Analysis of Static and Dynamic Pile-Soil-Jacket Behaviour

A thesis submitted in partial fulfillment of the
requirements for the degree of
Doktor Ingeniør
by

Mohammad Reza Emami Azadi

Trondheim, May 22, 1998

Department of Marine Structures
Faculty of Marine Technology
Norwegian Univeristy of Science and Technology

Abstract

This work deals with the non-linear interaction analysis of the jacket-pile-soil systems. A historic preview and the motivation for the study is described in introduction part(Ch.1).
To be able to study the non-linear response of the jacket systems under extreme loading conditions, initially the static behaviour of the pile-soil system is investigated in Chapter.2. In the initial part of this work, a review of the state of art pile-soil interaction models is performed. It is recognized that the most of the existing pile-soil models have been established based on large diameter pile tests on specific sites. The need for non-site specific and mechanistic pile-soil interaction models initiated the development of new (t-z) and (p-y) disk models.

Validation of the disk models is carried out by using the available database from recent large diameter pile tests in North-sea and Gulf of Mexico regions. The established static disk models are applied for non-linear static analysis of the jacket-pile-soil system under extreme wave loading.

Dynamic pile-soil interaction is studied in Chapter.4. Based on Wolf's initial pile-soil model a new disk-cone model is developed for the non-linear and non-homogeneous soils. The approach is based on strength of material and an indirect boundary element method. The differential equation of a single disk-cone system for non-linear and non-homogeneous soil is established. A semi-analytical solution of a single disk-cone system is obtained based on step-wise linearization of the established non-linear differential equation. Material and radiation damping are accounted for in the disk-cone model and the performance of the model is discussed.

The disk-cone model is applied in Chapter.4 for both surface and embedded disks in a soil layer with non-linear properties. The reflection and refraction mechanisms are discussed for various boundary conditions of the layer.

The system of multi-stack of disks-cones is used to discretize the pile-soil system. The solution of the discretized system is presented in both frequency and time domains. The idea of green friction is applied to establish the dynamic flexibility and hence stiffness matrix of the pile-soil system. The principle of superposition is used in frequency domain solution with and without considering the coupling effects between various disks. An incremental solution of the pile-soil

system is obtained in time domain by using Newmark's methods.

Equivalent simplified lumped models of pile-soil system such as SDOF,2DOF and 3DOF are also established for the aim of parametric studies in an efficient manner.

Validation of the dynamic stiffness functions computed according to disk-cone models is carried out by comparing the results with the more rigorous boundary element solutions and several verification cases of the pile-soil systems under dynamic loading are presented. The cases include vertical, horizontal and rocking motions of the pile-soil systems.

In Chapters.3 and 5, a new pushover analysis approach is presented based on wave height incrementation. Both the traditional load scaling and wave height incrementation methods are applied for the static as well as dynamic analyses of the jacket-pile-soil systems.

Simplified non-linear SDOF, 2DOF, 3DOF analysis methods as well as more complex MDOF analysis approach are employed in Chapter.5 to study the dynamic response of the jacket platform under extreme sea and seismic loading.

The ductility spectra analysis approach is introduced in Chapter.5 to facilitate the study of the dynamic performance of the jacket systems near collapse. Equivalent lumped models such as SDOF, 3DOF are applied and as a result simplified relationships are obtained for predicting the dynamic overload of the jacket-pile-soil system. The validation of the results of the SDOF based relationship is carried out against the results obtained from non-linear dynamic analysis of more complex MDOF systems.

Several case studies of SDOF, plane frames and MDOF jacket-pile-soil systems are performed in Chapter.5. The cases are examined to illustrate the effects of structural, foundation failure characteristics as well as dynamic loading effects on the overall performance of the jacket-pile-soil systems near ultimate collapse.

The influence of the pile-soil interaction modelling on the global behaviour of the jacket-pile-soil system near collapse are studied through considering various models of foundation such as linear spring to ground, non-linear plugged and un-plugged pile systems. The influence of the member fracture on the overall load carrying capacity of the system is also assessed by applying a simple CTOD criterion. The overall safety assessment of the jacket-pile-soil system is briefly described.

In Chapter.6, a reliability approach for the integrated analysis of the jacket-pile-soil system is applied. Modified versions of RELPS and GENSODM FORTRAN programs and NDDCAP MATLAB program are developed during the course of this work.

In the final chapter, concluding remarks and also recommendations for further investigations are given.

Dedication

"Dedicated to my parents"

Foreword

"Everything should be made as simple as possible, but not simpler"
Albert Einstein

Acknowledgment

This study has been carried out under supervision of Prof. Torgeir Moan from Dept. of Marine Structures of NTNU and Prof. Steinar Nordal from Dept. of Geotechnical Engineering of NTNU. Their Guidance and support during the course of this program is gratefully acknowledged.

Special thanks are given to Prof. Jørgen Amdahl from Dept. of Marine Structures of NTNU, Dr. Øyvind Hellan and Dr. Tore Holmaas from SINTEF Div. of Civil and Environmental Engineering, Dr. Ernst Eberg from Bygcon A.S and Dr. Geir Svanø at Div. of Geotechnical Engineering of SINTEF for their helpful discussions and valuable contributions to the work. The author expresses his gratitude to Prof. John Patrick Wolf of Swiss institute of Hydraulics and Dr.Friman Clausen from NGI for their helpful comments and discussions.

The author would like to express his gratitude towards the Dept. of Scholarship of Ministry of Culture and Higher Education of the Islamic Republic of Iran, Faculty of Marine Technology and Dept. of Marine Structures of Univ. of Science and Technology in Trondheim for their partial support during the period of this work.

The author also would like to thank his family for offering support during this work.

The author thanks the companies Norsk Hydro, NGI for allowing the use of their database during the course of this work.

Thanks are given to Mrs. Qi Ying Yang former Msc. graduate of Dept. of Marine Structures of NTNU for her contribution in preparing finite element and load models of several cases studied in this work under guidance of the author.

The author also thanks Mrs. Inger Rygh of SINTEF for redrawing some of the figures of this work.

Final thanks but not the least are given to Mrs. Sigrid Bakken Wold for her support during the course of this work.

Contents

List of Tables

List of Figures

Nomenclature

List of symbols

Roman symbols

a	Schmucker's ductility correlation factor
a_0	a normalized frequency parameter
a_{c0}	a damping function of HHT-method
a_{di}	dynamic attraction factor, design geometrical parameter
a_g	the ground acceleration
$a_{g,max}$	maximum ground acceleration
$a_{g,ref}$	reference ground acceleration
a_m	a material damping coefficient
a_n	the coefficients of base shear vs. wave height correlation with $n = 1, 2, 3, 4$
a_{m0}	a mass function of HHT-method
a_i	a transformation vector from element to assembled system
a_{ij}	the distance between source disk (i) and receiver disk (j)
a_k	the lateral earth pressure correlation factor
a_{k0}	a restoring force function of HHT-method
A	API's correlation factor for (p-y) soft clay mode
A_i	a transformation matrix from local to global(datum) coordinate system
A_l	cross-sectional area of cone on the incident wave side
A_r	cross-sectional area of cone on the refraction wave side
$A(z)$	cross-sectional area function of pile/cone etc.
b	Schmucker's ductility correlation factor(exponent)
c	the wave propagation velocity
c_h	wave propagation velocity in horizontal direction
c_b	the Bouc's hysteretic model parameter
c_l	the wave velocity on the incident wave side
c_n	Bouc'model parameters with $n = 1, 2$
c_p	the P-wave velocity
c_r	the wave velocity on the refraction wave side
c_R	the R-wave velocity

c_s	the S-wave velocity
c_v	wave propagation velocity in vertical direction
c_{tip}	a correlation factor for the pile tip resistance
$[C]$	the damping matrix
C_d	drag coefficient
C_M	coefficient of mass
C_n	empirical factors of API (p-y) model for sand with $n = 1, 2, 3$
C_p	damping coefficient of pile
C_{pf}	an augmented frictional damping coefficient of pile
C_{ps}	damping coefficient of pile-soil system
$C_{r,ps}$	a rotational dashpot coefficient of pile-soil system
$C_{r,sf}$	a rotational C_{sf}
C_{sf}	an augmented frictional damping coefficient of soil
C_{ve}	an augmented dashpot due to visco-elastic damping of soil
d	the pile penetration or soil layer depth(thickness)
dR	a difference(infinitesimal variation) of external force
d_i	the depth of soil layer (i)
D	the outer diameter of pile
$D(\zeta)$	outer diameter of pile as a function of normalized depth parameter
e	the embedment ratio of foundation
$exp(x)$	exponential function of x
E	the elastic(Young) modulus of material (steel, soil etc.)
$E(z)$	the elastic modulus of soil function with soil depth (z)
E_i	the initial elastic modulus of material
$E_{i,0}$	the initial elastic modulus of material at the reference depth
E^T	the tangent elastic modulus of material
f	the natural frequency of vibration
F_{100}	the 100-year environmental load
f_{di}	design value of material(strength) parameter
F_d	the damping force component
$F_{d,hys}$	the hysteretic damping force
$F_{d,max}$	the maximum damping force
F_D	the drag force component
F_e	the excitation force component
$F_{e,max}$	the maximum excitation(external) force
F_h	the hysteretic damping force
$F_{H1}(x)$	the annual probability of failure
F_i	the inertia force component
F_n	the non-linear restoring force
F_r	the restoring force component
$F_{r,max}$	the maximum restoring force component
$F_{r,res}$	the residual restoring force component
$F_{ref,max}$	the maximum reference (unscaled) load
F_{sea}	sea wave force

$f_{u,1}$	first order reliability function
$f_{u,2}$	second order reliability function
$F_{ult,st}$	the ultimate static force capacity of MDOF system
F_y	the first yield force
F_ν	the overload ratio
$g(x)$	the limit state function of a system
g_{bi}	a normalized ductility function for bi-linear SDOF system
g_i	the normalized initial shear modulus of soil
g_{ij}	the Green function of element (ij)
g'	the mirror image Green function
G	the shear modulus of soil
G_i	the initial shear modulus of soil
G_s	the secant shear modulus of soil
G_u	the Green function of a structural member
G^T	the tangent shear modulus of soil
G^t	the transpose of the Green function
$[G]$	the Green matrix or general dynamic flexibility matrix
$[G_{n-k}]$	the Green (flexibility) matrix at time step (n) for force at step (k)
h	height of the deck or a lumped mass from its base, height of a soil layer etc.
$h(t-\tau)$	unit impulse function at time (t) due to impulse at time τ
h_s	Svanø's CSM correlation factor
H	the wave height
H_1	the annual wave height
H^*_1	the most probable wave heights for 1-year
H_{100}	the 100-year wave height
H^*_{100}	the most probable wave height for 100-year
$H_{collapse}$	the collapse wave height
H_d	the deck height
H_{ps}	transfer function of pile-soil system
H_R	a hardening function
H_s	significant wave height
i	the square root of -1
I	the moment of inertia of pile
Im	the imaginary part of a variable
J_a	the depth coefficient of API soft clay model
k_a	the API's subgarde reaction modulus
k_{dpy}	API's (p-y) function
k_{dpz}	API's (t-z) and (q-z) function
k_{dy}	the dynamic spring parameter of soil
$k_{dy,h}$	the horizontal dynamic spring stiffness
$k_{dy,v}$	the vertical dynamic spring stiffness
$k_{dy,r}$	the rotational dynamic spring stiffness
k_e	the elastic stiffness
k_{eff}	the effective stiffness

k_{ep}	the elasto-plastic stiffness
k_i	the initial stiffness
k_{Re}	Reese's (p-y) stiffness parameter
k_r	the relative pile-soil stiffness
k_{sec}	the secant stiffness of a bi-linear SDOF system
k^T	tangent stiffness parameter of SDOF system
k'_p	the effective lateral earth pressure at rest
K	general system stiffness matrix
K_p	stiffness parameter of pile
K_{ps}	stifness of a SDOF pile-soil system
$K_{r,ps}$	rotational stiffness of pile-soil system
K_{st}	general static stiffness of cone-disk etc.
K^*	effective stiffness matrix
$K^T{}_i$	tangent stiffness at increment (i)
K_r	system stiffness matrix at step (r)
$[K_{dy}]$	the dynamic stiffness matrix
$[K_p]$	the pile stiffness matrix
$[K_{ps}]$	the pile-soil stiffness matrix
l_p	the pile length
L_{cr}	the critical length of pile
m	lumped mass of a SDOF system
m_{ij}	mass of element (ij)
M	bending moment
M_p	plastic bending moment
M_{pf}	an augmented mass of pile due to frictional damping
M_{ps}	mass of a SDOF pile-soil system
$M_{r,ps}$	a rotational mass of pile-soil system
M_s	lumped mass of soil
M_{sf}	an augmented mass of soil due to frictional damping
M_t	a trapped mass of soil
M_{ve}	an augmented mass of soil due to visco-elastic damping
M_x	bending moment about x-axis
M_y	bending moment about y-axis
M_z	bending moment about z-axis
$[M]$	a general mass matrix
$[M_{ps}]$	pile-soil mass matrix
n	the lateral earth pressure correlation factor (exponent term)
N	axial force, a general force function
$N(z)$	axial force function with depth (z)
$N(a_0)$	a normalized power (of transmitted energy) function
$N(\omega)$	general dynamic force(of uni-directional cone)
N_0	cyclic soil degradation reference number
N_{eq}	an equivalent number of cycles (load parcels)
N_m	cyclic soil degradation number

N_i	element interpolation function
N_l	the axial force of cone on the incident wave side
N_p	plastic axial force and the soil depth correlation factor of Janbu
N_q	API's pile tip resistance correlation factor
N_r	the axial force of cone on the refraction wave side
N_{ru}	an undrained shear strength factor
N_s	cyclic number related to shear stress degradation
p	the lateral soil pressure (load transfer)
p_i	the lateral soil pressure at τ_i
p_n	Reese's lateral soil resistance parameters with $n = 1, 2, 3, ...$
p_u or p_{peak}	the ultimate lateral soil pressure
p_{ud}	deep soil p_u
p_{us}	shallow soil p_u
$p^{'}$	the effective overburden pressure of soil
P_f	probability of failure
$P(\omega)$	general dynamic force
$P(g_a(x))$	an annual probability of failure function of a system
$P(R_a(x))$	an annual probability function of system strength
$P(S_a(x))$	an annual probability function of load
P_i	lateral force of a frictional damping element (i)
$P^k{}_{0,n}$	the kinematic component of pile-soil interaction force
$P^i{}_{0,n}$	the inertial component of pile-soil interaction force
q	a generalized displacement parameter or deviatoric stress component
q_{ps}	the pile tip resistance
q_{peak}	the ultimate pile tip resistance
q_u	the generalized coordinate system in u direction
q_v	the generalized coordinate system in v direction
q_w	the generalized coordinate system in w direction
$q^{'}$	the effective deviatoric stress component of soil
Q	shear force or a generalized force vector
Q_0	reference end bearing capacity of pile
Q_{di}	design load parameter
r	the radial distance from pile centre
r_0	the radius of a single (base) disk
r_i	the inner radius of pile/soil disk (i)
r_{id}	the outer radius of soil disk (i)
r_u	a resistance ratio associated with pore water pressure of soil
R	the vector of external forces
$R(x)$	strength function of a system
$R_a(x)$	the annual strength function
R_f	Kraft's stress-strain curve fitting factor
Re	the real part of a complex variable
s	the normalized shear stress parameter
s_N	Janbu's normalized resistance factor

$s_{p,ij}$	pile's equivalent dynamic stiffness parameter
S	general internal force vector
S_a	the annual load
$S(x)$	the load function of system
$S(\omega)$	a general dynamic stiffness function of cone-disk etc.
$S_0(x)$	reference value of S(x) function
S_i	the vector of internal forces of element (i)
S_{is}	the internal area of shaft
S_{plug}	the tip plug area
S_u	the undrained shear strength of soil
S_{ua}	the average undrained shear strength of soil
$[S_{dy}]$	general dynamic stiffness matrix
$[S_p]$	the dynamic stiffness matrix of pile
$[S_{ps}]$	the dynamic stiffness matrix of pile-soil system
$[S_{qs}]$	the quasi-static stiffness matrix of pile-soil system
t	time variable or the axial load transfer of pile-soil system
t_{min}	minimum required time step size
t_{is}	internal shaft friction skin
t_{peak}	the peak value of t_{ps}
$t^{pl}{}_{peak}$	the peak shaft skin friction with initial stress
t_{res}	the residual shaft skin friction
$t^{pl}{}_{res}$	the residual shaft skin friction with initial stress
T	the period of a wave or total shaft friction skin
T_0	reference shaft skin friction capacity of pile
T_d	the crest duration of the wave
T_{eff}	effective natural period of system
T_n	the natural period of a system
T_r	the r-year return period
T_{ref}	a reference period
T_s	the significant wave period
T_w	one cycle period of wave
T_z	zero mean-crossing wave period
$T^{-1}(u)$	tangent hyper-plane function in U-space
u	a nodal displacement or coordinate parameter
u_0	a reference(initial) displacement
$u_{,x}$	first derivative of u w.r.t x
$u_{,x...x}$	nth derivative of u w.r.t. x
u_{cu}	cyclic excess pore water pressure
$u_{dy;max}$	maximum dynamic displacement
u_e	elastic displacement component
u_{ep}	elasto-plastic displacement component
u_{fy}	first yield displacement
$u_{g,0}$	a reference ground displacement function
$u_{g,i}$	the harmonic component (i) of ground displacement function

u_{max}	the maximum sustainable global displacement
$u_{qs,max}$	the maximum quasi-static displacement of system
$u_{st,max}$	maximum static displacement
u_y	the first yield displacement of SDOF system
$\dot{u}$	velocity component
$\ddot{u}$	acceleration component
$\dddot{u}$	the third derivative of system
u^*	value of u at the design point
u^f	free-field displacement(motion) of soil
$u^p{}_{n+1}$	predictive displacement at incremental step (n+1)
$\bar{u}_n$	a memory displacement function at time step (n)
$\tilde{u}$	a predicted value of u
$\tilde{u}_{0,n}$	a predicted value of $u_{0,n}$
U	strain energy
v	a nodal displacement parameter
v_i	volume of element (i)
v_0	ground soil rotational displacement
v_e	an elastic displacement component
v_p	a plastic displacement component
V	the total volume of element
V_i	the coefficient of variation
w	a nodal displacement parameter
W_{hinge}	plastic hinge work
$W_{threshold}$	threshold plastic work
x_0	a reference parameter
x_i	a random parameter
x_p	a random pile parameter
x_{psi}	a random pile-soil interaction modelling parameter
x_s	a random soil parameter
x_{ss}	a random sea state parameter
x_{wlm}	a random wave load modelling parameter
X	a random vector
y	a coordinate parameter
y_{50}	the lateral displacement at $0.5p_u$
y_{ps}	the lateral pile-soil displacement
y_c	the pile-soil displacement at p_u
z	a vertical distance parameter
z_0	apex height of a single cone
z_b	Bouc model's parameter
z_c	the axial pile-soil displacement at t_{peak}
z_h	isotropic hardening (extension) parameter
z_i	cone's apex height parameter
z_l	cone's apex height on the incident wave side
z_{ps}	the axial displacement of pile-soil

z_r	cone's apex height on the refraction wave side
z_{rb}	the re-bound displacement of pile
z_{slipp}	the slippage displacement of pile
Z	the global soil depth parameter
Z_p	the plastic section modulus

Greek symbols

α	the material parameter of pile-soil, the Hilber-HHT integration parameter
α_{eff}	the effective stiffness factor
α_i	the root-square of importance factor for random variable x_i
α_{mf}	magnification factor of generalized Masing's rule
α_n	polynomial coefficients of disk or Bouc's model coefficients with $n = 1, 2, ...$
α_{res}	the residual strength parameter
α^*	α_i at the design point
β	kinematic hardening (shift) parameter, Bouc's model coefficient, Newmark's param , pile-soil material parameter, residual strength (ductility) parameter, reliability inc
β_{av}	the average value of β
β_m	the target reliability index
β_n	polynomial coefficients of disk (t-z), (p-y) curves with $n = 1, 2, ...$
β_u	the
β^*	the reliability index at design point
γ	shear strain, Newmark's integration parameter, unit weight of soil
γ_m	the safety factor of material parameters
γ_Q	the safety factor of load parameters
γ_θ	the circumferencial strain of soil
γ'	the effective unit weight of soil
$\gamma^*{}_R$	global safety factor of R^*
$\gamma^*{}_S$	global safety factor of S^*
Γ	the general yield surface function
Γ_b	bounding surface function
Γ_i	the yield surface function of element (i)
Γ_{ps}	the yield function of pile-soil interaction element
δ	a small increment of a quantity, pile-soil interface angle
$\delta(Z)$	axial deflection function of pile with depth (Z)
δ_c	consolidation displacement of pile
δ_{rb}	rebounding displacement of pile
δ_z	the differential displacement of pile
δ'	Dirac function of first type
δ''	Dirac function of second type
δ'	the effective pile-soil interface angle
$\delta r_{i,j}$	an iterative small variation of nodal displacement at incremental step (i) and iterat
$\delta R_{i,j}$	an iterative small variation of external force at incremental step (i) and iteration (j

Δ	an finite increment of a scalar, vector or matrix
$\Delta^i{}_{n+1}$	iterative quantity at increment step (n+1) and iteration (i)
$\Delta F^*{}_e$	effective external excitation force
ΔF_y	the reserve strength of a SDOF system
Δr_i	a nodal displacement increment at step (i)
ΔR_i	an external force increment at step (i)
$\Delta u_{1,g}$	a limit displacement at increment (1)
$\Delta u_{i,g}$	a limit displacement at increment (i)
$\Delta\sigma_d$	the deviatoric stress variation during cyclic loading of soil
ϵ	a general strain component
$\epsilon(\omega)$	a dynamic strain component
ϵ_1	the major principle strain component
ϵ_2	the intermediate principle strain component
ϵ_3	the minor principle strain component
ϵ_{50}	the strain at 50% of the major deviatoric stress component
ϵ_l	strain due to incident wave at soil layer boundary
ϵ_q	the deviatoric strain component
ϵ_r	the radial strain component, strain due to refraction from soil layer boundary
ϵ_u	the ultimate strain level
ϵ_θ	the circumferencial strain component
ζ	a normalized depth parameter
ζ_{if}	a pile-soil interface gap parameter
η	the soil disk radius parameter
η_{2d}	2D- radiation damping ratio
η_{3d}	3D- radiation damping ratio
η_j	the refraction factor of a soil layer
η_m	material damping ratio
η_r	radiation damping ratio
θ	the apex angle of cone
λ	a scalar variable
λ_i	cosine direction vector of element (i)
λ_R	Rayleigh wave length
λ_s	Svanø's CSM correlation factor
$\lambda^t{}_i$	transpose of the cosine direction of element (i)
μ	a ductility ratio
μ_{app}	an apparent ductility ratio
μ_{eff}	the effective ductility ratio
μ_{max}	maximum ductility ratio
μ_{x_i}	mean value of random parameters x_i
ν	the poisson ratio
ρ	density of a material
ρ_l	the density of the soil layer above (on incident wave side)
ρ_r	the density of the soil layer below (on refraction wave side)
σ	general stress component or vector

σ_1	the major principle stress component
σ_2	the intermediate principle stress component
σ_3	the minor principle stress component
σ_l	the stress induced by the incident wave
σ_r	the stress induced by refracted wave
σ_u	the ultimate stress
σ_y	the yield stress
σ'_a	the average effective stress component
σ'_c	the consolidated effective stress component
σ'_d	the deviatoric effective stress component
σ'_h	horizontal effective stress component
σ'_m	the mean effective stress component
σ'_v	vertical effective stress component
τ	general shear stress component
τ_i	the shear stress at the pile-soil interface
τ_{ps}	the peak shear stress at the pile-soil interface
ϕ	the internal friction angle of soil, a general shape function
ϕ_u	shape function of a beam element
ϕ_v	shape function of a beam element
ϕ_w	shape function of a beam element
Φ	the potential function of system
χ_a	soft clay correlation factor of API with depth
ψ_a	API's undrained shear strength correlation factor
ψ_k	Kraft's skin friction correlation factor
$\psi_r(r)$	shear strain distribution function over the radius of soil disk
Ψ	general stress-strain matrix
ω	the circular frequency of vibration
ω_n	the natural circular frequency of vibration

Operators

δ	an increment of a variable
Δ	an increment of a vector or matrix
λ	a scalar
∇	Laplasian (differential) of a function
∂	partial derivative
Σ	sum of quantities
$\int$	integration symbol
bar	a memory indicator
.	internal multiplication of vectors
*	external multiplication of vectors
/	external division of vectors
.*	element-by-element multiplication of vectors or matrices

$./$	element-by-element division of vectors or matrices
A^t	transpose of matrix A
Re	the real part a complex variable(vector or matrix)
Im	the imaginary part of a complex variable(vector or matrix)
$\frac{d}{dx}$	first derivative of a function w.r.t its variable for e.g. x
d^n/dx^n	nth derivative of a function w.r.t its variable for e.g. x
$inv(A)$	inverse of matrix A
log	logarithmic sign
ln	natural logarithmic sign
sgn	signum function
sin	trigonometric sinusoidal sign
cos	trigonometric cosine sign
tan	trigonometric tangent sign
$tanh$	tangent hyperbolic sign
tan^{-1}	arctangent sign
B_p	Bessel function
Y_n	Newman's function

Abbreviations:

BS	base shear function
COV	coefficient of variation
$CTOD$	crack tip opening displacement
DAF	dynamic amplification factor
DEP	degrading elasto-plastic system
DEQ	differential equation
EI	elastic(flexural) rigidity
EP	elasto-plastic system
EPP	elastic-perfectly-plastic system
$FORM$	first order reliability method
$GYEP$	gradually degrading elasto-plastic system
$LDEQ$	linear differential equation
$MDOF$	multi-degree-of-freedom system
NC	normally consolidated soil
ND	non-degrading system
$NDEQ$	non-linear differential equation
NPD	Norwegian petroleum directorate
OC	over-consolidated soil
PFS	plane frame system
PI	plasticity index of soil
RDU	ultimate dynamic resistance
RFY	first member failure(global yield) resistance
RNP	resistance of non-plugged system
RQS	quasi-static resistance

RRES	residual resistance
RSU	ultimate static resistance
SCF	scaling factor of load, acceleration etc. (ref to WLI approach)
SMDU	safety margin associated with the ultimate dynamic capacity of MDOF system
SORM	second order reliability method
SMQS	safety margin associated with quasi-static resistance of MDOF system
SQS	square sinusoidal shape wave
STI	triangular shape impulse or wave
SWL	still water level
WHI	wave height incrementation method
WLI	wave load incrementation method

CHAPTER 1

INTRODUCTION

1.1 Historical preview

The design of jacket type offshore platforms has been until recently done by the linear elastic design methods based on component strength such as first yield or low cycle fatigue of the structural element. The recent advent of computer technology made it possible to utilize new methods such as non-linear finite element and establish new methodologies for the design and the analysis of the jacket structures based on system's (overall) resistance rather than component strength .

To this aim, new structural models such as phenomenological model, general non-linear finite element and plastic hinge beam models were developed in the past years. These models have been implemented into the recent finite element codes such as USFOS (Søreide et al, 1994).

In this connection, new non-linear analysis methods such as pushover approach are developed in the recent years by Stewart et al, (1988,1993,1995), Hellan et al, (1991, 1995) Bea et al, (1993, 1995) and applied extensively (mainly) for static analyses of the Jacket systems. The advantages of such pioneering methods are now recognized in the offshore industry and to a large extent recent codes have authorized their use as the state of practice tools for the jacket system design.

However, recent events such as extreme storms(Hurricanes), severe earthquakes and subsidence of the jacket foundations highlighted the needs of offshore industry for the new models and methods to take into account the jacket- pile-soil foundation interaction as well as the non-linear dynamic performance/loading effects.

In the recent five years, several initial studies were carried out for this purpose such as works by Bea et al, (1993), Stewart et al, (1993 and 1995), Schmucker et al, (1994 and 1996), Emami et al, (1995, 1996 and 1998) and Moan et al, (1997). The focus of the current investigation is towards meeting some of these new challenges facing the offshore industry.

1.2 General(Background)

The dynamic pile-soil-jacket interaction has been the focus of recent studies and developments in the field of fixed trussed frame (jacket type) offshore platforms. In particular, the dynamic performance of the pile-soil-jacket systems under extreme environmental loading such as sea waves, currents and earthquakes is of great interest for re-assessment and limit state of collapse(integrity) studies of such structures.

Within this context, the issues such as different behavior of various jacket platforms in the same region exposed to an extreme storm (or hurricane) or a severe earthquake loading, response of a particular platform exposed to different loading time histories but with the same intensity, and the significance of the pile-soil interaction on the overall behavior of the platform, may be discussed.

A number of SDOF and MDOF studies on the dynamic performance of jacket platforms have been conducted in the recent years to address the aforementioned issues. Some of these investigations have neglected the nonlinear pile-soil-structure interaction. Some of the most recent MDOF studies have considered a nonlinear model for soil by adopting a Winkler type spring model. The need to verify such existing nonlinear pile-soil models, so-called t-z and p-y models, is great due to the uncertainties involved in their developments. The uncertainties may be related to the empirical development of such models. Majority of these pile-soil interaction models have been established on a specific onshore site with the soil and the pile characteristics. Wider application of the t-z and p-y models in the recent offshore pile-soil design requires more studies to be conducted on the topics of static, cyclic and dynamic pile-soil interactions.

The ductility analysis of the complex MDOF system may provide a valuable re-assessment of an existing jacket platform or offer accurate results for the design purposes, but they are much more costly than those of equivalent simplified systems such as (SDOF, 2DOF and 3DOF). On the other hand, simplified models are more efficient for use in spectral analysis and would also offer a valuable insight into the global behavior of the pile-soil-jacket system.

1.3 Motivations for the work

The motivations for the initiation of the present work may be stated as the current needs of the offshore industry for:

. re-assessment of the existing jacket platforms facing extreme loading such as hurricanes or winter storms, subsidence of the foundation of the jacket platforms in areas such as North-sea or Gulf of Mexico.

. new jacket platform's design for the use in the next decades

. moving towards an integrated jacket-pile-soil system analysis approach

. considering the combined structural and dynamic loading effects hence moving ultimately towards an integrated dynamic pushover analysis approach

. simple models for screening the jacket platforms before opting for more costly non-linear dynamic pushover analysis approach

1.4 Scope of the study

The scope of this work is to establish :

. an in-depth knowledge about the static and dynamic pile-soil interaction behaviour

. the methodology for the non-linear static and the dynamic integrated analyses of the jacket-pile-soil systems near the ultimate collapse(ULS check)

For this aim, the following items are considered:

. extensive literature study of state of practice and art pile-soil models

. establishment of static and dynamic disk/cone-disk pile-soil models based on soil-structure mechanics theory

. validation of the static disk and dynamic disk-cone models against large diameter pile test results as well as refined numerical methods

. establishment of a new pushover static/dynamic approach based on wave height incrementation

. introduction of a ductility spectra analysis approach to quantify the structure/foundation characteristic as well as dynamic loading effects on the global behaviour of the jacket-pile-soil systems near ultimate collapse

1.5 The organization of the work

The thesis has been organized as follows:

In Chapter 1 a preview and introduction of the thesis work is given.

In Chapter 2, a review and performance study of several widely used existing pile-soil interaction models is presented. In Chapter 2, two new t-z and p-y models are presented and validated

against the available data from the recent large diameter pile tests. Five case studies are included at the end of this Chapter.

In Chapter 3, two different methods for (integrated) static pushover static analysis of jacket-pile-soil systems are described and the results of three case studies are presented.

In Chapter 4, the dynamic pile-soil interaction is discussed and a dynamic model based on disk-cone idealization of the pile-soil system is presented.

In Chapter 5, the ductility demand analysis approach is described for simplified models as well as more complex MDOF systems and the results of the several case studies are discussed.

In Chapter 6, a reliability study of a pile-soil-jacket system is presented.

Finally Chapter 7, summarizes the main findings of this study and the recommendations for further investigations.

CHAPTER 2

STATIC PILE-SOIL INTERACTION

2.1 Introduction

This chapter deals with the static pile-soil interaction problem. The term pile-soil modelling is used throughout this study to refer to the idealization of the interaction between the pile and the surrounding soil in a force-deformation(or stress-strain) sense. The pile-soil interaction behaviour is often described by the load transfer- displacement curves, known as (t-z) and (p-y) curves, respectively, for axial and lateral loading.

The current practice (t-z) and (p-y) models have been developed based on either the pile test results or theoretically by Winkler spring idealization of the pile-soil system. The empirical models such as those recommended by API RP2A 1993, Reese's (p-y) model, Dunnavant et al (p-y) model have been established based on a limited number of large diameter pile tests mostly carried out on onshore sites. The reason for such limited database is the enormous costs of conducting large diameter pile tests. Alternative cost effective solutions such as triaxial tests or model (centrifuge) tests have proven to be far less reliable. A third solution is sought during the present work, which is based on a simplified theoretical approach validated against a number of large diameter pile test results.

Extensive studies in the past two decades have been conducted to establish the existing databases of API and NGI such as works by Barton et al, (1983), Bea et al, (1984) and (1986), Bond, (1992), Broms ,(1964), Clarke et al, (1992), Chow, (1996), Cox et al, (1974), Dunnavant et al, (1989), Fugro-McClelland, (1989), Gazioglu and O'Neill, (1984), Hamilton and Murff, (1988), Hamilton and Dunnavant, (1992), Janbu et al,(1976, 1985), Jardine and Lehane, (1994), Karlsrud et al, (1992), Kraft et al, (1981), Madshus,(1997), Matlock, (1970), Lacasse and Nadim, (1992), Langen,(1991), Langø,(1991), Nadim and Dahlberg, (1996), Nogami and Novak, (1977), Nordal et al, (1985), Poulos and Davis, (1980), Randolf, (1983) and (1992), Reese et al, (1974,1975), Svanøet al, (1992,1993), Sullivan et al, (1980) and Vijayvergiya, (1977) etc.

In the recent years several large diameter pile tests have been carried out worldwide such as those by BP and NGI (Clarke et al, 1992) at Pentre and Tilbrook sites in UK and by the University of Houston (Dunnavant et al, 1992) at Houston site in USA, respectively. These recent LDPT tests have provided extensive data on the static pile-soil behaviour during axial and lateral loading. The selection of these tests were based on the evaluation of the soil conditions at each site which appear to be representative of the offshore soils particularly encountered in the North sea.

The new (t-z) and (p-y) models presented in this Chapter are developed based on an uncoupled finite disk idealization of the pile-soil system. The establishment of these models are based on the initial works by Grande and Nordal, (1979), Svanø et al, (1993), for drained and undrained type soils, respectively. The basic idea is to model the pile-soil interaction in each direction with a multi-stack of disks (uncoupled finite disks). Each soil disk in the stack carries the pile loading into the surrounding soil.

Also in this Chapter the presented disk models will be validated against the recent large diameter pile test cases. A verification study of several pile- soil models discussed in this Chapter will be presented at the end of the Chapter.

2.2 Axial pile-soil interaction models

The piles are primarily subjected to the axial loading due to their own weight and other gravity loads transferred from the superstructure(jacket) which they support. In addition of the gravity loads the pile foundation is supposed to carry the axial loads induced by the environmental loading such as waves, currents and earthquakes on the superstructure.

The axial loads on the piles are resisted by the pile-soil reaction which is characterized by the pile-soil axial interaction(t-z) curves. The pile-soil axial resistance either is provided by the skin friction resistance of the pile shaft or the pile tip resistance or both. In the case of floating piles only the shear resistance at the pile-soil interface contributes to the pile's axial resistance, while for the end bearing piles a significant portion of the axial loads may be carried through the pile tip. The shaft (interface)resistance of the piles are the main focus of discussion throughout this Chapter , however (the current practice) tip resistance model for the end bearing piles will be briefly described.

2.2.1 API's axial modelling of pile-soil

The empirical(t-z) models such as those recommended by API 93 have been established based on a very limited number of large diameter pile test results. By measuring the settlement (or axial displacement) of the pile at several points along its shaft and at its head, an axial displacement function (δ) may be obtained which varies with the soil depth (Z). The static equilibrium of a slice of pile with thickness dZ and outer diameter D(Z) shown in Fig.2.1 can be written as

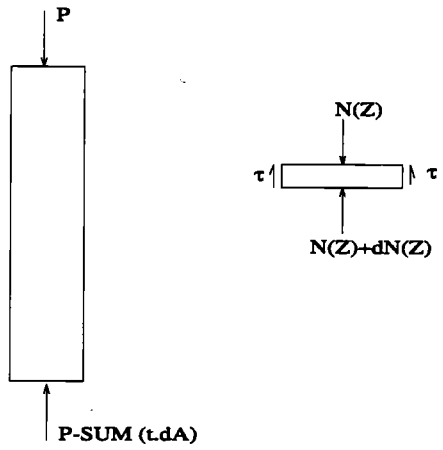

Figure 2.1: A schematic illustration of an axially loaded pile-soil system

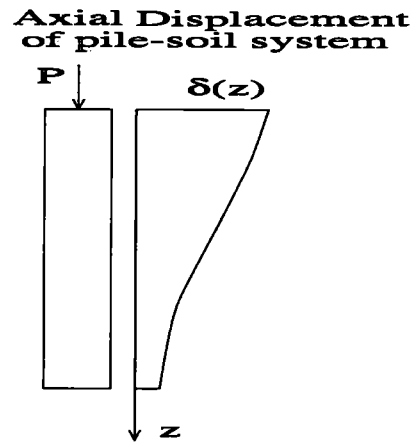

Figure 2.2: A fitted axial deflection curve $\delta(Z)$

follows:

$$t(Z).\pi D(Z).d(Z) + N(Z) + dN(Z) - N(Z) = 0 \tag{2.1}$$

thus:

$$t(Z) = -\frac{1}{\pi D(Z)}.\frac{dN(Z)}{dZ} \tag{2.2}$$

where $t(Z)$ is the mobilized shaft friction function on the unit area of pile's surface, Z is the vertical distance of the pile-soil element from the pile head and N(Z) is the axial force at the point Z.

If the deformation of the pile-soil during the axial loading is measured at several stations along the pile shaft, then an approximate deformation function $\delta(Z)$ may be fitted to the measured data points as illustrated on Fig.2.2.

The axial force at any point along the pile shaft may be obtained from simple continuum mechanics theory for small strains as:

$$N(Z) = EA\epsilon(Z) = -EA\frac{d\delta}{dZ} \tag{2.3}$$

By substituting Eq.2.3 into Eq.2.2 , t(Z) may be obtained as a function of N :

$$t(Z) = -\frac{1}{\pi D(Z)}\frac{d}{dZ}(-EA\frac{d\delta(Z)}{dZ}) = \frac{EA}{\pi D(Z)}\frac{d^2\delta(Z)}{dZ^2} \tag{2.4}$$

If $\delta(Z)$ function is already assumed or found numerically from the test data, then t(Z) will be known as a function of depth (Z) from Eq.2.4 for a number of axial load increments $\Delta N_i(Z)$ ($i = 1, 2, ..., n$ and n the total number of load increments), then a (t-z) curve can be easily obtained for each depth (Z).

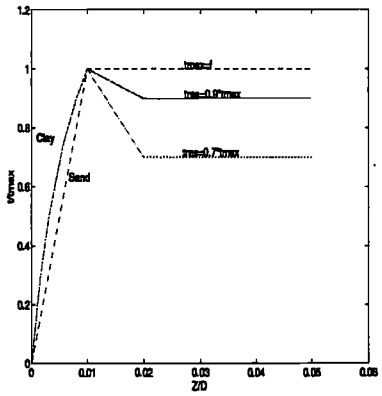

Figure 2.3: API RP2A 1993 (t-z) curves for clay and sand

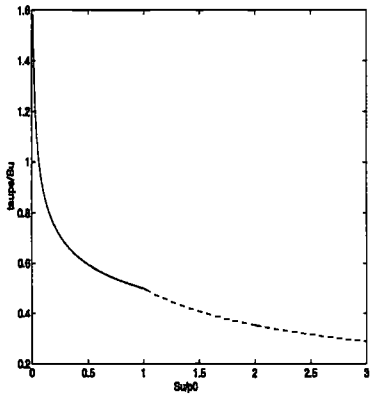

Figure 2.4: t_{peak} vs. S_u relationship according to API RP2A 1993

The basic empirical method described above may be modified to accommodate, large shear strains by considering the second order strain components in Eq.2.3. The empirical (t-z) relationship for cohesive soils according to API RP2A 1993 is shown in Fig.2.4 in which the peak skin friction t_{peak} has been correlated with respect to the shear strength S_u and the effective overburden pressure of soil p'_0 as follows:

$$\begin{aligned} t_{peak} &= 0.5 S_u \psi^{-0.5} \quad ; \psi \leq 1.0 \\ t_{peak} &= 0.5 S_u \psi^{-0.25} \quad ; \psi \geq 1.0 \end{aligned} \tag{2.5}$$

where $\psi = S_u/p'_0$, S_u is the undrained shear strength of soil, and p'_0 is the effective overburden pressure of soil.

The axial load transfer-pile displacement (t-z) relationships for clay and sand are shown in Fig.2.3. It is seen in Fig.2.3, (t-z) curves recommended by API RP2A 93 for clay have a post-peak softening part with the residual skin friction value range between 0.7 and 0.9 which may be determined as a function of stress-strain behaviour, stress history, pile installation method, pile loading sequence and other relevant factors.

The residual pile-soil resistance ratio t_{res}/t_{peak} could be found from direct shear tests or large scale pile tests. It is verified in Sec.2.5 that this ratio may vary from about 1.0 near the soil surface to nearly 0.7 close to the pile tip which agrees with the API recommendations.

2.2.2 Kraft's theoretical (t-z) model

This subsection briefly describes the theoretical (t-z) model proposed by Kraft et al,(1981) , which has been widely used in the offshore industry for the axial pile-soil interaction analysis.

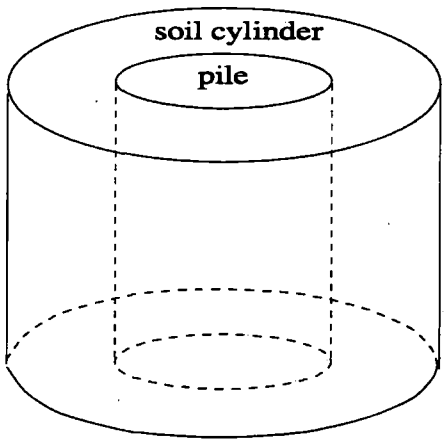

Figure 2.5: Idealization of pile-soil with concentric cylinders after Kraft et al, 1981

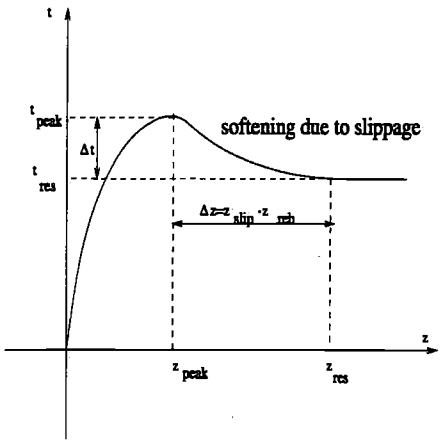

Figure 2.6: An idealized post-peak (t-z) relationship and Illustration of the slippage displacement (after Kraft et al, 1981)

Kraft's (t-z) model has been recommended by the practice codes such as API RP2A 1993 practice code and widely used in the past 15 years in the design of jacket foundations.

Kraft's (t-z) model has been developed in two separate stages, namely pre-peak and post-peak. Pre-peak portion of Kraft's model has been constructed based on the elasticity theory by using a concentric cylinder idealization of the pile-soil system. This approach assumes the pile-soil axial displacement as an equivalent to the deformation of concentric cylinders under shearing from the central shaft, as illustrated in Fig.2.5 (For details of derivation confer Kraft et al, 1981).
The load transfer-displacement relationship of concentric soil cylinder can be obtained according to the continuum mechanics theory as follows:

$$z = tr_i \int_{r_i}^{r_l} \frac{dr}{Gr} \tag{2.6}$$

where r_i = pile radius, r_l =the radial distance beyond which shear stresses are negligible (i.e. the radius of the outer cylinder) and G = the shear modulus of the soil which is assumed to vary nonlinearly as a function of the radial distance r and the shear strain or displacement z.

Kraft et al, (1981) has integrated Eq.2.6 by assuming a nonlinear G function based on soil's shear stress-strain behaviour as follows:

$$z = \frac{tr_i}{G_i} \ln\left(\frac{r_l/r_i - \psi_k}{1 - \psi_k}\right) \tag{2.7}$$

where G_i =the initial shear modulus of soil, $\psi_k = R_f/t_{peak}$ and R_f = a stress-strain curve fitting factor (a soil material parameter) and the other parameters are as defined above.

The response of the pile-soil system after reaching the peak friction capacity at the interface can not be simulated only by considering the shear stress-strain behaviour as described above, because of the slippage occurring at or near the pile-soil interface.

The slippage is often associated with large shear deformations at the pile-soil interface which may be simulated through direct shear or ring shear test techniques. The additional deformations may be added due to rotation of the principal stress axes after the failure. The whole phenomenon may be modelled by a post-peak strain softening part.

From direct shear tests on various soils, the slip displacement has been found(Kraft et al, 1981) to be between 0.9mm and 1.3mm beyond the displacement at the peak shear stress point. The direct shear test data indicated that t_{res}/t_{peak} ratio may be in the range of 0.8-1.0 for sand specimens and between 0.6-1.0 for clay samples.

This approach may not be a perfect way to simulate post-peak behaviour of the pile-soil system due to assumptions such as constant total normal stresses during the direct shear tests, non-homogeneities in the soil layer, the geometrical and dimensional effects etc. Therefore, the empirically simulated post-peak response may be modified by subtracting the rebound displacement at the pile-soil interface during shear stress drop from t_{peak} to t_{res}, from that of the deformation caused by the slippage as follows:

$$\delta z = z_{slip} - \frac{r_i t_{peak}}{G_i} \ln[\frac{(r_l/r_i - R_f)(1 - \alpha_{res} R_f)^{\alpha_{res}}}{(1 - R_f)(r_l/r_i - \alpha_{res} R_f)^{\alpha_{res}}}] \tag{2.8}$$

in which δz denotes the difference between the slippage and re-bounding displacements. α_{res} denotes the residual stress ratio which is defined as:

$$\alpha_{res} = \frac{t_{res}}{t_{peak}} \tag{2.9}$$

The limit of the above expression may be obtained as $z = z_{slip}$ (i.e. $\delta z_{rb} = 0$) when α_{res} and R_f are assumed to be equal to unity. The physical meaning of this limit is that for the deepest soil near the pile tip the axial rebound displacement after failure may be neglected which seems to be quite rational w.r.t very small displacements often occurring near the pile tip. It is assumed that the pile base is supported in a firm layer and hence the possibility of a punch through is not considered here.

Fig.2.6 shows the characteristic shape of Kraft's (t-z) curve. A quite significant post-peak softening can be seen in the post-peak region which is due to the combination of slippage and shearing as discussed above.

2.2.3 Disk modelling of the axial pile-soil interaction

The idea of finite disk or strip idealization of soil medium around the pile has been introduced in the recent years by Authors such as Grande and Nordal, (1979), Nogami and Konagai, (1988),

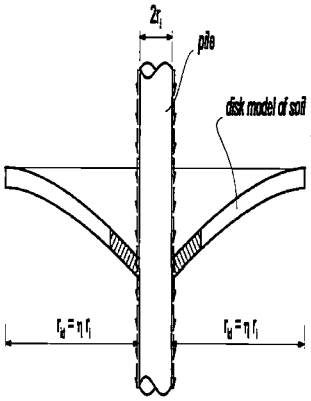

Figure 2.7: Disk idealization of pile-soil system under axial loading

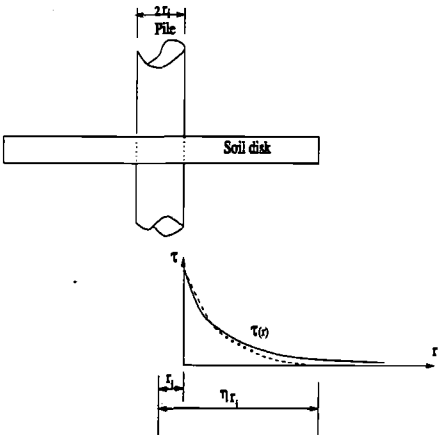

Figure 2.8: The stress and strain distribution over the soil disk around the pile

Wolf and Meek, (1992) and Svanø et al, (1993). The concept is based on idealization of the pile-soil interaction as finite uncoupled circular disks as illustrated in Fig.2.7. Various forms of soil disks have been used so far such as rigid, elastic deformable and hyper elastic deformable and elasto-plastic disks.

In this section a new (t-z) model is introduced which is developed based on the idealization of the pile-soil system by a set of uncoupled imaginary finite disks. Each disk as shown in Fig.2.7 represents the axial interaction between the pile and the soil.

The new model is an extended version of Grande and Nordal, (1979) and Svanø's initial disk models. The differences are in terms of stress distribution for a soil disk based on energy radiation theory in soil which is described in Chapter.4, the tangent stiffness formulation instead of secant stiffness as applied in the previous model and also analytical solution obtained by the author for the particular cases(see appendix.A). The maximum mobilized shear stress at the pile-soil interface is determined based on Mohr-Coulomb theory. The approach is rather simple and different from previous model. The axial force in the pile is carried and distributed through these imaginary disks to the ground. The induced shear stresses may be assumed to vary exponentially towards zero at the edges of each disk. Plane strain conditions are assumed over each pile-soil disk (i.e. strain components do not vary along the pile (shaft) axis).

The soil condition is assumed to be undrained(clay) under short term loading hence its volume could be considered constant after undergoing shear deformations. The radius of each finite disk r_{id} is assumed to be η times the radius of the pile r. Where η factor may be chosen in the range of 10-20 to be sufficient for approximation of the shear strain distribution in the soil.

From simple continuum mechanics, the shear strain of the pile-soil γ may be calculated as follows:

$$\gamma = \int_{\tau_0}^{\tau} \frac{d\tau}{G^T} \tag{2.10}$$

where τ is the shear stress around the pile and G^T is the tangent shear modulus of the soil which may be calculated from the following empirical relationship obtained by Langø, (1990) and Svanø et al, (1993) through a series of triaxial tests on clay:

$$G^T = G_i(1 - \alpha s)^{\beta} \tag{2.11}$$

where G_i is the initial shear modulus of clay, α and β are material parameters found by Svanø et al, (1993) for different soil type. The practical range of β is between 1 and 4. Equivalent values of α and β are derived for sand type soil according to soil data(Daghigh, 1993) given in appendix.A. s is the normalized shear stress factor defined as:

$$s = \frac{\tau}{\tau_{ps}} \tag{2.12}$$

where τ_{ps} is the shear stress at failure and the variation of the shear stress around the pile may be assumed as follows:

$$\tau = \tau_i \exp^{(\frac{r_i - r}{2r_i})} \tag{2.13}$$

where τ_i is the shear stress at the interface, r_i is the radius of the pile or the radial distance of the interface section from the pile center and so r is the corresponding radial distance at any point around the pile (see Fig.2.8).

The radius of the soil disk r_{id} around the pile is η times the radius of the pile r_i. From Eq.2.13, the shear stress τ value approaches zero at the edges of the assumed pile-soil disk. As illustrated on Fig.2.7, the axial loading on the pile is resisted through the shear stresses at the pile-soil interface which cause distortion of the soil disk around the pile. Hence, the axial displacement at the pile-soil interface may be obtained by integrating the shear strain γ over the radius of the disk. By inserting $\tau(r)$ from Eq.2.13 into Eq.2.10 and after integrating, the following expression may be obtained:

$$\gamma = \frac{\tau_{ps}}{G_i\alpha(1-\beta)}[1 - (1 - \alpha\frac{\tau_i}{\tau_{ps}}\exp^{(\frac{r_i - r}{2r_i})^{1-\beta}}]dr \tag{2.14}$$

and so the axial pile-soil displacement may be obtained as :

$$z = \int_{r_i}^{r_{id}} \gamma(r)dr = \frac{\tau_{ps}}{G_i\alpha(1-\beta)} \int_{r_i}^{r_{id}} [1 - (1 - \alpha\frac{\tau_i}{\tau_{ps}}\exp^{(\frac{r_i - r}{2r_i})})^{1-\beta}]dr \tag{2.15}$$

The integration of Eq.2.15 may then be performed either numerically or analytically. The analytical solution may only be achieved for the integer values of soil parameter β while the numerical solution may be preferred to find answer for any possible real value of β. For $\beta \leq 2.5$, the following tangent hyperbolic (t-z) relationship is fitted to the result of the numerical integration of Eq.2.15 which is plotted on Fig.2.9:

$$t = \frac{t_{peak}}{0.5\alpha(\beta+1)} tanh(\frac{\alpha G_i z}{0.9\beta D t_{peak}}) \qquad ;\beta \leq 2.5 \tag{2.16}$$

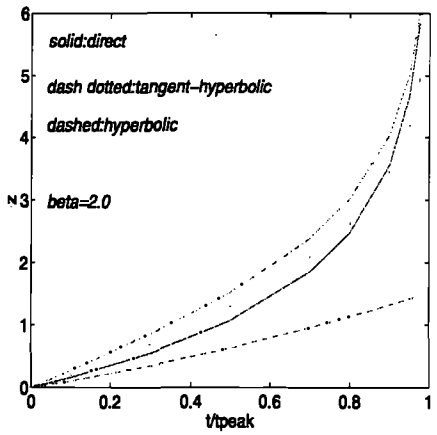

Figure 2.9: Numerical integration result vs. the fitted (t-z) function($\beta < 2.5$)

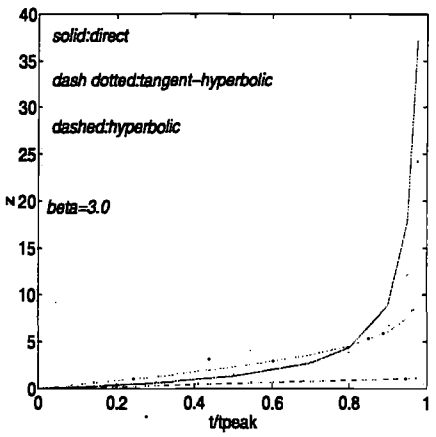

Figure 2.10: Numerical integration result vs. the fitted (t-z) function($\beta > 2.5$)

For $\beta \geq 2.5$, the following (t-z) function would provide the best correlation with respect to the numerical integration data, as shown on Fig.2.10:

$$z = \frac{t}{G_i} D t_{peak} \left(\frac{\alpha_1}{t_{peak} - t} - \frac{\alpha_2}{t_{peak}}\right) \tag{2.17}$$

Eq.2.17 can be re-written as follows:

$$t = t_{peak}\left(-\frac{\alpha_1}{2\alpha_2} + 0.5 - \frac{z}{2\alpha_{xd}\alpha_2} + \sqrt{(\alpha_{xd}{}^2(\alpha_1{}^2 + \alpha_1^2 - \alpha_1\alpha_2) + z^2 + \alpha_{xd}(\alpha_1 + 3\alpha_2)z)}\right) \tag{2.18}$$

where G_i is the initial shear modulus of the soil, α_1 and α_2 are curve fitting factors which are obtained numerically to be equal to $\beta - 0.83$ and $\beta - 0.67$, respectively. α_{xd} is obtained as: $\beta(1 - 0.27\beta)$. All other parameters in Eqs.2.16 and 2.17 are as defined in Table.2.1.

Fig.2.11 quantifies the influence of the soil's overconsolidation on the tangent shear modulus of soil. The linear relationship represents an ideal overconsolidated soil with the β and α equal to unity. While the non-linear $G^T - t/t_{peak}$ relationships represent normally consolidated soils. Practical range of β is obtained from the triaxial database (Svanø et al, 1993), (Langø, 1991) and (Daghigh, 1993) to be approximately between 1.0 and 4.0.

From Fig.2.11, α is found to be less than or equal to unity. According to the triaxial test results (Svanø et al, 1993 and Langø, 1991) practical range of α for clayey soils may be between about 0.5 and 1.0. Eq.2.15 is valid for $\beta > 1.0$. For an ideal linear $G - s$ relationship for OC soil (i.e. with $\beta = 1.0$), a simpler $(t - z)$ relationship can be derived through Eqs.2.10 and 2.11(see appendix.A). The peak skin friction t_{peak} may be computed from the Mohr-Coulomb criteria for both normally consolidated (NC) and overconsolidated (OC) soils.

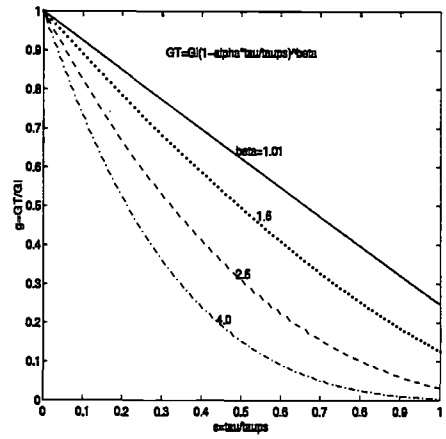

Figure 2.11: The normalized tangent shear modulus of soil vs. a normalized shear stress of soil

For contractant type soil such as NC clay, the (p'-q) stress path indicates some degradation (fall back) which is illustrated schematically on Fig.2.12. On the contrary, for OC type clay, the (p'-q) stress path does not exhibit any degradation. As illustrated in Fig.2.12 the deviatoric stress q increases as the mean effective pressure p' increases. This distinct behaviour may be attributed to the soil's tendency to hold together due to a possible new formation of the soil structure during shearing. Hence, the OC clay tends to dilate during the subsequent loading which allows the increase of its shearing capacity. The shear strength of the dilatant soil increases almost linearly by increasing the mean effective stress p'. The increase of p' means that the excess pore water pressure decreases and the effective stress on soil particles increases.

This means that the orientation of the principal stresses at the pile-soil interface will be different from that of the NC soil as illustrated in Fig.2.13.

Comparing the principal stress orientations shown in Fig.2.13, for OC soils, the major principal stress σ_1 is 90 degrees rotated with respected to the case of NC soil. This can be mathematically explained by k'_0, the lateral earth pressure factor as (Janbu, 1973):

$$k'_0 = \frac{\sigma'_h + a}{\sigma'_v + a} \tag{2.19}$$

For NC soil, $\sigma'_v \geq \sigma'_{h=h_0}$ thus $k' \leq 1$. For OC soil: $\sigma'_{h=h_c} \geq \sigma'_v$ and so $k' \geq 1$.

Another distinct feature of stress path of NC soil (in particular clay) as shown on Fig.2.13, is that as the soil reaches the failure (Coulomb) line, the shear stress approaches an almost constant level, while the soil contracts at strain levels in the magnitude of $0.5 - 2.0\%$.

This stress level may be defined as the undrained shear strength of NC soil (Janbu, 1973). After this constant shear stress q stage, by increasing the shear strain $\epsilon_q = 1/2(\epsilon_1 - \epsilon_3)$. the stress path (state) moves almost linearly back along the Coulomb failure line and then at larger strains

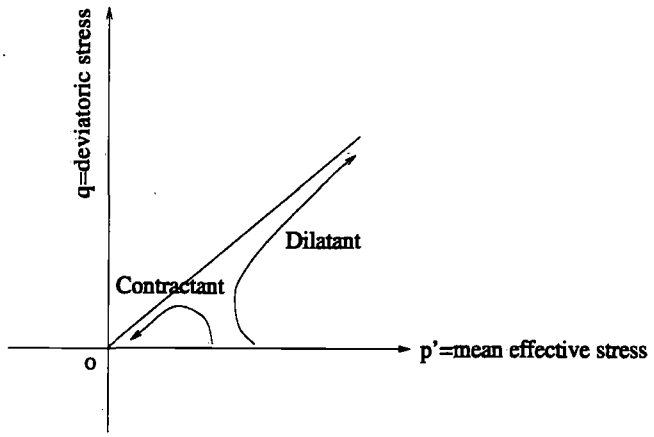

Figure 2.12: A schematic illustration of p'-q undrained stress paths for dilatant and contractant type soil behaviour

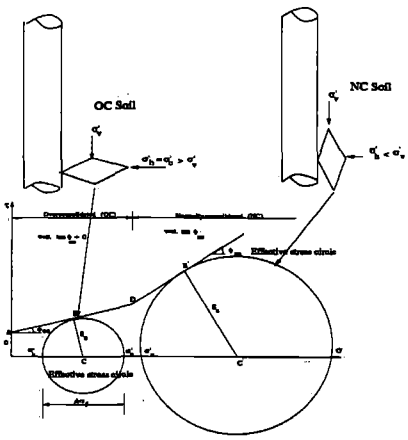

Figure 2.13: The orientation of principal stresses in NC and OC soils around the axially loaded pile

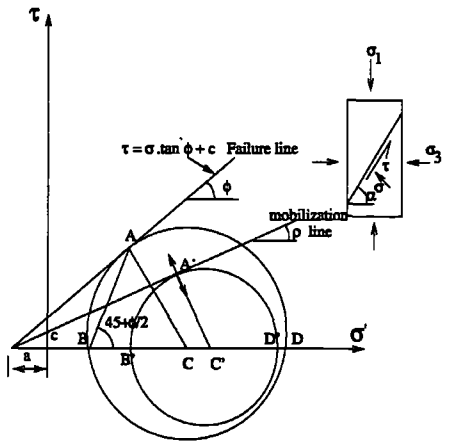

Figure 2.14: Definitions of soil failure and mobilization lines based on Mohr-Coulomb criteria

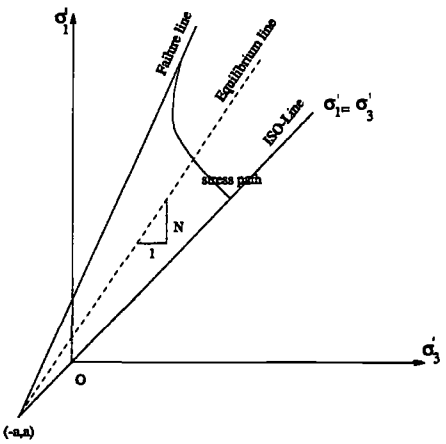

Figure 2.15: Definition of ISO, equilibrium and Failure lines for an ideal coulombian material

($\epsilon_q \geq 4$ percent -5 percent), it curves down in a parabolic shape until soil reaches its contraction limit (rupture).The latter behaviour may be defined as the strain softening response of the NC soil in the face of contraction.

In contrast, the stress paths of OC soils indicate a linear dilatant failure behaviour up to very large strains in magnitude of $\epsilon_q = 5\% - 10\%$ (LDPT database of Clarke et al, 1992).

In analogy with the NC soil, the undrained shear strength (S_u) of the OC soil may be defined as the shear stress level at reaching the p'-q stress path to the failure line (i.e. the shear stress corresponding to the intersect point of the stress path with the Coulomb failure line).

By outlining these basic assumptions, the peak shaft friction (t_{peak}) may be obtained as τ_{ps} from the intersection of the Mohr's circle and the pile-soil interface failure line l_{if}.

$$\tau_{ps} = \sigma_a^{'}(\frac{tan\delta}{1+tan^2\delta})(1 \pm \sqrt{1-(1+tan^2\delta)(1-\frac{tan^2\phi}{1+tan^2\phi})}) \tag{2.20}$$

Eq.2.20 may be simplified and re-arranged as follows:

$$\tau_{ps} = \frac{1}{2}sin2\delta\sigma_a^{'}(1 \pm \sqrt{1-(\frac{cos\delta}{cos\phi})^{2.0}}) \tag{2.21}$$

where $\sigma'_a = 1/2(\sigma'_1 + \sigma'_3)$ is the average of the effective major and minor principal stresses, denoted respectively with σ'_1 and σ'_3 ($\sigma'_1 \geq \sigma'_2 \geq \sigma'_3$). Note that for triaxial test conditions: $\sigma'_2 = \sigma'_3$. From Eq.2.45, two values emerge for τ_{ps}, a minimum and a maximum which correspond respectively to $\tau_{ps,1}$ and $\tau_{ps,2}$ as shown on Fig.2.16.

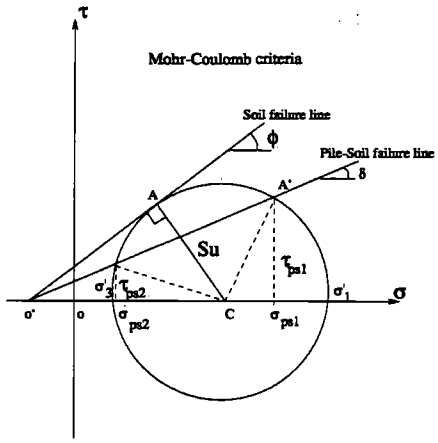

Figure 2.16: Mohr-coulomb criteria for an axially loaded pile-soil system

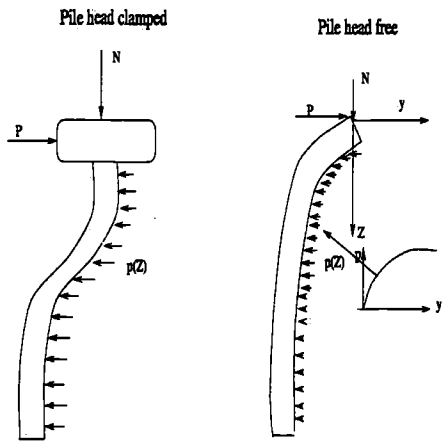

Figure 2.17: An example of a laterally loaded pile-soil system with clamped and free heads

Based on the above discussion on NC and OC soil behaviour, which were visualized on Fig.2.12, the maximum mobilized shear stress (or skin friction) for NC case, may be calculated as $\tau_{ps,1}$, while for OC situation $\tau_{ps,2}$ may be calculated as the peak mobilized shear stress (or t_{peak}).

The undrained shear strength S_u of soil is defined by(see Fig.2.18):

. Initial effective stress state

. Pre-loading stress history i.e. contractant (NC) or dilatant type(OC)

. Coulomb failure line of soil or pile-soil

The shear strength in effective stress approach might be determined in a simple manner as illustrated in Fig.2.20(Nordal, 1986):

$$M = \frac{3(N-1)}{3+(1+b)(N-1)} \tag{2.22}$$

in which M represents the slope of soil(Coulombian) failure line as shown in Fig.2.20. Parameters b and N are defined as follows:

$$b = \frac{\sigma'_2 - \sigma'_3}{\sigma'_1 + \sigma'_3} \tag{2.23}$$

$$N = \frac{1+sin\phi'}{1-sin\phi'} \tag{2.24}$$

where ϕ' denotes the effective internal friction angle of soil. For an undrained condition, the variation of excess pore water press $\Delta p'$ due to loading may be approximately taken as constant (Note that in reality $\Delta p'$ may vary with the total stress level σ_1 and σ_3). Fig.2.20 illustrates an effective stress path by assuming that $\Delta p' = constant$. According to this definition the

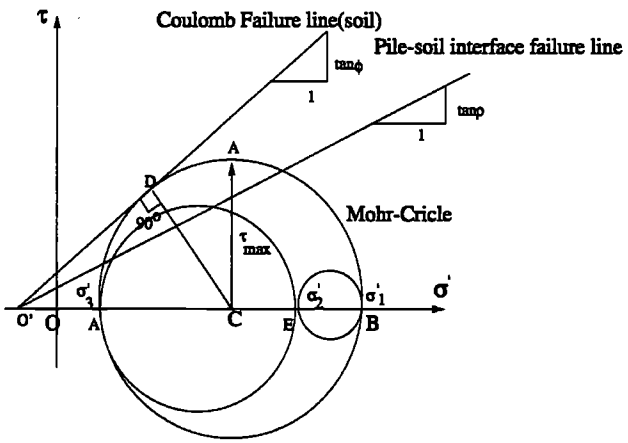

Figure 2.18: Definition of effective stress circle according to Mohr-Coulomb criteria

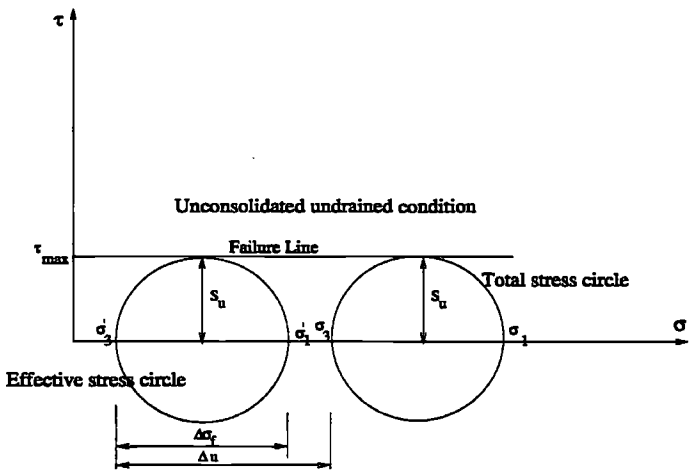

Figure 2.19: Definition of S_u according to total stress approach for unconsolidated undrained condition

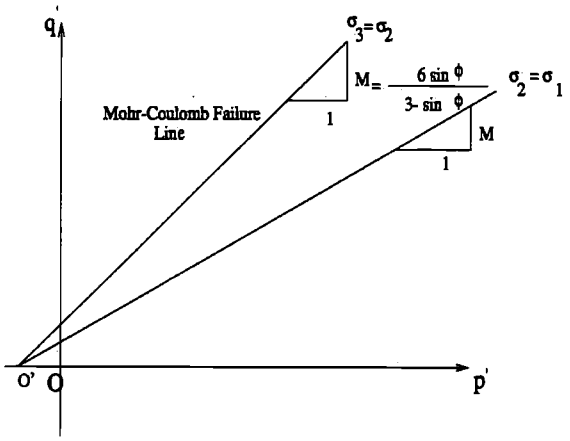

Figure 2.20: Definition of failure lines according to Mohr-Coulomb criteria for different effective stress conditions

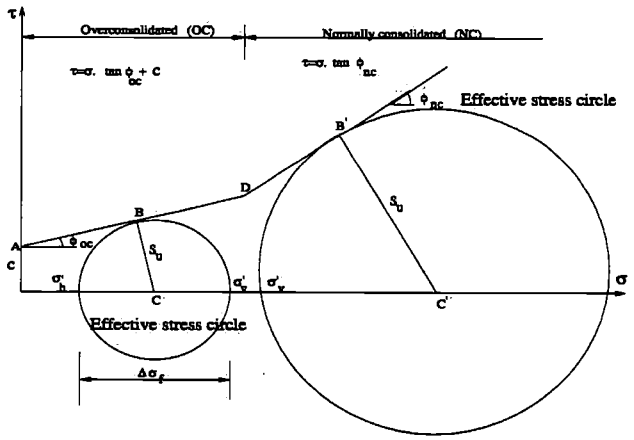

Figure 2.21: Comparison of effective stress based Mohr-Coulomb criteria for NC and OC soils

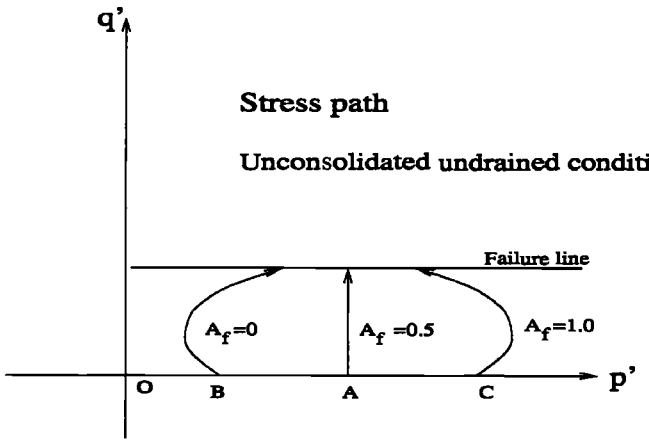

Figure 2.22: Dependency of stress path on the effective stress in the soil(Skempton's theory)

undrained shear stress S_u may be approximately expressed as follows:

$$S_u = \frac{1}{2}qN = \frac{1}{2}M(p_0' + a_d) \tag{2.25}$$

where $q = \sigma_1 - \sigma_3$ and p_0' the effective overburden pressure at rest may be defined as:

$$p_0' = \frac{1}{3}(\sigma_{v0}' + 2\sigma_{h0}') \tag{2.26}$$

a_d denotes the dynamic attraction of soil and might be defined as the tensile strength of soil under isotropic stress condition(see for e.g. Janbu, 1985).
The lateral earth pressure at rest may be defined as follows:

$$k_0' = (\frac{\sigma_h' + a_d}{\sigma_v' + a_d}) \tag{2.27}$$

For a NC soil condition as illustrated in Fig.2.13: $\sigma_1' = \sigma_v'$ and $\sigma_3' = \sigma_h'$ and $\sigma_v' > \sigma_h'$. Hence from Eq.2.27: $k_0' < 1$.

For an OC soil condition as shown in Fig.2.13: $\sigma_1' = \sigma_h' = \sigma_c'$ and $\sigma_3' = \sigma_v'$ and $\sigma_h' > \sigma_v'$. Hence from Eq.2.27: $k_0' > 1$.
Neglecting the small attraction term of a_d compared to much larger σ_1' or σ_3' then k_0' may be simplified from Eq.2.27 as:

$$k_0' = \frac{\sigma_h'}{\sigma_v'} \tag{2.28}$$

Combining Eqs.2.26 and 2.28 will result:

$$p_0' = \frac{1}{3}\sigma_{v0}'(1 + 2k_0') \tag{2.29}$$

For a condition of : $a_d << p'_0$, S_u of soil will be:

$$S_u = \frac{1}{2} M p'_0 = \frac{M(1+2k'_0)}{6} \sigma'_{v0} \tag{2.30}$$

For e.g. for a clayey soil with $\phi' = 30$ from triaxial compression test, from Eq.2.22 $M \approx 1$. For e.g. for NC soil with: $k'_0 = 0.5$ from Eq.2.30, $S_u = 0.33\sigma'_{v0}$. For e.g. for OC soil with: $k'_0 = 2.0$ from Eq.2.30, $S_u = 0.9\sigma'_{v0}$

The undrained shear strength (S_u) for the stress conditions represented in Fig.2.16 may be defined as the radius of the Mohr's circle which is normal to the failure line at the point of intersection :

$$S_u = \sigma'_a \sin\phi \tag{2.31}$$

Note that for an isotropic stress condition the above definition may not be applicable. Another definition of undrained shear strength is given by Das, (1985) for unconsolidated undrained condition as follows:

$$S_u = \frac{\Delta\sigma_f}{2} \tag{2.32}$$

where $\Delta\sigma_f = \sigma_1 - \sigma_3$ as the deviatoric stress at failure.
From Mohr-Coulomb failure criteria S_u can be approximately obtained as follows:

$$\begin{aligned} S_u = \frac{1}{2}(\sigma_1 - \sigma_3) &= \frac{1}{2}(N-1)(\sigma'_3 + a_d) \\ &= \frac{1}{2}(\frac{N-1}{N})(\sigma'_1 + a_d) \\ &= \frac{sin\phi}{1+sin\phi}(\sigma'_1 + a_d) \end{aligned} \tag{2.33}$$

For e.g. for OC clay with $a_d << \sigma'_c$, Eq.2.33 may be simplified as follows:

$$S_u = \frac{1}{2} sin\phi \sigma'_c \tag{2.34}$$

Ladd, (1974) has introduced a correlation between S_u , OCR and σ'_v of soil as follows:

$$S_u = 0.22\sigma'_v OCR^{0.8} \tag{2.35}$$

where OCR is defined as the ratio of the consolidated stress to the current effective stress:

$$OCR = \frac{\sigma'_c}{\sigma'_v} \tag{2.36}$$

Combining Eqs.2.36 and 2.35:

$$S_u \approx 0.22\sigma'_c \tag{2.37}$$

The latter approximation is quite close to the one obtained from the approximate Eq.2.34 for $\phi' = 20 - 30$ deg.

k_0' can also be obtained for contractant soils as follows:

$$k_0' = (\frac{1 - sin\rho}{1 + sin\rho}) \tag{2.38}$$

And for the dilatant (OC) soils, the following expression may be obtained from Eq.2.28:

$$k_0' = (\frac{1 + sin\rho}{1 - sin\rho}) \tag{2.39}$$

where ρ = the mobilized friction angle prior to loading.

It can be seen that the lateral earth pressure for OC soils is always greater than or equal to 1, while the coefficient k_0' is always less than or equal to unity. The Jaky's approximate formula for the lateral earth pressure which is expressed as:

$$k_0' = 1 - sin\phi \tag{2.40}$$

which may be compared with Eq.2.38. For overconsolidated soils Meyerhof et al, (1976) has modified Jaky's formula as follows:

$$k_0' = (1 - sin\phi)\sqrt{OCR} \tag{2.41}$$

For the typical average friction angle of OC soil 28-34 deg and OCR greater than unity in the range of 1-30, Eqs.2.39 and 2.41 give respectively, values in the range of 2.0-3.0 and 0.5-3.0. The measured average values of the coefficient of the lateral earth pressure for such soils are in the range of 1.7-3.5 which are quite close to the results of the Eq.2.19 above,
Janbu, (1985) presented an approximate formula for the OC soils as follows:

$$S_u \approx \frac{1}{2} sin\phi' \sigma_c' \tag{2.42}$$

In which σ_c' = the maximum past pre-consolidation stress in the soil which is given or measured between 600-1200 KPa for the North sea offshore sites. The latter then results in the undrained shear strength values in the range of 150-300 KPa which are typical of the North sea.

However, Janbu, (1985) has rejected any direct correlation between OCR and S_u, since based on the Mohr-Coulomb criteria no such direct relationship may be established. Alternatively one may relate k_0' to the OCR ratio as follows:

$$k_0' = a_k OCR^{1/n} \tag{2.43}$$

The correlation coefficient a_k and the exponent term n are defined by Janbu, (1985). The following approximate correlation may be obtained for non-cohesive soils:

$$k_0' \approx 2sin\phi' \tag{2.44}$$

The results of latter expression may be compared with those of API and NGI for plugged and unplugged piles in silica and carbonate sands. The mean values recommended by API are 0.8

and 1.0 for open and close ended piles, respectively. In comparison NGI survey (Lacasse, 1992) has given the mean values 0.88 and 0.46 for silica and carbonate sands, respectively. The correlation above gives values which are about 20 – 35 percent higher than the mean values given by NGI and API.

By combining Eqs.2.45 and 2.31, the maximum skin friction at the pile-soil interface may be written as :

$$\tau_{ps} = \tau_{max} \frac{\sin 2\delta}{2 \sin \phi} (1 \pm \sqrt{1 - \frac{\cos^2 \phi}{\cos^2 \delta}}) \tag{2.45}$$

where τ_{max} denotes the maximum shear stress at soil failure according to Mohr-Coulomb failure criteria. Eq.2.45 may be compared with the API formulations given in Eq.2.5.

The expressions derived above are consistent with those of API for S_u in their limits. For a practical range of ϕ, this limit may be approximately expressed as follows:

$$0.5 S_u \leq \tau_{ps} \leq S_u \tag{2.46}$$

or by substituting for S_u from Eq.2.46, the above inequality 2.33 may be expressed as follows:

$$0.5 \sigma'_a \sin \phi \leq \tau_{ps} \leq \sigma'_a \sin \phi \tag{2.47}$$

which may give the following inequality for ϕ varying in the range of 20-30 deg:

$$0.2 \sigma'_a \leq \tau_{ps} \leq 0.5 \sigma'_a \tag{2.48}$$

The above expression may also be expressed in terms of the conventional mean effective stress σ'_m, the deviatoric stress component σ'_d and the major stress component σ'_1.

For cohesive soils, the adhesion (c) or the equivalent attraction parameter a_d may be included in the above equations. The soil's attraction which is often denoted by a_d, may be defined (Janbu, 1973) as an apparent hydrostatic tensile strength of soil. To include such an effect mathematically, a_d may be added to σ'_a component in all above derivations.

2.3 Lateral pile-soil interaction

Pile foundations of offshore platforms are subjected to frequent lateral loading induced by the action of the environmental loads such as waves, currents, winds and earthquakes etc. The induced lateral loading on the pile head is resisted through the non-linear lateral pile-soil reaction which is characterized by (p-y) curves.

The lateral pile-soil behaviour may simply be expressed by the following differential equation (see Fig.2.17):

$$\frac{d^2 M}{dZ^2} + p(y) = 0 \tag{2.49}$$

If the action of the axial forces on the pile is also included then Eq.2.49 may be modified as follows:

$$EI\frac{d^4y}{dZ^4} - \frac{d^2(Ny)}{dZ^2} + p(y) = 0 \tag{2.50}$$

If $N = f(Z)$ and $p(y)$ are assumed or obtained from measurements then the above equation could be easily solved to give (y) the pile-soil lateral deflection and so the shear force and bending moment distribution along the pile shaft.

2.3.1 API's (p-y) model

2.3.1.1 (p-y) model for clay

The lateral pile-soil interaction (p-y) models recommended by API RP2A 1993 have been developed empirically. The empirical establishment of such (p-y) models have been based on the data acquisition from large diameter pile tests under lateral loading in the form of the voltage data. Such voltage variations initially were calibrated against simple tubular beam bending tests at the lab. So that M_i is related to V_i, the measured voltage changes at the sensor (gauge) station installed along the pile's shaft then are transformed to the corresponding bending moment data via such earlier obtained (M,V) correlations. Then the lateral load transfer(p) and the associated pile deflection (y) can be computed from beams theory as follows:

$$p = \frac{d^2M}{dZ^2} \tag{2.51}$$

$$y = \int\int \frac{M}{EI} dZ dZ \tag{2.52}$$

By incremental loading δL, the corresponding bending moment at the pile will increase from M to $M + \delta M$ and so the corresponding lateral pressure p to $p + \delta p$ and the lateral displacement y to $y + \delta y$, hence a set of (p-y) data could be obtained in an incremental way. (p-y) curves which are obtained in this manner are generally nonlinear with an early initial yield and then followed by a work hardening part.

The empirical (p-y) models which have been proposed by API RP2A 93 for lateral loading in clay briefly described in this subsection. The method has been initially proposed for soft clayey soils, moreover API RP2A 93 has suggested that the (p-y) model recommended for soft clay has to be modified for use in stiff clay situations. Due to more brittle behaviour of stiff clay soils compared to soft clay, particularly the post-peak part of the (p-y) curves have to modified by considering the possible degradation. The degree to which this degradation might be considered depends strongly on the specific stiff clay soil. For e.g. in fully saturated(deep water) condition with likely hydraulic scour effects a larger post-peak degradation might be considered(see for e.g. Dunnavant et al, 1989 and Hamilton and Dunnavant, 1992).

It has to be noted that the API recommended (p-y) envelope curves are design curve. This means that they may offer lower estimate of lateral or axial soil resistance. The (p-y) behaviour as shown in Fig.2.23 is completely nonlinear with no post-peak degradation except for cyclic loading which

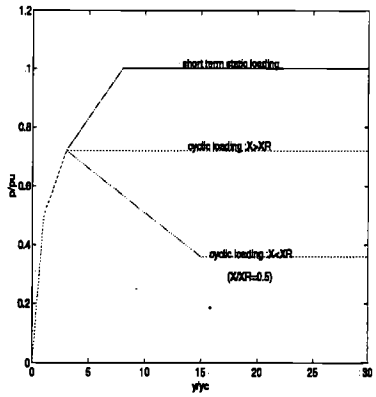

Figure 2.23: API (p-y) curves for soft and stiff clayey soils under short term static loading

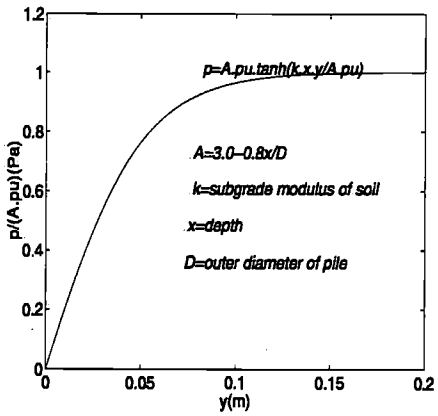

Figure 2.24: API-RP2A 1993 (p-y) curve for sand under static loading

will be discussed in Chapter.4. The peak lateral resistance ($p_u = p_{peak}$) is correlated against the undrained shear strength of soil (S_u). For deeper soil layers API RP2A 93 recommended $p_u = (9 - 12)S_u$, while for shallow parts of soil, it has given the following criterion:

$$p_u = 3S_u + \gamma Z + J\frac{S_u(Z)}{D(Z)} \qquad Z < Z_r \tag{2.53}$$

and

$$p_u = \chi S_u \qquad Z > Z_r \tag{2.54}$$

where $D(Z)$ = the pile's outer diameter at depth Z, γ = the effective unit weight of soil, in weight density units, J = empirical constant varying from 0.5 for the Gulf of Mexico to 0.25 for stiffer clayey soils such as those encountered in North sea area, Z = depth at the point along the pile shaft (positive downwards), Z_r = depth at the point along the pile at the bottom of the reduced resistance zone (top soil) and $\chi = 9 - 12$.

Z_r may be obtained by solving Eqs.2.53 and 2.54 simultaneously as follows:

$$Z(\gamma + \frac{JS_u(Z)}{D(Z)}) = (\chi - 3)S_u(Z) \tag{2.55}$$

where $\chi = \frac{p_u(Z \geq Z_r) - p_u(Z=0)}{S_u} = 9 - 12$. If $S_u(Z) = cte$ and $D(Z) = cte$ then Z_r may be obtained from Eq.2.55 as follows:

$$Z_r = \frac{(\chi - 3)D}{J + \frac{D\gamma}{S_u}} \tag{2.56}$$

In general S_u would vary with depth so the solution of Z_r may be obtained by solving Eq.2.55 numerically or graphically. API RP2A 93 has recommended that Z_r should not be less than 2.5

times the average diameter of the pile D_a as:

$$D_a(Z) = \int_0^Z \frac{D(Z).dZ}{Z} \tag{2.57}$$

2.3.1.2 (p-y) model for sand

API RP2A 93 has proposed the following empirical (p-y) model for sand:

$$p = Ap_u tanh(\frac{kZy}{Ap_u}) \tag{2.58}$$

where $A = (0.3 - 0.8Z/D) \geq 0.9$, k = the initial modulus of subgrade reaction which can be determined graphically from Fig.2.26 as a function of the internal friction angle of soil ϕ.

The ultimate lateral resistance p_u or p_{peak} of sand has been empirically found to vary with the depth, according to the following equations:

$$p_{us} = (C_1 Z + C_2 D_a(Z))\gamma' Z \tag{2.59}$$

$$p_{ud} = C_3 D_a(Z)\gamma' Z \tag{2.60}$$

where p_{us} and p_{ud} represent the ultimate lateral soil resistance for shallow and deep soils. API RP2A 93 recommended that p_u at any given depth to be calculated as the minimum values of Eqs.2.59 and 2.60:

$$p_u = min(p_{us}, p_{ud}) \tag{2.61}$$

where in Eqs.2.59 to 2.60, γ' = the effective soil weight, in weight density units. $D_a(Z)$ = the average outer diameter of the pile from near surface to the depth Z. C_1, C_2 and C_3 = the lateral resistance coefficients which are determined from Fig.2.25 as a function of ϕ.

2.3.2 Reese's (p-y) model

A semi-empirical (p-y) model has been proposed by Reese et al, (1975) for lateral analysis of the pile in stiff clay. The model has been developed based on analysis of the an instrumented pile in hard and saturated clay. The initial condition of test site has been reported (Reese et al, 1975) to have salty water which then has been inundated with fresh water before lateral pile test. The following describes briefly the original (p-y) model by Reese et al, (1975).

The general procedure for deriving the lateral load transfer (p) and the corresponding pile-soil displacement (y) is described in Sec.2.3.1. The characteristic shape of the (p-y) curve proposed by Reese et al, (1975) is given Fig.2.27, which consists of an initial linear elastic part followed by a nonlinear elasto-plastic part until reaching the peak. The post-peak portion of the (p-y) curve shows a rapid degradation (strain softening) of soil's lateral resistance to a residual value which is far smaller than (p_{peak} or p_u).

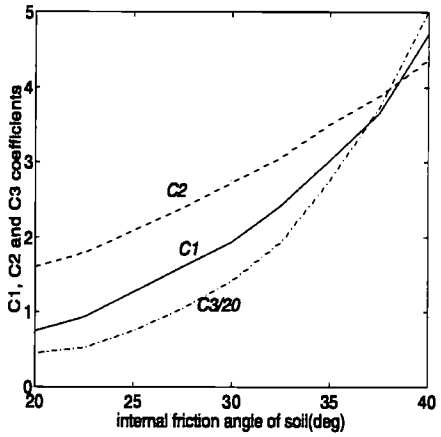

Figure 2.25: The ultimate resistance coefficients for API's (p-y) model for sand

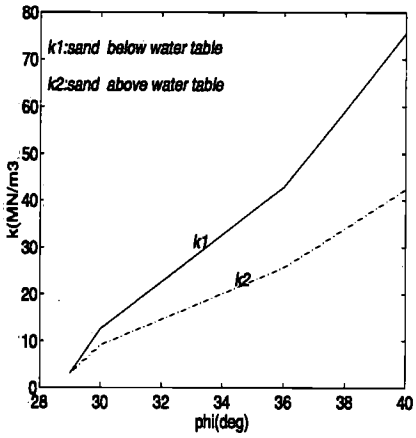

Figure 2.26: Subgrade modulus of soil k for sand under lateral loading according to API-RP2A 1993

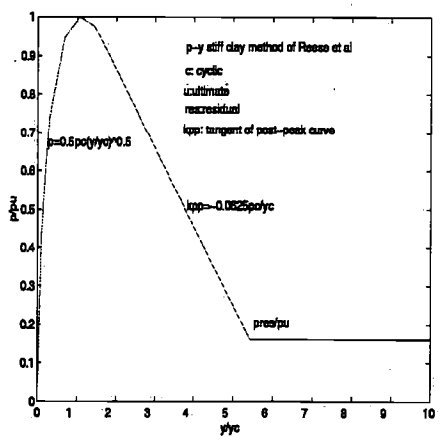

Figure 2.27: Reese's (p-y) curve for stiff clay under static loading

The extent of post-peak degradation that is simulated by this model may be attributed to the particular soil condition in which the pile test has been conducted. The saturated clay at the site has been reported (Reese et al, 1975) to contain salty water and it has been inundated by fresh water before the pile test. The rapid post-peak degradation of the Reese's (p-y) model may have been the result of either the slackness or the hydraulic erosion of the soil.

In contrast the initial response of Reese's (p-y) model is very stiff which will be discussed later in Sec.2.7. The initial stiffness and peak response of this model are governed by the following equations:

$$p_1 = k_{Re} Z y \qquad ; y < y_0 \tag{2.62}$$

where k_{Re} = an empirical stiffness correlated parameter which varies with S_u between 0.14-0.55. The associated nonlinear pre-peak (p-y) response described as follows:

$$p_2 = 0.5 p_{peak} (\frac{y}{y_c})^{0.5} \qquad ; y_0 \leq y \leq A y_c \tag{2.63}$$

where $y_c = \epsilon_c D(Z)$, ϵ_c = strain at the half the peak resistance, and varies from about 0.007 for hard clay to about 0.004 for very stiff clay (Reese et al, 1975).

The post-peak behaviour of the model is expressed by the following equations:

$$p_3 = 0.5 p_{peak} (\frac{y}{y - y_c})^{0.5} - 0.055 p_{peak} (\frac{y - A y_c}{A y_c})^{1.25} \qquad ; A y_c \leq y \leq 6 A y_c \tag{2.64}$$

$$p_4 = 0.5 p_{peak} (6A)^{0.5} - 0.411 p_{peak} - \frac{0.0625}{y_c} p_{peak} (y - 6 A y_c) \qquad ; 6 A y_c \leq y < 18 A y_c \tag{2.65}$$

$$p_5 = 0.5 p_{peak} (6A)^{0.5} - 0.411 p_{peak} - 0.75 p_{peak} A \qquad ; y \geq 18 A y_c \tag{2.66}$$

In the above equation, y_c is the corresponding displacement of the peak resistance point on the Reese's (p-y) curve and A = is an empirical non-dimensionalized parameter which correlates, the mobilized lateral resistance with the soil depth (see Fig.2.28). The ultimate lateral resistance of the pile-soil system p_{peak} is computed from the following empirical relationships:

$$p_{peak,1} = 2 S_{u_a} D(Z) + \gamma' D(Z) + 2.83 S_{u_a}(Z) \qquad ; Z \leq Z_r \tag{2.67}$$

$$p_{peak,2} = 11 S_u(Z) \qquad ; Z > Z_r \tag{2.68}$$

And p_{peak} will be :

$$p_{peak} = min(p_{peak,1}, p_{peak,2}) \tag{2.69}$$

where Z_r = is the depth corresponding to the bottom of the reduced resistance zone or the top soil as defined in section 2.3.1. Reese et al does not present any specific criterion for Z_r. It only indicates that Eq.2.67 could be used for depths near the surface while Eq.2.68 may be used for the intermediate and deeper depths.

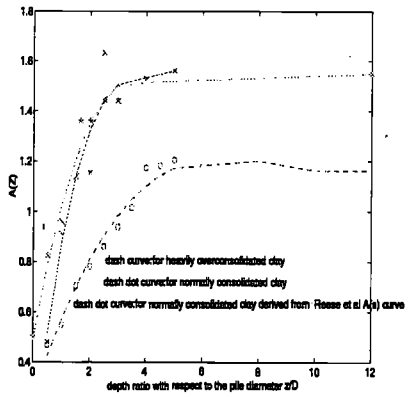

Figure 2.28: The correlation factor A (modified after Reese et al, 1975)

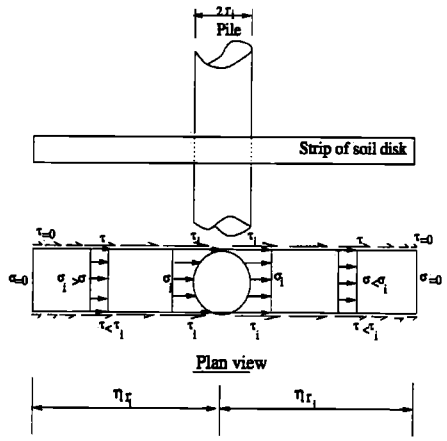

Figure 2.29: A disk idealization of pile-soil system under lateral loading(a "strip" of soil disk)

2.3.3 Disk modelling of the lateral pile-soil interaction

A new (p-y) model is developed in this section on the basis of disk modelling of the pile-soil system in a similar way to the (t-z) model which is derived in Sec.2.2.3. Several simplifying assumptions are made based on our initial understanding of the lateral pile-soil behaviour under monotonic loading. Again as for the axial loading case, the pile-soil interaction will be modelled by a number of uncoupled finite disks which encircle the pile. Fig.2.29 gives a schematic view of a pile section with a strip of soil disk around it and the normal/shear stress distribution over the strip of soil disk.

Each disk may be assumed to have a radius several times of that of the pile. This is to enable the pile-soil disk to distribute sufficiently the lateral load from pile to the soil. Based on the failure theory of Janbu et al, it may be assumed that the normal stresses imparted into the soil disk from the lateral loading of the pile-soil system could be resisted in the form of shear stresses around the soil disk. Again it may be assumed that for each uncoupled pile-soil disk a plane strain condition exist (i.e. the stress components may not vary with the disk thickness or pile depth). Moreover, it is assumed that the clay is in undrained condition, i.e. the soil element volume will remain constant or:

$$|\epsilon_r| = |\epsilon_\theta| \tag{2.70}$$

The shear distortion γ then may be computed as:

$$\gamma = \epsilon_r - \epsilon_\theta \tag{2.71}$$

By combining Eqs.2.70 and 2.71, then the radial strain will be:

$$\epsilon_r = \frac{\gamma}{2} \tag{2.72}$$

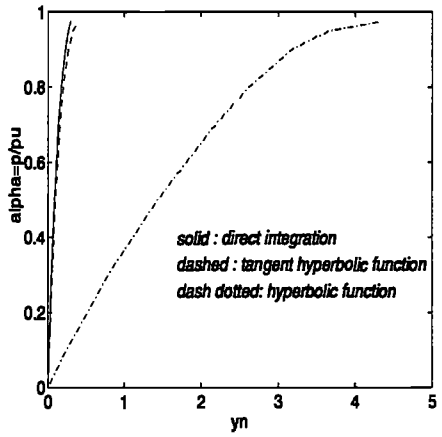

Figure 2.30: Numerical integration of Eq.2.77 vs. the fitted hyperbolic function Eq.2.78 for $\beta < 2.5$

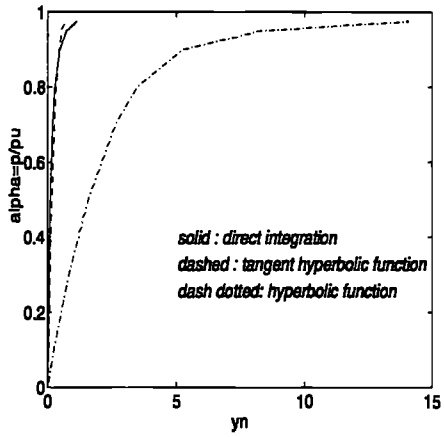

Figure 2.31: Numerical integration of Eq.2.77 vs. the fitted hyperbolic function Eq.2.78 for $\beta \geq 2.5$

From Mohr's circle and by making use of the latter assumption, the radial strain around the pile in the direction of y-axis may be calculated as follows:

$$\epsilon_r = \frac{1}{2}\int_0^\tau \frac{d\tau}{G^T} \tag{2.73}$$

where τ_i is the shear stress close to the pile and G^T is the tangential shear modulus of soil which is calculated from Eq.2.11.

The shear stress distribution along a horizontal"compression-elongation" column may be assumed in an exponential form as expressed in Eq.2.13 which satisfies the boundary condition at the pile-soil interface. The second boundary condition is also satisfied at the infinity distance from the pile-soil interface. However, for a soil disk of a finite radius, this may be approximately satisfied by assuming that $r_{id} = (\eta = 10 - 20)r_i$. According to Janbu's concept, the lateral pressure at the pile-soil interface might be resisted through the shear stresses on a failure surface as shown on Fig.2.29 up to failure point. Recalling Janbu's empirical relationship ultimate lateral resistance of pile-soil and the failure shear stress at failure as:

$$S_u = \frac{\zeta_{if} p_u}{N_{ru}} \tag{2.74}$$

where ζ_{if} = a pile-soil interface factor, ranging approximately between 1 and 2, for no gap and full gap conditions, respectively. p_u = the ultimate lateral resistance, in terms of stress units, N_{ru} = an undrained shear strength correlation factor which is between 4-5 down to depth 5D(Z) from soil surface, varies almost linearly between 5 and 8 for depths between 5D(Z) and 8D(Z) and further down may be assumed constant in the range of 8-10.

Janbu's empirical relationship may be used to correlate the lateral pressure at the pile-soil interface to the resisting shear stresses over the uncoupled disks as follows:

$$\tau_i = \frac{\zeta_{if} p_i}{N_{ru}} \tag{2.75}$$

where p_i = the lateral pressure at the pile-soil interface, τ_i = the mobilized shear stress at the pile-soil interface, τ_{ps} =the maximum shear stress at the pile-soil interface at failure and other parameters are as described above. The lateral displacement y may be obtained by integrating the radial strains along the pile-soil disk as follows:

$$y = \int_{r_i}^{r_l} \epsilon_r dr = \frac{1}{2}\int_{r_i}^{r_l}\int_0^{\tau} \frac{d\tau}{G^T}.dr = \int_{r_i}^{r_l} \frac{\tau_{ps}}{2G_i\alpha(1-\beta)}[1-(1-\alpha\frac{\tau_i}{\tau_{ps}}\exp^{(\frac{r_i-r}{r_i})}]^{1-\beta}.dr \tag{2.76}$$

where r_l is the radius of the imaginary finite disk. By combining Eqs.2.75 and 2.76, (p-y) relationship may be obtained as follows:

$$y = \int_{r_i}^{r_l} \frac{\tau_{ps}}{2G_i\alpha(1-\beta)}[1-(1-\alpha\frac{\zeta_{if} p_i}{N_{ru}D(Z)\tau_{ps}}\exp^{(\frac{r_i-r}{2r_i})})^{1-\beta}].dr \tag{2.77}$$

where τ_{ps} may be found as a factor of Su from Mohr - Coulomb failure criterion as given in Eq.2.45 of Sec.2.2.3. After the numerical integration of Eq.2.77, various mathematical forms may be tried to fit the data. In this case a simple tangent hyperbolic function is fitted (Fig.2.31) to the integration data as :

$$p = \frac{p_u f(\phi',\delta')}{0.5\alpha(1+\beta)} tanh(\frac{2\alpha G_i y}{0.9\beta p_u f(\phi',\delta')D}) \tag{2.78}$$

where $f(\phi',\delta')$ is obtained from Eq.2.45 as follows:

$$f(\phi',\delta') = \frac{1}{2}sin(2\phi')(1+\sqrt{1-\frac{cos^2\phi'}{cos^2\delta'}}) \tag{2.79}$$

For practical range of the effective internal friction angle of soil ϕ' and the effective pile-soil interface friction angle δ', the above function $f(\phi',\delta')$ might vary approximately between 0.5 and 1.0. By assuming that the α parameter might vary practically between 0.5 and 1.0 for various NC and OC soils, then from Eq.2.78, the following ratio may be obtained at large displacements where the value of the tangent hyperbolic function may approach unity.

$$\frac{p}{p_u} = \frac{f(\phi',\delta')}{\alpha} \tag{2.80}$$

The latter ratio may be defined as the overconsolidation influence factor. From Eq.2.80 is that for dilatant soils with $\alpha = 1.0$ and the same ϕ' or δ' angles, the p/p_u ratio would be greater than that for the contractant soils with $\alpha < 1.0$. The implication of introducing this factor here is that the larger bias (Horsnell and Toolan, 1996), (Lacasse and Nadim, 1996) often associated with using Eq.2.5 of API RP2A 1993 or similarly Eq.2.45 for NC soils will be reduced. The latter will be discussed further in Chapter 6 within the context of reliability study of pile-soil-jacket failure.

From Eq.2.78, the initial modulus of soil's lateral response may be obtained as follows:

$$k_i = \frac{dp}{dy}_{y=0} \tag{2.81}$$

which after differentiation may be re-written in the following form:

$$k_i = \frac{4N_{ru}G_i}{0.9\beta(\beta+1)D} \tag{2.82}$$

in which χ as the numerical correlation factor is obtained to be about as 2.22 and the other parameters involved are as defined earlier. Eq.2.81 can be compared with the correlation given by Yoshida, (1972) as follows:

$$k_i = \zeta_i(1+\nu)G_i \tag{2.83}$$

where the correlation factor ζ_i is given as between 2.4 and 3.6. Svanø et al, 1993 has obtained the lateral modulus of soil as $5G_i$ which is closer to the average value of k_i from Eq.2.81 about $5.12G_i$ for $\beta_{av} = 2$ near the surface where $N_{ru} = 4.0$. As shown in Eq.2.81, the initial modulus of soil in lateral loading is a function of the depth, pile's diameter and shear stress-strain behaviour.

2.3.4 Dunnavant's (p-y) model

Dunnavant and O'Neill,(1989) have proposed a new (p-y) model based on back analysis of data from large diameter pile tests carried out at Houston site. This (p-y) model has been basically developed for lateral loading of submerged, stiff and heavily overconsolidated clays. The soil condition based on which the model has been developed, resembles the offshore soil conditions. The soil condition at Houston site will be described at Sec.2.7 which is dedicated to LDPT case studies.

The model has been modified by Dunnavant and O'Neill, (1989) for cyclic loading effects. The recent design codes such as API RP2A 93 have also considered this method in their commentary. The empirical establishment of the model has been based on the general procedure described in Sec.2.3.1. Further details of the derivation of the criteria is given by Dunnavant and O'Neill, (1989). Two distinct features about this (p-y) model are a) taking into account hydraulic scour (gap) effects. b) elastic coupling between various (p-y) curves.

The degrading effects of developing gaps around the piles during cyclic lateral loading are particularly severe. This will be discussed in Chapter.4. Meanwhile, the static lateral capacity of saturated stiff clay could be reduced substantially by previous gap formations, during past storms or earthquakes. Such degradation effects are simulated through softening of the (p-y) response of the pile-soil system.

Dunnavant's (p-y) model includes the elastic coupling of the nonlinear (p-y) curves through introduction of a relative pile-soil lateral stiffness parameter (K_r) as follows:

$$K_r = \frac{EI}{E_s L^4} \tag{2.84}$$

where E = the elastic modulus of pile's material, I = the moment of inertia of the pile, E_s = the soil's elastic modulus, L = the pile's length.

The results of previous study by Baguelin et al, (1977) have indicated that the soil's subgrade modulus may vary with the flexural rigidity of the pile and thus as a nonlinear function of pile's diameter.

According to the results of study by Gazioglu and O'Neill, (1984) the critical pile length L_{cr} may be obtained as:

$$L_{cr} = 3D(Z)(\frac{EI}{E_s D(Z)^4})^{0.286} \tag{2.85}$$

the critical pile length given above is defined as the pile length beyond which the lateral pile-soil resistance may not be mobilized considerably. The critical length may be defined as effective length for flexible long piles under lateral loading. In the following sections, by means of numerical simulations it is shown that the lateral pile-soil mobilization is often limited to such as limited depth for e.g. defined by Eq.2.85.

Dunnavant's empirical (p-y) model is expressed as follows:

$$p = 1.02 p_u tanh[0.537(\frac{y}{y_{50}})^{0.7}] \qquad ; y \leq 8y_{50} \tag{2.86}$$

where p_u = the ultimate lateral resistance of pile-soil has been obtained empirically by Dunnavnt and O'Neill, (1989) as follows:

$$p_u = N_p S_u D(Z) \tag{2.87}$$

where N_p = an undrained shear strength correlated parameter which is calculated as :

$$N_p = 2 + \frac{\sigma'_v}{S_{ua}(Z)} + 0.4\frac{Z}{D(Z)} \leq 9 \tag{2.88}$$

where σ'_v = the effective vertical stress and S_{ua} = the average undrained shear strength from the soil surface to the depth in question (Z):

$$S_{ua} = \frac{\int_0^Z S_u(Z)dZ}{Z} \tag{2.89}$$

In Eq.2.86, y_{50} is the corresponding displacement at the one half of the ultimate pile-soil resistance which is correlated against K_r as:

$$y_{50} = 0.0063\epsilon_{50} D(Z) K_r \tag{2.90}$$

where ϵ_{50} and $D(Z)$ as defined in Sec.2.3.1.

Dunnavant's pile-soil test results indicated that $N_p \leq 6$ for ultimate mobilization of the degraded stiff clay may be achieved (see Fig.2.32).

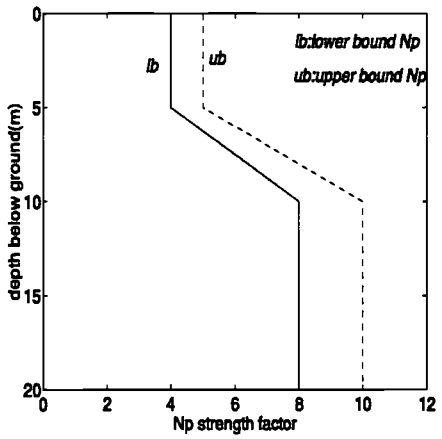

Figure 2.32: Janbu's N_p correlation factor and LDPT test vs. depth

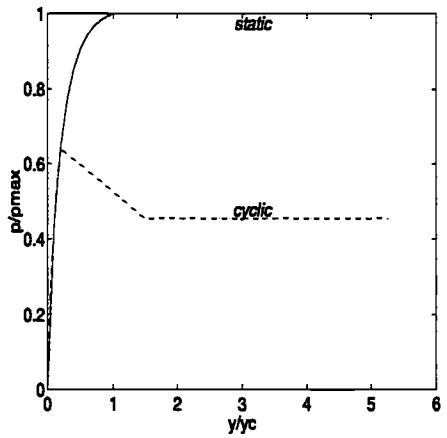

Figure 2.33: p-y criteria of Dunnavant et al for static loading

2.4 Calibration of pile-soil disk models

The disk models presented in Secs.2.2.3 and 2.3.4 were established theoretically based on some simplifying assumptions such as uncoupling, plane strain and undrained conditions etc. The calibration of the presented models against the empirical results would constitute an important part of their developments. The presented models are calibrated against the recent empirical results from Pentre and Tilbrook sites (Clarke and Mc Clelland, 1992).

2.4.1 Calibration of the axial disk model

The disk model presented for axial loading of pile-soil in Sec.2.2.3 is calibrated against the large diameter pile tests at Pentre and Tilbrook sites, respectively. First, the initial axial stiffness of the (t-z) model will be calibrated with respect to the tests. The influence of residual stresses induced during pile installations may be considerable. The residual skin friction may be caused by rebounding of the pile to the surface and/or consolidation of the soil (see Fig.2.35).

This may lead to an increase or decrease of the overall pile-soil stiffness. If at the depth of interest the sign of residual skin friction is negative, it will result in an increase of axial pile-soil stiffness in compression and vice versa in reduction of axial stiffness in tension. Otherwise will be true for the case of positive residual skin friction.

Although, the LDPT results show an apparent effect on the maximum mobilized skin friction (t_{peak}) due to the presence of the residual skin friction, but there is no definitive criterion to take it into account. Hence, the Eq.2.16 may be modified according to the empirical results, as

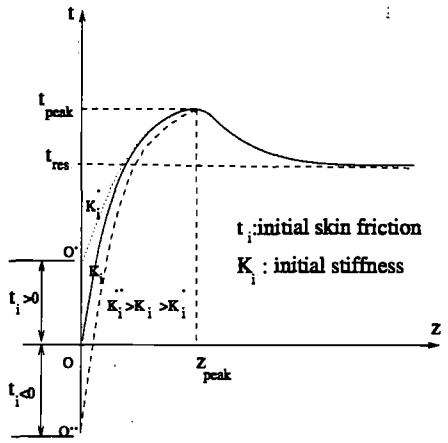

Figure 2.34: The initial stiffness changes due to existence of negative or positive residual skin friction at the pile-soil interface

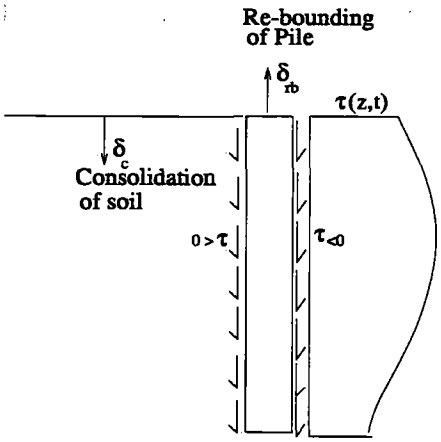

Figure 2.35: The residual skin friction at the pile-soil interface caused by the rebounding of the pile and consolidation of the soil

shown on Figs.2.33 and 2.34, to allow for pre-loading stresses:

$$t = \frac{t_{peak} tanh(\frac{\alpha K_i D(Z) z_{res}}{t_{peak}})}{tanh[tanh^{-1}[\alpha(\beta + 0.3)] - tanh^{-1}[\alpha(\beta + 0.3)(\frac{t_{res}^{pl}}{t_{peak}})]]} \tag{2.91}$$

in which t_{res}^{pl} denotes initial skin friction at pile-soil interface. The above equation may hold true for $t_{res}^{pl} \geq 0$. For negative values of t_{res}^{pl}, the load transfer-pile 's axial displacement relationship may be assumed linear up to the zero load level ($t = 0$), with the same stiffness as the initial stiffness of the pile-soil at $t = 0$ according to Eq.2.16:

$$z_{res}^{pl} = \frac{t_{res}^{pl}}{K_i D(Z)} \tag{2.92}$$

And hence the modified (t-z) relationship may look like:

$$t = \frac{t_{peak} tanh(\frac{\alpha K_i D(Z) z_{res}}{t_{peak}})}{tanh[tanh^{-1}[\alpha(\beta + 0.3)] - \alpha\beta']} \tag{2.93}$$

where $\beta' = \frac{t_{res}^{pl}}{t_{peak}}$. According to the measured data by Lambson et al, (1992), the stress path p'-q for both sites show very little degradation effects (see Fig.2.36). The measured peak skin friction profile (Clarke et al, 1992) does also verify the non-degrading nature of Pentre clay despite the fact that it's being assumed as normally consolidated. The stress history on most part of Pentre soil profile (Fig.2.36) shows a dilatant behaviour, which is in contrast to the definition of the NC soils as illustrated in Fig.2.12. This may be due to two different reasons, first the clay at Pentre site may not be considered as essentially NC because of the k' profile which indicates that lateral earth pressure coefficient k_v' for large extent of the pile penetration depth

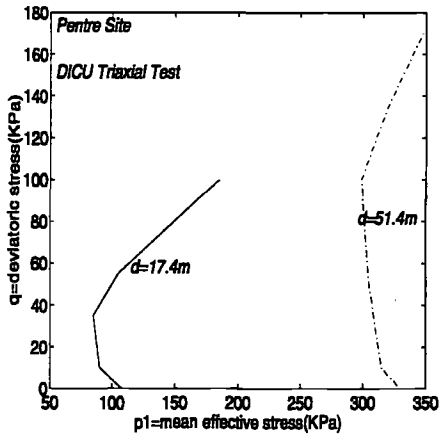

Figure 2.36: The stress path p'-q for various depths at the Pentre site (after Lambson et al, 1992)

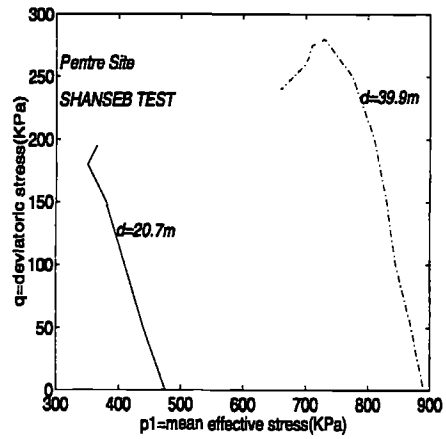

Figure 2.37: Isotropically consolidated-undrained (SHANSEP) stress path of Pentre site (LDPT database-Lambson et al, 1992)

is greater than unity (or the effective horizontal stress is greater than the effective vertical stress).

Secondly, the stress path plotted on Fig.2.36 have been obtained from triaxial tests on disturbed undrained samples of the Pentre clay. Hence, one might expect that the stress history of those samples may have been altered. The latter is verified by means of Fig.2.37 which indicates that the stress path of the samples which are subjected to some pre-stress to remove the sampling alteration stress, have shown quite different behaviour which are expected to be true response of normally consolidated Pentre soil. Although at certain depths there are some tendencies towards increase of shear stress, however, these are not significant and in-situ behaviour can be considered as contractant with moderate degradation.

The OCR profile measured at NC Pentre site by Lambson et al, (1992) indicates that the over-consolidation ratio is greater than unity (which means that the soil has been pre-loaded to some extent in the past, due to some possible geological changes or water level variations.

Therefore, assuming the greater value of t_{peak} from Eq.2.45, will be valid in this case. The latter can also be verified by dividing the measured peak skin data by the S_u profile. The ratio of $N_s = \frac{t_{peak}(Z)}{S_u(Z)}$ derived from tests and Eq.2.45 are plotted in Figs.2.70 and 2.71 for Pentre and Tilbrook sites, respectively. As shown the theoretical N_s ratio varies with depth between 0.1 and 0.85 for OC and 0.4 and 0.8 for NC sites, respectively. These results are in rather good agreement with the measured ones.

Thus the stress path plot of the soil could determine the use of either sign in Eq.2.45 as described in Sec.2.2.3. The post-peak skin friction resistance of the pile-soil system may be assumed to be less than or equal to the peak skin friction value. The $\alpha_{res} = t_{res}/t_{peak}$ is assumed simply

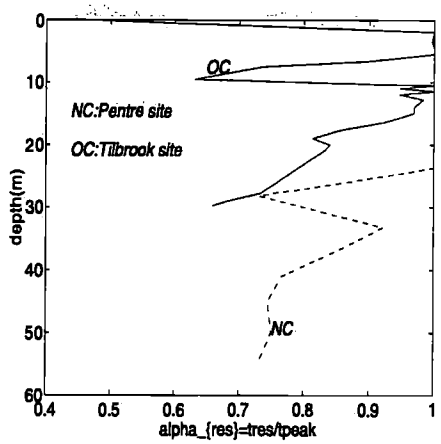

Figure 2.38: Residual skin friction α_{res} ratio derived from LDPT database (Clarke et al, 1992) vs. assumed range

to vary linearly from 1.0 near the soil surface to about 0.7 near the pile tip. This simplifying assumption is based on the cyclic degradation of the upper soil near the ground level during pile installation. Fig.2.38 compares the measured and assumed trends of α_{res}. The measured trends, as shown between about 0.97 near the surface to about 0.65 near the pile tip.

The post-peak softening behaviour due to slippage or rotation of principal stress axes, as

Table 2.1: The polynomial coefficients of (t-z) curve computed according to disk model of pile-soil system

polynomial coefficient	
α_1	$\beta - 0.83$
α_2	$\beta - 0.67$
α_3	-11.0670
α_4	47.8700
α_5	7.2700
α_6	0.5384
α_7	-0.0182
α_8	0.0002

described in Sec.2.2.2, may be calibrated either against direct shear tests results or against the (t-z) probe data during pile tests. The relative pile-soil displacement from the peak point until reaching the residual skin friction resistance may be correlated numerically as follows:

$$\delta z = z_{slip} - z_{rb} \tag{2.94}$$

Hence, using Eqs.2.16 or 2.17 and accounting for slippage by inclusion of z_{slip} as a function of $t_{peak} - t_{res}$ determined from (t-z) probe data (Fig.2.6), a numerical post-peak correlation may

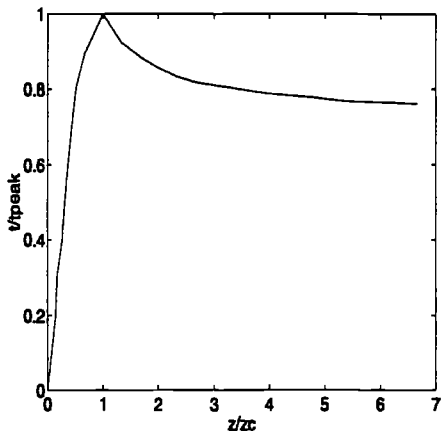

Figure 2.39: The post-peak softening due to slippage and/or rotation of principal stress axes

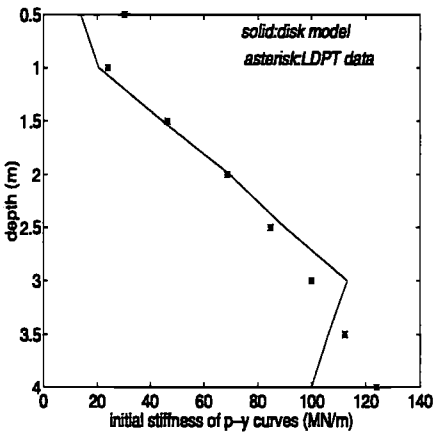

Figure 2.40: Comparison between the measured(Clarke et al, 1992) and the predicted initial stiffness of (p-y) according to the lateral disk model

be established as follows:

$$t = t_{peak}[1 - \frac{0.3Z}{Z_{tip}} \sum_{i=3}^{8} \frac{\alpha_i (z - z_c)^{i-3}}{z_{res} - z_c}] \tag{2.95}$$

where Z_{tip} = the pile tip depth or penetration depth and α_i are the fitted 5th order polynomial coefficients given in Table.2.1.

2.4.2 Calibration of the lateral disk model

The (p-y) disk model presented in Sec.2.3.3 is calibrated against the large diameter pile test results available from Tilbrook and Houston sites.

The effects of the previous (cyclic) lateral loading during past storms or earthquakes may be accounted for by either modifying the static Eq.2.78, (see Chapter 4), for such cyclic loading effects, or through introduction of the gap factor (ζ_i) which has been modelled in Eq.2.78. The effects of pile driving on the static lateral response of the pile-soil system may be considered through adding the initial skin friction on the pile shaft. The initial (residual) skin friction induced by for instance pile driving process may influence the initial stiffness of the pile under axial loading.

The (intact) initial stiffness of the pile-soil disk model is given in Eq.2.81. A good correlation is obtained between the initial stiffness of the (disk) (p-y) model and the test results (see Fig.2.40).

The peak lateral resistance of the pile-soil system calculated from Eq.2.74 is compared with the measured peak resistance results on Figs.2.42 and 2.43. As shown, satisfactory correlations are

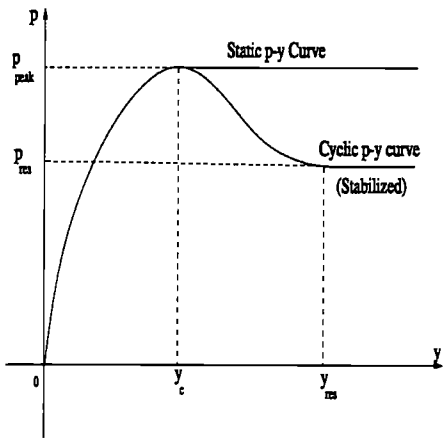

Figure 2.41: The characteristic shape of the modified post-peak (p-y) curves for cyclic effects

obtained between the disk model and the test results.

The correlation between the lateral disk model and the LDPT test results at large displacements particularly at shallow depths, indicates a post-peak softening (degradation) behaviour for the stiff and heavily overconsolidated soils even under static loading. Thus Eq.2.78 may be empirically calibrated to simulate the brittle post-peak behaviour of stiff clay which are often encountered in offshore North sea sites. Fig.2.41 illustrates the proposed modification of the original (p-y) curve derived in Sec.2.3.3 for non-degrading soils.

The calibrated (p-y) relationship may be written as follows:

$$p = f(y - y_c)(Z) \qquad ; y_c \geq y \leq y_{res} \tag{2.96}$$

$$p = p_{res}(Z) \qquad ; y \geq y_{res} \tag{2.97}$$

where $p_{res}(Z)$ = the residual lateral resistance of the pile-soil system for stiff OC soil, which varies with the soil depth. For depth below Z_r, as described in Sec.2.3.1, no post-peak degradation may be considered :

$$p_{res}(Z) = p_{peak}(Z) \qquad ; Z \geq Z_r \tag{2.98}$$

2.5 Computational procedure

The computational steps are summarized as follows:

1) simulation of the pile-soil behaviour by means of (t-z) and (p-y) interaction curves described above

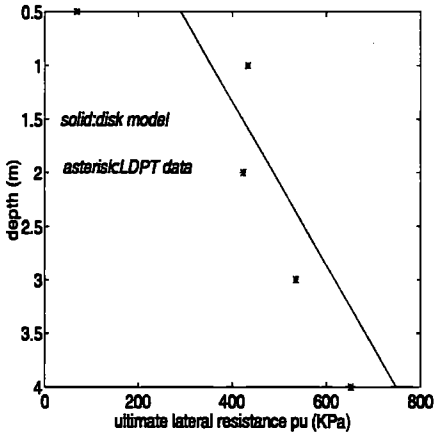

Figure 2.42: Comparison between the measured (Clarke et al, 1992) and the predicted p_u at Tilbrook site according to the lateral disk model

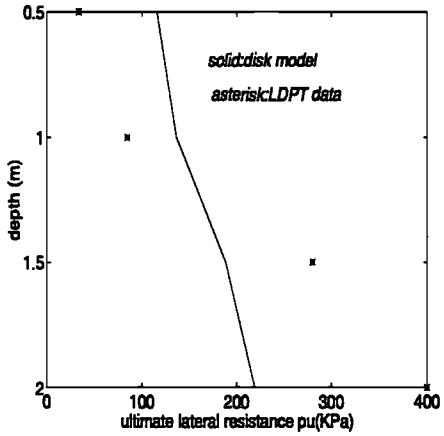

Figure 2.43: Comparison between the measured (Dunnavant et al, 1989) and the predicted p_u at Houston site according to the lateral disk model

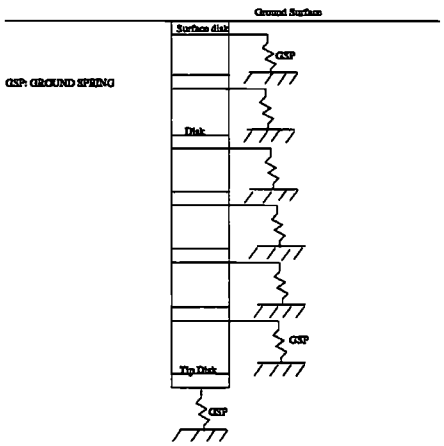

Figure 2.44: A finite element model of the pile-soil system

2) modelling the pile by means of two node beam elements (Fig.2.44)

3) using an incremental loading scheme for the analysis of the case

The (t-z) and (p-y) data are generated by FORTRAN program GENSODM and other MATLAB programs(see Emami, 1998) and incorporated into a nonlinear FE analysis program USFOS (Søreide et al, 1994) as a number of uncoupled non-linear spring/disk elements. The pile element model can be generated either manually or automatically by the aid of computer program PREFRAME (Dnv, 1992).

The solution approach may be a pure incremental method or combined with iterations. An advanced arc-length technique (Crisfield, 1991) is used for numerical solution of the system which is described in Chapter.3.

2.6 Verification of pile-soil interaction models(case studies)

Reliable application of the described pile-soil models would require a number of case studies. Through such case studies, the predictive ability of various (t-z) and (p-y) models, as described in secs.2.2.1 to 2.3.4, may be assessed and some practical recommendations may be proposed.

In the following subsections, all together five cases will be studied which comprise, respectively:

1) A static compression pile test at Pentre site

2) A static compression pile test at Tilbrook site

3) A static tension pile test at Tilbrook site

4) A static lateral pile test at Tilbrook site

5) A static lateral pile test at Houston site

The reason for selection of these test cases and an overview of the soil conditions at each site is give in the following subsection.

2.6.1 Selection of test cases

After a survey of several large diameter pile tests (LDPTs) which were carried out in the recent years in the North sea and the Gulf of Mexico regions (UK and US) a total number of five tests were selected.

The selection of the LDPTs were based on the following criteria:

. Pile size (diameter)

. Pile depth (length)

. Quality of the tests

. Soil type

. Undrained shear strength of the soil (Su)

. Overconsolidation of the soil (OCR)

. Plasticity of the soil (PI)

The selected test piles had diameters in the range of 0.76m-1.22m which were comparable to those used for the platforms in the North sea, where pile diameters of 2 to 3 m are common.

Pile length less than 30m is not sufficient practically to represent the offshore pile behaviour under axial loading. However, in the case of lateral loading this restriction may not be applied, since the soil resistance may not be utilized in deeper depths and thus increasing the pile length will have virtually no significant impact on its lateral capacity.

The soil type in the selected sites were considered to be predominantly silty clay to clayey silt with very little gravel/cobble portions (Lambson et al, 1992). The details about the mineralogy of Pentre, Tilbrook and Houston sites have been reported by Lambson et al, (1992) and Dunnavant et al, (1989). The soil profile of Pentre site contained higher silt content than Tilbrook and Houston sites which are presented in Figs.2.51 and 2.57. The studied sites were different in terms of isotropy. The soil at Pentre and Houston sites were considered to be more uniform than Tilbrook site (Lambson et al, 1992 and Dunnavant et al, 1989).

The average undrained shear strength of soil Su varies from over 100 KPa (stiff) for Pentre site to about 450KPa (very stiff) for Tilbrook Site. The stress history of the selected sites were quite different while Tilbrook site and Houston sites were heavily overconsolidated, Pentre site was essentially normally consolidated.

The overconsolidation ratio (OCR) profiles are presented in Figs.2.47, 2.53 and 2.59. As it will be discussed later, studying the effective stress path p'-q or similarly the lateral earth pressure would be useful to understand the stress history of each site. From these kind of information one might gain a little more insight into the pre-loading behaviour of the soil and be able to predict correctly the principal stress directions at the pile- soil interface prior and during the loading. To enable the reader to comprehend the lateral earth pressure factor, the effective overburden pressure (vertical stress) parameter is examined for each site in the following sections.

The plasticity index of soil is considered to be one of important parameters to describe the soil condition for various sites. The selected sites, Pentre, Tilbrook Grange and Houston had mean PI about 30 percent −40 percent which indicated that they are not too plastic (Lambson et al, 1992).

The soil profiles which are presented in following subsections 2.1 to 2.3 are derived from the LDPT data (Lambson et al, 1992), Clarke et al, (1992) and Dunnavant and O'Neill, (1989).

2.6.2 Pentre site

The grain profile of soil at Pentre site as shown on Fig.2.45 comprises several silty clay to clayey silt layers (with varying silt content, which is maximum at the upper layers near the soil surface and decreases with the depth and also becoming much stiffer. However, occurrence of a thick silty clay has been detected below depth 45m.

The plasticity index for Pentre site is presented on Fig.2.46 , PI ranges between 10 percent −30 percent which seems higher with respect to the clay sized fraction which is below 20 percent. The latter has been attributed to the geological features of the site (Lambson et al, 1992).

The overconsolidation ratio (OCR) of Pentre site has been estimated from PI (Plasticity index) correlation and also directly from oedometer tests. Fig.2.47 shows the OCR profile obtained for the Pentre site. It is seen that OCR decreases rapidly from about 5.2 near the surface to about 1.2 at 60m depth.

The undrained shear strength (Su) profile for Pentre site is shown in Fig.2.48. The (Su) profile is selected from tests on undisturbed and unconsolidated samples in accordance with API RP2A 1993 recommendations. The measured trend on Fig.2.48 shows a nearly linear variation with the depth. An idealized line is fitted to the test data as shown Su varies from about 50KPa near the top of cased part of the pile (15m below ground level) to about 140KPa at the pile tip.

The average bulk unit weight of the soil at Pentre site is about 19.46 KN/m3.. ϵ_{50} of the soil at Pentre which has been derived from the triaxial test results (Lambson et al, 1992) varies between 0.05 near the ground level to about 0.003 at 51.4m depth(see Fig.2.49).

The shear modulus of soil G has been plotted in Fig.2.50. The selected data has been taken from pressuremeter measurements and compared with the (t-z) probe (Lambson et al, 1992). The G value varies from about 28MPa near the ground level to about 65MPa close to the base.

2.6.3 Tilbrook Grange site

Fig.2.45 presents the soil description at the Tilbrook Grange site tested by BP Int. and NGI. The stratigraphy of the site is rather uniform with two main strata, an 18m lowestoft Till overlying a

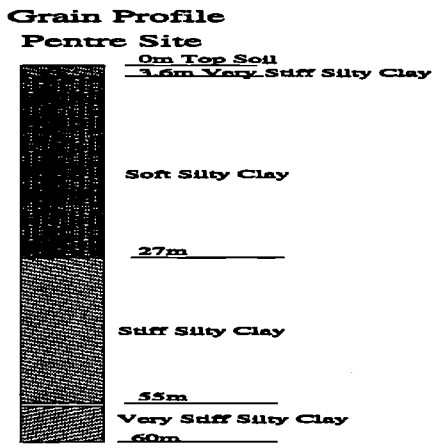

Figure 2.45: Grain profile of soil at Penter site

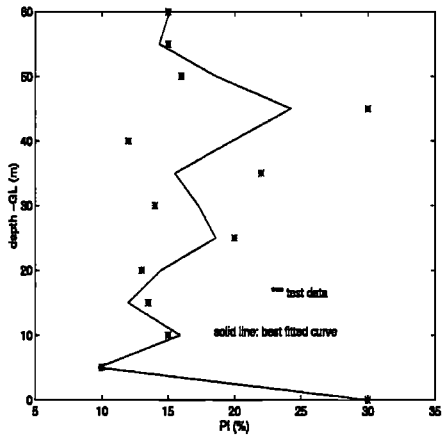

Figure 2.46: Plasticity Index (PI) Profile of Pentre Site

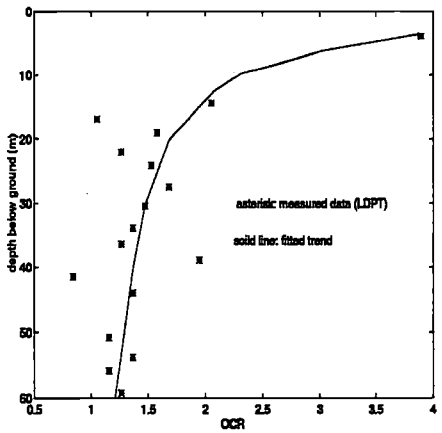

Figure 2.47: Over-Consolidation Ratio (OCR) Profile of Pentre Site

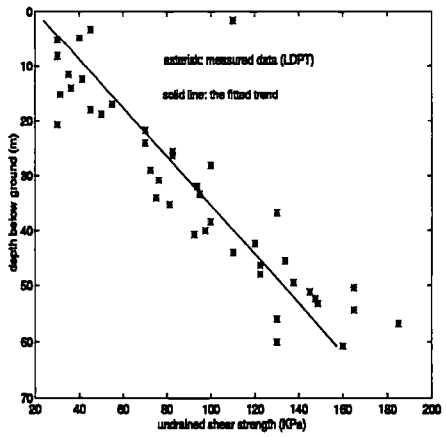

Figure 2.48: Undrained Shear Strength (SU) Profile of Soil at Pentre Site

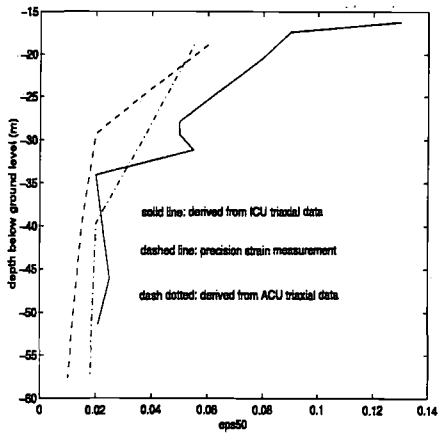

Figure 2.49: ϵ_{50} Profile of NC clay at Pentre Site

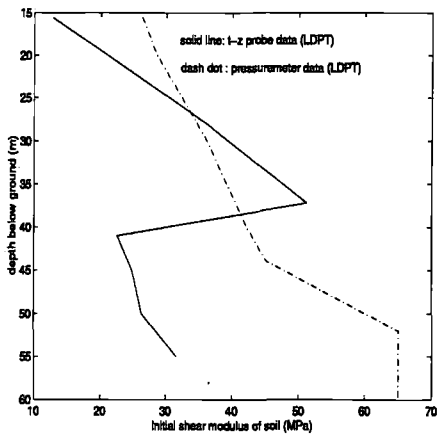

Figure 2.50: Profile of Soil's Shear Modulus G at Pentre Site

lower and thicker Oxford clayey stratum. The upper stratum is considered to be clay dominated (Lambson et al, 1992). The upper layers consist of very stiff silty clay with medium plasticity index (20% – 30%) (see Fig.2.52). Meanwhile the lower stratum comprises a hard fissured clay with silt partings with high plasticity index (20% – 40%).

The OCR profile for the Tilbrook has been given in Fig.2.53, it decreases from nearly 30 at about 2m below the soil surface to about 3.2 near the pile tip. It is therefore considered as heavily overconsolidated (OC) site.

Fig.2.54 summarizes the undrained shear strength (Su) data (Lambson et al, 1992) for Tilbrook site. The measured S_u trend shows a large variation of (Su) with the depth. The idealized variation of (Su) is fitted to the test data in Fig.2.54. The average Su is more than 400KPa which indicates the clay type is very stiff.

The average total unit weight of soil is about 21.2 KN/m3. ϵ_{50} of the soil at Tilbrook site which has been derived from the triaxial test results (Lambson et al, 1992) varies between 0.023 near the ground level to about 0.007 at 51.4m depth (see Fig.2.55).

The shear modulus of soil G is presented in Fig.2.56. The G data has been chosen from the pressuremeter measurements (Lambson et al, 1992) and compared with the (t-z) probe (Clarke et al, 1992). The G values from seismic cross-hall tests were several times higher than G profile derived from (t-z) probe.

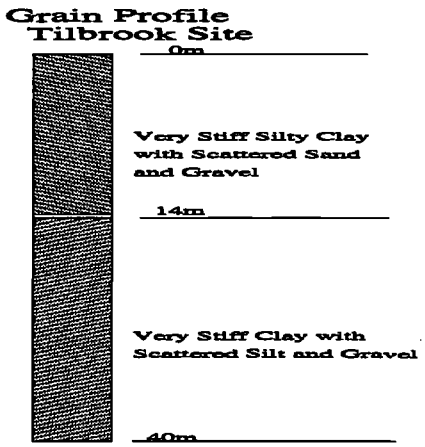

Figure 2.51: Grain profile of soil at Tilbrook site

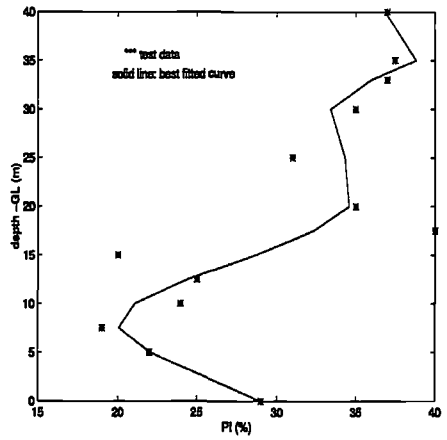

Figure 2.52: Plasticity Index (PI) Profile of Tilbrook Site

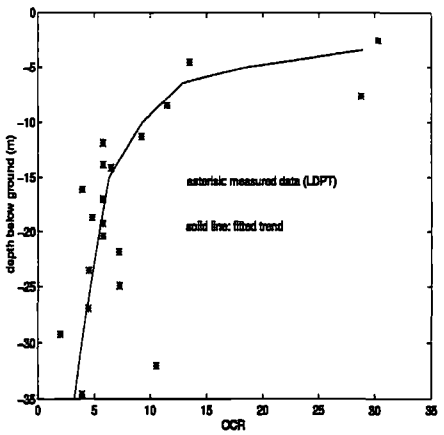

Figure 2.53: Over-Consolidation Ratio (OCR) Profile of Tilbrook Site

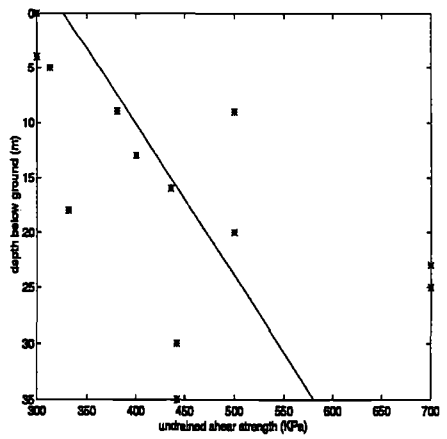

Figure 2.54: Undrained Shear Strength (SU) Profile of Soil at Tilbrook Site

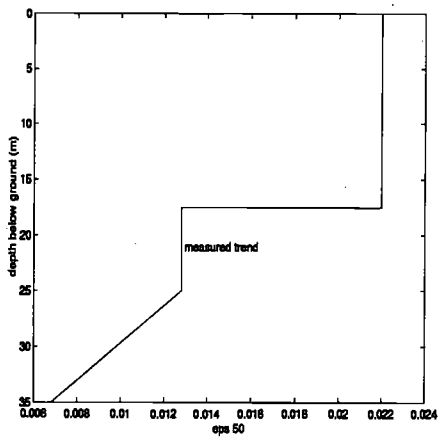

Figure 2.55: ϵ_{50} Profile of OC clay at Tilbrook Site

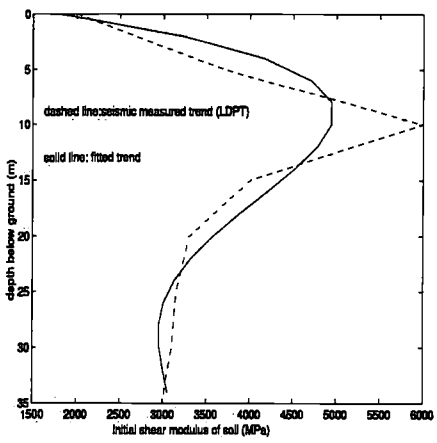

Figure 2.56: Profile of Soil's Shear Modulus G at Tilbrook Site

2.6.4 Houston Site

A brief description of the soil input data used for the comparative study of the Houston pile tested by Dunnavant and O'Neill, (1989) is given in this section. The details of the test are given by Dunnavant and O'Neill, (1989).

The grain profile of the soil is plotted in Fig.2.57 which represents a stiff clayey soil with variation of silt and scattered sand. The plasticity index PI of the soil is derived based on the correlations given by Ladd and Foott, (1974) and Das, (1985) for various clayey soils. This correlation is further calibrated against Pentre and Tilbrook LDPT data. As shown on the soil's structure's profile this site has higher plasticity index in average than Pentre and Tilbrook sites.

The OCR and Su profiles are shown in Figs.2.59 and 2.60, respectively, which indicate that the clay type of Houston site is stiff and heavily overconsolidated. OCR of this site varies from about 30 near the soil surface to about 6 close to the pile tip. The strain at half the maximum principal stress ϵ_{50} as plotted in Fig.2.61 does not vary considerably with the depth and in average is about 0.0125 which is somewhat higher than the recommended values by API RP2A 1993 and Reese et al., (1975).

The corresponding average unit total weight of soil is about 21MN/m3. The shear modulus profile for Houston site has been derived from (p-y) probe data based on Eq.2.82(see appendix.A). G varies between 20MPa near the surface to 120MPa at the maximum penetration depth.

Table 2.2: Description of the layouts of the LDPT test piles

LDPT test Pile	O.D (m)	t_w (m)	L (m)	d_p (m)
Pentre(NC)	0.762	0.015	58.5	55.0
Tilbrook(OC)	0.762	0.030-0.040	33.5	30.0
Houston(OC)	1.220	0.016	11.4	11.0

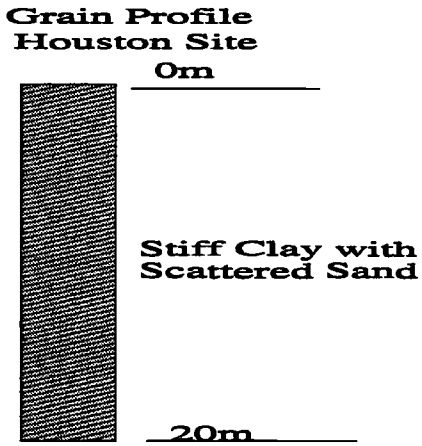

Figure 2.57: Grain profile of soil at Houston site

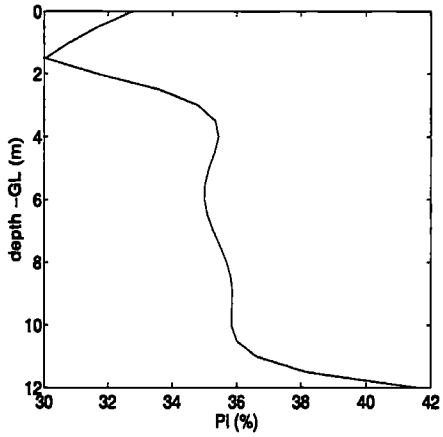

Figure 2.58: Plasticity Index (PI) Profile of Houston Site

2.6.5 Summary of pile's structural description

The structural characteristics of the selected piles resembled those of the piles used as foundation of North sea offshore Jacket platforms.

Pentre pile has been tested as cased at its upper 15m length. Therefore soil resistance is not considered for this part. Details about fabrication and calibration of piles are given by (Cox et al, 1992), (Clarke et al, 1992) and (Karlsrud et al, 1992). Fig.2.63 gives a schematic view of the Pentre, Tilbrook and Houston piles layouts. Table.2.2 describes the outer diameter, thickness and the length and penetration depth of these three LDPT piles.

2.7 Axial loading cases

Three case studies of Pentre pile in compression, Tilbrook pile in both Tension and compression are presented in the following subsections. The results of predictions by using different methods described in Secs.2.2 and 2.3 are compared with the pile test results (Clarke, 1992). Both (t-z) and the overall axial behaviour of the pile-soil systems are examined.

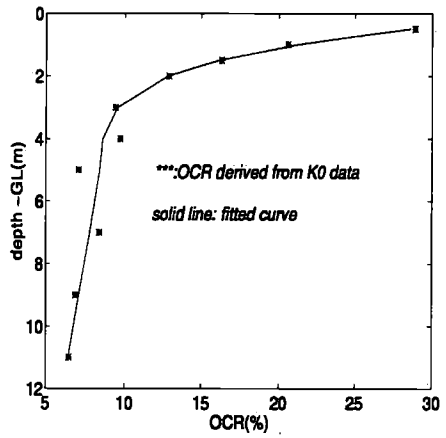

Figure 2.59: Over-Consolidation Ratio (OCR) Profile of Houston Site

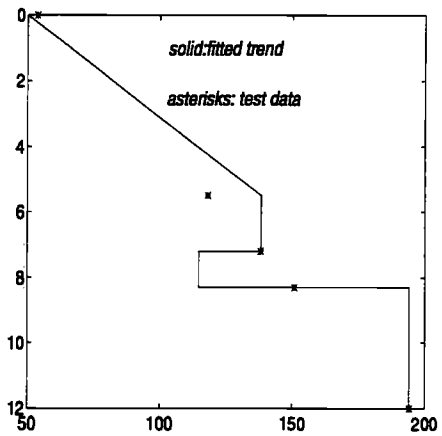

Figure 2.60: Undrained Shear Strength (SU) Profile of Soil at Houston Site

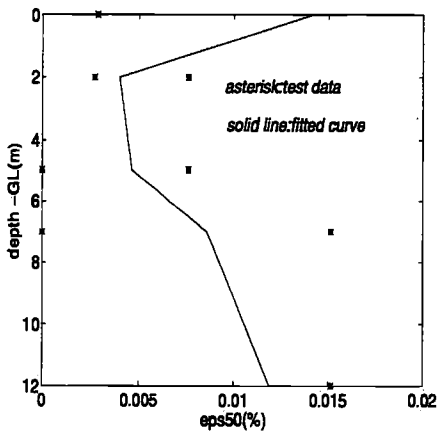

Figure 2.61: ϵ_{50} Profile of OC clay at Houston Site

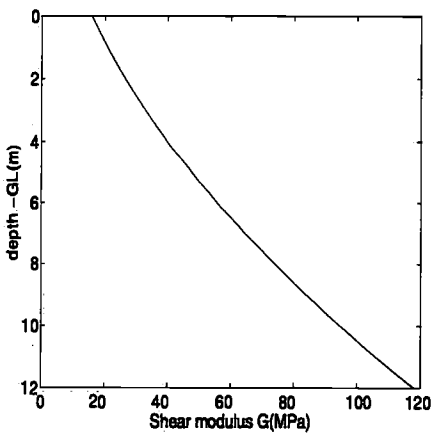

Figure 2.62: Profile of Soil's Shear Modulus G at Houston Site

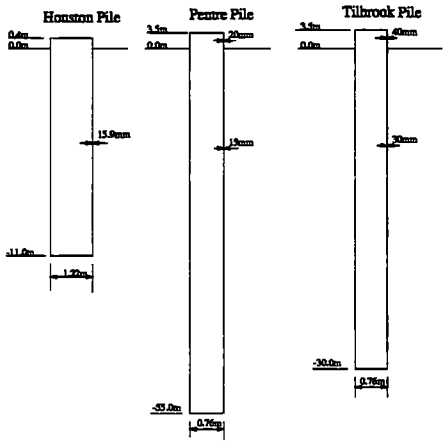

Figure 2.63: Pile Layouts at Houston, Tilbrook and Houston sites

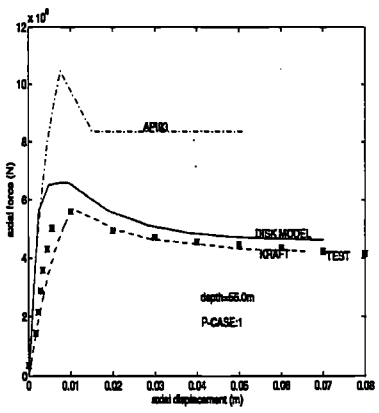

Figure 2.64: Predicted versus measured (t-z) response of the pile-soil system at Pentre site

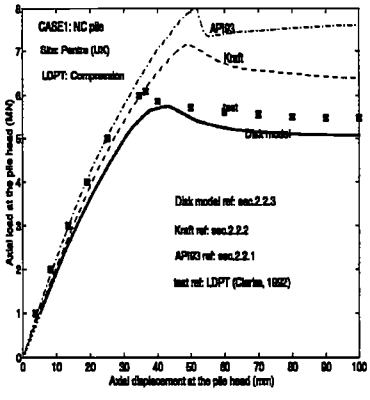

Figure 2.65: Predicted versus measured axial load-deflection response for NC pile at Pentre site

2.7.1 Pentre pile

2.7.1.1 (t-z) response

Figs.B.1 to B.17 compares the generated (t-z) curves for Pentre (NC) site with the measured curves at different depths. The measured (t-z) curves have distinct shapes in the deeper depths (below z=-21m), with a prominent peak and a clear strain softening behaviour at the post-peak region. Meanwhile the (t-z) curves probed (Cox et al, 1992) at the upper depths (near the surface) have no well defined (distinct) shape. The latter curves have peaks close to their nominal residual capacities at large displacements without any appreciable strain softening. This might be due to cyclic degradation of upper soil layers caused by pile driving. The latter will be briefly discussed within the context of the dynamic modelling of pile-soil in Chapter 4.

It is observed that the (t-z) response of Pentre pile has been overpredicted by the (t-z) method recommended by API RP2A 1993. The corresponding ultimate capacities are about 30 to 50 percent in average higher than the measured ones. This can be easily explained by Eq.2.5, in which for NC soils with $\psi = S_u/p'$ ratio far less than unity it results in a t_{peak}/S_u ratio near the unity. In this case, the ratio ψ is about 0.27 which resulted in t_{peak}/S_u ratio about 0.97 while the average measured t_{peak}/S_u as shown on Fig.2.70 is about 0.59. Meanwhile the average t_{peak}/S_u ratio obtained from Eq.2.45 for the lower and upper bounds of the disk model as shown on Fig.3.4.3.3 are about 0.60 and 0.68 which are very close to the actual measured value. It is seen in Fig.2.64 that the disk model has fairly well predicted the trend and the average values far better than API 93 but the local responses are stiffer near the surface, softer in the intermediate depths and closer to the measured trend at the deeper depths near the pile tip.

The presented Kraft (t-z) curves in Fig.2.64 are calculated based on an idealized trend to the measured LDPT data(Clarke, 1992) to see the match between the predicted (t-z) shape and the measured curves. The comparison of the predicted peak and residual skin friction values of Pentre pile according to Kraft et al, (1981) are discussed by Gibbs et al, (1992).

In this Chapter the (t-z) curves referred to as Kraft et al, (1981) are calculated according to the method described in Sec.2.2.2. It appears that (t-z) curves generated by the theoretical model of Kraft do match well the test results for Pentre pile. The discrepancies observed in Fig.2.64can be attributed to the idealization of the test data and the inherent bias in the concentric model's assumptions (see Sec.2.2.2 and Kraft et al, 1981).

Table 2.3: The load-displacement response of the Pentre pile under compression test

Method/Capacity	**Peak Capacity** (MN)	**Residual Capacity** (MN)	**Bias**
API RP2A 1993	8.00	7.63	1.31
Kraft (t-z) model	7.16	6.38	1.18
Disk model	5.74	5.07	0.94

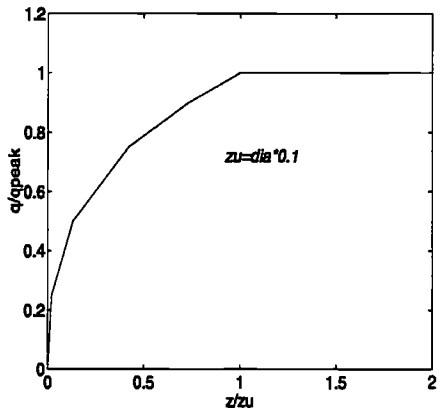

Figure 2.66: The characteristic shape of API's (q-z) curve

2.7.1.2 Global pile response

The global load-deflection response of the NC pile at the Pentre site which is predicted by the (t-z) methods described in Sec.2.2 are compared with the measured response in Fig.2.65. It can be seen that various approaches have well predicted the initial response. However, Kraft's (t-z) and the presented disk models have slightly underpredicted the initial stiffness of the pile. The amount of discrepancies have considerably increased by increasing the pile's axial load above $3MN$ level. Above this level, Kraft's proposed model has provided rather stiffer response compared with the disk model.

Near the failure the latter response curve has become much softer due to successive yielding of soil. In the post-peak region there is considerable difference between the different response curves. The post-peak softening simulated according to disk model is gradual while a slightly steeper degradation can be observed in the response of Kraft's (t-z) model. In contrast to the Kraft and disk models, the predicted residual response of the Pentre pile based on the API model is quite different. The response predicted according to API (t-z) model softens very suddenly just after peak and then it hardens steadily due to full mobilization of the shaft skin friction prior to that (i.e. at the peak) and then drop in the shaft skin friction to its residual limit which occurs simultaneously with increase in the pile tip displacement and gradual mobilization of it's capacity.

In overall the axial load-deflection behaviour of the Pentre pile has been very closely predicted by the presented disk model. While the recommended (t-z) model by API RP2A 1993 has provided the stiffest response compared with the measured and other predictions. The corresponding peak and residual capacities have been given in Table.2.3. As shown the bias in computed peak capacity is the highest for API 93 (t-z) model about 1.31 compared with 1.18 for Kraft's (t-z) model and 0.94 for the current disk model. Note that the bias throughout this Chapter is referred to the ratio of the predicted to measured capacity.

2.7.1.3 tip (q-z) response

To be able to compare the performance of the (t-z) models, the load-deflection response of the piles in this Chapter are computed according to API RP2A 1993 model. Fig.2.66 shows the characteristic shape of the API's recommended (q-z) curve. As shown, the yield gradually occurs at the pile tip with the first soil yield at a displacement of about 0.002 and the ultimate yield at a displacement of about 0.1 times the outer diameter of pile.

The peak tip resistance q_{peak} for non-cohesive soils such as sand and gravel are obtained as:

$$q_{peak,nc} = N_q p' \tag{2.99}$$

where p' represents the effective overburden pressure at the pile tip and N_q denotes an empirical tip resistance correlation factor which is given as a function of the pile-soil friction angle δ according to API RP2A 1993. N_q varies from 8 to 50 for δ varying from 15 deg to 35 deg. It is known from soil mechanics experiments(Nordal et al, 1989) and also the Mohr-Coulomb criteria that the pile shaft friction and tip resistance may not vary linearly with the effective overburden pressure of soil. After a certain depth given by the practice codes such as API, the peak skin friction and the tip resistance may reach a limit.

For very long piles, the effective overburden pressure p' at the pile tip can be very large and hence applying Eq.2.99 might overestimate $q_{peak,nc}$. API RP2A 1993 specifies a limit for q_{peak} as 12MPa.

For cohesive soils such as clay and silty clay, the peak tip resistance of the pile is determined as follows:

$$q_{peak,c} = c_{tip} S_u \tag{2.100}$$

where c_{tip} is given as 9 according to API RP2A 1993 and S_u denotes the undrained shear strength of the soil. c_{tip} is empirically obtained and might vary depending on the soil's brittleness and overconsolidation factor. For soft clayey soils, a value of 9 is relevant while for heavily overconsolidated stiff clays such as those encountered in the North-sea region a value of 12 seems to be more appropriate(see for e.g. Janbu, 1985, Clarke et al, 1992, Lacasse and Nadim, 1996).

2.7.2 Pentre pile in Tension

2.7.2.1 (t-z) response

The discussion of the local (t-z) response is given in previous subsection.

2.7.2.2 Global pile response

To investigate further the capability of the presented (t-z) models in tension, the Pentre pile is considered here without end-bearing. Since there has not been any direct measurement of the tensile capacity of the Pentre pile available, the measured compressive response curve as presented in Fig.2.65 is used to derive the tensile capacity by simply subtracting the measured end-bearing(Clarke et al, 1992) from it. It is therefore assumed here that the contribution of

Table 2.4: The load-displacement response of the Pentre pile under tension test

Method/Capacity	Peak Capacity (MN)	Residual Capacity (MN)	Bias
API RP2A 1993	7.75	6.97	1.48
Kraft (t-z) model	6.84	5.69	1.31
Disk model	5.42	4.38	1.04

the pile-tip resistance may be neglected in tension.

The corresponding measured and computed response curves are plotted in Fig.2.67. As observed, all three models have well predicted the initial response of the pile-soil system under tensile loading. The discrepancies have appeared above a threshold of 1MN load level. This point is the onset of the local yield at pile-soil element level (i.e. initial (t-z) yield at or near surface). As the axial loading increases towards the failure, the amount of discrepancies increase rapidly. However, the disk model response becomes gradually softer compared to the predicted response curves by Kraft and API 93 models, which become increasingly stiffer until reaching the peak. The proximity of the disk model prediction to the derived (measured) response is even better than the previous compressive case. This may indicate that some of the discrepancy observed in Fig.2.65 the compression case might have been due to the uncertainty(bias) involved with the prediction of end bearing behaviour of the Pentre pile (which were used according to API RP2A 1993).

At the post-peak region very significant discrepancies is observed between the predicted residual capacities according to API93 and Kraft (t-z) models. While the Kraft (t-z) model has simulated a considerable post-failure softening after the full mobilization of the shaft's frictional capacity, the API RP2A (t-z) method has given a sudden steep drop towards a constant residual axial capacity due to the shape of it's (t-z) curves as shown in Fig.2.64.

The associated peak and residual capacities are given in Table.2.4 and the corresponding bias with each peak is calculated against the measured one. As seen, the amount of bias is greater than 1.0 (about 1.04) for disk model in the case of tensile loading compared with the value 0.94 obtained for the compression case. The bias again is larger for API 93 (t-z) model about 1.48 compared to Kraft's (t-z) model which is approximately 1.31. The design implication of such large bias in the case of NC clay may be to use an alternative effective stress based method as disk model or modify the current API RP2A 1993 formulation Eq.2.5 as recently discussed by other authors (Lacasse and Nadim, 1996 and Horsnell and Toolan, 1996). It has to be noted that the partial safety factors such as those given by API code are not applied for the pile capacity values obtained throughout this Chapter.

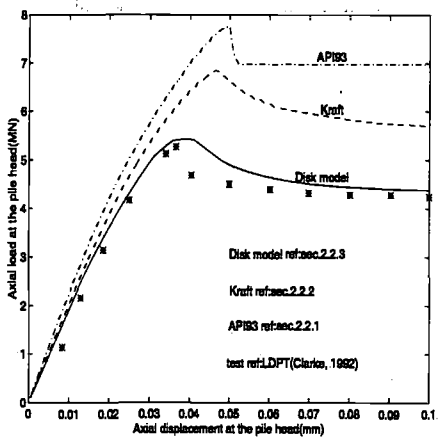

Figure 2.67: Predicted versus measured load-deflection response of Pentre pile (NC) in Tension

2.7.3 Tilbrook pile in compression

2.7.3.1 (t-z) response

Load transfer-pile displacement (t-z) curves evaluated at several depths for the OC pile at the Tilbrook Grange site are presented in Fig.B.18 to B.34 in conjunction with the measured curves. The scatter is very wide at the shallow soil depth down to the 12m below ground level.

Both API RP2A and disk model have very significantly overestimated the axial pile-soil resistance at the these depths (0-12m). However, the misleading fit between the Kraft's (t-z) curves in Figs.B.18 to B.34 is because of using the measured trend data instead of λ or α methods as presented previously by Gibbs et al, 1992.

The measured peak skin friction(Clarke et al, 1992) is an order of magnitude less than what can be predicted rationally based on empirical API RP2A 1993 model or the presented disk model based on soil mechanics theory.

It may be concluded that the difference is due to the other pre-loading degradation effects such as pile driving effects, whip phenomenon as briefly discussed by previous authors such as Hamilton and Dunnavant, (1992), Hobbs, (1992) and Gibbs et al, (1992) or possibly due to cyclic degradation caused by pile driving which will be discussed briefly in Chapter.4.

The following tensile pile measurements by Cox et al, (1992) has confirmed this to a large extent. The latter case will be studied in the following subsection. Gibbs et al, (1992) has concluded that due to pre-loading degradation the peak skin friction capacity of Tilbrook Grange (OC) pile has dropped to its residual capacity. Other authors such as Randolph, (1992) have analyzed this based on the effective stress basis at the pile-soil interface and concluded that some changes in the principal stress axes of soil may have occurred due to the pile installation.

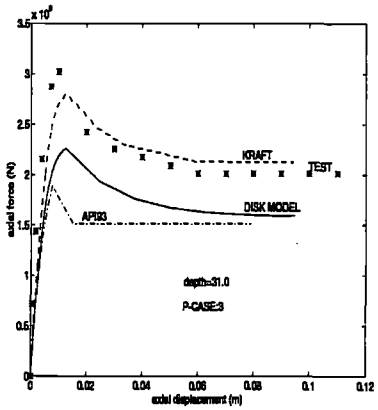

Figure 2.68: Predicted versus measured (t-z) response of the pile-soil system at Tilbrook site in compression

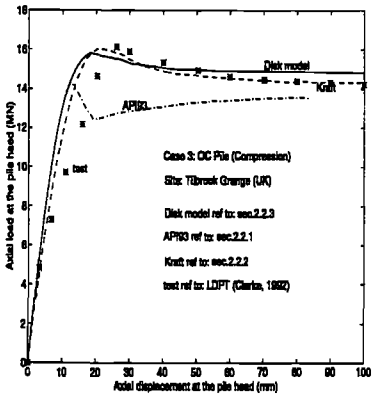

Figure 2.69: Predicted versus measured axial load-deflection response for OC pile at Tilbrook site in compression

In contrast to the upper soil levels, at the intermediate depths particularly (from 12.0m to 19.0m) the correspondence between the computed and the measured (t-z) curves is good. From depth 22.0 to 30.0m near the pile tip the measured skin friction capacity is much larger than the predicted values. Fig.2.71 compares the predicted and the measured t_{peak}/S_u ratios with the depth for Tilbrook pile. The average measured t_{peak}/S_u ratio is about 0.38 compared with the mean ratios of 0.41 and 0.61 obtained for the lower and upper bounds of the presented disk model. The average t_{peak}/S_u of API 93 model computed according to Eq.2.5 is about 0.36 which is very close to the test result. Eq.2.5 for $S_u/p^{'}$ ratios far greater than 1.0 gives smaller t_{peak}/S_u than 0.5 which is a reasonable agreement with the predictions of the disk model with two different set of upper and lower α and β soil parameters (see the appendix.A for the input data).

Table 2.5: The load-displacement response of the Tilbrook pile under compression test

Method/Capacity	**Peak Capacity** (MN)	**Residual Capacity** (MN)	**Bias**
API RP2A 1993	14.33	13.54	0.89
Kraft (t-z) model	16.04	14.32	0.99
Disk model	15.80	15.28	0.98

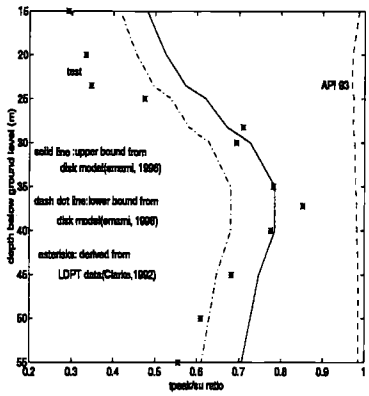

Figure 2.70: Predicted vs. measured t_{peak}/S_u for (NC) Pentre Site

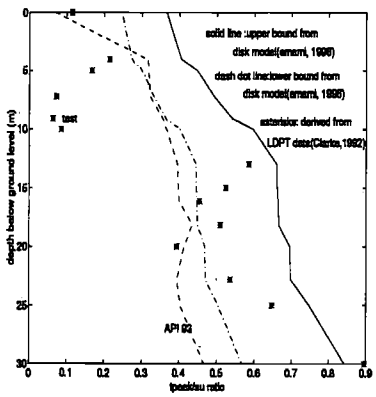

Figure 2.71: Predicted vs. measured t_{peak}/S_u for (OC) Tilbrook Site

2.7.3.2 Global pile response

The predicted versus measured global response of the Tilbrook pile under compression are summarized in Fig.2.69 and Table.2.5. As can be seen, there is a good match between the predicted responses and the LDPT data (Gibbs et al, 1992). However, as the load level exceeds the threshold of 5MN, the measured response appears to be softening which is associated with the local yields at the element level at a faster rate than what's anticipated by various predictive methods.

The latter may be related to the observed softer (t-z) response of the pile-soil at the upper layers near the ground level, which somewhat contradicts the general shape of the (t-z) curves as described in Sec.2.2

Despite softer pre-peak response, the near failure response of the Tilbrook pile has been well predicted by Kraft's (t-z) and the disk models. Although, API93 approach has resulted in a lower anticipated peak capacity, nevertheless the ultimate residual capacity has been well predicted at larger displacements near the 80mm. The latter observation can easily be interpreted by means of mathematical equations previously described in the Secs.2.2.1 to 2.2.3.

The API RP2A 1993 peak skin friction formulation (Eq.2.5) do somewhat underestimate the t_{peak} values close to the pile tip where $S_u/p^{'}$ ratio is much larger than 1.00, as shown in Fig.2.71. As seen, the average discrepancy at these depths (below 25m) is about 20-25%. Since the major contribution to the pile-soil's axial capacity in compression comes from these deeper depths near the pile's base, therefore one may expect such an underprediction of the peak axial resistance as observed which is about 5 percent in this case.

On the other hand, due to the compressibility of the pile (flexible pile $EI \neq \infty$ with an embedded length about 30m, the difference between the axial displacement at the top and the tip of

the pile will cause delayed phase in the full mobilization of the end-bearing compared to that of the pile shaft.

As shown on Fig.2.69, while the overall axial capacity of the pile-soil system drops at the peak point due to shear failure occurring at the interface after full mobilization of the frictional capacity throughout the pile, only a small portion of the pile's tip resistance which is about less than one third of it has been activated by moving end into the soil. Thus by passing the peak a gradual hardening occurs due to this activation. The slope of post-peak softening and subsequent hardening depends on a number of parameters such as the ratio between the tip maximum resistance or end-bearing capacity to the shaft resistance and also the shape of the response q-z curve. In the current study, the q-z curves for all cases are computed according to API RP2A 1993 recommendations. This is to enable us to investigate the performance of (t-z) models.

2.7.4 Tilbrook pile in tension

The incentives for studying the tensile behaviour of the large diameter pile at Tilbrook site have been:

. to assess the ability of various (t-z) methods in predicting the pile-soil behaviour in tension

. to study the skin friction differences between tensile and compressive loading of the pile

. to quantify (indirectly) the influence of the end- bearing on the overall axial capacity of the pile

. to verify the possible effects of soil degradation and excess pore water pressure generated by driving of the reaction piles during the earlier compression test

2.7.4.1 (t-z) response

The measured (t-z) curves for tensile loading of the Tilbrook pile are plotted in Fig.2.72 versus the calculated (t-z) curves. The predicted (t-z) curves have not shown any considerable post-peak degradation except at elevation -28m where also a typical (t-z) response for intermediate depths is observed. The ratio tres/tpeak ratio is about 0.80. The peak skin friction at the upper to intermediate layers have been mobilized at displacements between 20-35 mm.

The measured tensile (t-z) curves as shown, are closer to their predicted counterparts than the compressive ones. This may explain that observed scatter in the previous compression case might have been caused by other phenomena such as pile driving and prior cyclic degradation which will be discussed in Chapter.4.

It is observed that at depth about 6m below the ground level, the disk and API93 models have well predicted the response of pile-soil, whereas the Kraft's (t-z) method has largely overpredicted the tensile resistance of the pile-soil system. At 13m depth, the measured response is higher than

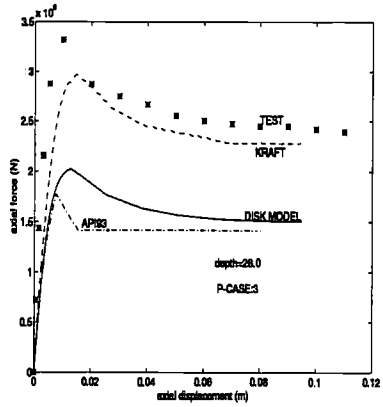

Figure 2.72: Predicted versus measured (t-z) response of the pile-soil system at Tilbrook site in Tension

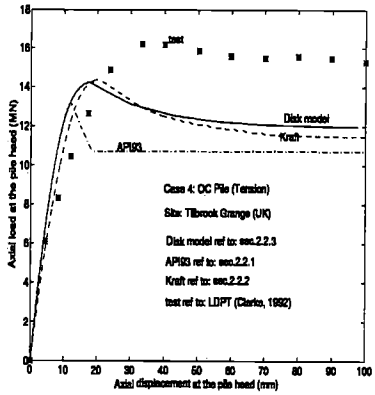

Figure 2.73: Predicted versus measured tensile behaviour of the pile at Tilbrook site

all other predictions. However the agreement between the predicted and the measured ultimate tensile resistance of pile-soil at 25m depth below the ground level is good.

Table 2.6: The load-displacement response of the Tilbrook pile under tension test

Method/Capacity	**Peak Capacity** (MN)	**Residual Capacity** (MN)	**Bias**
API RP2A 1993	13.15	10.71	0.82
Kraft (t-z) model	14.36	11.46	0.89
Disk model	14.24	11.98	0.88

2.7.4.2 Global pile response

The predicted and measured load-deflection curves of the tensile pile at Tilbrook site are compared in Fig.2.73 and Table.2.6. It is observed that the initial response(stiffness) of all the presented methods are very close to the measured one up to the load level about 6MN. However, the peak and the ultimate capacities of the pile-soil system have been significantly underestimated by all the applied (t-z) methods. Initially, it looks surprising that the measured tensile capacity of the OC pile(Clarke et al, 1992) is even higher than its compressive capacity, since it has been assumed that the tip resistance would be negligible in tension as confirmed by the measurements. However, further investigations showed that the possible effects of soil's consolidation and dissipation of the generated excess pore pressure in the elapse time between the previous compression test and the later tensile test would have caused an increase in the effective stresses in the soil and thus the shear strength according to Eq.2.45. This further increases the

peak skin capacity according to Eq.2.45 or Eq.2.5. Meanwhile the combined effect of reaction frame piles and the direction of the loading on altering the orientation or magnitude of the major effective stresses can not be neglected.

From effective stress point of view, it can be argued that the shear strength as mentioned earlier is related to the lateral earth pressure factor k_0' as expressed in Eq.2.19 which is a function of the major and minor effective stresses σ'_1 and σ'_3. The effective vertical stress may be altered from what is often assumed as the effective overburden pressure p' in Eq.2.5 The latter change then may affect the lateral earth pressure and so the shear strength and the failure stress level as discussed above. Such combined effects however have not resulted in very significant change in the case of tensile loading of Tilbrook pile as observed.

As seen on Fig.2.73, the proximity of the Kraft's (t-z) model with the measured peak skin friction data used as input indicates that the bias and uncertainty in the characteristic form of the model is far less than the bias related to his λ and α peak skin methods as previously shown by Gibbs et al, (1992).

The close results between Kraft's and disk model may be explained in this way, the Kraft's (t-z) and disk models as described in Sec.2.2.2 and 2.2.3 , respectively, have been developed based on the theories of non-linear elasticity with using different techniques. By looking at the basic derivation of two models, it may be said that Kraft's (t-z) model is a particular case of disk model with assuming β equal to unity. Bearing in mind that for heavily overconsolidated soil as Tilbrook β value normally varies between 1.0 to 2.5 according to the interpretation of the triaxial and the shear modulus data, it is easy to understand why these two theoretical models would give closer results than other methods.

2.8 Lateral loading cases

In the following subsections the behaviour of Tilbrook and Houston piles under lateral loading are studied. The p-y and the global lateral responses of the pile - soil are predicted by using API's soft clay approach, stiff clay method of Reese et al, (1975), criteria of Dunnavant and O'Neill, (1989) and the presented modified (p-y) method.

2.8.1 Tilbrook pile

2.8.1.1 (p-y) response

The predicted load transfer (p-y) curves are compared with the measured data (Clarke et al, 1992) in Figs.C.2 to C.8.

The measured load transfer (p) has been obtained simply by double differentiation of the measured bending moment (M) along the pile and (y) the pile displacement has been found through

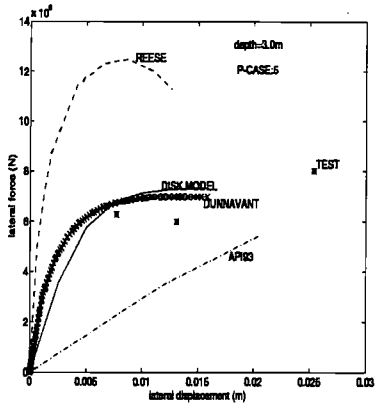

Figure 2.74: Predicted versus measured (p-y) response curves for Tilbrook site

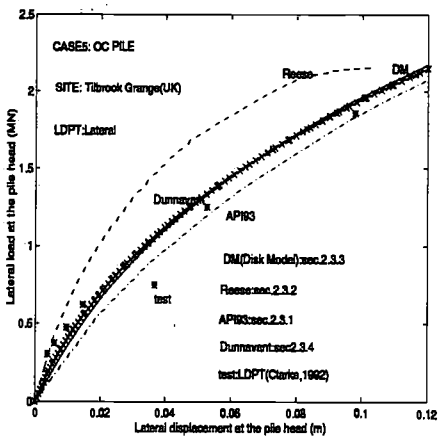

Figure 2.75: Predicted versus measured global lateral response of the pile at Tilbrook site

double integration of (M).

The predicted (p-y) curves based on API RP2A 1993 recommendations for soft clay, Reese's stiff clay approach, Dunnavant's p-y and disk models for various depths are plotted in Fig.C.2 to C.8. It is seen that the (p-y) response predicted according to API RP2A 1993 recommendations are generally much softer than the measured and other predicted curves for their initial parts. In contrast to the measured curves and those predicted according to the stiff clay method of Reese, these curves do not exhibit any post peak degradation and yield at much higher ultimate capacity for lateral displacements larger than 100 mm.

The (p-y) curves predicted by the stiff clay method of Reese et al, (1975) have peaks much higher than the measured response and also have exhibited very significant post-peak degradation which resulted then in much lower ultimate lateral resistance of soil. The reason for this sort of behaviour may be sought in the empirical foundation of this method. Reese's stiff clay method as described briefly in Sec.2.3.2 have been derived from lateral loading tests in a stiff clay soil with high degree of hydraulic degradation in the soil (see Reese et al,1975). It may be worth of notice that this intensity of post-peak degradation may be expected during cyclic loading of the pile-soil.

In comparison with the test data, Dunnavant's stiff clay method has resulted in slightly stiffer initial response but closer ultimate response. The agreements between the result of disk model, Dunnavant's method and test are very good.

Table 2.7: The bending moment response of the Tilbrook pile under lateral loading test

Method/Capacity	Lateral load (MN)	Maximum bending moment (MN.m)	Bias
API RP2A 1993	1.85	2.98	0.63
Reese (p-y) model	1.85	2.92	0.62
Disk (p-y) model	1.85	3.82	0.81
Dunnavant (p-y)model	1.85	4.73	1.00

2.8.2 Global lateral response of pile

The predicted and measured (Clarke et al, 1992) lateral load versus displacement curves at the (OC) pile head are summarized in Fig.2.75 and Table.2.7.

The observed initial response of the Tilbrook pile has been rather softer than the anticipated behaviour by the empirical and theoretical models described in Sec.2.3. The reason for the existing discrepancy might be the effects of the cyclic loading prior to the static loading. Also the LDPT data (Clarke et al, 1992) has been taken from the end of the first cycle loading which may not exclude completely such cyclic effects, however it is assumed that such measured data would be representative of a short term (monotonic type) static loading.

The studied models Dunnavant 's (p-y) model, Dunnavant (p-y) model and the presented disk model have resulted in fairly close responses.

The stiff clay approach of Reese has overpredicted the initial lateral load by about 20 percent to 50 percent whereas its ultimate response is less stiffer response. This is because of the observed significant post-peak degradation of the local (p-y) response curves in Figs.C.2 to C.8 lateral load.

It may be argued that since the initial phase of (p-y) curves will mostly be utilized for the case of design storms in the offshore piles, thus the existence of a larger bias in the initial response might reduce the reliability of the designed platform. However, the latest studies (see Chapter.6) have shown that the reliability index of the jacket-pile-soil system near collapse might be less influenced by the uncertainties in (p-y) modelling.

Some improvement in the larger lateral displacements is observed. However, it's expected that the Reese response curve would be softened faster as the displacement increases further thus under-estimating the ultimate response.

As far as API soft clay (p-y) model is concerned, it has given the stiffest response by far. Because of non-degrading nature of these (p-y) curves as shown in Fig.C.2 to C.8, it may be anticipated that the amount of over-estimation would increase further.

Similar trends can be observed for the induced maximum bending moment versus the lateral pile head load from Fig.2.76. However, the amount of the discrepancies are lesser which may be

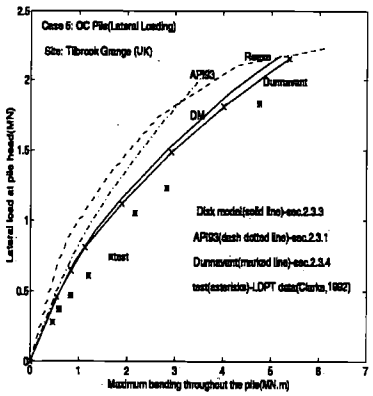

Figure 2.76: Predicted versus measured maximum bending moment response for lateral loading of Tilbrook pile

beneficial from the point of view of the pile design.

The proposed disk (p-y) method has given fairly good predictions of both initial and ultimate responses. The corresponding maximum discrepancy varies between $7 - 23$ percent with penetration depth of pile. The discrepancies in predicting the bending moment are less than those related to the load-deflection response. This low sensitivity to the choice of the (p-y) method used in the analysis of pile will be a beneficial factor for the offshore pile designer. On the other hand, relatively larger differences in the pile head lateral load and stiffness calculations would have an adverse effect on the global behaviour of the platform under sea loading(see Chapter 3 and 5).

2.8.3 Houston pile

2.8.3.1 (p-y) response

The derived and predicted (p-y) curves for the tested pile of Dunnavant and O'Neill, (1989) may be compared in Fig.C.9 to C.12. The deviations are comparatively larger than those observed for Tilbrook lateral pile test. However, the (p-y) trends and the range of peaks in the curves are fairly well predicted by the described methods.

As seen in the case of Tilbrook pile, the peaks and post-peak degradation have been overpredicted by Reese's stiff clay method while API's soft clay approach has not taken into account any such degradation but still has resulted in softer (p-y) curves.

Closer correlations have been obtained for the proposed (p-y) method based on disk modelling of pile-soil. The initial response has been well predicted according to Dunnavant 's (p-y) method

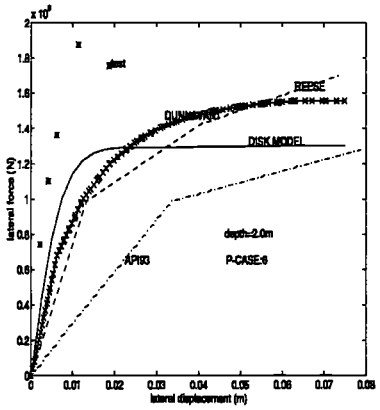

Figure 2.77: Predicted versus measured (p-y) response curves for Houston site

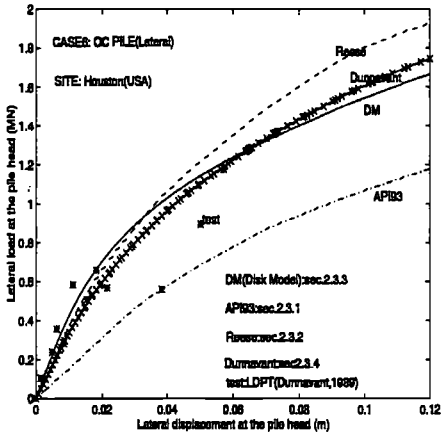

Figure 2.78: Predicted versus measured global lateral response of the pile at Houston site

while the ultimate lateral resistance of the soil has been overestimated. This method might produce even stiffer response by using the recommended values $\epsilon_{50} = 0.005$ and 0.01 instead of the measured value of 0.025(Lambson et al, 1992).

Table 2.8: The bending moment response of the Houston pile under lateral loading test

Method/Capacity	Lateral load (MN)	Maximum bending moment (MN.m)	Bias
API RP2A 1993	0.82	1.97	0.98
Reese (p-y) model	0.82	2.07	1.03
Disk (p-y) model	0.82	1.88	0.94
Dunnavant (p-y)model	0.82	1.82	0.90

2.8.3.2 Global response

The measured (Dunnavant, 1989) and predicted behaviour of the pile under static lateral loading are presented in Fig.2.78 and Table.2.8. It is seen that the (p-y) disk model presented in Sec.2.3.3 has provided the best prediction.

In comparison, the soft clay approach recommended by API RP2A 1993 has given much softer lateral response which may be due to the large uncertainty(bias) involved in estimating the key model parameter y_c as described in Sec.2.3.1.

While Dunnavant and O'Neill, (1989) (p-y) model has resulted in fairly close prediction to the test and the disk model, the stiff clay (p-y) approach of Reese et al, (1975) has overestimated

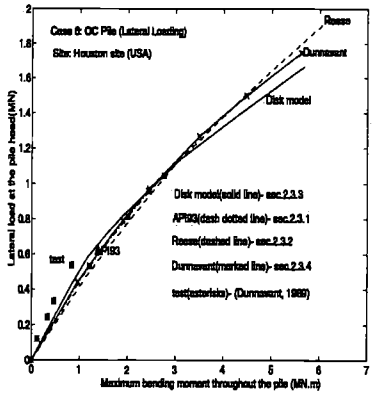

Figure 2.79: Predicted versus measured maximum bending moment response of Houston pile

the capacity.

It can be seen on Fig.2.79 that the computed maximum bending in the pile is less sensitive to the choice of (p-y) method which may benefit the pile design. However, the large scatter observed in Fig.2.78 in terms of the pile head stiffness based on API model may demand the use of an improved empirical model such as Dunnavant's method or a mechanistic and non-specific model based on stress-strain behaviour of soil such as disk model. The response of the jacket platform under extreme loading condition might depend on the stiffness and the ultimate capacity of the pile foundation. This issue will be discussed in Chapter.3.

2.9 Concluding remarks

The pile-soil interaction problem may be studied efficiently by means of (t-z) and (p-y) models. The current practice (t-z) and (p-y) models have been established mostly based on one or few onshore pile tests or based on elastic half and nonlinear subgrade modulus theories.

Two new (t-z) and (p-y) models were developed based on Mohr-Coulomb failure criteria and disk modelling of pile-soil system. The presented disk models were calibrated against the the LDPT test results at Pentre, Tilbrook and Houston sites.

The performance of the current practice pile-soil interaction models recommended by API RP2A, Reese, Kraft and Dunnavant, were assessed in extreme offshore soil conditions by means of five case studies.

Satisfactory correlations were obtained between the predictions and the LDPT test data for Kraft's (t-z) model, Dunnavant's (p-y) model. More improved correlations were obtained for the

calibrated disk models.

Predictive ability of various models generally improved with the depth. The maximum discrepancies were found near the soil surface due to possible top soil degradation during pile driving. Comparatively larger discrepancies were found for the lateral loading cases which showed the limits of the lateral pile-soil models.

The observed discrepancies might be partly due to the soil degradation near the surface prior to loading, the nature of the test data used for calibration of the model which may contain some bias and the underlying simplifying assumptions of model. Despite such uncertainties, the bending moment response were predicted well by all the studied models.

CHAPTER 3

NONLINEAR STATIC ANALYSIS OF JACKET-PILE-SOIL SYSTEM AT THE ULTIMATE COLLAPSE

3.1 Introduction

The aim of the current Chapter is to investigate the static behaviour of the jacket-pile-soil system at ultimate collapse. In this connection, the influence of the pile-soil foundation on the global performance of the system near the ultimate collapse will be the main topic of this Chapter.

When a jacket platform is subjected to the environmental loads such as those induced by extreme waves and currents or severe earthquakes, the system might exhibit a non-linear behaviour due to possible yields in either soil or structure or both. This possible non-linear behaviour demands a different treatment than the traditional methods of linear elastic analysis of such system. In the recent years, several tools have been developed to account for the non-linear behaviour of mainly jacket structures. Among those are phenomenological models developed by for e.g. Marshall et al, (1977) and Zayas et al, (1980) and general non-linear beam models by for e.g. Sugmimoto and Chen, (1985) and Chan, (1989) and plastic hinge beam-column models by (Nonaka, (1973), Ueda and Rashed, (1974), Rashed, (1980), Moan et al, (1985), Søreide et al, (1986), Abbassian, (1991), Eberg et al, (1993) and Hellan, (1994)). The developments of the pile-soil interaction models in the past two decades such as those empirical models by Matlock, (1970), Reese et al, (1975), Dunnavant and O'Neill, (1989) Hamilton and Dunnavant, (1992) and theoretical/semi-empirical models by Grande and Nordal et al, (1979) , Kraft et al, (1981), Svanøet al, (1992 and 1993), Gabr, (1994) and Emami et al, (1998) have provided necessary tools for an integrated jacket-pile-soil analysis. Within the context of this Chapter, we shall employ the plastic hinge beam model of Søreide et al, (1986, 1994) and the pile-soil interaction disk and API RP2A 1993 recommended models as described in Chapter.2 to assess the overall static response of the jacket-pile-soil system.

3.2 General

As mentioned in the introduction, the jacket platform is exposed to the environmental loads induced by the extreme waves and currents or earthquakes. The imposed forces on the structure are transferred into the soil through the piles supporting the jacket platform. Such imparted extreme loads may cause partial or complete yield of soil either in tension or compression or under lateral loading or a combination of these. It may be noted that a torsional type shear failure in the soil may be neglected because of the load transfer mechanism of the jackets.

The resulting potential failure modes of the jacket foundation might be either pull out failure or plunging or the plastic hinge failure in the pile or a combination of these failure modes. Since the wave induced axial and lateral forces and bending moments act simultaneously on the pile head, hence, the failure mechanism of pile foundation of a jacket platform may involve a combination of the pile-soil failure modes.

The soil failure usually starts at the upper layers near the mudline due to the potential weakness of the top soil and also because of the base shear transfer mechanism into the soil which only involves a limited depth of soil from mudline. For a base shear type failure mode of the jacket platform the soil yield under lateral loading and consequently plastic hinge formation in the pile are likely scenarios of the foundation failure. Whereas for an overturning type collapse mode of platform, the pull out or plunging of piles might be considered as the likely forms of pile-soil collapse. As mentioned, a combined failure mode can occur for a case which involves comparably large base shear and overturning moments at the pile-soil-jacket interface.

The soil failure can affect the structural member failure mechanisms by changing the bending moment or axial force transfer in the critical members. The foundation failure may change the stiffness and/or the ultimate collapse strength of the jacket-pile-soil system. The term jacket-pile-soil interaction which is used in this Chapter will refer to any of these possible effects.

The main focus of this study is near failure type interaction between the jacket structure and its foundation. However, the linear elastic type interaction will not be excluded from this definition.

It is shown within the cases studied in this Chapter that the potential of the jacket and pile-soil foundation interaction whether is linear or non-linear may not be ignored. Since, such ignorance may result in an unrealistic estimation of the initial stiffness, the peak ultimate collapse capacity and residual strength of the system.

However, the consequence of the jacket-pile-soil interaction can be more crucial for the ultimate limit state of collapse assessment of the jacket platforms particularly with the usual uncertainties in the soil's resistance parameters. The latter issue will be pursued further in the Chapter.6.

In most of the previous studies, the jacket-pile-soil interaction has been ignored such as recent works by Eberg et al, (1993), Hellan et al, (1993), Sigurdsson et al, (1993), Stewart et al, (1993). Other most recent works have included the nonlinear pile-soil-structure interaction by using uncoupled Winkler spring models, such as studies by Bea et al, (1993), Emami et al, (1995-1996)

and Schmucker, (1996). The current Chapter will consider both the existing and the developed pile-soil models, as described in Chapter 2.

Two different analysis methods exist for progressive collapse analysis of jacket-foundation system, respectively:

. Jacket-pile-soil interface analysis approach

. fully integrated analysis method

The interface analysis approach is implemented into a linear structure and non-linear pile-soil system interaction analysis program SPLICE(Dnv, 1992) and also implemented for dynamic analysis of a simplified non-linear jacket-pile-soil model (see for e.g. Emami et al, 1996). The integrated jacket-pile-soil analysis approach will be discussed throughout this Chapter.

To be able to make proper comparisons and quantify the effects of pile-soil-jacket interaction on the overall behaviour of the platform, throughout this Chapter three different supporting systems are considered as follows:

. fixed support system

. linear spring support (lumped system)

. non-linear pile-soil system (consistent FE system)

The influence of the pile tip plug (end-bearing) on the ultimate collapse response of the jacket-pile-soil systems is investigated within this Chapter.

Concerning the loading, both gravitational loads(dead plus live loads) and environmental loads induced by waves and currents are considered.

Two different static pushover analysis methods are applied namely, traditional wave load incrementation (WLI)method(Emami et al, 1995 and Hellan, 1995) and a more refined wave height incrementation(WHI) approach. The influence of wave load modelling is illustrated within the cases studied in this Chapter.

To illustrate the methods, 2D and 3D jacket models with the different soil and foundation models will be analyzed throughout this Chapter. The results of some of these static pushover analyses will be later compared with those of cyclic quasi-static and dynamic analyses in Chapter 5.

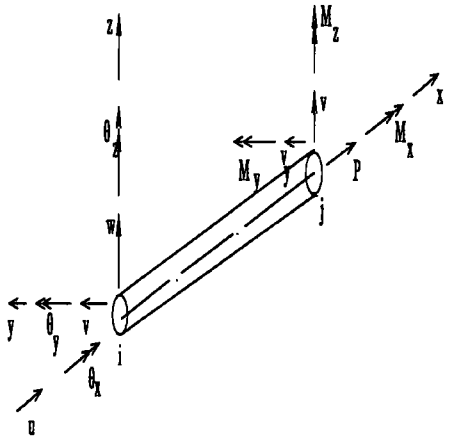

Figure 3.1: A two node finite beam element with 6DOFs at each node

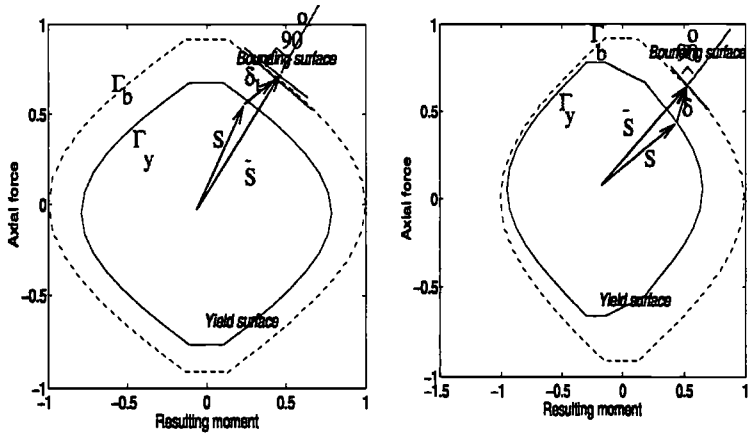

Figure 3.2: The yield and bounding surface concept associated with a 2node beam element

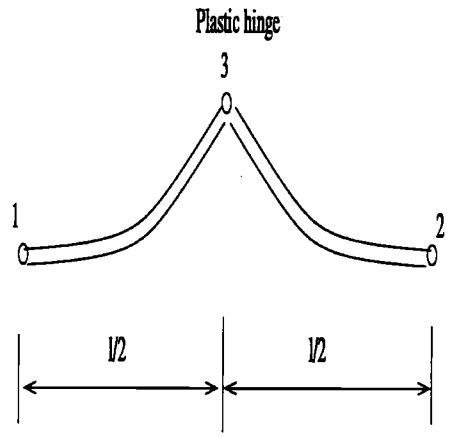

Figure 3.3: Dividing a beam element into two sub-elements after plastic hinge formation at the mid-span of element

3.3 Integrated pile-soil-jacket interaction analysis

3.3.1 Elasto-plasticity formulation of two node beam element

In the integrated jacket-pile-soil analysis approach, the changes in the stiffness of structure and foundation is considered through updating the system stiffness matrix at each step of the analysis as described in the following.

The procedure involves the establishing the elastic element stiffness matrices of both structural and pile-soil elements. Applying plasticity theory to establish the elasto-plastic (tangent) stiffness matrices of the structural and pile-soil elements and then transforming them into the global system stiffness matrix. Applying an incremental load and solving the system of non-linear force-displacement equations by means of familiar methods such as Newton-Raphson, Arc-length, Load limit point etc.

3.3.1.1 Element definition

Each actual structural member is modelled by using a two node beam element. Each node of beam element has 6DOFs as shown in Fig.3.1. A new node is introduced at the mid-span of the element after a plastic hinge is formed(see Fig.3.3). The beam element is then divided into sub-elements and the stiffness matrix of each sub-element is established and then incorporated into the super-element's stiffness matrix through a static condensation method.

3.3.1.2 Element (elastic) stiffness

A potential energy approach is formulated in an incremental form in USFOS program (Søreide et al, 1994) to compute the tangent stiffness matrix K^T of each finite two node beam element

shown in Fig.3.1. An approximate Von-Karman form of Green strain function is used to calculate the strain as follows:

$$\epsilon_x = u_{,x} + \frac{1}{2}v^2{}_{,x} + \frac{1}{2}w^2{}_{,x} \tag{3.1}$$

with u,v and w denoting the displacement components in x,y and z directions, respectively (see Fig.3.1). The strain energy expression is established by using virtual work principle as follows:

$$U = \frac{1}{2}\int_v \sigma^T.\epsilon.dv \tag{3.2}$$

in which σ, ϵ and v denote the general stress, strain vectors at their final values and the element volume. Eq.3.2 is referred to Clapyron's theorem. Considering the general stress-strain relationship according to continuum mechanics theory, we will have:

$$\sigma = \Psi.\epsilon = \begin{bmatrix} \sigma_{xx} \\ \sigma_{yy} \\ \sigma_{zz} \\ \sigma_{xy} \\ \sigma_{xz} \\ \sigma_{yz} \end{bmatrix} = \frac{E}{(1+\nu)(1-2\nu)} \begin{bmatrix} 1-\nu & \nu & \nu & 0 & 0 & 0 \\ \nu & 1-\nu & \nu & 0 & 0 & 0 \\ \nu & \nu & 1-\nu & 0 & 0 & 0 \\ 0 & 0 & 0 & \frac{1-\nu}{2} & 0 & 0 \\ 0 & 0 & 0 & 0 & \frac{1-\nu}{2} & 0 \\ 0 & 0 & 0 & 0 & 0 & \frac{1-\nu}{2} \end{bmatrix} \begin{bmatrix} \epsilon_{xx} \\ \epsilon_{yy} \\ \epsilon_{zz} \\ \epsilon_{xy} \\ \epsilon_{xz} \\ \epsilon_{yz} \end{bmatrix} \tag{3.3}$$

in which Ψ is a matrix relating the stresses and strains in a linear elastic body such as two node beam. E and ν denote the Young modulus and the poisson ratio respectively. For e.g. for a unidirectional stress-strain, we may write according to Hook's law:

$$\sigma = E.\epsilon \tag{3.4}$$

Now substituting for σ in Eq.3.2 from Eq.3.4, we may obtain the following relationship for the strain energy contribution due to the axial force in a bar element:

$$U = \frac{1}{2}EA\int_0^l (u_{,x} + \frac{1}{2}v^2{}_{,x} + \frac{1}{2}w^2{}_{,x})^2.dx \tag{3.5}$$

Similarly the bending moment contribution can be added to the R-H-S of Eq.3.5 as :

$$U = \frac{1}{2}EA\int_0^l (u_{,x} + \frac{1}{2}v^2{}_x + \frac{1}{2}w^2{}_x)^2.dx + \frac{1}{2}\int_0^l (EI_z v^2, xx + EI_y w^2, xx).dx \tag{3.6}$$

where the indices ,x and ,xx denote the first and the second derivatives with respect to x. Now taking a variational form of the strain energy according to Eq.3.6 will yield:

$$\begin{aligned} \delta U = {} & EA\int_0^l u_{,x}.\delta u_{,x}.dx + \int_0^l EI_z(v_{,xx}\delta v_{,xx} - \frac{N}{EI_z}v_{,x}\delta v_{,x})dx \\ & + \int_0^l EI_y(w_{,xx}\delta w_{,xx} - \frac{N}{EI_y}w_{,x}\delta w_{,x})dx - \int_0^l (N + EAu_{,x})\delta u_{,x}.dx \end{aligned} \tag{3.7}$$

Considering the general shape function relating the deformation of any point on the two node beam to the nodal displacement will yield:

$$\begin{aligned} u &= \phi_u^T q_u \\ v &= \phi_v^T q_v \\ w &= \phi_w^T q_w \end{aligned} \tag{3.8}$$

where ϕs denote the shape functions corresponding to the displacement components of the two node beam element in directions (i.e x,y and z) as:

$$\begin{aligned}\phi &= [coshkx/l \quad sinhkx/l \quad kx/l \quad 1] \\ &= [coskx/l \quad sinkx/l \quad kx/l \quad 1]\end{aligned} \tag{3.9}$$

where the buckling coefficient k is given as : $k = \sqrt{N/EI_z}$. in which N and EI_z denote the axial force and the flexural rigidity of the beam-column member. The coefficients of the generalized coordinate q are obtained according to the boundary conditions of the beam-column element. For the beam elements without axial force a third order polynomial shape function is used instead and an analytical (closed form) solution is obtained for the tangent stiffness matrix relationship in USFOS(see Søreide et al, 1994). A variational form of the incremental strain energy would be expressed as:

$$\delta\Delta U = \delta u^T \int_0^l EA\phi_{u,x}\phi_{u,x}^T dx\Delta u \tag{3.10}$$

$$\begin{aligned}&+\delta v^T \int_0^l EI_z(\phi_{v,xx}\phi_{v,xx}^T - \frac{N}{EI_z}\phi_{v,x}\phi_{v,x}^T)dx\Delta v \\ &+\delta w^T \int_0^l EI_y(\phi_{w,xx}\phi_{w,xx}^T - \frac{N}{EI_y}\phi_{w,x}\phi_{w,x}^T)dx\Delta w \\ &+\delta v^T \int_0^l EA\phi_{v,x}v_{,x}\phi_{u,x}^T dx\Delta u + \delta u^T \int_0^l EA\phi_{u,x}v_{,x}\phi_{v,x}^T dx\Delta v \\ &+\delta w^T \int_0^l EA\phi_{w,x}w_{,x}\phi_{u,x}^T dx\Delta u + \delta u^T \int_0^l EA\phi_{u,x}w_{,x}\phi_{w,x}^T dx\Delta w \\ &+\delta v^T \int_0^l EA\phi_{v,x}v^2{}_{,x}\phi_{v,x}^T dx\Delta v + \delta w^T \int_0^l EA\phi_{w,x}w^2{}_{,x}\phi_{w,x}^T dx\Delta w \\ &+\delta w^T \int_0^l EA\phi_{w,x}w_{,x}v_{,x}\phi_{v,x}^T dx\Delta v + \delta v^T \int_0^l EA\phi_{v,x}v_{,x}w_{,x}\phi_{w,x}^T dx\Delta w\end{aligned} \tag{3.11}$$

After arranging the integral terms in Eq.3.11, the components of the USFOS beam element (elastic) stiffness matrix is expressed as follows:

$$K_e = \begin{bmatrix} k_{uu} & k_{uv} & k_{uw} \\ k_{vu} & k_{vv} & k_{vw} \\ k_{wu} & k_{wv} & k_{ww} \end{bmatrix} \tag{3.12}$$

in which the subindices denote the submatrices which are given in order as integral terms in Eq.3.11. As seen, both linear elastic terms and second order terms due to rotation of the beam element are present in the above formulation. The coupling between the two translational degrees of freedom v and w (see Fig.3.1) are also present as the last integral term in Eq.3.11.

3.3.1.3 Plasticity formulation

The increment of plastic displacement is normal to the yield surface which is often referred to as normality rule expressed as follows:

$$\delta v_p = \begin{bmatrix} g_1 & 0 \\ 0 & g_2 \end{bmatrix} \begin{bmatrix} \Delta\lambda_1 \\ \Delta\lambda_2 \end{bmatrix} = G_u\Delta\lambda \tag{3.13}$$

in which Δu_p = an increment of the plastic displacement, g_1 and g_2 are the green function element of USFOS beam model which are defined in the following. $\Delta\lambda$ is a vector containing scalar values of $\Delta\lambda_1$ and $\Delta\lambda_2$.

$$g^T{}_i = \frac{\partial\Gamma}{\partial S_i} \tag{3.14}$$

where Γ defines a plastic interaction function for the tubular section as:

$$\Gamma = cos(\frac{\pi}{2}\frac{N}{N_p}) - \frac{\sqrt{M^2{}_y + M^2{}_z}}{M_p} = 0 \tag{3.15}$$

S_i in Eq.3.14 refers to a general force vector at node i of beam element. A kinematic (strain) hardening rule and partial yield formulation is used for the beam element according to a bounding surface concept(Dafailas and Popov, 1975 and Hilmy, 1984). The concept is illustrated in Fig.3.2. This model consists of a yield surface which is encircled by an outer bounding surface representing the ultimate limit state of collapse as shown. The inner and outer surfaces in Fig.3.2 represent the initial (fiber) yield and the full plastification of the element cross section. The region inside the inner yield surface represents the elastic state of the stress. According to the consistency law the stress state must remain on the yield surface that is:

$$\Delta\Gamma = 0 \tag{3.16}$$

Hence, the transition from the initial yield state to full plastification can be achieved by the translation of the inner yield surface towards the outer plastic surface in a unidirectional manner(the gradients of the stress vector are unidirectional at both surfaces). At the point of contact the stress state reaches the full plastification of the cross section. To avoid the intersection of these two translating surfaces, the shape of each surface is maintained however the size of the yield surfaces may vary(Isotropic hardening). The additional strain hardening may be modelled as follows:

$$\Gamma_b = f(\frac{\bar{S}_i - \beta_u}{z_b \sigma_y Z_p}) \tag{3.17}$$

in which Γ_b represents the bounding surface function, $\bar{S}_i$ = the mapping of the stress vector onto the outer bounding surface, β_u = is a shift (translation) parameter, z_b = an extension parameter, σ_y = the yield stress of the beam element material(such as steel) and Z_p =the plastic section modulus of the element. The kinematic hardening may be used to account for Bauschinger effects, however, for cyclic plasticity the changes of the yield and bounding surface may be considered due to changes in the elastic region of the material. The material parameters β_u and z_b can be obtained from the standard material and cyclic tests. Hellan et al, (1991) and (1995) has calibrated these parameters against the cyclic tests results of Granli, (-) and Ogawa et al, (1987). It is recognized that the changes in the size of the yield and bounding surfaces can take place gradually during a cyclic load process. However, in the current USFOS model, the transition from monotonous state to a stabilized cyclic state is set instantaneously. The cyclic transition is assumed to take place when the accumulated plastic work at the plastic hinge of element exceeds a threshold value as follows:

$$W_{hinge} = \sum_{i=1}^{n} S^T{}_i \Delta u^i{}_p > W_{threshold} = \theta_{threshold} \cdot M_p \tag{3.18}$$

in which W_{hinge} and $W_{threshold}$ denote the work consumption at the plastic hinge and a threshold set for the plastic work in USFOS. $\theta_{threshold}$ similarly denotes the threshold for the formation of a plastic hinge in the beam elements. The tangent(elasto-plastic) stiffness matrix K^T of each finite two node beam element of Fig.3.1 can be established as follows. The incremental force -displacement relationship reads in matrix form:

$$\Delta S = K^T \Delta v_e \tag{3.19}$$

in which Δv_e represents the elastic displacement increment as follows:

$$\Delta v_e = \Delta v - \Delta v_p \tag{3.20}$$

Combining Eqs.3.19, 3.20 and 3.13, the following emerges:

$$\Delta S = K^T(\Delta v - G_u \Delta\lambda) \tag{3.21}$$

The consistency rule requires that the force vector during yield has to remain on the yield surface that is:

$$\Delta\Gamma = \frac{\partial\Gamma}{\partial S}.\Delta S = G_u^T.\Delta S = 0 \tag{3.22}$$

Pre-multiplying both sides of Eq.3.21 with G_u^T and using the consistency rule of Eq.3.22, the following can be written:

$$G_u^T.\Delta S = G_u^T K^T(\Delta v - G_u \Delta\lambda) = 0 \tag{3.23}$$

Hence, $\Delta\lambda$ is obtained from Eq.3.23 as follows:

$$\Delta\lambda = (G_u^T K^T G_u)^{-1} G_u^T K^T \Delta v \tag{3.24}$$

Substituting for $\Delta\lambda$ from Eq.3.24 in Eq.3.21 leads to the tangent stiffness relationship as follows:

$$\begin{aligned} \Delta S &= K^T(\Delta v - G_u(G_u^T K^T G_u)^{-1} G_u^T K^T \Delta v) \\ &= (K^T - G_u(G_u^T K^T G_u)^{-1} G_u^T K^T)\Delta v \\ &= K_{ep}\Delta v \end{aligned} \tag{3.25}$$

An integrated pile-soil-jacket analysis is performed by considering the pile-soil elements as a part of the whole structure. This method would allow to establish a global system stiffness matrix with inclusion of pile-soil interaction effects in it. Likewise an integrated frame structure analysis, in which interaction between various members are reflected through the changes of the tangent stiffness system stiffness matrix such as buckling, plastification of elements, redistribution of forces and elastic unloading, etc.

3.3.2 Elasto-Plasticity formulation of General one node spring equivalent to disk

A general elasto-plasticity model for a general one node spring has been implemented into USFOS program(Eberg, 1996) which is described in the following. This model is used here with the

stiffness characteristics (load transfer-displacement) (t-z) and (p-y) curves calculated according to the disk model as described in Secs.2.2.3 and 2.3.3 of Chapter.2. The main features of the static disk and the non-linear one noded spring models are the same. In a sense, the spring is an idealization of the static disk in a finite element sense. The basic assumption of the model may be described as follows:

. Plasticity model includes an isotropic type hardening/softening which implies the extention or contraction of the yield surface is allowed.

. Hardening or softening may be associated with the presented disk model for axial and lateral loading of pile-soil system.

. The model accounts for the change in the loading direction in the XY plane by means of an interaction surface(Eberg, 1996).

. No scaling of load step due to plastification of the pile-soil interaction element is performed.

. No coupling is allowed between the axial and lateral disks(or springs).

3.3.2.1 Element definition

One node spring element (equivalent to the soil disk) with 6 DOFs are defined as follows:

$$u = [w \quad \phi] \tag{3.26}$$

where w and ϕ denote the subvectors of translational and rotational degrees of freedom, respectively. Each containing 3 DOFs.

3.3.2.2 Element stiffness (Linear)

The elastic stiffness matrix of the pile-soil system may be established as follows:

$$S = K_e u \tag{3.27}$$

where k_e is a 6x6 matrix in general, however, the rotational DOfs often set to zero and then k_e reduces to a 3x3 matrix.

3.3.2.3 Plasticity formulation

Generalized strains can be computed as follows:

$$u = \phi^T q \tag{3.28}$$

$$S = \phi^T Q \tag{3.29}$$

Decomposing the incremental displacement as follows into an elastic and another plastic part, we will have:

$$du = du_e + du_p \tag{3.30}$$

The corresponding elastic force-deformation relationship can be written as follows:

$$dS = k_e du_e \tag{3.31}$$

The corresponding plastic strain rate then can be written according to the normality law as follows:

$$du_p = d\lambda \frac{\partial F}{\partial s} \tag{3.32}$$

The isotropic hardening relationship can be applied as follows:

$$dR = H_R.d\lambda \tag{3.33}$$

The yield condition then can be written as follows:

$$\Gamma = |S - X| - R(u_p) = 0 \tag{3.34}$$

The gradient to the yield surface then can be computed as follows:

$$g = \frac{\partial F}{\partial S} \tag{3.35}$$

$$g_R = \frac{\partial F}{\partial R} \tag{3.36}$$

The elasto-plastic stiffness may be established by considering the consistency condition:

$$\partial F = \frac{\partial F}{\partial S} dS + \frac{\partial F}{\partial R} dR = 0 \tag{3.37}$$

Combining Eqs.3.27 to 3.37, the following matrix relationship can be written:

$$g^T k_e (du - g d\lambda) + g_R H_R d\lambda = 0 \tag{3.38}$$

Re-arranging Eq.3.38, we get:

$$(g^T k_e g - g_R H_R) d\lambda = g^T k_e du \tag{3.39}$$

Hence, $d\lambda$ can be obtained as:

$$d\lambda = (g^T k_e g - g_R H_R)^{-1} g^T k_e du \tag{3.40}$$

The elasto-plastic incremental relationship can then be written as follows:

$$\begin{aligned} dS = k_{ep} du &= k_e (du - du_p) \\ &= k_e (du - g d\lambda) \\ &= k_e du - k_e g (g^T k_e g - g_R H_R)^{-1} g^T k_e du \\ &= [k_e - k_e g (g^T k_e g - g_R H_R)^{-1} g^T k_e] du \end{aligned} \tag{3.41}$$

It can be seen in Eq.3.41 that the elasto-plastic stiffness of the pile-soil system can be calculated as a function of elastic non-linear stiffness, gradient and the isotropic hardening.

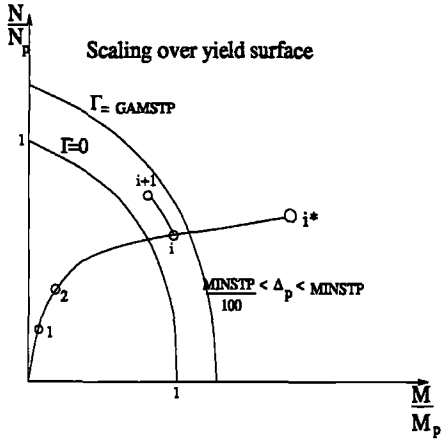

Figure 3.4: Scaling the load vector back to the yield surface

3.3.3 System stiffness formulation

The computed structural and pile-soil element matrices are transformed from local into the global coordinate system as follows:

$$k^i{}_{ep,g} = \lambda^T{}_i k^i{}_{ep} \lambda_i \tag{3.42}$$

in which λ_i indicates the cosine direction vector of element (i) (see for e.g. Przemieniecki, 1968 and Zienkiewicz, 1989). The transformed element matrices then are assembled in a global system stiffness matrix as:

$$K_r = \sum_i^n A^T{}_i k^i{}_{ep,g} A_i^T \tag{3.43}$$

in which A_i is a transformation matrix of nxn size relating the element dofs to the global dofs(see for e.g. Przemieniecki, 1968 and Reddy, 1985). Alternatively a superposition approach might be utilized to assemble the element stiffness matrices into the system stiffness matrix. The system stiffness matrix K_r is updated after each incremental step.

3.3.4 Solution procedures

3.3.4.1 Size of load increment

The load increment size is primarily set to capture the load-displacement response of the jacket-pile-soil system. In particular, smaller sizes are used as the load level reaches the ultimate collapse. However, the load control algorithm in USFOS scales the load increment as soon as plastification of an element takes place or a maximum specified displacement increment is exceeded in Arc-length approach. The scaling of the load is done to ensure that the load vector remains at the yield surface after element plastification occurs. Fig.3.4 illustrates schematically how the scaling of the load back to the yield surface is performed.

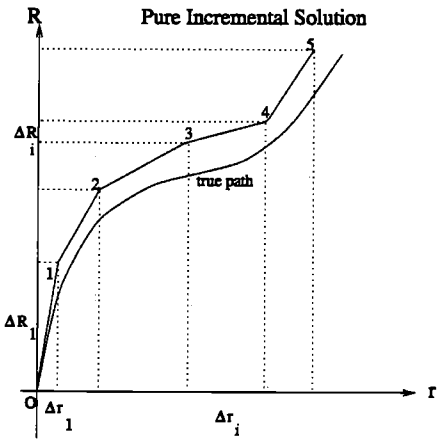

Figure 3.5: A schematic illustration of pure incremental solution method

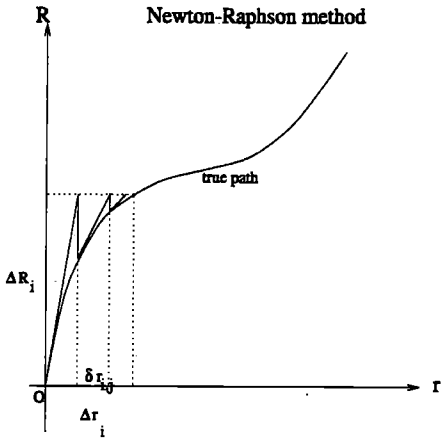

Figure 3.6: A schematic illustration of Newton-Raphson(Incremental/Iterative) solution method

To control the possible drift-off from the yield surface due to plastic hinge formation in the structural elements or yield of pile-soil elements, the following scaling criteria is applied in USFOS(Søreide et al, 1994):

$$\Delta u_{i,g} \leq \rho_{max} \Delta u_{1,g} \tag{3.44}$$

and $\Delta u_{i,g}$ is determined as follows:

$$\begin{aligned} \Delta u_{i,g} &= \Delta u^k{}_i w_k \qquad , k = 1, n \qquad , n = 1 \\ &= \sqrt{\frac{\sum \Delta u^k{}_i w_k{}^2}{\sum w_k}} \qquad , k = 1, n \qquad , n \geq 1 \end{aligned} \tag{3.45}$$

in which $\Delta u_{1,g}$ and $\Delta u_{i,g}$ refer to the limits of displacement increment at step 1 and i, respectively. u_k and w_k refer to the displacement and weighting factors in various dofs. The sign of the load increment is defined according to a current stiffness parameter (Bergan et al, 1978):

$$S_i = \frac{\Delta u^T{}_1 . \Delta R_1}{(\Delta \lambda_1)} \cdot \frac{(\Delta \lambda_i)}{(\Delta u^T{}_i) . \Delta R_i} \tag{3.46}$$

where Δu and ΔR are the incremental displacement and forces vectors. S_i indicates the current stiffness parameter at incremental step (i). If the S_i becomes zero indicates an unstable (bifurcation) point for the system which occurs at the collapse(peak) point.

If S_i becomes negative, the system is softening and a global un-loading is occurring. In a spring-back behaviour S_i after reaching zero at peak collapse point then starts increasing rapidly as the system un-loads. The increase of S_i is often reversed after reaching a new equilibrium of external and internal forces in the system.

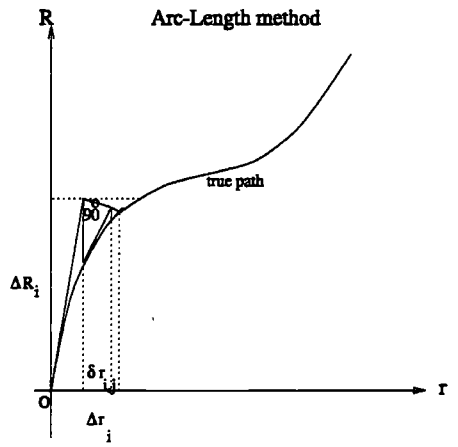

Figure 3.7: A schematic illustration of Arc-length solution method

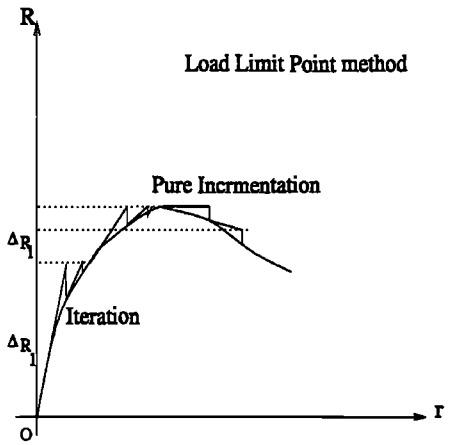

Figure 3.8: A schematic illustration of load limit point solution method

3.3.4.2 Pure incremental solution method

The matrix load-displacement relationship of the system may be solved by using a pure incremental method by updating the system tangent stiffness matrix after each incremental step as a function of the calculated displacement response. However, as illustrated in Fig.3.5 due to accumulation of the un-balance forces between the external and internal forces of the system at the end of each load step often an undesirable drift-off occurs from the true path of response. The magnitude of the drift-off might be controlled by varying the size of the load increment step. For e.g. a minimum load increment step size of 0.001 times the first load increment is often used in static pushover analysis in USFOS which yields reasonably accurate results.

However, the smaller load increment size requires far larger number of analyses steps which is often too costly to perform. For e.g. a static pushover analysis of a 3D jacket-pile-soil system with only 0.001 step size near collapse and at post-peak consumed 15 times more CPU time than that of an incremental analysis with only 0.01 step size. The pure incremental matrix solution may be expressed as follows:

$$K^T{}_i.\Delta r_i = \Delta R_i \tag{3.47}$$

where $K^T{}_i$, Δr_i and ΔR_i represent the tangent stiffness matrix, the increment of displacement vector and the increment of external forces vector at the incremental step (i). Since no iterations are allowed hence, $K^T{}_{i-1}$ is calculated instead from the response values at previous step. Thus, the equilibrium of the external and internal forces will read:

$$\Delta R_i = K^T{}_{i-1}.\Delta r_i + \delta R_i \tag{3.48}$$

in which δR_i represents the unbalance force at end of incremental step (i). The total forces are then computed by simply summing up the contribution of various steps as follows:

$$R_i = R_{i-1} + \Delta R_i \tag{3.49}$$

Similarly the total displacements r_i are computed as follows:

$$r_i = r_{i-1} + \Delta r_i \tag{3.50}$$

3.3.4.3 Newton-Raphson incremental/iterative solution method

To avoid the large drift-off from the true path of response and reducing the load increment to a very small size, a combined incremental/iterative procedure might be used which is referred to as the Newton-Raphson's method(see for e.g. Crisfield, 1991). The procedure involves computing first the tangent stiffness matrix at each load step according to Eq.3.48 and then performing correction iterations as follows:

$$K^T{}_{i-1,j-1}.\delta r_{i,j} = \delta R_{i,j} \tag{3.51}$$

The iterations are performed until reaching the true path as illustrated in Fig.3.6. In practice a limit (tolerance) is set for termination of iterations during each incremental step. If the convergence criterion is satisfied, the algorithm proceeds with a new incrementation. The updated incremental displacement response at the increment step i after jth iteration can be obtained as follows:

$$\Delta r_{i,j} = \Delta r_{i,j-1} + \delta r_{i,j} \tag{3.52}$$

There are several versions of incremental-iterative procedures such as Newton-Raphson, modified Newton-Raphson and the initial stress method(Crisfield, 1991). The technique so-called as predictor-corrector is also a version of incremental/iterative method.

3.3.4.4 Arc-length solution method

The arc-length approach in essence is an incremental/iterative approach. But the difference between this method and the Newton-Raphson type method is that after each iteration the position of the un-balance force is obtained through a normal in the direction of the arc passing from the intersection point between the force increment vector which is tangent to the load-displacement path at the point of incrementation and a constant total force level line as illustrated in Fig.3.7. The detail mathematical formulation can be found for e.g. in Crisfield, (1991).

3.3.4.5 Load limit point solution method

The iterative procedure sometimes fails to converge at the point of bifurcation. To find a stable solution, a switch can be set so that after detecting a change in the sign of current stiffness parameter or the determinant of the tangent stiffness matrix, the iteration procedure is halted until reaching a stable load-displacement path again. During the un-stable path(around the bifurcation point) a pure incremental approach is therefore used. After reaching the stable points, the iterations once again are switched on(see Fig.3.8). The latter is referred to as load limit point approach.

3.4 Case studies

In order to investigate the influence of the pile-soil interaction on the progressive collapse of the jacket system, the static pushover analyses are performed with considering three different

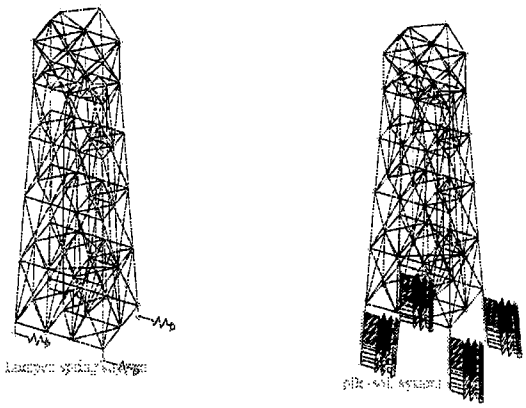

Figure 3.9: Lumped spring to ground and pile-soil foundation models

supporting conditions:

. a fixed support condition

. a linear spring support system

. a non-linear pile-soil system

For the fixed support case, the pile-soil interaction is disregarded. Thus only the collapse will occur due to failure of the structure (jacket), such as buckling of the legs, buckling and tensile failure of bracings, joint failure, loss of global stability ($p - \delta$) or a combination of these failure modes. However, in the real pile-soil-jacket system, either linear or nonlinear interaction would exist between the pile-soil and the structure.

For a foundation system which is too stiff compared to the structure, an equivalent linear spring model could be used. The linear stiffness of the equivalent spring may be obtained from the initial tangent stiffness of the pile-soil system at the mudline, as a first order approximation to the real pile head stiffness value.

Using a linear spring model may only be justified for small displacements of the pile-soil system. Fig.3.9 illustrates different support conditions for the jacket system.
These two different models are considered in the following case studies.

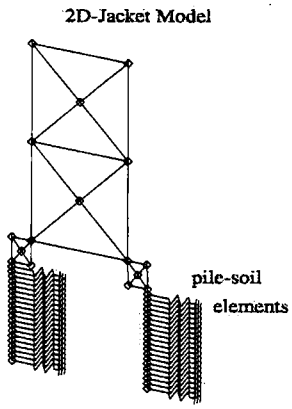

Figure 3.10: FE Model of the 2d Jacket frame with pile-soil foundation

Table 3.1: Structural member description of 2D Jacket case

Structural Member	**O.D/H** (m)	t_w/B (m)
Legs	2.0	0.06
Braces	1.5	0.05
Deck beam	2.0	0.06
Piles	2.5	0.06
Sleeves	2.6	0.05
Shear Plates	1.0	0.05

3.4.1 CASE 1: A 2D-Jacket Frame

3.4.1.1 Structure description

The jacket structure is considered to be a two storey plane frame, as shown in Fig.3.10. The load carrying system consists of two vertical main legs connected with horizontal and the cross bracings to provide the necessary redundancy and the reserve strength. The deck structure has been modelled as an equivalent horizontal tubular beam whose dimensions are given in Table.3.1. The pile-soil connections which consist of shear plates and sleeves have been modelled by equivalent frames.

Fig.3.10 shows the finite element model of the jacket and the pile-soil system. As shown, each real structural member is modelled by one two node beam element and the top deck module supporting system (truss) is modelled with one single horizontal beam element with equivalent stiffness. The pile sleeves are modelled with two connection frames with the vertical elements modelling the sleeves and and the horizontal and cross bracings replacing the shear plates. The topside facilities are not modelled in the frame model shown in Fig.3.10.

This kind of simple two dimensional model may be analyzed to simulate the behaviour of the equivalent frames of the complex 3D jacket in the direction of the its main planes (end on or broadside) or any other dominant wave angle. The equivalent stiffness of the plane frame can be determined by a simple linear elastic analysis. The integrated non-linear pile-soil-structure analysis then can be performed on 2D plane frame which is less costly than analysis of 3D jacket with pile-soil system.

Table 3.2: Linear lumped spring stiffness data for 2D Jacket case

k_{11}(N/m)	k_{22}(N/m)	k_{33} (N/m)
1.889E+08	2.053E+09	7.557E+09

Table 3.3: NC clay soil description for 2D Jacket case

Layer	Z(m)	γ(t/m3)	ϕ(deg)	Su(KPa)	G0(MPa)	ϵ_{50}	T_{max}(KPa)
1	1.0	20.5	-	7.5	500	0.01	4.33
20	20.0	20.5	-	150.0	1200	0.01	86.56

Table 3.4: OC clay soil description for 2D Jacket case

Layer	Z(m)	γ(t/m3)	ϕ(deg)	Su(KPa)	G0(MPa)	ϵ_{50}	T_{max}(KPa)
1	1.0	20.5	-	150.0	500	0.025	2.72
20	20.0	20.5	-	300.0	1200	0.025	81.91

3.4.1.2 Pile-Soil description

The foundation of the jacket comprises two single vertical piles driven 20m deep into the soil. The piles are tubular sections made of steel with yield strength of 470 MPa. The structural characteristics of the piles are described in the Table.3.1.

The piles are considered to be plugged from the equilibrium of the internal shaft friction and the tip plug resistance as follows:

$$\int t_{is} dS_{is} = \int q_{tip} dS_{plug} \tag{3.53}$$

where t_{is} = the internal shaft skin friction, q_{tip} = the tip resistance S_{is} = the internal area of the shaft and S_{plug} = the tip plug area.

Two different soil conditions are studied for this case, namely, NC and OC clay. The corresponding soil data are summarized in Tables.3.3 and 3.4. As seen, the average shear strength of the soil is about 80KPa and 225 KPa for NC and OC clay profiles. The OCR varies between 30 and 2.8 for OC soil and for NC clay OCR is taken as unity. The average strain at half principle

stress ϵ_{50} of the soil are 0.01 and 0.025 for NC and OC soils, respectively.

The pile-soil interaction is modelled by several non-linear disks connecting the pile to the surrounding soil. The pile members connecting these disks are modelled by two node beam elements as the other structural members.

The values of α and β parameters related to tangent stiffness of soil disks as described in Secs.2.2.3 and 2.3.3 of Chapter.2 are assumed to vary between 0.75-0.99 and 1.5-2.5 for NC clay and for OC clay 0.75 and 1.0, respectively.
API RP2A 1993 soft clay and (t-z) and (p-y) disk models are applied as described in Chapter.2.

Table 3.5: Load description for 2D Jacket case

load	(MN)
Vertical(Dead + wave)	20
Horizontal(wave+ current)	22

3.4.1.3 Load description

The loading on the jacket system consists of gravity and environmental loads. The equivalent vertical and horizontal joint loads are applied at the specified nodes of the structure in Table.3.5. The concentrated vertical loads are the sum of the dead weight of the structure and foundation, the weight of topside facilities and vertical component of the wave and current load. The concentrated horizontal loads are the sum of the wave and current induced loads only.

The wave is simply simulated by a deterministic regular wave and its kinematics are calculated by WAJAC program(DnV, 1992) according to a modified Airy theory(Dean and Dalrymple, 1984). The current velocity profile varies stepwise with the water depth from 0 at mud-line to about 1.05m/sec at the still water level.

The wave and current combined forces on the structure are calculated by using a computer program WAJAC (DnV,1992) based on the modified Morison's equation(Dnv, 1992).

Table 3.6: Pushover static analyses results for 2D-Jacket case with various foundation models

	Static(pushover)		
	Fixed support	Linear spring	Non-linear spring
First member failure(RFY)	1.99	1.94	.158
Ultimate collapse(RSU)	3.15	2.89	.802
Residual strength(RRES)	2.92	2.56	-

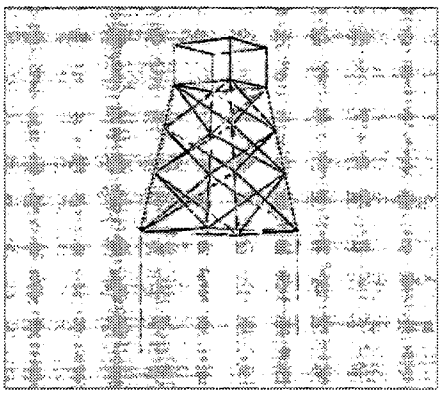

Figure 3.11: FE Model of 4leg (Malaysian) jacket platform

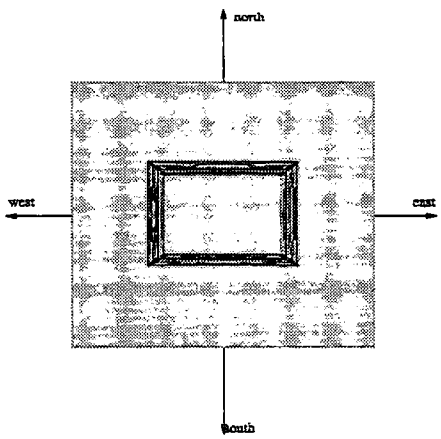

Figure 3.12: Plan view of 4leg jacket platform

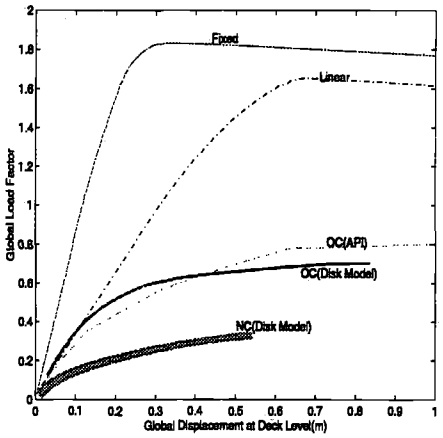

Figure 3.13: Global Load-displacement response of 2d jacket frame

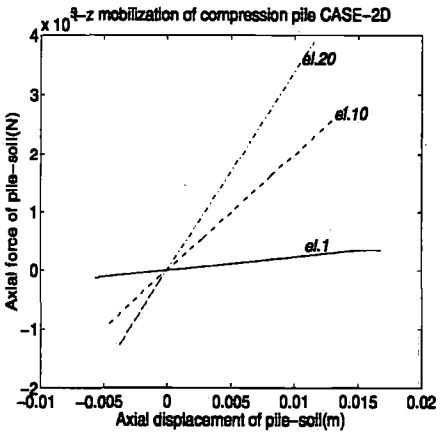

Figure 3.14: Axial mobilization curves of the compression pile

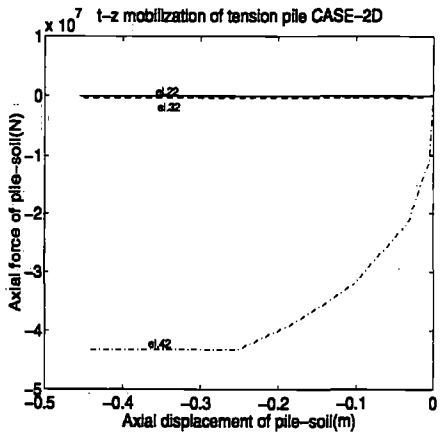

Figure 3.15: Axial mobilization curves of the tension pile

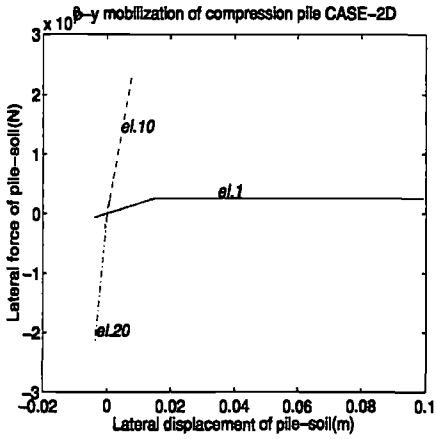

Figure 3.16: Lateral mobilization curves of compression pile

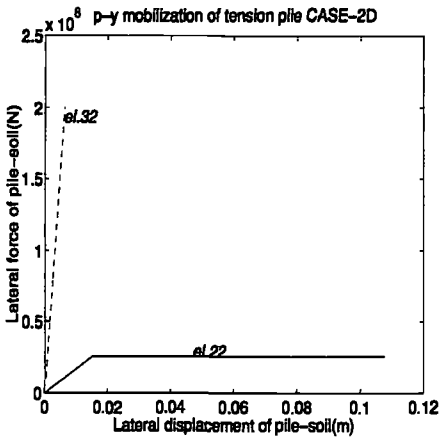

Figure 3.17: Lateral mobilization curves of the tension pile

3.4.1.4 Summary of results

Table.3.6 and Fig.3.13 summarize the global load-displacement response of the 2D jacket-pile-soil system with fixed, linear lumped spring and non-linear pile-soil support systems.

As observed the initial stiffness of the jacket with fixed support system is comparatively much higher than that with linear and non-linear foundation systems. The linear spring modelling in this case has offered an improvement with respect to the initial response of the structure in the range of small displacements for e.g. serviceability limit state(SLS) design. However, as seen the linear support system has failed to predict well the ultimate collapse response of the system. The ultimate capacity of the jacket-pile-soil system has been over predicted almost twice with respect to the non-linear pile-soil system.

In a more realistic non-linear model of the pile-soil system, the collapse of the system is observed far earlier than the structural failure as observed for the fixed and linear spring support systems because of the pull-out of the tension pile. Figs.3.14 and 3.15 show the axial pile-soil mobilization (t-z) curves for the compression and tension piles at the mudline level, 10m depth below mudline level and near the pile tip. It can be seen that el.22 and 42 connected to the left tension pile have been fully mobilized. The displacement at the head of tension pile is almost the same as pile tip about 450mm.

For the latter two cases, the failure of the system has occurred due to the plastic hinge formation at the leg near the ground support. These failure points are represented in the colour pictures of the deformed model of the structure by the red colours(see also colour display in appendix.H).

With respect to the minimum requirements for the ultimate limit state design (ULS) for which the safety factor may be calculated as:$\eta_r = \gamma_E.\gamma_M$ where η_r is the required level of safety factor

related to the combined effect of environmental loads and structural/foundation resistance for the jacket-pile-soil system, γ_E = the partial safety factor related to the environmental loading for e.g. as 1.3 according to NPD rules, (1992) γ_M = the partial safety factor related to the material strength of the jacket. γ_M is taken as 1.15 for steel material according to NPD rules, (1992) and as 1.2 and 1.3 for the soil material for an effective stress and the (undrained) total stress based pile-soil analyses, respectively.

In the current case study, the pile-soil load -displacement transfer curves are generated according to the disk model of soil as described in secs.2.2.3 and 2.3.3 based on an effective stress approach. Hence, a partial safety factor of 1.2 may be applied for the soil material. η_r will therefore be computed as 1.56. A more elaborate approach is introduced by Moan et al, (1997) for safety assessment of jacket-pile-soil systems near the ultimate collapse. This approach involves application of safety factors on both environmental and structural as well as pile and soil elements simultaneously. The latter method is not applied here. Table.3.6 shows that for the non-linear model of the pile-soil system this requirement can not be met. This means that the design of the foundation in this case is inadequate to comply with ULS requirements. It is observed that in this case the pre-mature failure of the system occurs due to pull-out failure of the tension(left corner) pile. To meet the required level of safety by NPD regulations for e.g. the following remedies may be considered:

i) increasing the length of the pile to provide sufficient skin friction in tension

ii) increasing the diameter of the pile which will proportionally increase the skin friction capacity of the pile both in tension and compression

iii) to build a resisting block at the tip of the pile or grouting the pile tip to the surrounding soil by cement (see Pile design methods for e.g. Poulos, 1978)

iv) insert an additional skirt pile to provide sufficient axial and lateral strength

Methods (iii) and (iv) may be considered for re-strengthening an existing (built) pile foundation while the other options described may be appropriate for a preliminary design of foundation. There might be restriction regarding increase of pile diameter for the piles inserted through(inside) the leg of the jacket, however, this method could be used for the skirt pile design. For a constructed skirt pile foundation, the possibility of grouting the pile tip may also be considered. Detail of re-design or re-strengthening of the pile foundation is out of the scope of the current study and will not be discussed further in this Chapter.

3.4.2 CASE 2:A 4-leg jacket case

3.4.2.1 Structure description

The structure is a light 4-leg jacket installed in shallow waters offshore Malaysia. The finite element model of the jacket and its 4 single pile foundation is shown in Fig.3.11. The bracing system of the jacket comprises only cross (X-type) bracings. The deck supporting module has

Table 3.7: Structural member description for 4-Leg(Malaysian) Jacket case

Structural Member	**O.D/H** (m)	t_w/B (m)
Legs	0.6	0.03
Braces	0.4	0.02
Deck beam	0.6	0.03
Piles	0.6	0.05

been modelled by an additional light frame at the top of the jacket with a height of about 7.5m above mean water level. The jacket-pile connections have not been modelled. The plan view of the jacket and the wave directions are shown in Fig.3.12. Table.3.7 describes the key structural characteristics of the jacket.

Table 3.8: Linear lumped spring stiffness data for 4-Leg(Malaysian) Jacket case

k_{11} (N/m)	k_{22}(N/m)	k_{33}(N/m)	k_{44}(N/m)	k_{55}(N/m)	k_{66}(N/m)
1.45E+08	1.45E+08	1.065E+09	3.49E+08	3.49E+08	10.00E+10

Table 3.9: Sand soil description for 4-Leg(Malaysian) jacket case

Layer	Z(m)	γ(t/m3)	ϕ(deg)	Su(KPa)	G0(MPa)	ϵ_{50}	T_{max}(KPa)
1	1.5	20.0	34.5	-	-	-	5.04
30	45.0	20.5	37.5	-	-	-	151.19

3.4.2.2 Pile-soil description

The foundation of the jacket consists of only single vertical piles as shown in Fig.3.11. The piles are made of steel tubular sections with a yield strength of 470MPa which are driven into a depth of about 45m. The pile cross sectional data is given in Table.3.7. The piles are supposed to be un-plugged and hence the most contribution to the axial resistance of the pile is from shaft (external and internal) friction.

Three different soil types are studied namely, sand, NC clay and OC clay. The corresponding soil input data are summarized in Tables.3.9, 3.10 and 3.11.

The load transfer-displacement (t-z), (p-y) and (q-z) curves are generated according to API RP2A 1993 and disk model as described in Secs.2.2.1 to 2.3.3 in Chapter.2.

3.4.2.3 Load description

The load vector consists of gravity, wave and current induced components. The gravity load on the structure is computed as the sum of the jacket selfweight , the weight of deck top facilities and

Table 3.10: NC clay soil description for 4-Leg(Malaysian) jacket case

Layer	Z(m)	γ(t/m3)	ϕ(deg)	Su(KPa)	G0(MPa)	ϵ_{50}	T_{max}(KPa)
1	1.5	20.0	-	47.40	500	0.025	20.57
30	45.0	20.5	-	70.49	1200	0.025	57.73

Table 3.11: OC clay soil description for 4-Leg(Malaysian) jacket case

Layer	Z(m)	γ(t/m3)	ϕ(deg)	Su(KPa)	G0(MPa)	ϵ_{50}	T_{max}(KPa)
1	1.5	20.0	-	94.75	1000	0.025	29.16
30	45.0	20.5	-	600.49	3000	0.025	277.35

that of piles(see Table3.12). The selfweight of jacket is distributed over the joints of structure proportionally. The weight of topside deck is distributed at four corner nodes of deck 510,520,530 and 540, respectively. The corresponding wave and current input data is given in Table.3.13.

3.4.2.4 Summary of results

Fig.H.1 shows the failure mode of the 4-leg jacket with a fixed supporting system. As seen, the main leg element 110 at the lower right corner (first bay) has buckled (elasto-plastically) due to combined compression and bending moment induced by the lateral wave +current load and vertical gravity loads on the jacket.

The red colour fringe of the element represents the plastic interaction value of 1.0. The axial force and bending moment interaction curve, the yield and bounding surfaces of el.110 are plotted on Figs.3.19, 3.20 and 3.21 which indicate that at the peak load of collapse, most of the force contribution in the critical leg element 110 is compressive force. As the plastic hinge forms at mid span of element 110 and it starts buckling the axial force is reduced and the bending moment portion increases significantly. The shift of yield surface with respect to the bounding surface as shown in Fig.3.21 is considerable and is due to the kinematic type hardening associated with the material model of element 110.

The plastic utilization of other elements are much lower than unity which shows the dependence of the system collapse on only one critical leg element. The global load-deflection response of the platform shows almost no reserve strength beyond the first member failure as plotted in Fig.3.30. Also seen that the ratio of the ultimate residual to the peak capacity of the jacket system with the fixed support system is about 1.7/3.0 which is due to the lack of properly designed redundancies in this lattice structural system. However, with respect to the applied 100-year design wave combined with the current induced load and the existing gravity loads on the structure, the obtained ultimate capacity of 1.7 times this design load normally satisfies the requirement for the ultimate limit state design(see for e.g. NPD rules or API RP2A 1993 code). However, this may not be sufficient to declare this structure safe since in the case of a weak(soft) soil supporting the jacket, the assumption related to fixed support system may not be valid.
To investigate any possible soil-structure interaction a lumped linear spring to ground model of foundation is considered for the 4-leg jacket. The static pushover analysis of the 4-leg jacket

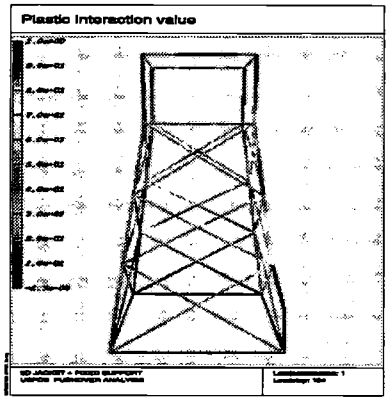

Figure 3.18: Failure mode of 4-leg (Malaysian) Jacket with fixed support (For colour display see Appendix.H)

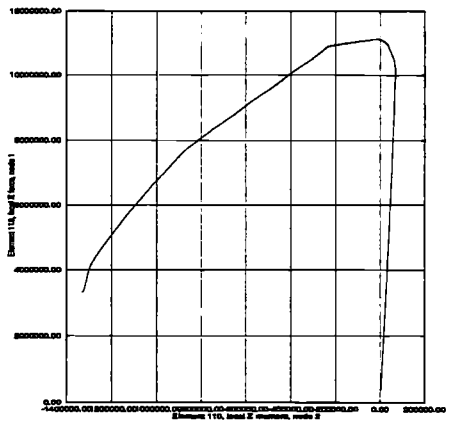

Figure 3.19: The local axial force vs. local bending moment interaction of el.110 of 4-leg (Malaysian) Jacket with fixed support

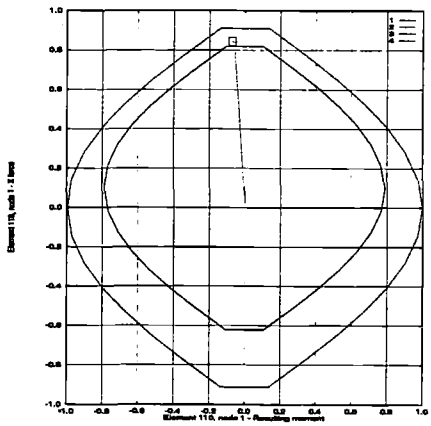

Figure 3.20: The stress state at reaching the yield surface of el.110 of 4-leg (Malaysian) Jacket with fixed support

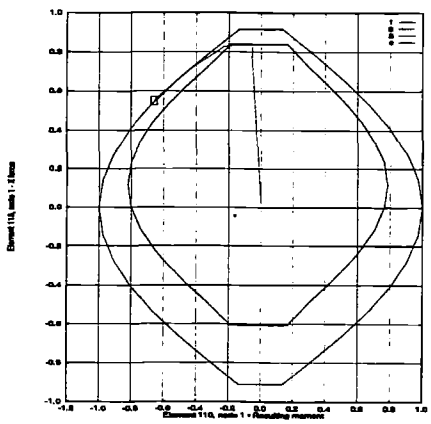

Figure 3.21: The stress state at reaching the bounding surface of el.110 of 4-leg (Malaysian) Jacket with fixed support

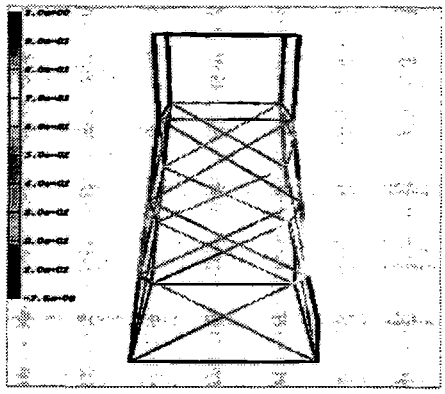

Figure 3.22: The Failure mode of the 4-leg (Malaysian) Jacket with linear spring to ground (For colour display see Appendix.H)

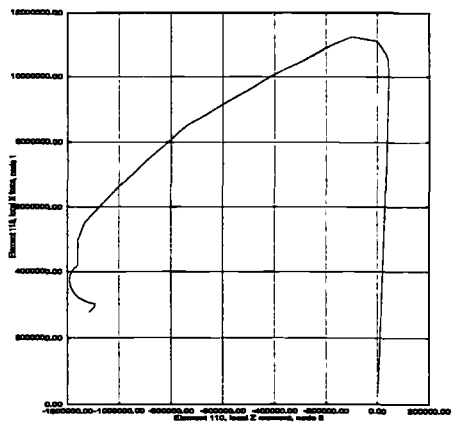

Figure 3.23: The axial force vs. bending moment interaction curve of el.110 of the 4-leg (Malaysian) Jacket with linear spring to ground model

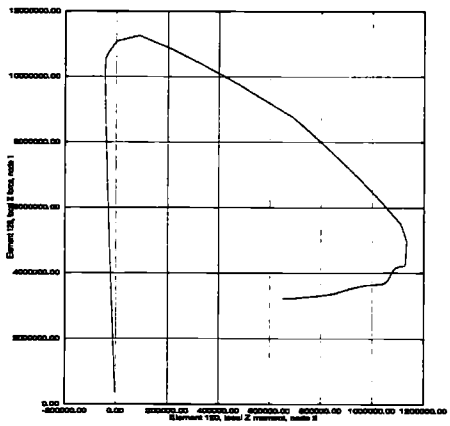

Figure 3.24: The axial force vs. bending moment interaction curve of el.120 of the 4-leg (Malaysian) Jacket with linear spring to ground

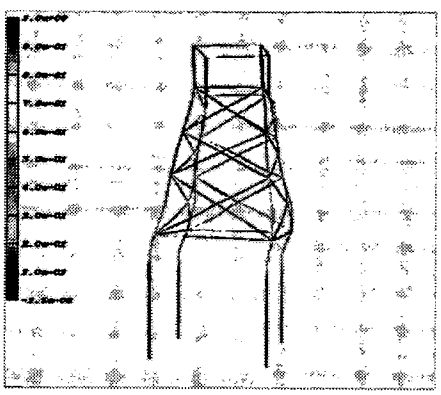

Figure 3.25: The Failure mode of the 4-leg (Malaysian) Jacket with non-linear pile-soil model(NC clay) (For colour display see Appendix.H)

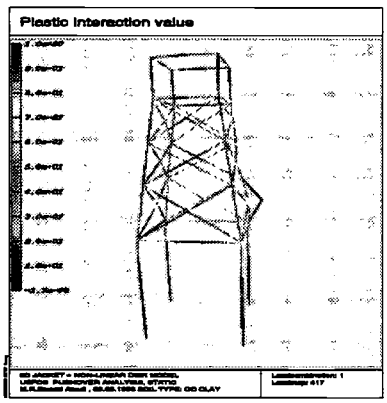

Figure 3.26: The Failure mode of the 4-leg (Malaysian) Jacket with non-linear pile-soil model(OC clay) (For colour display see Appendix.H)

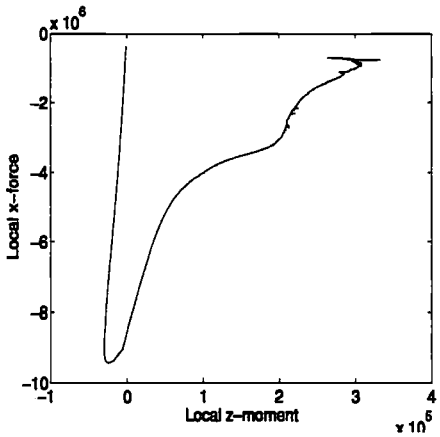

Figure 3.27: The axial force vs. bending moment interaction curve of el.120 of the 4-leg (Malaysian) Jacket with non-linear pile-soil model(OC clay)

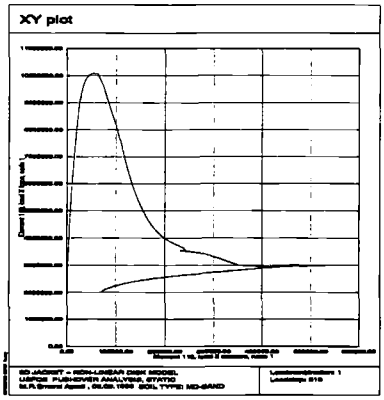

Figure 3.28: The axial force vs. bending moment interaction curve of el.110 of the 4-leg (Malaysian) Jacket with non-linear pile-soil model(sand)

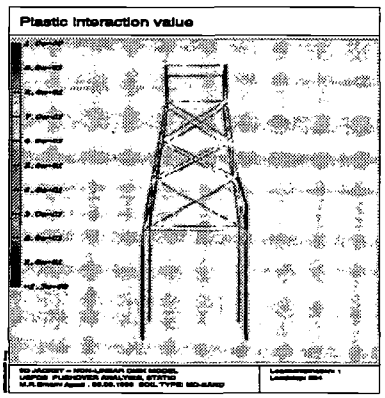

Figure 3.29: The failure mode of the 4-leg (Malaysian) Jacket with non-linear pile-soil model(sand) (For colour display see Appendix.H)

Table 3.12: Load description for 4-Leg(Malaysian) Jacket case

load	(MN)
selfweight of jacket	2.977
weight of topside deck	9.810
horizontal wave+current force	1.646
vertical wave+ current force	-0.552

Table 3.13: Wave and current description for 4-Leg(Malaysian) Jacket case

Water depth(d)	47.5m
100 year wave height(H_{100})	24.0m
Wave period(T_{100})	12.0sec
Current velocity(V_c)	0.7m/sec
Wave direction (α)	West-East
Drag coefficient(C_d)	0.77
Inertia coefficient(C_m)	2.0
Friction coefficient(C_x)	0.0001

with linear support system has been performed and the global load-displacement response is shown on Fig.3.30.

The pre-peak stiffness of the jacket-pile-soil system as seen is lower than that of the fixed jacket due to the additional displacement at the deck level induced by the deformation of the linear spring to ground.

As seen, the ultimate (peak) capacity of the system in this case is just slightly higher than that of fixed support system.

The post-peak softening behaviour of theses two models are also quite similar. The unloading has occurred in both systems after the plastic buckling of the two main leg members (el.110 and el.120). The equilibrium of the forces after the leg member failure required to reduce the total external forces on the jacket. The residual capacity of the linear supported system is about 1.24 compared to 1.69 of fixed system. Regarding the ultimate limit state design of the jacket, the rapid degradation of post-peak strength in the case of linear spring supported system may pose a risk.

Fig.H.2 shows the failure mode of the jacket with linear spring to ground system. In comparison the failure mode is more symmetric for the jacket system with the linear spring system.

The axial force-bending moment interaction curves are shown in Figs.3.23 and 3.24 for the buckled leg elements 110 and 120 which were visualized in Fig.H.2. Similar to the fixed system, as the legs started buckling plastically, the contribution of the bending moment has increased considerably due to rapidly growing lateral displacement at the mid-span of buckled element. Hence

Table 3.14: Pushover static analyses results for 4-Leg(Malaysian) Jacket case with various foundation models

	Static(pushover)		
	(RFY)	(RSU)	(RRES)
Fixed support	2.786	3.027	1.692
Linear spring	2.752	3.050	1.238
Non-linear pile-soil (NC Clay)	0.200	1.560	1.395
Non-linear pile-soil (OC Clay)	0.301	2.497	1.294
Non-linear pile-soil (SAND)	0.311	2.716	1.165

the axial force contribution has been reduced which is quite well understood from static point of view since the plastic interaction formula of a beam column (see for e.g. Søreide, 1986) is based on a combination of axial force and bending moment components and as the bending moment increases in the member's cross section at full plastification, the axial load has to be reduced to satisfy the plastic equilibrium of forces.

Though the lumped linear spring model could in a simplified manner simulate the soil-structure interaction but it is still not known whether any such large forces carried through the pile to the soil would likely result in soil yield and hence influencing the global response of the jacket-pile-soil system or not? To answer this question, a non-linear finite element model of the pile-soil has to be considered. This model enables us to simulate any possible yield in the soil or any possible buckling or plastic hinge formation in the pile itself induced due to large axial forces or excessive lateral deformations in the surrounding soil. The pile-soil failure may influence the super-structure's (jacket) response and vice versa the failure of the jacket structure may influence the near collapse behaviour of the pile-soil system. Such interaction is analyzed here through an integrated jacket-pile-soil analysis by means of USFOS program(Søreide at al, 1994). The non-linear pile-soil interaction is represented by static disk model as described in Secs.2.2.3 and 2.3.3 of Chapter.2 and generated by a number of Matlab language programs(see Appendix.C). Three main soil types are also investigated namely, normally consolidated clay, overconsolidated clay and medium dense sand.

As first non-linear soil case, a NC clayey soil is considered as described in Table.3.10. The global load-displacement response of the jacket-pile-soil system is much softer than the response of the fixed and linear spring supported jacket as compared in Fig.3.30. The peak (ultimate) collapse strength of the jacket is about 1.6 compared with 3.03 and 3.05 for the fixed and linear spring supported jacket systems, respectively. The ultimate residual strength of the jacket-non-linear pile-soil system is about 1.40 compared to 1.69 for fixed and 1.24 for linear spring supported jacket. As shown on Fig.H.5 a plastic hinge formation is seen in the upper parts of piles close to the mudline level which is the result of excessive lateral soil deformation in upper soil parts.

This can be verified visually through inspecting the deformed model of the jacket-pile-soil system and numerically through the pile-soil mobilization (t-z) and (p-y) curves for both tension(left) and compression(right) piles. The mobilization curve of el.200123 at the tip of the tension (left) pile in Fig.3.32 does not indicate the failure of the tension pile. While inspecting the tip (t-z)

mobilization curves of els.200002 and 200030 suggests collapse of the right corner pile in compression. The lateral mobilization (p-y) curves plotted in Fig.3.33 show that the soil has yielded near the surface under lateral loading. The maximum lateral soil displacement at depth 1.5m below the mud-line level is about 110mm. It is also seen that the soil has been mobilized only down to depth about 12.0m below the mud-line. The results of this case study indicates that, applying a fixed or linear spring type soil support system will significantly overestimate the collapse load of the jacket in a soft clay soil condition as described above.

The global load-displacement response of the jacket-pile foundation on OC clay is also represented in Fig.3.30. As seen, the spring back behaviour occurs just after the ultimate collapse of the system due to buckling of a critical leg member el.120(see Fig.H.4). This behaviour is not observed in the case of soft NC clay for which the global failure of system was governed by the pile-soil failure in compression and under lateral loading.

The spring back response in this case is due to the very stiff overconsolidated soil which has not reached its collapse (peak) point under the imposed loading on the jacket. Since after the plastic buckling failure of leg els.110 and 120 the external loading on the jacket had to be reduced to compensate for the loss of these two main load carrying elements, the only possibility left for the attached pile-soil system has been to unload elastically because the plastic un-loading (softening) can not be allowed for the soil. While in the case of NC soil such behaviour is not seen due to slide(yield) of the pile-soil which has initiated the global collapse of the system. Also the mechanisms of the collapse for fixed and linear support systems are mainly dependent on the structural behaviour since for the fixed case no ground displacement is allowed and for the linear foundation case the deformation of the linear support has been quite small compared to that of structural distortion. Its effect can be seen in the hardening/softnening of the post-peak unloading part.

The axial and lateral mobilization curves for the OC case do not indicate a pile pull-out or plunge failure. Although as shown on Figs.3.34 and 3.35, the axial mobilization of soil near the mud-line is much higher. The mobilization curve of el.200002 at the top of compression (right) pile shows that the soil at this point has initially yielded in compression due to the transferred compressive forces from the jacket but just after the buckling of the leg member in compression the axial stress in el.200002 has been reversed through an elastic un-loading and then started re-loading in tension. This behaviour is manifested in a global spring back response as shown on Fig.3.30. The same kind of un-loading is also observed for the el.200030 at the tip of the compression pile as plotted in Fig.3.34.

The axial force and bending moment interaction curve for the critical leg member (el.120) is given in Fig.3.27. The peak point of this curve corresponds to the peak collapse load on the jacket which implies that the failure mainly has occurred due to compressive force in the member while as seen after the peak point the contribution of the bending moment has increased dramatically which is accompanied with the plastic buckling of the member at its mid-span.

The lateral mobilization curve of el.200002 also verifies the above conclusion concerning the

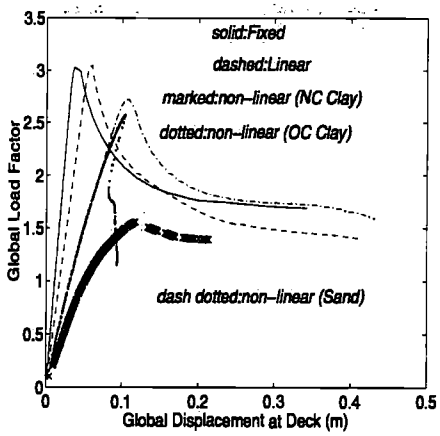

Figure 3.30: Global Load-displacement responses of the 4-leg jacket with various support systems

elastic un-loading of the soil element and the lack of full lateral mobilization of the soil. The influence of the OC clay on the ultimate collapse capacity of the jacket-pile-soil system is observed to be considerable by reducing it from 3.03 for the fixed system to about 2.50. The post-collapse strength of the jacket supported on OC clay as shown is considerably lower than that of the fixed jacket system due to very brittle behaviour of the soil.

As a last case, the influence of the sand type soil on the global response of the 4-leg jacket is investigated through a static pushover analysis. The pile-soil interaction curves are generated according to API RP2A 1993 (t-z) model for sand. The global load deflection response of the latter system is plotted in Fig.3.30 and compared with the other soil models. As seen the initial (pre-peak) response of the system supported on the sand is almost the same as the system supported on OC clay up to load level of 2.2 and small discrepancy is observed after this load level. The peak capacity of the system is given in Table.3.14 which is quite close to that of system supported on OC clay but their post-collapse responses are completely different.

The latter model's post-peak response is much softer due to sandy soil's response nature under axial and lateral loading. As seen on Fig.H.6 the collapse of the system though has been initiated by soil's yield but no pull-out or pile plunge failure is observed in this case. In terms of the residual strength of the system, the reduction has been less severe for the case of sand which is obtained to be about 1.17 compared to 1.69 for the fixed jacket model.

The global failure mode of the pile-soil-jacket system, as shown in Fig.H.6 is initiated by the yield of the top soil elements. However, the collapse of the system is observed to occur after the buckling of the main legs (els. 110 and 120) due to increase in the bending moment which is induced by the excessive soil deformation near the mudline.

The plastic interaction value of the element 110 clearly illustrates the generated failure mecha-

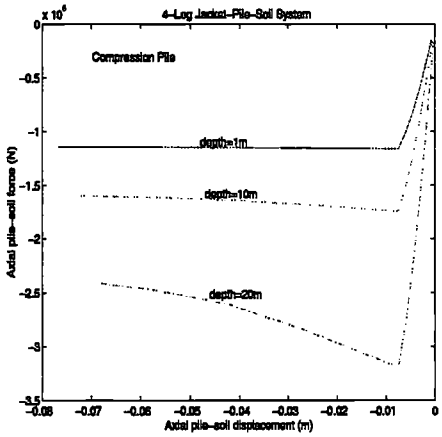

Figure 3.31: Axial mobilization curves of compression pile at three different depths for NC clay

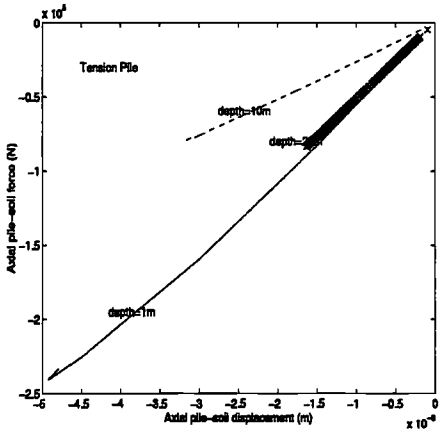

Figure 3.32: Axial mobilization curves of tension pile at three different depths for NC clay

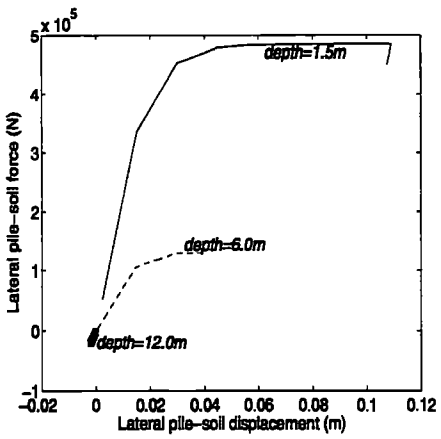

Figure 3.33: Lateral mobilization curves of compression pile system at three different depths for NC clay

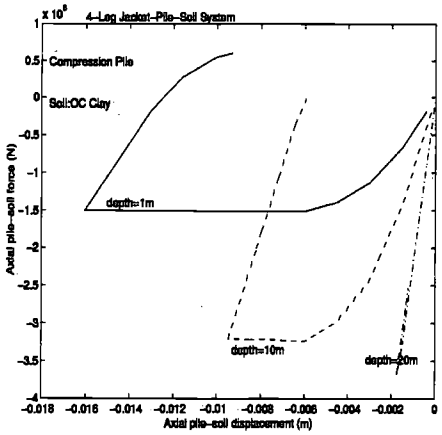

Figure 3.34: Axial mobilization curves of compression pile at three different depths for OC clay

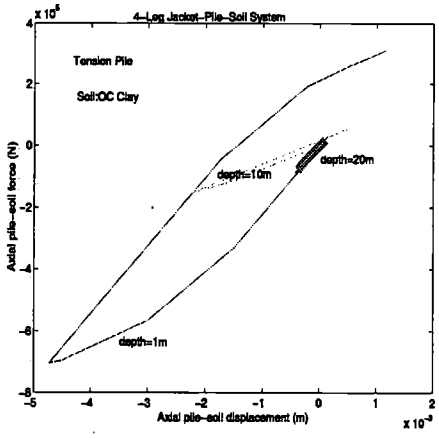

Figure 3.35: Axial mobilization curves of tension pile at three different depths for OC clay

nism by the pile-soil displacement. As seen in Fig.3.30 at the point of first plastic hinge formation, the axial force has dropped considerably while the contribution of the bending moment has been maximum. The axial force versus the lateral displacement at the mid-span of the element 110 is shown in Fig.3.28 for 4-leg jacket with pile foundation in sand. It is apparent that the buckling capacity of the leg has been reduced by introduction of pile-soil non-linearities by about 12%.

3.4.3 CASE 3: An 8-leg Jacket-Pile-Soil system

3.4.3.1 Structural model

The finite element model of the jacket structure used in the case study is shown in Fig.3.9. The structure consists of two longitudinal and four transversal frames. Longitudinal frame's bracing system comprise mainly single diagonal braces and only X-braces at the first and the fifth storeys. The transversal frames have only K-braces. The supporting deck has been modelled as a truss and the top deck facilities have been modelled by a pyramid frame. Tables.3.15 and 3.16 summarize the descriptions of the structural and non-structural elements of the 8-leg jacket platform.

3.4.3.2 Foundation model

The foundation of the jacket system in this study is modelled as equivalent single piles penetrating to a depth of 28m below the mud-line. Due to the relatively short lengths of the designed skirt piles in this case, they have been grouted at the bottom where the piles have penetrated into a sand layer. Hence, the pile-tip is considered to be plugged to ensure end-bearing. Since the lateral resistance may be mobilized at the upper part of the soil, the designed pile condition is not modified and will be used in the first part of this study. The pile-soil interaction is

Table 3.15: Structural member description of 8-Leg Jacket case

Structural Member	**O.D/H** (m)	t_w/B (m)
Legs	1.60-3.00	0.147-0.060
Braces(horizontal-l.1)	0.90-1.30	0.025-0.035
Braces(diagonal-l.1)	0.60-1.60	0.020-0.050
Braces(horizontal-l.2)	0.90-1.00	0.025-0.035
Braces(diagonal-l.2)	1.00	0.035
Braces(horizontal-l.3)	1.40	0.030
Braces(diagonal-l.3)	1.20-1.40	0.035-0.040
Braces(horizontal-l.4)	1.00-1.20	0.045-0.030
Braces(diagonal-l.4)	1.10	0.050-0.055
Deck:Braces(horizontal-l.5)	0.90-1.10	0.035-0.050
Deck:Braces(diagonal-l.5)	1.60	0.075
Piles	2.88	0.04

modelled as non-linear disks as described above. The detail description of soil profile is given in Table.3.17.

3.4.3.3 Hydrodynamic model

Two different hydrodynamic models are used in the present study. The main difference being the modelling of non-structural elements, such as anodes etc. These two models therefore yield different loads corresponding to the 100 year-design wave heights and so the given global load factors associated with collapse. For clarity, these two models and their results are treated separately. However, the results obtained by each model can be used to study the effect of for instance wave load scaling vs. wave height incrementation approach.
The 100-year wave height and period and the current velocity are described in Table.6.4.

In the early part of our study, we used Model-1(WAJAC) as the reference. However, since it was not possible to use this model in cyclic analysis Model-2(USFOS) was adopted.

Model-1(WAJAC load model) contains non-structural members as risers, conductors, landing docks, bottle legs and pile guides. Drag and mass coefficients are 0.77 and 2.0, respectively. Model-2(USFOS load model) does include boat landings and pile guides and uses drag and mass coefficients of 0.7 and 2.0, respectively. In Model-1 no marine growth was specified whereas in Model-2 marine growth profile was assumed to vary from zero at mudline level to about 10cm at mean water level.

Model-1 was primarily applied to perform static pushover analyses and recently to study the wave height vs. wave load incrementation as well as foundation effects. The more recent Model-2 was applied to study the cyclic (quasi-static) response of the jacket-pile-soil system.

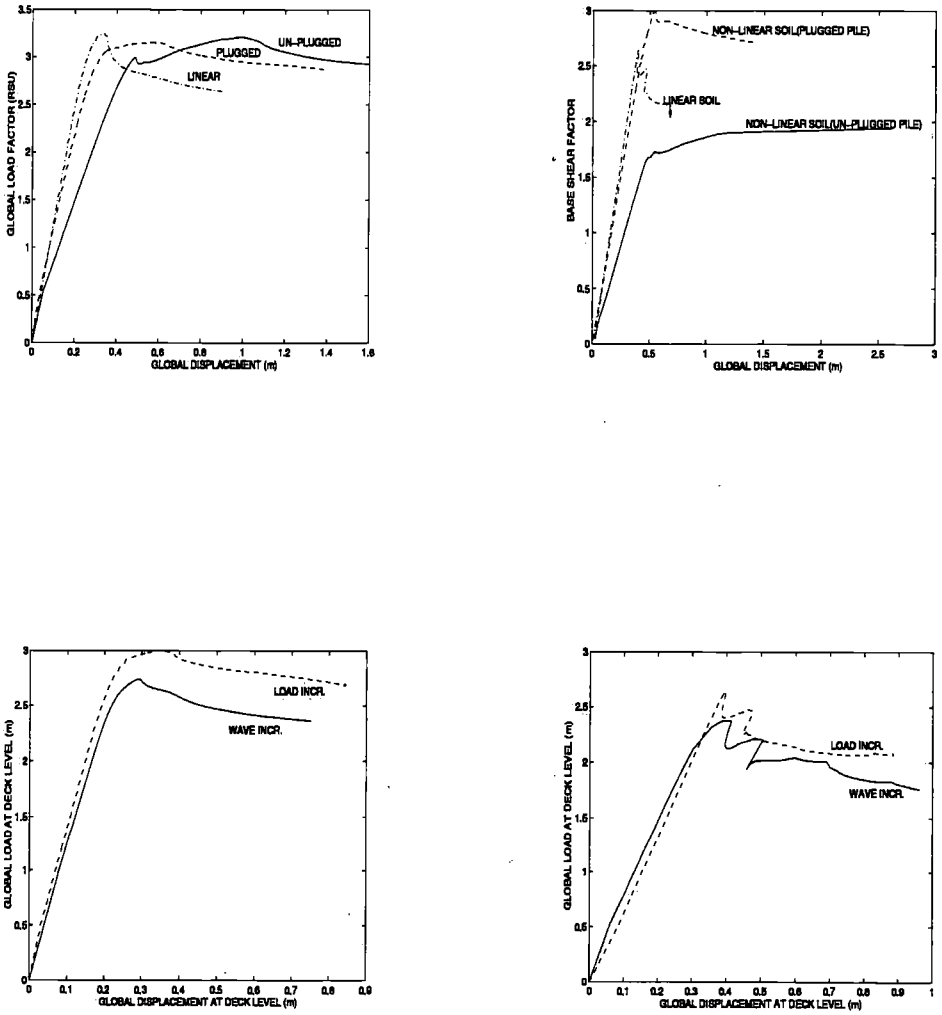

Figure 3.36: Static response of the jacket(hydrodynamic Model-1) with non-linear pile-soil vs. linear support system under a) end-on loading b)broad-side loading c) wave height incrementation method vs. conventional wave load incrementation method for end-on loading d) modified vs. conventional for broad-side loading]

Table 3.16: Hydrodynamic(non-structural) member description of 8-Leg Jacket case

Non-structural Member	**O.D/H** (m)	C_d	C_m
Conductors	4.59-11.1	0.7	0.339-0.168
Conductor guide	0.94-5.20	0.77	0.72-2.0
Risers	12.75"-36"	0.7-1.0	2.0
Docking sleeve	2.70-5.40	0.7	1.10-0.72
Boat landing	-1.0	0.432	2.0
Walkways	-1.0	0.7	2.0
J-tubes	-1.0	0.64-0.7	2.0
Fire and sea caissons	-1.0	0.66-1.02	2.0
Launch legs	1.8-4.1	0.77-1.5	2.0-1.30
Pile guide	-1.0	0.18	2.0
Bottle legs	1.8-13.24	0.77	2.0-2.5

3.4.4 Static behaviour

The static response of hydrodynamic Model-1 and 2 under end-on and broad-side loading are summarized in Tables.3.19 to 3.22 and plotted in Fig.3.36. The global load factors corresponding to the first member failure(RFY), the ultimate static capacity(RSU) and residual strength(RRES) of the system under end-on and broad-side loading are given in Tables.3.19 to 3.22 respectively, for hydrodynamic Models 1 and 2. (Note that the reference load for these global factors is the 100 year wave load). In general good consistency is seen between the results with respect to the different structural, foundation and hydrodynamic models used in each studied case which will be described in the following.

3.4.4.1 Static response of the platform under end-on loading(without the effect of pile-soil)

As seen from the static analyses results(see Fig.3.36 and Tables 3.19 and 3.20), the structure(both hydrodynamic models) under end-on loading exhibits quite substantial reserve strength beyond the first member failure (about 30% or more of the ultimate static capacity). This kind of behaviour is mainly attributed to the load shedding capacity of the bracing system of the longitudinal frames which enable the jacket system to re-distribute smoothly the forces after the first member failure. The equilibrium of the forces is very quickly achieved after first member failure and hence the system has not lost any considerable strength. Successive failures of several diagonal and horizontal braces occur before the ultimate collapse of the system is reached when all the remaining reserve strength in the system has been exhausted gradually.

The post ultimate response of the system(Model-1) show a slow degradation of the strength and hence a rather ductile behaviour. The post-peak strength degradation of the system is only about $7-8\%$ for the end-on loading.

Table 3.17: Soil description for 8-Leg(North-sea) jacket case

Layer	Z(m)	γ(t/m3)	ϕ(deg)	Su(KPa)	G0(MPa)	ϵ_{50}	T_{max}(KPa)
1	3.5	20.5	37.0	0	31.5	0	10.3
2	4.5	20.5	37.0	0	47.5	0	23.5
3	5.5	20.5	37.5	0	53.1	0	30.0
4	6.5	20.5	38.0	0	58.2	0	36.6
5	8.5	20.5	38.0	0	65.1	0	45.8
6	10.5	20.5	38.0	0	73.3	0	58.0
7	12.5	20.5	38.0	0	80.6	0	70.3
8	14.5	20.5	38.0	0	87.3	0	82.5
9	15.9	20.5	38.0	0	92.6	0	94.0
10	18.5	21.6	0.0	174	58.0	0.013	99.7
11	23.5	20.5	34.0	0	109.6	0	104.2
12	25.5	21.6	0.0	180	60.0	0.011	121.4
13	29.5	20.5	37.0	0	125.7	0	115.8

Table 3.18: The wave and current description for 8-leg Jacket platform

The wave direction	**wave height** (m)	**wave period** (s)	**current velocity** (m/s)
West-East wave	30.2	16.7	1.1
North-South wave	27.3	15.8	1.05

3.4.4.2 Influence of foundation model on the static behaviour of system under end-on loading

To investigate the influence of foundation modelling and in particular the pile-soil failure effects on the near collapse behaviour of the jacket platform, the response of three different foundation models was studied considering, namely, linear spring to ground, non-linear plugged pile and un-plugged pile.

The pre-collapse response of the jacket platform with plugged type pile foundation and linear type foundation model are stiffer than that of the un-plugged system(see Fig.3.36). The softening of the response for the latter case may be attributed to the rapid yield occurring in the soil along the pile shaft with a relatively smaller contribution than the tip resistance. The proximity of the pre-collapse response of the linear and the plugged case is due to far larger end-bearing contribution than the un-plugged pile foundation (an order of magnitude higher than the total skin friction along the pile). This may indicate that for a design load level a linear spring idealization of the platform might be as good as plugged model of the pile-soil system. However, the linear idealization apparently would be quite unconservative with an un-plugged pile. With respect to the plugged design of the foundation for this platform, a linear spring to ground assumption may be considered to be an appropriate model for serviceability analysis. For the ultimate limit state design, the results indicate that even an initially stiff linear lumped spring system of foundation is unconservative, especially w.r.t the broad-side loading of the platform(with un-plugged piles).

Table 3.19: Pushover response of the jacket platform with plugged pile foundation under end-on loading(Model-1)

	Static(pushover)	
	Wave Load Incr.	Wave Height Incr.
First member failure(RFY)	1.99	1.94
Ultimate collapse(RSU)	3.15	2.89
Residual strength(RRES)	2.92	2.56

Table 3.20: Pushover response of the jacket platform with plugged pile foundation under end-on loading(Model-2)

	Static	
	Wave Load Incr.	Wave Height Incr.
RFY	1.99	1.96
RSU	2.79	2.55
RRES	2.58	-

The interaction between soil-pile(plugged case) and jacket has resulted in increased system capacity as observed in Fig.3.36. The axial resistance of the plug at the pile tip(about 325MN) has allowed the system to carry higher overturning moment at the mud-line level. It is observed here that the jacket with the linear spring foundation model has failed at a global load level about 2.6 under broad-side loading , while the same jacket Model-1 with the plugged type pile foundation has resisted about 15% higher load. Under end-on loading, the ultimate static strength of the system apparently has not been influenced much by the different foundation modelling.

It is also seen that the plugged piles have provided sufficient ductility for the system at the post-collapse range, while the jacket with the linear spring system was found to be less ductile. The implication of this fact on dynamic response of the system will be discussed in Chapter.5.

3.4.4.3 Static response of the platform under broad-side loading (without the effect of pile-soil)

For the jacket with linear spring to ground system, a dramatic load shedding can be seen just after the collapse. As seen, the behaviour of the system is linear elastic up to the collapse and the system does not possess any noticeable reserve strength beyond first member buckling. This behaviour is attributed to the K-brace configuration of the transversal frames. When the compression member of a K-brace system failed, the axial force in both members of the bracing have to be reduced to satisfy the equilibrium of the forces. This corresponds to the peak(ultimate collapse) point and after that when the lateral displacement increases the load drops further in the system, since both tensile and compressive members of K-bracing system are shedding force at the same rate(Stewart, 1995 and Hellan, 1995).

Table 3.21: Pushover response of the jacket platform with plugged pile foundation under broad-side loading(Model-1)

	Static	
	Wave Load Incr.	Wave Height Incr.
First member failure(RFY)	2.05	1.79
Ultimate collapse(RSU)	2.99	2.73
Residual resistance(RRES)	2.71	-

Table 3.22: Pushover response of the jacket platform with plugged pile foundation under broad-side loading(Model-2)

	Static	
	Wave Load Incr.	Wave Height Incr.
RFY	2.15	1.89
RSU	2.52	2.32
RRES	2.06	-

3.4.4.4 Influence of foundation on the static behaviour of system under broad-side loading

The static load-deflection response of the jacket with hydrodynamic Models 1 and 2 with plugged foundation under broad-side loading are summarized in Tables 3.21 and 3.22. The jacket system with plugged pile foundation is seen to possess considerable amount of reserve strength beyond its first member failure(ranging from $17-30\%$ of the ultimate capacity). This reserve strength has been induced by the ductility provided by the gradual yield of the soil particularly at the pile tips. It can be seen from Fig.3.36 that the jacket's ultimate static capacity with plugged pile foundation is about 15% higher than that with a linear spring support system. It can also be seen in Fig.3.36 that the pre-ultimate response of the plugged system is somewhat softer than that of jacket with linear support system. The post-ultimate response of the plugged system in this case is comparatively much stiffer than that of the jacket with linear support system.

The residual strength of the jacket with a plugged pile foundation system is found to be about 82% of the ultimate static capacity while the residual strength of the jacket-linear spring to ground system is found to be less than 75% of the ultimate static capacity.

In comparison, the static load-deflection response of the jacket with un-plugged pile system is much softer than that of the jacket with plugged and linear spring support system. The ultimate capacity of the jacket with un-plugged pile system has been mobilized at a lateral displacement of about 2.0m which is 5 times higher than that for the plugged system. The corresponding ultimate capacity is only about 2/3 of the jacket with the plugged pile foundation system. Inspecting the global failure mode of the latter system shows that the platform has failed due to the pull out of the tension piles.

3.4.5 Comparison of wave height incrementation(WHI) and wave load incrementation(WLI) approaches

In a conventional static pushover approach, the environmental loading such as that induced by wave and current are imposed incrementally on the structure until the ultimate collapse occurs. This method does not take into account the variation of the sea surface elevation during each increment of loading.

The variation of the sea surface elevation changes the wet zone on the platform and hence the resultant total base shear and the overturning moment. Additional forces may be imparted on the structure if the extreme wave's crest reaches the cellar or main deck areas. With respect to these effects, a new pushover approach is established based on incrementing the wave height. The procedure involves several increment of the wave height and if a wave on deck is encountered then the additional deck forces are calculated according to the draft Sec.17 of API 1994.

It is seen that the ultimate strength factors(for both hydrodynamic models of jacket) obtained in conventional static pushover analyses are about $8-9\%$ larger than those corresponding to the wave height incrementation method.

Fig.3.36 compare the results of pushover analyses based on load and wave height incrementation methods for end-on and broad-side loading. It is seen that the near collapse response of the platform during wave height incrementation is more soft. The maximum discrepancy which occurred near the ultimate collapse, is about 9 percent. This is mainly due to the additional forces imparted on the upper part of the structure including part of the cellar deck (about 1.1 m at collapse), and to changes in the distribution of the forces over the structural elements. It is seen that the ductility of the jacket has not been changed in a significant manner. Since only the wave height is incremented, while the current velocity is kept fixed, there is still some place for speculation whether the observed trends might be really due to wave height incrementation. However, recent investigation by excluding the current induced loads show the same tendency.

3.5 Conclusion

It is shown that the influence of soil types as well as pile-soil modelling can be significant on the global static behaviour of the jacket-pile-soil system. In particular, stiff OC type and sand show much stiffer behaviour than soft NC clay on the global response of the system.

It is shown that a linear modelling of foundation may provide a significant improvement over a fixed support system without any account for structure-soil interaction. However, the latter might overestimate particularly the overall stiffness of the pile-soil foundation. It is also shown that in some cases the linear model of soil may result in a significant overestimation of the ultimate static capacity of the jacket-pile-soil system.

A more realistic non-linear pile-soil model is applied for the cases studied in this Chapter and shown that a significant yield in the soil can result in pile failure either in tension, compression or

under lateral loading which might significantly influence the global load-displacement response of the jacket near the collapse.

It is observed that a plugged pile foundation may exhibit quite different response than that of an un-plugged one. The influence of the pile tip load transfer-displacement modelling is shown to be quite significant on the overall response of the jacket-pile-soil system. It is shown that for e.g for a short pile system, the plug resistance may have much more significant contribution than the total shaft skin friction resistance. The associated response of the jacket with plug pile foundation is found to be much stiffer than that of un-plugged case.

It is concluded that the effect of wave load modelling can be important on the ultimate static resistance of the jacket-pile-soil system. It was observed that a wave load modelling based on wave height incrementation resulted in $8-9\%$ lower ultimate static strength than the traditional wave load scaling approach for the studied case here. The latter discrepancy may be attributed to the change of wave load distribution, shift of load centroid due to variation of wet zone over structure and the other possible effects due to large deformation and accumulated (cyclic) plasticity.

CHAPTER 4

DYNAMIC ANALYSIS OF PILE-SOIL INTERACTION

4.1 Introduction

The response of a jacket platform under the action of environmental loading such as waves or earthquakes may be influenced by the interaction between the pile and soil. As described earlier in Chapters 2 and 3, the collapse behaviour of such systems as jacket-pile-soil are often considered as quasi-static due to the relatively low frequency associated with the environmental loads such as extreme waves and currents. However, due to comparatively higher frequency of vibration associated with earthquakes and other possible dynamic loading on the jacket platform such as collision with ship or explosion on the deck etc., the static pile-soil interaction models such as disk model described in Chapter.2 may not be relevant since the dynamic stiffness of the pile-soil foundation may vary significantly with the frequency of vibration. Several basic modelling approaches have been developed to analyze the dynamic interaction between the pile and soil such as continuum finite element representation of the soil(see for e.g. Langø, 1991), boundary element modelling(see for e.g. Kaynia and Kausel, (1982) and their combinations or extensions). These are referred to as rigorous methods and are often applied for refined analysis of a foundation.

Although these methods may offer very accurate solutions, they are nevertheless very time consuming and hence very costly to apply for analysis of a large number of piles. Other alternative solutions which have been developed in the recent years are mainly based on a plane strain idealization of soil and are similar in principles to the static models presented in Chapter.2, however, with addition of dynamic properties (see for e.g. Nogami and Konagai, 1986 and 1988).

In the most recent years, a new soil dynamic approach referred to as cone modelling was presented by Meek and Wolf, (1992), which is on the basis of strength of material method. The

cone modelling is an indirect boundary element approach with respect to the cone's geometrical extension to the inifinity.

The basic derivations by Meek and Wolf, (1992) were based on linear-elastic and homogeneous soil assumptions. The idea was developed by Wolf et al, (1994) for pile-soil foundations with a rigid or flexible pile embedded in an elastic soil half space. As illustrated in Fig.4.6, a multi-stack of disks represents the pile and the cones are used to model the interaction between the pile and the surrounding soil.

The interaction between the disks via cones are illustrated schematically in Fig.4.1. This interaction via the soil cones may be referred to as coupling which represented by equivalent springs in Fig.4.7. This coupling between disks actually represents the displacement contribution at the location of each disk caused by the loads acting on the other disk or equivalently displacement generated at the position of other disks. In physical sense, coupling is due to the transmission of the wave through soil media from a point at pile (source disk connected to the pile) back to the pile at another point(receiver disk) via cones(see Fig.4.3). In a sense, the coupling between disks represents the interaction which takes place from one cone to another in the full space of soil.

The coupling between disks in this Chapter is only applied for the linear elastic type soil since it is based on the principle of superposition.

The pile itself can be represented in this model by elastic beam elements. The mass of the soil inside the pile may be removed from that of the system(Wolf and Meek, 1992) and the mass of the pile can be condensed at the disks(nodes). The model is capable to include both material and radiation damping.

The radiation damping is an inherent property of the cone model due to its geometry which extends (rapidly)towards infinity and thus carries away a significant proportion of the input excitation energy. The material damping may be considered to be less important than the radiation damping for the cone-disk system. However, the influence of material damping on the dynamic response of the pile-soil system will be investigated. The material damping is included as visco-elastic or linear hysteretic for an elastic type soil.

An extension of the cone model for non-homogeneous and/or non-linear soil behaviour is presented in this Chapter. Also two different models are used within this Chapter to represent the non-linear elasto-plastic type pile behaviour. These are namely, USFOS beam model (Søreide et al, 1994), which is briefly described within the context of Chapter.3 and the Bouc's general purpose non-linear hysteretic structural element model(Bouc, 1968).

Various models of pile-soil are formulated in frequency and time domains such as 1) rigid pile and linear elastic soil, 2) flexible(elastic) pile and linear elastic soil with linear hysteretic damping 3) flexible(elastic and elasto-plastic) pile and non-linear(elasto-plastic and hyper-elastic) soil with non-linear hysteretic type damping.

In the frequency domain analysis, the first two pile-soil models are applied while the non-linear soil models are considered in the time domain analysis. As mentioned, the coupling between various disks is considered in the frequency domain analysis but only in each loading direction not between the horizontal and vertical motions of disk. However, in the non-linear time domain analysis the coupling between disks is not applied. A kinematic hardening rule is used for the elasto-plastic soil model. Both static disk and dynamic cone-disk models are implemented in the time domain analyses and the influence of the excitation frequency is accounted for by modifying the the static stiffness of the disk model.

Extreme wave and seismic response analyses of pile-soil systems are performed here. Due to the low frequency of sea waves, the corresponding dynamic stiffness is estimated to be close to that of the static stiffness of pile-soil system. The impedance functions of several piles in half space of soil obtained according to the cone-disk model are verified against the results of existing rigorous methods such as boundary element solution(Kaynia and Kausel, 1982), direct boundary integral method (Apsel and Luco, 1987) and the analytical approaches of Nogami and Konagai, (1986) and (1988).

Simplified equivalent (non-linear) lumped models such as SDOF, 2DOF and 3DOF of pile-soil are also used to get further physical insight into the dynamic pile-soil behaviour by performing a number of parametric studies. The influence of several important soil and pile parameters on the pile-soil system's dynamic stiffness coefficients and interaction are investigated through these simplified analyses.

4.2 Cone-Disk modelling of soil

4.2.1 General

The idea of linear cone modelling of soil was initiated by Meek and Wolf, (1992) based on the well known Boussinesq theory of soil mechanics and the results obtained from rigorous elastic wave propagation analysis of Miller and Pursey, (1955), boundary element analyses by Kaynia and Kausel, (1982), direct integral method of Gazetas et al, (1984) and (1987), direct integral method of Apsel and Luco, (1987). Based on the Boussineseq's theory, the stress/strain distribution in an elastic half space of soil under a concentrated vertical load is illustrated in Fig. 4.8. It is shown that the stress/displacement contours form cones (or wedges) with their apex points taken at a distance above the loaded surface. The stress/strain distribution in the horizontal direction near the loaded plane is neglected according to this theory. Meek and Wolf, (1992) considered these unidirectional unfolded cones to carry the applied load at a given point in soil to the infinity. Nonetheless, in the linear cone model of Wolf et al,(1994) the radiation in the horizontal direction is neglected. This neglected radiation is particularly related to the near loaded plane of soil. Fig. 4.9 shows schematically that the stress or energy can be transmitted through soil within spheres (or semi-sphere) in radial directions.

The neglected radiation energy may be represented in this model by the cut off areas(see Fig.4.8). It can be seen that the ratio of the neglected (cutoff) energy may be small compared to the total

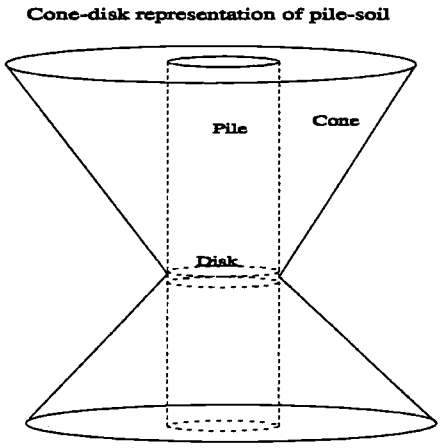

Figure 4.1: A double cone representation of the dynamic pile-soil interaction

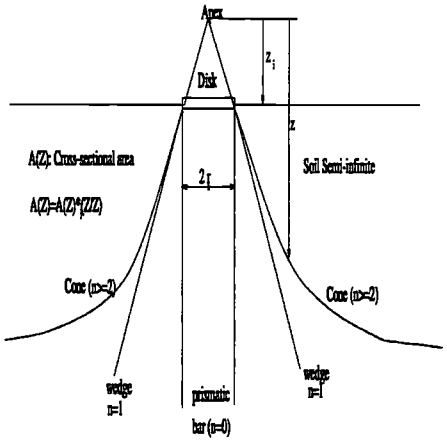

Figure 4.2: A single cone representation of the semi-infinite soil medium under a loaded disk located at the surface (with special cases of cone as wedge and a prismatic bar)

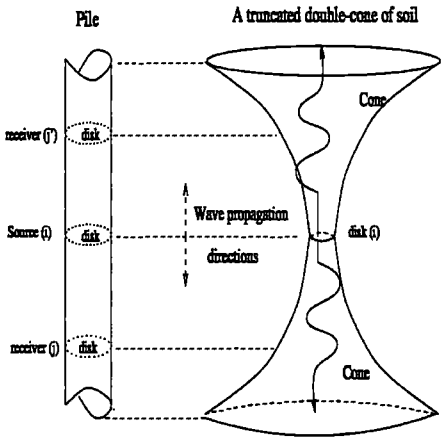

Figure 4.3: Illustration of interaction(coupling) between various disks via their associated double-cones in (the fullspace) of soil

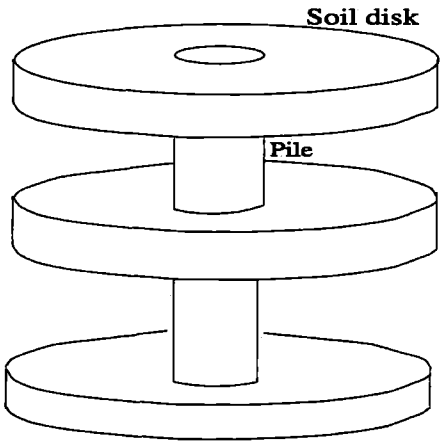

Figure 4.4: A multi-stack of deformable pile-soil interaction disks connected via pile elements

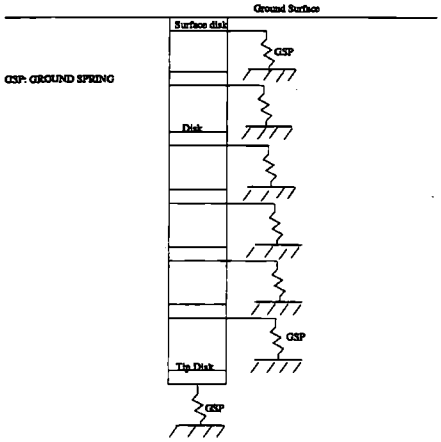

Figure 4.5: A multi-stack of rigid disks connected to the ground via equivalent non-linear springs representing the pile-soil interaction

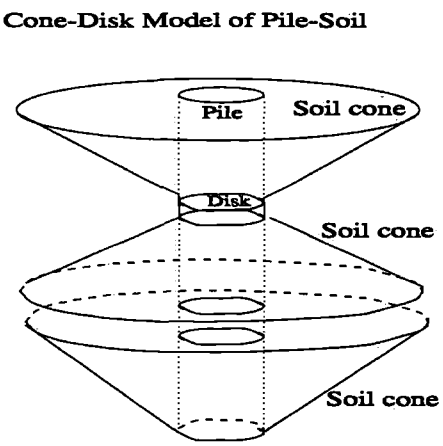

Figure 4.6: A multi-stack of the rigid pile disks connected to each other via pile elements and to the ground via soil cones representing the interaction between the pile and soil

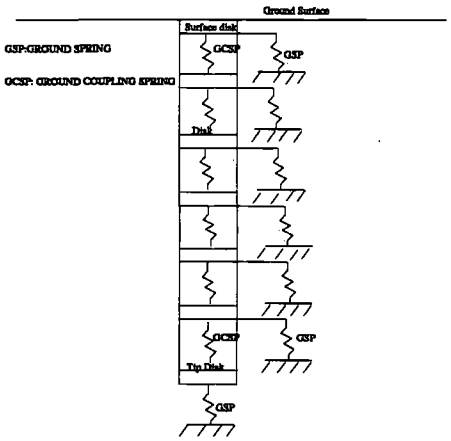

Figure 4.7: A multi-stack of rigid disks connected to each other via pile elements and also coupling (ground) springs and attached to the ground via. equivalent non-linear springs representing the pile-soil interaction

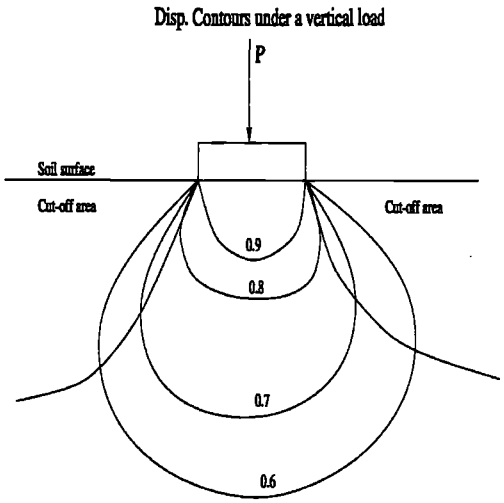

Figure 4.8: Displacement contours of Boussinesque under a (concentrated) loaded disk in an elastic half-space of soil

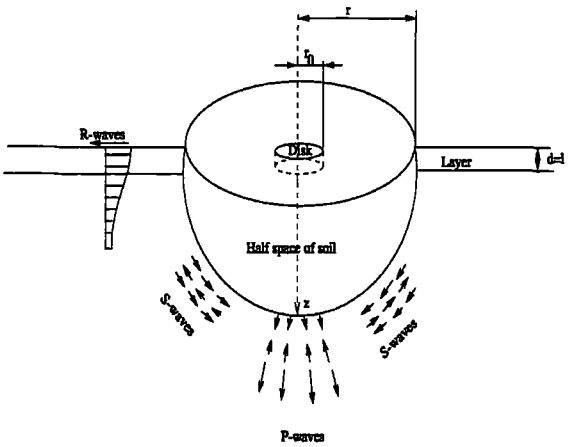

Figure 4.9: A schematic illustration of wave energy transmission sphere in soil(After Wolf, (1994)

amount of the energy transmitted. In analogy to the surface disk concept, the idea of embedded disk has been introduced by Meek and Wolf, (1992), which constituted the basis for a multi-stack of disks model. Similar to a loaded surface disk, it is assumed that for the embedded disk the stress distribution can take place within a double-cone as illustrated in Fig. 4.10. These double cones intersect at the disk plane, the intersect area as shown is equal to the cross-sectional area of the rigid loaded disk.

Wolf's disk model basically consists of a multi-stack of uncoupled rigid disks with their associated linear double cones which can transmit any translational as well as rotational motion into the soil separately. The rigid disks are connected to each other via rigid or linear elastic beam (or rod) elements (see e.g. Timoshenko and Goodier , 1982).

The extension of initial cone idea(Meek and Wolf, 1994) to a non-linear pile-soil system is described in the following. Different methods might be used for solution of the non-linear cone model. The first approach was introduced by Emami and Moan, (1996) involves modification of the linear cone model of the Wolf and Meek, (1994) based on non-linear disk assumption. The idea is to modify the corresponding linear cone properties such as the soil's shear modulus G and hence the corresponding wave velocities c_p and c_s as functions of the displacement response of the pile-soil system. In other words, this approach is an indirect solution of the non-linear cone model of soil.

In the second approach, a non-linear version of Wolf's cone model is directly obtained based on general non-homogeneous and non-linear soil medium assumptions. The disks in the model shown in Fig.4.7 are coupled in each loading direction, axial, lateral and rocking but are uncoupled between these degrees of freedom, except between the lateral and rocking motions. The

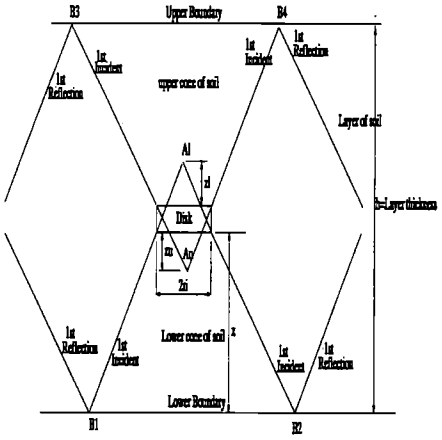

Figure 4.10: A schematic illustration of the double-cone concept of soil (after Meek and Wolf, 1992)

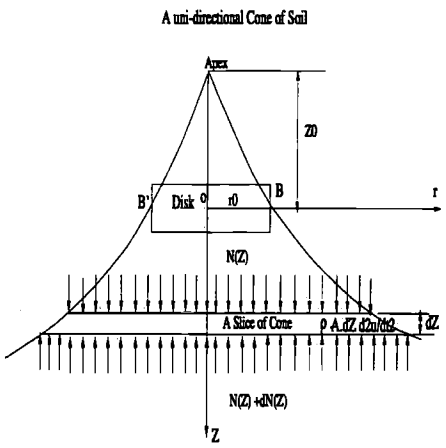

Figure 4.11: Equilibrium of dynamic forces for a thin slice of soil cone

interconnecting elements of the disks are assumed to be deformable and in general as elasto-plastic beam (rod) elements(see Bouc, 1967 and Przemieniecki, 1967). The geometric as well as material non-linearities are considered for the interconnecting finite two node beam elements.

A more sophisticated two node beam element of USFOS(Søreide et al, 1994) for pile including material and geometrical non-linearities is also used. The pile-soil interaction is modelled by Winkler type springs as shown in Fig.4.5. The damping is hence modelled only as hysteretic damping in the soil which occurs due to its yielding. Two different types of soil behaviour are considered namely, elasto-plastic and hyper-elastic. The latter type does exclude any hysteretic soil damping and is only used to quantify the soil's in-elastic damping effects on the response of the pile-soil system. The structural model of USFOS is described in Chapter.3.

4.2.2 Geometrical properties of a non-linear cone model

In this section, geometrical properties of the soil cone are defined by means of a simple case of wedge (a special case of cone see Fig.4.2). These common properties will have the same meaning for all types of soil cones discussed here.

The geometry of a cone in general is defined by two parameters, namely, the apex height (or similarly apex angle) and the radius of the disk associated with the cone as illustrated in Fig.4.12. The apex angle of a non-linear cone in general will vary with the soil depth and the time. However, for simplicity it may be assumed that the associated angle of each cone would remain constant.

In a more realistic analysis, the variations of cone angle can be considered at specific discrete

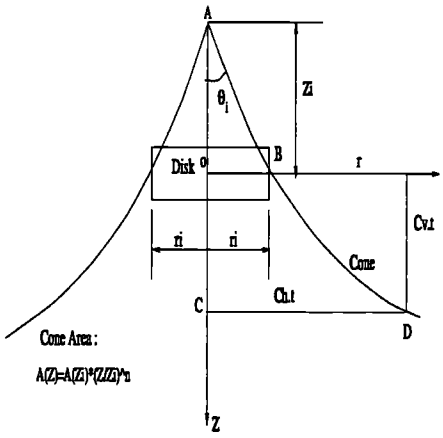

Figure 4.12: Geometrical properties of the non-linear cone of soil under various motions

points of soil space such as location of disks (or nodes in finite element model of pile-soil system) and at the boundaries of various layers. For the disk i located within a layer of soil shown in Fig. 4.12, the apex height and associated disk radius with the cone are denoted as z_i and r_i, respectively. The aspect ratio $\frac{z_i}{r_i}$ and the corresponding apex angle of a non-linear cone θ_i can be related to the velocity ratio of the vertically and horizontally propagating waves towards infinity as shown in Fig. 4.12. In triangles ACD and AOB, the following geometrical relationship can be written:

$$tg\theta_i = \frac{\bar{CD}}{\bar{AC}} = \frac{\bar{OB}}{\bar{AO}} = \frac{r_i}{z_i} \tag{4.1}$$

where $\bar{CD}$ can be written as:

$$\bar{CD} = r_i + c_h.t \tag{4.2}$$

and $\bar{AC}$ can be written as:

$$\bar{AC} = z_i + c_v.t \tag{4.3}$$

thus: $\frac{c_h}{c_v} = \frac{r_i}{z_i} = tg\theta_i$ Assuming the shear wave velocity in general as a function of the tangent shear modulus and poisson ratio of soil as:

$$c_i = f_i(G^T, \nu) \qquad ; i = h, v, r \tag{4.4}$$

in which h,v and r refer to the horizontal, vertical and rocking motions, respectively and the tangent stiffness modulus of soil $G^T = f_{G^T}(u, z, r)$, hence the opening angle of a layered soil cone may be written as:

$$\theta_i = tg^{-1}\left(\frac{f_h(f_G(u,z,r),\nu)}{f_v(f_G(u,z,r),\nu)}\right) \tag{4.5}$$

The corresponding θ_i and z_i/r_i ratios for particular cases of disk's motion are given in appendix.D

4.2.3 Dynamic formulation of the cone model in a half space of soil(with only radiation damping)

According to Meek and Wolf, (1992) a soil medium around a dynamically loaded rigid disk may be modelled as a single (or double cone) as illustrated in Fig.4.10 and 4.11. The basic dynamic equation of equilibrium may be obtained for a slice of cone with an infinitesimal thickness as shown in Fig. 4.11 as follows:

$$dN(\omega) - \rho dv \frac{\partial^2 u(\omega)}{\partial t^2} = 0 \tag{4.6}$$

for a harmonic type of excitation, that's : $u(\omega) = Csin(\omega t)$ or $Ccos(\omega t)$, we will have:

$$\frac{\partial^2 u(\omega)}{\partial t^2} = -C\omega^2 sin(\omega t) \tag{4.7}$$

Hence, we will have:

$$dN(\omega) + \rho A.dz\omega^2 u(\omega) = 0 \tag{4.8}$$

Knowing that the force-stress relationship is:

$$N(\omega) = \sigma(\omega).A(z) \tag{4.9}$$

And the stress-strain relationship may be written as:

$$\sigma(\omega) = E.\epsilon(\omega) \tag{4.10}$$

Substituting the latter in Eq. 4.9 will result in:

$$N(\omega) = E.\epsilon(\omega).A(z) \tag{4.11}$$

Now differentiating $N(\omega)$ with respect to z will give:

$$dN(\omega) = \frac{\partial E}{\partial z}.\epsilon(\omega).A(z).dz + E.\frac{\partial \epsilon(\omega)}{\partial z}.A(z).dz + E.\epsilon(\omega).\frac{\partial A(z)}{\partial z}.dz \tag{4.12}$$

Combining Eqs. 4.8 and 4.12, we get:

$$\frac{\partial E}{\partial z}.\epsilon(\omega).A(z) + E.\frac{\partial \epsilon(\omega)}{\partial z}.A(z) + E.\epsilon(\omega).\frac{\partial A(z)}{\partial z} + \rho A(z).\omega^2.u(\omega) = 0 \tag{4.13}$$

According to the simple continuum mechanics theory with the assumptions of small strain $\epsilon(\omega)$ may be written as follows:

$$\epsilon_z = \frac{\partial u}{\partial z} \tag{4.14}$$

By substituting for $\epsilon(\omega)$ in Eq. 4.13, we will have:

$$\frac{\partial E}{\partial z}.\frac{\partial u}{\partial z}.A(z) + E.\frac{\partial^2 u}{\partial z^2}.A(z) + E.\frac{\partial u}{\partial z}.\frac{\partial A(z)}{\partial z} + \rho.A(z).\omega^2.u(\omega) = 0 \tag{4.15}$$

For non-linear and non-homogeneous soil, the elastic modulus of soil E may be written in general as a function of shear strain in the soil(see Appendix.D). Since the soil displacement can be related to the shear strain (see Secs.2.2.3 and 2.3.3), hence E can be written as:

$$E = F_E(z_0, r_0, u, \dot{u}, ...) \tag{4.16}$$

in which z_0,r_0 refer to cone's apex height and disk radius and u and $\dot{u}$ represent the soil displacement and its first derivative with respect to z.

Also E can be related to the tangent shear modulus of soil, G^T via ν as follows:

$$E = 2(1+\nu)G^T \tag{4.17}$$

E can be re-written as follows:

$$E = E_i(z,r).f_E(u,\dot{u},...) \tag{4.18}$$

in which E_i indicates the initial elastic modulus of soil which in general is a function of z and r which may be approximately decoupled as follows:

$$E_i = f_{E_i}(z,r) = f_{E_i,z}(z).f_{E_i,r}(r) \tag{4.19}$$

Now combining Eqs. 4.17 and 4.18, we will have:

$$E_i(z,r).f_E(u,\dot{u},...) = 2(1+\nu)G^T \tag{4.20}$$

Thus:

$$G^T = \frac{E_i(z,r)}{2(1+\nu)}.f_E(u,\dot{u},...) = G_i(z,r).f_E(u,\dot{u},...) \tag{4.21}$$

On the other hand, the shear modulus of soil G^T can be written in general as:

$$G^T = f_{G^T}(\tau) \tag{4.22}$$

The tangent shear modulus of the soil G^T may be defined as:

$$G^T = \frac{\partial \tau}{\partial \gamma} \tag{4.23}$$

By inserting the shear stress function τ in Eq. 4.23, G^T may be obtained theoretically(see Appendix.D).

The normalized tangent shear modulus g^T may then take the following form:

$$g^T = g_i + \alpha_1 s + \alpha_2 s^2 + \alpha_3 s^3 + ... + \alpha_n s^n \tag{4.24}$$

in which g_i and s are the normalized shear modulus and stress parameters:

$$g = \frac{G}{G_i} \tag{4.25}$$

$$s = \frac{\tau}{\tau_{ps}} \tag{4.26}$$

where τ_{ps} here is considered as the failure shear stress at the pile-soil interface as determined in Sec.2.3.2 based on the soil mechanics theory (Mohr-Coulomb criteria). The coefficients of general Eq. 4.24 may be determined through procedure described in appendix.D.

For example a truncated form of Eq. 4.24 has been proposed by Svanø et al, (1993) for clayey soils which is described in Secs.2.2.3 and 2.3.3. Other relationships have been proposed by Ramberg-Osgood, (1943), Hardin-Drnevich, (1972), Richart, (1975), Janbu, (1976), Hara, (1980), Molenkamp, (1980) , Finn and Lee , (1982), for both sand and clay. Langø, (1991) obtained similar correlations from cyclic triaxial tests on several clayey sites in Norway and he applied the CSM model of Svanø, (1992) to fit his obtained triaxial test results. Due to efficiency of Svanø's model in having only two unknown parameters which can capture main characteristics of the soil, it is adopted here for the current study and has been calibrated for sand by using Finn's more complex cyclic model (see appendix.D).

A particular form of G^T is derived based on the CSM model of Svanø et al, (1993) for clay as follows:

$$G^T = \frac{G_i(\sigma'_m + a_d)(1 - \frac{\lambda_s \gamma G_i}{\lambda_s \gamma G_i + 1})}{\sqrt{1 + 4\frac{h_s \gamma G_i}{\lambda_s \gamma G_i + 1}}} \tag{4.27}$$

In which λ_s and h_s are material related coefficients which are obtained for e.g. by Langø, (1991) and Svanø et al, (1993) for NC and OC clays. Eq.4.27 may be used for sand by calibrating the appropriate parameters (see appendix.D).

Another mathematical form of G^T can be expressed as(Svanø et al, (1993):

$$G^T = G_i(1 - \alpha.s)^\beta \tag{4.28}$$

In which α and β are the material parameters of soil which may be obtained directly (from triaxial tests) or can be obtained from h_s and λ_s by equating the right hand sides of Eqs.4.28 and 4.27 (see appendix.D)

Hence, comparing Eqs. 4.21 and 4.28, we will have:

$$f_E(u, ...) = (1 - \alpha s)^\beta \tag{4.29}$$

$$\tau = f_\tau(u) \tag{4.30}$$

where $f_\tau(u)$ is often referred to as (t-z), (p-y) and (q-z) functions(see Chapter.2). Combining Eq. 4.29 and Eq. 4.30, the following can be written:

$$f_E(u, ...) = (1 - \alpha.\frac{f_\tau(u)}{\tau_{ps}})^\beta \tag{4.31}$$

and from Eq. 4.18 as:

$$E = E_i.(1 - \alpha\frac{f_\tau(u)}{\tau_{ps}})^\beta \tag{4.32}$$

E_i may be in general expressed as:

$$E_i = E_i(z = z_0, r = r_0).f_{E_i}(z, r) \tag{4.33}$$

By combining Eqs. 4.32, 4.33, 4.19 may be re-written as follows:

$$E = E_{i,0}.f_{E_i,z}.f_{E_i,r}.(1 - \alpha\frac{f_\tau(u)}{\tau_{ps}})^\beta \tag{4.34}$$

Now differentiating E with respect to z will result in:

$$\frac{\partial E}{\partial z} = E_{i,0}.\frac{\partial f_{E_i,z}(z)}{\partial z}.f_{E_i,r}(r).f_{E,u}(u) + E_{i,0}.f_{E_i,z}(z).f_{E_i,r}(r).\frac{\partial f_{E,u}(u)}{\partial z} \tag{4.35}$$

The following part by part partial derivative equation can be written:

$$\frac{\partial f_{E,u}(u)}{\partial z} = \frac{\partial f_{E,u}(u)}{\partial u}.\frac{\partial u}{\partial z} \tag{4.36}$$

For a non-homogeneous soil the following simple and convenient variation with the soil depth may be assumed:

$$f_{E_i,z}(z) = (\frac{z}{z_0})^m \tag{4.37}$$

in which m is the order of distribution function. Thus, we will have:

$$\frac{\partial f_{E_i,z}(z)}{\partial z} = \frac{m}{z_0}(\frac{z}{z_0})^{m-1} = \frac{m}{z}.f_{E_i,z}(z) \tag{4.38}$$

inserting the latter into Eq. 4.35, will yield:

$$\frac{\partial E}{\partial z} = E_{i,0}.f_{E_i,z}.f_{E_i,r}.(\frac{m}{z}.f_{E_i,u} + \frac{\partial f_{E,u}}{\partial u}.\frac{\partial u}{\partial z}) \tag{4.39}$$

$A(z)$ also can be in general assumed to vary with z as:

$$A(z) = A(z_0)(\frac{z}{z_0})^n \tag{4.40}$$

thus:

$$\frac{\partial A(z)}{\partial z} = A(z_0)\frac{n}{z_0}(\frac{z}{z_0})^{n-1} = \frac{nA(z)}{z} \tag{4.41}$$

Substituting for $\frac{\partial A(z)}{\partial z}$, $\frac{\partial E}{\partial z}$ into Eq. 4.15 and re-arranging the terms will produce:

$$\frac{\partial^2 u}{\partial z^2} + \frac{1}{f_{E,u}}.\frac{\partial f_{E,u}}{\partial u}.(\frac{\partial u}{\partial z})^2 + (\frac{m+n}{z})\frac{\partial u}{\partial z} + \frac{\rho.\omega^2}{E_{i,0}f_{E,z}.f_{E,u}}.u(\omega) = 0 \tag{4.42}$$

in which $f_{E_i,r}$ is dropped, since it is assumed that E_i profile only varies with depth (z).

4.2.4 Discussion about different solution procedures for non-linear cone model

In this section several different methods for solution of non-linear cone model are discussed. Adhering to our simple to more complex approach which is followed throughout this work, we adopted first a much more simplified method for solution of a non-linear cone model based on modification of the Green functions associated with the linear cone model of Meek and Wolf, (1992) and Wolf et al, (1992).

The second approach is introduced in the following subsection as a semi-analytical solution of the cone model based on a step-wise linearization of the non-linear differential equation in an incremental form. Although this approach is more complex than the first method, it still is approximate and does not account for the non-linear terms in the differential equation emerging from the variation of the tangent shear modulus of soil within a small incremental step(see Eq.4.42).

To avoid deviation from the true path of response due to neglecting the non-linear terms associated with variation of f_E with respect to displacement (u), a predictor-corrector approach may be applied which is outlined in the following.

The fourth solution approach may be applied based on the finite difference method. This numerical method might be slightly more costly due to discretization of the cone and solution of the differential equation over all the discretized nodes of the cone, nevertheless it is more reliable than the three first methods.

The most complex and costly solution approach might be a continuum mechanic solution based on full discretization in space and time. This approach is based on finite elements of soil cone or in general the soil surrounding the pile.

4.2.5 Indirect solution of non-linear disk-cone model

Based on the disk-cone idealization(Meek and Wolf, 1992 and Wolf et al, 1994) an efficient approach is introduced for the solution of a non-linear pile-soil system. Evaluation of the associated dynamic stiffness of an embedded foundation such as pile-soil system is provided by Emami and Moan, (1996). The non-linear response functions of the system approximated by a synthesis of impulse response functions which are classified according to Wolf et al, (1994) to horizontal, vertical and rocking motions. Each impulse function g_{ij} is obtained as the displacement response of the soil medium at a distance a_{ij} from the point of source disk (i) as shown in Fig.4.13.

The differential equation for a unit load impulse is given in appendix.D. The displacement due to unit impulse function at time(t) due to impulse generated at time (τ) may be obtained as follows:

$$g_{ij} = g(a_{ij}, t-\tau, c) + g(a_{ij'}, t-\tau, c) \tag{4.43}$$

where g_{ij} is a function of distance between the receiver disk (j) and the source disk (i) a_{ij} as shown in Fig.4.13, time interval between the present time (t) and the time of load impulse τ at the source disk (i)(This time interval is often referred to as the retardation time) and also the wave velocity (c). The frequency dependent Green function $g(a,\omega)$ can be computed through a Fourier transformation from $g_{ij}(a,t,c)$. As expressed each g_{ij} impulse function is dependent on the wave propagation velocity in soil (c). c may be expressed as a function of tangent shear modulus of soil G^T as:

$$c = \sqrt{\frac{f(\nu)G^T}{\rho}} \tag{4.44}$$

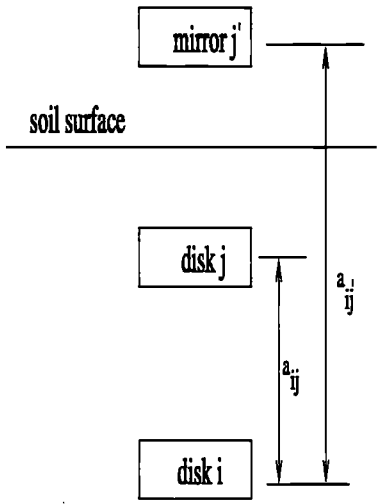

Figure 4.13: Representation of source, receiver and mirror of source disks

where the explicit forms of the $f(\nu)$ function is given in Appendix.D for P, S and R-waves. G^T might be related to the shear stress τ at the pile-soil interface as follows:

$$G^T = G_i(1 - \alpha\frac{\tau}{\tau_{ps}})^\beta \tag{4.45}$$

Combining Eqs.4.44 and 4.45 may lead:

$$c = \sqrt{\frac{f(\nu)G_i}{\rho}}.\sqrt{(1 - \alpha\frac{\tau}{\tau_{ps}})^\beta} \tag{4.46}$$

For e.g. for a particular case of normally consolidated soil with $\beta = 2$, from Eq.4.46 a simple

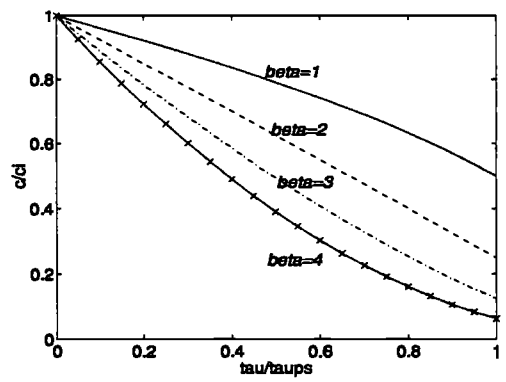

Figure 4.14: Variation of shear wave velocity vs. shear stress at pile-soil interface

linear relationship is obtained between c and τ as:

$$c = c_i(1 - \alpha.\frac{\tau}{\tau_{ps}}) \tag{4.47}$$

c/c_i vs. τ/τ_{ps} relationships for different values of β are plotted in Fig.4.14. It is observed that c/c_i varies with τ/τ_{ps} ratio depending on the β parameter. The plotted limits $\beta = 1.0$ to 4.0 represent a practical range from heavily overconsolidated to essentially normally consolidated soils. It can be seen that the shear wave velocity (c) decreases more rapidly with the increase of shear stress for a normally consolidated soil than a heavily overconsolidated one. For e.g. at a half collapse shear stress level (i.e. $\tau/\tau_{ps} = 0.5$) the wave velocity for OC soil($\beta = 1$) is about 0.78 times the initial wave velocity (c_i) while at the same stress level the wave velocity (c) is only about 0.37 times the initial wave velocity (c_i) for NC soil with ($\beta = 4.0$). Now substituting for c from Eq.4.47, in green functions in Eq.4.43, we can obtain:

$$c_h = f_h = f_h(h, t, c_i\sqrt{1 - \alpha\frac{f_\tau(u, G^T, \alpha, \beta)}{\tau_{ps}}}) \tag{4.48}$$

Similarly f_v and f_r can be obtained. The mass, however, is not affected by the variation of the tangent shear modulus G^T. Hence, it is possible to compute the dynamic response of the embedded foundation(pile) in the time domain taking into account the non-linear properties of soil such as G^T, c, α and β.

The complex Green functions for an elasto-plastic soil half space may be Modified after Meek and Wolf, (1992) as follows:

$$g^n{}_{ij} = g^n{}_{ij}(t, a_{ij}, c(G^T, \nu)) + g^n{}_{ij}(t, a'_{ij}, c(G^T, \nu)) \tag{4.49}$$

where a_j and a'_{ij} represent respectively, the distances from the source disk j and its mirror image to the receiver disk i as shown in Fig.4.17. The superindex (n) indicates the integration step and c represents the wave propagation velocity in the soil which is a function of tangent shear modulus G^T and the poisson's ratio ν of soil(see also appendix.D). Combining Eqs.4.49 and 4.45 may result in:

$$g^n{}_{ij} = g^n{}_{ij}(t, a_{ij}, c(G_i(1 - \alpha.\frac{f_\tau(u)}{\tau_{ps}})^\beta, \nu)) + g^n{}_{ij}(t, a'_{ij}, c(G_i(1 - \alpha.\frac{f_\tau(u)}{\tau_{ps}})^\beta, \nu) \tag{4.50}$$

where f_τ relationship for e.g for the axial loading of disk is obtained according to Sec.2.2.3 as follows:

$$u = \phi_a(\tau) = \frac{\tau_{ps}}{G_i\alpha(1-\beta)}\int_{r_i}^{r_{id}}\left[1 - (1 - \alpha\frac{\tau_i}{\tau_{ps}}\psi_r(r))^{1-\beta}\right]dr \tag{4.51}$$

hence, after inversing, we obtain:

$$f_\tau(u) = \phi_a^{-1}(\tau) \tag{4.52}$$

4.2.6 An approximate semi-analytical solution of non-linear cone model

Considering an incremental form of Eq. 4.42 as:

$$\frac{\partial^2 \delta u}{\partial z^2} + \frac{1}{f_{E,\delta u}} . \frac{\partial f_{E,u}}{\partial u} . \left[\frac{\partial u}{\partial z} \frac{\partial \delta u}{\partial z} + (\frac{\partial \delta u}{\partial z})^2 \right] + (\frac{m+n}{z}) \frac{\partial \delta u}{\partial z} + \frac{\rho . \omega^2}{E_{i,0} f_{E,z} . f_{E,\delta u}} . \delta u(\omega) = 0 \quad (4.53)$$

By assuming that the tangent shear modulus or equivalently $f_{E,u}$ is approximately constant within a sufficiently small incremental step δu then the second term in Eq.4.53 may be neglected which results in the following step-wise linearized form:

$$\frac{\partial^2 \delta u}{\partial z^2} + (\frac{m+n}{z}) \frac{\partial \delta u}{\partial z} + \frac{\rho . \omega^2}{E_{i,0} f_{E,z} . f_{E,\delta u}} . \delta u(\omega) = 0 \quad (4.54)$$

The general solution of the following linearized differential equation may be obtained through an iterative procedure as follows:

$$z^m \delta \ddot{u}_i + (m+n) z^{m-1} \delta \dot{u}_i + B_p \delta u = 0 \quad (4.55)$$

where $f_{E,\delta u}$ determined from the response known at the previous incremental step as follows:

$$f_{E,\delta u} = (1 - \frac{f_\tau (u_{i-1} + \delta u_i)}{\tau_{ps}})^\beta \quad (4.56)$$

where δu_i is initially predicted for e.g from previous step as δu_{i-1}.

The predicted solution of the linearized differential Eq.4.55 then will become:

$$\delta u_{i,p} = z^{\frac{1-m-n}{2}} \left[c_1 J_{\frac{m+n-1}{2}} (\pm \sqrt{B_p} z^{\frac{2-m}{2}}) + c_2 Y_{\frac{m+n-1}{2}} (\pm \sqrt{B_p} z^{\frac{2-m}{2}}) \right] \quad (4.57)$$

where p: predicted value
$J_{\frac{m+n-1}{2}} = \frac{(m+n-1)}{2}$ Bessel function of first order and first kind.
$Y_{\frac{m+n-1}{2}} = \frac{(m+n-1)}{2}$ Newman function of first order and first kind. (see for e.g Spiegel, 1968)

The predicted value of B_p as coefficient of the last term on R-H-S of Eq.4.57 will be:

$$B_p = \frac{\rho \omega^2 {z_0}^m}{E_{i,0} f_{E,\delta u,p}} \quad (4.58)$$

c_1, c_2 = coefficients of Eq.4.57 can be determined from B.C. conditions as:

$$\begin{aligned} \delta u(z=0) &= \delta u_0 \\ \delta u(z \to \infty) &\to 0 \end{aligned} \quad (4.59)$$

where m = exponent of E function, n = the order of the cone. The corrected $f_{E,\delta u}$ will be :

$$f_{E,\delta u,c} = (1 - \frac{f_\tau (u_{i-1} + \delta u_{i,p})}{\tau_{ps}})^\beta \quad (4.60)$$

δu_i can be corrected from solution of linearized differential equation above as:

$$\delta u_{i,c} = z^{\frac{1-m-n}{2}} \left[c_1 J_{\frac{m+n-1}{2}} (\pm\sqrt{B_c} z^{\frac{2-m}{2}}) + c_2 Y_{m+n-1} 2(\pm\sqrt{B_c} z^{\frac{2-m}{2}}) \right] \tag{4.61}$$

The above steps may be repeated until the desired convergence is obtained:

$$\delta u_{i,c} = \delta u_{i,p} + tol(\delta u_i) \tag{4.62}$$

where $tol(\delta u_i)$ =the tolerance value of δu_i which depends on the desired level of accuracy. Iterations may be switched off or only one iteration used depending on the need for greater speed in calculations.

A truncated from of the latter might also be applied for the pile-soil system where the last nodes in each mesh of cone could be considered at the tip of the pile. For the long piles under action of dynamic loads applied at the pile head this procedure may be correct because the displacement at or near the tip may be assumed to be negligible even in dynamic case compared to the upper layers of soil near the pile head. Nevertheless, for the seismic ground motion which may propagate from tip of the pile upwards the latter assumption may not be applicable.

For a high frequency case a series solution may be found by inspection as follows:

$$\delta u(\omega) = \delta u_0(\omega).(\frac{z_0}{z})^{\frac{n+m}{2}}.e^{\frac{-i\omega}{c}(z_0-z)} \tag{4.63}$$

It can be verified that the latter is the general solution(i.e. for all values of ω) for a particular case of the cone with $n+m = 0, 2$. Wolf and Meek, (1994) presented a proof of the initial version of Eq. 4.63 with one parameter n. This implies $n = 0, 2$ for homogeneous soil for which $m = 0$, $n = -1, 1$ for linear soil profile $m = 1$ and $n = 0$ for a parabolic soil profile $m = 2$. $n = 0$ according to Eq. 4.40 represents a constant area or a prismatic rod(see Fig.4.2), $n = 1 or -1$ represent linearly varying (decreasing or increasing) in area (translational wedges) and $n = 2$ denotes a parabolically varying (transnational cone) etc.

For $\omega = 0$ (the static case), the general solution of non-linear cone can be obtained in series form as follows :

$$\delta u = C_1 z^{C_2} + C_3 z^{C_4} \tag{4.64}$$

Substituting for δu from latter in Eq. 4.54, we may obtain, the following characteristic solution:

$$\delta u = C_1 + C_3 z^{1-(m+n)} \tag{4.65}$$

where $C_2 = 0$ and $C_4 = 1-(m+n)$, the coefficients C_1 and C_3 can be obtained from the boundary conditions of the cone system. The displacement of the disk at $z = z_0$ is assumed to be known or $\delta u(z) = \delta u(z = z_0)$. The second boundary condition may be imposed as $\delta u(z \to \infty) = 0$ or $\delta u(z = z_{tip}) = \epsilon$. The application of the latter is described later for a particular case of the cone model. For $(m+n) > 1$ the coefficients C_1 and C_3 can be obtained as follows: C_1=0 and $C_3 = \delta u(z_0).z_0^{(m+n)-1}$. Inserting these in Eq. 4.65, we will have:

$$\delta u = \delta u(z_0).(\frac{z}{z_0})^{1-(m+n)} \tag{4.66}$$

For a prismatic bar ($n = 0$) and homogeneous soil ($m = 0$), the above solution may not be valid since the condition $m + n > 1$ is not met for the boundary condition related to the infinity. However, the practical solution of this may be sought through use of second (a modified) boundary condition such as one described above. For the latter case, we may obtain the following solution:

$$\delta u = \frac{\delta u_0 z_{tip}}{z_{tip} - z_0} + \frac{\delta u_0 z}{z_0 - z_{tip}} = \delta u_0 (\frac{z_{tip} - z}{z_{tip} - z_0}) \tag{4.67}$$

in which it may be assumed that $\frac{z_0}{z_{tip}} = 0$. It is evident that the latter assumption may not be valid for a disk with the associated cone or double-cone located at or near the pile-tip. Hence, for the upper disks located near the pile head, we may have a simpler approximate form for small strain condition from Eq. 4.67 as:

$$\delta u \approx \delta u_0 (1 - \frac{z}{z_{tip}}) \tag{4.68}$$

For a long pile, the latter approximate form (Eq. 4.68) is valid since it satisfies the boundary conditions both at the surface and the tip which is also valid only for small incremental displacement.

The solution obtained here is similar to the initial linear cone model solution of Wolf and Meek and Wolf, (1994). The differences are the replacement of the variables with their incremental forms, and addition of a new parameter m for the non-homogeneous soil condition:

$$\delta u(z) = \delta u(z_0) \sum a_n (\frac{z_0}{z})^{(n+m)-1} \tag{4.69}$$

where the coefficients of the series on the right hand-side of Eq. 4.69 can be easily determined from a numerical trial procedure. For a simpler single term, the summation sign can be dropped.

The static and dynamic stiffness of the soil cone can be obtained by using the Eq.4.11 as follows:

$$\delta N(\omega) = E.\epsilon(\omega).A(z) \tag{4.70}$$

By substituting for $\epsilon(\omega)$ from Eq.4.14 we will have:

$$\delta N(\omega) = E.\frac{\partial \delta u(\omega)}{\partial z} A(z) \tag{4.71}$$

By combining the latter and Eq.4.63, we will have:

$$\delta N(\omega, z = z_0) = E(z = z_0) A(z = z_0) \frac{\delta u_0}{z_0} (-\frac{n+m}{2} - \frac{i\omega z}{c}) \tag{4.72}$$

Now the interaction force increment $\delta P(\omega, z = z_0)$ at the disk-cone interface can be easily obtained as:

$$\delta P(\omega, z = z_0) = -\delta N(\omega, z = z_0) = E(z = z_0) A(z = z_0) \frac{\delta u_0}{z_0} (\frac{n+m}{2} + \frac{i\omega z}{c}) \tag{4.73}$$

The corresponding dynamic stiffness $S(\omega)$ may be obtained as follows:

$$S(\omega) = \frac{\delta P(\omega, z = z_0)}{\delta u} \tag{4.74}$$

By inserting Eq.4.73 in the latter, the following expression emerges:

$$S(\omega) = \frac{E(z=z_0)A(z=z_0)}{z_0}[(\frac{n+m}{2}) + \frac{i\omega z_0}{c}] \tag{4.75}$$

Comparing the latter equation with the general expression of dynamic equation of motion:

$$M\ddot{u} + C\dot{u} + Ku = f(\omega) \tag{4.76}$$

where $f(\omega)$ = a harmonic excitation force for e.g as $f_0 exp(i\omega t)$. Now assuming that $u(\omega) = u_0 exp(i\omega t)$ and substituting into Eq.4.77 will yield:

$$(-M\omega^2 + Ci\omega + K)u(\omega) = \lambda u(\omega) \tag{4.77}$$

where $\lambda = f_0/u_0$. Eq.4.77 represents a standard complex eigen-value problem which can be re-written as:

$$(S(\omega) - \lambda I)u(\omega) = 0 \tag{4.78}$$

where I denotes the unit matrix and $S(\omega)$ represents the dynamic complex stiffness of the cone-disk in general as:

$$S(\omega) = K + i\omega C - \omega^2 M \tag{4.79}$$

From which for a free-undamped SDOF system, the natural frequency emerges as:

$$\omega_n = \sqrt{\frac{K}{M}} \tag{4.80}$$

Based on Eq.4.75, the dynamic stiffness parameter K and the damping parameter C may be obtained at the location of the disk $z = z_0$ as:

$$K = (\frac{n+m}{2})\frac{E(z=z_0)A(z=z_0)}{z_0} \tag{4.81}$$

$$C = \frac{E(z=z_0)A(z=z_0)}{c} \tag{4.82}$$

For a special case of the cone with $m + n = 2$, the corresponding dynamic spring and dashpot coefficients can be obtained from Eqs.4.81 and 4.82 as follows:

$$K = \frac{E(z=z_0)A(z=z_0)}{z_0} = \frac{\rho c^2 A(z_0)}{z_0} \tag{4.83}$$

$$C = \frac{E(z=z_0)A(z=z_0)}{c} = \rho c A(z_0) \tag{4.84}$$

It can easily be shown from Eq.4.63 that in general ($z \neq z_0$), K and C will be functions of ω. Eq.4.79 in a general form can be re-written as follows:

$$S(\omega) = K_{st}(k_{dy}(\omega, c) + i\omega c_{dy}(\omega, c)) \tag{4.85}$$

where K_{st}, k_{dy} and c_{dy} represent the static spring stiffness, dynamic (spring)coefficient and the dynamic dashpot coefficient, respectively. For the special case of $z = z_0$, we have for e.g $k_{dy} = 1$ and $c_{dy} = \frac{z_0}{c}$.

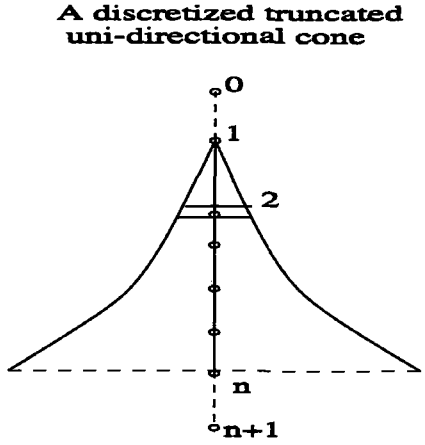

Figure 4.15: A discretized truncated (uni-directional) cone of soil along its central axis

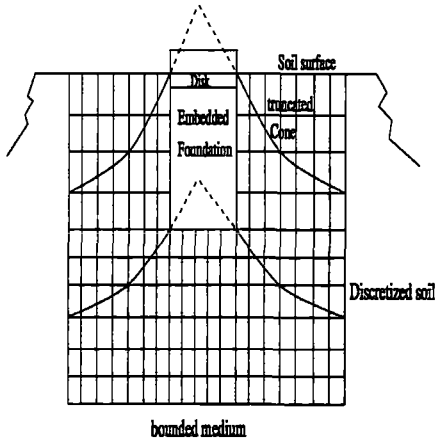

Figure 4.16: Discretization of a bounded soil medium around an embedded foundation by general (continuum) finite elements and uni-directional cone elements

4.2.7 A predictor-corrector based semi-analytical solution of non-linear cone model

To avoid the inaccuracies due to neglecting the non-linear terms related to variation of f_E with respect to u on the left hand side of Eq.4.53, a predictor-corrector approach might be applied to overcome this difficulty. The approach involves first a predicted solution of the linearized differential equation (Eq.4.54). After determining the predicted response u_p from Eq.4.57, the initially neglected non-linear terms on the L-H-S of Eq.4.54 can be determined as a function of displacement response u. The obtained unbalance term may be equated with an equivalent last term of Eq.4.54 to obtain the modified equivalent terms as $B_{p,eq}$. The updated linearized differential equation with inclusion of unbalance term can be easily obtained from Eq.4.57.

This procedure can be applied iteratively until the corrected displacement response u_c is obtained from the last iteration $u_c^i \leq u_c^{i-1} + tol(u)$ where $tol(u)$ represents a pre-set tolerance value for termination of the response calculation.

4.2.8 A numerical solution of non-linear cone model based on finite difference approach

Based on finite difference approach, the first and the second derivatives of the response can be expressed as follows:

$$\frac{\partial u}{\partial z} = \frac{u_{i+1} - u_i}{\Delta z} \tag{4.86}$$

$$\frac{\partial^2 u}{\partial z^2} = \frac{u_{i+2} - 2u_{i+1} + u_i}{\Delta z^2} \tag{4.87}$$

$f_{E,u}$, $f_{E,z}$ can be determined numerically according to Eqs.4.31 and 4.34 at point (i) of the cone mesh shown on Fig.4.15. Then the differential Eq.4.42 can be written in a finite difference form as follows:

$$\frac{u_{i+1}-2u_i+u_{i-1}}{\Delta z_i^2}+\frac{1}{f_{E,ui}}\left(\frac{u_i-u_{i-1}}{\Delta z_i}\right)^2+\left(\frac{m+n}{z_i}\right)\frac{u_i-u_{i-1}}{\Delta z_i}+\frac{\rho\omega^2}{E_{i,0}f_{E,zi}f_{E,ui}}u_i=0 \qquad (4.88)$$

Writing Eq.4.88 over all the nodes of the cone's mesh (1 to n), n equations are established with (n+2) variables. Two more needed equations may be obtained from the boundary conditions for nodes (0) and (n+1). The B.C. may be expressed as follows: $|u_0| = |u_2|$ and $|u_{n+1}| \approx |u_n|$ w.r.t the geometry of the cone. Node (0) can be assumed as the mirror image of node (2) and hence its displacement would be the same as node (2) from the upper cone. While node (n+1) is far outside the cone's mesh and hence the displacement associated with it may be taken approximately as that of node (n), since node n is assumed at the far field of soil.

Solving (n+2) non-linear algebraic equations by means of classical numerical engineering methods (see for e.g. Przemieniecki, 1968, Clough and Penzien, 1968 etc) in terms of (n+1) variables of response at the discretization points might yield the solution of the non-linear cone problem in a numerical manner.

4.2.9 General finite element solution approach for an embedded foundation in a bounded medium

The most complex approach to solve the embedded foundation problem (in particular a pile) would be to make use of continuum type finite elements for a bounded medium of soil. In this approach as shown in Fig.4.16 a truncated area of bounded medium can be discretized by using 3D continuum finite elements with various shapes(see for e.g. Zeinkiewich, 1989). The appropriate boundary conditions have to enforced so that the missing soil effect could be accounted(such as reflection, refraction from the boundary) and also the size of the soil's global stiffness matrix and the number of elements needed could be limited.

Several previous studies have employed this more rigorous method either for linear elastic soil for e.g. Wolf and Song, (1995) and Wolf et al, (1996) and also with utilizing the general plasticity rules for the non-linear soil such as Langen, (1991) and Madshus, (1997). This method is considered to be extremely demanding in terms of computational time required particularly for time domain analysis of pile-soil system. Therefore, the application of this approach has been so far limited to some relatively small size or very sensitive problems such as design of pile foundation of nuclear power plant etc. Due to numerical complexity and time consumption it is recognized that this approach may not be very feasible at the current stage of offshore technology for analysis of pile foundation of jacket platforms. However, advances in terms of supercomputing systems might allow the designer and analysts to apply such more rigorous and accurate methods in near future.

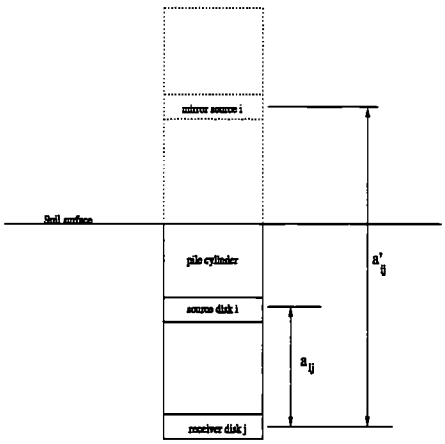

Figure 4.17: Geometrical properties of the non-linear cone of soil under various motions

4.3 Material damping associated with the cone model

4.3.1 General

The radiation damping as illustrated in the previous section is an inherent property of the dynamic cone model. While the radiation damping is considered to account for the most significant loss of energy in the soil medium, nevertheless some material damping will always be present in the pile-soil system. This material damping is mainly due to the friction between the soil particles and also partly caused by the friction between the pile's steel material and the soil.

A proper physical model to describe this kind of damping is perhaps the frictional damping model itself which can also be based on the degree of soil's frictional mobilization or indirectly based on the normal force components inducing the frictional loss in the soil or between the pile and the soil. Except frictional damping, there are other forms of material damping which can be applied such as visco-elastic(Voigt type), linear hysteretic(non-causal) and non-linear hysteretic type damping.

Although linear hysteretic and Voigt's VE models are in essence of the same family of dampers, nonetheless, there is a substantial difference between these two models. According to the Voigt's visco-elastic model the damping may be assumed to be linearly proportional to the frequency of vibration ω while in the linear hysteretic (non-causal) model, the material damping is considered to be constant. The corresponding damping ratio often is obtained according to each mode of the vibration. These two models are often applied for frequency domain analysis of the pile-soil systems.

On the other hand, the non-linear hysteretic model can also be applied for material type energy absorption in the soil. The corresponding energy loss is assumed to take place within each cycle of vibration as represented for a half cycle by the shaded area in Fig.4.18. The area enclosed

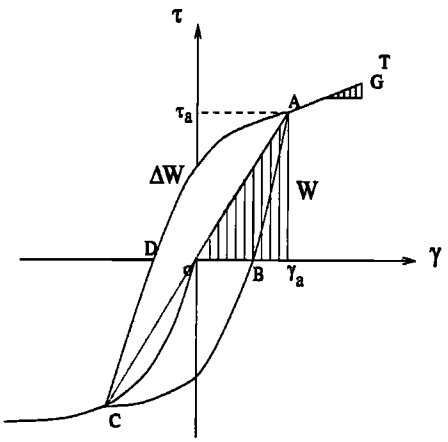

Figure 4.18: Illustration of hysteretic energy loss during cyclic loading of soil

within each hysteresis loop actually represent the amount of the total energy in one cycle. This part of work or energy as equivalently used can not be recovered even after unloading the pile-soil system. Non-linear hysteretic behaviour of soil will be discussed further subsequently.

An overview of each of these material damping models and their applications are given in the following subsections.

4.3.2 Voigt's visco-elastic damping

The basic kind of material damping which can be applied for the dynamic cone-disk model of soil is the Voigt's visco-elastic type damping. The Voigt model postulates that the damping can be defined as a linear function of frequency of excitation ω. Thus the model is suitable for pile-soil analysis in the frequency domain. According to the correspondence principle, the stiffness and damping coefficient of the dynamic system may be modified to accommodate the linear material damping $\eta_m = a_m\omega$ according to Eq.4.85. a_m is a coefficient which is inversely proportional to the natural frequency of the vibration of the cone ω_n.

The correspondence principle may be described as : "A linear hysteretic material damping can be introduced into the dynamic system by multiplying a complex term as $1+2i\eta_m$ corresponding to the material damping ratio η_m with the elastic stiffness properties of the soil such as shear modulus G(see for e.g. Wolf and Meek, 1994 and Appendix.D)". Hence, the shear velocity and its functions such as K_{st}, k_{dy} and c_{dy} will be modified accordingly. The dynamic stiffness function with considering the material damping from Eq.4.79, then can be decomposed as derived in Appenix.D, by assuming that the η_m is often small, thus its square may be omitted:

$$[real(S(\omega))]^* = -M\omega^2 + (1+i\eta_m)^2 K_{st} k_{dy}(\omega, c(1+i\eta_m)) \tag{4.89}$$

$$[imag(S(\omega))]^* = (1+i\eta_m)\omega K_{st} c_{dy}(\omega, c(1+i\eta_m)) \tag{4.90}$$

in which *asterisk* symbols indicates a modified form of $S(\omega)$, a_m is the linear material damping

coefficient. M represents the mass of the soil which will be considered as trapped (added) mass underneath of disk, while the mass of the soil inside the pile cylinder will be excavated mathematically, hence, here M in this Eq.4.89 will be substituted by M_t representing the trapped mass of soil. It may be worth noting that this trapped mass might only exist for the disk located at the pile tip.

Eqs. 4.89 and 4.90 can be re-written as:

$$K^*(\omega) = -M_t\omega^2 + (1 + 2ia_m\omega)K \tag{4.91}$$

$$i\omega C^*(\omega) = (1 + ia_m\omega)iC\omega \tag{4.92}$$

And Eqs. 4.91 and 4.92 can be simplified as follows:

$$K^*(\omega) = (-M_t\omega^2 + K) + 2ia_m\omega K = (K - M_t\omega^2) + i\omega C_{ve} \tag{4.93}$$

$$i\omega C^*(\omega) = i\omega C - a_m\omega^2 C = i\omega C - \omega^2 M_{ve} \tag{4.94}$$

As mathematically shown in Eqs. 4.93 and 4.94, introducing a linear frequency dependent visco-elastic damping results in modifying the initial dynamic system by augmenting a dashpot with a coefficient of $C_{ve} = 2a_m K_{st} k_{dy}(\omega, c^*)$ and a mass of $M_{ve} = a_m K_{st} c_{dy}(\omega, c^*)$. Therefore, in general, the dynamic stiffness parameters of visco-elastically damped model are non-linear functions of frequency of excitation ω.

4.3.3 Linear hysteretic (non-causal) damping

The linear hysteretic damping which is also known as non-causal damping(Wolf et al, 1994) is another version of linear hysteretic damping which as mentioned above assumes that damping ratio is constant and can be obtained according to each eigen-mode of vibration.

If we replace the frequency dependent material damping in Eqs. 4.93 and 4.94 with a constant material damping η_{cm} another modified dynamic stiffness system is obtained as a function of ω in general. If the k_{dy} is considered as a linear function of ω and introducing a constant material damping as η_{cm}, it will still be a linear function of ω. Figs.4.19 through 4.24 compare the spring and dashpot parameters of the dynamic system computed according to the described damping models.

As shown in Fig.4.19 k_{dy} decreases linearly with the frequency of excitation. By taking an inverse Fourier transformation of the response according to the frequency independent linear hysteretic damping model, no causing force can be obtained at the initial part of the response. This spurious response theorem has been investigated by Meek and Wolf, (1992) for the case of unmodified k_{dy} (i.e only K_{st} is assumed to be affected by the material damping).

As discussed by Meek and Wolf, (1992), this kind of spurious response despite its non-causality is accurate and valid in comparison with causal Voigt type damping or other experimental test results.

The dynamic stiffness expression with the presence of linear hysteretic type material damping may be obtained as follows(see Wolf and Meek, (1994) and appendix.D):

$$S^*(a_0) = -M_t\omega^2 + K(1 + 2ia_m\omega) + i\omega C(1 + ia_m\omega) \tag{4.95}$$

After re-arranging and substituting the relevant terms in latter, the stiffness will be(see also appendix.D):

$$S^*(a_0) = K_{st}\left[1 - \frac{\mu}{\pi}\frac{c_s^2}{c^2}\frac{z_0}{r_0}a_0^2 - \eta_m\frac{z_0}{r_0}\frac{c_s}{c}a_0\right] + ia_0K_{st}\left[\frac{2\eta_m}{a_0} - 2\eta_m\frac{\mu}{\pi}\frac{c_s^2}{c^2}\frac{z_0}{r_0}a_0 + \frac{z_0}{r_0}\frac{c_s}{c}\right] \tag{4.96}$$

in which all the parameters are as defined above. The dynamic spring and dashpot coefficients then follows from the real and the imaginary parts on the R-H-S of Eq. 4.96 as:

$$k^*_{dy}(a_0) = 1 - \frac{\mu}{\pi}\frac{c_s^2}{c^2}\frac{z_0}{r_0}a_0^2 - \eta_m\frac{z_0}{r_0}\frac{c_s}{c}a_0 \tag{4.97}$$

$$c^*_{dy}(a_0) = \frac{2\eta_m}{a_0} - 2\eta_m\frac{\mu}{\pi}\frac{c_s^2}{c^2}\frac{z_0}{r_0}a_0 + \frac{z_0}{r_0}\frac{c_s}{c} \tag{4.98}$$

For a vertical motion of disk for $\nu \leq 1/3$ the trapped mass is omitted (i.e. $\mu = 0$), hence the dynamic stiffness parameters given in Eqs.4.97 and 4.98 will be simplified as follows:

$$k^*_{dy,v}(a_0) = 1 - a_0\eta_m\frac{z_0}{r_0}\frac{c_s}{c} \tag{4.99}$$

$$c^*_{dy,v}(a_0) = \frac{2\eta_m}{a_0} + \frac{z_0}{r_0}\frac{c_s}{c} \tag{4.100}$$

With the visco-elastic material damping assumption (i.e. $\eta_m = a_{m,ve}\omega$) and knowing that $\omega = a_0c_s/r_0$, we will have:

$$\eta_m = \frac{a_{m,ve}a_0c_s}{r_0} \tag{4.101}$$

Substituting Eq. 4.101 into Eq. 4.99 and 4.100, the coefficients of dynamic stiffness for visco-elastic type material damping becomes:

$$k^*_{dy,v}(a_0) = 1 - a_{m,ve}\frac{c_s}{r_0}\frac{z_0}{r_0}\frac{c_s}{c}a_0^2 \tag{4.102}$$

$$c^*_{dy,v}(a_0) = 2a_{m,ve}\frac{c_s}{r_0} + \frac{z_0}{r_0}\frac{c_s}{c} \tag{4.103}$$

Eqs. 4.99 and 4.102 are plotted in Fig. 4.19 with solid and dashed lines, respectively(marked with LH and VE).

Though the visco-elastic and non-causal linear hysteretic dampers may provide the basis for the dynamic analysis of damped pile-soil systems in frequency domain but they may not be very relevant for the time domain analysis of such systems.

4.3.4 Frictional type material damping

A frictional damping model might be more relevant for a pile-soil system in the sense that the actual material damping in the soil arises from friction between the soil particles caused by the rubbing. Similarly at the pile-soil interface, frictional stress exists between the soil and steel material of pile. It is observed that the frictional force N may be created by the lateral forces P in the soil as follows(modified after Wolf et al, 1994):

$$N(\omega) = \sum_{i}^{3} C_i P_i tan(\delta_i) sgn(u_i, \dot{u}_i, \ddot{u}_i, ...) \tag{4.104}$$

in which δ represents the friction angle of the soil. sgn is a sign function which determines the sign of the argument inside the parentheses. It is observed that the frictional force in general will be non-linear w.r.t the sgn function. If the sgn function is dropped in Eq.4.104 and δ is assumed as a constant friction angle of soil (Coulombian response), $N(\omega)$ will be a linear function of u. Index i in Eq.4.104 is an indicator of various components of dynamic force(restoring, damping and inertia, respectively). C_i coefficient in Eq.4.104 is obtained as : $C_1 = 2C_2 = C_3 = 1.0$.
The lateral force P may be decomposed into its components as follows:

$$P = K|u - u_0| + C|\dot{u} - \dot{u}_0| + \Delta M|\ddot{u} - \ddot{u}_0| \tag{4.105}$$

The first term on the R-H-S of Eq. 4.105 is the contribution of the spring force, the second term is that of dashpot and the last term is related to the trapped mass underneath the disk which can be considered for an incompressible soil (Wolf et al, 1994):

$$\Delta M = \mu \rho r_0^3 \tag{4.106}$$

where μ is a coefficient obtained as follows:

$$\begin{aligned} \mu &= 2.4\pi(\nu - 1/3) && ;1/3 < \nu \leq 1/2 \\ &= 0 && ;\nu \leq 1/3 \end{aligned} \tag{4.107}$$

Thus by combining Eqs.4.104 and 4.105, $N(\omega)$ may be re-written as follows:

$$N(\omega) = K|u-u_0|tan(\delta)sgn(\dot{u}-\dot{u}_0) + \frac{C}{2}|\dot{u}-\dot{u}_0|tan(\delta)sgn(\ddot{u}-\ddot{u}_0) + \Delta M|\ddot{u}-\ddot{u}_0|tan(\delta)sgn(\dddot{u}-\dddot{u}_0) \tag{4.108}$$

The following dynamic stiffness functions can be obtained(see appendix.D):

$$k^*_{dy}(a_0) = 1 - \eta_m . \frac{4}{\pi} \frac{c_s}{c} \frac{z_0}{r_0} . a_0 - \frac{\mu}{\pi} (\frac{c_s}{c})^2 \frac{z_0}{r_0} . {a_0}^2 \tag{4.109}$$

$$c^*_{dy}(a_0) = \frac{c_s}{c} \frac{z_0}{r_0} + \frac{8}{\pi} . \frac{\eta_m}{a_0} - \frac{\mu}{\pi} . \frac{z_0}{r_0} (\frac{c_s}{c})^2 \frac{8}{\pi} \eta_m a_0 \tag{4.110}$$

Applying Eq.4.108 the impedance functions related to a frictional damping system are derived by inclusion of the inertia terms(see appendix.D).

Comparing Eqs. 4.109 and 4.110 with Eqs. 4.97 and 4.98, it can be seen that the first terms on both spring and dashpot terms are the same but the difference is a factor $4/\pi$ instead of one in the terms involving the material damping factor η. If the damping parameter η_m in the latter equation is replaced by $(\pi/4)\eta_m$ then the truncated frictional damping relationship for the spring coefficient will turn out to be exactly the same as the linear hysteretic model. In geotechnical practice, the observed maximum difference of about 0.17 may not be considered very significant.

4.3.5 Discussion about the influence of visco-elastic and linear hysteretic damping on dynamic stiffness coefficients of the cone

In this section, we discuss the influence of various types of material damping described in the previous subsections on the dynamic stiffness coefficients of soil cone. To illustrate these variations particularly with the frequency of vibration, initially we consider the Voigt's VE and Linear hysteretic(non-causal) type damping. To observe the limits of such variations, lower and upper bounds of the soil compressibility as $\nu = 0$ and $\nu = 0.5$ respectively are considered. The soil's compressibility is defined with its ability to dilate and contract. The compressible soils such as dry sand or clay may be considered to propagate the compressive or P-waves into the infinity while perfectly incompressible soils such as saturated clays could be considered as less able to expand or contract hence less able to radiate P-waves towards the infinity. At the limit for a perfectly incompressible soil with ($\nu = 0.5$), there is no possibility for the soil rod to contract to dilate even for a very long wave, therefore, the energy can not be transmitted as P-waves.

It is shown in the following, this characteristic of soil will also play an important role in determining the impedance functions of the cone-disk model which are essential in predicting the dynamic response of the pile-soil system.

As illustrated in Figs.4.19 and 4.20, the spring coefficient $k^*_{dy,v}$ at $a_0 = 0$ is equal to unity according to both visco-elastic and non-causal linear hysteretic damping models.

This verifies the consistency of the dynamic stiffness relationship with the static case. However, significant differences in terms of shape or degradation of damped spring coefficient $k^*_{dy,v}(a_0)$ are observed in the dynamic range ($a_0 > 0$). For visco-elastic type damping model, the degradation is parabolic with a_0 and approaches $-\infty$ when $a_0 \to \infty$. At $a_0 = \sqrt{\frac{1}{a_{m,v}} \frac{r_0}{c_s} \frac{r_0}{z_0} \frac{c_p}{c_s}}$, $k^*_{dy,v}(a_0) = 0$ which physically represents a cutoff frequency for the cone's spring coefficient under vertical motion of disk. Since the ω values for which this cut off occurs, are in the order of 100 HZ, therefore this certainly will not cause any problem for the extreme sea waves with very low dominant frequencies in the range of 0.05 to 0.1HZ. For the extreme seismic motions of soil with typical main frequencies in the range of 0.5 to 50HZ, the cone spring coefficient will be a positive value.

In comparison, the spring coefficient $k^*_{dy,v}$ decreases linearly with a_0 for a linear hysteretic damping model as shown in Fig. 4.19. The degradation in this case is slower than that for the visco-elastic case for higher frequencies. As shown, the addition of the trapped mass beneath the pile-soil disk (for compressible soil) changes the linear variation of $k^*_{dy,v}$ to a parabolic re-

lationship but decreases with a smaller magnitude than that of the visco-elastic model without considering the trapped mass. The dashpot coefficient $c^*_{dy,v}$ as plotted in Fig. 4.20 is constant for the visco-elastic damping model with a magnitude of $2a_m\frac{c_s}{r_0}+\frac{z_0}{r_0}\frac{c_s}{c_p}$, while for the linear-hysteretic model it is a hyperbolic function which decreases rapidly with a_0 and approaches an asymptotic value of about $\frac{z_0}{r_0}\frac{c_s}{c_p}$ at very large frequency of excitation(i.e. $a_0 \rightarrow \infty$) which is represented by a dashed curve. Inclusion of the trapped mass also changes the damping parameter considerably for large frequencies ($a_0 >> 1.0$). As shown in Fig. 4.20 $c^*_{dy,v}$ is zero at $a_0 = \pi c/(2\eta_m \mu c_s)$ and negative after that. Hence, this point can be considered as the cut off frequency of the corresponding cone under vertical motion.

In the following section horizontal, vertical and rocking motions of disk are considered and for each case the spring and the dashpot coefficients(i.e. impedance functions) are obtained for different material properties.

(I) For vertical motion of the disk:

$c = c_p$;$0 \leq \nu \leq 1/3$; (compressible soil)

$c = 2c_s$;$1/3 < \nu \leq 1/2$ (incompressible soil)

$\frac{z_0}{r_0} = \frac{\pi}{4}(1-\nu)(\frac{c}{c_s})^2$

$$k^*_{dy,v}(a_0) = 1 - \frac{4}{\pi}\frac{z_0}{r_0}\frac{c_s}{c}\eta_m a_0 - \frac{\mu}{\pi}\frac{{c_s}^2}{c^2}\frac{z_0}{r_0}{a_0}^2; \tag{4.111}$$
$$= 1 - \eta_m(1-\nu)\frac{c}{c_s}a_0 - \frac{\mu}{4}(1-\nu){a_0}^2$$

For e.g. for $\nu = 1/3$, $\eta_m = 0.25$ and $\mu = 0$, we have:

$$k^*_{dy,v}(a_0) = 1 - 0.33a_0 \tag{4.112}$$

for which the cut-off frequency is about $a_0 = 3$ or $\omega_0 = \frac{3c_s}{r_0} = 150HZ$. This actually represents a high frequency which is often associated with the machine vibration. For lower frequency seismic and sea waves, the corresponding spring coefficient will be positive.

The dashpot coefficient for the vertical motion of the soil disk can be obtained as follows:

$$c^*_{dy,v}(a_0) = \frac{z_0}{r_0}\frac{c_s}{c} + \frac{2\eta_m}{a_0}\frac{4}{\pi} - \frac{\mu}{\pi}\frac{z_0}{r_0}\frac{{c_s}^2}{c^2}\frac{8}{\pi}\eta_m a_0 \tag{4.113}$$
$$= \frac{\pi}{4}(1-\nu)(\frac{c}{c_s}) + \frac{2\eta_m}{a_0}\frac{4}{\pi} - \frac{2\mu}{\pi}(1-\nu)\eta_m a_0$$

For e.g. $\nu = 1/3$, $\eta_m = 0.25$ and $\mu = 0$ gives:

$$c^*_{dy,v}(a_0) = \frac{\pi}{2}(1-\nu) + \frac{2}{\pi a_0} \tag{4.114}$$

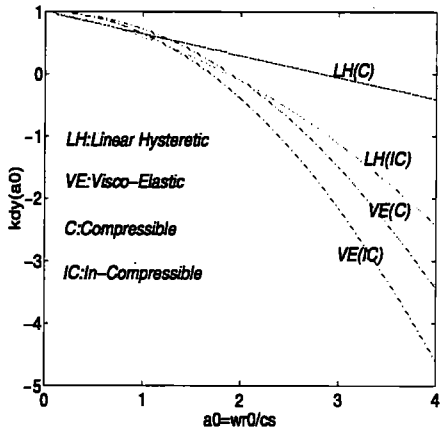

Figure 4.19: Modified dynamic coefficient of single pile-soil system under vertical motion vs. non-dimensional frequency a0 for non-causal linear hysteretic and visco-elastic type damping

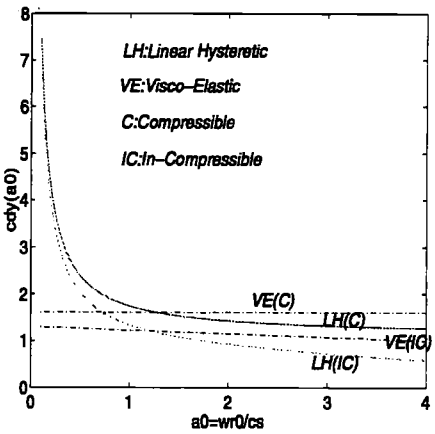

Figure 4.20: Modified vertical dashpot coefficient of single disk-cone system under vertical motion vs. non-dimensional frequency a0 for non-causal linear hysteretic and visco-elastic type damping

Fig. 4.19 shows lower and upper bounds of $k^*_{dy,v}(a_0)$ corresponding to $\nu = 0$ perfectly compressible soil and for $\nu = 1/2$ perfectly incompressible soil, respectively.

The dynamic spring coefficient is seen to be higher for the compressible soil than that of the incompressible soil. Nevertheless, the differences are smaller for visco-elastic damping for two types of soil.

The dashpot (damping) parameter $c^*_{dy,v}(a_0)$ is plotted in Fig. 4.20 for incompressible as well as compressible soils. The damping relationship is seen to be non-linear (hyperbolic) type for both cases, however, is smaller for the incompressible soil than that for the compressible one. The ultimate damping coefficient for very high frequency is about $\sqrt{2}\pi/4$ for $\nu = 0$ which is $\sqrt{2}$ times of that for the perfectly incompressible soil $\nu = 1/2$ for which $c_p(\nu = 1/2) = \sqrt{2}c_s$. This conclusion is physically sound based on our understanding of frictional loss in the soil. A nearly incompressible soil, the soil can not be compressed or dilate to allow for the P waves to propagate, while in a partially saturated or dry soil the compressive waves can propagate by compressive deformation of the soil elements which can be allowed by filling the void space in the soil volume. Thus comparatively, the total amount of the energy which can propagate towards infinity is much higher for the latter type soil.

(II) For horizontal motion of the disk we have:

$c = c_s$; for all ν values

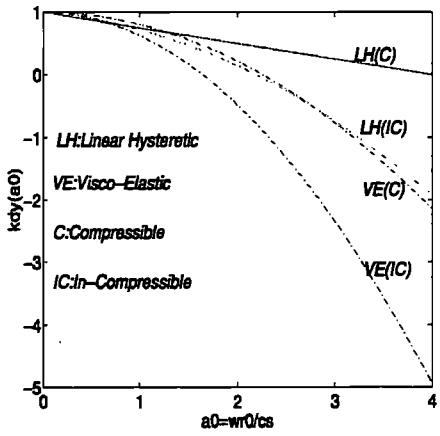

Figure 4.21: Modified dynamic spring coefficient of single disk-cone system under horizontal motion vs. non-dimensional frequency a0 for non-causal linear hysteretic and visco-elastic type damping

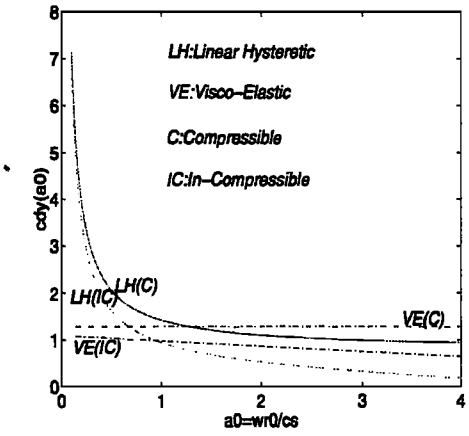

Figure 4.22: Modified dashpot coefficient of single disk-cone system under horizontal motion vs. non-dimensional frequency a0 for non-causal linear hysteretic and visco-elastic type damping

$\frac{z_0}{r_0} = \frac{\pi}{8}(2-\nu)$

Hence, the spring and the dashpot coefficients ($k^*_{dy,h}(a_0)$ and $c^*_{dy,h}(a_0)$) will be computed as follows:

$$k^*_{dy,h}(a_0) = 1 - \frac{4}{\pi}\frac{z_0}{r_0}\frac{c_s}{c}\eta_m a_0 - \frac{\mu}{\pi}\frac{{c_s}^2}{c^2}\frac{z_0}{r_0}{a_0}^2 \tag{4.115}$$
$$= 1 - \frac{\eta_m}{2}(2-\nu)a_0 - \frac{\mu}{8}(2-\nu)\frac{{c_s}^2}{c^2}{a_0}^2$$

The $k^*_{dy,h}(a_0)$ which is plotted in Fig. 4.21 starting from unity at $a_0 = 0$ and decreasing linearly with a_0 and approaching $-\infty$ at $a_0 = \infty$. $k^*_{dy,h}(a_0) = 0$ at $a_0 = \frac{2}{\eta_m(2-\nu)}$ (for $\mu = 0$) which indicates the cut off of the cone's spring coefficient.

In a similar manner, the dashpot coefficient $c^*_{dy,h}(a_0)$ can be derived as follows:

$$c^*_{dy,h}(a_0) = \frac{z_0}{r_0}\frac{c_s}{c} + \frac{2\eta_m}{a_0}\frac{4}{\pi} - \frac{\mu}{\pi}\frac{z_0}{r_0}\frac{{c_s}^2}{c^2}\frac{8}{\pi}\eta_m a_0 \tag{4.116}$$
$$= \frac{\pi}{8}(2-\nu) + \frac{8}{\pi}\frac{\eta_m}{a_0} - \frac{\mu}{\pi}(2-\nu)\frac{{c_s}^2}{c^2}\eta_m a_0$$

which is a hyperbolic relationship in terms of a_0 as shown in Fig. 4.22 decreasing from infinity at $a_0 = 0$ to an asymptotic value of $\frac{\pi}{8}(2-\nu)$ at very large frequencies $a_0 \to \infty$ for $\mu = 0$.

(III) For the rocking motion of the disk:

$c = c_p$; for $0 \leq \nu \leq 1/3$

$c = 2c_s$; for $1/3 < \nu \leq 1/2$

$\frac{z_0}{r_0} = \frac{9\pi}{32}(1-\nu)(\frac{c}{c_s})^2$

Hence, the dynamic spring coefficient follows from Eq. D.26 as follows:

$$k^*_{dy,r}(a_0) = 1 - \frac{4}{\pi}\frac{z_0}{r_0}\frac{c_s}{c}\eta_m a_0 - \frac{\mu}{\pi}\frac{{c_s}^2}{c^2}\frac{z_0}{r_0}{a_0}^2 \tag{4.117}$$
$$= 1 - \frac{9}{8}(1-\nu)(\frac{c}{c_s})\eta_m a_0 - \frac{9\mu}{32}(1-\nu){a_0}^2$$

For e.g. $\nu = 1/3$ and $\eta_m = 0.25$, we obtain:

$$k^*_{dy,r}(a_0) = 1 - \frac{3}{8}a_0 \tag{4.118}$$

which is zero for $a_0 = 8/3 \approx 2.67$. The spring coefficient is plotted in Fig. 4.23 vs. a_0 for both compressible and non-compressible soil types. It is observed that $k^*_{dy,r}(a_0)$ decreases for both cases from a unity at $a_0 = 0$ towards $-\infty$ for $a_0 = \infty$. As observed for the vertical motion of the disk, the spring parameter is larger for the compressible soil than that of incompressible one.

The dashpot parameter for the rocking motion of the soil disk can be obtained from Eq. D.26 as follows:

$$c^*_{dy,r}(a_0) = \frac{z_0}{r_0}\frac{c_s}{c} + \frac{2\eta_m}{a_0}\frac{4}{\pi} - \frac{\mu}{\pi}\frac{z_0}{r_0}\frac{8}{\pi}\eta_m a_0 \tag{4.119}$$
$$= \frac{9\pi}{32}(1-\nu)(\frac{c}{c_s}) + \frac{2\eta_m}{a_0}\frac{4}{\pi} - \frac{9\mu}{4\pi}(1-\nu)\eta_m a_0(\frac{c}{c_s})^2$$

For e.g. $\nu = 1/3$ and $\eta_m = 0.25$, we have:

$$c^*_{dy,r}(a_0) = \frac{3\pi}{8} + \frac{2}{\pi a_0} \tag{4.120}$$

For in-compressible soils($c = 2c_s$) then we can obtain:

$$c^*_{dy,r}(a_0) = \frac{9\pi}{16}(1-\nu) + \frac{8\eta_m}{\pi a_0} - \frac{\mu}{\pi}\frac{z_0}{r_0}\frac{8}{\pi}\eta_m a_0 \tag{4.121}$$

For e.g. for a perfectly non-compressible type of soil $\nu = 1/2$ and $\eta_m = 0.25$, we can obtain:

$$c^*_{dy,r}(a_0) = \frac{9\pi}{32} + \frac{2}{\pi a_0} - \frac{9\mu}{4\pi}(1-\nu=\frac{1}{2})(\eta_m = 0.25)4a_0 \approx \frac{9\pi}{32}(1-0.4a_0) + \frac{2}{\pi a_0} \tag{4.122}$$

Fig. 4.23 compares the dashpot coefficient vs. a_0. It is seen that the relationships are hyperbolic for both soil types, but with higher magnitude for the compressible soil compared to that of incompressible one. The limit values of $c^*_{dy,r}(a_0)$ are $-\infty$ and $9\pi\sqrt{2}/32 \approx 1.25$ for $\nu = 1/2$ and $\nu = 0$, respectively. This observation is consistent with that made for the vertical motion of the disk above.

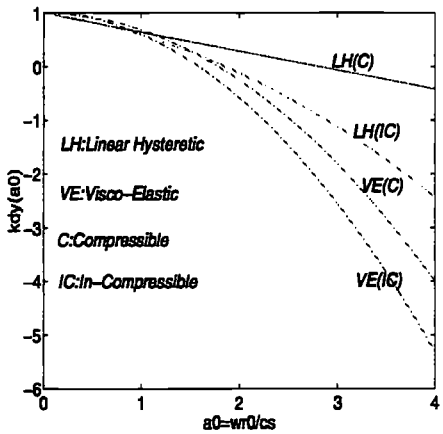

Figure 4.23: Modified dynamic spring coefficient of single disk-cone system under rocking motion vs. non-dimensional frequency a0 for non-causal linear hysteretic and visco-elastic type damping

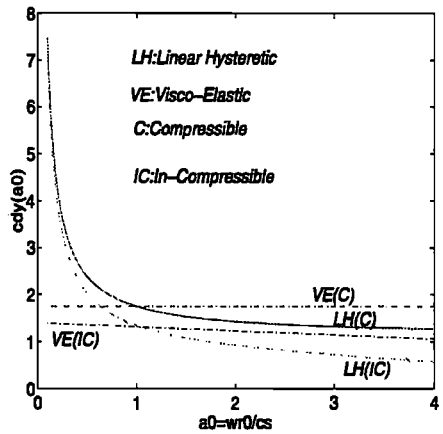

Figure 4.24: Modified dashpot coefficient of single disk-cone system under rocking motion vs. non-dimensional frequency a0 for non-causal linear hysteretic and visco-elastic type damping

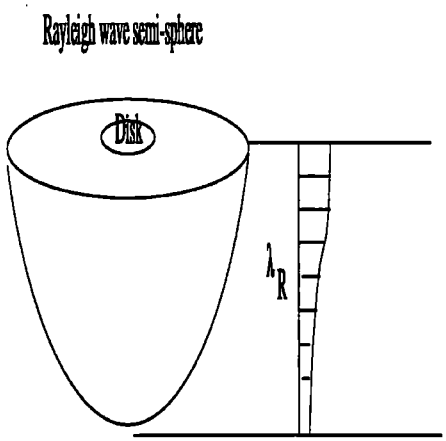

Figure 4.25: Rayleigh wave transmission in the radial direction

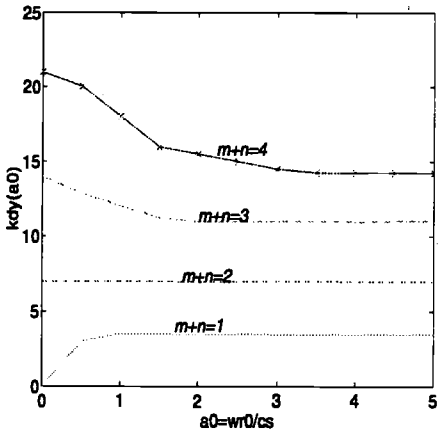

Figure 4.26: Comparison of k_{dy} of a 2D-wedge and a 3D-cone model of soil

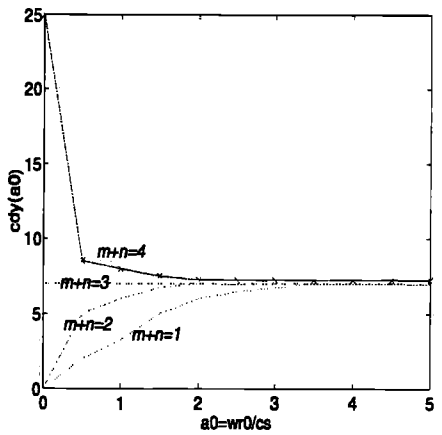

Figure 4.27: Comparison of c_{dy} of a 2D-wedge and a 3D-cone model of soil

4.3.6 Discussion about negative dynamic stiffness properties of a cone-disk model

As illustrated in the previous section, the dynamic stiffness coefficients $k_{dy}(a_0)$ and $c_{dy}(a_0)$ can be negative for a range of frequencies. This phenomenon can be physically interpreted as well as using the mathematical relationships obtained above.

Let us first consider an undamped dynamic system consisting of a rigid disk on a half space or a layer of soil with its associated cone. For poisson ratio ν of soil less than 1/3 (for compressible type soil) such as dry sand, as the disk starts vibrating under the applied loading, there will be no trapped mass of soil to vibrate with the disk hence the dynamic stiffness will be only dominated with the spring and dashpot of the disk-cone system. Hence, the corresponding $k_{dy}(a_0)$ and $c_{dy}(a_0)$ coefficients will remain positive for all frequencies of excitation.

However, for an incompressible soil such as saturated clay with a poisson ratio of $1/3 < \nu \leq 1/2$, a trapped mass will exist underneath the disk which will start vibrating in phase with the disk, hence, it will influence the dynamic stiffness and damping coefficients. The tendency towards negative stiffness occurs when the inertia takes over from the spring. The resonance or spring cut-off occurs also due to the influence of the trapped mass of soil. Although the mass is moving in phase with the disk but due to the negative sign of inertia force in the dynamic stiffness term as $:S_\omega = K + i\omega C - \omega^2 M$ and also the square term of frequency the dynamic stiffness then becomes negative after the cut-off frequency as defined above. For soils with $\nu < 1/2$ the dynamic stiffness can reach a peak negative value and return to become positive by increasing the frequency.

This recovery may be physically explained as follows. As the frequency of vibration increases beyond a critical value, the trapped mass either vanishes (detaches from the disk) or possibly

moves in negative phase with the disk's motion. For a perfectly incompressible soil($\nu = 1/2$), however, this kind of stiffness or damping recovery is not observed. Physically speaking, in the latter case, the trapped soil mass moves the whole time with the disk in phase and does not vanish.

So far we discussed the negative dynamic stiffness phenomenon for the undamped cone-disk systems. However, in reality every dynamic system such as cone-disk possesses some material damping whose effect on modifying the dynamic stiffness properties of the cone-disk system were described through the mathematical relationships which presented in the previous section.

It is shown above that the linear hysteretic damping results in modification of the stiffness properties of the cone-disk model through augmenting equivalent spring and dashpot elements which are proportional to the original damping and spring coefficients of the cone-disk system C and K, respectively, and also proportional to the material damping coefficient of soil a_m. Hence, the dynamic stiffness can be written as:$S(\omega) = (K - K_{lh}) + i\omega(C + C_{lh}) - \omega^2(M_t)$. where K,C as earlier are the original stiffness parameters, K_{lh} and C_{lh} are the augmented spring and dashpot which are added due to the presence of the linear hysteretic material damping.

It is evident that the spring action will be dominated by an augmented frequency dependent spring K_{lh} in parallel with the original spring K. The augmented spring K_{lh} increases parabolically with the frequency of excitation but with an opposite sign and rapidly takes over from its original counterpart. Hence, the result will be cut-off and then negative spring stiffness. On the contrary, the augmented dashpot term C_a which is proportional to the original spring stiffness K has the same sign as the original dashpot (positive sign) and is frequency independent will not cause any variation in terms of k_{dy}.

On the other hand, in the case of a visco-elastic type hysteretic material damping which is linearly frequency dependent, as described in the previous, there will be an added mass proportional to the damping coefficient C as $M_{ve} = -2a_mC\omega^2$ and another augmented dashpot proportional to the original spring stiffness K as $C_{ve} = 2a_mK\omega^2$. For this case, the dynamic stiffness of the system will be:$S(\omega) = K + i\omega(C + C_{ve}) - \omega^2(M_t + M_{ve})$. When this system starts to vibrate, the inertia term may not reduce significantly the dynamic stiffness for lower frequencies but as the frequency of vibration increases the effect of added masses (trapped and augmented) will start to dominate the cone-disk model's dynamic response. This will result in resonance and then by increasing further the frequency will result in negative value for the real part of $S(\omega)$ which corresponds to the spring's stiffness.

In contrast to the half space of soil, the dynamic stiffness for a disk on a layer of soil might recover due to possible reflections from the boundaries of the system which is discussed in a subsequent section. Though the trapped mass effect may not be so significant as the augmented mass or spring, nevertheless it will reduce the spring stiffness in the same manner as the other added mass. The variation of dashpot coefficient c_{dy} with the material damping though is not significant as for the spring parameter k_{dy}, but nevertheless implies that the material damping does indeed affect the radiation damping.

As observed in earlier section, in certain frequencies, the linear hysteretic material damping may result in the cut-off of the energy transmission. Depending on the frequency of excitation, damping and poisson ratios of soil, an effective added mass can be defined which relates to the active mass or inertia term for each range of these parameters.

It is shown that a considerable non-linear material damping caused by the yield of soil might reduce the amount of radiation damping through soil cone. Analogously, any discontinuity such as gapping or separation of pile from soil might result in partial or complete cut-off of radiation damping (see for e.g El Naggar and Novak, 1995). The effect of the non-linear material damping is discussed in the following section.

4.3.7 Non-linear hysteretic type material damping of soil

The strain and displacement dependent material damping can also be associated with the cone model. Such models might be more relevant for the time domain analysis of pile-soil systems than the visco-elastic, linear hysteretic and the frictional models as described above. In a following subsection, we will illustrate the effects of using each of these models on two simplified 2DOF and 3DOF systems. However, before that a simple concept of strain dependent material damping is given in this subsection. For a single uni-directional cone, a relationship may be obtained between the displacement and its derivative strain according to the theory of continuum mechanics as $\epsilon_c = f(u_c, \dot{u}_c, ...)$. Such relationship then can be combined with the material damping relationship as:

$$\eta_m = a_m \frac{f(u_c, \dot{u}_c, ...)}{\alpha_s} \tag{4.123}$$

Inserting Eq. 4.123 into the dynamic equation of motion of SDOF the cone, we will have:

$$M\ddot{u}_c + K(1 + 2ia_m \frac{f(u_c, \dot{u}_c, ...)}{\alpha_s})u_c = F_e(t) \tag{4.124}$$

The imaginary term in Eq. 4.124 may be replaced by its real counterpart as follows:

$$C = ia_m K \frac{u_c \frac{f(u_c, \dot{u}_c, ...)}{\alpha_s}}{\dot{u}_c} \tag{4.125}$$

In a more advanced dynamic soil mobilization type non-linear hysteretic damping model (for e.g Svanø et al, 1992-1993 and Madshus, 1997), the linear stiffness term in Eq. 4.124 is replaced with a non-linear tangent stiffness function as $K_c = f(G_0, z, r, u_c, \sigma'_m, \omega, ...)$ with the parameters involved as described in previous subsection. Hence, the damping in this case is more inherent property of the soil's inelastic behaviour.

By utilizing the Green function approach and the dynamic properties of the non-linear cone, the latter model might be capable of taking material non-linearity through u variable, geometrical non-homogenity through z and r variables, pore-excess or cyclic degradation effect through σ'_m parameter and the frequency of excitation effect by ω parameter.

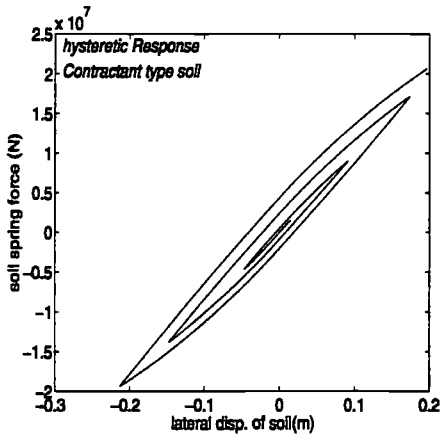

Figure 4.28: A tangent stiffness model of pile-soil with the hysteretic behaviour for contractant type (NC) soils

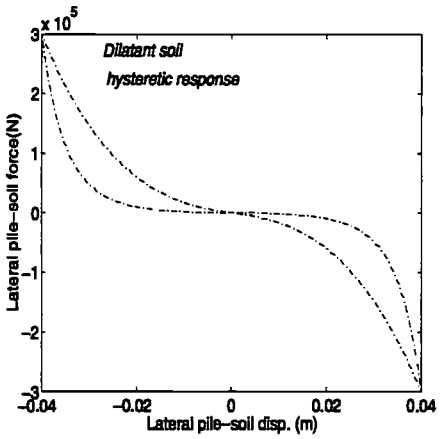

Figure 4.29: A tangent stiffness model of pile-soil with the hysteretic behaviour for dilatant type (OC) soils

The cyclic behaviour of the soils have been the subject of extensive investigations in the past years. As outcome of numerous cyclic tests on both clay and sand, several non-linear hysteretic models have been developed most of them for non-dilatant type soils such as normally consolidated soft clays (see for e.g Ramberg-Osgood, (1943), Hardin-Drnevich, (1972), Richart, (1975), Janbu, (1976), Hara, (1980), Molenkamp, (1980) , Finn and Lee , (1982), Langø, (1991), Svanø, (1992) and Madshus, (1997)). Most of these models assume that the soil behaviour during cyclic loading can be simulated by hysteretic loops which are established by using a characteristic backbone curve similar to one shown on Fig.4.28. The shown backbone curve connects the tips of the hysteretic loops.

For the dilatant soils such as OC clay or dense sand, the hysteretic shear stress- strain behaviour of the soil may be essentially different from that of soft contractant clay, as illustrated in Fig.4.29. For this kind of soil, the tangent stiffness of soil increases as the shear strain increases since the mean effective stress increases with the increase of the shear stress in the soil while the soil dilates during each loading cycle. For a laterally loaded pile-soil system, an inactive displacement zone may be considered within which the mobilized shear stress of the soil is almost zero. This inactive displacement zone may be considered to diminish with the soil depth as illustrated in Fig. 4.28. The depth at which the apex of the immobilized zone is located may be defined as the critical depth of the full strength mobilization.

To get better idea about the dilatant type soil behaviour during cyclic loading, the cyclic stress path $q' - p'$ is illustrated in Fig.4.30. It is observed that the mean effective stress p' initially decreases on the first loading branch with the increase of the deviatoric stress component q'. This might be attributed to the immediate increase of the excess pore pressure of water in the soil just after loading, however, as shown the mean effective stress after reaching a limit(on

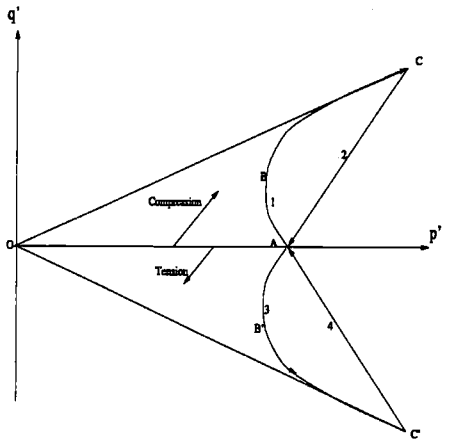

Figure 4.30: A characteristic (butter fly) type q'-p stress path for dilatant type soils

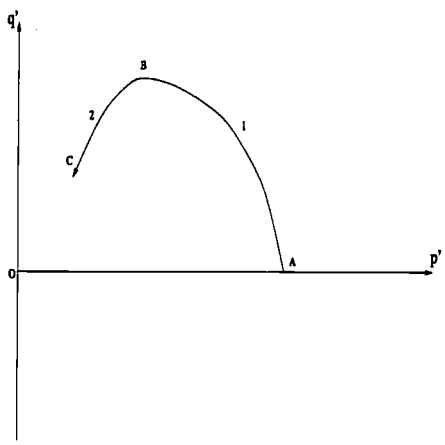

Figure 4.31: A characteristic type q'-p stress path for contractant type soils

branch 1), again increases as the loading proceeds and the deviatoric stress which is an indicator of the magnitude of shearing which occurs in the soil. The shear stress vs. mean effective stress relationship is almost linear for this part of loading. It is observed that upon the unloading(on branch 2) both the deviatoric and the mean effective stress decrease almost linearly proportionally. On the re-loading branch(3) on the negative shear stress side. (see Fig.4.30), a mirror of stress pattern in branch 1 is observed. The branch 4 is also similar to branch 2 on unloading part. This kind of behaviour as discussed by Madshus, (1997) may be considered by a non-associative plastic flow rule (for e.g a Fuzzy type model Klisinski et al, 1988).

Fig.4.31 shows a different kind of soil response which is often observed for essentially normally consolidated type soils. It is seen that the excess pore pressure p' decreases as the shearing in the soil increases up to a peak point denoted here by B. After this point, the deviatoric stress component decreases as the excess pore water pressure further increases.

Throughout this Chapter, it is assumed that the soil response(yield and/or bounding surface) might be shifted during the cyclic loading. The latter is better known as an associated kinematic hardening rule. We applied this kind of kinematic, hardening rule based on a direct distance from the yield surface to the bounding surface which is discussed in a general form in Chapter.3.

4.4 A cone model for layered soil

4.4.1 General

The idea of unfolded cone model is basically derived from the Boussinesq displacement and stress contours (see for e.g Das, 1985 or Wolf et al, 1994) for a statically loaded disk resting on the surface of an elastic half space of soil which is illustrated in Fig. 4.8.

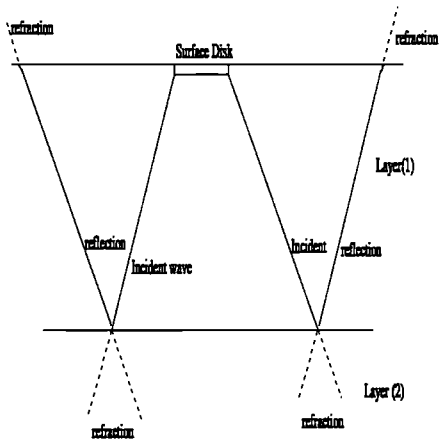

Figure 4.32: A cone model of a near surface layer of soil

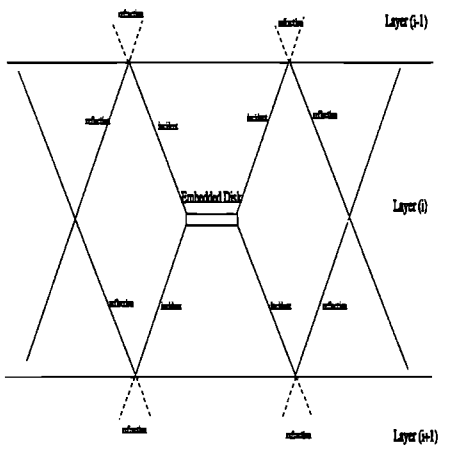

Figure 4.33: An embedded disk with double cone model of soil

The linear and non-linear cone models which were described above are applicable for a uniform half space of soil which extends to infinity. However, in a real situation the soil may consist of several layers with different properties(such as shear modulus and poisson ratio). Each layer may be confined within its own boundaries with adjacent layers such as free surface, a bed rock surface or a flexible layer surface. While in a semi-infinite soil medium, it may be assumed that no wave would reflect or refract, in a layered medium, however, it might be the case, particularly for a layer with a rigid boundary such as rock underlying it and a free surface boundary overlying it. For sub-sea strata, similar conditions may be encountered such as a layered soil overlying a bed-rock.

Based on the echo phenomenon from the physics of acoustics, Meek and Wolf, (1992) proposed a cone model for layered soil which is derived initially for a surface layer as described above which can be extended for sub-surface layers with different boundary conditions as well. The following subsections describe the basic model of Meek and Wolf, (1992) and its extension to sub-surface layers with general assumption of the cone's geometry and non-linearities of the soil.

4.4.2 A disk on a surface layer with associated single cone model

Let us consider a layer of soil as shown in Fig.4.32 which is located between the surface and an underlying bedrock. Due to the relatively much higher rigidity of the bedrock compared with the overlying soil, it may be assumed that no transmission of motion would take place through bedrock or the displacement at the bedrock surface may be assumed as zero. This implies that the displacement components of the incident and the reflected waves must have the same magnitude with opposite signs. On the other hand, the boundary condition for the free surface is to have zero stress there which means that it can deform freely. Thus the displacement components of the incident and the reflected waves must be the same which is mathematically shown later.

Now if a rigid disk located on the surface of the considered layer is excited by a concentrated load such as P_i, the waves will propagate from this surface downwards towards the underlying bedrock carrying the energy within the associated single cone with its apex at a distance z_i above the surface as described in the previous subsection. The emitted wave from the surface after traveling a distance of h_i encounters the bedrock surface where it can not pass through and hence will be reflected back towards the surface. In analogy with the Boussinesq distribution, it may be assumed that the angles of both incident and reflected envelopes are the same. The latter is analytically and also numerically proven by Miller and Pursey, (1955) and Meek and Wolf, (1992) and (1994) for elastic homogeneous type soil.

By assuming the identical apex angles of the incident and the reflected cones, their apex height ratio may be obtained as: $\frac{z_i}{z_i+h}$ and hence the intersection area of the reflected(upward) cone at the surface will be proportionally larger than that of the downward one(Fig. 4.32). The reflected waves from bedrock after reaching the free surface of the layer will reflect back towards the bedrock due to the separation or cutoff in the free boundary.

For a mudline surface, of course, the vertical stress would be equal to that of the hydrostatic and hydrodynamic pressure of water column above the mud-line. Hence, the assumption of free surface can not be applied at mud-line level.

The successive reflection of the propagating waves within their corresponding folded cones as shown in Fig. 4.32 would carry the energy to the infinity horizontally. As described by Wolf et al. according to the echo phenomenon of physics the horizontal radiation would require longer travel distance and hence longer time than the spherical or cylindrical forms of radiation in a unified half space as described above. This is also simulated numerically in a following subsection. Based on the above outlined basic concept of Wolf et al, the extended non-linear cone model for a near soil surface layer is described in the following subsection.

4.4.3 An embedded disk in a sub-surface layer with associated double cone model

Let us consider somewhat more general case, a sub-surface layer of soil located between two arbitrary boundaries with the given properties. A loaded disk which may be associated with a pile-soil system is considered at a point of space within this layer as shown in Fig.4.33. The loaded disk generate waves which can propagate both upwards and downwards in general. It is assumed that the propagation takes place within identical cones(double cones) but with opposite apex positions(see Fig.4.33).

The generating displacement function for a given point in a cone space at a distance a_i from the loaded disk (i) may be defined as(Wolf et al, 1994): $u_i(t - \frac{a_i}{c})$ where the index i refers to the position of disk i and c denotes the wave velocity in the soil layer. u_i represents the generating function at the location of disk (i) as shown in Fig.4.33. The fraction in the argument of

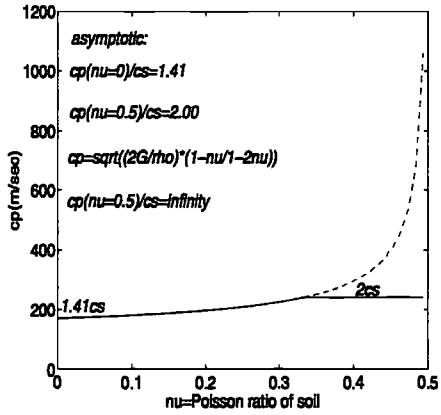

Figure 4.34: Variation of dilatational wave velocity with ν

generating displacement represents the delay or retardation time which is needed for the wave to travel from the disk (i) to the point at the distance a_i from it. (For compressible soils with the poisson's ratio $0 < \nu \leq 1/3$, the wave velocity may be assumed as c_p while for the incompressible soils $(1/3 < \nu \leq 1/2)$ as $2c_s$). The limit of the P-wave for $\nu = 1/2$ will become:

$$limc_{p_{\nu \to 1/2}} = lim \sqrt{\frac{2G}{\rho} \frac{1-\nu}{1-2\nu}} \to \infty \tag{4.126}$$

while c_p's limit for $\nu = 1/3$ at the boundary between the compressible and incompressible soil is:

$$limc_{p_{\nu \to 1/3}} = lim \sqrt{\frac{4G}{\rho}} = 2c_s \tag{4.127}$$

Hence an asymptotic value of $2c_s$ is applied for $1/3 < \nu < 1/2$ as shown in Fig.4.34.
For a non-homogeneous and non-linear soil type, c may vary as a function of both distance a_i and also the displacement response itself $u(t, a_i)$, and hence the displacement response at a certain point within the layer can be expressed as: $u = u_i(t - \frac{a_i}{c(t,a_i)})$. At the boundary position the propagating wave may partly reflect and partly refract(or pass through with a change in the angle of propagation with respect to the incident wave angle). The reflected wave may be considered to travel back within a cone with a modified angle due two reasons, first the change in the properties of the soil(material damping) and secondly due to the portion of the energy refracted(radiation damping). If we consider a non-linear hysteretic energy dissipation within the distance a_i and the time t, then the angle of opening of the cone model may be written as(see appendix.D for details):

$$\frac{\phi_i}{\phi} = \frac{u_i(t - \frac{a_i}{c(t,a_i)})}{u_i(t - \frac{a_i}{c(0,0)})} \tag{4.128}$$

However, if we consider the angle of the cone to remain constant then the only consideration is to account for the refracted energy. We consider the ratio of the refracted wave energy to the

incident wave energy as: η_i. Hence, the displacement response of the incident wave propagating along the upper cone will be:

$$u_{ui,1} = \frac{z_i}{h + z_i - z} u_{i,r}(t - \frac{h - z}{c(t, h - z)}) \tag{4.129}$$

in which z_i is the apex distance from the surface of the disk (i), z is the distance between the disk (i) and the underlying layer. It is seen in Eq. 4.129, the displacement amplitude varies as an inverse function of the corresponding distance measured from the apex of the cone.

It can be assumed that a part of incident wave reflects from the boundary and other portion of it could pass through the boundary (refract). In general, the reflected portion of wave energy may be assumed to be: $u_{i,r}(t, a) = (\eta - 1)u_i(t, a)$. In which η may be called refraction factor of wave which may be considered as:

$\eta = 0$ for rigid bed-rock boundary for which the whole portion of incident wave will reflect

$\eta = 1$ for two adjacent layers with the same material properties $G_{i-1} = G_i$ a special case of a uniform half-space of soil

$\eta = 2$ for a free-surface for which stress-free condition must be ensured, hence $u_{i,r} = u_{i,inc}$

for a surface subjected to stress such as the mud-line at sea-bed which is subjected to the combined hydrostatic pressure of still water column and hydrodynamic pressure induced by the action of waves the refraction factor η may be obtained by enforcing the stress condition as follows:

$$(2 - \eta_j)E(z)\left[\frac{-z_i}{(z_i + 2h)^2}\bar{u}(t - \frac{2h}{c}) - \frac{z_i}{z_i + 2h}\frac{1}{c}\frac{d\bar{u}}{dt}(t - \frac{2h}{c})\right] = q(z) \tag{4.130}$$

From which η_j can be easily derived as follows:

$$\eta_j = 2 - \frac{q}{E(z)(\frac{-z_i}{(z_i+2h)^2}\bar{u}(t - \frac{2h}{c}) - \frac{z_i}{z_i+2h}\frac{1}{c}\frac{d\bar{u}}{dt}(t - \frac{2h}{c}))} \tag{4.131}$$

It is evident from Eq.4.131 that for zero stress condition $\eta_j = 2$. However, for an arbitrary two soil layer boundary η_j may be assumed or obtained from the physics of wave refraction between two layers with given material properties as refraction coefficients(see Appendix.D).

The reflected wave's amplitude from the upper boundary can be computed as follows:

$$u_{ur,1} = (\eta_1 - 1)\frac{z_i}{h - z + z_i} u(t - \frac{h - z}{c(t, h - z)}) \tag{4.132}$$

This reflected wave travels down towards the lower boundary of the layer where its amplitude decreases as follows:

$$u_{li,1} = (\eta_1 - 1)\frac{z_i}{2h - z + z_i} u(t - \frac{2h - z}{c(t, 2h - z)}) \tag{4.133}$$

A part of this incident wave on the lower boundary will reflect back towards the upper boundary as:

$$u_{lr,1} = (\eta_1 - 1)(\eta_2 - 1)\frac{z_i}{2h - z}u(t - \frac{2h - z}{c(t, 2h - z)}) \tag{4.134}$$

At reaching the upper boundary the amplitude of this wave will be:

$$u_{ui,2} = (\eta_1 - 1)(\eta_2 - 1)\frac{z_i}{3h - z}u(t - \frac{3h - z}{c(t, 3h - z)}) \tag{4.135}$$

The subindices 1 and 2 denote the number of wave reflections and differentiate between the portions of each reflection depending in general on the traveled distance from the origin of propagation and the non-linear and non-homogenity of the layer boundaries in the soil space. The sequence of incident and reflected waves can continue towards infinity and as obtained from Eqs.4.132 to 4.135, the amplitude of the reflected waves decrease with the traveled distance and will diminish after a finite number of wave reflections. The series converge quite fast and hence only a few first terms may be sufficient.

Waves will also propagate at the same time along the downwards cone as shown in Fig. 4.10. The first incident wave from the downwards cone can be computed as follows:

$$u_{li,1} = \frac{z_i}{z + z_i}u(t - \frac{z}{c(t, z)}) \tag{4.136}$$

The reflected wave then will be:

$$u_{lr,1} = (\eta_1 - 1)\frac{z_i}{z + z_i}u(t - \frac{z}{c(t, z)}) \tag{4.137}$$

The reflected wave from the lower boundary after traveling a distance of h across the layer will strike on the upper boundary with an amplitude of:

$$u_{ui,1} = (\eta_1 - 1)\frac{z_i}{h + z + z_i}u(t - \frac{z}{c(t, h + z)}) \tag{4.138}$$

This wave then reflect back with an amplitude of :

$$u_{ur,1} = (\eta_1 - 1)(\eta_2 - 1)\frac{z_i}{h + z + z_i}u(t - \frac{z}{c(t, h + z)}) \tag{4.139}$$

Continuing the above transmission in a successive manner, the amplitude of response at any point of time may be obtained as follows:

$$u = \sum_{j=0}^{n} \frac{(\eta_j - 1)^j z_i}{z_i + z + 2jh}u_i(t - \frac{z + 2jh}{c(t_j, z + 2jh)}) + \sum_{j=1}^{n} \frac{(\eta_j - 1)^j z_i}{2jh - z + z_i}u_i(t - \frac{2jh - z}{c(t_j, 2jh + z)}) \tag{4.140}$$

where η_j, z_i, h denote the reflected portion of energy, the apex height of the original double cone (i) and the thickness of the layer (i). Eq.4.140 is formulated at the lower boundary of the layer (i).

The first summation term on the right hand side of Eq. 4.140 represents the contribution from all the upwaves and downwaves striking and reflecting, respectively from the boundary (e.g. lower

boundary) generated from the initial lower cone and the second summation term represents the contribution of all the upwaves and downwaves associated with the upper cone.

It may be argued that with assuming that the direction of the loading is downwards then if the upper cone is activated, it should indeed propagate tensile waves which are usually in the case of soil neglected. Hence, for a single concentrated uni-directional load, only the first or the second summation term will be sufficient. It is evident from Eq. 4.140 that at the location of the disk (i) where $z = 0$ the first summation term on R-H-S of Eq. 4.140 for $j = 0$ will yield $u_i(t)$ which is the assumed generating response function at the disk location. It is seen from the latter equation, the higher terms of both summations will be smaller and approach zero as the j increases towards infinity.

Eqn. 4.140 can be re-written in a compact form as:

$$u = \sum_{j=0}^{n} (\eta_j - 1)^j \zeta_{j,d} u_i(t - T_{j,d}) + \sum_{j=1}^{n} (\eta_j - 1)^j \zeta_{j,u} u_i(t - T_{j,u}) \tag{4.141}$$

in which the first sum indicates the contribution from the upper and the lower cones, respectively. The second sum denotes the contribution of all one sided cones with a geometry parameter $\zeta_{j,u} = \frac{z_i}{2jh - z + z_i}$, $\zeta_{j,d} = \frac{z_i}{z_i + z + 2jh}$ and an echo time as $T_{j,d} = \frac{z + j2h}{c(t, z + 2jh)}$ and $T_{j,u} = \frac{2jh - z}{c(t, 2jh + z)}$. The above function inside the sum may be referred to as cone's echo function. The other dynamic properties related to the echo function will be utilized in a following section.

4.4.4 Dynamic properties of a layered cone

By having a general sub-surface layered cone model relationship established in the previous section, it is possible to obtain the corresponding dynamic stiffness properties by means of a Fourier transformation as follows:

$$\int_0^\infty e^{-i\omega t} f(t - a) dt = e^{-ia\omega} f(\omega) \tag{4.142}$$

where $f(t - a)$ may be replaced with the R-H-S of Eq. 4.141 which will yield:

$$u(\omega) = \int_0^\infty e^{-i\omega t} u dt = \sum_{j}^{n} (\eta_j - 1)^j (\zeta_{j,d} e^{-iT_{j,d}\omega} + \zeta_{j,u} e^{-iT_{j,u}\omega}) u_i(\omega) \tag{4.143}$$

The force-displacement relationship in the frequency domain may be written as:

$$u_i(\omega) = \frac{P(\omega)}{K(k + i\omega c)} \tag{4.144}$$

Substituting for $u_i(\omega)$ from Eq. 4.143 into Eq. 4.144 yields:

$$u(\omega) = \sum_{j}^{n} (\eta_j - 1)^j (\zeta_{j,d} e^{-iT_{j,d}\omega} + \zeta_{j,u} e^{-iT_{j,u}\omega}) \frac{P(\omega)}{K(k + i\omega c)} \tag{4.145}$$

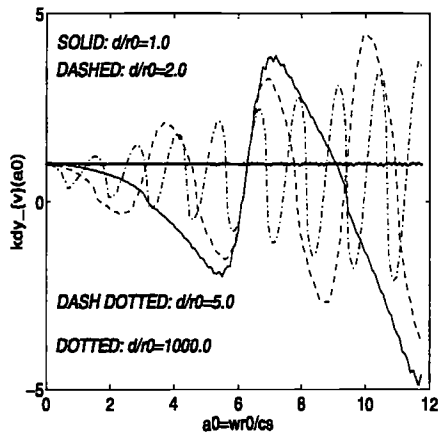

Figure 4.35: Dynamic axial stiffness of a single disk embedded in a soil layer vs. non-dimensionalized frequency of excitation for different layer thickness ratios $d/r0$

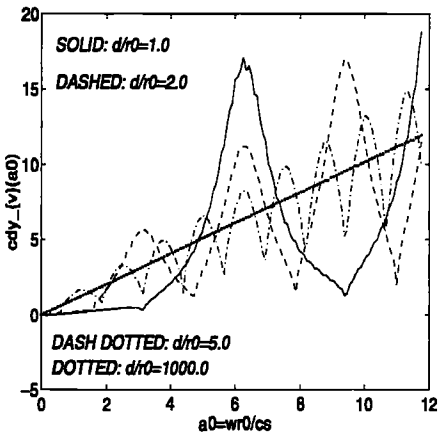

Figure 4.36: Dynamic axial dashpot parameter of a single disk embedded in a soil layer vs. non-dimensionalized frequency of excitation for different layer thickness ratios $d/r0$

By knowing that the dynamic stiffness in frequency domain $S(\omega)$ can be written as:

$$S(\omega) = \frac{P(\omega)}{u(\omega)} \tag{4.146}$$

then by combining the latter with Eq. 4.145, we would have:

$$S(\omega) = \frac{K(k + i\omega c)}{\sum_{j=0}^{n}(\eta_j - 1)^j \zeta_{j,d} e^{-iT_{j,d}\omega} + \sum_{j=1}^{n}(\eta_j - 1)^j \zeta_{j,u} e^{-iT_{j,u}\omega}} \tag{4.147}$$

By decomposing Eq. 4.147 to real and imaginary parts, the corresponding spring and dashpot coefficients of the sub-surface layered (non-linear) cone can be obtained for example numerically for a finite but sufficiently large value of j.

Figs.4.35 and 4.36 show the variation of the dynamic spring and dashpot parameters with the non-dimensionalized frequency of excitation $a_0 = \omega r_0/c_s$ for a single disk embedded in a layer of soil with varying thickness $d/r0$ from unity to a very large value of 1000 which represents physically a semi-infinite layer. It is observed that for certain frequencies the dynamic stiffness and damping parameters approach zero which represent the resonance of the system. It is observed that for the layer with a thickness ratio as unity almost perfect resonance occur at a_0 corresponding to the eigenfrequencies of the layer as $\omega_i = \pi/T_{echo}$ which can be explained as follows:

$$\begin{aligned} t = \frac{\frac{\lambda}{2}}{c} &= \frac{2d}{c} = T_{echo} \\ &= \frac{T_n}{2} = T_{echo} \end{aligned} \tag{4.148}$$

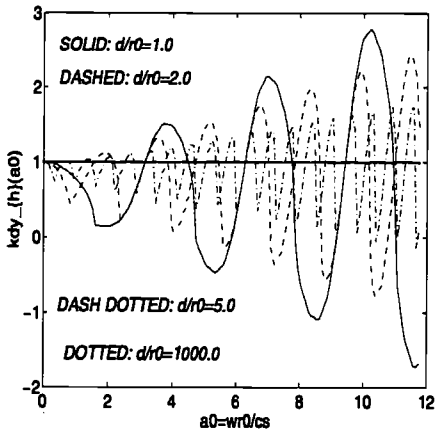

Figure 4.37: Dynamic lateral stiffness of a single disk embedded in a soil layer vs. non-dimensionalized frequency of excitation for different layer thickness ratios $d/r0$

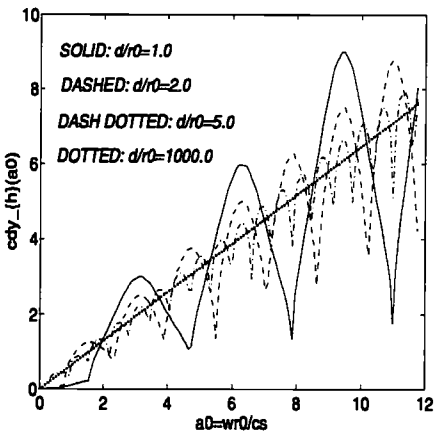

Figure 4.38: Dynamic lateral dashpot parameter of a single disk embedded in a soil layer vs. non-dimensionalized frequency of excitation for different layer thickness ratios $d/r0$

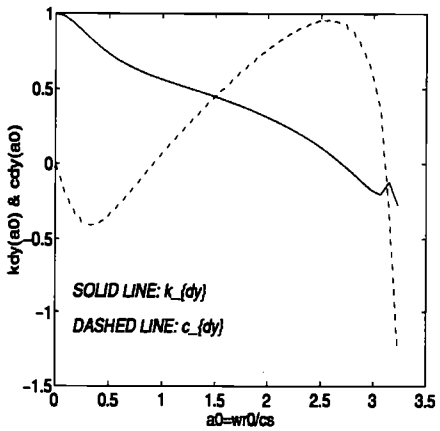

Figure 4.39: Dynamic stiffness properties of a non-linear (NC clay) layer with $\beta = 1.1$ and depth ratio $d/r0 = 1$ under vertical motion of an embedded disk vs. non-dimensionalized frequency of excitation $a_0 = \omega r_0/c_s$ with an upper free-surface and a lower bed-rock boundaries

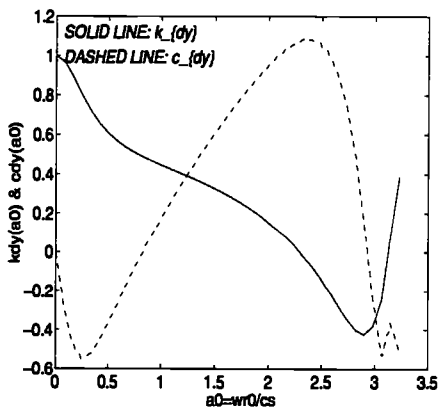

Figure 4.40: Dynamic stiffness properties of a non-linear (NC clay) layer with $\beta = 1.5$ and depth ratio $d/r0 = 1$ under vertical motion of an embedded disk vs. non-dimensionalized frequency of excitation $a_0 = \omega r_0/c_s$ with an upper free-surface and a lower bed-rock boundaries

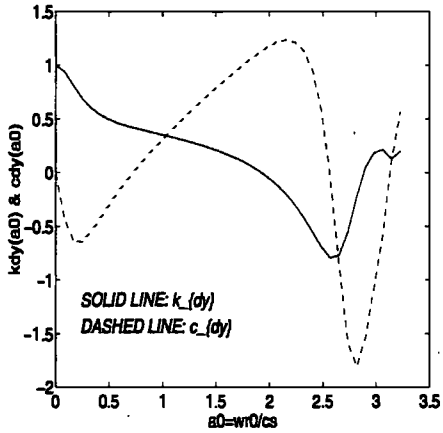

Figure 4.41: Dynamic stiffness properties of a non-linear (NC clay) layer with $\beta = 2.0$ and depth ratio $d/r0 = 1$ under vertical motion of an embedded disk vs. non-dimensionalized frequency of excitation $a_0 = \omega r_0/c_s$ with an upper free-surface and a lower bed-rock boundaries

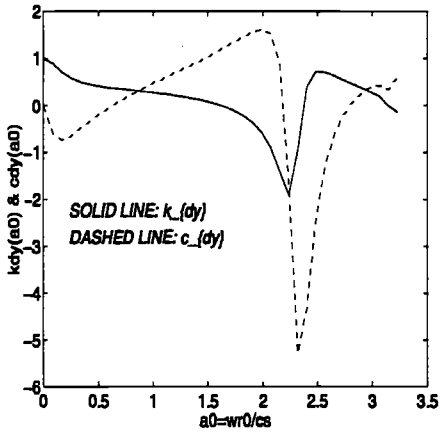

Figure 4.42: Dynamic stiffness properties of a non-linear (NC clay) layer with $\beta = 2.5$ and depth ratio $d/r0 = 1$ under vertical motion of an embedded disk vs. non-dimensionalized frequency of excitation $a_0 = \omega r_0/c_s$ with an upper free-surface and a lower bed-rock boundaries

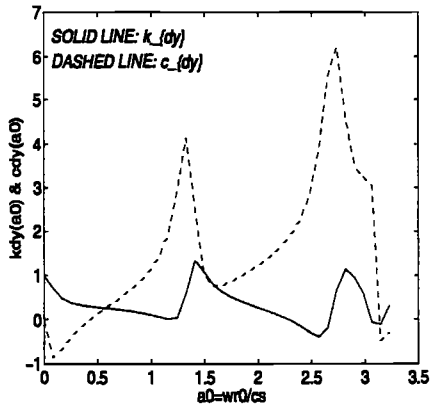

Figure 4.43: Dynamic stiffness properties of a non-linear (NC clay) layer with $\beta = 2.5$, $\alpha = 0.99$ and depth ratio $d/r0 = 1$ under vertical motion of an embedded disk vs. non-dimensionalized frequency of excitation $a_0 = \omega r_0/c_s$ with an upper free-surface and a lower bed-rock boundaries

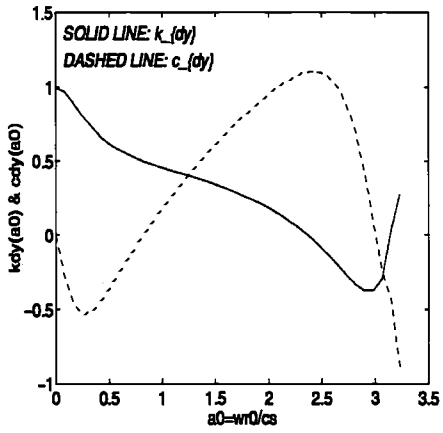

Figure 4.44: Dynamic stiffness properties of a non-linear (NC clay) layer $\beta = 1.0$, $\alpha = 0.75$ and a depth ratio $d/r0 = 1$ under vertical motion of an embedded disk vs. non-dimensionalized frequency of excitation $a_0 = \omega r_0/c_s$ with an upper free-surface and lower rigid bed-rock boundaries

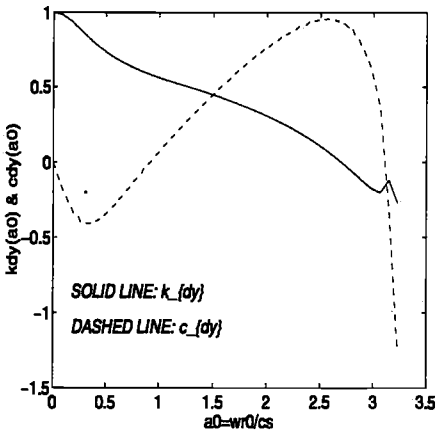

Figure 4.45: Dynamic stiffness properties of a non-linear (NC clay) layer with a depth ratio $d/r0 = 1$ under vertical motion of an embedded disk vs. non-dimensionalized frequency of excitation $a_0 = \omega r_0/c_s$ with an upper free-surface and a lower bed-rock boundaries

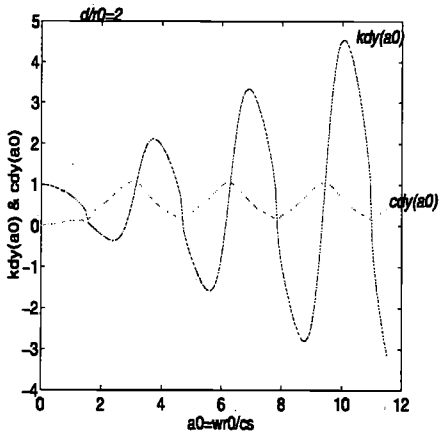

Figure 4.46: Comparison of dynamic stiffness properties of a non-linear (NC clay) layer with depth ratios $d/r0 = 2$ under vertical and horizontal motions of an embedded disk vs. non-dimensionalized frequency of excitation $a_0 = \omega r_0/c_s$ with upper and lower rigid bed-rock boundaries

By substituting $T_n = 1/f_n$ in Eq.4.148, and $f_n = \omega_n/2\pi$, the following can be obtained:

$$\omega_n = \frac{\pi}{T_{echo}} = \frac{\pi c}{2d} \tag{4.149}$$

in which ω_n represents the eigenfrequency of the soil layer with a thickness of d and the wave propagation velocity of c. As observed in Fig. 4.36, for the vertical motion of the disk in the layer with a thickness ratio of $d/r_0 = 1$, the corresponding resonance frequencies occur at $a_0 = \pi, 3\pi, 5\pi, ..., 2m + 1\pi$ which is investigated as follows: For the vertical motion of disk:

$$T_{echo} = \frac{2d}{c} = \frac{2r_0}{2c_s} = \frac{r_0}{c_s} \tag{4.150}$$

Substituting the latter into Eq.4.149, we will have:

$$\omega_n = \frac{\pi c_s}{r_0} \tag{4.151}$$

The corresponding a_0 emerges as:

$$a_0 = n\pi \qquad ; n = 2m + 1 \qquad ; m = 0, 1, 2, .., n \tag{4.152}$$

It is also seen that as the depth ratio of the layer increases towards infinity k_{dy} and c_{dy} approach to asymptotic values with average of about unity. This can also be easily verified by considering that in a semi-infinite layer the echo time according to Eq.4.148 becomes nearly infinity and

hence the corresponding eigen-frequency of the semi-infinite layer approaches zero which means no oscillations as observed in Figs.4.39 to 4.44. The amplitude becomes unity by vanishing the echo functions in the denominator of Eq.4.147.

It is observed that the dynamic spring changes sign with increasing the frequency of excitation, this phenomenon is associated with the reflection functions in the denominator of Eq.4.147. Physically speaking, this means a phase angle from zero to 2π for the spring parameter which are caused by the procession of the reflections up and down the layer which arrive at 180 deg phase with the applied load at the disk position at the same time of t for particular frequencies as simulated in Figs.4.39 through 4.44.

As for the dashpot coefficient c_{dy} no such phase angle or sign change is observed. The radiation damping is either positive or zero. The increase in the amplitude of k_{dy} for lower layer thickness is associated strongly with the echo phenomenon in the layer as described above. As observed, by increasing the layer thickness to infinity no wave can travel back within the allowed time and hence no fluctuation occurs. However, for a semi-infinite (half-space) of soil there will be oscillations which are actually associated with activated slices between the disks in a pile-soil system. This kind of layering which is not a soil structure's property rather related to the finite-element discretization of the pile-soil system allows to have finite slices (layers) of soil in between the disks and hence the overall dynamic stiffness at the pile head may vary with the frequency though not very significantly. This aspect is illustrated in a subsequent section.

Fig. 4.45 illustrates the variation of the dynamic stiffness of a disk embedded in a layer of soil with a thickness ratio of $d/r_0 = 1$ and normally consolidated clayey soil condition with a poisson ratio of $\nu = 1/3$. As shown, the normalized spring coefficient k_{dy} which is represented by a solid line decreases non-linearly from unity at $a_0 = 0$ for the static case and reaches a cut-off point at the normalized frequency of about $a_0 = 2.7$ which corresponds to $6\pi/7$. The spring stiffness has an opposite phase with the displacement response after this point as shown in the plot.

The dashpot coefficient c_{dy} plotted with a dashed line in Fig. 4.45 decreases non-linearly from zero at zero frequency towards a negative peak of about 0.4 at about $a_0 = 0.4 \approx \pi/8$ and then increases towards a positive peak of about 1.0 at a frequency of about $a_0 = 2.5 \approx 4\pi/5$. Thereafter, the dashpot coefficient falls very rapidly towards a second cut-off and negative damping values. Hence, the observed cut-off frequencies of dashpot in this cases are about $\pi/4$ and π.

Fig. 4.46 is another example to show how the layer cut-off occurs for the spring and dashpot properties at certain frequencies corresponding to a layer with a thickness ratio of $d/r_0 = 2$ and elastic behaviour with double rigid boundaries. It is observed that the spring cut-offs in this case occur at nearly peaks and valleys corresponding to c_{dy} and hence with half the frequency intervals as those of damping of the layer. Apparently the damping cut-offs correspond in this case to the normalized frequencies of $a_0 = \pi, 2\pi, 3\pi$ (i.e. both odd and even multiples of the layer's fundamental natural period). It is interesting to see that the cut-off for doubly rigid boundaries occurs more often than that of the layer with a free upper boundary and a lower rigid bed-rock.

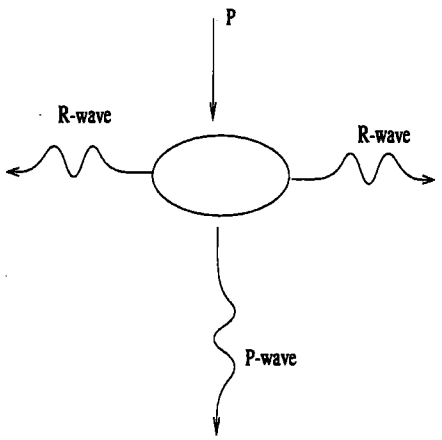

Figure 4.47: Propagation of waves from a vertically loaded disk in horizontal and vertical planes

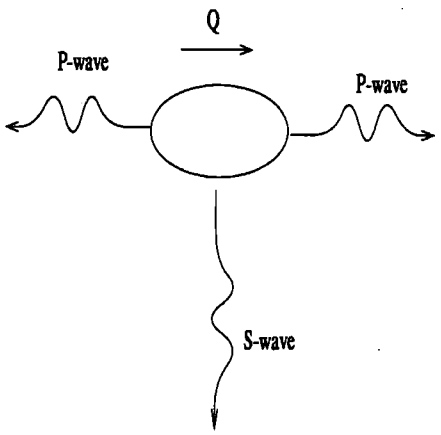

Figure 4.48: Propagation of waves from a horizontally loaded disk in horizontal and vertical planes

This phenomenon may be explained as follows, in the case of double rigid-bed rock the waves generated at the embedded disk which propagate upwards and downwards the whole energy is reflected and of course with an elastic assumption of the soil there is no plastification or yield in the soil to absorb any part of the input energy, thus the occurrence of the peaks and valleys are absolutely distinct and quite frequent which can be easily predicted from the echo return period as described above. However, in the case of a free upper boundary and lower rigid rock boundary with an elasto-plastic soil the energy of the generated wave partly can be absorbed in the soil as material(near field) damping and the remaining energy reaches the edges of the layer and the part of upward travelling waves do not hundred percent as the case for rigid boundary reflect and result in deformation of the surface this also alters the outcome of the frequency of cut-off as illustrated. Hence, It is naturally expected to observe larger intervals for the cut-off in the latter case. This conclusion is verified here for a layer with much larger thickness ratio for which the period of return of the downward propagating waves are so long that there is no visible fluctuation in the dashpot and spring curves.

4.5 Discussion about the validity range of dynamic cone and static disk models

Each loaded disk transmits the waves into the soil's infinity via cones. The waves are spread as compressive-dilatational (P), shear(S) and Rayleigh (R) waves into the soil. It is well known from physics of wave propagation that the P-waves take a more significant portion of the transmitted energy under a vertical motion of disk-cone while shear waves have a more significant contribution to energy dissipation under a horizontal loading. Fig.4.50 schematically illustrates

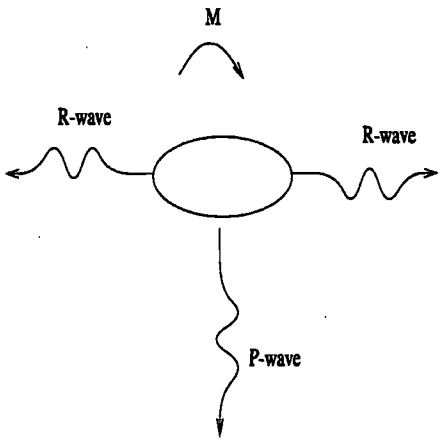

Figure 4.49: Propagation of waves from a disk under rocking motion in horizontal and vertical planes

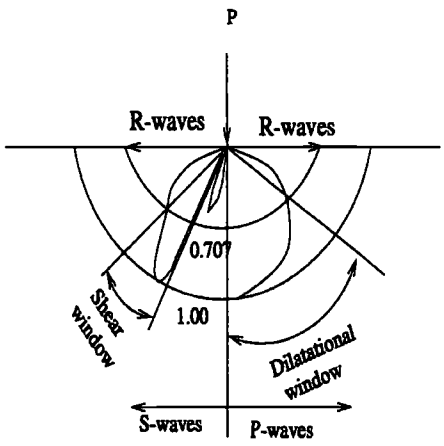

Figure 4.50: Partition of energy related to P, S and R waves in a semi-infinite medium of soil

the energy partition of the P,S and R waves.

Although the cone model is capable to predict the dynamic response of the soil half space (incl. layered medium of soil) very well with respect to its underlying assumptions and its performance for higher frequency range. However, its validity limits with respect to the Rayleigh wave transmission and the frequency range of application have to be discussed.

In this section, we will examine the different underlying assumptions for disk-cone model and discuss why they work and for what range of frequencies? For this aim, we may consider the horizontal propagation of the waves known as Rayleigh. Fig. 4.25 illustrates schematically a radial propagation of waves around a loaded disk located in the soil. The radius of this semi-sphere is about half times that of Rayleigh wave length λ_R which is assumed to be proportional inversely to the frequency of vibration ω and its depth is equal to one Rayleigh wave length λ_R(Wolf et al, 1994). It is evident that as the frequency of the vibration approaches zero both the radius and also depth of the semi-sphere approaches infinity. Hence, for this static limit, an idealization of radial disk with a much larger radius than that of pile is justifiable.

On the contrary, as the frequency increases towards infinity the depth of the Rayleigh cylinder approaches zero and the boundary of the far-field and near-field of the soil is shifted towards the pile's shaft at the upper limit. This signifies that first of all application of static radial disk for such high frequency range is invalid, secondly the Rayleigh (horizontal)wave propagation becomes almost zero for such high frequencies of vibration and third implication is that for this high frequency limit no radial spreading of the waves occurs and hence the uni-directional assumption related to the cone model is exact at this limit.

The above discussion would imply that for low frequency vibrations such as those induced by the extreme sea waves the static disk model which is based on the assumption of shear stress-strain distribution in horizontal planes as described in Secs.2.2.3 and 2.3.3 might be more relevant than cone model, whereas for the high frequency vibrations such as those induced by seismic ground motion or machine vibrations, the cone model will be applicable.

To quantify the rate of energy transmission, a power function $N(a_0)$ may be defined as follows:

$$N(a_0) = \frac{1}{T}\int_0^T dN(\omega)\frac{du(\omega)}{dt}dt \tag{4.153}$$

in which T refers to one period of wave as:$T = \frac{2\pi}{\omega}$ and $N(\omega)$ and $u(\omega)$ denote the force and the displacement response, respectively.
Fig. 4.51 shows the normalized power rate $N_v(a_0)$ of a disk under vertical loading versus the normalized frequency of excitation $a_0 = \omega r_0/c_s$ for the range $a_0 = 0-10$. The soil is assumed to be homogeneous with a shear modulus of $G = 35MPa$ and ν ranging from 0.01 0.499 corresponding to perfectly compressible and incompressible soils, respectively. It can be seen that distinguished peak occurs for the upper limit of ν. In Fig. 4.51 the peak point of power (or resonance in a sense) occurs at about $a_0 = 1.16$ whereas the dashed and solid curves corresponding to $\nu = 1/3$ and 0.01, respectively, have no peaks within the plotted range and approach unity near $a_0 = 10$. The resonance of power for the case $\nu = 0.499$ is due to the added mass of the soil underneath

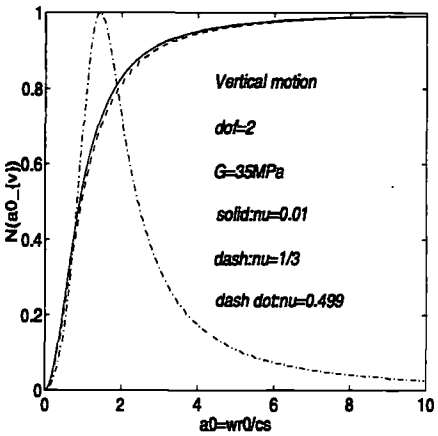

Figure 4.51: Variation of power rate of a disk $N_v(a_0)$ with a_0 under vertical motion for $\nu = 0.01, 1/3$ and 0.499

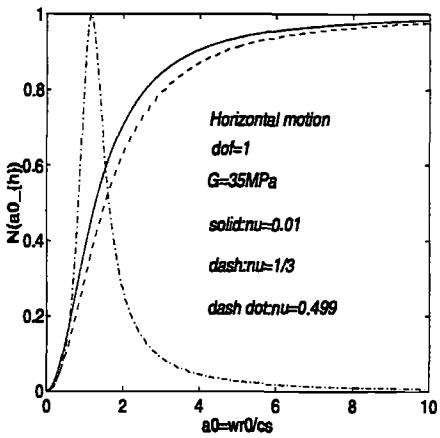

Figure 4.52: Variation of power rate of a disk $N(a_0)$ with a_0 under horizontal motion for $\nu = 0.01, 1/3$ and 0.499

the disk.

Fig. 4.52 shows the results of normalized power $N(a_0)$ under horizontal motion vs. a_0 for a disk in the latter soil type for $\nu = 0.01, 1/3$ and 0.499, respectively. The same trend is also observed here, there is a distinguished peak for the higher limit of $\nu = 0.499$. While for the compressible soil cases $\nu = 0.01, 1/3$ there are no such distinguished peak at least within the plotted range of a_0.

It is observed that the magnitude of power rate is dependent on ν. But the maximum observed value of power is unity and independent of poisson ratio of soil. The peak value of power rate as vertical case occurs at about $a_0 = 1.16$. The power rate $N(a_0)$ as seen in Figs.4.51 and 4.52 approaches exponentially towards zeros at higher frequencies (i.e.$a_0 \to 10$). This means that in a perfectly incompressible soil no energy is transmitted at very high frequencies. This is of course, physically correct, since at very high frequencies of vibration of disk, the Rayleigh wave transmission becomes zero and the only way wave can propagate is downwards vertically. Since in an incompressible soil $\nu = 0.499$, the dilatational waves are not possible, hence the power becomes zero at higher a_0.

On the other hand for the rocking motion of disk as shown in Fig. 4.53, the peak normalized power for the $\nu = 0.499$ (dash dotted line) occurs at about $a_0 = 4$ which much higher than translational cases but with the same magnitude as unity. The post-peak magnitude of power decreases almost linearly with a_0. For two other compressible soil cases with $\nu = 0.01, 1/3$, there is no peak within the range of a_0 plotted and the difference is very small in terms of magnitude of $N(a_0)$ (almost independent of ν).

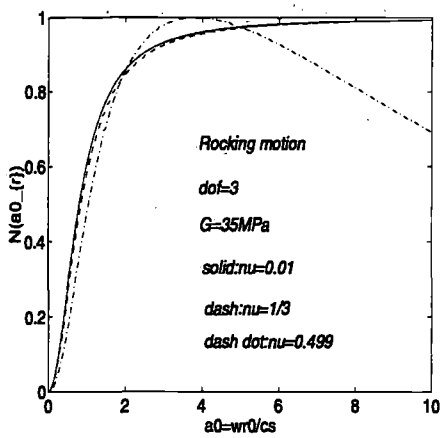

Figure 4.53: Variation of power rate of a disk $N(a_0)$ with a_0 under rocking motion for $\nu = 0.01, 1/3$ and 0.499

4.6 Discussion about dimensional performance of the cone model

As described above, the cones are three dimensional whose geometry are defined by their apex angle and the disk radius at least for linear and homogeneous soil. It can be shown that the three dimensional cone model($n = 2$) compared to the two dimensional wedge model ($n = 1$) is more accurate in dealing with an axially symmetric foundation such as pile-soil system.

It can be shown that the damping coefficient of the wedge model approaches infinity at the zero frequency limit while the high frequency limit of c_{dy} approaches $\rho c A_0$ which is derived from Eq.4.63.

For the three dimensional cone, however, the lower frequency limit (static) starts from $(n - 1)\rho c^2 A_0/z_0$ as derived from Eq.4.69 and the high frequency limit of it approaches $n\rho c^2 A_0/2z_0$. Hence, the high frequency limit of the dashpot coefficient is the same for both three dimensional cone and a two dimensional wedge.

Analogous to Eqs.4.89 and 4.90, the radiation damping can also be represented separately in the dynamic stiffness $S(a_0)$ based on the correspondence principle as:

$$S(a_0) = K_{st} k_{dy}(1 + 2i\eta_m + 2i\eta_r) \tag{4.154}$$

in which parameters η_m and η_r are the material and radiation damping coefficients, respectively. Comparing the latter with a general form of the dynamic stiffness as follows:

$$S(a_0) = K_{st}(k_{dy}(a_0) + i a_0 c_{dy}(a_0)) \tag{4.155}$$

and neglecting the material damping will result in radiation damping expression as:

$$\eta_r = \frac{a_0 c_{dy}(a_0)}{2k_{dy}(a_0)} \tag{4.156}$$

Hence, the damping ratio η_r can be defined as half the ratio between the imaginary and real parts of the dynamic stiffness $S(a_0)$, approaches infinity for the two dimensional wedge model compared to a far smaller value for the three dimensional cone model. This difference in radiation damping property of the two and three dimensional models are often misinterpreted based on their inherent geometrical properties.

It is often assumed by nature that a three dimensional soil model can radiate energy at higher rate than its two dimensional counterpart. This basic assumption is considered to be due to the cross sectional area of the cone at each given depth. However, a closer examination reveals that in fact the opposite is true, that's the two dimensional cone model radiates energy more than the corresponding three dimensional soil model. The reason is that for a given frequency of excitation the radiation damping which is defined in Eq.4.156 is inversely proportional with the dynamic spring coefficient k_{dy}. It is observed that k_{dy} is smaller for the two dimensional cone than that of a three dimensional one (see Fig. 4.26). This implies that with assuming the same c_{dy}, the ratio of radiation will be greater for the two dimensional wedge model than the three dimensional cone system.

Comparing the rigorous elastodynamic boundary element of soil solutions with the two dimensional cone model results, it is shown in a subsequent section that the discrepancies in terms of k_{dy} and c_{dy} are quite small and for practical purposes can be neglected.

For cone models with material damping the radiation damping ratio can approach zero and infinity for particular cases of spring and dashpot cut-off, respectively. For instance, it was observed above that for a particular frequency limit k_{dy} may approach zero while the corresponding c_{dy} may be a positive value. This means that the radiation damping ratio η_{rad} may approach infinity as follows:

$$\eta_r^* = \frac{c_{dy}(a_0)a_0^*}{2k_{dy}(a_0^*)} \to \infty \tag{4.157}$$

in which the particular frequency a_0^* is illustrated in Figs.4.26 and 4.27. While for the corresponding three dimensional model with only radiation damping allowed, the damping ratio is far less than infinity.

The radiation damping ratio for lower and higher frequency limits can be obtained from Figs.4.26 and 4.27 according to Eq.4.156 as follows:

$$\eta_{2d}(a_0 = 0) \to \infty \tag{4.158}$$

$$\eta_{3d}(a_0 = 0) = 0 \tag{4.159}$$

$$\eta_{2d}(a_0 \to \infty) = \frac{a_0 z_0}{c} \tag{4.160}$$

$$\eta_{3d}(a_0 \to \infty) = \frac{a_0 z_0}{2c} \tag{4.161}$$

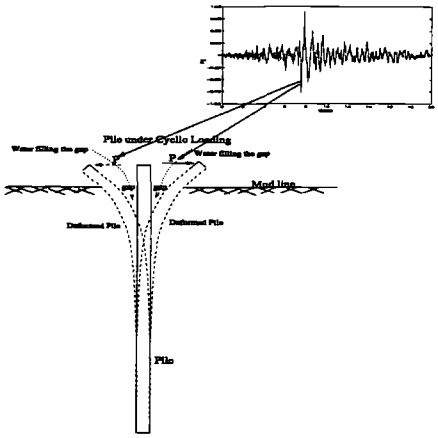

Figure 4.54: A schematic illustration of a cyclic degradation "slotting" phenomenon caused by the gap at the pile-soil interface

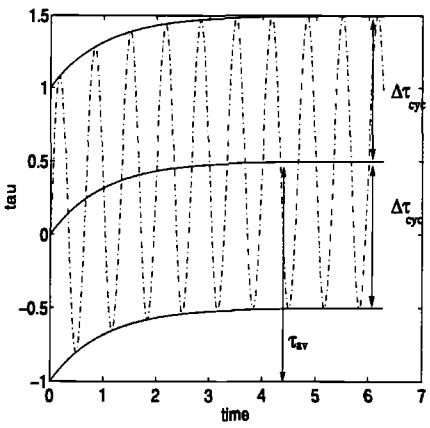

Figure 4.55: A two way cyclic shear stress at the pile-soil interface

Eq.4.158 shows that the radiation damping for static case in a two dimensional wedge type model is infinity whereas the true damping ratio is zero for static case as obtained by the three dimensional cone model in Eq.4.159. While it is shown in Eqs.4.160 and 4.161 that the radiation damping for the two dimensional model is twice as that for the three dimensional cone for the higher frequency limit.

The cut-off limit in the dynamic stiffness of the cone is observed to occur at very high frequencies. Since the frequency range of the extreme sea and seismic waves are usually less than these high frequency limits, thus the overestimation of radiation damping would be less significant.

4.7 Discussion about the loading rate effects

Previous studies by Bea et al, (1980, 1982), Bradshaw et al, (1984), Polous, (1982), Randolf, (1990), Rigden and Semple, (1983) show that the dynamic loading rate effect may increase significantly the ultimate capacity of the axial or laterally loaded piles. In particular, Bea et al, (1980, 1982) observed that in large scale pile tests, the dynamic ultimate shaft skin friction has a linear lognormal relationship with the rate of the loading. Bea and Audibert, (1979) obtained that for low cycle extreme waves the rate effect factor $\beta_u = \frac{\tau_{dy,peak}}{\tau_{st,peak}}$ might be in the order of 1.0-1.5 while for high frequency loading such as those induced by earthquakes the increase in the ultimate capacity of the pile might be in order of 0.8-1.0 times the static capacity(i.e. $\beta_u = 1.8-2.0$).

For e.g. Polous, (1982) presented a lognormal relationship between the dynamic shaft skin

friction and that of static loading as:

$$\tau_{dyn,peak} = \tau_{st,peak}(1 + F_\rho log\frac{\lambda}{\lambda_s}) \tag{4.162}$$

in which $\tau_{dyn,peak}$, $\tau_{st,peak}$ represent the dynamic and static peak shaft skin friction capacities, respectively. λ and λ_s denote the loading induced displacement rate and a reference displacement rate(see Poulos, 1982). Poulos suggested $0.1 < F_\rho < 0.25$.

Randolf et al, (1990) has also suggested that the resistance of the pile during a dynamic loading process for e.g. driving may be affected by the inertia and damping reaction forces. Randolf, (1990) has presented the following relationship for the dynamic skin friction stress adjacent to the pile:

$$\tau_{dy,peak} = \tau_{st,peak}[1 + \alpha(\frac{\Delta v}{v_0})^\beta] \tag{4.163}$$

where Δv is the relative velocity at the pile-soil interface and v_0 is a reference velocity of 1m/sec. The α and β parameters in Eq.4.163 are suggested as 1.0 and 0.2, respectively(Randolf, 1992). For e.g. considering an average relative velocity of pile-soil as 0.1m/sec at the ultimate collapse of the jacket-pile-soil system, which is induced by the pile-soil failure in tension, we may obtain $\tau_{dy,peak} = 1.63\tau_{st,peak}$. This increase of about 60% in the shaft skin friction seems to be unconservative w.r.t to the slow motion(strain rate) of the pile under an extreme wave loading. This might be due to the fact that the parameters defined on the R-H-S of Eq.4.163 have no direct dependency on the loading rate or strain rate etc. A better estimate might be obtained from Eq.4.163 for low and intermediate type loading rates, if the parameters α and β are determined as function of the loading rate or even frequency of vibration of the pile-soil system.

The increase in the dynamic shaft friction capacity of the pile might be due to the activation of the inertia and damping forces in the soil surrounding the pile(Randolf, 1990), the breaking the bonds between the soil and pile material(Bea et al, 1982) and also re-structuring the soil itself due to high frequency vibrations, rapid changes in the excess pore water pressure in the soil volume (Nordal, 1998).

4.8 Discussion about the counteracting effects of cyclic and dynamic loading

In the previous section, the positive effect of the dynamic loading effect on the increase of the pile's mainly shaft skin friction capacity is briefly discussed. Such positive effects may be counteracted by the cyclic loading effects such as 'slotting' or 'post-holding'. This phenomenon is schematically illustrated in Fig.4.54.

During the cyclic loading of the offshore pile, a gap may develop between the pile and the surrounding soil which is often larger near the surface and decreases with the depth. This gap may be filled by water during cyclic loading in the opposite side as shown in Fig.4.54 which would result in the loss of the effective interface area between the pile and the soil and hence

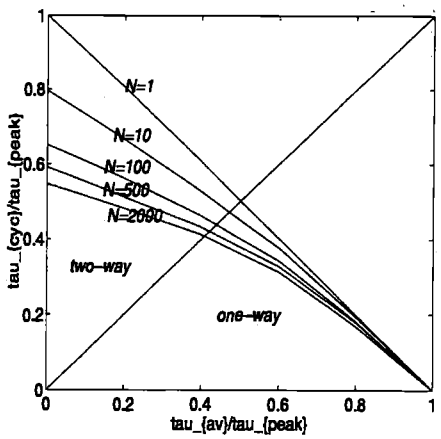

Figure 4.56: The cyclic to static peak shear stress at pile-soil interface as a function of number of shear stress cycles(After Svanø et al, 1992)

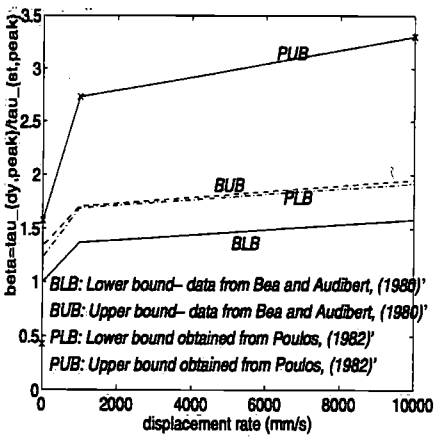

Figure 4.57: The dynamic rate effects on the ultimate dynamic shear stress at collapse of the pile-soil system(Data from Bea and Audibert, (1980) and Poulos, (1982)

reduce the static capacity of the pile either in axial or lateral loading. It may be noteworthy that the gap is mainly the result of the lateral cyclic loading of the pile which is often combined with the axial loading in the case of jacket pile foundations.

The cyclic degradation effects on the pile's axial and lateral capacities have been the subject of several investigations such as works by Bea et al, (1980), Janbu et al, (1976 and 1985), Nadim and Dahlberg, (1996), Rigden and Semple, (1983), Svanø et al, (1993) etc. These investigations showed that the pile's shaft skin friction capacity may be reduced considerably due to the cyclic loading induced by the extreme waves etc. Recent investigations by Nadim and Dahlberg, (1996) , Langø, (1991), Svanø et al, (1993) indicated that the cyclic loading effect also depends on the average shear stress in the soil τ_{av}, the ratio of the cyclic increment to the average shear stress $\Delta\tau_{cyc}/\tau_{av}$ and the ratio of the cyclic shear stress to the peak shear stress at collapse of the pile-soil system($\Delta\tau_{cyc}/\tau_{peak}$), as illustrated in Fig.4.55. As shown, the average shear stress may indicate that the cyclic loading is one-way or two-way (i.e. one-way cycling of soil if always $|\Delta\tau_{cyc}|/\Delta\tau_{cyc} > 0$, and two-way cycling of soil if exists $|\Delta\tau_{cyc}|/\Delta\tau_{cyc} < 0$).

For e.g., for a two-way cyclic loading with assuming an average shear stress as zero, the ultimate cyclic shear stress for 10 cycles of extreme wave loading might be about 0.8 times that of the static loading. While for a cyclic one-way loading with an average shear stress to peak shear stress ratio of about 0.5, the cyclic shear stress at collapse might be less than 0.4 times that of static loading(see Fig.4.56).

Theses negative effects may be counter balanced with the positive effects of the inertia and damping. Hence, the effective cyclic (dynamic) peak shear stress associated with the pile-soil

failure might be obtained as:

$$\tau_{cyc,dy,peak} = \frac{\tau_{dy,peak}}{\tau_{st,peak}} . \frac{\tau_{cyc,peak}}{\tau_{st,peak}} \tag{4.164}$$

$\tau_{cyc,dy,peak}$ then would be written in general as:

$$\tau_{cyc,dy,peak} = f(\Delta\epsilon/\epsilon, \Delta u/u, N, \omega, \Delta\tau_{cyc}/\tau_{av}, , \Delta\tau_{cyc}/\tau_{av}, \tau_{st}, ...) \tag{4.165}$$

in which $\Delta\epsilon$, ϵ, Δu, u, ω and N represent the increment of the shear strain, shear strain, the increment of excess pore water pressure and excess pore water pressure in the soil, the frequency of the vibration of the soil and the number of shear stress cycles. Other parameters are as pre-defined.

There is still great deal of debate and skepticism in the offshore industry about inclusion of any bias greater than one(observed greater than computed capacity) in the current practice codes. This may be due to the lack of extensive test database related to cyclic, dynamic large diameter pile tests, the relative high safety of the designed pile foundations of the jackets in the past two to three decades based on a static ultimate capacity approach, the other recent problems such as subsidence at the sea-bed facing some of the existing jacket platforms in the North-sea and other areas.

In the following case studies, it is assumed that the dynamic loading rate effects are counteracted by the negative cyclic soil degradation effects and hence the ultimate capacity of the pile-soil system are assumed as the same as static one. However, the dynamic stiffness is assumed as a function of the frequency of the vibration of the pile-soil system and the embedment ratio of the pile(e/r_0) as described in the previous subsections. The cyclic stiffness degradation is formulated (see appendix.D), but it is not implemented in the response calculations.

Hence, in overall, we believe that our response calculation approach might be rather conservative with regard to the above discussion. This decision was taken due to the lack of precise data on the cyclic degradation of the pile cases studied in Chapter.4. However, it is recommended that in the cases that there is sufficient evidence supporting the cyclic degradation or rate effects, the ultimate capacity of the pile-soil may be modified accordingly.

4.9 Analysis methods of pile-soil system

4.9.1 General

In general two different methods for dynamic analysis of pile-soil system exist as any other mechanical system, namely, frequency and time domain analysis methods. In the frequency domain analysis, the time history of the input excitation is decomposed by means of spectral analysis into its contents harmonic(see for e.g Clough and Penzien, 1968). The dynamic response of the pile-soil system subjected to each single harmonic force component can be computed after establishing a matrix stiffness relationship of system. By applying all the force components associated with the frequency contents of the input excitation force.

The response of the pile-soil system under the given dynamic load then can be obtained by superimposing all the individual responses of the system. The applied principle of superposition in frequency domain analysis might only be valid for linear elastic soil. By assuming a linear elastic behaviour of soil, it is also possible to apply the coupling between various pile disks as illustrated in Fig.4.7. Since a linear soil behaviour is assumed in the frequency domain analysis throughout the following section, therefore linear hysteretic or Voigt type visco-elastic material damping are considered as relevant.

Although traditionally linear assumptions are applied for frequency domain analysis due to the resulting efficiency in computation of response, nonetheless, the non-linear analysis of pile-soil system can also be performed in the frequency domain(see for e.g Angelides and Rosset, 1980) but this approach is computationally very time consuming.

The time domain analysis of pile-soil systems will be performed with assuming a non-linear soil behaviour. The procedure involves establishing a stiffness formulation of the pile-soil system based on the dynamic equation of motion and considering the non-linearities of soil hence using a tangent stiffness approach.

A recursive approach(Wolf et al, 1994) is applied to calculate the necessary Green functions instead of direct integration the Duhamel's integral. The approach is computationally more efficient than direct integration of Duhamel's integral. Then a numerical integration over a finite number of time steps is performed by means of a standard scheme such as Newmark β method. Special considerations are given to the elastic response of the pile-soil system with a small mass of pile and a smaller trapped mass of soil disk. In such cases, an additional numerical damping is introduced to avoid the numerical instabilities (see for e.g Nogami and Konagai, 1988 and Wolf et al, 1994 etc.).

Although frequency and time domain analysis methods are completely independent, nonetheless, it is possible to transfer from frequency domain to time domain by means of Fourier transformations(see for e.g. Clough and Penzien, 1968). This approach has been extensively applied for foundation analysis of gravity type platforms in the North sea region by Madshus, (1997).

4.9.2 Dynamic stiffness formulation in frequency domain

4.9.2.1 A rigid pile and linear soil

The dynamic equation of motion for a pile-soil system according to D'Almbert's principle may be written as follows:

$$P(\omega) = [M_{ps}]\ddot{u}(\omega) + [C_{ps}(\omega)]\dot{u}(\omega) + [K_{ps}(\omega)]u(\omega) \tag{4.166}$$

which for a harmonic excitation with linear hysteretic damping as described above, Eq. 4.166 can be expressed as follows:

$$P(\omega) = [K_{ps}(\omega)(1 + 2i\eta_m) - \omega^2 M_{ps}]u(\omega) \tag{4.167}$$

where $K_{ps}(\omega)$ is the undamped dynamic stiffness of the pile-soil system. If we consider a massless disk system then Eq. 4.167 will be reduced to a quasi-static type of interaction formula as follows:

$$P(\omega) = [K_{ps}(\omega)(1 + 2i\eta_m)]u(\omega) = [S_{qs}(\omega)]u(\omega) \tag{4.168}$$

Holding the inertia (mass) term in Eq. 4.167 and re-writing it:

$$P(\omega) = [S_{dy}(\omega)]u(\omega) \tag{4.169}$$

where $[S_{dy}(\omega)]$ can be called the damped dynamic stiffness matrix of the rigid pile-linear soil system. K_{ps} can be computed as the inverse of the flexibility matrix $[G(\omega)]$:

$$[K_{ps}(\omega)] = [G(\omega)]^{-1} \tag{4.170}$$

Hence, the dynamic stiffness matrix may be expressed as:

$$[S_{dy}(\omega)] = [G^{-1}{}_{dy}(\omega)(1 + 2i\eta_m) - \omega^2 M] \tag{4.171}$$

The dynamic flexibility matrix $[G(\omega)]$ can be established as(Wolf et al, 1994):

$$[G(\omega)] = [g_{ij}(a) + g_{ij'}(a')] \qquad ; i, j = 1, 2, ..., n \tag{4.172}$$

in which the elements of the dynamic flexibility matrix can be computed independent of the pile-soil displacement. $g_{ij}(a)$ element referred to as Green function element for the receiver disk i and the source disk j and its image j', is defined as the displacement at the receiver disk i due to the unit force applied at the source disk j and its image j'. $[S_{dy}(\omega)]$ can be determined according to the Green function approach (Meek and Wolf, 1992) as functions of double cone parameters of soil and the seismic wave velocities (the compressive and the shear wave velocities c_p and c_s). The latter are functions of soil's elasto- plastic properties such as the shear modulus G and the poisson ratio ν. It is assumed that g_{ij} in this case is constant w.r.t u. Therefore Eq. 4.172 can be computed independent of the pile-soil displacement (see appendix.D). $g_{ij}(a)$ function in general may be expressed as follows:

$$g_{ij}(a) = g_{ij}(a, r_0, z_i, G, \nu, w) \tag{4.173}$$

In which a, r_0 and z_i are the double cone parameters (Wolf and Meek and Wolf, 1994) as shown in Fig. 4.12. As shown here, the dynamic stiffness matrix of the virgin soil S_{dy} is coupled via Green's functions g_{ij}. Now considering Eq.4.168 it is seen that the disks are coupled through the full-space of soil as modelled by cones and also via beam elements of pile itself.

The displacement response of the pile-soil system may then be obtained from Eq. 4.167 as follows:

$$u(\omega) = [S_{dy}(\omega)]^{-1}P(\omega) \tag{4.174}$$

By knowing the applied loads and the boundary conditions (I.C and B.C) then the reduced matrix equation may be solved to obtain the unknown displacement and reaction forces. For example for a seismic input case the force vector $P(\omega)$ on the right hand side of Eq. 4.174 may consist of the ground acceleration vector times the corresponding mass matrix as follows:

$$P(\omega) = [M_{ps}]\ddot{u}_g \tag{4.175}$$

where we have:

$$\ddot{u}_g = [\ddot{u}_{g,1}\ddot{u}_{g,2}...\ddot{u}_{g,n}] \tag{4.176}$$

in which $u_{g,i}$ represents the ground acceleration time histories at the location of soil disk (i). In practice, it is usually assumed that the earthquake time histories are fully correlated for a small area with a dimension such as a single pile, thus $u_{g,i} = u_{g,0}$ which refers to the center of the pile-soil field or any other base point at the vicinity of that where the ground acceleration is given for. If such measurements are not directly available for the given site, then a record from far field for the virgin soil (halfspace) may be used with a filtering procedure in general:

$$u_g = H_{ps}u_{g,0} \tag{4.177}$$

in which H_{ps} is called the site-specific transfer function (see for e.g Caltech 1995, Bessason, 1993) which filters the measured remote earthquake to the site specific response. H_{ps} can be a function of various parameters such the spherical coordinate of the site relative to the station (the great and local seismic circles) and the material properties of the site. A random type excitation such as an earthquake record can be decomposed to its primary harmonic components which may be used as input in Eq. 4.174 to determine the individual response components as follows:

$$u_g = \sum u_{g,i}sin(w_i t + \phi_i) \tag{4.178}$$

in which $u_{g,i}, w_i$ and ϕ_i are the amplitude, frequency and the phase angle of each component. Thus the total response may be obtained by superposition of all individual responses according to Eq. 4.174 as follows:

$$u(\omega) = \sum -[S_{dy}(w_i)]^{-1}[M_{ps}]\omega_i^2 u_{g,i}sin(w_i t + \phi_i) \tag{4.179}$$

4.9.2.2 A flexible pile and linear elastic soil

The dynamic equation of motion expressed in Eq. 4.167 may be modified to account for the flexibility of the pile as follows:

$$P(\omega) = ([K_{ps}](\omega)(1 + 2i\eta_m) + [K_p] - \omega^2[M_{ps}])u(\omega) \tag{4.180}$$

in which the added term $[K_p]$ corresponds to the static stiffness of the non-rigid pile ($EI \neq \infty$) which may be obtained according to the beam (rod) theory of elasticity (see for e.g Timoshenko and Goodier (1982)).

A classic finite element method can be applied to establish $[K_p]$ from the corresponding pile element stiffnesses (see for e.g Przemieniecki, (1968), Reddy, (1985) and Zienkiewicz and Taylor, (1989) etc.).

Wolf and Meek, (1994) considered a mathematical subtraction of the soil properties from Eq. 4.174 to replace the soil cylinder with that of the pile. Since the elastic modulus of the soil cylinder is much smaller than that of the pile, hence neglecting the subtraction of soil stiffness from pile may not effect the dynamic stiffness matrix $[S_{dy}(\omega)]$ appreciably. However, the subtraction of the mass may be applied. Considering an added mass of the soil around the pile and a trapped

mass inside the pile then the effect of the mass subtraction from inside the pile may diminish. A complete procedure may involve all the mentioned items.

It may be worth mentioning that while the pile's stiffness contribution enters as purely static (independent of ω), however the stiffness of the pile-soil disk elements is a function of frequency w. To reconcile this with the explicit expressions established by Wolf and Meek, (1994), we may consider the associate mass or inertial contribution (terms) or in other words if we decompose Eq. 4.180 into two separate parts we will get:

$$P(\omega) = [S_{ps}(\omega) + S_p(\omega)]u(\omega) \tag{4.181}$$

where $[S_p]$ and $[S_{ps}]$ are the dynamic stiffness contributions of the pile and the interaction between the pile and soil, respectively as:

$$[S_{ps}(\omega)] = [K_{ps}(\omega)(1 + 2i\eta_m)] \tag{4.182}$$

$$S_p(\omega) = [K_p - \omega^2 M] \tag{4.183}$$

The latter equation shows that all the material damping is considered in the form of linear hysteretic soil damping and the pile is assumed to be linear elastic.

The procedure for computing the displacement and reaction forces may be the same as described in the previous subsection. The dynamic stiffness at the pile-soil head may be obtained by applying unit displacements at the pile head in each direction.

$$P(\omega) = [00...1...0] \tag{4.184}$$

By combining Eqs. 4.181 and 4.184,we may obtain the corresponding stiffnesses as follows:

$$[S_{i,d}] = (([S_p(\omega) + S_{ps}(\omega)]^{-1})_{ii})^{-1} \tag{4.185}$$

4.9.3 Dynamic stiffness formulation in time domain

The direct time domain stiffness formulation presented by Wolf, (1994) may be modified to obtain the dynamic response of a non-linear pile-soil system without any need for Fourier transformation from frequency domain solution as presented in the previous section.

The basic dynamic interaction formula for an embedded foundation (Wolf et al,1994) can be modified for a non-linear single pile-soil system by using appropriate tangent stiffness matrices of pile-soil system as follows:

$$P_{0n} = [S_{ps}(t) + S_p(t)]u_n - [S_{ps}(t)]\bar{u}_n - [M]\ddot{u}_n - [S_{ps}(t)]u^f{}_n \tag{4.186}$$

In which P_{0n} is the interaction forces at the pile-soil interface and consists of two components as follows:

$$P_{0n} = P_{0n}^k + P_{0n}^i \tag{4.187}$$

where superscripts k and i refer to the kinematic and the inertial components, respectively expressed as follows:

$$P_{0_n}^k = [S^g(t)](u(t) - u_g(t)) = -[S^f(t)]u^f(t) + [S^g(t)]u(t) \tag{4.188}$$

where $u_g(t)$ denotes the displacement of the ground system and is given as (Wolf et al, 1994):

$$u_g(t) = [S^g(t)]^{-1}[S^f(t)]u_f(t) \tag{4.189}$$

where $S^g(t)$ and $S^f(t)$ represent the dynamic stiffness matrices of the ground soil system and that of the free field soil, respectively. $u^f(t)$ is the free field motion of the pile-soil nodes (disks). The inertia component $P_{0_n}^i$ can be expressed as follows:

$$P_{0_n}^i = [M](\ddot{u}(t) - \ddot{u}_g(t)) \tag{4.190}$$

in which $\ddot{u}(t)$ and $\ddot{u}_g(t)$ stand for the accelerations of the pile-soil system (total) and the ground system (excavated). The mass matrix $[M]$ can be established as concentrated at the disks (lumped) follows:

$$[M] = [m_{ij}] \qquad ; i, j = 1, 2, ..., nd \tag{4.191}$$

where $m_{ij} = 0$ for $i \neq j$ and $m_{ij} \neq 0$ for $i = j$. Considering a kinematic interaction the Eq. 4.186 may be re-formed to produce the Eq. 4.188. Hence the kinematic interaction is inherent in Eq. 4.186. However, substituting the inertial interaction Eq. 4.190 into Eq. 4.186 only satisfies the equilibrium condition for the first term. Thus the remaining ground force($m\ddot{u}_g$) must be enforced on the system as the external load.

The term $[S_{ps}(t) + S_p(t)]$ denotes the combined stiffness of the pile-soil system. The non-linear dynamic stiffness matrix of the pile-soil multi-stack of disks system $[S_{ps}(t)]$ may be computed as a function of the non-linear Green functions as follows:

$$g_{ij}(t, a) = f_g(G^T, a, t) \tag{4.192}$$

in which $g(t, a)$ is a Green function element which represents the displacement of a receiver disk i due to the unit load at the location of a source disk and its mirror image (Wolf et al, 1994). G^T is the tangent stiffness of the pile- soil system as defined in Eq. 4.23. Now combining the Eq. 4.22, 4.30 and 4.192 will result in:

$$g_{ij}(t, a) = f_g(f_G(f_\tau(u, ...)), a, t) \tag{4.193}$$

The latter equation is formulated in a parametric form and may be solved numerically (see appendix.D)

The pile's non-linear stiffness matrix $[S_p(t)]$ can be established based on the classical beam (rod) theory (see for e.g Timoshenko) by accounting for the pile's both material and geometric non-linearities as follows:

$$[S_p(t)] = [S_p(t)]_m + [S_p(t)]_g = [f_{p,m}(u, \dot{u}_t, ...)] + [f_{p,g}(u, \dot{u}_x, ...)] \tag{4.194}$$

in which the first term on the right hand-side of the Eq. 4.194 corresponds to the tangent structural stiffness matrix and the second term denotes the geometric stiffness matrix which may become significant for large displacements.

The total displacements from Eq.4.186 can be applied, if $[S_{ps}(t)]$ matrix is established based on initial or a secant soil stiffness. However, in the case of tangent stiffness an incremental form has to be applied. This is because at the collapse of pile-soil system ,the term $[S_{ps}(t)]$ becomes zero which results in zero restoring force if the total form is applied. By using an incremental form, however, at the collapse the total restoring force increment becomes zero which is correct by definition.

An incremental form of Eq. 4.186 is considered by subtracting the force components at each time step from their values at the previous time step as follows:

$$\Delta P_{0n} = [S_{ps}(t) + S_p(t)]\Delta u_n - [S_{ps}(t)]\Delta \bar{u}_n - [M]\Delta \ddot{u}_n - [S_{ps}(t)]\Delta u^f{}_n - \delta\Delta P_{0n-1} \quad (4.195)$$

in which the last term on the R-H-S of Eq.4.195 indicates an unbalance force at the end of last time increment step (n-1) as:

$$\delta\Delta P_{0n-1} = \Delta P_{0n-1} - [S_{ps}(t)+S_p(t)]\Delta u_{n-1} + [S_{ps}(t)]\Delta \bar{u}_{n-1} + [M]\Delta \ddot{u}_{n-1} + [S_{ps}(t)]\Delta u^f{}_{n-1} \quad (4.196)$$

To solve Eq. 4.195, a numerical integration method may be applied such as Newmark family of β methods. Expressing the incremental velocity and the displacement terms at the time station (n) in terms of the incremental displacement ,velocity and the acceleration terms at previous time steps and the acceleration term at the same time step as:

$$\Delta \dot{u}_n = \Delta \dot{u}_{n-1} + \frac{1}{2}(\Delta t)\,[\Delta \ddot{u}_{n-1} + \Delta \ddot{u}_n] \quad (4.197)$$

$$\Delta u_n = \Delta u_{n-1} + (\Delta t)\Delta \dot{u}_{n-1} + (\frac{1}{2} - \beta)(\Delta t)^2 \Delta \ddot{u}_{n-1} + \beta(\Delta t)^2 \Delta \ddot{u}_n \quad (4.198)$$

For some particular values of β parameters a physical meaning may exist, such as $\beta = \frac{1}{4}$ or $\frac{1}{6}$ which correspond to the constant and linear acceleration methods. Combining the Eqs. 4.197, 4.198 and 4.186, the following may emerge:

$$([A]^T[S_{ps}(t) + S_p(t)]_0[A] - \frac{1}{\beta(\Delta t)^2}[M])\Delta u_n = \Delta P_{0n}^i + [A]^T[S_{ps}(t)]_0\Delta \bar{u}_n$$
$$+[M](-\frac{1}{\beta(\Delta t)^2}\Delta u_{n-1} + \frac{1}{\beta \Delta t}\Delta \dot{u}_{n-1} - \frac{0.5-\beta}{\beta}\Delta \ddot{u}_{n-1} + [A]^T[S_{ps}(t)]\Delta u_f) \quad (4.199)$$

in which term $\Delta \bar{u}_n$ denotes a recursive displacement vector which may be calculated based on the previous values of displacements as follows(Wolf et al, 1994):

$$\Delta \bar{u}_n = \sum_{k=1}^{n-1}[G_{n-k}]\Delta P_k \quad (4.200)$$

in which $[G_{n-k}]$ represents the Green matrix at time station n (i.e. $t_n = n\delta t$) due to a linearly varying load around time station k (i.e. increasing from zero at t_{k-1} to about unity at k and

then decreasing to zero at time station $k+1$). It is assumed here that for a non-linear pile-soil interaction, the off-diagonal members of the Green matrix $[G_{n-k}]$ are set to zero thus the coupling terms are avoided. However, for the linear elastic soil, the superposition principle is applied in calculation of the elements of $[G_{n-k}]$ matrix. Hence, the off-diagonal members are computed.

The last term on the right hand-side of Eq. 4.199 may be computed as follows:

$$\Delta P_{n-1} = [S_{ps}(t)]_{n-1}\Delta u_{n-1} - [S_{ps}(t)]_{n-1}\Delta \bar{u}_{n-1} \tag{4.201}$$

where the increment of displacement Δu_{n-1} has already been computed (known) at the previous time station (n-1). The first term on the right hand-side of Eq. 4.201 is the dynamic stiffness matrix of the pile-soil disk (free-field) which can be easily computed in terms of the Green functions $g_{ij}(t)$ (see appendix.D).

The Green function associated with the nth time station due to load at unit loads at the time station k th time station may be computed in a recursive manner as follows (see appendix.D for details):

$$\Delta u_{n=k+1} = a(e^{\frac{-2c\delta t}{z_i}} - 2e^{\frac{-c\delta t}{z_i}} + 1)\frac{z_i}{c\delta t}\Delta u_k \tag{4.202}$$

in which all the parameters are as defined above. For a unit impulse, the coefficient a will be equal to $\frac{1}{K}$. Combining Eqs. 4.199 and 4.202, the numerical integration can be performed over a given interval of time history.

The discussion of the stability of this method is given in the appendix.D and other literature concerning the Newmark's integration methods. However, it is worth mentioning that the existence of $[M]$ on the right hand-side of Eq. 4.199 may result in a numerical instability for particular values of β parameter such as $\frac{1}{4}$. The remedy may be to avoid the trapped mass at the tips of the stack. However, in practical cases due to the presence of a large mass of the super-structure which is connected to the pile (at the interface), the procedure seemed to be stable.

4.9.4 Bouc's non-linear hysteretic system stiffness

A modified form of Bouc's non-linear hysteretic model(Bouc, 1968) is adopted here to simulate the response of the equivalent SDOF model of pile. The model is well suited for non-linear dynamic analysis of oscillatory systems. The non-linear hysteretic response is illustrated in Fig. 4.58.

The dynamic equilibrium according to the modified Bouc's model may be expressed as:

$$p(u,\dot{u}) = m\ddot{u} + f_h(u,\dot{u}) + f_n(u) \tag{4.203}$$

in which $m\ddot{u}$, $f_h(u)$ and $f_n(u)$ are inertia, hysteretic and non-linear functions of the displacement response u(and its derivatives with respect to time). The latter equation may be expressed as

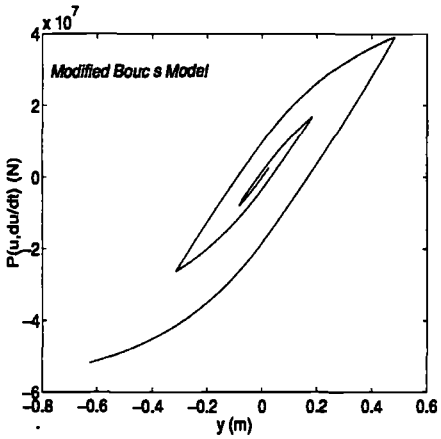

Figure 4.58: Modified Bouc's non-linear hysteretic model

follows (Constantinou and Tadjbaksh, 1985):

$$p(u,\dot{u}) = m\ddot{u} + \beta\frac{F_y}{u_y} + (1-\beta)F_y z_b \tag{4.204}$$

in which u_y and f_y are the initial yield displacement and force of the hysteresis damper and β is the ratio of the post-yield stiffness to the elastic initial stiffness. For e.g. $\beta = 1$ will simulate a linear elastic system, while by inserting $\beta = 0$ an elastic-perfectly plastic response can be simulated. $\beta < 0$ can simulate a system with post-peak degradation. z_b is a hysteresis parameter which is related to the displacement u and $\dot{u}$ through the following equation(Bessason, 1993):

$$u_y\dot{z}_b = -\alpha_1|\dot{u}||z_b|^{n-1}z_b - \alpha_2\dot{u}|z_b|^n + \alpha_3\dot{u} \tag{4.205}$$

in which α_1, α_2 are shape parameters, α_3 determine the amplitude of the restoring force (hysteresis) loop, n represents the elatso-plastic transition which determines the smoothness of the transition from elastic to plastic. It may be worth of noting that u excludes any rigid body motions of the pile and hence only represents the pile element's distortion.

The solution of Eq. 4.205 has been given for instance by (Spiegel, 1968):

$$z_b = z_i e^{c_b(u-u_0)} + \frac{\alpha_3}{u_y c_b}(e^{c_b(u-u_0)} - 1) \tag{4.206}$$

where $z_{b,i}$ and u_0 may be known from the initial conditions. And parameter c_b can be determined as follows:

$$c_b = -\frac{1}{u_y}(c_1\alpha_1 + c_2\alpha_2) \tag{4.207}$$

where parameters c_1 and c_2 can be determined as follows:

$$c_1 = 1 \qquad ;\dot{u} \geq 0 \qquad\qquad c_1 = -1 \qquad ;\dot{u} < 0 \tag{4.208}$$

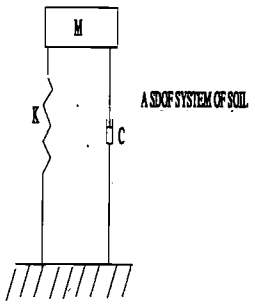

Figure 4.59: A NPS-SDOF system

$$c_2 = 1 \quad ; z_b \geq 0 \qquad c_2 = -1 \quad ; z_b < 0 \tag{4.209}$$

Since the value of c_2 depends on the sign of z_b which is also a function of c_2, it can be determined through an iterative procedure (see appendix.D).
The tangent stiffness parameter of the pile element then may be obtained as:

$$k_p^T = \frac{\partial P}{\partial u} = \beta \frac{F_y}{u_y} + (1-\beta) F_y (\frac{\alpha_3}{u_y} + c_b z_b) \tag{4.210}$$

The dynamic stiffness of an equivalent spring (lumped model of pile for e.g. SDOF system) then may be calculated in a simplified manner by modifying the elastic modulus of pile element E_p as a function of displacement u and the velocity $\dot{u}$ as follows:

$$s_{p,ij} = k_{ij} \cdot \frac{k_p^T(u, \dot{u})}{k_p^T(u = u_0, \dot{u} = \dot{u}_0)} \tag{4.211}$$

in which $s_{p,ij}$ and k_{ij} refer to the dynamic and static stiffnesses of ij of the pile, respectively. $k_p^T(u, \dot{u})$ and $k_p^T(u = u_0, \dot{u} = \dot{u}_0)$ denote the current and the initial values of the tangent stiffness parameter as described in Eq. 4.210.

The above procedure is well suited for the discrete element (lumped parameter) equivalent model of pile-soil system (such as SDOF, 2DOF and 3DOF systems). For time domain analyses which are carried out in this Chapter due to smaller plastic utilization of the pile, the elastic assumption for pile elements is considered as relevant. However, the pile behaviour is simulated by using a simplified equivalent model as described in this subsection and also by using a more sophisticated plastic hinge beam model of USFOS(Søreide et al, 1994) which is described in Chapter.3.

4.9.5 A nonlinear SDOF system

The simplest dynamic system may be used to model a single pile case with the nonlinear soil as shown in Fig. 4.59. The stiffness formulation of the nonlinear SDOF system in the time domain may be established as a special case of Eq. 4.186 in the following form:

$$m\Delta\ddot{u}_0 + m\Delta\ddot{u}_g + K_{ps}(u, \dot{u})\Delta u_0 = 0 \tag{4.212}$$

In which Δu_0 and $\Delta\ddot{u}_0$ and $\Delta\ddot{u}_g$ represent the displacement increment of the single degree of freedom system , its second derivative with respect to time. and the increment of the ground acceleration. K_{ps} is the tangent stiffness of the pile-soil system which is a function of the total displacement u and its first derivative $\dot{u}$. To solve Eq. 4.212 in the time domain, an explicit algorithm can be established by using a predictor-corrector technique based on familiar Newmark's family of methods (see Newmark, 1959). The incremental acceleration term $\Delta\ddot{u}_{0,n+1}$ at the time station $(n+1)$ may be obtained from Eq. 4.212 as:

$$\Delta\ddot{u}_{0,n+1} = -\frac{1}{m}(m\Delta\ddot{u}_{g,n+1} + K_{ps,n+1}\Delta u_{0,n}) \tag{4.213}$$

In Eq.4.213, $K_{ps,n+1}$ represents the pile-soil tangent stiffness at step (n+1). $K_{ps,n+1}$ is a function of u_{n+1} and $\dot{u}_{n+1}$ which represent the displacement and its first derivative at step (n+1). So far, only the values of the response are known at the end of the previous step n. Hence, $K_{ps,n+1}$ will be replaced with $K_{ps,n}$. This implies an unbalanced force which must be added to the R-H-S of Eq.4.212 to hold the equilibrium of the external and internal forces. Then the incremental acceleration at step (n+1) can be written as:

$$\Delta\ddot{u}_{0,n+1} = -(\Delta\ddot{u}_{g,n+1} + \frac{K_{ps,n+1}}{m}\Delta u_{0,n} - \Delta\ddot{u}_{0,n} + \Delta\ddot{u}_{g,n} + \frac{K_{ps,n}}{m}\Delta u_{0,n}) \tag{4.214}$$

The predictor equation for $\Delta u_{0,n+1}$ can be written as:

$$\Delta u_{0,n+1} = \Delta u_{0,n} + dt\Delta\dot{u}_{0,n} + \frac{dt^2}{2}\Delta\ddot{u}_{0,n} \tag{4.215}$$

and the predictor expression of $\Delta\tilde{\ddot{u}}_{0,n+1}$:

$$\Delta\tilde{\ddot{u}}_{0,n+1} = \Delta\dot{u}_{0,n} + \frac{dt}{2}\Delta\ddot{u}_{0,n} \tag{4.216}$$

and $\Delta\ddot{u}_{0,n+1}$ from Eq. 4.213 emerges as:

$$\Delta\ddot{u}_{0,n+1} = -\frac{1}{m}(m\Delta\ddot{u}_{g,n+1} + K_{ps}\Delta u_{0,n+1}) \tag{4.217}$$

The corrected incremental velocity term $\Delta\dot{u}_{0,n+1}$ can now be written as:

$$\Delta\dot{u}_{0,n+1} = \Delta\tilde{\ddot{u}}_{0,n+1} + \frac{dt}{2}\Delta\ddot{u}_{0,n+1} \tag{4.218}$$

The total displacement, velocity and acceleration terms then can be computed as:

$$\begin{aligned} u_{0,n+1} &= u_{0,n} + \Delta u_{0,n+1} \\ \dot{u}_{0,n+1} &= \dot{u}_{0,n+1} + \Delta\dot{u}_{0,n+1} \\ \ddot{u}_{0,n+1} &= \ddot{u}_{0,n+1} + \Delta\ddot{u}_{0,n+1} \\ v_{0,n+1} &= v_{0,n} + \Delta v_{0,n+1} \end{aligned} \tag{4.219}$$

$$\begin{aligned} \dot{v}_{n+1} &= \dot{v}_{n+1} + \Delta\dot{v}_{n+1} \\ \ddot{v}_{n+1} &= \ddot{v}_{n+1} + \Delta\ddot{v}_{n+1} \end{aligned} \tag{4.220}$$

It can be shown that above explicit algorithm is conditionally stable which means that for time step size larger than $dt > \frac{T}{\pi}$ the solution may not converge (Hahn, 1991). This explicit algorithm is quite efficient in dealing with simple nonlinear systems such as simplified equivalent models of pile-soil systems. The procedure described here is applied for the analysis of the simplified non-linear model of pile-soil system in the following.

A 2DOF SYSTEM OF PILE-SOIL

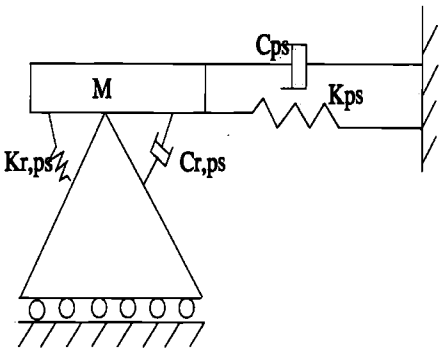

Figure 4.60: A NPS-2DOF system

4.9.6 A 2DOF non-linear system

A non-linear 2 degree of freedom system as shown in Fig. 4.60 system can represent another class of pile-soil system. For instance a single rigid pile with horizontal and rocking degrees of freedom which may be considered as coupled in a pile-soil system. The basic equation of motion again can be derived from Eq. 4.186 as follows:

$$m\Delta\ddot{u}_g + m\Delta\ddot{u}_0 + mh\Delta\ddot{v}_0 + K_{ps}\Delta u_0 = 0 \tag{4.221}$$

$$m\Delta\ddot{u}_g + m\Delta\ddot{u}_0 + mh\Delta\ddot{v}_0 + K_{r,ps}\Delta v_0 = 0 \tag{4.222}$$

where Δu_0, Δv_0 represent the translational(for e.g horizontal) and rotational (e.g rocking) movements of the rigid pile foundation, respectively. Δu_g represents the displacement of the effective ground motion. K_{ps} and $K_{r,ps}$ represent the corresponding translational and rotational stiffnesses of the rigid pile and non-linear soil system which can be computed according to the relationships described in previous sections (see Sec.4.3.2.1). Hence, in this simple 2DOF system, the input excitation force $m\Delta\ddot{u}_g$ will be resisted through the inertia of the pile and the non-linear hysteretic damping of soil.

The procedure for solving the latter non-linear 2DOF system may be established in analogy to the non-linear SDOF system described in the previous subsection. First for e.g, we consider the translational incremental displacement $\Delta u_{0,n+1}$, it can be calculated from the values known at the previous station according to the following truncated (Taylor) expansion:

$$\Delta u_{0,n+1} = \Delta u_{0,n} + \Delta\dot{u}_{0,n}dt + \Delta\ddot{u}_{0,n}\frac{dt^2}{2} \tag{4.223}$$

Then the corresponding incremental velocity term may be predicted at the current time step n as follows:

$$\Delta\tilde{\dot{u}}_{0,n+1} = \Delta\dot{u}_{0,n} + \Delta\ddot{u}_{0,n}\frac{dt}{2} \tag{4.224}$$

From Eq.4.221 the incremental acceleration term can be obtained as follows:

$$\Delta\ddot{u}_{0,n+1} = -\Delta\ddot{u}_{g,n+1} - h\Delta\tilde{\ddot{v}}_{0,n+1} - \frac{K_{ps,n}}{m}\Delta u_0 \tag{4.225}$$

where $\Delta\tilde{\ddot{v}}_{0,n+1}$ refers to the predicted acceleration at the current time station and since its actual value is not yet known at this stage of calculation, thus we may use its value from the previous time station (n) i.e: $\Delta\tilde{\ddot{v}}_{0,n+1} = \Delta\ddot{v}_{0,n}$.

The predicted value of the velocity from Eq.4.224 now can be corrected as follows:

$$\Delta\dot{u}_{0,n+1} = \Delta\tilde{\dot{u}}_{0,n+1} + \frac{\Delta\ddot{u}_{0,n+1}}{2}dt \tag{4.226}$$

Similar expression can be obtained for the (rotational) rocking motion of rigid pile. The rotational displacement increment at the current time station n $\Delta v_{0,n+1}$ can be computed as follows:

$$\Delta v_{0,n+1} = \Delta v_{0,n} + \Delta\dot{v}_{0,n}dt + \Delta\ddot{v}_{0,n}\frac{dt^2}{2} \tag{4.227}$$

The rotational velocity increment $\Delta\dot{v}_{0,n+1}$ can be predicted as follows:

$$\Delta\tilde{\dot{v}}_{0,n+1} = \Delta\dot{v}_{0,n} + \frac{\Delta\ddot{v}_{0,n}}{2}dt \tag{4.228}$$

The rotational acceleration increment $\Delta\ddot{v}_{0,n+1}$ is obtained from the Eq.4.222 as follows:

$$\Delta\ddot{v}_{0,n+1} = -\frac{\Delta\ddot{u}_{g,n+1}}{h} - \frac{\Delta\ddot{u}_{0,n+1}}{h} - \frac{K_{r,ps,n}\Delta v_{0,n+1}}{mh} \tag{4.229}$$

in which all the terms on the R-H-S are known or computed previously(see Eqs.4.227 and 4.225).

Now the rotational velocity increment $\Delta\dot{v}_{0,n+1}$ can be corrected as follows:

$$\Delta\dot{v}_{0,n+1} = \Delta\tilde{\dot{v}}_{0,n+1} + \frac{\Delta\ddot{v}_{0,n+1}}{2}dt \tag{4.230}$$

We recall that on the R-H-S of Eq.4.225, $\Delta\ddot{v}_{0,n+1}$ is assumed as its previous value for the first iteration. Now we can substitute for $\Delta\ddot{v}_{0,n+1}$ with the value obtained in Eq.4.229 and hence repeat the calculations from Eq.4.225. This iterative procedure can be used until the corrected value of each acceleration term becomes approximately the same as its predicted value at the previous step of iteration scheme as:

$$\Delta\ddot{u}_{n+1,i+1} - \Delta\ddot{u}_{n+1,i} < tol(abs(\Delta\ddot{u}_{n+1})) \tag{4.231}$$

The algorithm is stable with the following condition:

$$dt < \frac{T_{min}}{\pi} \tag{4.232}$$

in which T_{min} is the smallest eigenperiod of the system. However, the efficiency of this algorithm is in fast and easy use in non-linear structures with fewer degrees of freedom such as the two

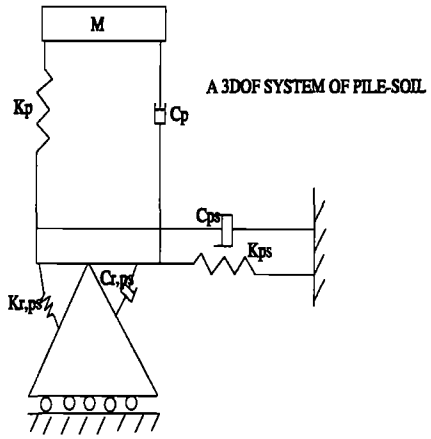

Figure 4.61: A NPS-3DOF system

last examples. For a non-linear MDOF system, this scheme may not be very efficient due to the above stability criterion for the highest vibration mode of the system. Thus within the specified limitations, this technique is expected to perform well. It's also worth mentioning that the accuracy of the response of the non-linear system will depend on how the (seismic or sea wave) loading time history is sampled. (i.e. the time step length). For illustration, an example would be a system such a 2DOF as discussed in this section, it's observed that the governing criterion will be the latter one. (i.e. to define sufficient samples within each cycle (wave) of the loading time history). Sometimes with fewer point in each cycle some secondary variations such as local peaks or valleys may not be simulated). Also for wave and seismic loading, it's sometimes customary to filter the original record for variety of reasons, more importantly, for creating a high pass or low pass filtered data which does not have the corrupted components, diffracted and splash waves from other neighboring structures etc. And also sometimes the original record may be altered to create synthetic loading histories (see for e.g. Bea et al, (1993)).

4.9.7 A lumped 3DOF pile-soil system with frictional damping

The dynamic equations of equilibrium of a 3dof system consisting of a translational dof for the soil, a rotational dof for soil and a translational degree of freedom for the pile with a frictional type material damping of soil as illustrated in Fig. 4.61 may be written as follows:

$$m\ddot{u}(t) + m\ddot{u}_0(t) + mh\ddot{v}_0(t) + K_p|\bar{u}(t)|tg\delta sgn(\dot{u}) + C_p|\bar{\dot{u}}(t)|\frac{tg\delta}{2}sgn(\tilde{u}) = -m\ddot{u}_g(t) \quad (4.233)$$

$$m\ddot{u}(t) + m\ddot{u}_0(t) + mh\ddot{v}_0(t) + K_{ps}|\bar{u}_0(t)|tg\delta sgn(\dot{u}_0) + C_{ps}|\bar{\dot{u}}_0(t)|\frac{tg\delta}{2}sgn(\ddot{u}_0) = -m\ddot{u}_g(t) \quad (4.234)$$

$$m\ddot{u}(t) + m\ddot{u}_0(t) + mh\ddot{v}_0(t) + K_{r,ps}|\bar{v}_0(t)|tg\delta sgn(\dot{v}_0) + C_{r,ps}|\bar{\dot{v}}_0(t)|\frac{tg\delta}{2}sgn(\ddot{v}_0) = -m\ddot{u}_g(t) \quad (4.235)$$

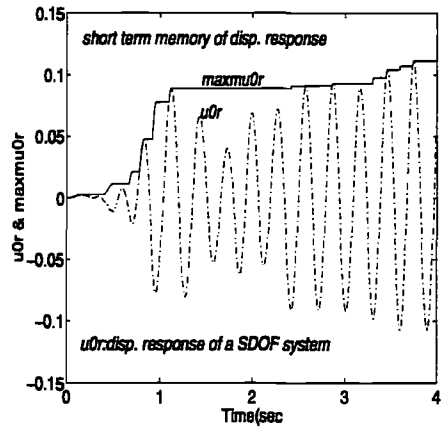

Figure 4.62: A short-term memory of the augmented frictional dynamic elements

The following set of predictor-corrector equations can easily be written:

$$u_n = u_{n-1} + \delta t \dot{u}_{n-1} + \frac{\delta t^2}{2}\ddot{u}_{n-1} \tag{4.236}$$

$$\tilde{\dot{u}}_n = \dot{u}_{n-1} + \frac{\delta t}{2}\ddot{u}_{n-1} \tag{4.237}$$

$$u_{0,n} = u_{0,n-1} + \delta t \dot{u}_{0,n-1} + \frac{\delta t^2}{2}\ddot{u}_{0,n-1} \tag{4.238}$$

$$\tilde{\dot{u}}_{0,n} = \dot{u}_{0,n-1} + \frac{\delta t}{2}\ddot{u}_{0,n-1} \tag{4.239}$$

$$v_{0,n} = v_{0,n-1} + \delta t \dot{v}_{0,n-1} + \frac{\delta t^2}{2}\ddot{v}_{0,n-1} \tag{4.240}$$

$$\tilde{v}_{0,n} = \dot{u}_{0,n-1} + \frac{\delta t}{2}\ddot{u}_{0,n-1} \tag{4.241}$$

From Eq.4.233 the acceleration term $\ddot{u}_n$ can be obtained as:

$$\ddot{u}_n = \frac{-\ddot{u}_{g,n} - \tilde{\ddot{u}}_{0,n} - h\tilde{\dot{v}}_{0,n} - K_p/m|\bar{u}_n|\frac{4}{\pi}tg\delta\tilde{\dot{u}}_n}{1 + C_p/m|\tilde{\dot{u}}_n|\frac{2}{\pi}tg\delta} \tag{4.242}$$

where term $\tilde{\ddot{u}}_{0,n}$ and $\tilde{\dot{v}}_{0,n}$ refer to the predicted acceleration terms which for the first iteration may be assumed as: $\ddot{u}_{0,n-1}$ and $\dot{v}_{0,n-1}$, respectively. The velocity term $|\tilde{\dot{u}}_n|$ in the denominator of the R-H-S of Eq.4.242 refers to the predicted absolute value of the velocity term $\dot{u}$ from the starting time station until time station n as illustrated in Fig. 4.62.

Similarly from Eq.4.234 the acceleration term related to soil $\ddot{u}_{0,n}$ can be obtained as follows:

$$\ddot{u}_{0,n} = \frac{-\ddot{u}_{g,n} - \ddot{u}_n - h\tilde{\dot{v}}_{0,n} - K_{ps}/m|\bar{u}_{0,n}|\frac{4}{\pi}tg\delta\tilde{\dot{u}}_{0,n}}{1 + C_{ps}/m|\tilde{\dot{u}}_{0,n}|\frac{2}{\pi}tg\delta} \tag{4.243}$$

The velocity term $|\tilde{\dot{u}}_{0,n}|$ in the denominator of the R-H-S of Eq.4.242 refers to the predicted value of the velocity term $\dot{u}_0$ from time zero to the current time station n.

And from Eq.4.235 the rotational acceleration term $\ddot{v}_{0,n}$ would be obtained as follows:

$$\ddot{v}_{0,n} = \frac{-\ddot{u}_{g,n} - \ddot{u}_n - \ddot{u}_{0,n} - K_{r,ps}/m|\bar{v}_{0,n}|\frac{4}{\pi}tg\delta\tilde{\dot{v}}_{0,n}}{h + C_{r,ps}/m|\tilde{\dot{v}}_{0,n}|\frac{2}{\pi}tg\delta} \tag{4.244}$$

where term $|\tilde{\dot{v}}_{0,n}|$ denotes the predicted absolute value of the velocity term $\dot{v}_0$ from time zero until current time station n. After obtaining the above acceleration terms at the time station n the predicted velocities in Eqs.4.237 through 4.241 can be corrected as follows:

$$\dot{u}_n = \tilde{\dot{u}}_n + \frac{\delta t}{2}\ddot{u}_n \tag{4.245}$$

$$\dot{u}_{0,n} = \tilde{\dot{u}}_{0,n} + \frac{\delta t}{2}\ddot{u}_{0,n} \tag{4.246}$$

$$\dot{v}_{0,n} = \tilde{\dot{v}}_{0,n} + \frac{\delta t}{2}\ddot{v}_{0,n} \tag{4.247}$$

The above predictor-corrector scheme can be repeated to also correct the values of the acceleration terms until the convergence criterion is satisfied that 's : $\ddot{u}_{n,i} = \ddot{u}_{n,i-1} + (tol(\ddot{u}) << \ddot{u}_{n,i-1})$

4.10 Numerical examples

In this section, we will analyze several cases of the pile-soil foundation systems to illustrate the predictive ability of the methods described in the the previous sections. We will consider different soil behaviour such as elasto-plastic, hyper-elastic and also study different soil models such as static disk model, dynamic cone-disk model, Winkler-spring model of API-RP2A 1993, also simplified lumped models such as SDOF, 2DOF and 3DOF. Different loading types will be considered such as impulse load, wave load applied at the pile head, seismic ground motion applied along the pile and at its tip. Two different solution method as described above will be used namely, frequency and time domain approaches.

The focus will be on the axial and lateral motions of the pile which are of primary importance for the analysis of jacket pile foundations. However, we will also consider rocking motion combined with a horizontal motion of a rigid pile in a simple 2DOF system analysis. The results of the cone-disk models will be verified against those obtained based on rigorous methods such as boundary element method and other analytical approaches.

In the last part of this section, we shall present the results of several simplified equivalent pile-soil analyses. These parametric studies are mainly aimed to give more physical insight into the dynamic behaviour of single pile-soil systems. In particular, the influence of key soil and pile parameters on the stiffness properties of the pile-soil system and the interaction between pile and soil are of interest.

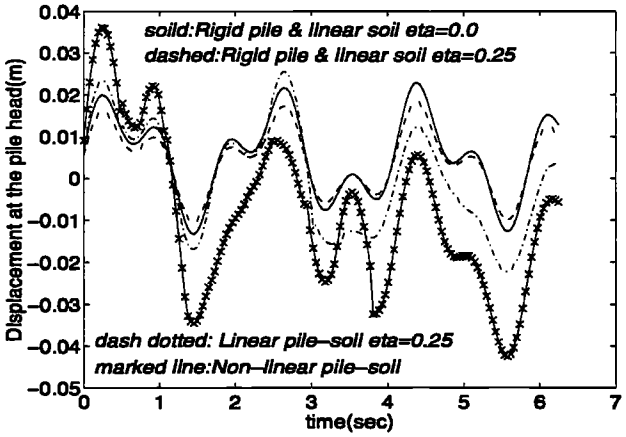

Figure 4.63: Comparing the displacement responses of a single pile-soil system under an idealized earthquake

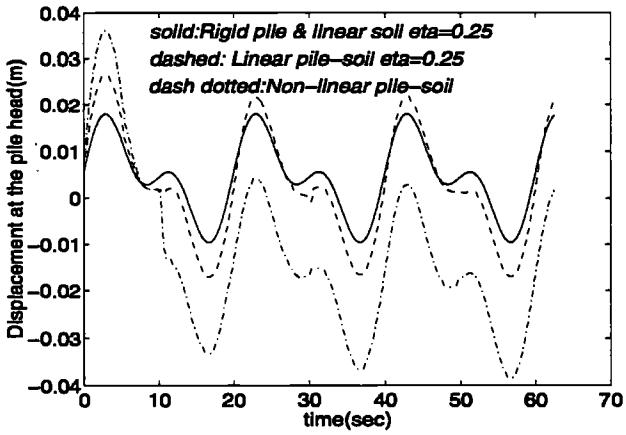

Figure 4.64: Comparing the displacement responses of a single pile-soil system under an idealized sea load ($Tn = 12.5 - 15.0sec$)

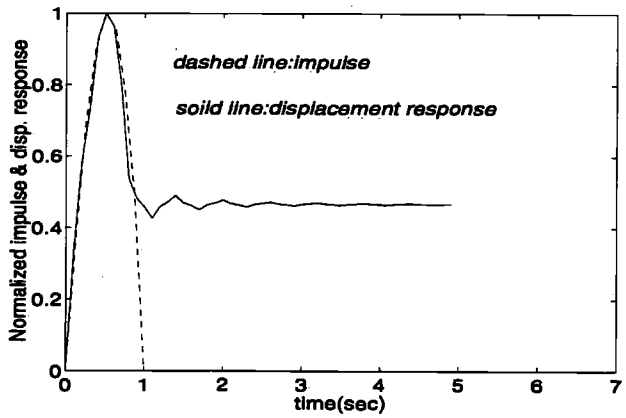

Figure 4.65: Displacement response of a single pile-soil system under an impulse(STI) loading ($T_d = 1.0sec$)

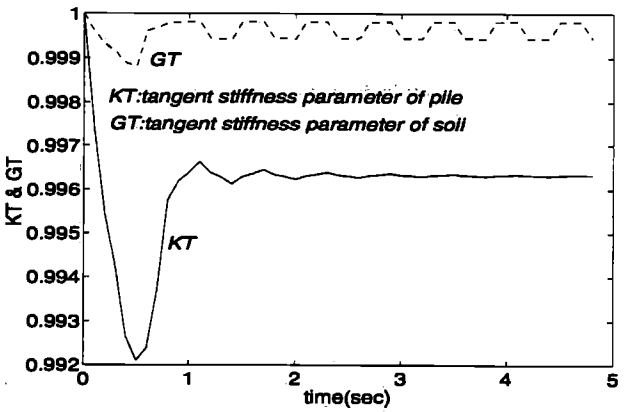

Figure 4.66: Tangent stiffness of pile versus simulation time for an impulse(STI) loading ($T_d = 1.0sec$)

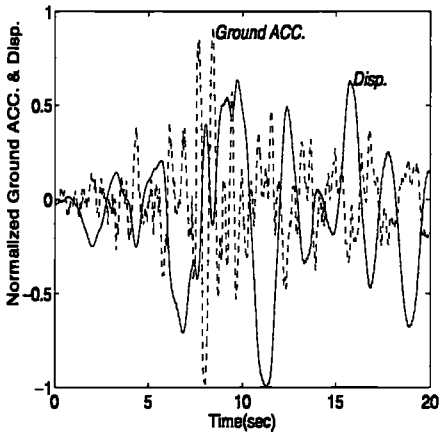

Figure 4.67: The ground acceleration vs. global displacement history at the pile-head under Taft-EQ-ground acceleration for Tilbrook pile at OC clayey soil

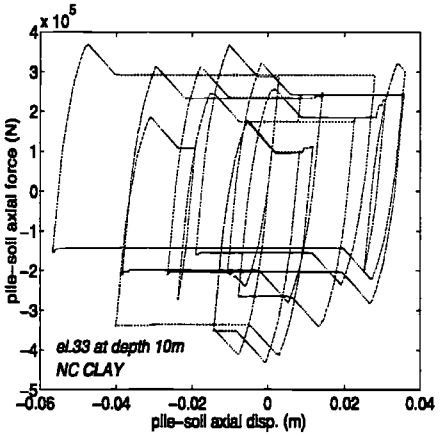

Figure 4.68: A sample mobilized t-z hysteretic curves at 10m depth below the ground surface under Taft-EQ-ground acceleration for Tilbrook pile at OC clayey soil

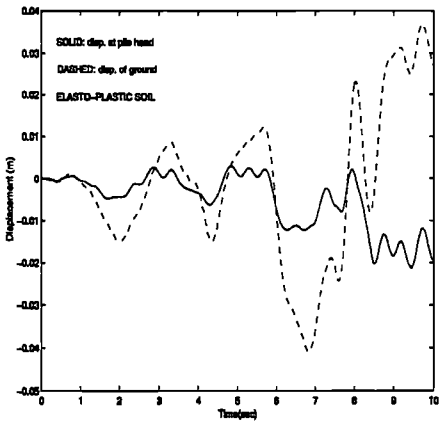

Figure 4.69: The prescribed displacement history vs. the displacement response at the pile-head under Taft-EQ-ground for Tilbrook pile in OC clayey soil(elasto-plastic)

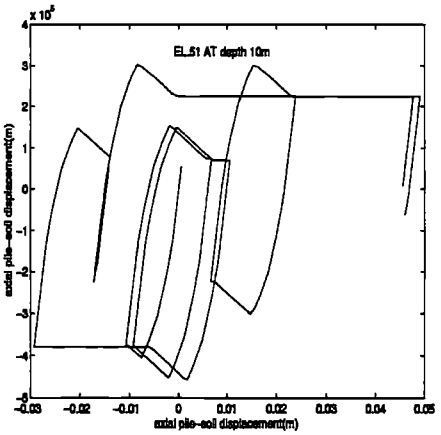

Figure 4.70: A sample mobilized t-z hysteretic curves at 10m depth below the ground surface under Taft-EQ-ground acceleration for Tilbrook pile in OC clayey soil(elasto-plastic)

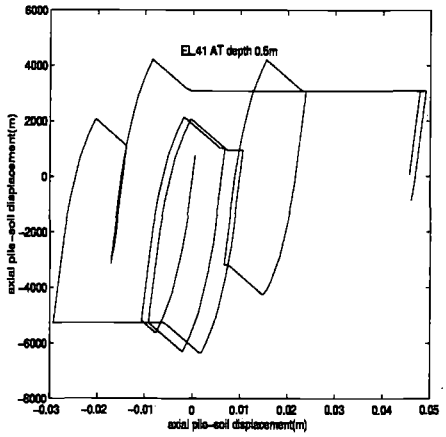

Figure 4.71: A sample mobilized t-z hysteretic curves at 0.5m depth below the ground surface under Taft-EQ-ground acceleration for Tilbrook pile in OC clayey soil(elasto-plastic)

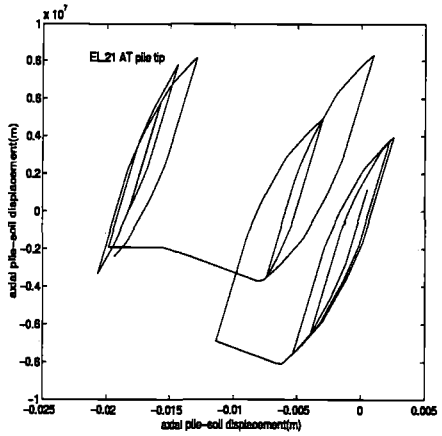

Figure 4.72: A sample mobilized t-z hysteretic curves at depth 31 below the ground surface (pile-tip) under Taft-EQ-ground acceleration for Tilbrook pile in OC clayey soil(elasto-plastic)

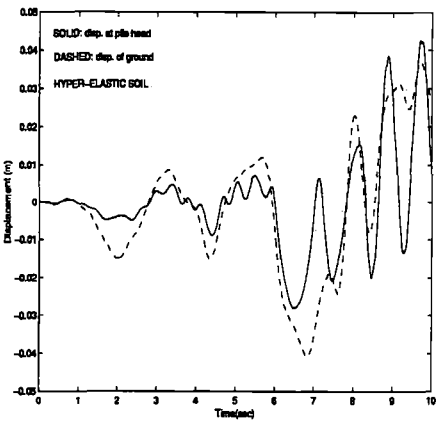

Figure 4.73: The ground acceleration vs. global displacement history at the pile-head under Taft-EQ-ground acceleration for Tilbrook pile at OC clayey soil(hyper-elastic)

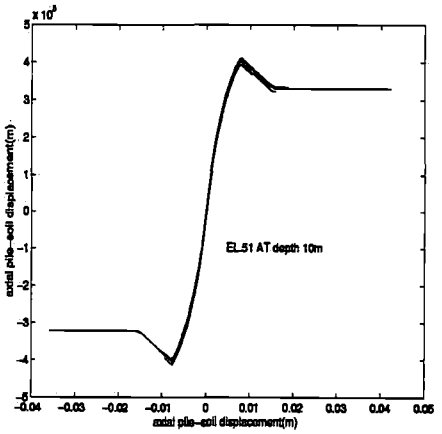

Figure 4.74: A sample mobilized t-z hysteretic curves at 10m depth below the ground surface under Taft-EQ-ground acceleration for Tilbrook pile at OC clayey soil(hyper-elastic)

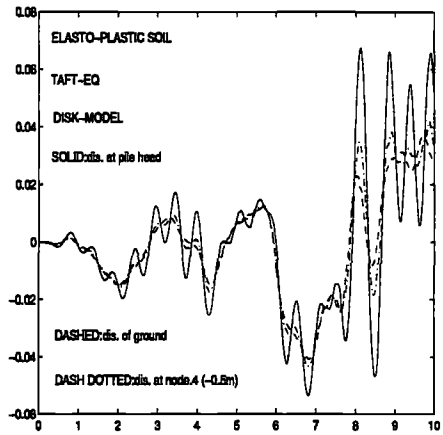

Figure 4.75: The lateral displacement response at the pile-head under Taft-EQ-ground acceleration for Tilbrook pile at OC clayey soil(elasto-plastic)

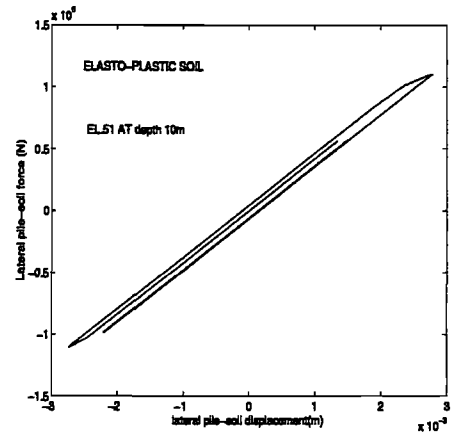

Figure 4.76: A sample mobilized p-y hysteretic curves at 10m depth below the ground surface under Taft-EQ-ground acceleration for Tilbrook pile at OC clayey soil(elasto-plastic)

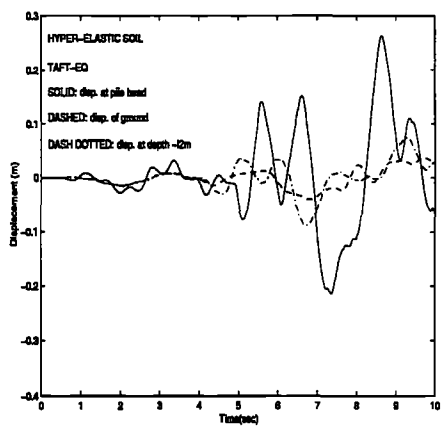

Figure 4.77: The lateral displacement response at the pile-head under Taft-EQ-ground acceleration for Tilbrook pile at OC clayey soil(hyper-elastic)

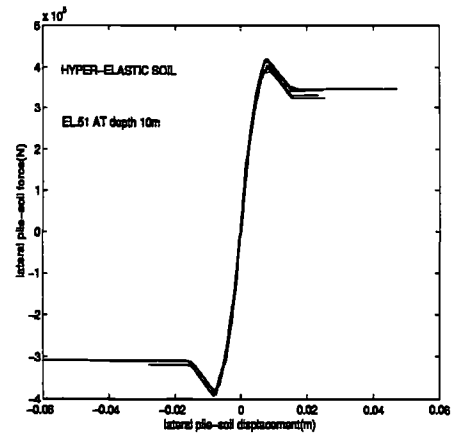

Figure 4.78: A sample mobilized p-y hysteretic curves at 10m depth below the ground surface under Taft-EQ-ground acceleration for Tilbrook pile at OC clayey soil(hyper-elastic)

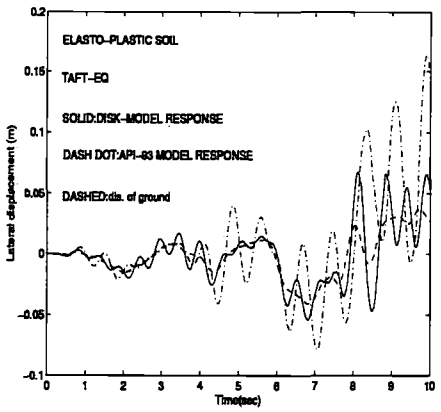

Figure 4.79: Comparison of the lateral displacement response at the pile-head under Taft-EQ-ground acceleration for Tilbrook pile at OC clayey soil(elasto-plasic) of a)disk model-1a and b) API-RP2A 1993 p-y model

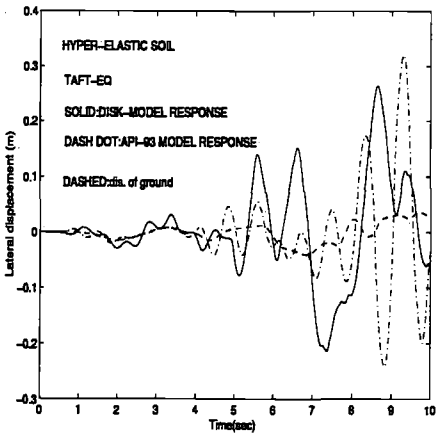

Figure 4.80: Comparison of the lateral displacement response at the pile-head under Taft-EQ-ground acceleration for Tilbrook pile at OC clayey soil(hyper-elastic) of a)disk model-1a and b) API-RP2A 1993 p-y model

4.10.1 Axial case(vertical motion of the pile)

An example of a non-linear pile-soil analysis in the time domain is presented in the following. The pile has an outer diameter of about $1.0m$ and a thickness of about $0.03m$ and a length of about 30m. The soil condition is normally consolidated soft clay with an average shear modulus of about $G = 35MPa$ and the poisson ratio of about $\nu = 0.45$ which is typical for highly saturated soils. The pile-soil system is subjected to a short sinusoidal type impulse load with a duration period of about 1.0 sec which resembles an idealized low intensity(scaled) earth-quake loading half-cycle. The choice of this type load is intended to show the free damped vibration of a nearly elastic pile-soil system.

The analysis is carried out in the time-domain according to Eq.4.199. It is seen on Fig. 4.65, the plotted normalized response curve (dashed line), the displacement response quickly dies out after the impulse time due to the numerical damping introduced by a $\gamma = 0.6 > 0.5$ and also a non-linear hysteretic damping of soil. Fig.4.66 shows that the tangent stiffness degradation is very small in this case, hence, the magnitude of the hysteretic damping (for this case with lower intensity of impulse load) is regarded to be quite small compared to the numerical damping. The latter was taken to prevent any numerical instability due to minus sign of the inertia term on the L-H-S of Eq.4.199. By using a small time step and due to relatively smaller mass of the pile-soil system some numerical instability may occur for linear systems. As will be shown in the following cases, for a non-linear pile-soil with high degree of soil's yield the effect of this numerical damping will be overridden by the dominant hysteretic damping. Hence, it is not necessary to introduce any numerical damping in such non-linear pile-soil cases.

Fig. 4.63 compares the response of a rigid pile and linear soil without and with linear hysteretic damping($\eta = 0.25$), a linear pile-soil system with the specified damping $\eta = 0.25$ and a non-linear pile-soil system with in-elastic hysteretic damping under an idealized earthquake. The pile-soil data are described in Table.D.5 of Appendix.D. It is seen that the response of the rigid pile-linear soil system is quite regular with participation of two main frequencies of vibration which are manifested in the form of double peaks. The response of the same pile-soil system with introducing a linear hysteretic damping with a ratio of $\eta = 0.25$ is somewhat lower but the pattern of response basically is the same which verifies that the linear hysteretic damping may not change the eigen-periods of the system in this case.

The response of the linear pile-soil system with a linear hysteretic damping of about $\eta = 0.25$ is plotted in Fig. 4.63 by a dash dotted line which is even somewhat higher than that of the un-damped rigid-pile and linear soil system. This is because, for the linear pile-soil system the deformation of the pile has increased the amplitude of the vertical displacement at the pile head. The peak vertical displacement of the linear pile-soil system is slightly less than $25mm$ compared to about $17mm$ in this case of the rigid pile-linear soil system with exactly the same damping. The pattern of response It is observed that has also been altered for the linear system due to pile's own deformation. However, the frequency of the forced response has not been considerably changed.

The marked line in Fig. 4.63 shows the response of the non-linear pile-soil system with in-elastic hysteretic damping, It is observed that the amplitude of the response is significantly higher in the case, due to the lower stiffness which is the result of gradual yield in the soil. The peak vertical displacement at the pile head in this case is about $44mm$ compared with about $23mm$ and $17mm$ for the linear pile-soil and rigid pile-linear soil cases, respectively.

It is also shown that the pattern of the response has changed (for e.g the occurrence and proportion of the secondary peaks and valleys in the response are altered and also there is a shift in the response towards the negative displacement due to the significant yield in the soil.

Fig. 4.67 shows the response of Tilbrook pile at OC clay under Taft earthquake excitation applied at the head of the pile. The related pile and soil data for this case are described in Chapter.2. The pile-soil is modelled as illustrated in Fig. 4.5. The displacement response is represented by the solid line in the plot whose peaks can be compared with the peaks in the ground acceleration. A phase is observed between the response and the predominant eigen-period of the response corresponding to that of the ground input displacement.

The axial pile-soil mobilization hystereses are plotted in Fig. 4.68 which show that the soil at depth 10m below the ground level has been fully mobilized. The shift in the peaks of the hystereses manifest the kinematic hardening in the soil. The maximum observed vertical displacement at the depth 10m is about $0.058m$.

Fig. 4.69 shows the displacement response at the head of a 31m long pile with an outer diameter of $O.D = 0.762m$ at heavily over- consolidated clayey soil with elasto-plastic behaviour with an

average shear soil modulus of $G = 35MPa$ an average undrained shear strength of $S_u = 75KPa$. The site is subjected to the strong motion of Taft-earthquake (record, 1966) which has been modified (Caltech, 1995).

It is seen that the time history of vertical pile head displacement has followed more or less that of the ground but with participation of higher eigen-frequencies of the pile's response in the vertical direction (the higher frequencies effects are represented by the secondary peaks in the aforementioned history response denoted by the solid curve in Fig. 4.69).

Due to the plastic yield occurring in the soil under vertical motion of the pile as identified in the axial pile-soil (interaction) mobilization hystereses plotted in Figs.4.70, 4.71 and 4.72, the displacement response curve at the pile head has shifted towards negative displacement after $t = 8sec$ ref. to the acceleration history plot of the ground and the corresponding displacement history which is denoted in the same plot Fig. 4.69, the highest peaks have occurred just after this time ($t = 8sec$).

The observed magnitude (amplitude) of the displacement response at the pile head in this case is lower than that of the ground displacement due to the observed plastic yields in the pile-soil elements (springs) which has absorbed significant part of the energy in the form of hysteretic energy or analogously part of the ground displacement has been dissipated in the form of permanent deformation (or plastic displacement) of soil (see for e.g. Fig. 4.71 etc.).

The corresponding fundamental eigen-frequency of this pile-soil system is about (0.82) which is closer to that of the ground displacement but far larger than that of the velocity or acceleration of the ground. As shown, the linear dynamic magnification effects have been heavily damped out by the in-elastic yield in the soil.

On the other hand, the magnitude of the displacement response is computed to be closer or even larger than that of the ground for the same site with hyper-elastic soil behaviour as plotted in Fig. 4.73. It is seen that displacement response at the pile head for the latter case has been magnified due to dynamic (DAF) effects after $t = 8sec$, the observed dynamic amplification factor is ($DAF = 0.043/0.0375 = 1.15$). This amplification factor is allowed due to the lack of the hysteretic soil damping which is observed in the previous elasto-plastic case to absorb very significant portion of the ground displacement input energy. Since plastic utilization of pile steel material itself for both cases have been insignificant (about $0.02 - 0.04$), hence no considerable damping has occurred in the pile itself.

It can be seen that for the latter hyper-elastic case, the pile response oscillations denoted by solid line in Fig. 4.73 has closely followed those of the ground as denoted by the dashed curve in the same figure. Again the higher frequency effects can be seen particularly in the initial part of the response up to $t = 6secs$ in the form of secondary peaks.

As mentioned above, in both these (vertical motion of pile) cases, the response has been sensitive to the ground displacement not to the ground acceleration or velocity because of higher eigen-

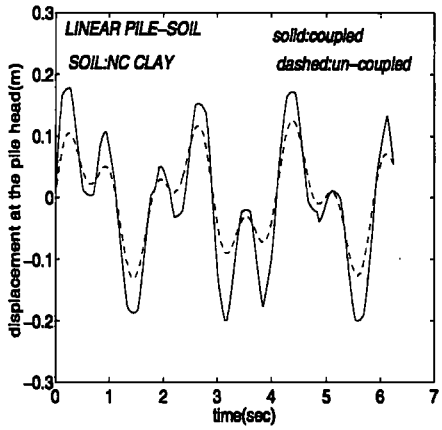

Figure 4.81: Influence of coupling between double cones(disks) on the displacement response of a single flexible pile-soil system

period of the pile-soil which is in the range of dominant frequency of the effective displacement input of ground. Of course, for a pile alone without assigning the mass of the super-structure (for e.g jacket which carries a mass comparatively several order of magnitude higher than that of a single pile), the natural period of the pile-soil system would be far smaller for e.g as given in simpler examples above $T_n = 0.043sec$ etc. whose response as observed are quite different and more sensitive to the ground acceleration or velocity.

The effects of coupling on the response is illustrated through the following example of a single pile-soil analysis. The coupling between the disks as described above are both introduced through the soil full-space between the cones and also through the interconnecting pile elements. The results are plotted in Fig. 4.81 which show an increase in the dynamic flexibility of the pile-soil system due to presence of off-diagonal Green functions g_{ij}s. To verify that this coupling has only taken place between the same degrees of freedom associated with the disks, another simulation is performed by using relatively rigid pile elements $E = 2.1e+14Pa$, the coupling effect between cones has vanished due to the full coupling between the disks in the rigid pile.

4.10.2 Comparison of dynamic lateral response of disk and API-93 models

The dynamic response of Tilbrook pile at OC clay under prescribed TAFT-EQ ground acceleration is analyzed according to the presented multi-stack of disks model as shown in Fig. 4.4 and the p-y model recommended by API-RP2A 1993.

The results are plotted in Figs.4.75 through 4.80 for elasto-plastic and hyper-elastic soil behaviour, respectively. It is seen that for the elasto-plastic soil type, the API-RP2A 1993 soft

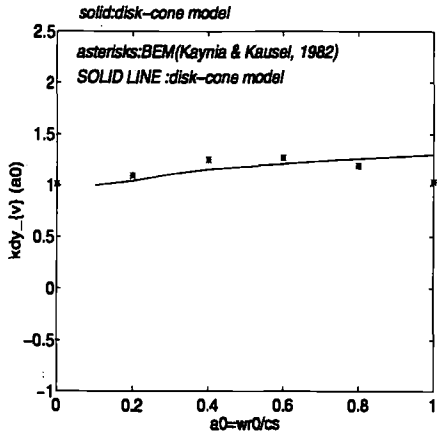

Figure 4.82: Comparison of impedance function $k_{dy,v}$ of disk-cone model and boundary element solution of Kaynia and Kausel, (1982)

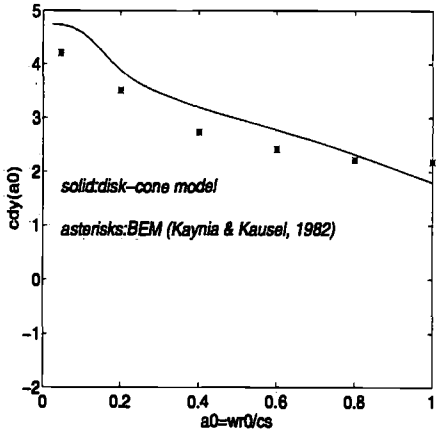

Figure 4.83: Comparison of impedance function $c_{dy,v}$ of disk-cone model and boundary element solution of Kaynia and Kausel, (1982)

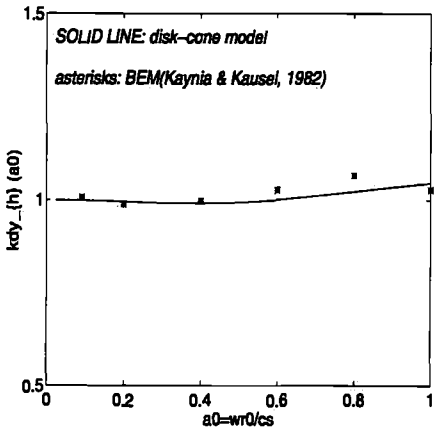

Figure 4.84: Comparison of impedance function $k_{dy,h}$ of disk-cone model and boundary element solution of Kaynia and Kausel, (1982)

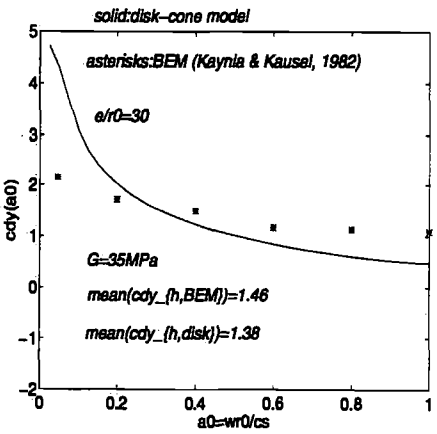

Figure 4.85: Comparison of impedance function $c_{dy,h}$ of disk-cone model and boundary element solution of Kaynia and Kausel, (1982)

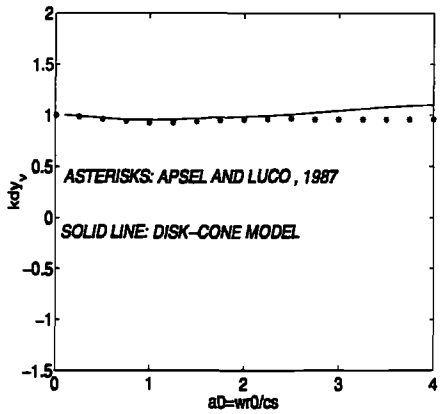

Figure 4.86: Comparison of impedance function $k_{dy,v}$ of disk-cone model and boundary element solution of Apsel and Luco, (1987)

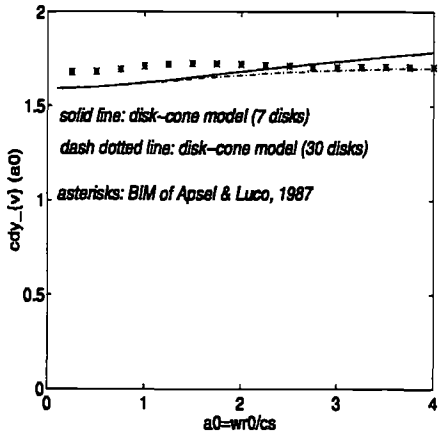

Figure 4.87: Comparison of impedance function $c_{dy,v}$ of disk-cone model and boundary element solution of Apsel and Luco, (1987)

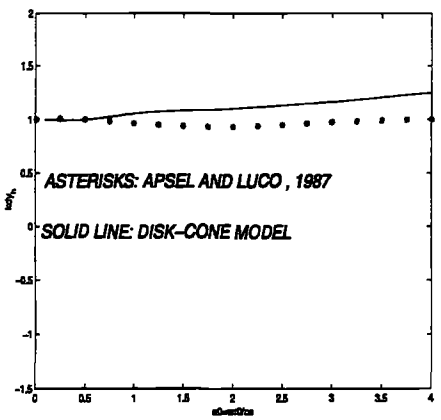

Figure 4.88: Comparison of impedance function $k_{dy,h}$ of disk-cone model and boundary element solution of Apsel and Luco, (1987)

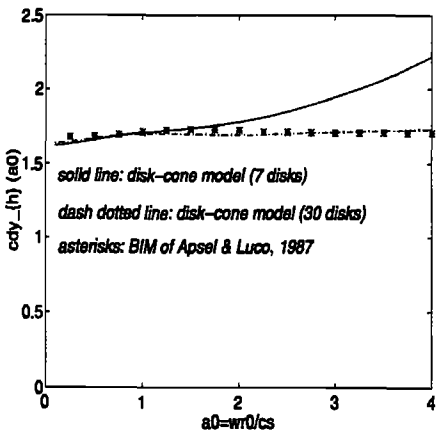

Figure 4.89: Comparison of impedance function $c_{dy,h}$ of disk-cone model and boundary element solution of Apsel and Luco, (1987)

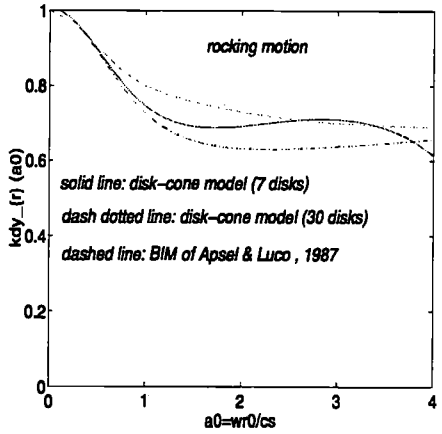

Figure 4.90: Comparison of impedance function $k_{dy,r}$ of disk-cone model and boundary element solution of Apsel and Luco, (1987)

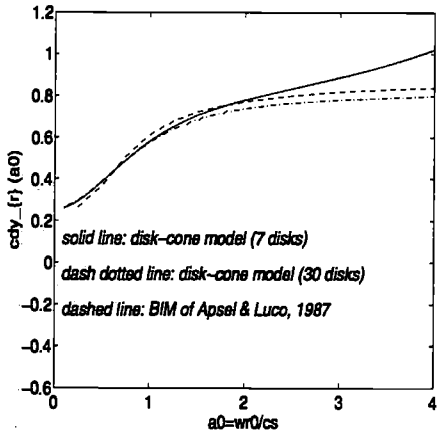

Figure 4.91: Comparison of impedance function $c_{dy,r}$ of disk-cone model and boundary element solution of Apsel and Luco, (1987)

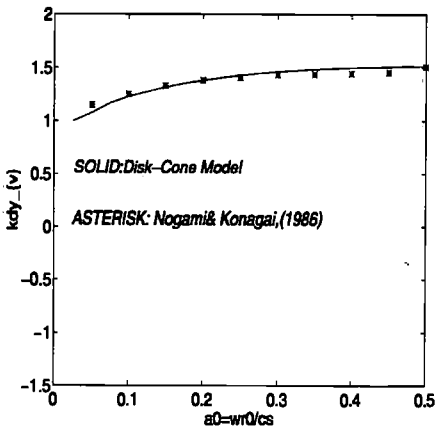

Figure 4.92: Comparison of impedance function $k_{dy,v}$ of disk-cone model and boundary element solution of Nogami and Konagai, (1986)

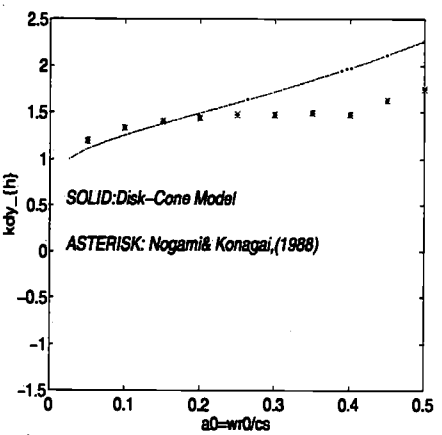

Figure 4.93: Comparison of impedance function $k_{dy,h}$ of disk-cone model and boundary element solution of Nogami and Konagai, (1988)

clay p-y model, has given much larger response than that of the disk model. The fundamental eigen-period of the response associated with the dash dotted curve of API-93 model, is apparently slightly higher than that of the solid line corresponding to the response of the disk model. This is because the corresponding stiffness of API-93 p-y model is less than that of the disk model. This was also observed for the static case in Sec.2.5 of Chapter.2.

The participation of the higher eigen-frequencies are visible in the disk model response curve whereas not seen in the displacement response of API-93 model. The largest peak according to disk model occurs at $t = 8sec$ while for the API-93 model peak resonance is seen at $t = 9.9sec$. A more considerable shift is observed in the API-93 response curve after $t = 8sec$ when the largest ground displacement peak is observed.

In comparison, the response of the disk model has less shifted after $t = 8sec$. The latter observation can also be easily verified by examining the p-y mobilization hysteretic curves for e.g. at depths 0.5m and 10m below the ground as plotted in Fig.4.76.

On the other hand, the peak responses of the two aforementioned models are comparatively closer for the hyper-elastic soil case as shown in Fig. 4.80. It is seen that for the latter case, the disk model response as denoted by the solid line in Fig. 4.80 has a peak of about 0.27m at time $t = 8.66sec$. The response of API-93 model as denoted by dash dotted curve has a peak of about 0.32m at $t = 9.31sec$.

The maximum discrepancy related to the peak response is only about $15\% - 18\%$ which is quite satisfactory in geotechnical terms. However, the eigen-periods of the two responses are quite different as seen, the fundamental eigen-period of the disk model's response in the region of $t = 6 - 10sec$ is almost twice as large as that of API-93 model. This can be verified by examining Fig.4.79. It is observed that the API-93 mobilized p-y curve which is much softer than its disk model counterpart has not reached at the prescribed horizontal motion of ground to its peak point and still can be considered as semi-elastic with much higher current stiffness value than that of the disk model which has already reached the collapse and consequently has resulted in comparatively larger eigen-period of response. This problem is actually due to displacement controlled nature of the response while in a load controlled system one may expect opposite to happen.

4.10.3 Verification cases of impedance functions of pile-soil

The dynamic stiffness parameters so called the impedance functions at the head of pile-soil system are computed for a wide range of frequencies of excitation as $a = 0.01$ to 0.5, 1.0 and compared against rigorous boundary element by Kaynia and Kausel, (1982), the results of direct boundary integral solution by Apsel and Luco, (1987) and also the rigorous solution of Nogami and Konagai, (1986) and (1988) for vertical, horizontal and rocking motions of the pile.

Fig. 4.82 shows the dynamic stiffness function $k_{dy,v}$ as a function of non-dimensionalized frequency $a_0 = \omega r_0/c_s$ for a pile with an embedment ratio of $e/r_0 = 30$ in homogeneous soil with shear modulus of $G = 150MPa$ (see also Table.D.7 of Appendix.D). It is seen that $k_{dy,v}$ of

disk-cone model varies from 1.0 at $a_0 = 0.$ to about 1.3 at $a_0 = 1$ compared to the rigorous BE solution of Kaynia and Kauasel which shows a slight fluctuation about the obtained solution here. The agreement is very good with respect to the selected range of frequencies. The mean value of $k_{dy,v}$ is about 1.18 according to BEM and about 1.14 according to the disk-cone model solution.

Fig. 4.84 shows a comparison between the dynamic impedance function $k_{dy,h}$ for horizontal motion of a foundation with an embedment ratio of $e/r0 = 30$(see Table.D.7of Appendix.D). A slight variation is observed in the dynamic stiffness of the system with increase of the frequency of excitation a_0 from 0 to 1.0. The agreement between the disk-cone results presented here by a solid line and those of boundary element solution of Kaynia and Kausel, (1982) are quite good. The mean values of $k_{dy,h}$ according to BEM and disk-cone models are 1.02 and 1.12, respectively.

The dashpot coefficient $c_{dy,v}$ of a deeply penetrated pile with an embedment ratio of about $e/r_0 = 30$ under vertical motion in a homogeneous soil with the shear modulus of $G = 150MPa$(see Table.D.7) is plotted in Fig. 4.83. The solid line represented the impedance function obtained here by using the disk-cone as described above whereas the asterisks show the BEM results of Kaynia and Kausel, (1982). The correlation between the results are quite good. The average discrepancy is about 6.5 percent for the overall range of a_0. As observed here, the damping coefficient begins from nearly 4.8 at about $a_0 = 0$ and decreases quite rapidly with increasing the frequency of excitation up to about $a_0 = 1$ and afterwards it decreases almost linearly with increasing the frequency of vibration. At the highest limit of the plot $a_0 = 1$ the damping ratio is around 2.0 which is only 42 percent of its static value!

Fig. 4.85 shows the damping function $c_{dy,h}$ for the latter pile-soil system under horizontal motion of ground. The damping coefficient calculated according to the disk-cone model as denoted by the solid line on Fig. 4.85 decreases non-linearly(almost exponentially) from nearly 4.8 at the static case to about 0.50 at $a_0 = 1$.

Fig. 4.92 compares the disk-cone model solution with that of rigorous solution by Nogami and Konagai, (1986) for axial loading of a very deeply embedded pile $e/r_0 = 75$ in a homogeneous layer of soil with a thickness of $d/r_0 = 150$ which is overlying a bed-rock surface(see Table.D.7 of Appendix.D).

It is observed that there is a considerable increase in the vertical dynamic stiffness of the pile-soil system $k_{dy,v}$ over a practical range of frequencies of excitation $a_0 = 0-0.5$. The dynamic stiffness has smoothly increased from unity at or near $a_0 = 0$ to about 1.5 at $a_0 = 0.5$. The agreement for this range of e/r_0 and a_0 is very good.

Fig. 4.93 verifies the results of disk-cone model for $k_{dy,h}$ by using the results obtained by Nogami and Konagai, (1988) for a laterally loaded pile-soil system whose details as given in Nogami and Konagai, (1988).

The results of disk-cone model are also verified against those of a more rigorous direct bound-

ary integral method of Apsel and Luco, (1987) for both axial and lateral loading of embedded foundations. Apsel and Luco, (1987) have presented results for embedment ratios of $e/r_0 = 2.$ which are used in Figs.4.86 through 4.91 for comparison.

The dynamic impedance function $k_{dy,v}$ of the foundation as described in the latter case is compared in Fig. 4.86 with those obtained by Apsel and Luco, (1987). Similar to the horizontal case, the normalized dynamic axial stiffness of the analyzed shallow foundation varies slightly from unity (its static stiffness). These results may imply that for a small embedment ratio, the translational dynamic stiffness of foundation can be assumed as the static stiffness for a time-domain analysis.

The impedance function $k_{dy,h}$ of a shallow foundation with an embedment ratio of about $e/r0 = 2$ under horizontal motion computed according to the disk-cone model and the rigorous boundary integral method of Apsel and Luco, (1987) are compared in Fig. 4.88. It is observed that the normalized lateral stiffness has a small variation about the unity, for the overall agreement between the results of disk-cone model and those of the Apsel and Luco, (1987) is quite good. The mean discrepancy is about 8 percent.

Fig. 4.90 shows the dynamic impedance function $k_{dy,r}$ for the rocking motion of an embedded foundation with an embedment ratio of $e/r0 = 2$ in a homogeneous soil with shear modulus of $G = 35MPa$ and $\nu = 0.4$ (see Table.D.7 of Appendix.D).

It is observed that the dynamic stiffness response computed by disk-cone model as described above, well agrees with the results of rigorous boundary integral method by Apsel and Luco, (1987). The solid line represents the $k_{dy,r}$ computed by modelling the foundation system with only 7 disks while the dash dotted line represents the $k_{dy,r}$ computed based on a much finer model of 30 soil disks. It can be seen that even with only 7 disks the dynamic response of the foundation is very closely predicted. For this shallow foundation, using 5-7 disks provides quite satisfactory results in practical terms. The normalized rocking stiffness is about unity for the static case $a_0 = 0$ while it decreases rapidly for higher frequencies up to $a_0 = 1$ for frequencies higher than $a_0 = 1$ there is slight variation of $k_{dy,r}$.

The dashpot coefficient of the latter foundation under vertical motion $c_{dy,v}$ is plotted in Fig. 4.87. The solid line represents the response of the disk-cone model by using only 7 disks whereas the dash dotted line denotes the computed response according to much finer model of 30 soil disks. These results are compared in the same plot with the dynamic vertical stiffness obtained by Apsel and Luco, (1987) based on boundary integral method. It is observed that though there is small discrepancy for the frequency range lower than about $a_0 = 2$, nevertheless, the overall agreement is quite good. For the finer mesh of 30 disks the obtained dynamic stiffness for the higher frequency range (i.e. $a_0 > 2.5$) is almost exact in comparison with the rigorous BIM solution of Apsel and Luco, (1987).

The plotted response in Fig. 4.87 compares the modelling effect on the dynamic impedance function as well. The solid line represents the response of the disk-cone model by using only 7 disks

whereas the dash dotted line denotes the computed response according to much finer model of 30 soil disks. These results are compared in the same plot with the dynamic vertical stiffness obtained by Apsel and Luco, (1987) based on boundary integral method. It is observed that though there is small discrepancy for the frequency range lower than about $a_0 = 2$, nevertheless, the overall agreement is quite good. For the finer mesh of 30 disks the obtained dynamic stiffness for the higher frequency range (i.e. $a_0 > 2.5$) is almost exact in comparison with the rigorous BIM solution of Apsel and Luco, (1987).

Fig. 4.89 shows the damping coefficient $c_{dy,h}$ under horizontal motion of the latter described foundation. The solid line represents the computed $c_{dy,h}$ according to the disk-cone models with 7 elements, while the dash dotted line indicates the results obtained here by using 30 disk-cone elements. The asterisks denote the results obtained by Apsel and Luco, (1987) based on boundary integral method. The correspondence between the these latter results is extremely close. The discrepancy in this case is even less than one percent.

The dashpot coefficient $c_{dy,r}$ of the latter foundation under rocking motion is shown in Fig. 4.91. It is observed that damping coefficient starts from nearly 0.21 at $a_0 = 0$ for the static case and increases non-linearly with the frequency of excitation a_0 towards an asymptotic value of about 0.8 near $a_0 = 4$. It is seen that the damping coefficient computed according to the disk-cone model by using about 7 disks which is represented by solid line on Fig. 4.91 has been well estimated for the lower frequency range of $a_0 = 0 - 2$, while it has been overpredicted for higher frequencies than this. The dash dotted line corresponding to a pile modelled by 30 disk elements, has represented more accurately the response of disk-cone model with only 2-5 percent discrepancy for the overall range of a_0. The obtained results are excellent with considering the simplicity of the disk-cone model compared to the referred rigorous solution methods.

4.10.4 Economic comparison of disk-cone and rigorous methods

The computer(CPU) time required to calculate these dynamic stiffness and damping properties of disk-cone model ranges between 1-5 minutes compared to several hours needed for the rigorous methods such as boundary element method.

For a single pile-soil system modelled by 30 disks the required time was about 5 mins compared to 1min for a 5 disk model of the same system.

4.11 Illustrative examples of simplified systems

Figs.4.95 through 4.99 show three examples of simple SDOF systems under the earthquake acceleration.

The natural eigen-period of the first SDOF system is about $T_n = 1.74sec.$ The response of linear and non-linear systems are plotted in Figs.4.95 and 4.94, respectively.

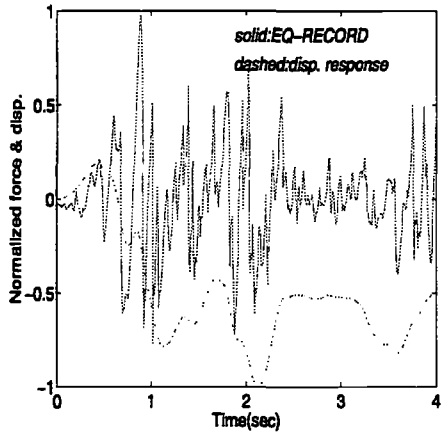

Figure 4.94: Normalized ground acceleration and displacement response histories of a nonlinear SDOF system under seismic loading $Tn = 1.74sec$

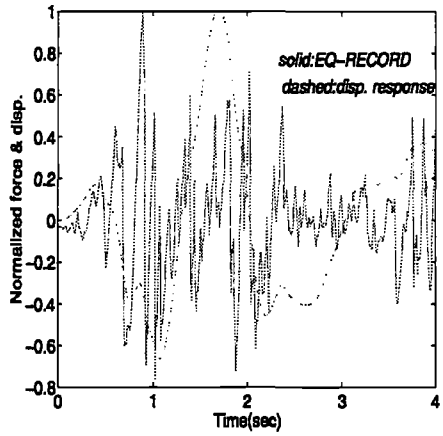

Figure 4.95: Normalized ground acceleration and displacement response histories of a linear SDOF system under seismic loading $Tn = 1.74sec$

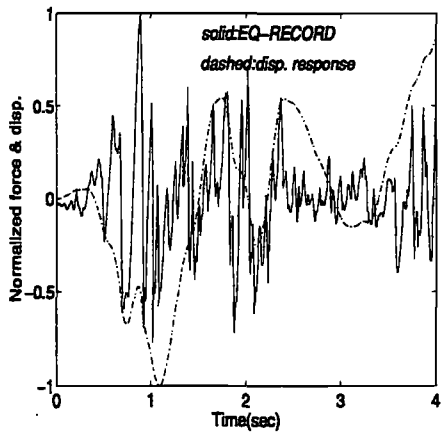

Figure 4.96: Normalized ground acceleration and displacement response histories of a nonlinear SDOF system under seismic loading $Tn = 0.43sec$

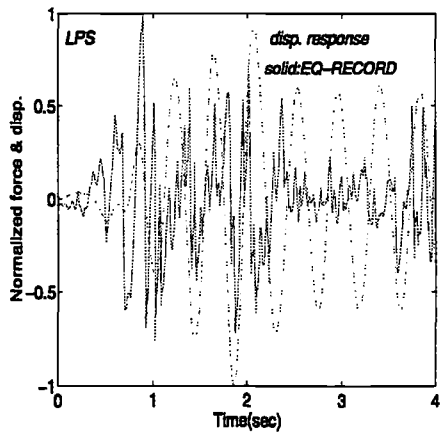

Figure 4.97: Normalized ground acceleration and displacement response histories of a linear SDOF system under seismic loading $Tn = 0.43sec$

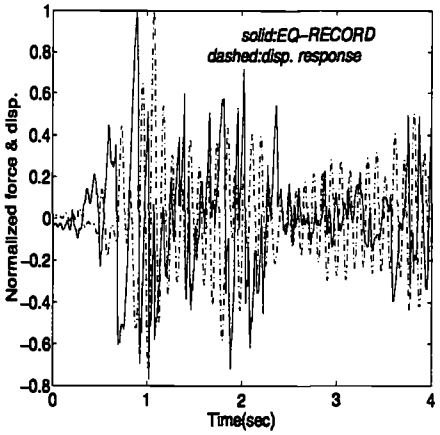

Figure 4.98: Normalized ground acceleration and displacement response histories of a non-linear SDOF system under seismic loading $Tn = 0.087sec$

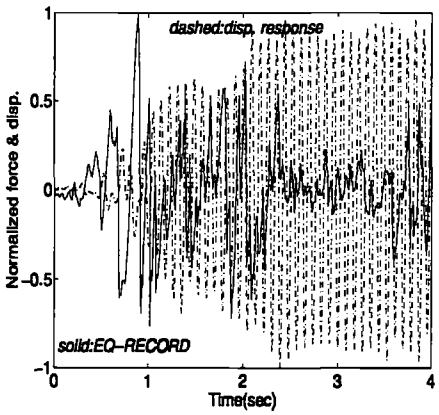

Figure 4.99: Normalized ground acceleration and displacement response histories of a linear SDOF system under seismic loading $Tn = 0.087sec$

The peak displacement response of the linear system as plotted in Fig. 4.95 has occurred at $t = 1.75secs$ while the peak acceleration of the ground has been observed at about $t = 0.87sec$. The displacement response for the linear case corresponds to the ground displacement rather than the ground acceleration.

In comparison, for the nonlinear soil system, the peak displacement response as shown in Fig. 4.94 has occurred at about $t = 2.2secs$, whereas the maximum ground acceleration is observed at $t = 0.87sec$. The peak displacement response is about $0.076m$ for this simple system.

The displacement response of a linear SDOF system with a natural period of about 0.43 is plotted in Fig. 4.97. It is observed that the peak displacement has occurred at $t = 1.85secs$ which has about 1.0 sec time lag with that of the peak ground acceleration. In contrast, the response of the non-linear pile-soil system shows a peak at about $t = 1.1sec$ which is about 0.25 sec after that of the peak ground acceleration. The eigen-period of the response is apparently influenced by the soil non-linearities. This has been manifested in the increased eigen-period of the response due to reduced stiffness after yielding of the soil. The peak ground displacement is 0.24m in this case compared with the smaller value of 0.125m in the linear case.

Fig. 4.99 shows the displacement response of another SDOF system with a natural period of $0.087sec$ under the plotted acceleration of the ground. It is observed that a resonance has occurred just after the peak acceleration of the ground. The observed resonance is due to the proximity of the natural fundamental period of the system to that of the ground input motion. By contrast, the resonance effect is not observed in Fig. 4.98 for the non-linear soil case due to the in-elastic hysteretic damping occurring in the soil and changes in the natural period of the system as a function of the system's tangent stiffness. The peak displacement in the system is

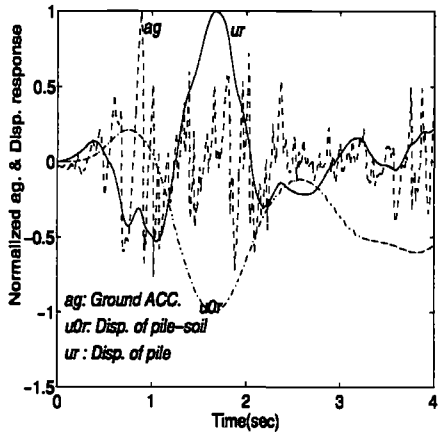

Figure 4.100: The normalized ground acceleration and the displacement response of a linear 2DOF system under a scaled EQ-record with max Acc=3.42g on an OC type clayey soil

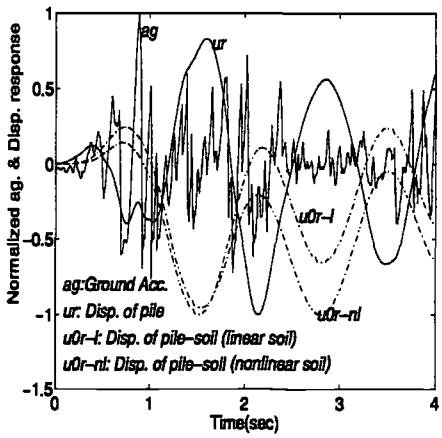

Figure 4.101: The normalized ground acceleration and the displacement response of a non-linear 2DOF system under an un-scaled EQ-record with max.acceleration=0.34g on an OC type clayey soil with linear and non-linear soil response

about 26mm which is sufficient to cause yield of the soil.

As an example of a simple system of pile-soil, Figs.4.100 and 4.101 show the displacement response of linear and non-linear 2DOF systems, respectively, in which one degree of freedom represents the displacement response of the soil and the other dof denotes the distortion of the pile's structural element.

Fig. 4.102 shows the displacement response of another equivalent lumped model of pile-soil system with 3DOFs representing, the translational motion of pile and soil and rotational displacement of soil, respectively. The mass of the system is subjected to an acceleration history of a corrected earthquake (Taft-EQ) for a duration of only 4secs (time of the record is scaled by a factor of 5). The maximum acceleration of the ground which is un-scaled is about 0.34g at time 0.87sec.

The soil condition is assumed to be heavily overconsolidated (OC) clay as typical of North-sea offshore sites. The solid line represents the distortion of the pile element itself while the dash dotted and heavy solid lines denote those of the soil. Amplification of the response is observed after the peak ground acceleration has passed which is due to the eigen-period of the system which is very close to that of the ground-disp $1.23sec$. The peak distortion of the pile is about 0.06m at time $t = 3.4sec$ vs. peak displacement of soil as $0.05m$ at $t = 3.2sec$ and that of the pile-soil system rotation as 0.0025rad at $t = 3.4sec$. The rotational displacement shows that foundation has tilted towards one side and also the translational response of soil has shifted

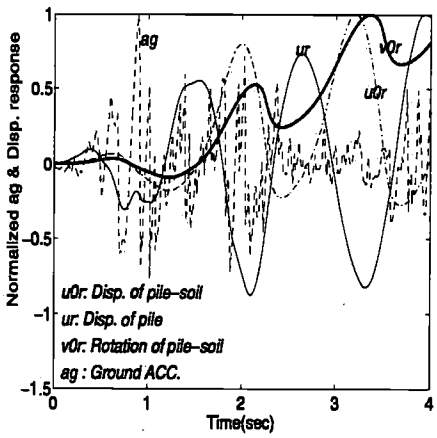

Figure 4.102: Normalized ground acceleration and Displacement response ur of pile distortion, $u0r$ the pile-soil displacement and $v0r$ the pile-soil rotation a non-linear 3dof system with a natural period of $T_n = 1.23s$ ($T_d = 4sec$)

somewhat due to its plastic yield.

4.12 Summary of other parametric studies by using simplified methods

The Fig. 4.103 through 4.108 show the results of the analysis by applying the described simplified pile-soil systems in the previous sections.

These first set of plots show that the normalized dynamic stiffness coefficient of a single rigid pile under vertical motion. It's assumed that the embedment ratio $e/r0$ varies between 10 to about 30 to simulate shallow to very deep foundations. r_0 is considered as the radius of the pile and throughout this section is assumed as 0.5 or diameter of pile as 1.00. The other pertinent parameters are given in Appendix.D.

Each embedded foundation (or pile) is subjected to a seismic wave which induces the loading on each assumed pile-soil disk idealizing the pile-soil interaction as defined earlier in Chapter.2. It may be assumed that an initial incident dilatational type (compressive or P) has induced the vertical motion of the disks (pile-soil). The pile is assumed as rigid and no material damping is introduced into the system. Hence, the reducing effects of the linear hysteretic damping as discussed earlier and that of attached trapped mass underneath the pile-soil disk will not be considered in this set of parametric study.

It is observed that the spring coefficient or the real part of the dynamic stiffnesses does not

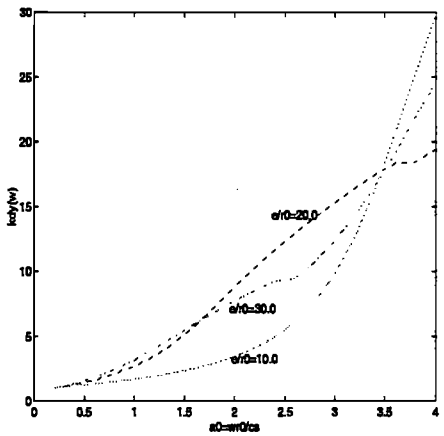

Figure 4.103: Dynamic axial spring coefficient of pile-soil system vs. non-dimensional frequency a0 for embedment ratios $e/r0$ =10,20 and 30

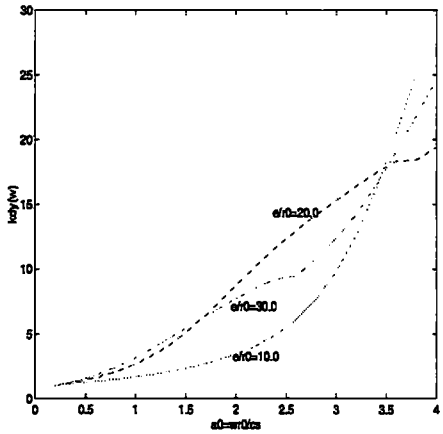

Figure 4.104: Dynamic axial dashpot coefficient of single pile-soil system vs. non-dimensional frequency a0 for embedment ratios $e/r0$ =10.0,20 and 30

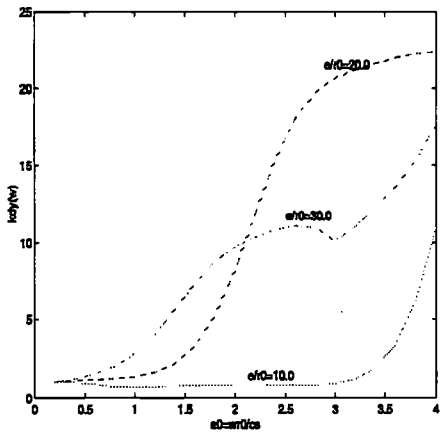

Figure 4.105: Dynamic lateral spring coefficient of single pile-soil system vs. non-dimensional frequency a0 for embedment ratios $e/r0$ =10,20 and 30

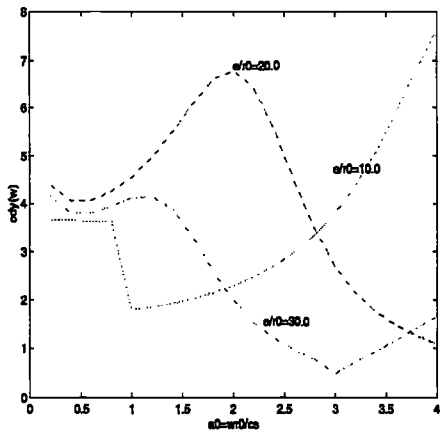

Figure 4.106: Dynamic lateral dashpot coefficient of single pile-soil system vs. non-dimensional frequency a0 for embedment ratios $e/r0$ =10.0,20 and 30

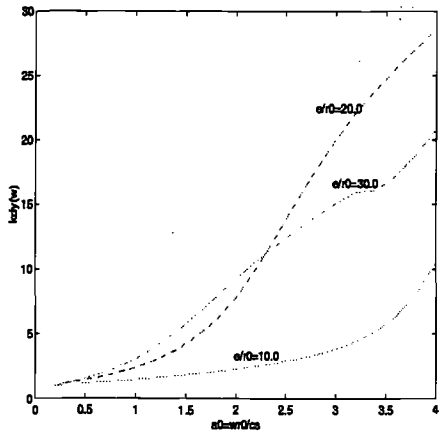

Figure 4.107: Dynamic rotational(rocking) spring coefficient of single pile-soil system vs. non-dimensional frequency a0 for embedment ratios $e/r0$ =10,20 and 30

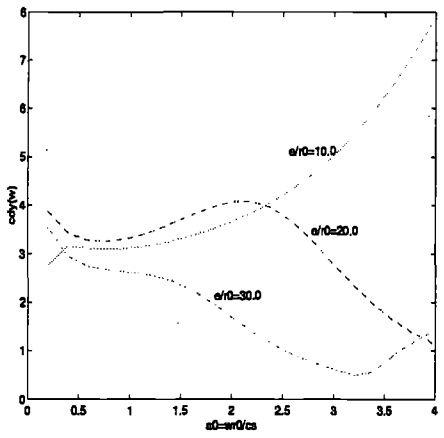

Figure 4.108: Dynamic rotational(rocking) dashpot coefficient of single pile-soil system vs. non-dimensional frequency a0 for embedment ratios $e/r0$ =10.0,20 and 30

vary very significantly for the range of frequency of excitation typical for extreme sea waves or even low seismic waves. However, there are significant variations for the higher frequencies of vibration than for e.g. ($a_0 = 0.5$). It may be noteworthy that this sort of variations may not be seen in the real pile-soil system with the corresponding embedment ratios, due to the reducing effects of inertia associated with the pile/soil mass, the material damping effects and the pile's flexibility(possible yield). This example is intended to only illustrate the variability of the stiffness parameters of the pile-soil with the frequency of vibration.

It can also be observed that the dashpot coefficient is also more or less constant with increasing the frequency of input excitation ω for the range of extreme sea waves.

The other feature about these results is that, the dynamic spring and dashpot coefficients increase by an increase in embedment ratio $e/r0$. However, the rate of increase is not linear and as shown in the plot. But even for the case of a rigid pile, there is a difference between the two curves (K_s vs. $e/r0$ and C_d vs. $e/r0$).

The dynamic stiffness coefficients for a rigid pile under horizontal motion are simulated in Figs.4.105 and 4.106 . It is assumed that the piles (foundations) have been subjected to vertically propagating shear waves (S_v).

The plotted k_{dy} and c_{dy} curves in Figs.4.103 to 4.106 show somewhat variation with the non-dimensionalized frequency $a_0 = \frac{\omega r_0}{c_s}$ for the typical range of frequency of excitation of extreme sea waves or low frequency seismic waves, however these fluctuations are not very significant and can be neglected for practical purposes. Thus using an equivalent non-linear static stiffness

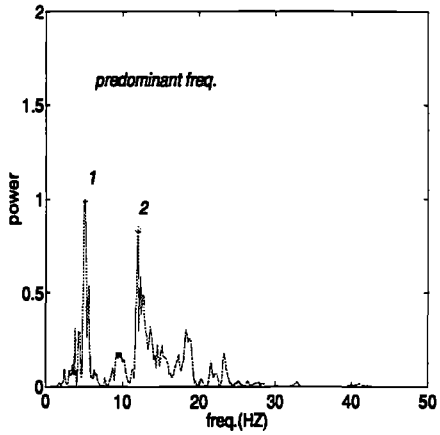

Figure 4.109: Power spectrum of the ground effective input acceleration

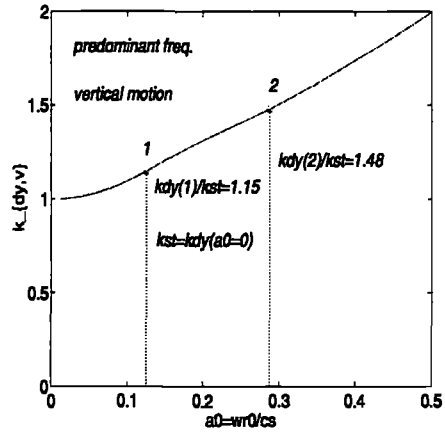

Figure 4.110: k_{dy} for dominant frequency of excitation

$k_{ps}(\omega = 0)$ and $c_{ps}(\omega = 0)$ may not result in a significant loss of accuracy in a dynamic stiffness formulation.

It is observed that the stiffness parameter $k_{ps}(\omega)$ increases non-linearly and almost exponentially with increasing the depth of the foundation $e/r0$. It may be worth mentioning that in a real practical case where a pile has a finite stiffness (flexible) the latter results may not be applied particularly for larger $e/r0$ ratios. In the latter cases, the pile -soil interaction as shown in Chapter.2 for a static case, can only be mobilized down to a certain depth of pile and increasing the pile may be considered approximately fixed at that level against any lateral movement so that further adding the pile length may not increase the lateral capacity of the pile. Such effective length of the pile may also be implemented explicitly in the above procedure for a rigid pile calculation to obtain reasonable results for practical cases with large $e/r0$ ratios as:

$$(e/r0)^{flexible} = \alpha_{eff}(e/r0)^{rigid} \tag{4.248}$$

where α_{eff} represents the effective pile length ratio. The evaluation of the dynamic stiffness values for rocking and torsional degrees of freedom have also been shown in Figs.4.107 and 4.108.

It is observed that the response under the rocking (rotational) motion is significantly different from vertical and horizontal (translational) cases as observed before. In the latter case the dynamic spring coefficient $k_{ps}(\omega)$ and the dashpot coefficient $c_{ps}(\omega)$ vary dramatically and non-linearly from near zero to much larger values than unity at higher frequencies $a_0 \geq 3-4$ or $\omega = (3-4)c_s/r0$.

Also the $c_{ps}(a_0)$ curves have an asymptotic part which as described above for larger $a_0 \geq 3-4$ may be approximately considered constant for low embedment ratios(shallow type foundations).

On the other hand, the dynamic spring coefficient, $k_{ps}(a_0)$ varies with lesser intensity with a_0 for shallow foundations. However, the rate of variation as for other previous rigid pile cases increases rapidly and exponentially as the embedment ratio increases towards large numbers (about 100 i.e. infinitely long piles).

It may also be assumed that for shallow foundations $k_{ps}(\omega) = cte$. However, it would be more relevant to determine the dynamic stiffness coefficient according to the dominant frequency of the excitation ω_{peak}. As illustrated in Figs.4.109 and 4.110 for an example of the seismic analysis of a pile-soil system in a homogeneous layer of OC clayey soil with $G = 35MPa$ and $\nu = 0.4$ and pile embedment ratio of $e/r_0 = 30$ subjected to a vertical ground acceleration with the plotted power spectrum, the peak powers occur at two distinct frequencies of ground oscillation, $\omega_1 = 5.1HZ$ and $\omega_2 = 12HZ$ which are typical of a high frequency seismic oscillation. The corresponding dynamic stiffness of the predominant peaks denoted by 1 and 2 are shown in Fig. 4.110. The ratio of the corresponding dynamic stiffness of the pile-soil system to its static one $k_{dy,v}(1)/k_{st} = 1.15$ and $k_{dy,v}(2)/k_{st} = 1.48$, where $k_{st} = k_{dy,v}(a_0 = 0)$.

These obtained ratios indicate that the axial dynamic stiffness of the pile-soil system can be significantly modified due to the acceleration of the ground. It may be shown that for a low frequency of vibration such as corrected and scaled TAFT-EQ used in simulations above, the predominant frequencies associated with the peak powers as plotted in Fig. 4.109 are far lower than 2HZ (0.51HZ and 1.2HZ, respectively). The corresponding normalized dynamic axial stiffnesses of the pile-soil system are about 1.007 and 1.01 which are quite close to that of the static one ($k_{dy,v} = 1$). This would indicate that taking the static stiffness for the time-domain analysis in the related simulations is well justified.

However, for the cases that the time axis of the earthquake or the duration was scaled which resulted in higher frequency vibrations, the dynamic stiffness and damping coefficients were obtained from the frequency domain analyses and used for the time-domain analysis. In this manner, the frequency effects are also taken into account in the time domain analysis. For very low frequency of excitation, $k_{ps}(\omega)$ can be assumed as the static spring coefficient or $k_{ps}(0)$.

It is observed that for the higher frequency of excitation than $a_0 = 3 - 4$, the dynamic stiffness of a rigid-pile in elastic half-space dramatically increases. In contrast, for a flexible pile with non-linear soil assumption, the maximum dynamic stiffness for $a_0 = 3 - 4$ is several times smaller. However, for the extreme sea waves and strong seismic motions, the dominant frequency of content is usually lower than this range for which the discrepancy can be expected to be small.

$$\epsilon_{ks} = \frac{dk_{ps}}{de/r0} \tag{4.249}$$

in which ϵ_{ks} may characterize the variability of the dynamic stiffness of the spring with respect to the embedment ratio. It is evident that the influence of the pile's stiffness is more significant for the case of rocking and torsional degrees of freedom.

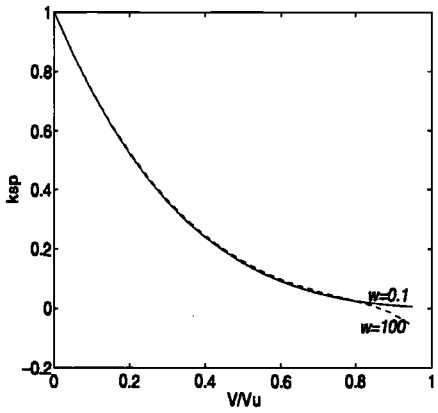

Figure 4.111: Dynamic axial spring coefficient of single pile-soil system vs. vertical loading ratio V/V_u for ω =0.1 and 100HZ with embedment ratio $e/r0 = 10$

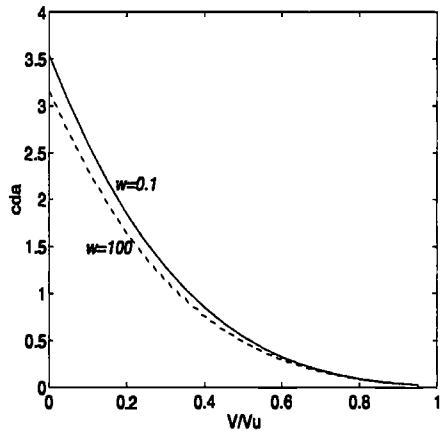

Figure 4.112: Dynamic axial dashpot coefficient of single pile-soil system vs. vertical loading ratio V/V_u for $\omega = 0.1$ and 100HZ with embedment ratio $e/r0 = 10$

It can be seen that for higher frequencies than $a_0 = 4$, the dynamic spring coefficients may decrease for even translational motions (horizontal). Such variations may imply taking some degree of caution in applying any constant value of spring coefficient in general.

Figs.4.111 through 4.128 show the results of parametric study by using above described models. The effects of several key parameters in the dynamic response of the pile-soil can be studied through these results.

The studied parameters include, the hysteretic damping ratio for the pile and soil, the radiation damping effects, the pile's slenderness or embedment effects etc. The influence of the non-linear and hysteretic energy absorption on the equivalent pile-soil system response is also considered.

The cost effective feature of the applied approach together with the good performance of the models discussed would be a preference in comparison to accurate but rigorous elasto-dynamic solutions as boundary element method of Kaynia and Kausel, (1982) and other less accurate and much more time consuming non-linear approaches such as Pseudo-dynamic methods etc.

The effects of several key parameters such as load ratio, frequency of excitation and embedment ratio on the dynamic stiffness and damping coefficients for vertical, horizontal and rocking motions for a semi-infinite homogeneous soil are shown in Figs.4.111 through 4.128. It is observed that the dynamic stiffness of the embedded foundation decreases almost exponentially towards zero with the increase of the loading ratio towards unity. For higher frequency limits ($\omega = 100$), significant variations are observed in the value of the $k_{dy,v}$ function for axial load ratio $v/v_u > 0.5 - 0.7$. For deeper embedment ratios $e/r_0 = 50$, the observed fluctuations begin from

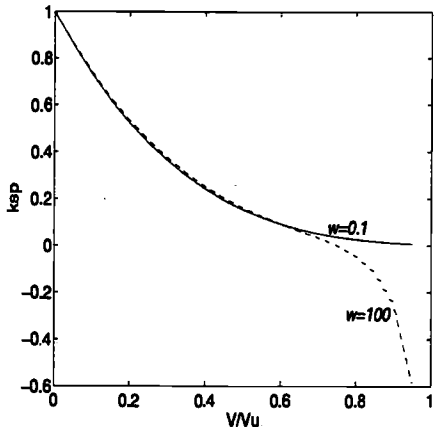

Figure 4.113: Dynamic axial spring coefficient of single pile-soil system vs. vertical loading ratio V/V_u for $\omega = 0.1$ and 100HZ with embedment ratio $e/r0 = 20$

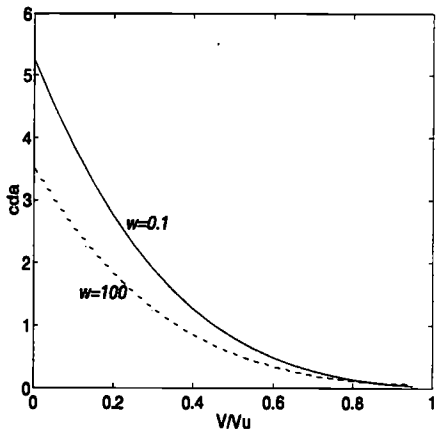

Figure 4.114: Dynamic axial dashpot coefficient of single pile-soil system vs. vertical loading ratio V/V_u for $\omega = 0.1$ and 100HZ with embedment ratio $e/r0 = 20$

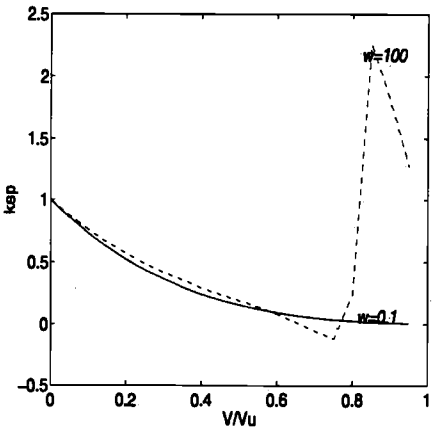

Figure 4.115: Dynamic axial spring coefficient of single pile-soil system vs. vertical loading ratio V/V_u for ω =0.1 and 100HZ with embedment ratio $e/r0 = 50$

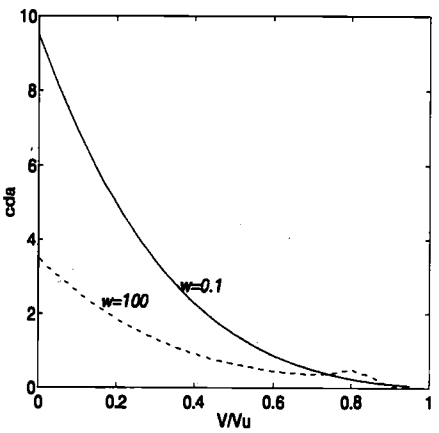

Figure 4.116: Dynamic axial dashpot coefficient of single pile-soil system vs. vertical loading ratio V/V_u for $\omega = 0.1$ and 100HZ with embedment ratio $e/r0 = 50$

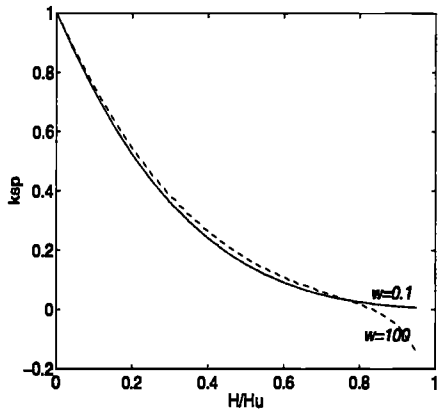

Figure 4.117: Dynamic lateral spring coefficient of single pile-soil system vs. horizontal loading ratio H/H_u for ω =0.1 and 100HZ with embedment ratio $e/r0 = 10$

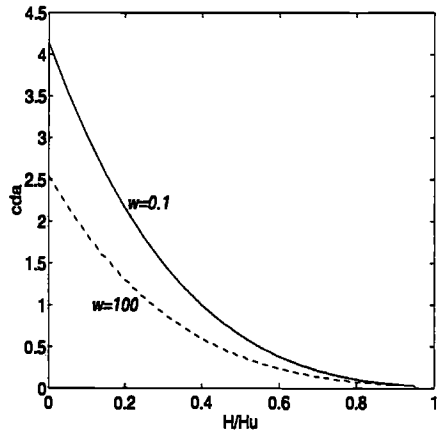

Figure 4.118: Dynamic lateral dashpot coefficient of single pile-soil system vs. horizontal loading ratio H/H_u for ω = 0.1 and 100HZ with embedment ratio $e/r0 = 10$

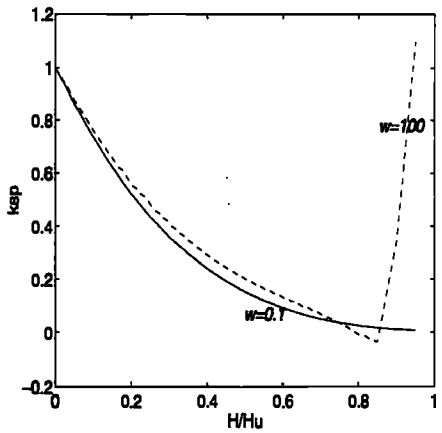

Figure 4.119: Dynamic lateral spring coefficient of single pile-soil system vs. horizontal loading ratio H/H_u for ω =0.1 and 100HZ with embedment ratio $e/r0 = 20$

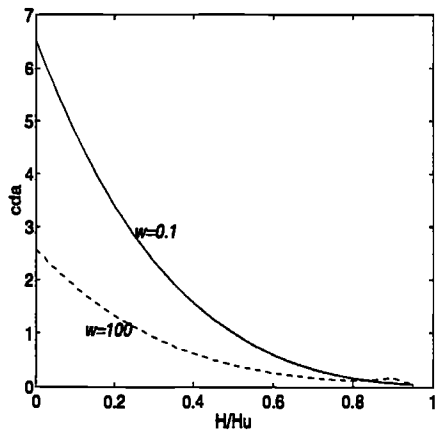

Figure 4.120: Dynamic axial dashpot coefficient of single pile-soil system vs. horizontal loading ratio H/H_u for ω = 0.1 and 100HZ with embedment ratio $e/r0 = 20$

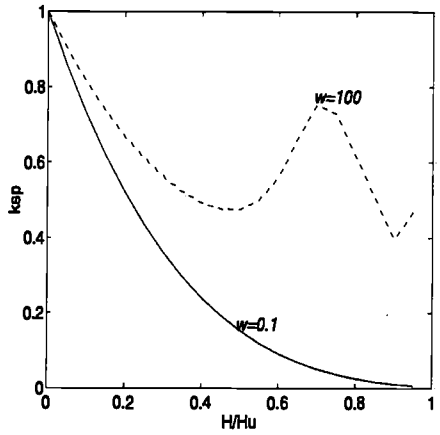

Figure 4.121: Dynamic lateral spring coefficient of single pile-soil system vs. horizontal loading ratio H/H_u for ω =0.1 and 100HZ with embedment ratio $e/r0 = 50$

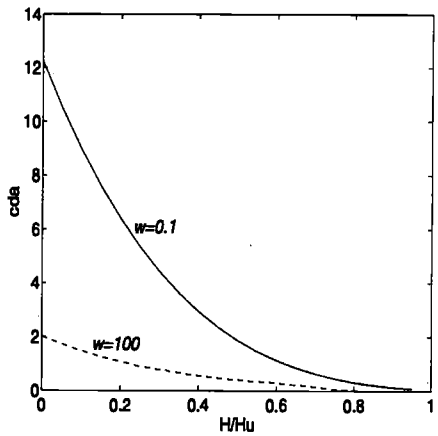

Figure 4.122: Dynamic lateral dashpot coefficient of single pile-soil system vs. horizontal loading ratio H/H_u for $\omega = 0.1$ and 100HZ with embedment ratio $e/r0 = 50$

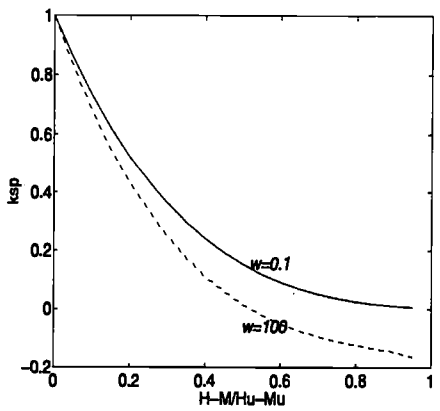

Figure 4.123: Dynamic rocking spring coefficient of single pile-soil system vs. bending moment ratio M/M_u for ω =0.1 and 100HZ with embedment ratio $e/r0 = 10$

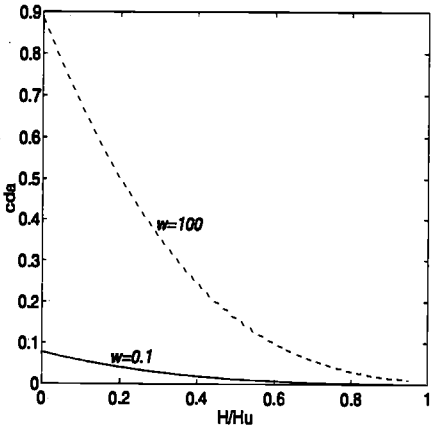

Figure 4.124: Dynamic rocking dashpot coefficient of single pile-soil system vs. bending moment ratio M/M_u for $\omega = 0.1$ and 100HZ with embedment ratio $e/r0 = 10$

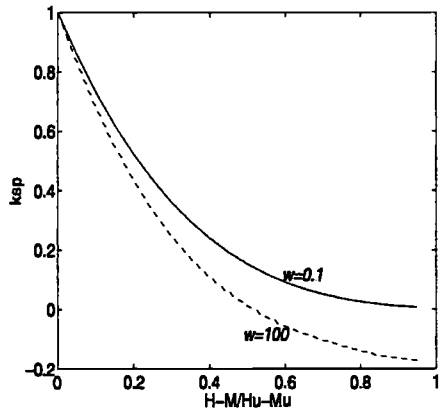

Figure 4.125: Dynamic rocking spring coefficient of single pile-soil system vs. bending moment ratio M/M_u for ω =0.1 and 100HZ with embedment ratio $e/r0 = 20$

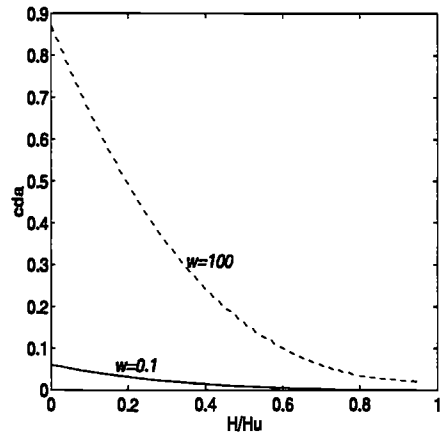

Figure 4.126: Dynamic rocking dashpot coefficient of single pile-soil system vs. bending moment ratio M/M_u for ω = 0.1 and 100HZ with embedment ratio $e/r0 = 20$

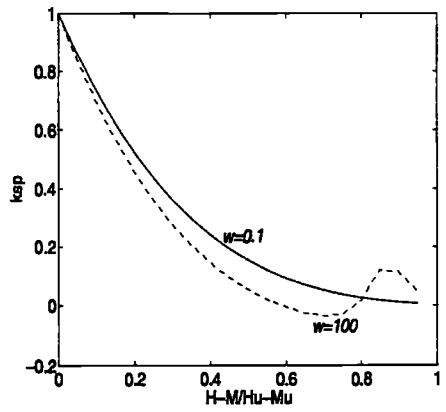

Figure 4.127: Dynamic rocking spring coefficient of single pile-soil system vs. bending moment ratio M/M_u for ω =0.1 and 100HZ with embedment ratio $e/r0 = 50$

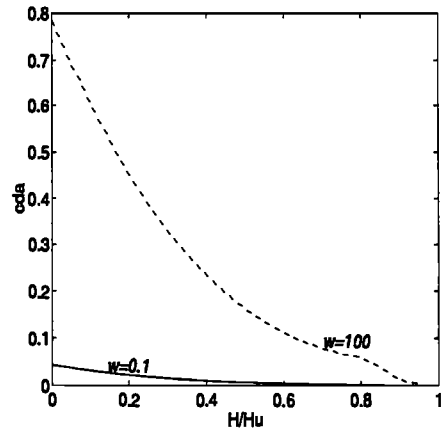

Figure 4.128: Dynamic rocking dashpot coefficient of single pile-soil system vs. bending moment ratio M/M_u for ω = 0.1 and 100HZ with embedment ratio $e/r0 = 50$

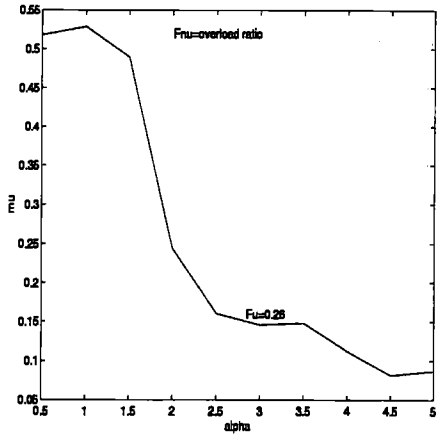

Figure 4.129: Ductility demand ratio of a single pile-soil system vs. the natural period ratio $\alpha = T_n/T_0$ for an overload ratio of $F_\nu = 0.26$

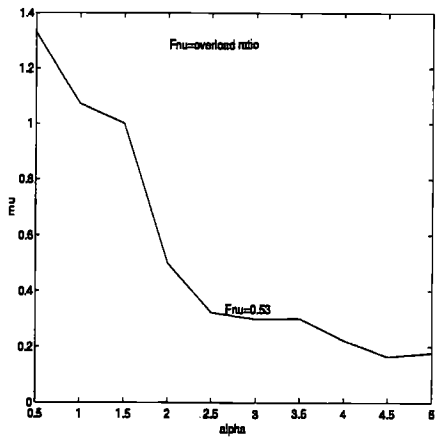

Figure 4.130: Ductility demand ratio of a single pile-soil system vs. the natural period ratio $\alpha = T_n/T_0$ for an overload ratio of $F_\nu = 0.53$

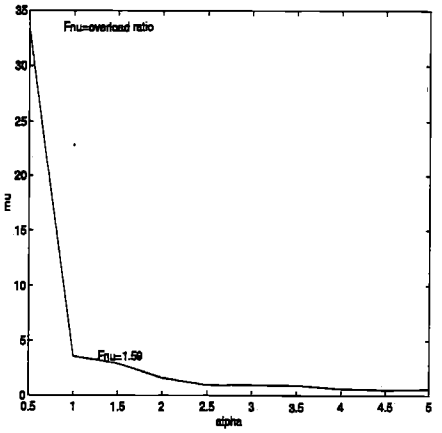

Figure 4.131: Ductility demand ratio of a single pile-soil system vs. the natural period ratio $\alpha = T_n/T_0$ for an overload ratio of $F_\nu = 1.59$

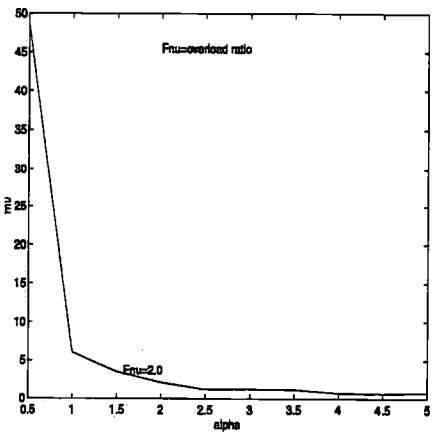

Figure 4.132: Ductility demand ratio of a single pile-soil system vs. the natural period ratio $\alpha = T_n/T_0$ for an overload ratio of $F_\nu = 2.0$

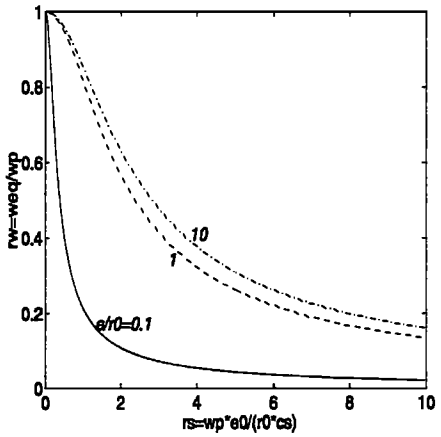

Figure 4.133: Variation of the frequency ratio $r\omega$ a single pile-soil system with the pile's embedment e

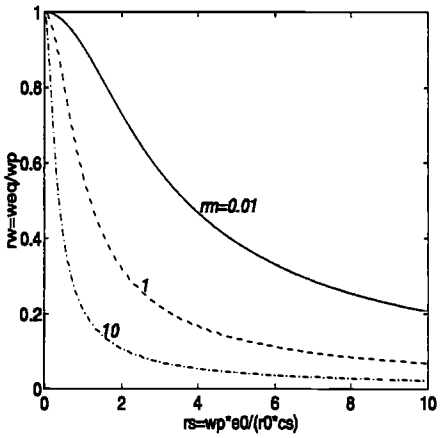

Figure 4.134: Variation of the frequency ratio $r\omega$ a single pile-soil system with the mass parameter $rm = m_{pile}/m_{soil}$

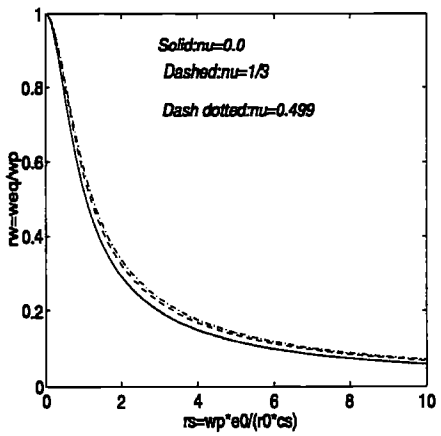

Figure 4.135: Variation of the frequency ratio $r\omega$ a single pile-soil system with the poisson's ratio of soil

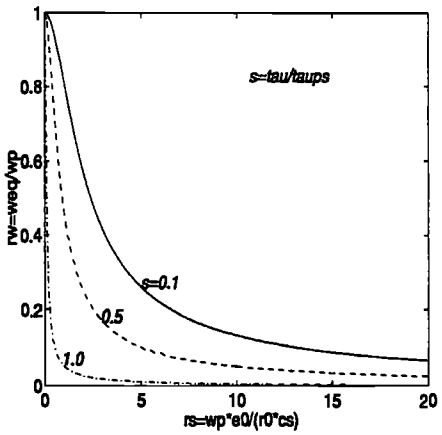

Figure 4.136: Variation of the frequency ratio $r\omega$ a single pile-soil system with the shear stress ratio of soil $s = \tau/\tau_{ps}$

$v/v_u > 0.6$ as seen in Fig. 4.115 while for the lower embedment ratio $e/r_0 = 10$, considerable variations occur after $v/v_u = 0.8$ as seen in Fig. 4.111. More significant variations are observed for the largest embedment ratio ($e/r_0 = 50$).

For the horizontal motion of the shorter pile, the dynamic stiffness $k_{dy,h}$ decreases almost exponentially up to the collapse load. For $e/r_0 = 50$, $k_{dy,h}$ decreases up to a load level of about $H/H_u = 0.4$ from where some fluctuations are observed in the value of the impedance function. As shown in Fig. 4.117, the amplitude of the variation of $k_{dy,h}$ decreases towards the ultimate capacity of the pile. In comparison for the deeply embedded pile with $e/r_0 = 20$, a very significant variation is observed at about $H/H_u = 0.9$. This may be interpreted as the change in the phase of response with respect to the wave propagation at this point due to change in the tangent stiffness of the pile-soil system which may have been caused the system to respond out of phase with the input excitation.

For the rocking motion, the near static (low frequency limit) of the normalized dynamic stiffness decreases exponentially from unity towards the zero at a bending moment ratio $M/M_u = 1.0$. A peak is observed for the high frequency range at about $M/M = 0.85$ for the embedment ratio of $e/r_0 = 50$. The amplitude of the variation generally decreases as the load ratio increases.

For the lower embedment ratio, the amplitude and the corresponding load levels, the fluctuations of the dynamic stiffness related to the higher frequency limit are smaller than those observed for higher embedment ratios.

For very deep foundation with $e/r_0 = 50$, the variation is much more significant and at much higher load level $M/M_u = 0.8 - 0.9$. At the observed peak in Fig. 4.127 the absolute value of the corresponding dynamic stiffness is about 6 times of that for static one.

The damping coefficient of the vertically loaded pile $c_{dy,v}$ decreases non-linearly from a static value towards zero. For the latter frequency limit the dynamic stiffness coefficient of dashpot is lower than that of the low frequency (static case) up to almost collapse. For the $e/r_0 = 50$ case, it exceeds that of the the low frequency limit after $V/V_u = 0.77$. A small peak is observed at a load level of about $V/V_u = 0.8$ which corresponds to the change in the dynamic characteristic of the system with respect to its tangent stiffness and the frequency limit.

It is seen in Fig. 4.116 the dashpot coefficient under vertical loading of the pile with embedment ratio of e/r_0 is far smaller for the high frequency limit of $\omega = 100$ than the low frequency limit, for the lower load ratios up to $V/V_u = 0.7$. At $V/V_u = 0.8$, the damping parameter $c_{dy,v}$ reaches a small peak and after that it decreases towards zero. The ratio of $c_{dy,v}$ of the high frequency to that of low frequency limit at zero load level is about 0.37. This reduction in the damping is also expected from the earlier discussion about the cone model's behaviour. We observed above that the damping ratio can be far greater for the low frequencies than that of high frequencies of vibration for translational motion of pile.

For the horizontal case, the same trend is observed. The damping coefficient for the high fre-

quency limit$\omega = 100$ is under the static values for the whole range of loading ratio $H/H_u = 0-1.0$ for $e/r_0 = 10$ case. The damping ratio of the dynamic high frequency case is about 0.25 times of the low frequency one at a load ratio of about $H/H_u = 0.35$ for an embedment ratio of $e/r_0 = 50$. The normalized $c_{dy,h}$ values are closer at zero load and near collapse where both stiffnesses approach zero. For the higher embedment ratio $e/r_0 = 20$, the dashpot coefficient related to the high frequency limit starts just under its static value and decreases up to the load ratio of about $H/H_u = 0.85$ thereafter it increases and attains a peak value of about 0.09 times at the zero load level.

Figs.4.123 to 4.128 compares the influence of the load ratio on the low and high frequency limits of the pile-soil's rocking vibration. Generally the observed rocking damping coefficient for the high frequency limit is far higher than that for the static case. At the zero load level, the static damping coefficient is an order of magnitude less than that of the high frequency limit. The damping ratio decreases very rapidly close to the collapse load level. The observed behaviour may be partly associated with the overall stiffness decrease. The physical explanation is that at higher load levels the soil yields and hence the radiation damping becomes less effective due to a kind of created imaginary bounding in the near field of the soil. In a real pile-soil loading also this can be observed due to creation of the gaps and hence discontinuity in the soil surrounding the pile which results in partial cut-off of radiation damping (see for e.g. El.Naggar and Novak, (1995)).

The observed gradient of the damping curve in Fig. 4.126 , of the dynamic high frequency corresponding to an embedded pile with $e/r_0 = 20$ is higher. For the deepest foundation with $e/r_0 = 50$, the slope of the low-frequency curve is quite slow with no fluctuations around it.The damping for the high-frequency limit starts from about 0.8 and decreases rapidly towards zero near the collapse load.

The potential damage of equivalent simplified pile-soil systems are investigated through ductility demand analyses. The corresponding spectra are plotted in Figs.4.129 through 4.132. It is shown that the ductility demand ratio μ which is defined as the ratio between the maximum displacement at the pile head and the first yield of the pile-soil system generally decreases with the increase of the pile-soil's effective natural period T_{eff} which is defined as:

$$T_{eff} = 2\pi\sqrt{\frac{M_{ps}}{f(K_{ps}^T(u)) = \alpha_{eff}K_{ps}}} \tag{4.250}$$

where M_{ps} is the total mass of the pile-soil system and $K_{ps}^T(u)$ is the tangent stiffness of the pile-soil system which is equal to the real part of the dynamic stiffness $S(a_0)$ as defined above, α_{eff} may be suggested as $0.001 - 0.01$ for relatively soft to very stiff soils.

As seen in the plotted spectra, the ductility ratio of pile-soil increases with the increase of the overload ratio F_ν which is defined as the ratio of the maximum dynamic acceleration to a reference acceleration which corresponds to the restoring force capacity of the system as:

$$F_\nu = \frac{a_{g,max}}{a_{g,ref}} \tag{4.251}$$

where $a_{g,max}$ is the maximum ground acceleration, and $a_{g,ref}$ is defined as:

$$a_{g,ref} = \frac{F_{r,max}}{M_{ps}} \tag{4.252}$$

where $F_{r,max}$ is the maximum restoring force(static capacity) of the pile-soil system. This topic is further discussed in the following Chapter.

The influence of pile's embedment ratio on the system's response is investigated through a frequency ratio $r_\omega = \omega_{eq}/\omega_p$ vs. a stiffness ratio parameter $r_s = \omega_s r_0/c_s$ as plotted in Fig.4.133. r_ω and r_s both characterize the interaction of the pile-soil system through an equivalent SDOF frequency parameter of ω_{eq} and a pile frequency parameter $\omega_p = \sqrt{k_p/m_p}$ where k_p and m_p are the stiffness and mass of the pile itself. Other parameters involved are the pile embedment parameter e, a reference embedment ratio e_0,the pile radius r_0 and the shear wave velocity c_s.

It is observed that the frequency ratio r_ω decreases exponentially by increasing the ratio r_s which can be interpreted as increasing the interaction between pile and soil as the soil becomes relatively softer(i.e. for e.g when c_s decreases). Since the ω_p parameter is at the numerator of the r_s relationship, it can be concluded that increasing the pile's stiffness relative to the soil, will also result in increased pile-soil interaction. Increasing the pile's embedment e increases the r_ω ratio which means that increasing the stiffness of the soil relative to the pile's stiffness and hence reduces the pile-soil interaction. The influence becomes smaller for larger values of embedment e, because for example in the case of a laterally loaded pile increase of pile length than $d = 10$ practically has far less effect on increasing its stiffness and failure capacity.

The effect of mass variation on the pile-soil response is investigated by using simplified equivalent SDOF and 3DOF systems which are shown in Fig.4.134. It is observed that increasing the mass of the pile-soil system reduces the frequency ratio r_ω which can be interpreted as increase of the pile-soil interaction.

The influence of two other important soil parameters as shear stress ratio and poisson's ratio are also studied here by means of the equivalent simplified lumped models. The results are shown in Figs.4.135 and 4.136. As observed, the effects of the shear strength is more pronounced than that of the poisson ratio of the soil on the change of the pile-soil's equivalent response eigenfrequency. As observed, by increasing the soil's shear stress τ_{ps} or decreasing s, the frequency ratio r_ω increases which means that the interaction effect is reduced. Also by increasing the soil's poisson ratio ν from 0.0 towards 0.499 (i.e. a saturated type) the r_ω slightly increases. Which means that the effect of equivalent pile-soil interaction is somewhat higher for a compressible soil than that of an incompressible one.

4.13 Concluding remarks

A non-linear disk-cone model for the pile-soil systems is established in this Chapter. The model is an extension of Wolf's linear disk-cone model. The formulation of the non-linear and non-

homogeneous cone model is introduced in an incremental form and solved analytically by using a step-wise linearization approach. Several other solution procedures of non-linear cone model are also disscussed.

It is shown that both radiation and material damping can be formulated into the disk-cone model. The radiation damping is shown to be an inherent property of the disk-cone model. It is illustrated that various material damping form can be formulated into the disk-cone model of pile-soil system. Voigt's visco-elastic, linear hysteretic, frictional and non-linear hysteretic damping are among those which are formulated and discussed within this Chapter.

It is shown that the Voigt's VE and linear hysteretic type damping can be conveniently considered in a disk-cone model formulation in frequency domain while non-linear hysteretic and frictional types of damping are more relevant for time domain analysis of the pile-soil system. It is also demonstrated that these damping can be easily implemented with simplified lumped models of pile-soil system such as SDOF, 2DOF and 3DOF etc. It is shown that physically a linear hysteretic type damping can be modelled as equivalent mass, spring and dashpot with their properties dependent on the original model's properties.

It is also demonstrated that the disk-cone model can be applied for both layered and homogeneous soil. In this connection, both surface and embedded disks are modelled with corresponding single and double cones. It is shown that various boundary conditions can be applied with the disk-cone model of pile-soil. Refraction as well as reflection of the waves from the boundaries are modelled.

It is illustrated that equivalent simplified lumped models can be quite efficiently applied for the dynamic analysis of pile-soil systems. The capability of these models are demonstrated in an extensive parametric study.

The disk-cone model of the pile-soil system is formulated both in frequency and time domains in a simple and familiar matrix form. The principle of superposition is applied for the solution of the pile-soil system in the frequency domain. The approach is illustrated for a rigid pile or elastic pile in a linear elastic soil. The matrix solution of the non-linear pile-soil system is derived in the time domain by applying a hysteretic type soil damping.

It is shown that the dynamic stiffness and damping properties of a single disk-cone depend significantly on the soil's non-linearities and non-homogenities as well. It is observed that the dynamic spring and dashpot coefficients of the disk-cone can vary significantly with the frequency of the vibration. It is shown that the dynamic stiffness of a disk-cone system can be negative (180deg) out of phase with the input excitation force.

The predictive ability of the disk-cone model are demonstrated in analyzing several examples of large diameter pile under for e.g. seismic ground excitation, simple impulse and harmonic loading at the pile head. Several comparisons of the disk-cone model predictions with those of other models such as API RP2A 1993 and also refined methods such as boundary element

method are performed. Satisfactory correlations are obtained for the studied cases. It is also shown that the accuracy of the predictions depends on the mesh size or number of disks nevertheless with modelling the pile-soil with only 5-7 disks still quite satisfactory results are obtained.

Some interesting results are obtained by using simplified equivalent pile-soil models such as the effects of loading rate and frequency of excitation on the dynamic stiffness and damping properties of the pile-soil systems, the influence of the embedment ratio and other important factors on the dynamic pile-soil interaction etc.

CHAPTER 5

NONLINEAR DYNAMIC ANALYSIS OF JACKET-PILE-SOIL SYSTEM AT THE ULTIMATE COLLAPSE

5.1 Introduction

The dynamic performance of jacket type fixed offshore platforms has been an important topic concerning the recent developments in the field of offshore structures. Until recent years, the general belief was that the behaviour of jacket type structures under environmental loading may be assumed to be quasi-static and hence the ultimate collapse response of jacket platforms were mainly analyzed by using conventional static pushover method as described in Chapter.3. As a consequence the tools which were developed for ultimate and progressive limit state designs did not include any dynamic(inertia) effects. The issue of nonlinear dynamic assessment of jacket platforms was highlighted after recent events such as hurricanes in the Gulf of Mexico and severe winter storms of extreme intensity in North sea area. On the aftermath of such extreme sea storms, the following questions were raised:

1) Why do the jacket platforms with different structural characteristics behave so differently under extreme sea waves and earthquakes?

2) How does a jacket platform behave under various loading time histories with the same intensity?

3) Whether a jacket platform designed for a static loading can sustain (pass safely through) a dynamic loading with a larger intensity?

4) What is the effect of pile-soil interaction on the overall dynamic performance of the structure?

Several recent studies(Bea and Young, 1993, Eberg et al, 1993, Emami et al, 1995 and 1996 and Fajfar et al, 1993, Moan et al, 1997 and Schmucker and Cornell, 1994 and 1996 and Stewart et al, 1993 and 1995) have addressed some of these issues. The current chapter will provide an overview of these recent findings and mainly focus on the work done by the author.

To get an insight into the non-linear dynamic behaviour of jacket platforms a ductility demand approach is developed based on the analyses of simplified systems such as SDOF, plane frames and also more complex MDOF systems.

The global ductility ratio of (structure-foundation)system is defined as the ratio between the maximum sustainable displacement(regarding the global stability of the structure) and the first global yield displacement of the platform at the deck level(see Fig.5.1). The dynamic overload (overcapacity) ratio is defined as the ratio between the maximum (ultimate) dynamic load and the ultimate static resistance of the structure(see Fig.5.2).

Since the near failure non-linear dynamic behaviour of the platform is influenced by changes in both its structural characteristics and also the dynamic loading effects, therefore a ductility spectrum method is developed to relate the natural period as a key measure of structural and foundation's stiffness and mass characteristics to the ductility ratio as an indicator of the overall maximum displacement response of the system and the dynamic overload ratio. These three parameters will be referred to hereafter as the main parameters in ductility spectra analysis.

Hence, the main focus of the ductility spectra analyses in this chapter will be on these three key parameters. However, the effects of other important parameters such as in-elastic hysteretic behaviour, post-peak degradation, equivalent viscous damping ratio, soil's shear modulus (stiffness), duration and the shape of the loading history, frequency content and randomness will also be among the topics which will be discussed in this chapter.

The ductility spectra can be applied either :

. to predict the maximum dynamic overload ratio(ultimate dynamic capacity) of a given platform system

. or to estimate the required maximum overall ductility(potential damage) for a given platform for an extreme loading history

. or to obtain a design natural period of the system to answer for the given limits of both ductility(maximum damage) and overload ratio

The ductility spectra method may provide a valuable tool for the global assessment of the jacket-pile-soil systems at the limit state of collapse. A procedure is established in this chapter for ductility demand analysis which involves following key steps:

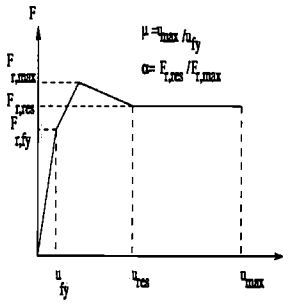

Figure 5.1: A schematic illustration of ductility characteristics of a SDOF system

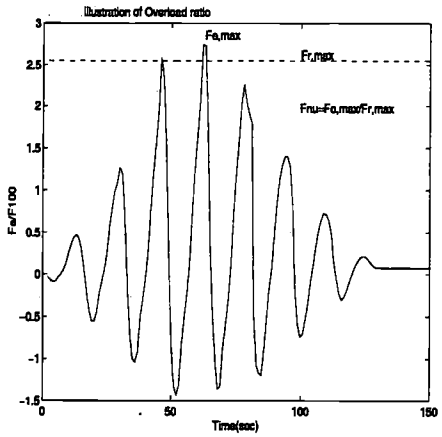

Figure 5.2: A schematic illustration of dynamic overload ratio

. a static pushover analysis as described in Chapter.3 to determine the ultimate and residual static resistance (factors) of the platform and its first global yield displacement which may be assumed as the first major yield or buckling event in the structure which results in a considerable change in its (lateral) stiffness (see Fig.5.1)

. a series of iterative-incremental dynamic analyses to obtain the ultimate dynamic collapse load and the maximum displacement associated with that

. finding the ductility ratio and the overload ratios for each studied system

. varying the stiffness or mass parameters of the SDOF or MDOF system and hence its natural period and obtaining the related overload and ductility ratios

The overload factor of a jacket system can be predicted by using either the established ductility spectra as described above or the relationships obtained based on analyses of simplified systems.

Hence, the methodology in this chapter involves using simplified approaches for e.g. based on SDOF systems to predict the overall ductility response of the more complex MDOF systems and utilizing the results of MDOF system analyses to validate the relationships established based on simplified models. Although the simplified relationships may not be able to precisely predict the dynamic performance characteristics of a more complex system due to their lack of account for the local member failure (such as plastic hinge, buckling) and interaction between various components, load distribution, p-δ effects etc, nevertheless, they could provide efficient tools for first order prediction(screening) of the overall dynamic response parameters of a more complex jacket-pile-soil system. Based on such initial predictions of the dynamic strength or ductility demand of the equivalent simplified model of a jacket-pile-soil system, the designer then can

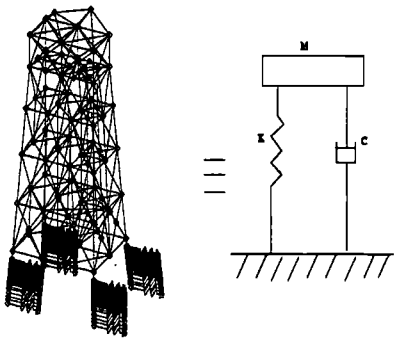

Figure 5.3: A SDOF idealization of overall jacket-pile-soil motion

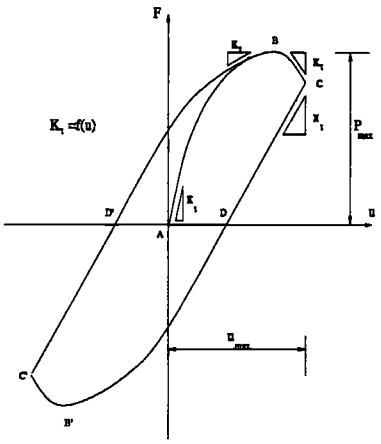

Figure 5.4: Tangent stiffness definition of a general restoring force system

decide whether or not to perform more refined MDOF analyses of system.

Within the context of this study, we shall also investigate the non-linear dynamic interaction between the jacket and the pile-soil system at the ultimate limit state of collapse and its effects on the overall ductility demand of the jacket platform.

5.2 Ductility demand analysis of simplified structural models

5.2.1 General

A simple non-linear single-degree-of-freedom (SDOF) system might be used initially to only indicate the overall dynamic behaviour of the jacket platform. The motion of SDOF system might only represent for example the jacket's lateral load-displacement response at the deck level(see Fig.5.3). The mass, spring and dashpot in this simple system can be used to represent the total mass, the overall lateral stiffness and the damping properties of the real jacket system. In the case of a non-linear SDOF system as is used in this chapter, the inherent in-elastic hysteretic damping in the non-linear spring's response is mainly considered. However, in some cases the equivalent viscous damping is also applied to account for other sources of damping in the system such as hydrodynamic, proportional structural and soil damping.

The tangent stiffness assigned to the SDOF system is a well known Bouc type hysteretic model which is described in Chapter.4. By varying the parameters of Bouc's model in special cases, elastic-perfectly-plastic and bi-linear models can also be represented. The fundamental natural period of the (equivalent) SDOF system is defined as $T_n = 2\pi\sqrt{m/k_i}$ where k_i is the initial stiffness of the system.

To establish the desired ductility relationships from analyses of SDOF systems, the amplitude of applied load history is scaled up successively to illustrate various overload ratios(F_ν). The mass of the SDOF system is also varied to simulate various levels of natural period ranging from about 0.5 to 5.0secs. The maximum displacement is determined after each analysis corresponding to a certain overload ratio and the mass(natural period). The corresponding first global yield displacement of the system can be obtained from an idealized form of the Bouc's stiffness model as shown in Fig.5.4. The displacement corresponding to the first yield point is assumed as the basis of the ductility calculations.
The spectra results for various loading histories are given in a following subsection.

5.2.2 Theory background

The dynamic equilibrium equation for a SDOF system can be expressed as follows:

$$F_i(t) + F_r(t) + F_d(t) = F_e(t) \tag{5.1}$$

in which $F_i(t)$ =the inertia force, $F_r(t)$ = the spring restoring force, $F_d(t)$ = the damping force and $F_e(t)$ = the excitation(external) force.

It is evident from Eq.5.1 that the ultimate dynamic capacity of a system can be greater than its maximum static resistance due to the contribution of the inertial $F_i(t)$ and the damping forces $F_d(t)$. A dynamic overload ratio F_ν can be defined as follows:

$$F_\nu = F_{e,max}/F_{r,max} \tag{5.2}$$

in which $F_{e,max}$ is the maximum dynamic excitation force and $F_{r,max}$ is the ultimate restoring force(or static capacity) of the system which may be determined from a pushover analysis. The global load factor corresponding to the first yield of the system may be expressed as:

$$RFY = F_{r,fy}/F_{100} \tag{5.3}$$

in which F_{100} corresponds to the 100-year wave load and $F_{r,fy}$ refers to the first global yield load. The static strength of the system is also conveniently expressed by the ratio RSU as:

$$RSU = F_{r,max}/F_{100} \tag{5.4}$$

The residual resistance factor of the system may be expressed as follows:

$$RRES = F_{r,res}/F_{100} \tag{5.5}$$

in which $F_{r,res}$ denotes the residual resistance of the system. Similarly dynamic ultimate strength factor RDU may be defined as:

$$RDU = F_{e,max}/F_{100} \tag{5.6}$$

Combining Eqs.5.2, 5.4 and 5.6, the overload ratio may be re-written as:

$$F_\nu = RDU/RSU \tag{5.7}$$

The associated ductility ratio μ of a non-linear system may be defined as follows:

$$\mu = u_{max}/u_{fy} \tag{5.8}$$

in which u_{max} is the maximum (sustainable) displacement of the system and u_{fy} is the displacement corresponding to the first global yield of the system (Fig.5.1). From the non-linear dynamic point of view, a system's overload factor would depend upon two counteracting effects, a beneficial inertia resistance and detrimental dynamic amplification.

For a non-degrading elastic-perfectly-plastic system which possesses sufficiently large ductility (i.e $\mu >> 1.0$) then the system can in principle accelerate to resist the overload factors up to infinity.

On the other hand, if the period of the excitation force matches the natural period of the system, the response will be dynamically amplified. For a brittle system($\mu = 1$), the dynamic amplification effect may reduce the overload factor F_ν. The effects of post-peak degradation may also be considered to further reduce F_ν (see e.g. Schmucker, 1996, Moan et al, 1997). These issues are discussed further subsequently.

For a non-linear and hysteretic Bouc's type SDOF system, Eq.5.1 may be re-written as follows:

$$m\ddot{u} + F_h(u, \dot{u}) + F_n(u) = F_e(t) \tag{5.9}$$

in which $F_h(u, \dot{u})$ = a hysteretic function of displacement and velocity responses of SDOF system and $F_n(u)$ = a non-linear function of the displacement response as given by Bouc, (1968). Double integrating Eq.5.9 with respect to time, we may obtain the following:

$$mu_{max} - mu_0 = \int_0^t \int_0^{t_{max}} [F_e(t) - F_h(u, \dot{u}) - F_n(u)]\, dt d\tau \tag{5.10}$$

where indices max and 0 indicate the maximum and the initial values of the displacement response, respectively. Hereafter, we will drop subindex max and refer to μ_{max} as simply μ. By knowing the initial conditions for example $u_0 = 0$ then the maximum displacement response and hence the ductility ratio μ of the non-linear and hysteretic SDOF system can be obtained as follows:

$$\mu = \frac{1}{mu_y} \int_0^{t_{max}} \int_0^t \left[F_e(t) - \beta \frac{F_y}{u_y} u - (1-\beta)(F_y z_i e^{c_b(u-u_0)} + \frac{\alpha_3}{u_y c_b}(e^{c_b(u-u_0)} - 1)) \right] dt d\tau \tag{5.11}$$

where all other parameters involved on the R-H-S of Eq.5.11 are as defined above and in Sec.4.8.1. DAF represents the dynamic amplification factor(displacement magnification factor) as:

$$DAF = \frac{u_{dy,max}}{u_{st,max}} \tag{5.12}$$

where $u_{st,max}$ and $u_{dy,max}$ denote the peak static and dynamic displacements, respectively. It is seen that, the ductility ratio might be obtained as a function of both the loading history and the response history. Thus the latter requires a numerical (time domain) integration of the response

first by using for e.g. the predictor-corrector technique based on Newmark's family of methods. The overload ratio in general may be expressed as follows:

$$F_\nu = f(\mu, T_n, T_w, \alpha_{res}, k_t) \tag{5.13}$$

where T_w, α_{res} and k_t denote the wave period, the residual ratio and the tangent stiffness parameter of the SDOF system. $\alpha_{res} = F_{r,res}/F_{r,max}$ is defined as the ratio of the residual to ultimate static capacity of the system. Based upon the time integration of Eq.5.11 and those of 3DOF systems the following simple relationship may be suggested:

$$F_\nu = \frac{1}{DAF}\left[1 + (\frac{\alpha_{res}.T_{ref}.T_n}{T_w}) log_{\mu_{max}}\mu.(\frac{16T_n}{T_{ref}.T_w})^{\frac{\beta}{2}}\right]\mu^{\frac{1-\beta}{2}} \tag{5.14}$$

β is an indicator of the collapse behaviour of the jacket system which is defined as:

$$\beta = 1 - \frac{F_{r,res}}{F_{r,max}}.\frac{T_n}{T_{eff}} \tag{5.15}$$

in which T_{eff} represents the effective natural period of the system which may be expressed as a function of the tangent stiffness of the system as:

$$T_{eff} = 2\pi\sqrt{\frac{m}{k_{eff}}} \tag{5.16}$$

which indicates that the effective natural period of an elastic-perfectly-plastic SDOF system will approach infinity at the collapse when the effective (dynamic) stiffness value becomes nearly zero. This implication is physically sound since at the ultimate collapse, the system can not oscillate back to its dynamic equilibrium state(i.e. the time needed to structure to shake down is infinity). $F_{r,res}$ and $F_{r,max}$ on R-H-S of Eq.5.15 represent the residual and the maximum restoring (static) strengths, respectively.

The ratio $\frac{T_n}{(T_w T_{ref})}$ represents the variability of the μ with the natural period of system T_n and also with the extreme wave period T_w. The base of the logarithmic function is set as μ_{max} which is considered to be about 10 for practical purposes. A damage level of $\mu_{max} > 10$ is considered to represent an ultimate collapse of the structure in practice.

The associated function with the period variability is considered to be exponential which decays as seen on the spectra with increase of T_n towards values greater than $3 - 5.0$ secs. T_{ref} may be defined as a reference period for e.g. .1sec. The exponent term of $T_n/(T_{ref}T_w)$ function is $\beta/2 = 1/2(1-\frac{F_{r,max}}{F_{r,res}}\frac{T_n}{T_{eff}})$ which is a function of the residual strength ratio, the natural period and the effective period of the oscillatory system. The physical importance of this is that the effect of natural period is associated with the system's non-linear response and thus with its stiffness and strength degradation, unlike linear SDOF assumptions made by Schmucker, (1996).

5.2.3 Discussion on physical aspect of T_n/T_w effect on μ

The effects of wave period duration are considered to be important on the damage inflicted on the structural system. Based on physics of SDOF system, it can be judged that the maximum

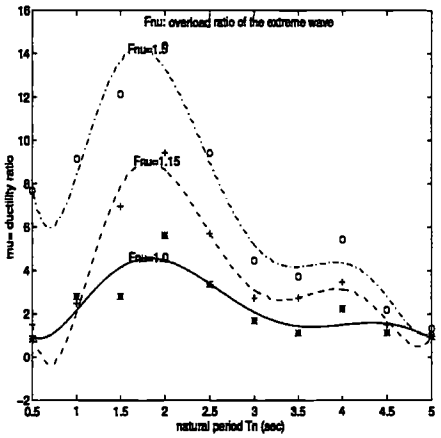

Figure 5.5: Ductility spectra for a simulated extreme wave($H_s = 15.0$ m, $T_z = 15.8$ sec)

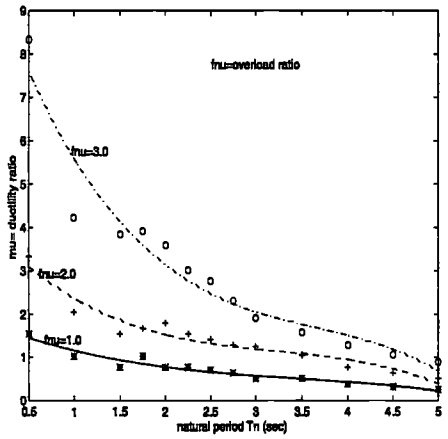

Figure 5.6: Extreme wave ductility spectra for a simulated wave($H_s = 12.75m$ and $T_z = 12.5s$)

displacement response of the system might increase as the wave period increases, because as the system accelerates during an extreme wave event beyond its static capacity limit to compensate for the dynamic overload, the time to reach to the maximum velocity and then return to the zero velocity(momentum) will strongly depend on the input force duration. If the input load is reduced (quickly) within a shorter duration period then the system would less likely to accelerate further and hence increase the displacement further beyond what statically is expected.

The amount of the effective overload will depend on the wave duration (period) and also the shape of the wave. If the wave shape allows to have a quicker unloading or deceleration to take place after the passage of crest then the time to reach to the zero velocity is shortened and hence the damage will be less on the system and it will likely survive the extreme wave. Schmucker, (1996) found that the waves of smoother shapes such as squared sinusoidal shape may be more damaging than the triangular shape waves. He in particular considered a duration period related to the crest passage of the wave and investigated these two type shape effects.

It can be argued that for asymmetric wave loading histories on the platforms which occur near the collapse when the wave height reaches upper parts of the jacket (for e.g. cellar deck or possibly main deck), the shape effects might play an important role. It might be expected that for such waves near collapse the wave becomes sharper which might lessen to some extent (slightly) the damaging effect of the wave compared to a squared or smoother shape but the exceeded forced which has to be balanced off in decelerative phase of response with the reduction of the wave load would possibly take place rather over longer time due to smaller and wider (flatter) part of the trough of the wave load. Sometimes, it might not be possible to balance off the input energy (force) during this trough period and the structure then encounters a new large wave before the velocity has really reached zero(i.e the displacement still increases at this point). The result

will likely be an incrementally increasing displacement response which in most cases causes the ultimate dynamic collapse of the system.

5.2.4 Discussion about selection of the β parameter

It is evident that if the system ideally could maintain its static ultimate collapse(peak) capacity up to very large displacements, then β will be simplified as:

$$\beta = 1 - \frac{T_n}{T_{eff}} \tag{5.17}$$

For a practical case, $0 < T_n < T_{eff}$ which means that $0 < \beta < 1$. It has to be noted that in Eq.5.14, we assumed that T_{eff} is an effective dynamic period near collapse which is neither the same as the natural period of a static system at that point nor is equal to the initial natural period. By this definition T_{eff} carries a notion of both inertia and the tangent stiffness.

The implication of the above relationship is that for a brittle system with ($\beta = 1$), no effective gain from positive inertia resistance can be expected. By definition, T_{eff} becomes equal to infinity at the collapse of a completely brittle system. For a dynamic system with a generous allowance of ductility as EPP, then of course, we may be allowed to include the observed beneficial inertia effects in T_{eff} taken to be as:

$$T_{eff} = 2\pi\sqrt{\frac{m}{\alpha k_i}} \tag{5.18}$$

where α may be taken in the range of for e.g $0.1 - 0.001$, with the lower and upper bounds corresponding to the very highly inertia effective and very low mass dominated systems, respectively. In analogy to the dynamic stiffness of pile-soil system, we may obtain the following general relationship for T_{eff}(see Appendix.E):

$$T_{eff} = 2\pi\sqrt{\frac{m}{Real(S(\omega))}} \tag{5.19}$$

where $S(\omega) = K_{eff} + i\omega C$.

5.2.5 Other simplified SDOF based F_ν vs. μ relationships

If we replace T_{eff} with T_n in Eq.5.15 and neglect the other effects such as the effects of natural period, wave period, shape factor, the following simplified relationship emerges which was obtained by Emami et al, (1995) for semi-ductile fixed type frames with $T_n = 0.5sec$:

$$F_\nu = \sqrt{\mu} \tag{5.20}$$

This relationship might be physically justified, since for an EPP-SDOF system which can maintain its ultimate(peak) capacity almost indefinitely, the ductility would allow the system to override any small linear dynamic effect, if exists in the system.

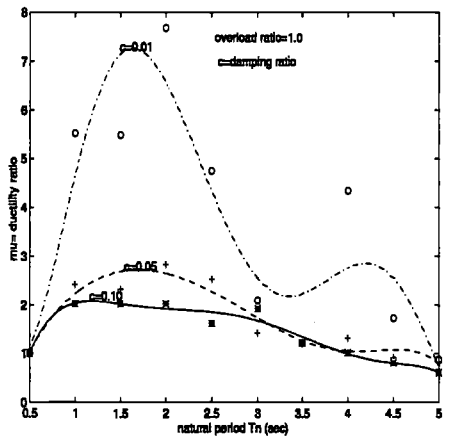

Figure 5.7: Extreme wave ductility spectra for variation of viscous damping

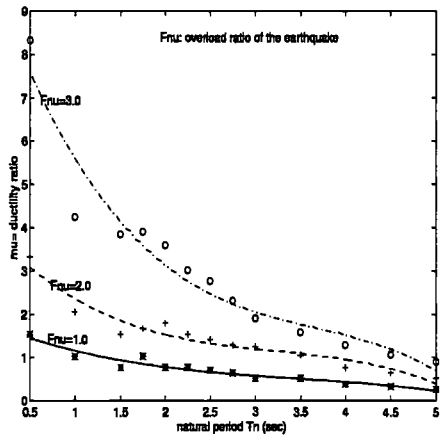

Figure 5.8: Ductility spectra for severe earthquake(El Centro, 1940)

In other words, the gain in terms of the positive non-linear inertia effect overrides the detrimental effect of dynamic amplification effect if included in Eq.5.20 as $F_\nu = 1/DAF\sqrt{\mu}$.

It can be seen from eq.5.20 that for an ideally ductile system the overload ratio can be infinitely large. On the contrary, for a very brittle system no real positive inertia contribution can be utilized and the system will be susceptible to detrimental dynamic effects even before reaching to its ultimate static capacity level. Therefore, the linear DAF effect has to be certainly present in the $F_\nu - \mu$ relationship which is the case in Eq.5.14.

For a very brittle system (i.e. $\alpha_{res} = 0$ hence; $\beta = 1$) with a ductility ratio very close to unity then from Eq.5.14 the dynamic overload-ductility relationship can be derived as follows:

$$F_\nu = \frac{1}{DAF} \tag{5.21}$$

This may indicate that for a brittle Jacket system with a natural period of much less than that of wave period, if the linear dynamic effects are neglected (i.e. $DAF = 1$) then the maximum dynamic overload ratio will be equal to unity. In general, for a very brittle system, the maximum dynamic capacity may be less than or equal to its peak static capacity).

For a semi-ductile jacket platform, the residual capacity can not be neglected as for a very brittle system(i.e. $0 < F_{res} < F_{r,max}$ or $0 < \beta < 1$). In terms of ductility classification, a semi-ductile system can be defined as a system with a ductility ratio ($1 < \mu << \infty$). However, in engineering practice, a structure may be considered as semi-ductile with a $0.7 < \alpha_{res} < 0.9$. For a semi-ductile system, the average overload ratio may be obtained to be in the range of $1.02 - 1.1$ for typical extreme sea waves with for example $T_w = 12 - 20$ secs for North-sea.

In comparison, for a ductile system with a maximum admissible ductility level for example for

a jacket type frame system as $\mu = 5 - 10$, the dynamic overload ratio may be in the range of $F_\nu = 1.1 - 1.2$, for typical extreme (sea) wave periods. It may be noteworthy that the maximum admissible μ may be required in practice with respect to the damage inflicted to the non-structural elements caused by very large deformation of the jacket, even if the global instability of the structure does not occur. Also other local restraints such as member fracture and joint flexibility limits may not allow the structure to sustain larger deformations such as $u_{res} = \mu.u_{fy} \geq (5 - 10)u_{fy}$.

Stewart et al, (1988) has suggested the overload ratios in the range of $1.0 - 1.07$ for a semi-ductile structure and overload ratio $F_{nu} \geq 1.2$ for ductile structures. For seismic waves, however, larger F_ν might be expected than those suggested here for the extreme sea waves due to typically smaller T_w values. For severe earthquakes, T_w typically is less than 1-2 secs and hence according to Eq.5.14, F_ν can be even larger than 2.0 for fixed type frame structures as jackets. The latter suggestion is also confirmed with the findings of Bea and Young, (1993) and Fajfar et al, (1993).

The following overload vs. ductility ratio relationship is obtained by Bea and Young, (1993) based on analyses of ND EP SDOF systems:

$$F_\nu = \sqrt{2\mu - 1} \tag{5.22}$$

The above relationship is suggested for a natural period of structure about $1.0sec$ and damping ratio of about 5%. Bea and Young, (1993) also suggested another relationship for an elasto-plastic SDOF system with post-peak strength degradation and for natural period range of 2.0sec and damping ratio of about 5% as:

$$F_\nu = \alpha_{res}.\mu \tag{5.23}$$

It has to be noted that these two relationships have been suggested for seismic analysis results(Bea and Young, 1993). The comparisons made here show that the latter two relationships might somewhat underestimate the overload ratio for ductility ratios closer to unity while they tend to overestimate the overload ratio for far larger ductility values than 1.0 for extreme wave loading. However, for quite moderate ductility ratios ($1 < \mu < 2$), the latter two relationships might provide rather reasonable estimates of F_ν even for extreme wave loading(see Bea and Young, 1993). For a very brittle system(i.e. $\alpha = 0$), Eq.5.23 gives a $F_\nu = 0$ which is far lower estimate. On the other hand, for a completely ductile system (i.e $\alpha_{res} = 1.0$), Eq.5.23 of Bea offers a proportional F_ν versus μ. It may be argued that the resulting overload ratio of 5-10 may not be attained for jacket systems under extreme wave loading even with a ductility ratio as high as 5-10(see also Steawrt, 1995). It seems that Eqs.5.22 provides better results under severe earthquake loading(Bea and Young, 1993). Hence, using these relationships to compare the results from MDOF analysis of jacket system under extreme waves with much larger duration period than earthquake loading seems less relevant.
Schmucker, (1996) obtained an overload-ductility ratio relationship based on analysis of an idealized bi-linear type elasto-plastic SDOF system as follows:

$$F_\nu = \frac{1}{DAF} + a\left[\frac{1}{4\pi^2}(\frac{T_n}{t_d})^2(\mu - 1)\right]^b \tag{5.24}$$

in which T_n and t_d denote the fundamental natural period of the structure and the crest duration(about half cycle period) of the sea wave, respectively. The coefficients "a" and "b" in

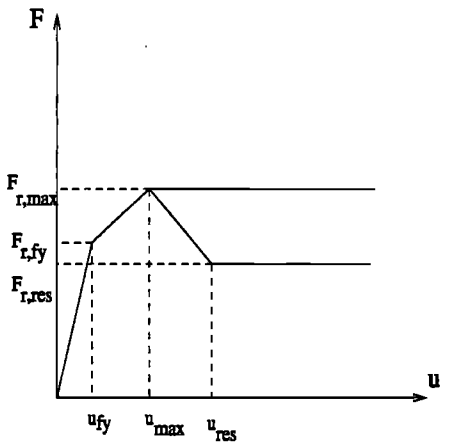

Figure 5.9: A schematic illustration of (bi-linear) elastic-perfectly-plastic and post-peak degrading SDOF systems

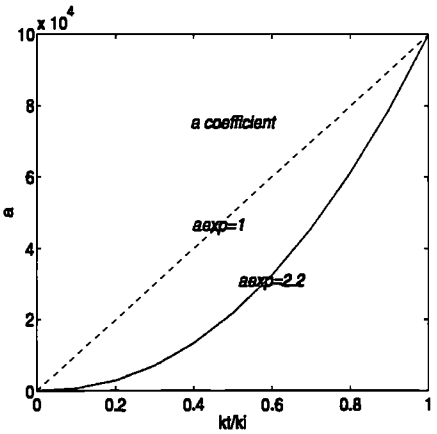

Figure 5.10: Variation of coefficients "a" in Eq.5.24 with k_t/k_i

Eq.5.24 depend on the load history "shape" and the structural natural period. Schmucker, (1996) has suggested that for squared-sinusoidal shape waves (similar to the shape of sea wave force) the coefficient "a" may be taken as 2.2 and the exponent term "b" as 0.5.

These suggested values are obtained for a bi-linear elasto-plastic SDOF system as shown in Fig.5.9 in which $k_t/k_i \rightarrow 0$. Although Eq.5.24 has been proposed for EP-SDOF systems, nonetheless, it is basically derived based on linear dynamics assumption(i.e the restoring force is assumed to vary linearly with displacement response of SDOF system) . Eq.5.24 of Schmucker indicates that the natural period of the system is taken as constant throughout the elasto-plastic response of SDOF system.

This may contradict the underlying assumptions for determining the coefficients "a" and "b" (see also Schmucker, 1996). Obviously this is not the case for a (gradually yielding) elasto-plastic SDOF system. For such a system the effective natural period of system may increase with the decrease of the system's tangent stiffness according to Eq.5.18.

5.2.6 Discussion on bi-linear SDOF based $F_\mu - \mu$ relationship

If T_n is replaced in Eq.5.24 with T_{eff} from Eq.5.16, then the following modified relationship is obtained:

$$F_\nu = \frac{1}{DAF} + a\left[\frac{1}{4\pi^2}(\frac{k_i}{k_t})(\frac{T_n}{t_d})^2(\mu - 1)\right]^b \tag{5.25}$$

The latter implies that for an EPP-SDOF system, regardless of its fundamental natural period at the collapse the overload ratio will approach infinity. However, this might only be correct for EPP-SDOF system with sufficient ductility (i.e. $\mu >> 1.0$). The last term in the latter

expression indicates that this infinity overload is possible for any $\mu > 1.0$. This is obviously not correct. We seek to find out why this effective natural period seemingly does not fit into the Eq.5.25 (i.e. what is the physical or mathematical reason behind this paradox?)

Based on Schmucker, (1996) own derivations for a bi-linear EP-SDOF system, it is possible to find the link as follows. We therefore here quote the three Equations obtained by Schmucker, (1996). For a quasi-static response of a bi-linear SDOF system as shown in Fig.5.9, the following can be written:

$$u_{max,qs} = u_y + \frac{F_{r,max} - F_{fy}}{k_t} \tag{5.26}$$

Eq.5.26 can be re-written as follows:

$$F_\nu = 1 + (\frac{k_t}{k_i})(\mu - 1) \tag{5.27}$$

The argument in the parentheses on the R-H-S of Eq.5.27 is given(Schmucker, 1996) as follows:

$$\bar{g}_{bi} = \frac{1}{4\pi^2}(\frac{T}{t_d})^2(\mu - 1) \tag{5.28}$$

where $\bar{g}_{bi}$ denotes a normalized loading history quantity which is defined by Schmucker, (1996) as follows:

$$\bar{g}_{bi} = \frac{m(u_{max} - u_{r,max})}{F_{r,max}t_d^2} \tag{5.29}$$

$\bar{g}_{bi}$ can be considered as equivalent term to μ, though as seen these two are mathematically quite different. The latter expression can be related to the loading history in a quasi-static manner (see for e.g Schmucker and Cornell, (1994)). By combining Eqs.5.27 to 5.29, Schmucker, (1996) has obtained the following:

$$F_\nu = 1 + 4\pi^2(\frac{t_d}{T})^2(\frac{k_t}{k_i})\bar{g}_{bi} \tag{5.30}$$

By comparing Eqs.5.30 and 5.24, Schmucker, (1996) has obtained the coefficient a as follows:

$$a = 4\pi^2(\frac{t_d}{T})^2(\frac{k_t}{k_i}) \tag{5.31}$$

Now by combining the Eqs.5.25 and 5.31, we obtain:

$$F_\nu = \frac{1}{DAF} + \left[(4\pi^2)(\frac{t_d}{T_n})^2(\frac{k_t}{k_i})\right]^{1-b}(\mu - 1)^b \tag{5.32}$$

Taking the limit of F_ν at the collapse point will yield:

$$lim F_{\nu k_t \to 0} = \frac{1}{DAF} \tag{5.33}$$

which for a quasi-static case without linear dynamic effects (i.e. $DAF = 1$) results in unity. This is certainly correct for only a quasi-static response of an EPP-SDOF system which means that it excludes the extra resistance gained by activation of the inertia forces. To include inertia

terms into the above relationships of Schmucker,(1996) for Q-static response, it can be suggested that the following form could be used :

$$F_{e,max} = F_y + \Delta F_{y,max} + F_{d,max} + F_{i,max} \tag{5.34}$$

where $F_{e,max}$ = the maximum excitation dynamic force, F_y = the corresponding first yield force, $\Delta F_{y,max} = F_{r,max} - F_y$ = the reserve strength of the SDOF system beyond the first yield(for a bi-linear system), $F_{d,max}$ =the damping force and $F_{i,max}$ = the maximum inertia force activated after first yield. If one assumes simply that the overload is related to the maximum displacement hence the damping force may be neglected since at $u = u_{max}$ the velocity response of SDOF system $\dot{u} = 0$.

It may be appropriate to take the F_d as nonzero at the time of the peak dynamic load. $F_{i,max}$ at the peak load will have nonzero value in general and it can be negative if there is any phase between the acceleration response and the input excitation force. However, we are interested in positive effect of inertia at this point.

The bi-linear relationship given by Schmucker, (1994) can be modified as follows:

$$F_\nu = \frac{1}{DAF} + a\left[\frac{1}{4\pi^2}(\frac{k_i}{k_{eff}})(\frac{T_n}{t_d})^2(\mu - 1)\right]^b \tag{5.35}$$

where k_{eff} may be taken for a gradually yielding system as $k_{eff} = f(k_t)$. Simple forms of this could be a secant stiffness:

$$k_{eff} = k_{sec} = \frac{F_{r,max}}{u_{r,max}} \tag{5.36}$$

or as a weighted function of the initial and tangent stiffness near collapse (for e.g with $k_t = (0.1 - 0.01)k_i$).

5.2.7 Comparison of SDOF based relationships by means of numerical examples

A numerical comparison based on $F_\nu - \mu$ relationships described above may allow us to judge their predictive abilities for the real jacket cases which will be considered subsequently. We consider primarily the relationship that we presented in the above section for e.g for a typical natural period range of jacket $T_n = 1 - 5sec$ and both with and without DAF effects, and ductile as well as brittle type of response. Then we also compare the results with the typical predictions of the other relationships as given for e.g by Bea and Young, (1993), Schmucker, (1996) and Stewart et al, (1988).

At this stage no comparisons are made with the plane frame and MDOF Jacket analyses. The aim is to see whether the results of these simple formulations for the typical range of parameters relevant for a jacket platform can be justified. The results for instance given in Appendix.E indicate that Eq.5.14 yields very reasonable results for the given range of parameters of interest. The upper and lower limits of F_ν are also in close agreement with the range suggested by Stewart

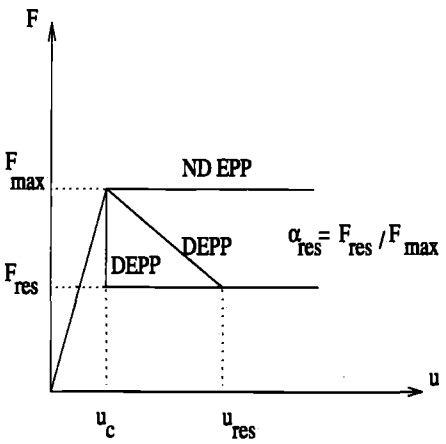

Figure 5.11: A schematic illustration of post-peak behaviour of SDOF systems

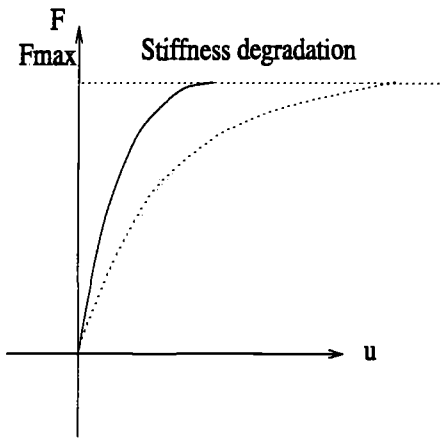

Figure 5.12: An illustration of stiffness degradation of a SDOF system

et al, (1988). We usually obtain overload ratios of about 0.9 to 1.3 for very brittle to quite ductile systems, respectively. The DAF is also applied to representative the jacket's superimposed resonance response under for e.g extreme waves or earthquakes.

The results obtained based on Schmucker's formula seems to be quite reasonable at least for the range of parameters investigated here. Nevertheless, if we apply Eq.5.31 for coefficient "a" in Eq.5.24 of Schmucker instead of his suggested 2.2 value, then it may significantly overestimate F_ν. Coefficient "a" in fact as plotted in Fig.5.10 increases exponentially with increase of k_t/k_i. The value of "a" is mathematically zero for $k_t/k_i = 0$ which results then in $F_\nu = 1/DAF$ (or 1.0 for the case of $DAF = 1$). We also obtained the same result through modified relationship given in Eq.5.35, which we referred to as a paradox. Thus we and Schmucker,(1996) have reached in principle the same conclusion that the value of "a" can not be taken neither at initial intact case nor at the ultimate collapse where $k_t = 0$. Hence effective values of a or Teff have to be used. The sort of paradox mentioned above and the need for such large scale calibration of coefficient "a" can be avoided by using a non-linear SDOF based relationships that we presented above.

The SDOF based $F_\nu - \mu$ initial relationships obtained by Bea and Young, (1993) and Emami et al, (1995) are considered to overestimate largely the overload ratio if the apparent ductility ratio is used as so far defined. If the underlying assumptions of these simple relationships are examined carefully, it can be easily understood that these relationships are obtained based on non-degrading elastic-perfectly-plastic assumption for SDOF systems. However, in most realistic cases, EPP assumption may not hold true, hence the associated relationships with it tend to overpredict the dynamic capacity of the corresponding jacket-pile-soil system.

If we bear in mind this fact, then the use of apparent ductility may not be permissible for all the cases. Therefore, we define an effective ductility ratio here which can be related to the apparent

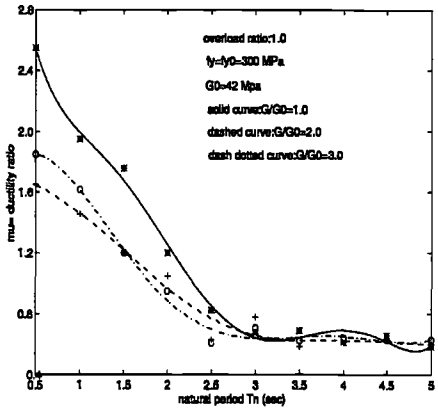

Figure 5.13: Seismic ductility spectra for variation of soil's shear modulus G(El Centro, 1940)

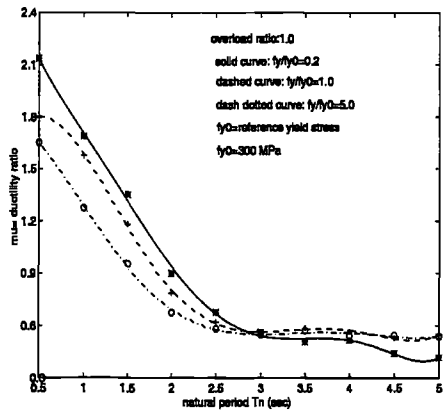

Figure 5.14: Seismic ductility spectra for variation of yield stress fy(El Centro, 1940)

ductility ratio and the residual strength ratio of the system in a simple manner as follows:

$$\mu_{eff} \approx \mu.\alpha_{res} \tag{5.37}$$

The three systems shown in Fig.5.11 have different effective ductility ratios. For system(a) which behaves absolutely brittle the and the residual strength drops to zero just after the peak capacity of the system is reached, both apparent and effective ductility ratios are zero by definition. For the system (b) which apparently possesses some ductility (i.e the maximum displacement is apparently larger than that of the first yield) but with sharp reduction in the system's load carrying capacity to a smaller level than that of the peak ultimate capacity the effective ductility is smaller than that of the apparent ductility($\mu_{eff}/\mu \leq 1.0$). For the system (c) the effective ductility ratio is the same as the observed(apparent) ductility ratio ($\mu_{eff} = \mu$). Now it is quite clear that the use of apparent ductility ratio must only be limited to the structures behaving like SDOF system (c).

5.2.8 The results of ductility analyses of simplified systems

The results of dynamic analyses of non-linear SDOF systems described above are presented in this subsection in the form of ductility spectra. As mentioned in the introduction, the concept of ductility spectrum is used here which enables us to relate several key parameters associated with the structural characteristics, response and the dynamic load history and the spring (stiffness).

For the ultimate collapse response, the best indicator of the damage can be the peak displacement(or its normalized form ductility ratio). For the extreme dynamic loading, the overload ratio may be used as an indicator of the loading intensity. Therefore, the main three parameters

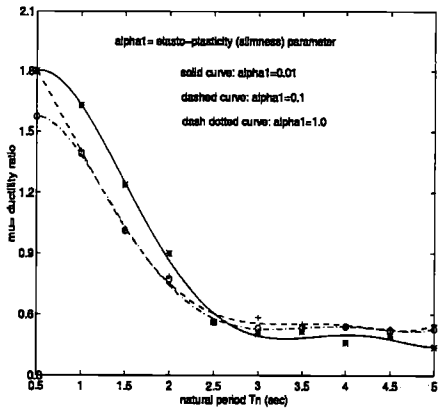

Figure 5.15: Seismic ductility spectra for variation of band-width parameter α_1(El Centro,1940)

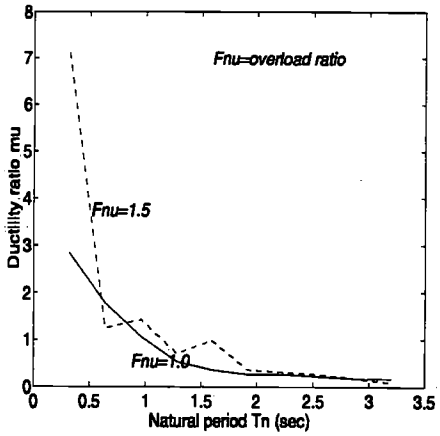

Figure 5.16: Seismic ductility spectra (Santa Cruz, 1989)

of ductility spectra are taken as the natural period of the system T_n, the ductility demand ratio μ and the overload ratio F_ν.

Of course, a dynamic system will in general have damping which reduces the damage to the oscillatory system. Equivalent viscous as well as in-elastic (hysteretic) damping are studied here. Both damping forms are considered in the ductility spectra analyses.

Concerning the dynamic loading history, other important parameters such as wave period T_n for example corresponding to the 100 year return period for the sea waves, the dominant ground shaking period for the seismic loading and the duration period of the loading history will also be studied in this section. The effect of randomness(periodicity) of loading history have been studied for e.g by Bea and Young, (1993).

Ductility spectra for different wave and earthquake conditions are given in Figs.5.5 to 5.19. The reference values for G, f_y and α_1 parameters are chosen to be 42MPa, 350MPa and 0.1, respectively.

It is seen that in the established spectra, the ductility demand ratio (μ) of system generally decreases by increasing its natural period. There are some peaks and valleys(humps) associated with the most of the spectra, which are especially in the range of $T_n \leq 2.0-3.0 secs$. They might be due to the resonance effects related to the multiples of the primary force harmonics(Morison, 1992). Meanwhile, for large overload ratios $F_\nu > 1.0 - 1.1$, the dynamic amplification effects might have been dominated by the dynamic overload related to the positive inertia effects.

The general trend as shown by the fitted curves in Figs.5.5 through 5.20 is the increase of (μ) by

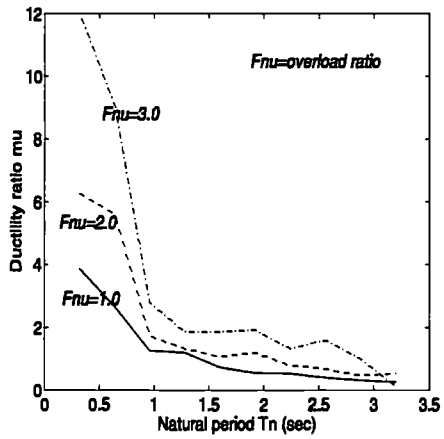

Figure 5.17: Seismic ductility spectra(Woodfords, 1995)

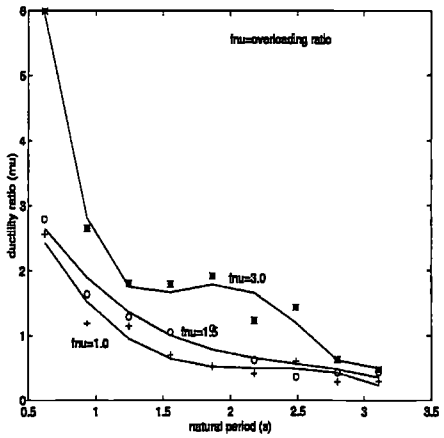

Figure 5.18: Seismic ductility spectra(Parkfield, 1994)

decreasing T_n towards $0.5sec$. As shown in the presented ductility spectra, the relative maximum displacement (ductility demand) of the system is highly dependent on the overload ratio (F_ν) for the range of $T_n \leq 2.0 - 3.0secs$.

The influence of the structural stiffness related parameters(of Bouc's model) such as the first yield strength f_y and the hysteretic width parameter α_1 as an indicator of the in-elastic energy absorption in the system are illustrated in Figs.5.14 and 5.15.

The observation is that increasing f_y or α_1 resulted in shifting the ductility spectra towards smaller T_n values. The latter might be interpreted as the change of effective (natural) period of the structure due to change in its stiffness. This seems to be a beneficial effect in the sense that the required ductility ratio is reduced. However, the peak ductility demand is not altered very much in Figs.5.14 and 5.15. It may be expected that the variations to be larger for higher overload ratios than 1.0. This is because for the overload ratio equal to unity there is not much ductility demand except for the range of about $T_n < 1.5$sec.

It can be seen on the tails of spectra plotted in Figs.5.14 and 5.15, the required ductility is even less than unity for higher natural periods for the given overload ratio of unity. This reduction may be attributed to the combined inertia and damping effect in the system. The latter can be mathematically proven by using one of the basic equations obtained based on EPP-SDOF system. Let us consider an expanded form of Eq.5.10 as follows:

$$\mu = 1.0 + \frac{4\pi^2}{{T_n}^2} \int_{t_{r,max}}^{t_{max}} \int_{t_{r,max}}^{t} \frac{F_{r,max}(F_\nu - 1) - F_{d,hys}(u, \dot{u})}{F_{r,max}} dt d\tau \tag{5.38}$$

in which $F_d(u, \dot{u})$ represents a general form of the non-linear hysteretic damping force in the

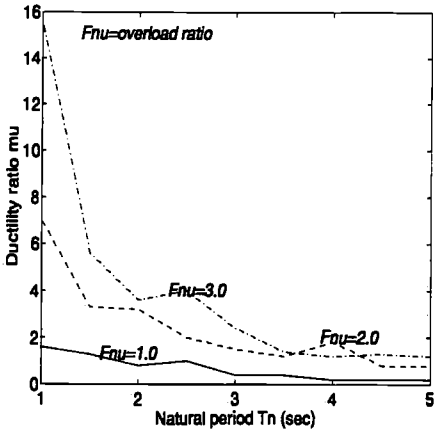

Figure 5.19: Seismic ductility spectra(Taft, 1952)

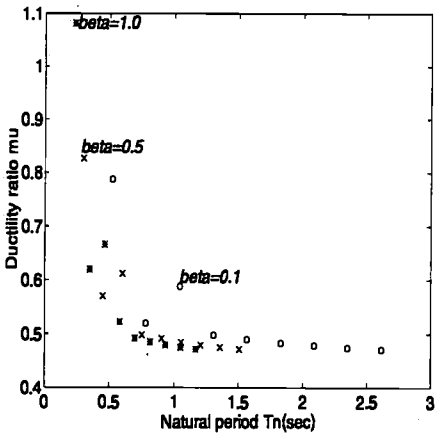

Figure 5.20: Variation of ductility ratio μ with β

SDOF system. For $F_\nu = 1$, Eq.5.38 can be re-arranged as follows:

$$\mu = 1 - \frac{4\pi^2}{T_n{}^2} \int_{t_{r,max}}^{t_{max}} \int_{t_{r,max}}^{t} \frac{F_{d,hys}(u,\dot{u})}{F_{r,max}} dt d\tau \tag{5.39}$$

If T_n is replaced with T_{eff} in Eq.5.39 , μ will be nonzero but can be less than unity due to existence of the the damping term.
The ductility spectra obtained by Bea and Young, (1993) for several extreme waves (hurricanes) and earthquakes show similar results. Bea and Young,(1993) obtained the ductility ratio μ up to a natural period of about 5 secs for overload ratios of 1 and even higher for e.g. 2. Those results show that for lower overload ratios in the range of 1.0-2.0 the tail of the required ductility can be less than 1.0.

If the linear damping such as equivalent viscous or linear hysteretic damping of soil are neglected in Eq.5.39, then μ will always be greater than or equal to unity. For e.g. Schmucker, (1996) suggested that $\mu - 1$ must appear under square root which implies that $\mu \geq 1.0$. It is easy to show mathematically by using Schmucker's proposed relationship that μ can be less than or equal to unity for $F_\nu = 1.0$. If for instance, we convert Eq.5.24 of Schmucker, (1996), μ can be obtained versus F_ν as follows:

$$\mu = 1 + (\frac{F_\nu - \frac{1}{DAF}}{a})^{1/b} 4\pi^2 (\frac{t_d}{T_n})^2 \tag{5.40}$$

It can be seen in Eq.5.40 that the limit of μ becomes unity for $F_\nu = 1.0$ and $DAF = 1.0$. But if $DAF > 1.0$ then $\mu > 1.0$ which is quite reasonable. For $DAF < 1.0$ case, the decay of response occurs due to the presence of damping in the SDOF system (which is not considered in Schmucker's original formulation) then it is evident from Eq.5.40 that for $F_\nu = 1.0$, we will have: $\mu < 1.0$. This is because the second term on the R-H-S of Eq.5.40 in this case is negative.

For an undamped SDOF system, μ will be unity if the resonance effects (DAF) could be neglected. However, in the case of extreme sea waves, some resonance effects might be present due to the odd and even multiples of the primary force components induced by the non-linear drag term in the Morison's equation. (see for e.g Moe and Moan et al, 1987 and Morison et al, 1992). These effects may be superimposed on the non-linear dynamic ductility response of the platform system (Bea and Young, 1993).

There could be other second order non-linearities added into the ductility demand of an idealized platform system induced by the combination of the sea surface fluctuation and the current stretching or extrapolation into the instantaneous water surface (see for e.g Hahn et al, 1995).

For the earthquake type loading, however, the resonance effects may be attributed to the high frequencies associated with the ground motions(e.g accelerations). In many cases the dominant frequencies which are associated with the peaks in the power spectrum of the energy(note that this is a different kind of spectrum on which the horizontal axis is taken as the frequency of vibration) might be close to the fundamental natural period of the system and hence they might induce some resonance in the ductility response. Such resonance may manifest itself in the form of either higher major peaks associated with the maximum non-linear dynamic demand or in the form of some secondary (smaller) peaks in the ductility spectra(see for e.g spectra in Figs.5.5 to 5.20).

The influence of soil's stiffness on the overall ductility demand of SDOF system is also investigated. The soil's shear modulus G is used as the main indicator of the soil's stiffness and varied between 0.3 to 3.0 times an initially taken shear modulus $G_0 = 42MPa$ as reference. The corresponding spectra are presented in Fig.5.13. It is observed that the peaks are reduced by increasing the soil's shear modulus particularly in the range of $T_n < 2.0 - 3.0$secs. These effects are comparable with those seen in Figs.5.14 and 5.15 for the structural stiffness parameters.

The influence of the equivalent viscous damping (with the assumption that it accounts for other sources of damping such as Hydrodynamic, soil and structural) is illustrated in Fig.5.7. It is observed that generally increasing the equivalent damping ratio reduces the ductility demand. The influence of the damping for shorter periods is much greater than that for larger periods. The higher damping as seen damps out the peaks in the spectra. The reduction in terms of the ductility peaks of spectra is a non-proportional with the damping ratio. Increasing damping ratio from 0.01 to 0.05 has reduced the peak ductility demand by a factor of about 2.8 compared to only 30% reduction of the peak demand for increase of damping from 0.05 to 0.10. It is hence, expected that increase of more damping will have less significant effect on reducing the maximum response of the system.

It may be worth noting that the effects of the in-elastic hysteretic damping for the response of the system under extreme loading can be expected to be more significant than the viscous damping. The latter can be investigated by comparing the maximum ductility demands for e.g observed in Figs.5.14 and 5.15 with those peak values in Fig.5.7. It is seen that, the magnitude of the maximum ductility demands for the in-elastic hysteretic damping is comparatively far

lower than those obtained for a SDOF system with equivalent viscous damping for the same overload factor(s).

It is also observed from Figs.5.5 through 5.20 that the ductility demands for extreme wave loading are higher than those for seismic loading for the same overload ratios. The difference might be due to the much longer duration of extreme waves than that of the earthquakes. The loading duration effect may cause the system to reach its ultimate capacity sooner than it might have been anticipated in a static loading.

It will be shown subsequently that the effects of such linear DAF effects are seemingly less pronounced for more ductile jacket systems than those with brittle behaviour. It is observed from Figs.5.5 through 5.20 that the ductility demands for extreme wave loading are higher than those for seismic loading for the same overload ratios.

The variation of the ductility demand for different waves and earthquake records can be seen on Figs.5.5 to 5.20. The highest peaks for a given overload ratio varies significantly for different earthquake or wave loading time histories. For e.g. for a significant wave height of $H_s = 12.75m$ with a corresponding mean crossing period of about $T_z = 12.5$ secs, the maximum ductility for an overload factor of unity is about one third of that for a significant wave height of about $H_s = 15m$ and a mean period $T_z = 15.8$secs.

This large difference may be attributed to the energy carried by each wave, as we know the energy carried through one cycle of the wave has a proportion with the square of the wave amplitude and also the wave we talking here is an irregular wave simulated based on Jonswap's energy spectrum which has non-linear proportionality in terms of generated wave height with the input H_s and T_z, besides the energy carried in each cycle depends strongly on the duration(period) of the wave cycle. Thus the outcome will be a nonproportional relationship between μ and H_s and T_z for the same structural system and overload ratio.

For the earthquake records studied here, significant variations are observed in terms of the ductility demand ratio. For e.g for Santa Cruz earthquake with a peak ground acceleration of about $a_g = 1.2m/s^2$ and a duration period of about $T_d = 53.5$sec the required ductility is about 50% higher than that for the Taft record with peak ground acceleration of about $a_{g,max} = 0.83m/s^2$ and duration period of about $T_d = 42.7sec$. The variability of the ductility demand with the periodicity of the earthquake is also studied by several authors (see for e.g Bea and Young, 1993, Bazzuro and Cornell, 1988). Bea and Young, (1993) found that for the synthetic seismic records the maximum ductility ratios are in average lower than those obtained for the recorded ones with the same maximum acceleration and the frequency content. The observed difference is attributed to the phasing(randomness) of the simulated earthquakes versus the recorded earthquakes.

However, for the extreme sea waves, it has been observed that the peak required ductility ratios are lower for the real recorded extreme waves such as recent Hurricanes (for e.g Andrew, Elena etc.) than the simulated waves with the same amplitude and frequency of content characteristics.

These results imply that the ductility spectra presented here (for the simulated extreme sea and the recorded earthquakes) might be somewhat conservative(see for e.g. Bea and Young, 1993).

5.3 Ductility analysis of plane frame systems

5.3.1 General

To establish the ductility-overload relationship for frame systems, we initially consider three simple portal frames (a) a single braced one storey plane frame (b) a double braced one storey plane frame (c) a double braced two storey plane frame.

The natural periods of both single and double braced one storey plane frames are taken as 0.5secs. This particular natural period is of interest for us since this may indicate the lower bound for the typical natural period range of jacket platforms. We selected this period also because it was observed from SDOF analyses in Sec.5.2 that for this lower bound of natural period, the ductility demand ratio μ is generally higher than those for the larger periods.

5.3.2 Ductility analysis of a one-storey plane frame

To determine the desired natural period of the plane frame a simple linear eigen-value analysis was performed for each case. The mass is lumped at the upper two nodes of the plane frame. The loading is considered as a concentrated horizontal at this upper beam level. The time history of the loading is shown in Fig.5.22 which is generated for a regular wave. First the static pushover analysis of plane frame is carried out to determine the ultimate peak capacity $F_{r,max}$ and the residual strength $F_{r,res}$, the displacement corresponding to the global first yield u_{fy}. The loading history is scaled up proportionally and applied successively and the corresponding maximum displacement response is obtained as u_{max}.

We may consider that $F_{e,max} = SCF.F_{ref,max}$, where $F_{ref,max}$ denotes the reference(unfactored) load history's maximum amplitude and SCF as a scaling factor. Then F_ν can be simply re-expressed from Eq.5.2 as follows:

$$F_\nu = SCF.\frac{F_{ref,max}}{F_{r,max}} \tag{5.41}$$

5.3.3 The results of ductility analysis of the one-storey plane frame

The results of the analyses of the single and double braced plane frame of Fig.5.21 are presented in Figs.5.23. A simple relationship is obtained by fitting a curve to the obtained data as represented by a solid line in Fig.5.23 as follows:

$$F_\nu = \sqrt{\mu} \tag{5.42}$$

This correlation fits well for the ductility data obtained for both single braced and the double braced plane frames. The results of single and double braced frame analyses are denoted by plus

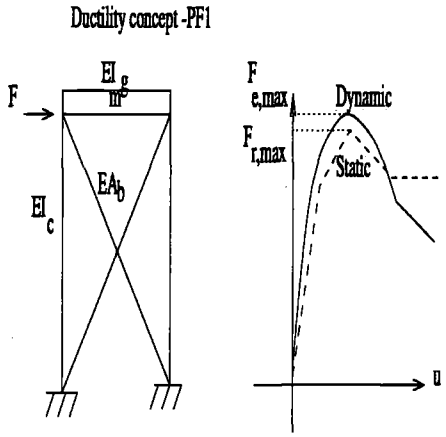

Figure 5.21: A double-braced one storey plane frame

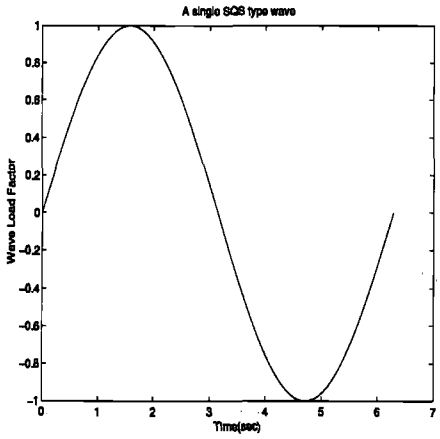

Figure 5.22: A single SQS type wave load imposed on one storey plane frame

and asterisks signs, respectively, in Fig.5.23. A larger scatter is seen for the larger values of μ.

The fitted relationship of Eq.5.42 is denoted by a solid line. It is seen that this correlation is somewhat unconservative for the larger values of μ than 5. This obtained simple correlation might only be applicable for fixed support type jacket frames(i.e with disregarding the effects of the soil-structure interaction) with a natural period of about $T_n = 0.5$ sec.

Fig.5.24 compares the results of equivalent single and double braced frames with those of SODF and MDOF analyses of a 12 leg drilling type jacket platform(Bea and Young, 1993). It is seen that the F_ν corresponding to the plane frame with a single brace is far lower than those obtained for plane frame with double bracing system, SDOF and MDOF analyses of the 12 leg jacket system. It is also observed that the Eq.5.42 matches well with the results of the plane frame analysis with single brace system and 5% damping. In comparison, the SDOF relationship of Bea and Young, (1993) has provided a better fit for the results of double braced plane frame analysis with 5% damping and those obtained from analyses of an equivalent SDOF system.

Eq.5.42 is a particular form of Eq.5.14 with $\beta = 0$. Eq.5.42 in essence is similar to the relationships obtained by Bea and Young, (1993) and Schmucker, (1996). The exponent term 0.5 is seen in all these three correlations, however, the coefficients terms are significantly different. Bea and Young,(1993) assumes a function of $2\mu - 1$, which implies a minimum value of $\mu = 0.5$, Eq.5.42 is valid for single irregular type waves. It is argued subsequently that including the multiple wave effects, the non-linear pile-soil interaction, incrementing the wave height instead of wave load scaling and varying T_n of the structure may lead to considerable changes in the overall ductility demand of the system.

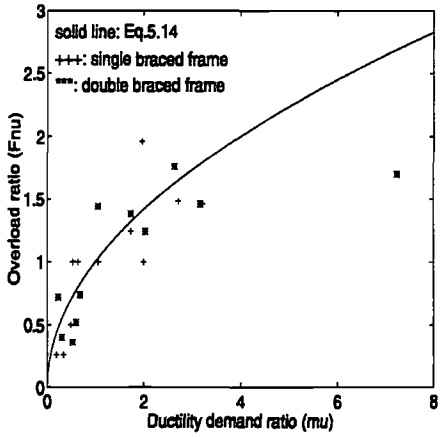

Figure 5.23: Overload vs. ductility ratio relationship of single and double braced one storey plane frames

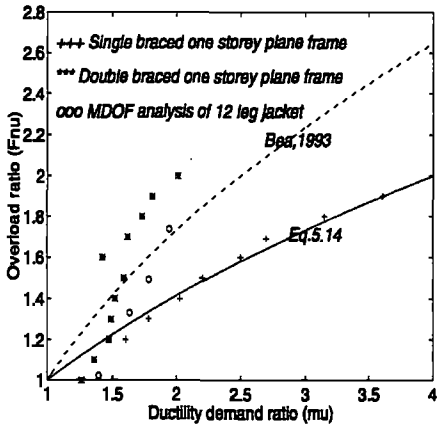

Figure 5.24: Comparison of the F_ν vs μ relationships from SDOF, MDOF and plane frame analyses results for the case of 12 leg jacket platform(Bea and Young, 1993)

5.3.4 Ductility analysis of double braced two storey plane frame system

To further investigate the effects of variation of T_n on the plane frame's ductility ratio, series of ductility demand analyses are carried out here by using another simple double braced two storey plane frame as shown in Fig.5.21. The stiffness and the mass of the plane frame system is varied to simulate the natural periods of interest close to 0.5 sec(the most demanding region in the ductility spectra).

The ductility demand analysis as described above is carried out for each case through proportional scaling of the load history. The corresponding maximum displacements response are normalized against the first global yield displacement of the plane frame. The first global yield of the plane frame system is obtained from the static pushover analysis. Figs.5.26 through 5.28 show the examples of the obtained dynamic overload and ductility ratios.

5.3.5 The results of ductility analysis of 2 storey plane frame

The plane frame is fixed at its base and the mass is concentrated at the upper two nodes of the structure as shown in Fig.5.25. The loading consists of gravity and seismic loading and applied at the same upper corner nodes where the mass is lumped.

The seismic excitation force is assigned by multiplying the seismic acceleration and the top mass. The aim of this simple model is to get some idea about the variation of the overload and ductility ratios for the loads with far shorter duration such as seismic excitations. From our study on SDOF and 3DOF systems, we found that the dynamic overload ratio may vary quite

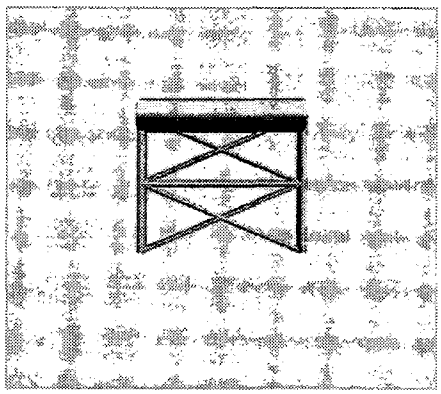

Figure 5.25: A double braced two storey plane frame model

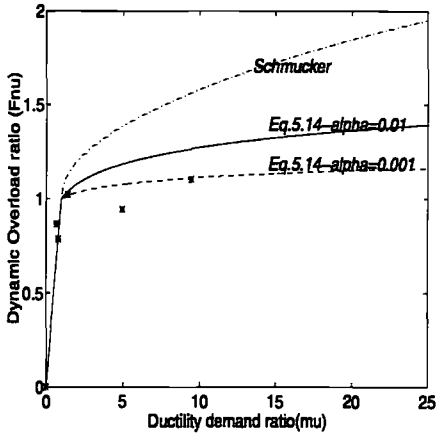

Figure 5.26: Ductility vs. overload response of the two storey plane frame with a natural period of $T_n = 0.28sec$

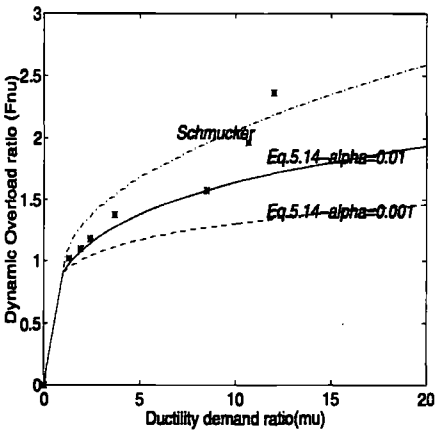

Figure 5.27: Ductility vs. overload response of the two storey plane frame with a natural period of $T_n = 0.56sec$

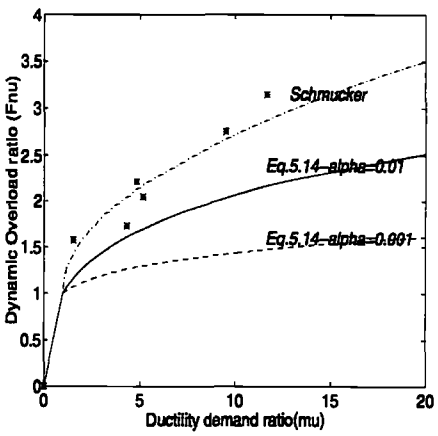

Figure 5.28: Ductility vs. overload ratio response of the two storey plane frame with a natural period of $T_n = 0.82sec$

significantly for the seismic loads compared to the wave loads. It is observed in the ductility spectra shown in Figs.5.5 to 5.20 that the ductility demand ratio μ is comparatively smaller for the seismic type loading.

The susceptibility of structure in the case of earthquake loading is higher to the linear dynamic (resonance) effects due to proximity of the natural period of the structure and the ground oscillation. As in the case of extreme sea waves, these resonance induced response will be superimposed on the non-linear response of the frame for overload ratios larger than unity.

In this section, dynamic analyses of the double braced two storey plane frame with three different natural periods 0.28, 0.55 and 0.82 secs are performed. These periods are chosen to represent the most demanding region in the ductility spectra based on the results of SDOF systems.

The corresponding dynamic analysis results of the plane frame are denoted by asterisks symbols and compared with the predicted F_ν vs. μ response curves based on Eq.5.14 obtained here and the Eq.5.24 obtained by Schmucker, (1996). It is seen that the Schmucker's relationship has provided an upper bound to the obtained frame results. In comparison, our relationship has given slightly lower F_ν values than the those of plane frame analyses. There is a scatter in terms of F_ν ratios obtained from the 2D-plane frame analyses which is mainly seen for the larger ductility ratios $\mu \geq 5.0$. The scatter related to the upper bound might be related to the termination of the response at a failure cycle before a complete passage these cases are assumed to represent a much higher overload ratio than mean predicted trend. In overall, the predicted response curves according to Eq.5.14 is much closer to the mean observed response trends.

For practical jacket type frame systems, the range of interest for ductility demand μ may be considered to be less than about 5(Stewart, 1995). This consideration is mainly due to the operational limits of the platform. The global instability and joint capacities to sustain μ larger than let say $5-10$ will be definitely limiting the maximum ductility demand for any jacket platform.

Referring to the observations in Fig.5.26, for $\mu < 1.0$ the relationship between F_ν and μ is almost linear. The major change in the capacity is seen to occur right after $\mu = 1$ level, where the static capacity is exceeded. If we take an average level of overload ratio for the μ range greater than 1.0, a mean dynamic overload of about $10\% - 20\%$ is obtained.

This beneficial effect due to reaction of inertia of system has been predicted by our simplified relationship Eq.5.14 by accounting for the changes (shift) in stiffness of the system through an effective period T_{eff} as described in Eq.5.16.

We have accounted for duration effect of the loading history through T_n/T_w ratio in Eq.5.14. The ratio is about 0.5 for this frame case and the result is seen as higher μ demand for $F_\nu > 1.1$. This is also seen in the presented ductility spectra for SDOF systems above. As the natural period of the system decreases, the ductility demand μ generally increases. μ becomes much higher for the smaller values of T_n than say 1.0sec. Now, we shall investigate a double braced two storey plane frame with a natural period of almost twice as the first case (i.e $T_n = 0.55sec$). The

results of plane frame analyses and the prediction based on simplified methods are presented in Fig.5.27 in the same manner(by using the same symbols) as for the previous case. It is seen that the maximum F_ν obtained for the latter case is about 1.95. This is mainly due to the effect of increase in the duration of the seismic loading cycles.

A significant yield is observed, when system surpasses its static capacity level which occurs around $\mu = 1.3$. An apparent hardening can be seen in $F_\nu - \mu$ response by increasing the maximum displacement (μ). This observation is also consistent with our findings based on the results of SDOF analyses.

At a maximum ductility of about $\mu >= 10$, the system's dynamic strength has become almost 1.5 times its static capacity (computed earlier as its total base shear). This signifies the fact that for a seismic loading with comparatively smaller duration period T_w, the dynamic overstrength of the system can be significantly higher than an extreme sea wave with much larger duration. With respect to above discussion, larger the wave duration period becomes more destructive it will be. It is noted that a ductility ratio of $\mu = 1.3$ is observed for an overload ratio of about $F_\nu = 1.0$. This indicates the presence of linear dynamic in the elastic range of response. This resonance is due to the proximity of the linear(initial) natural period of the system and the period of duration of seismic wave which is nearly 1.0 for this case.

The predicted $F_\nu - \mu$ curves are plotted in Fig.5.27 according to the described predictive relationships show a good fit for the practical range of $\mu < 4 - 5$ for jacket systems. Eq.5.14 has given a more conservative prediction compared to the analyses results. In comparison, the relationship of Schmucker, (1996) has somewhat over-predicted F_ν in this case.

A third case is studied which is a double braced two storey plane frame with a natural period of $T_n = 0.82sec$. The computed $F_\nu - \mu$ response of the plane frame is compared with those obtained based on simplified methods in Fig.5.28. Again a scatter is observed particularly in the initial part of this response. A large variation in terms of F_ν is observed which actually is related to different load cases. Although the structure is the same but different load cases have produced different maximum responses which are mainly associated with their static failure modes. However, a better trend is seen for the post collapse range of the response. The predictive relationship of Schmucker, (1996) has given the best estimate in this case. Our predicted $F_\nu - \mu$ response curve is more conservative in this case. The response predicted based on $\alpha = 0.01$ is closer than the prediction based on $\alpha = 0.001$.

It is evident that for these three cases with relatively low duration of seismic loading, an α value of greater than or equal to 0.01 more appropriate. This might also be associated with the relatively large inertia resistance in these cases.

It is also found here that the overload ratio F_ν is significantly larger for the system with the larger natural period than the one with the smaller period. The maximum predicted value of F_ν is obtained to be about 3.0 for the latter case compared to the frame with a natural period of $T_n = 0.28sec$ which was only slightly higher than 1.2. The general trend observed in the ductility

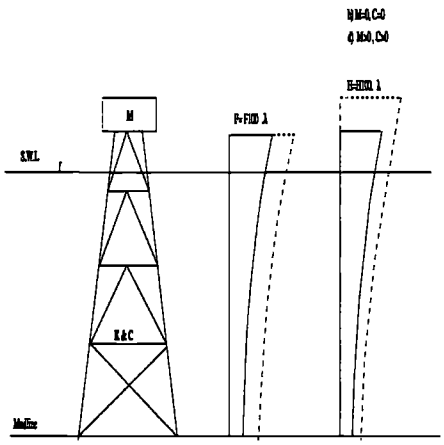

Figure 5.29: The wave load incrementation vs. wave height incrementation approach

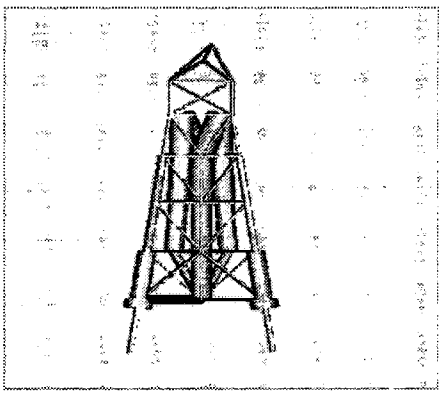

Figure 5.30: The new model of the 8-leg jacket-pile-soil system

spectra above hence is also partly verified here for 2D-framed systems. The significance of the duration therefore is highlighted for the seismic response of the framed systems with lower natural periods than for the systems with longer period of vibration exposed to the loading histories with larger duration such as extreme waves.

5.4 Ductility demand analysis of 3D-Jacket-pile-soil system

5.4.1 General

The dynamic performance of jacket platform under extreme loading might be influenced by the interaction between the structure and its foundation and the dynamic loading effects as well. The ductility behaviour of the structure and the pile-soil foundation will determine how much dynamic overload structure can sustain beyond its static capacity.

The jacket-pile-soil interaction might provide the required ductility level(beneficial effect) and also can be detrimental if it results in collapse of the pile-soil foundation prior to full plastic utilization of the structural members.

With respect to the pile-soil modelling, in the cases that the soil is much stiffer and the piles are sufficiently strong (i.e. for e.g plugged in the case of end bearing piles or very long in the case of floating piles), the pile-soil-structure interaction may be modelled as linear. In such cases, the overall ductility response of the system may be less influenced by the structure-foundation interaction.

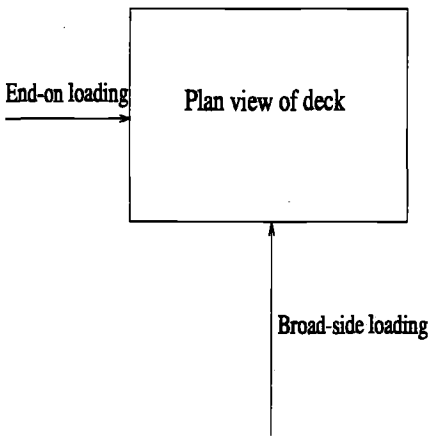

Figure 5.31: A plan view of deck w.r.t end-on and broad-side loading directions

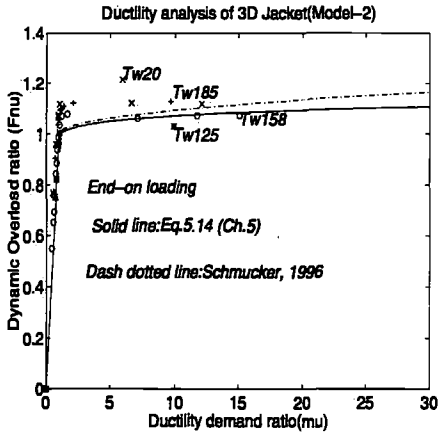

Figure 5.32: Ductility vs. overload ratio response of the original model of jacket platform under end-on loading(regular wave)

To study the effects of soil non-linearities on the dynamic response of jacket, we will consider both linear and non-linear soil-structure interaction throughout this section. The effects of pile tip modelling on the ultimate dynamic response of the system will also be studied in this section through considering plugged and un-plugged pile foundation systems.

The influence of the hysteretic soil damping on the potential damage to the system is also studied in the following.

5.4.2 Time domain dynamic analysis

A brief theory background and the solution strategy adopted in computer program USFOS(Amdahl and Eberg, 1992) for time domain dynamic analysis is described in the following subsections.

5.4.2.1 Equation of motion

Dynamic equilibrium of motion is expressed according to Eq.5.1.

5.4.2.2 Mass matrix

The inertia of the discretized system is represented by the consistent mass matrix:

$$M = \int_{i=1}^{nel} a_i^T \int_{V_i} \rho_i N^T N dV a_i \tag{5.43}$$

where ρ is the density and N the element interpolation polynomial vector. a_i is the transformation vector from element system to assembled system. A consistent mass matrix for a 4DOF beam with third order polynomial shape functions is used. Concentrated masses may be specified at nodes. Added mass for submerged elements will be included.

5.4.2.3 Damping

Based on the distributed material damping property C, the well known equivalent viscous damping model is given by:

$$F_d = C\dot{u} \tag{5.44}$$

where the damping matrix is given by:

$$C = \int_{i=1}^{nel} a_i^T \int_{V_i} C_i N^T N dV a_i \tag{5.45}$$

For computational (normal mode approach) reasons the damping matrix C is usually expressed in terms of mass and stiffness matrices of system in the form of Caughy series as follows:

$$C = \sum_{k=1}^{n} M(M^{-1}K)^k \tag{5.46}$$

The expansion reduces to a Rayleigh damping form when the series is truncated after two first terms and after adding a viscous term will have the following form:

$$C = C_0 + \alpha_1 M + \alpha_2 K \tag{5.47}$$

The α_j Rayleigh damping factors are calculated from modal damping data available for structure(see e.g Clough and Penzien, (1976) and Warburton, (1976)).

5.4.3 Solution procedures

The dynamic equation of motion is solved in the time domain by using $\alpha - HHT$ method (Hilber, 1976) instead of conventional Newmark's-β method. The governing equations are expressed as:

$$M\ddot{u}_{n+1} + (1+\alpha)C\dot{u}_{n+1} - \alpha C\dot{u}_n + (1+\alpha)Ku_{n+1} - \alpha Ku_n = (1+\alpha)F_{e,n+1} - \alpha F_{e,n} \tag{5.48}$$

$$\dot{u}_{n+1} = \dot{u}_n + \Delta t(1-\gamma)\ddot{u}_n + \Delta t\gamma\ddot{u}_{n+1} \tag{5.49}$$

$$u_{n+1} = u_n + \Delta t\dot{u}_n + \frac{\gamma t^2}{2}(1-2\beta)\ddot{u}_n + \Delta t^2\beta\ddot{u}_{n+1} \tag{5.50}$$

The only difference between Eqs.5.48 to 5.50 and the conventional Newmark's-β approach is introduction of some new terms in the stiffness, damping and load expressions. The incremental equations are developed as follows:

$$\begin{aligned} M(\ddot{u}_{n+1} - \ddot{u}_n) + (1+\alpha)C(\dot{u}_{n+1} - \dot{u}_n) + (1+\alpha)K(u_{n+1} - u_n) \\ = (1+\alpha)(F_{e,n+1} - F_{e,n}) + F_n - M\ddot{u}_n - C\dot{u}_n - Ku_n \end{aligned} \tag{5.51}$$

$$\Delta\ddot{u}_{n+1} = \ddot{u}_{n+1} - \ddot{u}_n = \frac{1}{\Delta t^2\beta}\Delta u_{n+1} - \frac{1}{\Delta t\beta}\dot{u}_n - \frac{1}{2\beta}\ddot{u}_n \tag{5.52}$$

$$\Delta\dot{u}_{n+1} = \dot{u}_{n+1} - \dot{u}_n = \frac{\gamma}{\Delta t\beta}\Delta u_{n+1} - \frac{\gamma}{\beta}\dot{u}_n - \Delta t(\frac{\gamma}{2\beta} - 1)\ddot{u}_n \tag{5.53}$$

Combining Eqs.5.51 to 5.53 yields:

$$\begin{aligned} \left[\frac{1}{\Delta t^2\beta}\Delta u_{n+1} - \frac{1}{\Delta t\beta}\dot{u}_n - \frac{1}{2\beta}\dot{u}_n\right]M + (1+\alpha)\left[\frac{\gamma}{\Delta t\beta}u_{n+1} - \frac{\gamma}{\beta}\dot{u}_n - \Delta t(\frac{\gamma}{2\beta} - 1)\tilde{u}_n\right]C \\ +(1+\alpha)\left[\Delta u_{n+1}\right]K = (1+\alpha)(F_{e,n+1} - F_{e,n}) + \alpha F_{e,n} - M\ddot{u}_n - C\dot{u}_n - Ku_n \end{aligned} \tag{5.54}$$

In which the only unknown is Δu_{n+1}. Collecting all unknown terms on the LHS yields:

$$\left[(1+\alpha)K + (1+\alpha)\frac{\gamma}{\Delta t\beta}C + \frac{1}{\Delta t^2\beta}M\right]\Delta u_{n+1} = (1+\alpha)(F_{e,n+1} - F_{e,n}) + \alpha F_{e,n} - M\ddot{u}_n$$
$$-C\dot{u}_n - Ku_n + \left[\frac{1}{\Delta t\beta}\dot{u}_n + \frac{1}{2\beta}\ddot{u}_n\right]M + \left[(1+\alpha)(\frac{\gamma}{\beta}\dot{u}_n + \Delta t(\frac{\gamma}{2\beta} - 1)\ddot{u}_n\right] \quad (5.55)$$

The damping term may be considered to consist of a viscous term and a proportional damping term as expressed in Eq.5.47. In this way, the governing incremental equation can be transformed into:

$$K^*\Delta u_{n+1} = \Delta F^*_{e,n+1} \quad (5.56)$$

where the effective stiffness becomes:

$$K^* = (1+\alpha)(1 + \frac{\alpha_2\gamma}{\Delta t\beta})K + (1+\alpha)\frac{\gamma}{\Delta t\beta}C_0 + \left[\frac{1}{\Delta t^2\beta} + (1+\alpha)\frac{\alpha_1\gamma}{\Delta t\beta}\right]M \quad (5.57)$$

which can be re-written in a compact form as:

$$K^* = a_{k0}K + a_{c0}C + a_{m0}M \quad (5.58)$$

where a_{k0}, a_{c0} and a_{m0} are functions of the integration parameters β and γ, the proportional damping coefficients α_1 and α_2 and the time increment size Δt according to Eq.5.57. The incremental force- displacement relationship then will follow as:

$$\Delta F_{e,n+1} = (1+\alpha)\left[F_{e,n+1} - F_{e,n} + (\frac{\gamma}{\beta}\dot{u}_n + \Delta t(\frac{\gamma}{2\beta} - 1)\ddot{u}_n)C\right] + (\frac{1}{\Delta t\beta}\dot{u}_n + (\frac{1}{2\beta} - 1)\ddot{u}_n)M + F_{e,n} - C\dot{u}_n - Ku_n \quad (5.59)$$

Similar to Newmark's-β method, the total displacements, velocities and accelerations at step $n+1$ can be computed as:

$$u_{n+1} = u_n + \Delta u_{n+1} \quad (5.60)$$
$$\dot{u}_{n+1} = \frac{\gamma}{2\beta}\Delta u_{n+1} + (1 - \frac{\gamma}{\beta})\dot{u}_n - \Delta t(\frac{\gamma}{2\beta} - 1)\ddot{u}_n \quad (5.61)$$
$$\ddot{u}_{n+1} = \frac{1}{\Delta t^2\beta}\Delta u_{n+1} - \frac{1}{\Delta t\beta}\dot{u}_n + (1 - \frac{1}{2\beta})\ddot{u}_n \quad (5.62)$$

The predictor-corrector approach is adopted as the solution procedure. Eqs.5.60 to 5.62 are split into two parts as:

$$\dot{u}^p_{n+1} = \dot{u}_n + \Delta t(1-\gamma)\ddot{u}_n \quad (5.63)$$
$$\dot{u}_{n+1} = \dot{u}^p_{n+1} + \Delta t\gamma\ddot{u}_{n+1} \quad (5.64)$$
$$u^p_{n+1} = u_n + \Delta t\dot{u}_n + \frac{\Delta t^2}{2}(1-2\beta)\ddot{u}_n \quad (5.65)$$
$$u_{n+1} = u^p_{n+1} + \Delta t^2\beta\ddot{u}_{n+1} \quad (5.66)$$

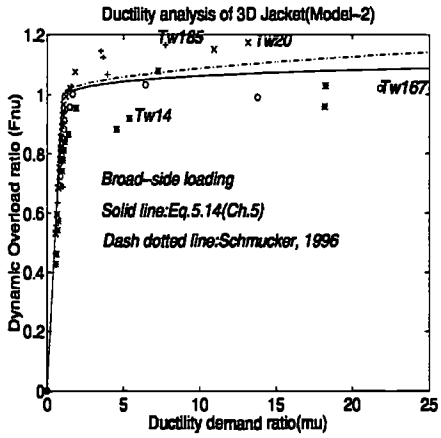

Figure 5.33: Ductility vs. overload ratio response of the original model of jacket platform under broad-side loading(regular wave)

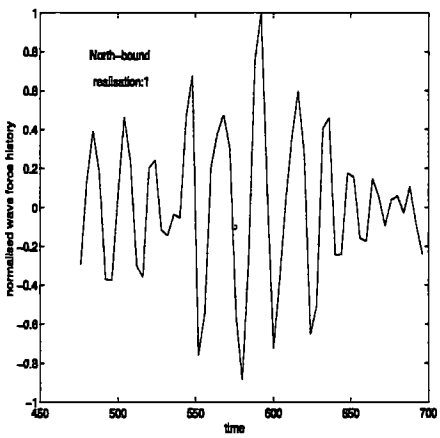

Figure 5.34: A realization of the sea state with its most intensive portion

The predictor equations which are denoted by a superscript p in the latter equations are evaluated on the basis of the values at step n. It is assumed that $\ddot{u}_{n+1}$ is zero in the predictor equations. Now the iterations can be performed by means of Eq.5.66 as follows:

$$u^{i+1}{}_{n+1} = u^{i}{}_{n+1} + \Delta^{i+1}{}_{n+1} \tag{5.67}$$

$$\ddot{u}^{i+1}_{n+1} = \frac{(u^{i+1}{}_{n+1} - \tilde{u}_{n+1})}{\Delta t^2 \beta} \tag{5.68}$$

$$\dot{u}^{i+1}_{n+1} = \tilde{\dot{u}}_{n+1} + \ddot{u}^{i+1}_{n+1} \Delta t \gamma \tag{5.69}$$

where superscript i denotes the iteration steps, Δ^{i+1} denotes the iterative displacements at the iteration step $i+1$ and $\tilde{u}$ denotes the corrected value of u. Using the predictor-corrector approach would reduce any possible large drift from the yield surface. Both effective load vector and effective stiffness matrix are non-linear functions of Δt and so various displacement components vary non-proportionally within each time step Δt. The time scaling may be achieved by means of a bi-section technique(Amdahl and Eberg, 1992).

This technique involves the solution of dynamic equilibrium equations in the corrector phase. Once the scaled time increment is determined the dynamic equilibrium is solved in the corrector phase keeping Δt constant. Equilibrium iterations will then ensure that the force vector position will remain on the yield surface hence the consistency criterion like for static case is also satisfied.

5.4.4 Ductility analysis(procedure) of 3D-Jacket system

Similar to analysis of SDOF model, a simple procedure can be established for ductility analysis of MDOF model of jacket-pile-soil system involving the following steps:

(i) a static pushover analysis based on for e.g the wave load scaling approach(WLI) as described above, to determine the ultimate static resistance (RSU) and the displacement corresponding to the first yield(u_{fy}) of the jacket-pile-soil system

(ii) a (cyclic) dynamic analysis for the given wave height(WHI) or wave load level(WLI) starting from a certain wave height for e.g 100 year wave height

(iv) scaling up successively the wave height(WHI) or load(WLI) to the ultimate collapse of the system and repeating the analysis for each wave height or load level

(v) computing μ and F_ν from the results of steps (i) to (iv) according to Eqs.5.2 and 5.8

(vi) varying T_n of the jacket-pile-soil system and repeating steps(i) to (v)

(vii) plot F_ν vs. μ and T_n

The design approaches may involve determining either:

a) $F_{\nu,max}$ from obtained ductility spectra for the given μ and T_n

or b)the required μ for the given F_ν and T_n

or c)T_n for the given F_ν and μ

It may be noted that for a jacket platform, the mass of the deck top facilities are usually obtained from design while the stiffness and strength capacities of the jacket and pile-soil might be varied. Since the mass of the jacket or pile-soil is often less than 1/3 of the deck itself, hence the mass may be assumed as constant then the stiffness can be varied. Varying the stiffness of the jacket-pile-soil system may result in change of μ. For e.g if RSU of system is kept fixed and K_i of the system is increased then u_{fy} will be reduced and thus the μ will increase, if u_{max} is also constant. Varying RSU instead, will result in change of F_ν. Hence, the desired T_n may be obtained iteratively.

5.4.5 Structural model

The finite element model of the jacket structure used in the case study is shown in Figure 5.3. The structure consists of two longitudinal and four transversal frames. Longitudinal frame's bracing system comprise mainly single diagonal braces and only X-braces at the first and the fifth storeys. The transversal frames have only K-braces. The supporting deck has been modelled as a truss and the top deck facilities have been modelled by a pyramid frame.

5.4.6 Foundation model

The foundation of the jacket system in the following case studies is modelled as equivalent:

a) lumped linear springs attached to the ground at each corner of the jacket

b) single end-bearing (plugged) piles penetrating to a depth of 28m below the mud-line

c) as (b) without plugs at the pile tips

The pile-soil interaction is modelled as:

i) non-linear springs recommended by API RP2A 1993

ii) non-linear disks as described in Secs.2.2.3 and 2.3.3

We will initially consider lumped linear spring to ground Model of foundation. Part of this investigation was carried out earlier by using WLI approach(see the hydrodynamic model) and reported by Emami et al, (1995). Another part of this study was performed recently by using a new WHI method(see the hydrodynamic model).

Subsequently we will use plugged model of foundation to investigate the dynamic near collapse behaviour of the jacket-pile-soil system. This corresponds to the initial design condition of the pile foundation. Due to the relatively short lengths of the designed skirt piles in this case, they have been grouted at the bottom where the piles have penetrated into a sand layer. Hence, the pile-tip is considered to be plugged according to the design to ensure sufficient end-bearing.

In the final part of this section, we shall also consider the influence of un-plugged type pile foundation on the global dynamic response of the platform near collapse.

5.4.7 Hydrodynamic model

Three different hydrodynamic models are used in the present study. The main difference being the modelling of non-structural elements, such as anodes etc. These three models therefore yield different loads corresponding to the 100 year-design wave heights and so the given global load factors associated with collapse. For clarity, these three models and their results are treated separately. However, the results obtained by each model can be used to study the effect of for instance wave load scaling vs. wave height incrementation approach and dynamic vs. static.

In the early part of our study, we used Model-0(WAJAC) as the reference(Emami et al, 1995). However, since it was not possible to use this model in cyclic analysis (WHI approach) Model-1(USFOS) was adopted.

Model-1(WAJAC load model) contains non-structural members as risers, conductors, landing docks, bottle legs and pile guides. Drag and mass coefficients are 0.77 and 2.0, respectively.

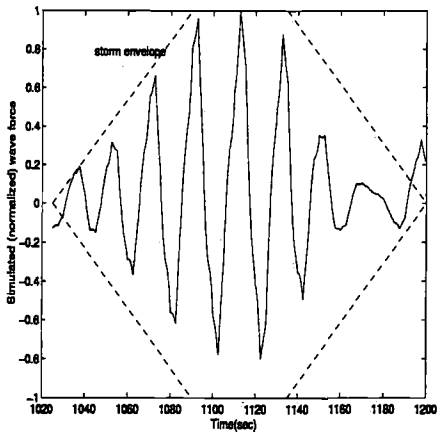

Figure 5.35: A simulated sea state according to the envelope approach

Model-1(USFOS load model) does include boat landings and pile guides and uses drag and mass coefficients of 0.7 and 2.0, respectively. In Model-1 no marine growth was specified whereas in Model-2 marine growth profile was assumed to vary from zero at mudline level to about 10cm at mean water level.

Model-2(USFOS) was recently created almost identical to Model-1(WAJAC) as cited above. This was done after new options became available in USFOS model to include specific hydrodynamic coefficients for various elements. This is done primarily to verify the USFOS model results and also to perform cyclic dynamic analysis without need for calibration of the base shear.

Model-1 was primarily applied to perform static pushover analyses and recently to study the wave height vs. wave load incrementation as well as foundation effects. The more recent Model-1 was applied to study the cyclic (quasi-static) as well as dynamic response of the jacket platform.

5.5 The influence of hydrodynamic modelling and wave load history on the dynamic performance of the jacket-pile-soil system

In the following subsections, we will consider the regular as well as irregular wave loading. The regular wave is initially applied to investigate the influence of the wave period T_w on the dynamic overload vs. ductility response of the platform. The duration of the regular wave is assumed to be one cycle. But in a real storm situation, the largest wave may be proceeded with several smaller waves and then after reaching a maximum peaks they are followed usually with few smaller waves(see for e.g Fig.5.34). In the recent years, several methods are introduced to model the extreme wave load with multiple cycles. For e.g. Tromans et al, (1991) presented a new

extreme wave theory which according to that an extreme sea state may be simulated sufficiently accurately by as few as may be two or three build up cycles with increasing height and then an extreme wave cycle (the largest corresponding to collapse) and then subsiding part of the storm towards the 100 year wave height. Stewart et al, (1993) also introduced a method to simulate a synthetic storm by taking a 100 year wave and scaling it up to the collapse height level and then decreasing it gradually to the 100-year wave height in successive cycles.

In this section, another approach is introduced for simulation of the extreme sea waves. The method is based on a successive scaling of the wave from nearly zero to the ultimate collapse wave height and proceeding for a period of two most extreme wave cycles and then decreasing linearly towards zero(see Fig.5.35).

The method is therefore based on a wave envelope which mimics the random sea state realizations (Fig.5.34) simulated by WAJAC program(DnV, 1992). It is seen that, the simulated random sea state varies somewhat from this idealized form nevertheless, it captures the main pattern of the extreme storm in its most severe portion. The current particle velocities are superimposed on the wave induced velocities in the Morison's equation to calculate the total wave induced load on the structure.

The irregular wave approach is applied with both Model-1 and Model-2 to be more representative of the sea state. The irregular wave is simulated for the duration of 8 cycles (about 150 secs). Due to the simulation length of about 150 secs and the number of analyses(at least 10-15) needed to achieve the ultimate collapse of the system, parametric(sensitivity) studies are considered to be less feasible option with this approach.

5.5.1 Ductility analysis of the jacket(Model-1) with plugged pile foundation under regular wave loading

Fig.5.32 shows the dynamic overload versus ductility demand ratio results obtained from several full 3D-Jacket analyses for harmonic wave periods of 12.5secs, 14.0secs, 15.8secs, 18.5secs and 20.0secs. Also on the same plot we have shown the predicted $F_\nu - \mu$ response curves according to bi-linear EPP-SDOF model of Schmucker, (1996) and gradually degrading EP-SDOF model established in Eq.5.14. It is seen that in the elastic range of response the discrepancies in terms of F_ν are far less significant than in near yield(or collapse) region of the response curves (close to $F_\nu = 1$ where the response has reached the ultimate static capacity).

Even slightly below this level, we observe some differences for different periods of wave loading. The smaller the wave period is the lesser the dynamic overload capacity has become. The trend is more visible for $\mu > 1.0$. The differences are particularly more significant for wave periods between 12.5 and 15.8secs. As the wave period has increased from 15.8secs towards 20secs (the upperbound period), the observed discrepancies have become less significant. The observation from our 3D-analyses here at the first glance looked paradoxical with respect to our initial understanding of SDOF systems under regular wave loading. But a closer examination later revealed that this can even be predicted based on SDOF analysis of the system with the proper

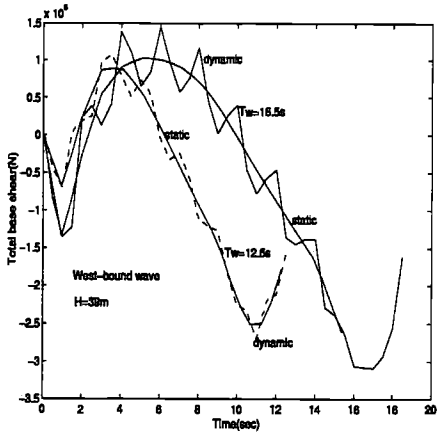

Figure 5.36: Comparison between the base shear response of the jacket platform(Model-1) under end-on loading with wave periods of $T_w = 12.5$ secs and 18.5 secs

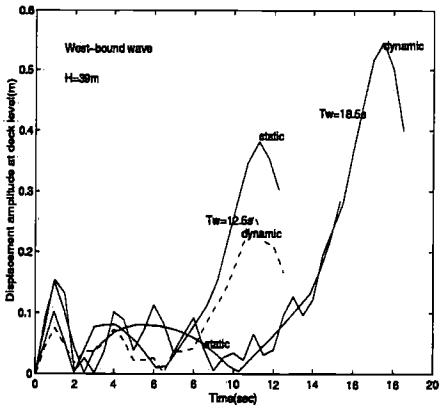

Figure 5.37: Comparison between the displacement histories of the jacket platform(Model-1) under end-on loading with wave periods of $T_w = 12.5$ secs and 18.5 secs

load history. We discuss this further in the following.

5.5.2 Discussion about the influence of wave period on F_ν

To be able to interpret the numerical observations in Sec.5.5.1, we need to examine the static and dynamic base shear and overturning moment as well as displacement histories for two cases with clear differences seen in terms of F_ν(or μ) between them. Let us consider for example two different periods 12.5 secs and 18.5 secs. The corresponding response histories are plotted for two points marked in Fig.5.32. These points correspond to the same wave heights 39m but not necessarily the same base shear or overturning moments. Due to different periods associated with these wave heights the corresponding velocity and acceleration terms calculated according to the relevant wave theory(for e.g stoke's 5th order) are different, hence, the computed drag and inertia terms from Morison's equation will be different.

According to the base shear histories plotted in Fig.5.36, the calculated total dynamic base shear for the wave with larger period of 18.5*secs* is considerably higher than that of wave with 12.5 secs duration period. The static base shear response histories indicate that the total imposed wave loading on the structure. It is seen that the dynamic base shear response curves show some superimposed oscillatory effects likely due to the superharmonics of the waves, the pre-peak stiffness degradation of the jacket-pile-soil system (and some other possible contributors of less importance which are out of the scope of this study).

The larger resonance effects can be seen in this case for the wave with the larger period(18.5secs)

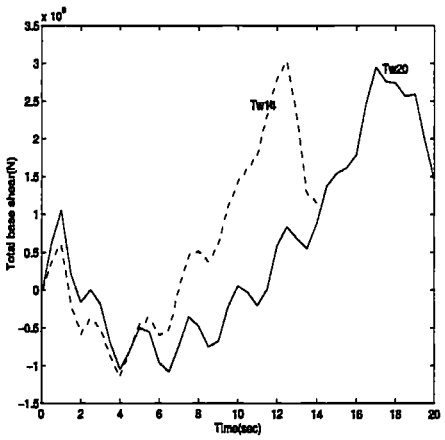

Figure 5.38: Comparison between the base shear histories of the (Model-1) jacket platform under broad-side loading with wave periods of $T_w = 14$ secs and 20 secs

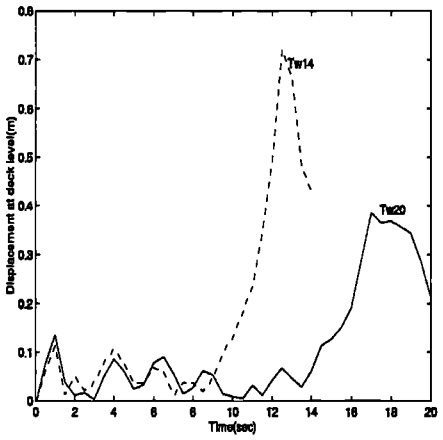

Figure 5.39: Comparison between the displacement response of the (Model-1) jacket platform under broad-side loading with wave periods of $T_w = 14$ secs and 20 secs

than the wave with smaller period(12.5secs). Comparing these base shear with the associated displacement response histories plotted in Fig.5.37 reveal that the dynamic displacement response has been smaller for the wave with 12.5secs period than the statically predicted response and far smaller than the maximum dynamic response corresponding to the wave with period of 18.5secs. It seems that for the smaller period the beneficial effects of inertia has reduced the maximum observed displacement.

On the contrary for the wave with larger period(18.5secs) the dynamic response has been

Table 5.1: Comparison of the maximum overturning moment according to wave load incrementation (WLI) and wave height incrementation (WHI) methods

	Static(pushover)	
	wave load incr.	wave height incr.
Maximum base shear(MN)	191.7*2.3568	451.8
Maximum overturning moment(MN.m)	32500	35780

generally higher prior to the collapse (largest observed peak) and at reaching this peak due to domination of the non-linear inertia the oscillatory effects have disappeared and both responses have almost converged at the onset of the major yield.

Other examples are given in Figs.5.38 and 5.39. It is seen that the maximum displacement response of the studied jacket system under a regular wave with period of 14 secs is significantly higher than that of a wave with a period of 20 secs. The corresponding maximum base shears are almost the same for both waves in this case. Fig.5.38 shows that the wave with a period of 14secs has a more rapid build-up than the wave with a period of 20secs. The jacket system

seemingly in this case had less time to compensate for the dynamic overload beyond its static capacity which is also combined with the observed linear dynamic effects. In contrast, the base shear history of the wave with the period of 20 secs is gradually increased to the same maximum value and the system probably had the possibility to compensate. This besides the fact that for the larger wave of 20secs compared to the jacket's initial natural period, the linear dynamic effect is less than that for the wave with a smaller period of 14secs.

Although the higher resonance effect can be considered as partly contributor to the difference in terms of dynamic overload ratios but it may not be the only cause. The other possible cause might be the shape of the wave load history. Other authors such as Bea and Young, (1993) and Schmucker,(1996) have also observed such effects. The trouble arises for a steeper wave with shorter period when the force input into system during the acceleration phase of response is either not well compensated during a subsequent unloading, or the gradual build up of the forces is not allowed and consequently system faces a kind of non-linear dynamic impulse (w.r.t the duration and magnitude of loading rate).

The observations indicate that the steeper waves induce more asymmetric and impulsive load history than flatter waves. More impulsive wave load history means possibility of higher potential damage to the structure. As we know, the steepness of the wave is characterized by the wave height and period parameters. Therefore, variation of the wave period might result in change of wave steepness and consequently the potential damage to the system.

The distribution of the wave forces on the structural members might also change as a result of variation in the corresponding wave period. The different distribution of the forces may change both base shear transfer mechanism and also the overturning moment calculated with respect to the mud-line.

It is believed that such effects could be more important for the overturning type failure modes of jacket-pile-soil systems which might be caused for e.g. by the pile pull-out or pile plunge, leg member buckling. However, as we found from visualization of the global collapse modes corresponding to these two wave periods, the governing failure mechanism has been base shear for both cases, since the main failure occurs in the bracings of the system and also plastic hinge in the pile is formed due to the failure of the soil under lateral loading.

The maximum overturning moment values given in Table.5.1 revealed that the difference in terms of overturning moments is considerable for the same maximum base shear. But this observed difference has not resulted in the change of overall failure mode from a base shear type to an overturning type. Nevertheless, the latter has contributed largely to the mobilization of soil in axial directions and hence it may have altered the overall jacket-pile-soil interaction.

In fact, due to existence of the plugs in the pile tips the increase in overturning moment associated with the higher wave height has not been able to cause the platform to overturn into sea. It will be later discussed that the consequence of such overturning moment increase can be quite different for jacket supported on the un-plugged type piles.

The predicted SDOF response curves as shown in Fig.5.32 are obtained according to Eqs.5.14 and Eq.5.24 of Schmucker, (1996) with assuming a 100 year return period of $T_w = 15.8$ secs for the this direction of wave. The observed correlations between the SDOF predicted response and the MDOF analysis of jacket are quite good considering that the simplified relationships do not take into account component failure of structure and only able to capture one degree of freedom response of the system. Nevertheless, they have been quite capable to capture the overall response of the system near failure. Our observation here and previous studies by Schmucker, (1996) showed that for jacket-pile-soil systems the failure response is often dominated by one single mode which can be easily simulated by an equivalent SDOF system. At most may be two or three degrees of freedom be enough to represent the collapse mechanism of jacket-pile-soil systems(see for e.g Emami et al, (1996)).

The SDOF based predicted response is in about $4-5\%$ of range of the response predicted for the west wave with a 100 year return period of 15.8secs. Since the likelihood of having an extreme wave with a height of say 42m with a duration period of less than that of a 100 year wave (with a far smaller height of about 27.3m for example the west direction) is very low in a probabilistic sense, therefore, considering the mean level for the predicted responses for the sake of comparison seems to be more rational. Comparing the predicted results in a deterministic manner also requires to choose a base curve corresponding to the same assumed 100year wave period.

From design point of view, since a most probable period associated with an overload factor of over 1.0 or 1.1 will likely be much higher than 15.8secs. Hence taking this point with the observed higher $F_\nu s$ for the larger periods than 15.8secs, we may conclude that the predicted response by SDOF relationships are even slightly conservative (in average about 5% for the end-on loading of jacket platform). With considering a deterministic under-estimation inherent in the studied SDOF systems for the practical range of $\mu = 1-5$, we may anticipate to have conservative estimate of response in most cases.

A similar investigation is launched for the broad-side response of the platform under action of North-bound wave. F_ν versus μ response curves obtained from MDOF and SDOF non-linear dynamic analyses of the 8-leg jacket-pile-soil system are plotted in Fig.5.33. As shown the predicted response based on SDOF methods are closer to about mean values of the response obtained from MDOF analyses denoted by discrete points for different wave periods.

As seen in Fig.5.39, the peak displacement (amplitude) corresponding to the shorter period $T_w = 14.0$secs is significantly larger than that of a wave with a longer duration(period) of about $T_w = 20.0$secs and for the same F_ν value.

The peak response has occurred at time about $t = 12.5$secs where the peak base shear at the mud-line level has also been observed. The peak displacement corresponding to the wave with a period of about 20 secs has occurred at about time $t = 17.0$secs when the maximum base shear is observed. The ratio between the maximum displacements is about $0.76/0.38 \approx 2.0$. We will discuss the reasons behind the observed difference for the considered wave periods.

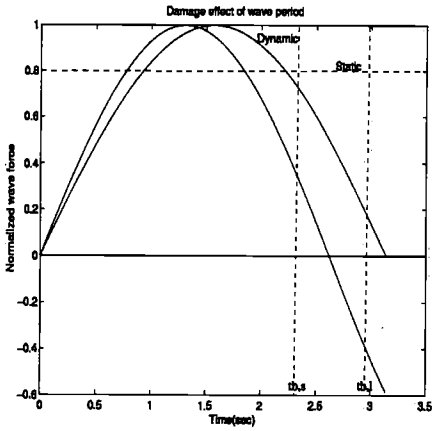

Figure 5.40: The effect of increasing wave period on the potential damage to the system

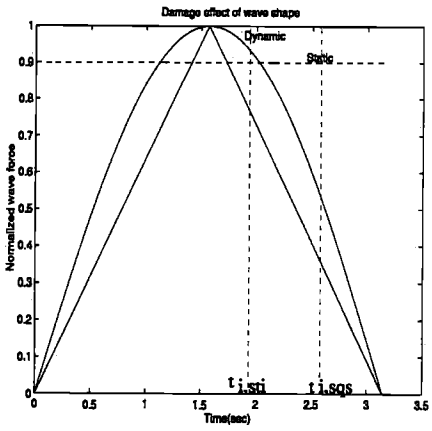

Figure 5.41: The effect of wave shape on the potential damage to the system

From our knowledge based on understanding of elasto-plastic type SDOF system's behaviour, we recall that for a wave with a larger period the damage (normalized maximum displacement) is expected to be larger than a wave with a shorter period. This point is also illustrated in Fig.5.40. As seen for instance for a simple harmonic wave with longer duration and an amplitude above the static capacity($F_\nu > 1.0$), the time which is required for system to balance this excess force denoted by $t_{b,l}$ is larger than that for a shorter wave length $t_{b,s}$. $t_{b,l}$ and $t_{b,s}$ physically indicate the duration periods within which system's inertia reaction force is active (or the inertia dominated phase of structure). As shown during these periods, the system's static resistance capacity is exceeded and hence it starts accelerating. The acceleration will go on until the excess force or energy is still added to the system that is until the time t_c when the excess force becomes zero. Thereafter the system enters a deceleration phase since the force is reduced from static capacity level and this phase may be called dynamic unloading of the system. Although the system at deceleration(negative acceleration) phase, but its velocity is not yet zero.

The system's momentum (velocity) becomes zero at the time when the whole unbalanced force is compensated which corresponds to times $t_{b,s}$ for e.g for shorter wave. A this point of time the displacement is maximum and hence the potential damage to structure will depend on this time length. If the time for balance of dynamic forces on the system becomes longer then the induced damage on the system will be larger. This implies that $F_\nu - \mu$ response curve has to be somewhat softer for a wave with longer duration period than that of a shorter wave.

Another point of view is related to the wave shape effect (Schmucker,1996). Referring to Fig.5.41. a steeper or sharper wave such as a triangular wave has less damaging effect than a squared-sinusoidal type or (smoother and flatter) wave with the same amplitude and duration period. This is because the unbalance area is smaller for the STI than SQS and thus the time needed to reach a balance is comparatively smaller. On the contrary to these implications the MDOF analyses of the full 3D-model of jacket in both loading directions indicate that the dynamic over-

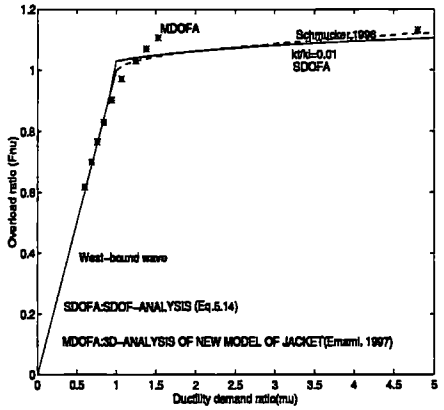

Figure 5.42: The ductility vs. overload ratio response of Model-2 of 8-leg jacket platform under end-on loading(irregular wave)

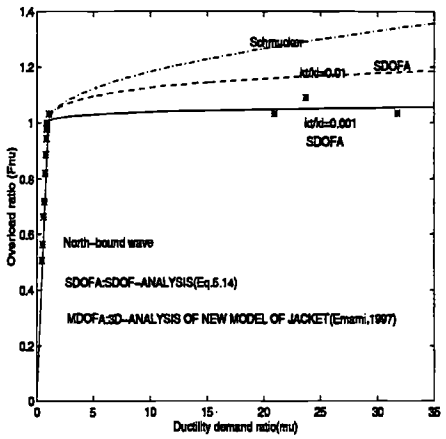

Figure 5.43: The ductility vs. overload ratio response of Model-2 of 8-leg jacket platform under broad-side loading(irregular wave)

load ratio in average is relatively smaller for the waves with shorter periods. Although we have too observed from 3D-Jacket-pile-soil system analysis for the end-on direction that in some cases the maximum displacement induced for the same wave height was larger for the longer wave. But it should be noted that the corresponding base shear has been different so the observations based on the same wave height have not changed the overall picture.

It seemed that the waves with smaller periods have induced wave load histories which are steeper than those of longer waves. These waves become more impulsive towards the collapse, the impulsive nature of the force does not allow the system to take the force gradually and hence might initiate undesirable dynamic effects. In addition to this, it is observed for e.g in Fig.5.38 that for wave height near failure the wave load history is becoming more asymmetric for shorter waves compared to longer ones. Recalling what we discussed above, the unbalance time will become longer for such a non-symmetric wave load because the system receives a larger amount of unbalance force above the static capacity level and has far smaller reduction in the trough side, hence the overall balance in one cycle is not achieved when it encounters another peak with added force which induces more acceleration.

It is evident that higher acceleration implies larger displacements (or damage). Sometimes this undesirable accumulation of dynamic unbalance forces leads to the ultimate collapse of the system. Therefore, it is not only the period and the maximum amplitude of dynamic force which determines the required ductility but also the shape of the load history which plays a significant role.

5.5.3 Ductility demand analyses of modified model(Model-2) of 8-leg jacket-pile-soil system

As described in the previous section, the dynamic performance characteristics of the jacket-pile-soil system is studied by two key parameters as the overload ratio and the maximum damage indicator(ductility demand ratio). The results given in Fig.5.42 show the relationship between the F_ν and μ for the west wave direction for the duration of the whole storm ($T_d = 150secs$).

The predicted response according to non-degrading type(ND EPP) and gradually yielding type elasto-plastic(GYEP) SDOF systems are also plotted in the same Figure. As shown the initial part of the response up to $\mu = 1$ is linear and the effects of linear dynamics are seen to be quite negligible. The maximum computed μ for a $F_\nu = 1$ is nearly 1.0. The post-ultimate response of the system is considered to be less hardening with respect to the inertia effects gained beyond the static capacity of the system. The predicted response according to the simplified models as seen are fairly conservative for the practical range of $\mu < 5.0$. The underprediction for this range of ductility is inherent in the nature of SDOF systems, because it is assumed that the inertia is activated rather for maximum displacement larger than the assumed sustainable maximum displacement for a jacket-pile-soil system.

However, from the MDOF analysis of the jacket system, we observe such considerable gain even for μ values far lesser than 5. This is because the inertia has been actually activated during the initial elastic part and also other initial cycles of the loading which has resulted in the increase of the F_ν. The activation of the inertia prior to the so-called inertia dominated phase is an issue which has been also studied by previous authors such as Schmucker, (1996). Schmucker, (1996) reported that due to changes in the stiffness of the system prior to the ultimate collapse and also possibly due to some linear dynamic effects , the $F_\nu - \mu$ relationship may change for this smaller range of ductility.

Furthermore, the damping effects present in both the structure and the pile-soil at the onset of ultimate collapse of the system might increase the dynamic resistance of the system according to Eq.5.1.

From $\mu = 1$ to $\mu = 1.25$ the SDOF models have slightly overpredicted the response. This may be related to the initial stiffness degradation and also resonance effects during the elastic range of the response accumulated and manifested in lowering slightly F_ν for this small range of μ. But as seen, the beneficial effects of the inertia soon has more than compensated for this small loss of capacity. As observed the response has hardened rapidly due to a combination of the inertia and damping resistance up to $\mu = 1.5$ where the dynamic resistance of the system has effectively exceeded 10% above the static capacity.

From this point on the MDOF response has become almost flat up to a ultimate collapse ductility obtained at about 4.8. Very slight increase of the dynamic overcapacity of only about less than 5% is observed for an increase of about 3.5 in terms of μ. This is because as the system accelerates in this range further, at the same time its static capacity is reduced to a post-peak (residual) level which is about 10% or slightly more less than that of its static ultimate capacity.

The total gain in terms of the inertia increases is likely over 20% as the μ increases. However, this benefit is at the expense of losing some static resistance due to failure of main load carrying components of the system. So the net benefit of the dynamic resistance then has become at the end something like 13% which is indeed a significant and absolutely realistic and achievable gain.

The predicted SDOF based response according to Eq.5.14 which accounts for the effective natural period changes due to the rapid degradation of the tangent stiffness of the jacket-pile-soil system is shown with solid line. The k_t/k_i is taken as 0.01 which has resulted in $T_{eff} = 10T_n$. This means that the β parameter according to Eq.5.14 has become about 0.91 which is an indicator of the system's residual strength and stiffness degradation effects.

The maximum predicted dynamic capacity according to our simple SDOF based model is about 1.11 at a ductility level of about 5. The ultimate discrepancy in terms of the predicted ultimate dynamic capacity of the system between SDOF and MDOF methods is about 2.3% in the range of $\mu = 4 - 5$. The maximum discrepancy between SDOF and MDOF methods in this case is about 5.3%. The linear dynamic effects combined with the pre-peak stiffness degradation effects totally account for about $2 - 5\%$ loss of capacity at μ range of 0.94 to 1.25.

The results obtained here are consistent with the recent findings of Stewart,(1995) on the fixed framed structures(such as jackets). He concluded that the overcapcity in terms of the dynamic resistance of such systems can be expected to be in the range of 1.1-1.2 with a ductile type response. The more realistic analyses carried out here confirm this suggestion and also our earlier findings in the previous sections from the analyses of plane frames.

In the following, we investigate the dynamic overload versus the ductility demand response of the same modified jacket-pile-soil system under broad-side(North-bound wave) loading. This direction of loading according to our earlier studies (see for previous section) was found to represent a more brittle response than the west bound direction. Even with inclusion of the non-linear pile-soil system, we found that the residual strength of the system is lesser for this direction than the west bound wave. The residual strength ratio is observed to be less than 0.8. To investigate the influence of the residual strength on the ultimate dynamic resistance of the system, we consider the lower and upperbound of k_t/k_i ratios as 0.01 and 0.001.

From our knowledge based on SDOF system analysis, the $k_t/k_i = 0.001$ might be considered as a reasonable value accounting for the rapid post-peak degradation effects.

The sensitivity of the $F_\nu - \mu$ relationship is also assessed to the changes in terms of T_{eff}. We discussed above that T_{eff} represents the effective dynamic stiffness of the system with accounting for inertia and damping effects. The predicted results based on these two values representing the lower and upper-bound for the k_t/k_i are plotted in Fig.5.43 together with the response obtained from MDOF analysis and also the predicted response according to Schmucker, (1996).

As we anticipated, the lower bound $k_t/k_i = 0.001$ matches well to the computed MDOF response

while the prediction based on $k_t/k_i = 0.01$ has overpredicted the dynamic capacity by about 10%. The response predicted according to EP-SDOF based relationship of Schmucker,(1996) has overestimated the ultimate response by about 28% at $\mu = 35$. Since this level of ductility is usually unattainable for system's such as jacket platforms as we discussed earlier, hence, a practical range of say $\mu <= 5$ is considered for our comparison. For this range the maximum discrepancy observed for response predicted based on SDOF approach of Schmucker,(1996) and the MDOF analyses results here is in the range of $10 - 15\%$.

It is worth mentioning that the observed $F_\nu - \mu$ response very well matches in the elastic range up to about $F_\nu = 1.0$ with the obtained results from 3D-Jacket analysis. The results obtained here and also the findings of Bea and Young, (1993), Stewart,(1995) might indicate that for semi-ductile type behaviour of the framed jacket system as studied here, the dynamic overstrength may be less than or equal to 1.05-1.10.

Comparing the results presented in Figs.5.43 with those presented in Fig.5.42, it can be seen that the ultimate F_ν obtained for the North-bound wave (broad side) loading is found to be about 10% less than the west-bound(end-on) loading. The reason is evident by comparison of the post-ultimate static behaviour of the jacket platform under the two different loading directions. While under the end-on loading the residual strength of the platform is about 0.9 times of its ultimate static capacity(ductile behaviour) under broad-side loading its response has been almost semi-ductile with a residual strength factor of slightly less than 0.8.

The consequence of this is that while the system has gained a lot(may be totally around $20 - 25\%$)from positive action of inertia by allowing for large displacements to develop due to the presence of plugged piles with sufficient axial resistance which has provided enough ductility compared to a linear or fixed foundation case (see for e.g the following sections). But this much gain plus the damping resistance has been just enough to compensate for the post-peak degradation of the static resistance for the broad-side loading and at the end we have obtained something like 5% net gain.

For the end-on loading, we have obtained over 10%(precisely about 13% net gain in terms of inertia) which is due to the less strength degradation at the post-peak range($\mu > 5$). Stewart, (1995) suggested that for a ductile jacket system, we may expect to gain in terms of positive inertia and damping, totally about $20 - 25\%$ if the system is semi-ductile. For e.g. for a semi-ductile system with a residual strength of about 0.8 times that of the ultimate static capacity, the dynamic overstrength of the system may be less than 10%.

For a system with very brittle behaviour, then the expectation would be a zero dynamic overstrength or even likely dynamic understrength(i.e $F_\nu < 1$) due to possible negative inertia(linear dynamic) effects(see the following sections).

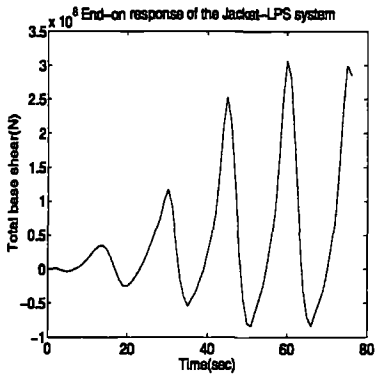

Figure 5.44: The base shear response of the jacket(Model-1) with linear spring to ground under end-on loading

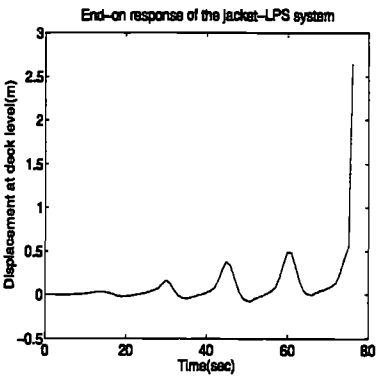

Figure 5.45: The displacement response of the jacket(Model-1) with linear spring to ground at deck level under end-on loading

5.6 The influence of foundation modelling on the dynamic vs. static response of the jacket system

5.6.1 Ductility demand analysis of Model-1 with linear spring to ground under end-on loading

The base shear response of the jacket with hydrodynamic Model-1 and linear spring to ground under end-on loading is shown in Fig.5.44. It is seen that the base shear history is strongly asymmetric with largest peaks in the crest side. This might be due to the addition of the current forces, the effect of wave reaching the cellar deck area during the passage of the crest which induces larger forces and possibly the effect of plastic deformation of the structure. The peak base shear response is observed at about $t = 60$ secs.

The displacement response of the jacket Model-1 with linear spring to ground is plotted in Fig.5.45. It is seen that the collapse of the system has occurred at the time between $t = 75 - 77$ secs. This time actually corresponds to the passage of the second largest wave crest through the upper frame above the jacket(the cellar deck level). It is interesting to note that the structure has passed safely through the first largest peak but it's collapsed during the subsequent peak of about 0.98 times the first peak at $t = 76$ secs.

The deck has moved about 3.5m in about 2 secs which implies a velocity of about $1.8m/sec.$ (It has to be noted that the displacement response near 77 secs is cut in the plot. This is done in some of the response plots where showing a very large displacement might have prevented visualizing the smaller peaks prior to the ultimate collapse). At near collapse the velocity of the deck is about 2m/sec. Viewing the deformed model of jacket shown on Fig.H.7, it is found that the diagonal bracings in the third floor have failed and subsequently plastic hinges have formed at the connection between the second and the third and the third and the fourth storeys of the

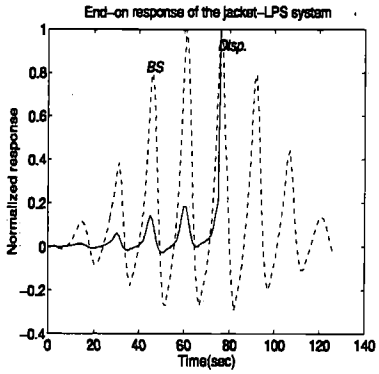

Figure 5.46: a)The normalized displacement vs. base shear response of the jacket (Model-1) with linear spring to ground under end-on loading

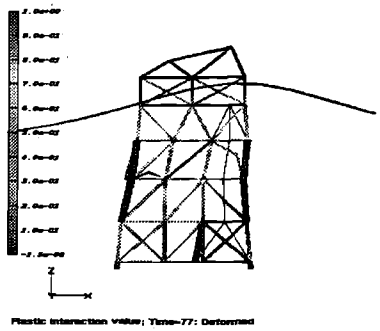

Figure 5.47: The deformed model of the Jacket(Model-1) with linear spring to ground under end-on loading (For colour figure see Appendix.H)

jacket (a frame mechanism).

Visualization of the response show that the left diagonal braces fail in tension and the one in the right bay buckles under compression at about t=76secs and then the lateral load is resisted through the frame action and by increasing the wave load finally a sway mode frame mechanism takes place at about $t = 77$ secs.

The base shear type failure mechanism is observed in the longitudinal frame of the jacket at the collapse at the third floor which also close to the centroid of the wave force on the structure. Very large permanent (plastic) deformation observed in the structure does not allow the platform to recover even after the passage of the largest crest at about 78 secs(incremental collapse). Subsequent smaller crest induce even larger displacement peak at deck level. With respect to the observed high plastic utilization of the structure and the global peak displacement of in order of 3m, the corresponding wave height of about 45.5m is considered as the ultimate collapse wave height.

5.6.2 Ductility demand analysis of Model-1 with linear spring to ground under broad-side loading

The base shear response of the jacket platform with hydrodynamic Model-1 and linear springs to ground under broad-side loading is plotted in Fig.5.48. The first largest peak has occurred at about $t = 67$ secs and the second one at about $t = 83$ secs with almost the same magnitude as the first largest peak. Fig.5.50 shows that the platform has passed safely through the first peak and collapsed during the second one.

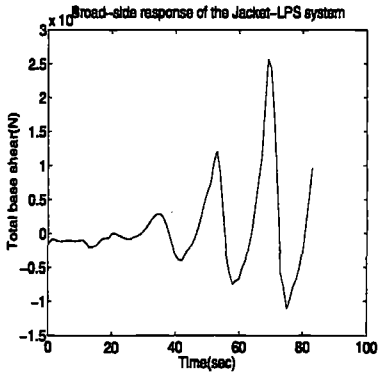

Figure 5.48: The base shear response history of the jacket (Model-1) with linear spring to ground under broad-side loading

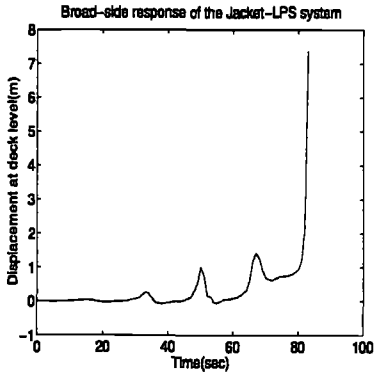

Figure 5.49: The displacement response history of the jacket (Model-1) with linear spring to ground at deck level under broad-side loading

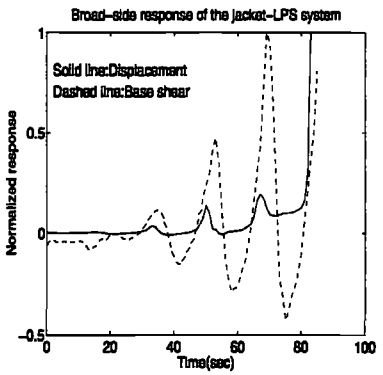

Figure 5.50: The normalized base shear vs. displacement response of the jacket (Model-1) with linear spring to ground under broad-side loading

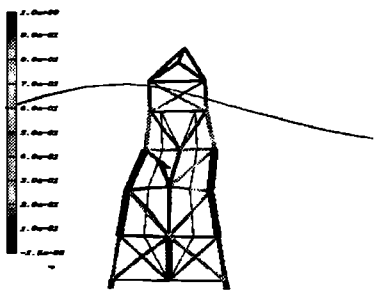

Figure 5.51: The deformed model of the jacket (Model-1) with linear spring to ground under broad-side loading (For colour figure see Appendix.H)

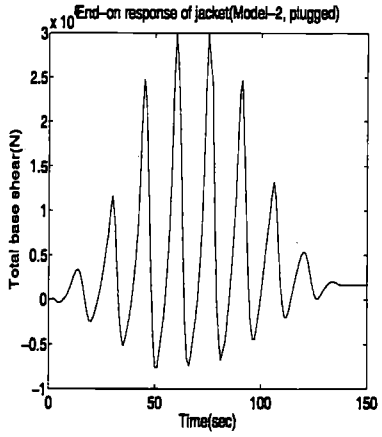

Figure 5.52: The base shear response of the jacket (Model-1) with plugged pile foundation under end-on loading

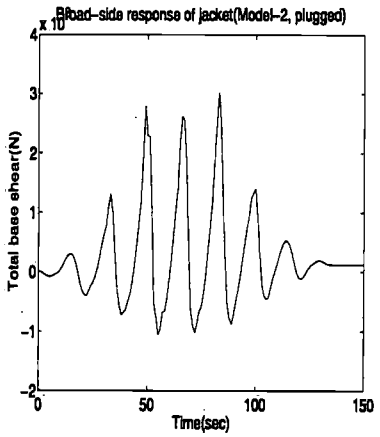

Figure 5.53: The base shear response of the jacket (Model-1) with plugged pile foundation under broad-side loading

The displacement response of the system is plotted in Fig.5.49. The deck of the platform has been displaced about 6m within 3 secs ($t = 80 - 83$ secs) which implies an average velocity of about 2m/sec. This is a quite considerable velocity compared to the water particle velocity of about 15m/sec induced by the ultimate wave height of 48.2m. Since the deck response is a slow motion type response, hence the relative velocity effect on the wave force distribution on the jacket members could be considerable. This subject will be further discussed in a following section.

The collapse of the system under broad-side loading has been caused by the increased base shear and the overturning moment. The deformed model of the jacket system with linear spring model of foundation under broad-side loading is shown in Fig.H.8. It is seen that the deck of platform has tilted during the passage of the second largest crest. The global failure of the structure is initiated by the collapse of the K-bracing system at the first peak and then by formation of the plastic hinges in the frame, the jacket system has ultimately collapsed.

5.6.3 Ductility demand analysis of Model-1 with (plugged) pile foundation under end-on loading

The base shear and displacement response histories of the platform obtained by dynamic collapse analysis under end-on loading are plotted in Figs.5.52 and 5.54, respectively. The observed base shear history is asymmetric with larger peaks occurring at crest loading as compared to trough. As seen from the displacement response history in Fig.5.54, the ultimate collapse of the platform occurs at time about $t = 76.5secs$ which corresponds to the largest peak of the wave loading (Fig.5.52). The vertical and horizontal response histories at the pile heads and

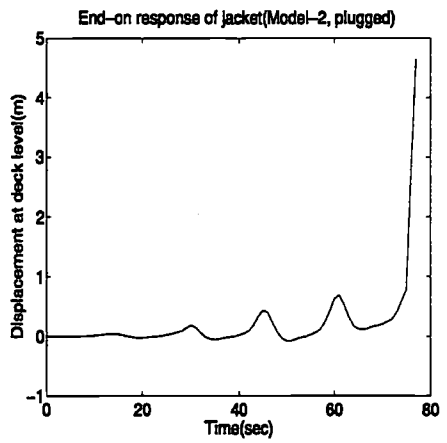

Figure 5.54: The displacement history at the deck level of jacket with plugged pile foundation and hydrodynamic Model-1 under end-on loading

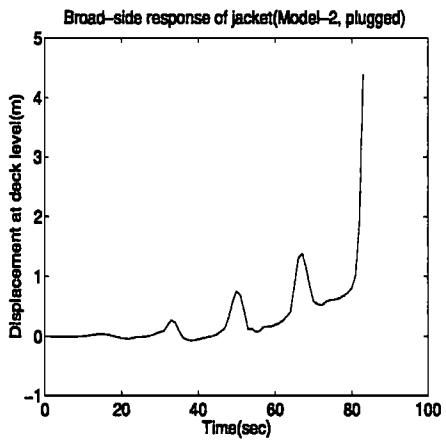

Figure 5.55: The displacement history at the deck level of jacket with plugged pile foundation and hydrodynamic Model-1 under broadside loading

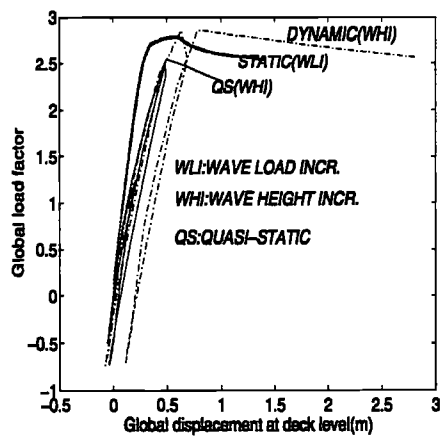

Figure 5.56: The global load-displacement(P-δ) response history of the jacket with plugged foundation model under end-on loading

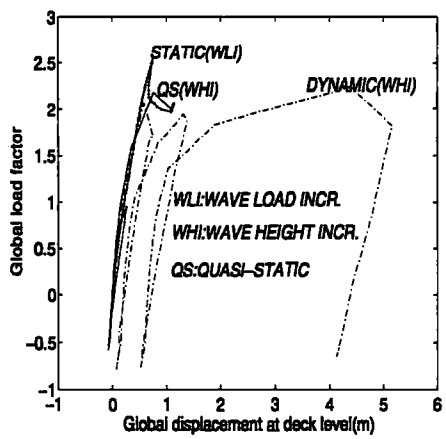

Figure 5.57: The global load-displacement(P-δ) response of the jacket with plugged foundation model broad-side loading

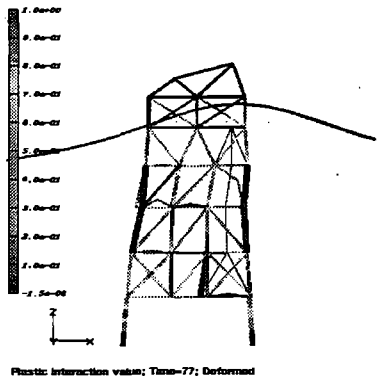

Figure 5.58: The deformed plastic interaction model of platform with plugged nonlinear pile-soil system under end-on loading(For colour display see Appendix.H)

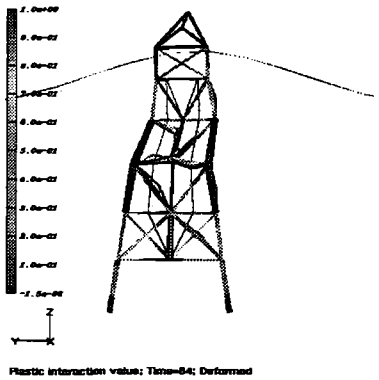

Figure 5.59: The deformed plastic interaction model of platform with plugged pile-soil system under broad-side loading(For colour display see Appendix.H)

tips are also examined which did not indicate any pile-soil pull-out, plunge or lateral collapse mode. A permanent plastic deformation is seen to have developed incrementally prior to the ultimate collapse which is also shown at the beginning of the dynamic response corresponding to the ultimate failure cycle (solid line in Fig.5.54).

The observed displacement response history of the platform at the deck level is asymmetric, with larger displacements occurring in the positive global X-axis(wave direction). This fact may be partly due to the loading asymmetry and partly due to the mentioned permanent (plastic) deformations developed in the jacket.

Fig.5.56 compares the static base shear-deflection (P-δ) response of the platform (plugged pile)with those from the failure cycles corresponding to quasi-static(cyclic) and dynamic analyses. It is shown that the quasi-static(cyclic) response curves have lower peaks due to the wave load modelling effects. Moreover, the dynamic response is somewhat stiffer than those of static and cyclic(quasi-static) ones mainly due to the inertial effects.

Table 5.2: Pushover response of the jacket platform with plugged pile foundation under end-on loading(Model-1)

	Static		Dynamic
	wave load incr.	wave height incr.	wave height incr.
RFY	1.99	1.96	2.38
RSU/RDU	2.79	2.55	2.86
RRES	2.58	-	-

Fig.H.11 shows the collapse mode of the plugged pile-soil-jacket system indicating that most of the plastically utilized members are located in this area. Also the horizontal members in the bottom bay connected to the main legs at the corners have buckled. A plastic hinge formation is seen in the left pile in Fig.H.11 at about upper one third of pile depth. This signifies that a lateral plastic interaction has taken place between the soil- pile at this point. This may be initiated mainly by the base shear transferred to the pile-soil system at the interface level. No axial failure mode(such as pull-out or plunge)is observed for the end-on loading of platform.

5.6.4 Ductility demand analysis of Model-1 with (plugged) pile foundation under broad-side loading

Fig.H.12 shows the collapse mode of the jacket with a plugged support system. The most plastically utilized (failed)members are situated at the second and the third bays from the bottom, and at the bottom bay all four horizontal bracing members have failed in compression.

As shown in Fig.3.36 (Chapter.3), the response under broad-side loading of the jacket with foundation modelled as linear springs at the sea-bed is rather brittle and the maximum RSU factor is about 2.64 compared to the 2.99 factor obtained with a plugged non-linear pile-soil model(WAJAC load).

This is mainly due to the ductility provided by the foundation which has changed the ultimate collapse mode from a brittle to a semi-ductile one. The effect of un-plugging on the ultimate collapse behaviour of the platform is even more pronounced, as seen in Fig.3.36 the *RSU* factor is then reduced to 1.94. The corresponding initial and near collapse (static) responses are closer to the linear spring case and much stiffer than the unplugged pile case(see Fig.3.36).

Table 3.21 shows the global load factors corresponding to first member failure (brace buckling), the ultimate collapse and the residual strength of the jacket -plugged pile-soil system under broad-side loading. The reserve strength of the system beyond its initial member failure is less than that for the end-on loading (see Tables 3.19 to 21). The ratio of residual to ultimate capacity of the system is lower than that for the end-on loading which indicates a post-peak degrading system under broad-side loading.

Table 5.3: Pushover response of the jacket platform with plugged pile foundation under broad-side loading(Model-1)

	Static		Dynamic
	wave load incr.	wave height incr.	wave height incr.
RFY	2.15	1.89	1.76
RSU/RDU	2.52	2.32	2.23
RRES	2.06	-	-

The dynamic ultimate resistance of the jacket under broad-side loading is about 22% lower than that under the end-on loading. This difference can be explained by examining the static load-deflection response of the jacket under these two loading directions. It is observed that the jacket-pile-soil system behaves in a more brittle manner under broad-side loading with a sharp reduction of about 20% in the residual strength of the system, while the end-on response is much softer with a smaller reduction in the system's capacity of about 9%. This is expected on the basis of the apparent ductility of the system.

Although the behaviour of this jacket-pile-soil system is mainly dominated by ductility(non-linear response), nevertheless some linear dynamic amplification (DAF) effects may have been present due to the odd and even multiples of the primary force components computed from the drag term of Morison's equation and surface elevation (Moe and Moan, 1984).These effects may be more pronounced for a random sea state with a range of frequency content. In the current simulation, however, the DAF effect may be considered as secondary to the main effects of F_ν and μ parameters.

Table 5.4 compares the results of MDOF dynamic analyses of jacket with plugged pile founda-

Table 5.4: The ultimate capacity and overload ratio of Jacket platform with plugged pile foundation (Model-1)

	RSU	RQS	RDU	F_ν
End-on	2.79	2.55	2.86	1.12
Broad-side	2.52	2.32	2.23	0.96

tion under end-on and broad-side loading, respectively.

The results given in Tables.5.2 and 5.3 indicate that the ultimate strength factors for quasi-static analysis based on wave height incrementation are about $8\% - 9\%$ lower than the ultimate strength values obtained by the traditional static pushover analysis based on wave load scaling approach. The observed difference may be mainly due to the change of the wet zone on the jacket (hence shifting the centroid of the forces on the structure upwards) and possibly due to the change in the wave load distribution on the structural members. As the centroid of the forces moves upwards, the shear wave transfer and also the resultant overturning moment change.

For base shear type failure mechanism, as observed in this case, shifting the centroid of the wave forces towards upper bays has likely reduced somewhat the ultimate capacity. The change is resulted not only because of the increased overturning moment but also due to the change in the shear force transfer mechanism as the result of shifted centroid. This is because the governing failure mechanism for this case(jacket with plugged piles) is base shear (see Fig.H.12).

The ultimate static capacity for the broad-side loading of the jacket is found to be about 10% lower than the ultimate capacity obtained for the end-on loading while the ultimate dynamic capacity for the broad-side loading is found to be about 20% less than that for the end-on loading. The observed reduction in the capacity is due to less static redundancy of the transversal frames compared with the longitudinal frames.

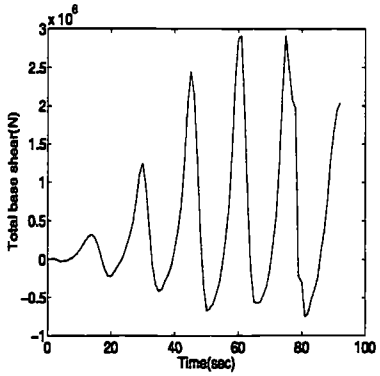

Figure 5.60: The base shear response history of the jacket (Model-1) with un-plugged pile under end-on loading

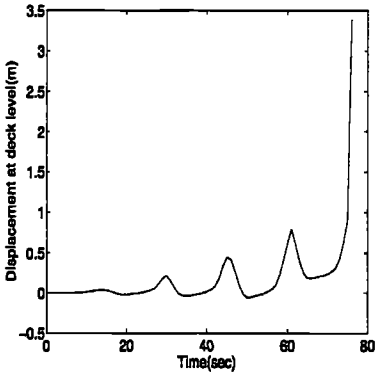

Figure 5.61: The dynamic displacement response of the jacket with un-plugged pile foundation under end-on loading

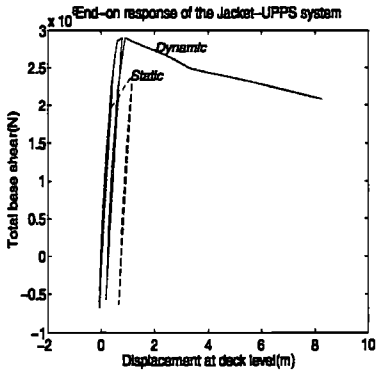

Figure 5.62: Comparison of dynamic and quasi-static(P-δ) response of the jacket system with hydrodynamic (Model-1) and un-plugged foundation model under end-on loading

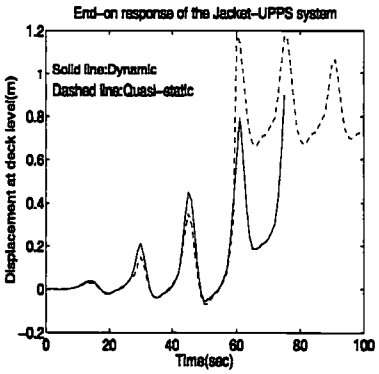

Figure 5.63: Comparison of dynamic and quasi-static displacement response of the jacket system with hydrodynamic Model-1 and un-plugged foundation model under end-on loading

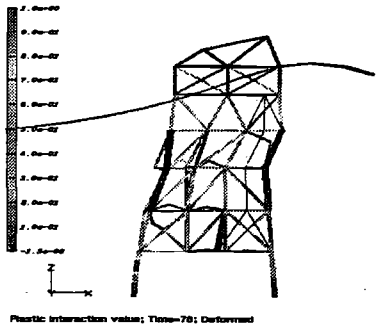

Figure 5.64: The deformed model and plastic interaction model of the jacket(Model-1) with un-plugged pile foundation under end-on loading(For colour figure see Appendix.H)

5.6.5 Ductility demand analysis of Model-1 with un-plugged pile foundation under end-on loading

The base shear response of the jacket with hydrodynamic Model-1 and un-plugged pile-soil model is plotted in Fig.5.60.

The deformed model of the system near ultimate collapse is visualized in Fig.H.9. It is seen that, the jacket-pile-soil system has collapsed at the passage of the largest crest at $t = 76$ secs. The maximum displacement of about 8m(which is not shown in the response plot to be able to visualize the smaller peaks) has occurred in about 5secs implying an average velocity of about 1.6m/sec. This is about 11% of the maximum water particle velocity. At the passage of the largest crest a sway mode frame mechanism is observed at the second and the third elevations(storeys) of the structure. The base shear frame mechanism has occurred after the failure of the main bracing system in all the three bays of the third floor. The diagonal braces at the left and the middle bays of this elevation have failed in tension and the one at the right bay has buckled under compression which is visible in Fig.H.9. Another diagonal member on the right bay of the fourth elevation has failed in tension. The compressive X-brace at the left bay of the first storey has too buckled under compression transferred from the higher elevations. Also the horizontal bracings at the left and middle bays of the second and the third floors have buckled.

Consequently the lateral force(base shear) has been transferred to the legs at the joints where the connected diagonal members have already failed. Subsequent increase of the wave load up to the crest point has resulted in plastic hinge formation at the connections between the third and fourth, third and the second floors at the right leg and also between the connections of the first and the second and the second and the third floors on the left leg. The transfer of the base shear to the soil via pile has resulted in a plastic hinge formation at the upper section of the left corner pile. This plastic hinge in the left pile indicates that the soil yield may have occurred under lateral loading transferred from superstructure at the mud-line.

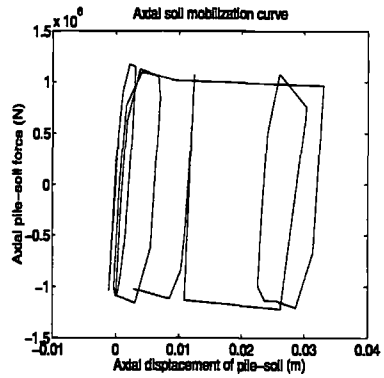

Figure 5.65: The axial pile-soil mobilization(t-z) curve at tension pile head near mudline(el.4701) for jacket(Model-1) with un-plugged pile system under end-on loading

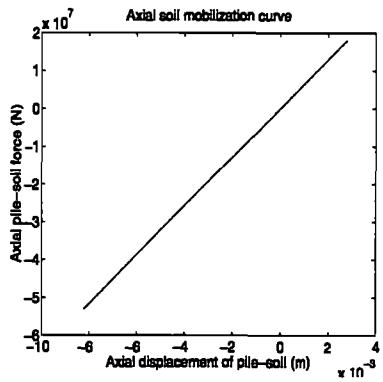

Figure 5.66: The axial pile-soil mobilization(t-z) curve at compression pile tip(el.6902) for jacket(Model-1) with un-plugged pile system under end-on loading

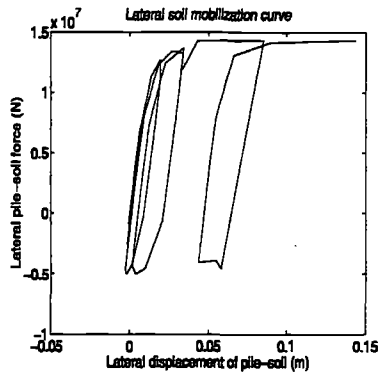

Figure 5.67: The lateral pile-soil mobilization(p-y) curve at position of plastic hinge near tension pile head near mudline(el.5201) for jacket(Model-1) with un-plugged pile system under end-on loading

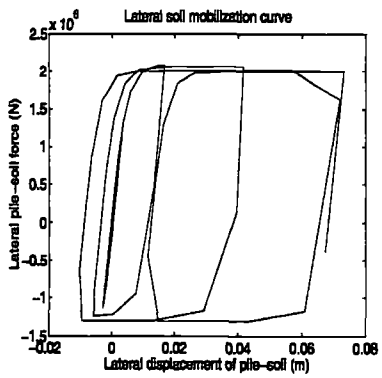

Figure 5.68: The lateral pile-soil mobilization(p-y) curve at compression pile head near mudline(el.4702) for jacket(Model-1) with un-plugged pile system under end-on loading

This can be easily verified by inspecting the lateral soil mobilization (p-y) curves plotted at the position of the plastic hinge on the left pile and the head of compression pile located on the opposite side (see Figs.5.67 and 5.68). The soil has deformed by about 140mm close to the tension pile shaft at the observed plastic hinge area. At the compression pile head(el.4702), the maximum lateral displacement of soil is more than 70mm. The large area under (p-y) curves also indicate a significant hysteretic soil damping under lateral loading at the upper parts of the piles.

Figs.5.65 and 5.66 show the axial mobilization(t-z) curves of soil close to the tension pile head and the compression pile tip. The vertical movements of the tension pile head and the compression pile tip are about 35mm and 8mm, respectively. These movements do not indicate any form of pile pull-out or plunge for this case.

Comparing the dynamic and quasi-static(WHI) displacement histories of the platform at the deck level in Fig.5.63, it is seen that significant dynamic amplification effects are present at the initial part of the response prior to collapse (up to $t = 50$ secs). The resonance is particularly significant at the second and third peaks at about $t = 30$secs and 45 secs. DAFs associated with these peaks are 1.42 and 1.29, respectively.

As the response approaches the onset of collapse (non-linear region), considerable deamplification occurs(about maximum 34% at the fourth peak at time $t = 60$ secs). At time $t = 77$ secs, the system has reached the ultimate dynamic collapse. For the purpose of comparison, we have excluded the dynamic response after this from Fig.5.63.

The base shear vs. global displacement of the platform (P-δ) curves related to the dynamic and quasi-static response(WHI) are given in Fig.5.62. The initial parts of dynamic and static P-delta curves have almost the same stiffness up to a total base shear of about 200MN corresponding to a global load factor of about 1.92. After this point a major difference seen between the dynamic and quasi-static response. The corresponding static stiffness is much lower than the dynamic stiffness due to the activation of the large inertia force in the deck. At a total base shear of about 239.6MN(RQS=2.30), an elastic unloading is observed in the quasi-static response after passage of the largest wave crests. This actually indicates a partial relaxation(shake down) of the system with sustaining considerable damage(a permanent deformation of in order of 1.0m at deck level).

Due to numerical problem associated with the plastic un-loading of the system during wave crest(increase of loading), we decided to terminate the quasi-static analyses at this level (an extreme maximum wave height of about 45.5m). With respect to structural collapse mode observed here we believed that the real RQS factor may be slightly higher by maximum $3-5\%$(RQS of 2.4 instead of computed value of 2.3).

On the contrary the dynamic response has been successfully predicted up to the ultimate collapse of the system as shown in Fig.5.62. The major yield in the dynamic response has occurred somewhat above the ultimate static response of the system due to combined effects of inertia and damping of the system.

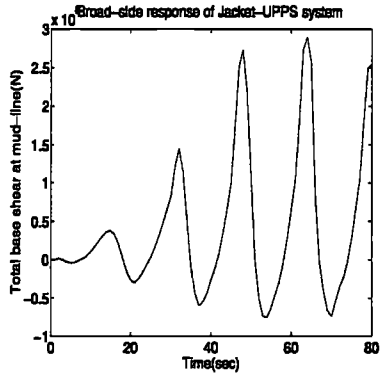

Figure 5.69: The base shear response history of the jacket(Model-1) with un-plugged pile under broad-side loading

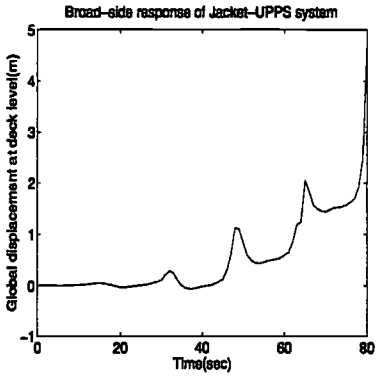

Figure 5.70: The displacement response history of the jacket(Model-1) with un-plugged pile under broad-side loading

The dynamic peak ultimate capacity is reached at the total base shear of about 291MN(corresponding to a global load factor: $RDU = 2.79$). The corresponding overload ratio F_ν is obtained as : $F_\nu = RDU/RQS = 1.16 - 1.21$. The lower bound of F_ν corresponds to the anticipated value of $RQS = 2.4$ while the upper bound of F_ν is related to the obtained value of $RQS = 2.3$ here.

5.6.6 Ductility demand analysis of Model-1 with un-plugged pile foundation under broad-side loading

Dynamic base shear and displacement response curves of the jacket platform with hydrodynamic Model-1 and un-plugged pile foundation under broad-side loading are shown in Figs.5.69 and 5.70. After the first major wave crest at the time $t = 50$ secs some plastification is observed in the response. The system has partially shaken down after the passage of the subsequent peak (the largest crest). But it has finally collapsed at the passage of the third largest peak at about time $t = 80$ secs. The deck has been displaced by about 3m from time $t = 77$ secs to $t = 80$ secs with an average velocity of about 1.0m/sec compared to the maximum water particle velocity of about 12.88m/sec. The latter may imply about 15% reduction in terms of drag force on the structural members.

It is evident that the displacement of the lower elevations of the structure is much less than this and hence the reduction of the total wave force would be far less than 5%. This topic is further discussed in the following.

Fig.H.10 shows the deformed model of the jacket with unplugged pile-soil system under broad-side loading. At the collapse the compression K-bracing members have buckled in the third storey along the four transversal frames. Meanwhile, the left pile has been partially uplifted and the opposite pile plunged into soil due to lack of plug at the pile tip.

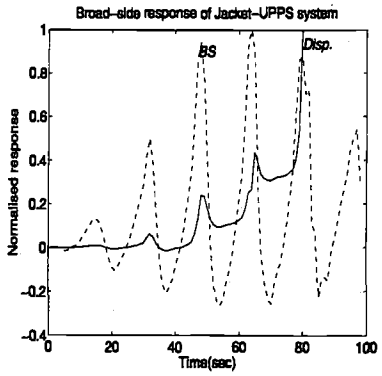

Figure 5.71: The normalized base shear vs. displacement response of the jacket(Model-1) with un-plugged pile foundation under broad-side loading

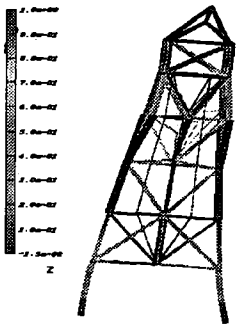

Figure 5.72: The deformed model and plastic interaction model of the jacket(Model-1) with un-plugged pile foundation under broad-side loading(For colour figure see Appendix.H)

Fig.5.78 compares the quasi-static and dynamic displacement response at the deck level for the jacket with hydrodynamic Model-1 and un-plugged pile foundation under broad-side loading. The response curves up to the time $t = 50$ secs are almost identical. Between the time $t = 50$ secs and $t = 80$ secs, some dynamic amplification of response is observed. The maximum DAF of 1.21 is observed at the time about 70 secs. The observed resonance might be due to the superharmonics of the wave induced by the drag term.

It is seen that the dynamic and quasi-static response curves have converged after the time $t = 78$ secs at the onset of the ultimate collapse of the system. It is worth of noting that a plastic deformation of about 1.5m is observed prior to the ultimate collapse.

The dynamic and quasi-static P-δ response curves of the system are compared in Fig.5.77. It is seen that the quasi-static response is somewhat stiffer than the dynamic response, particularly at the last(failure) cycle. The peak quasi-static capacity is about 295MN vs. the ultimate dynamic resistance of 289MN. The corresponding global load factors are $RQS = 2.18$ and $RDU = 2.14$, respectively. Thus the associated dynamic overload ratio is obtained as $F_\nu = RDU/RQS = 0.98$. This indicates a 2% reduction of the static capacity due to the deleterious effects of dynamics combined with the brittle behaviour of the structure. The obtained global load factors meet the minimum requirement of NPD,(1992) for ultimate limit state(ULS) design of jacket-pile-soil system for this case as 1.56. Significant safety margins are available as: $SMQS = RQS/RNP - 1 = 39\%$ and $SMDU = RDU/RNP - 1 = 37\%$.

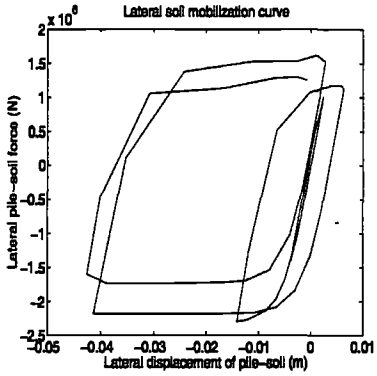

Figure 5.73: The axial(t-z) mobilization curves at the plastic hinge position in the left(tension) pile under broad-side loading

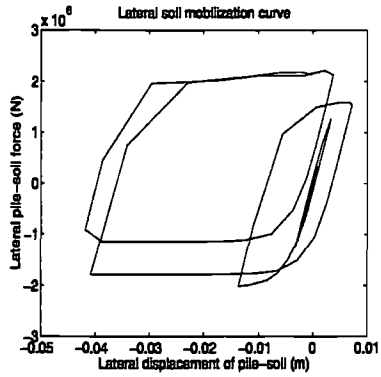

Figure 5.74: The axial(t-z) mobilization curves at the plastic hinge position in the right(compression) pile head under broad-side loading

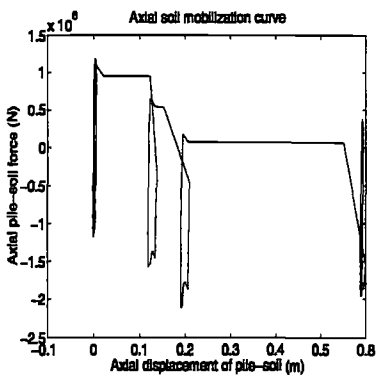

Figure 5.75: The lateral(p-y) mobilization curves at the tension pile head(el.4703) for the jacket(Model-1) with un-plugged foundation model under broad-side loading

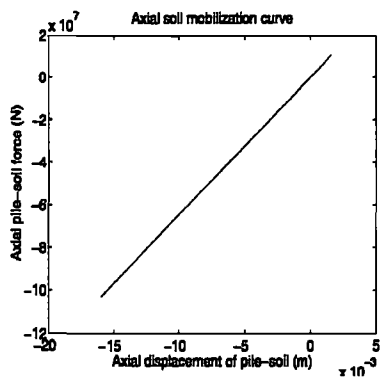

Figure 5.76: The lateral(p-y) mobilization curves at the compression pile tip(el.6902) for the jacket(Model-1) with un-plugged foundation model under broad-side loading

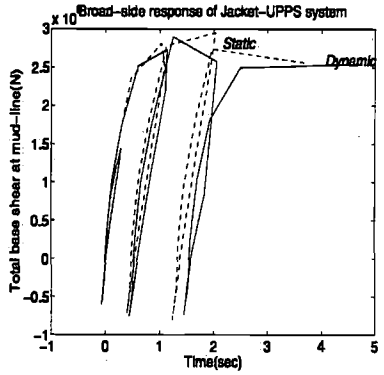

Figure 5.77: Comparison of (P-δ) dynamic and quasi-static response of the jacket system (Model-1) with un-plugged foundation model under broad-side loading

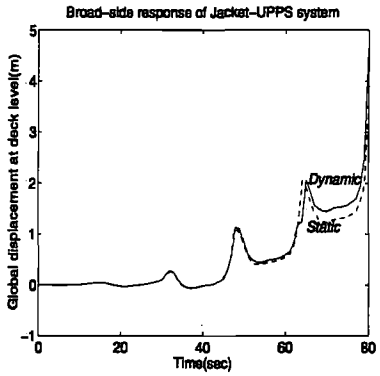

Figure 5.78: Comparison of dynamic and quasi-static displacement response histories of the jacket (Model-1) with un-plugged foundation model under broad-side loading

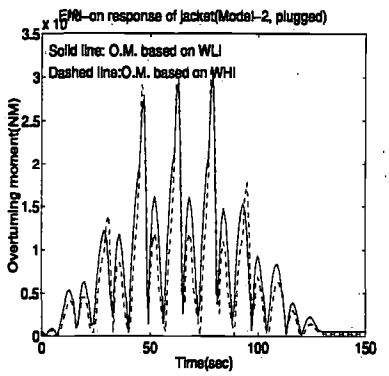

Figure 5.79: Comparison of overturning moment according to WLI and WHI approaches for the jacket(Model-1) with plugged pile foundation under end-on loading

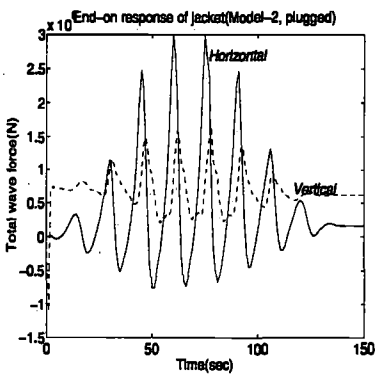

Figure 5.80: Comparison of vertical and horizontal components of the wave force for the jacket(Model-1) with plugged pile foundation under end-on loading

5.7 Comparison of the results(linear spring case) according to WLI and WHI approaches

Fig.5.79 compares the overturning moment histories for the jacket with plugged pile system and according to the wave load scaling approach (Emami et al, 1995) and the present study based on cyclic WHI approach. The maximum overturning moment corresponding to the latter method(WHI) is about $2.47/2.34 = 1.06$ times that for the former approach(WLI). The difference mainly due to the shift of the centroid of the loading on the structure and partly due to the load distribution pattern on the structure.

This 6% in terms of overturning moment may explain partly the observed different responses. However, the influence of vertical force may not be ruled out as we observe in the case of latter analysis the vertical forces vary with time and at the point of maximum base shear they seem to be negligible. With respect to the stabilizing effect of downward vertical forces, lack of such forces may cause the structure to loose its stability. Fig.5.80 shows the time history of the vertical force component.

It is seen that, the vertical force component varies with time and in some points of time is positive or upwards which means that the stabilizing force on the tension piles which is only gravity(vertical forces) has turned into an upward force pulling the pile out of ground. In contrast, the upward component of the wave does not exist in WLI method and the vertical forces are found to be positive during the history of the response and at the time of maximum base shear at the mud-line the gravitational(vertical) forces are negative or downwards which help to stabilize somewhat the tension pile. Hence, we observed a partial pull-out failure of pile in the case of scaled dynamic loading.

5.8 Influence of member fracture on the dynamic behaviour of jacket system

5.8.1 General

The jacket systems even with sufficient redundancy or global ductility may experience member or joint fracture due to the large global deformations near collapse.

The jacket platforms are usually manufactured of several sections of various sizes. There may be some small cracks developed during the manufacturing process of these components. After the platform enters its operation, these small size cracks may grow due to frequent or excessive loading such as those induced by extreme waves and earthquakes etc. If the crack growth continues, it may result in member or joint failure and hence loss of system's overall capacity.

If the joints are well manufactured such as cast nodes, they might be assumed as rigid. However, in the cases that joints are expected to behave as flexible, there is a possibility for the joint rupture due to development of large deformations near the collapse of the jacket system.

At the present study, we shall assume that the frame joints are rigid. Hence, we will investigate the influence of the member fracture on the global response of the jacket platform near failure.

The strain level in the members under tensile forces has to be checked and if it exceeds a certain limit, the member is considered to be ruptured. The forces then has to be distributed on the adjacent members connected to that member, this is done in for e.g. computer program USFOS, (Søreide et al, 1994) by introducing an internal load case. The external loading after the load re-distribution can continue on the fractured element.

The fracture check is based on the so-called "load 3" CTOD criterion(Næss, 1985). A simplified model is adopted here for calculating the strains in the plastic hinges. The crack tip opening displacement "CTOD" is computed on the basis of the nominal strain, the corresponding stress(which may be raised due to hardening) and an assumed crack length as follows:

$$CTOD - crit < \pi \epsilon_u . \frac{\sigma_u}{\sigma_y} a \tag{5.70}$$

in which CTOD-crit= the critical crack tip opening

ϵ_u = the ultimate strain at the rupture

σ_y = the yield stress of the member

σ_u = the ultimate stress at the fractured member(1.3 σ_y)

a = the flaw size

The choice of the flaw size depends strongly on the crack length growth mechanism and is a highly stochastic parameter related to the loading history, the geometry of the crack and other relevant parameters. Hence, an appropriate selection of this parameter must be made to reflect the uncertainties involved.

5.8.2 Ductility demand analysis of the fractured model of jacket with hydrodynamic Model-1 (without the effect of pile-soil) under end-on loading

Dynamic base shear and displacement histories of the fractured model of the jacket platform with linear spring to ground and hydrodynamic Model-1(without the effect of pile-soil) are plotted in Figs.5.81 and 5.82.

The displacement response of the intact and the fractured model of the jacket are almost identical prior to collapse. After time about $t = 76$ secs, a small discrepancy is observed between the results. The base shear response also indicates the same. However, the interesting difference

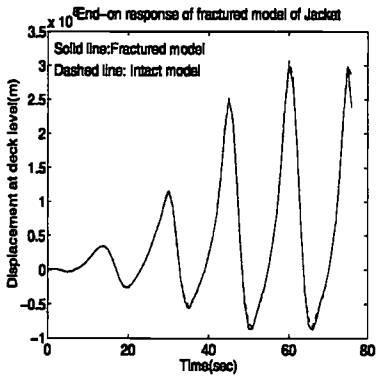

Figure 5.81: The base shear response of the fractured model of the platform(Model-1) with linear spring to ground under end-on loading

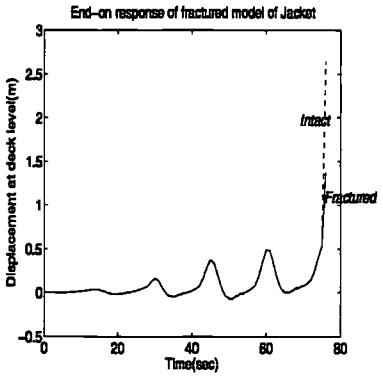

Figure 5.82: The displacement response history of the fractured model of the platform(Model-1) with linear spring to ground under end-on loading

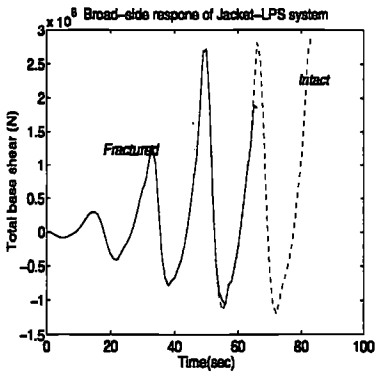

Figure 5.83: The base shear response of the jacket platform(Model-1) with linear spring to ground under broad-side loading

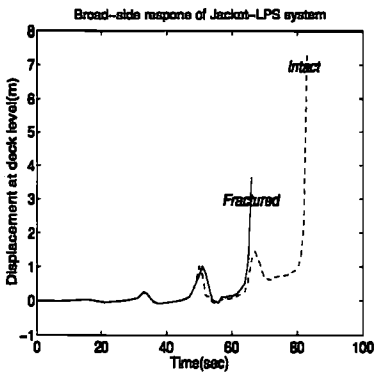

Figure 5.84: The displacement response history of the jacket platform(Model-1)with linear spring to ground under broad-side loading

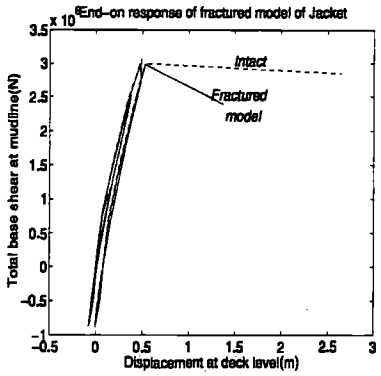

Figure 5.85: The dynamic vs. quasi-static (P-δ) response histories of the fractured model of jacket platform(Model-1) under end-on loading

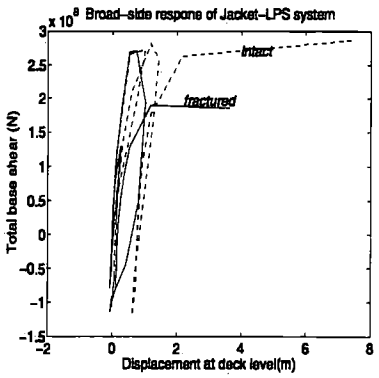

Figure 5.86: The dynamic vs. quasi-static (P-δ) response histories of the fractured model of jacket platform(Model-1) under broad-side loading

emerges in $P-\delta$ response curves plotted in Fig.5.85. It can be seen that the fractured model of jacket degrade at much faster rate(more brittle) than the intact model. The residual strength of the fractured model is about 0.8 compared to 0.93 for the intact model under end-on loading. This means that a ductile system has become a semi-ductile due to loss of member ductility.

It is seen that the ultimate dynamic capacity of intact and the fractured systems are almost the same. The wave heights corresponding to the ultimate collapse of the intact and fractured models are obtained as 45m and 45.5m, respectively. The corresponding RDU ratio is obtained to be: $RDU_{fractured}/RDU_{intact} = 0.98$. This indicates that for a ductile structure the member fracture check may not be very important compared to a more brittle structure. This topic is further pursued in the following.

5.8.3 Ductility demand analysis of the fractured model of jacket with hydrodynamic Model-1 (without the effect of pile-soil) under broad-side loading

The dynamic response time histories of the jacket platform with linear spring to ground and hydrodynamic Model-1 are plotted in Figs.5.83 and 5.84. It is observed in Fig.5.83 that the ultimate collapse base shear of the fractured model is about 0.95 times that of the intact model(without ruptured member).

Some discrepancy is observed in the displacement response of the fractured and intact models after time about $t = 50$ secs. It is seen that, the fractured model has collapsed at about time $t = 67$ secs about 18 secs prior to the ultimate collapse of the intact model. It is seen that the deck of the platform has moved about 6m within 3 secs implying an average velocity of about 2m/sec. This velocity may be compared to the maximum particle velocity of about 15m/sec for

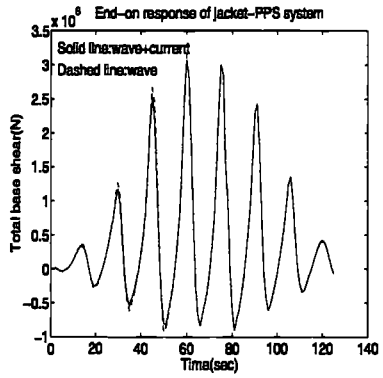

Figure 5.87: Comparison of the base shear response of the 8-Leg jacket(Model-1) with plugged pile foundation with and without current

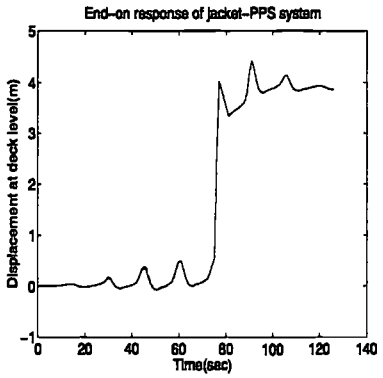

Figure 5.88: Comparison of the displacement response of the 8-Leg jacket(Model-1) with plugged pile foundation with and without current

the collapse wave height of about 48.25m.

Comparing the P-delta response of the two models in Fig.5.86, it is seen that the initial parts of the response are almost identical. The fractured model shows sign of rapid degradation than the intact one. The ultimate dynamic(base shear) capacity of the intact model is about 5% higher than the fractured one. The post-ultimate response of the fractured model is much softer than the intact one. For example at the failure cycle, the total base shear capacity of the intact model increases even after observing a global displacement in excess of 2m at the deck level. This is because of the activated inertia and damping reaction forces at such observed large displacements while the fractured model has not gained much from the positive inertia effects due to loss of member ductility.

5.9 Influence of current on the dynamic response of the jacket with hydrodynamic Model-1(without the effect of pile-soil) under end-on loading

Dynamic base shear and displacement(near collapse) histories of the jacket with hydrodynamic Model-1 (without the effect of pile-soil) under end-on loading (with and without current) are plotted, respectively, in Figs.5.87 and 5.88. Fig.5.89 compares the P-δ response of the 8-Leg jacket with linear to ground model of foundation under end-on loading(with and without current).

The response of the system without current load included appear to be somewhat stiffer compared to the response associated with combined wave and current loading. The ultimate collapse

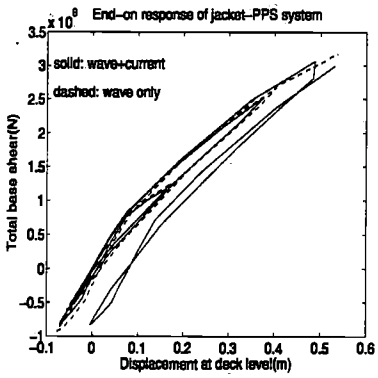

Figure 5.89: Comparison of P-δ response of the 8-Leg jacket(Model-1) with plugged pile foundation with and without current

factor of the jacket under wave load is about 5% higher than that for combined wave and current loading. This discrepancy can be compared to that of static response obtained in Chapter.3 which is about 7.5%. The slight difference may be attributed to the inertia and damping effects.

The response of the system under combined wave and current loading appears to be more asymmetric compared to that obtained under only wave loading action. The difference may be attributed to the change in the water particle velocity due to the combined wave and current action and distribution of the drag and inertia forces on the structural members. Since the current is on-line with the wave, hence at the crest the peak wave load is larger than that for the trough where the direction of the current is opposite to that of the wave.

5.10 Relative velocity vs. absolute velocity based dynamic overstrength

It is observed that during the recent investigation that relative velocity of the jacket near the collapse might have a considerable influence on the ultimate load factor of the system. For e.g Schmucker, (1996) found that the relative velocity based wave force calculation may result in $10-15\%$ reduction of the overall base shear for relatively slender jackets compared to a fixed based system.

Our investigation showed that for the relatively stiffer jacket system (with plugged pile foundation), the reduction in the total base shear is about 5%. The difference between our finding here and those of Schmucker, (1996) can be explained as follows.

The magnitude of the modification of the drag term in the Morison's equation depends on the amplitude of the water particle velocity and the velocity of the jacket structure itself. It is evident that the velocity of a more rigid structure will be less than that of a more flexible one.

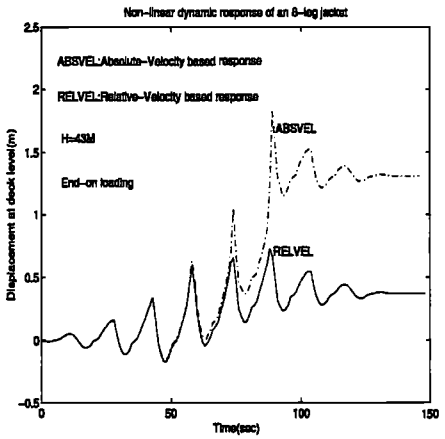

Figure 5.90: Comparison between response histories calculated based on relative and absolute velocity methods

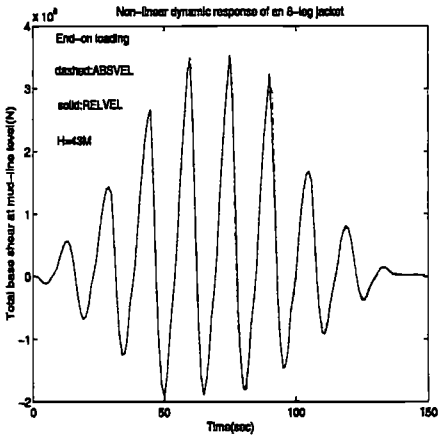

Figure 5.91: Comparison between total base shear histories calculated based on relative and absolute velocity methods

Also the ultimate collapse wave height of the stiffer structure would be higher than a more flexible one. For e.g for slender jackets which were studied by Schmucker, (1996), the ultimate wave height at the collapse of the structure was in the range of 60-75ft(about 18m-22.5m).

Comparing these with our example of the 8-leg North-sea jacket with a 100 year wave height in the range of 27.3-30.2m and the collapse wave heights in the range of 40-50m for different wave directions and also considering that the water depths is about 109.5m. These will imply that for the larger wave heights the water particle velocity are higher in this case than those associated with the relatively smaller wave heights as studied by Schmucker, (1996). The result is the smaller structural velocity compared to much larger water particle velocity (say about $1-2\%$) which has yielded slight modifications of drag force in Morison's equation.

Our analyses showed that the maximum wave height corresponding to the ultimate dynamic collapse of the jacket (Model-1) is increased from 42m for the end-on loading to about 43m as shown in Fig.5.90. This corresponds only to about 4% increase in terms of the ultimate dynamic capacity of the system. For the broad-side loading of the Model-1 of the 8-leg jacket platform, a maximum wave height of about 42m is obtained here corresponding to the collapse of the system vs. a wave height of about 41m which represents again about 4% increase in terms of the ultimate dynamic(base shear) capacity.

It is observed that jacket platform with un-plugged pile foundation which deforms much larger due to pull-out of the tension pile, the ultimate wave height is increased by about 1.5-2m (from 41.m to about 42.75m)for the end-on loading of the system. The increase in terms of the total dynamic capacity was obtained to be about 7% compared to about 4% as we obtained for the

previous cases of the modified jacket with plugged piles.

Based on these recent findings, it may be expected to have about $5-15\%$ gain with respect to the relative velocity of structure. The lower bound may be considered for much stiffer jackets with higher collapse wave heights as the cases we studied and the higher bound for more flexible jackets with lower associated collapse wave height.

If we combine the effects of positive inertia and relative velocity of structure, a gain of up to $20-25\%$ can be achieved beyond the ultimate static strength for ductile systems. This desirable effect can not be neglected in the re-assessment studies of of the most jacket platforms particularly those which are facing other problems such as subsidence in the sea-bed and wave in deck forces and are at the limit of being declared unsafe. The implication of an increase of ultimate dynamic capacity of the system by about $10-20\%$ might be quite significant for such systems in terms of avoiding lots of costs for restrengthening and frequent monitoring/inspection which otherwise have to be sustained.

Table 5.5: The predicted versus computed overload ratios of jacket platform with plugged pile foundation under end-on and broad-side loading(Model-1)

Predictive Method	F_ν (end-on)	F_ν (broad-side)
MDOF(abs.velocity)	1.12	0.96
MDOF(rel.velocity)	1.16	0.99
Stewart et al, 1993	1.10-1.20	$\leq$1.00
Schmucker, 1996	1.04	0.91
Eq.5.14	1.13	0.96

5.11 Comparison of the MDOF and SDOF analyses results

The predicted dynamic overload values according to SDOF and MDOF analyses are summarized in Tables.E.15 to E.18 of Appendix.E. The cases include the original and the modified models of the 8-leg jacket platform with different foundation models as described above. The predictive methods are based on MDOF and simplified SDOF analyses of the systems as outlined in the previous sections.

Generally good correlations are obtained between the results of the simplified SDOF and MDOF analyses methods. In particular the simplified relationship presented in this chapter has offered very close predictions of the ultimate dynamic capacity of the jacket system. There is also good correlation in most cases between the presented relationship here and that of Schmucker, (1996) based on a bi-linear idealization of an elasto-plastic SDOF system. The latter relationship is shown to give somewhat higher estimates of the overload ratio for brittle systems (with larger

post-collapse degradation). Schmucker's approach is found to be rather conservative for ductile and semi-ductile systems with less load shedding after the ultimate collapse load.

In contrast, the simplified approach based on gradually yielding SDOF system indicated fairly very good predictive capability w.r.t the overload capacity of the brittle as well as ductile systems studied here.

It is seen that the correspondence is quite good between the results obtained from recent analyses based on varying sea surface elevation(WHI method). While the overload factors obtained from previous analyses of jacket platforms(Bea and Young, 1993 and Emami et al, 1995) based on a fixed sea surface elevation(WLI approach) seem to be somewhat conservative. In particular, an overload ratio of about 1.36 is obtained from analysis of the jacket platform(Model-1) with linear spring model of foundation under end-on loading(Emami et al, 1995).

Similarly overload ratios of somewhat higher than 1.2-1.3 obtained by Stewart, (1995) for a plane frame of a jacket model without accounting for foundation failure and member fracture effects. Bea and Young, (1993) also obtained overload factors of slightly higher than 1.3 from analysis of a 12-leg jacket platform as quoted in Table.5.4. On the contrary, the results of the recent analyses of the 8-leg jacket platform with varying the sea surface elevation and accounting for the structure-foundation interaction, has resulted in more realistic overload ratios which are in the range of 1.12-1.16 for the ductile and 0.96 to 1.07 for the brittle to semi-ductile response of the jacket system. These results well match the predicted results based on Eq.5.14 and other simplified formulations as presented in Table 5.4.

The results obtained by Stewart, (1995) also indicated that the jacket platform might possess dynamic overstrength in the range of 1.1-1.2 for ductile system while for semi- ductile type system up to 1.05 and for more brittle systems with DAF effects less than or equal to 1.0.

It seems that the relationship based on ND EPP SDOF system as presented previously by Bea and Young, (1993) and Emami et al, (1995) for particular range of natural periods may be valid for the jacket systems without accounting for strength and stiffness degradation. Such relationship seems to offer fairly reasonable first order estimates of overload ratio under seismic loading with much shorter duration than the extreme sea waves.

Our proposed relationship(Eq.5.14) also gives good estimates for the seismic ductility demand of the jacket type fixed frames. For smaller values of (T_w/T_n) typical for seismic loading, Eq.5.14 results in higher values of F_ν than those obtained for the studied wave load periods. As shown in Sec.5.3.1, overload ratios in the range of 2-3 can be obtained for a double braced two storey plane frames with natural periods of 0.3-0.8 secs under seismic loading with duration period of 0.5-1.0 sec.

5.12 Concluding remarks

It is shown that the dynamic performance of a jacket-pile-soil system near the ultimate state of collapse may depend on structural, pile-soil as well as dynamic load characteristics. In the present work, we studied some of the most important parameters related to the dynamic performance of the system.

The concept of ductility spectra is developed to facilitate the study of the key parameters such as ductility, overload ratio and the natural period of the system. Simplified non-linear SDOF as well as more complex MDOF models of jacket-pile-soil systems are employed. The ductility spectral analysis concept based on simplified SDOF and 3DOF systems is introduced. This approach offers efficient means to study the influence of key structural as well as loading parameters on the dynamic response of the system near collapse.

A procedure is developed to establish the ductility spectra based on static and dynamic pushover analyses of equivalent simplified models. A simple relationship is obtained based on the results of analyses of simplified models. The predictive capability of the obtained formulation is assessed against the results of more complex 3D-Jacket analyses, 2D-plane frame analyses and also other existing relationships.

It is shown that the suggested relationship here offers reasonably good first order estimate of the dynamic overload ratio of the system. The capability of the model is attributed to the account taken of several important parameters such as gradual yield of the system(tangent stiffness variation), the post-peak strength degradation, the wave duration, natural period of the system and the wave shape and height effects.

The obtained SDOF based relationships seem to offer good first order estimates of the ductility demand or dynamic overload of a more complex MDOF jacket system. These simplified models may provide useful tools for a preliminary assessment(screening)of the dynamic performance of the jacket systems.

The inertial resistance of the structure is shown to be important in providing an additional reserve strength for structures with sufficient ductility. It may also be concluded that the effect of ductility can be significant in providing an overload factor of large than unity. Overload factors in the range of 1.1-1.2 were obtained for the systems with ductile behaviour. On the contrary, overload ratios slightly lower or closer to unity were found for systems with semi-brittle type behaviour.

The foundation modelling is found to have significant influence on the near collapse behaviour of the system. Hence, it is concluded that realistic (nonlinear) pile-soil models should be used in the ULS based analysis.

The effects of superimposed harmonics are shown to be important in reducing the overload ratio for brittle behaving systems. Such reduction for jacket system under wave loading studied here found to be less than about 5%.

It is observed that for the relatively stiff(rigid) jacket systems studied in this chapter, the ultimate dynamic collapse capacity is increased in the range of $3-7\%$ through accounting for relative velocity in the wave load calculation. The smaller influence was obtained for the linear spring type foundation model and the plugged type pile foundation with relatively smaller displacement response at the deck level compared to the jacket with un-plugged pile for which we found a greater influence.

In the cases studied here, it is observed that the maximum displacement response of the jacket at the deck level often exceeds the largest diameter of the leg member and also found that no high frequency motion is involved at the deck level. The observations indicate that the relative velocity effect on the ultimate near collapse behaviour of the jacket-pile-soil system may not be neglected.

CHAPTER 6

RELIABILITY ANALYSIS OF JACKET-PILE-SOIL SYSTEM AT THE LIMIT STATE OF COLLAPSE

6.1 Introduction

There is a need for reliability based analysis of jacket-pile-soil system due to uncertainties associated with the structural, pile-soil resistance as well as environmental loading. The uncertainties might be related to both geometrical and material parameters of the structure and pile-soil foundation as well as ultimate resistance calculation models associated with both structure and foundation. In a similar manner, the sea state parameters are considered to be random (by nature) and also the wave and current load calculation model is associated with some degree of uncertainty.

In the past two decades, various methods for reliability based analysis of fixed jacket type offshore platforms have been developed. These methods are either based on component or the system reliability assessment such as works by Bea, (1991), Baker and Vrouwendvelder, (1992), Karamchandani, (1990), Moses and Liu, (1992), Olufsen and Moan, (1989), Shetty, (1992), Sigurdsson et al, (1993), Wu and Moan, (1989). In the recent studies, the effects of pile-soil-jacket interaction have been analyzed such as works by Bea, (1993, 1995), Hansen et al, (1995), Samier et al, (1994).

While systems reliability approaches are not yet applied in the design of new structures, they are used in reassessment of existing jackets when simple conservative methods are insufficient(API 1994, Digre et al, 1995). This is because more realistic and complex procedures would then pay off in making decisions which affect safety and significant costs of replacing or modifying the

structure. Use of system based reliability assessment approach is initially motivated by the significant reserve strength beyond the first member failure which is the basis for the conventional design methods(Lloyd and Clawson, 1983).

The so-called "direct" system reliability approach may require very significant computational efforts when it comes to consider the jacket-pile-soil interaction. Such direct methods so far mostly applied for re-assessment of fixed jacket platforms (for e.g. Sigurdsson et al, 1993). Hence, the recent research is focused on establishing computationally efficient system reliability methods(for e.g. Bea, 1993, Hansen et al, 1995, Samier et al, 1994 and Vugts and Edwards, 1992). Such simplified methods are often based on a system limit state function which relates the system resistance (R) to the total base shear at mudline for e.g. as an indicator of the load (S). After establishing the appropriate uncertainty measures related to various jacket, pile-soil, sea state and wave load model, the failure probability is evaluated by using first order and second order reliability methods (FORM/SORM), bounding techniques or other simulation techniques(see for e.g. Madsen et al, 1986, Moan, 1997 etc).

The annual maximum load parameter (S) is defined as the total base shear(BS) and related to a specific wave height,i.e.100 year wave height(H_{100}). The $BS - H_{100}$ relationships are established for two main wave directions, namely, North and West. The wave load calculation procedure is modified based on the draft version of API RP2A, (1994).

The annual system strength parameter(R) is considered as a probabilistic function of the random pile, soil parameters and pile-soil interaction modelling and a function of the model uncertainty in structural strength calculation, sea-state parameters and wave load model.

A simplified linearized relationship is used to relate S to the deterministic base parameter S_0 and the first derivatives of S with respect to all pile-soil random parameters. An iterative scheme is adopted to converge at the design point. The inaccuracy introduced into the reliability calculations by this linearization is compensated by the performed iterations.

Two different approximations of the failure surface in the vicinity of the design point are used for reliability analysis respectively a first and a second order methods.

The uncertainties in the wave load modelling is accounted for by introduction of a model uncertainty in wave load calculation and modelling the maximum annual wave height as random. The structural uncertainty is also considered through a model uncertainty in system strength (R) calculation.
A simulation procedure is established for generating the pile-soil resistance characteristic (t-z), (p-y) and (q-z) curves, system ultimate strength, wave and current induced load calculation and reliability analysis of the jacket-pile-soil system under extreme wave loading by using computer programs GENSODM (Emami, 1994), USFOS(Søreide et al,1994), WAJAC(DNV, 1992) and RELAP (Hovde, 1995), respectively. (see Appendix.G).

Reliability analysis program RELAP (Hovde, 1995) is formulated based on an annual probabil-

ity failure function for the ultimate limit state of collapse of the pile-soil-Jacket system. The annual failure probability function is defined as the probability that the annual maximum load parameter(S) exceeds the (annual)system strength (R).

To study the effects of the uncertainties in the soil and pile parameters, the pile-soil interaction modelling and the wave load modelling on the near failure behavior of the pile-soil-Jacket systems, a series of simulations are performed for each of random parameters involved. The importance factors for each set of random parameters and the reliability indices are computed for both wave directions.

6.2 Theory background

6.2.1 Ultimate limit state failure function of the pile-Soil-jacket system

The collapse behaviour of pile-soil-jacket systems is a function of non-linear structural behavior, pile-soil interaction, load pattern and their interaction. Each of theses parameters are subject to uncertainties which are either inherent or due to fabrication, measurement and modelling.

For instance, the structural uncertainties might be due to randomness in geometrical and material properties as well as model uncertainty associated with non-linear structural analysis particularly at large displacements near the ultimate collapse of the platform.

An extensive study of uncertainties affecting the strength of the jacket-pile-soil system has been carried out by (Hovde and Hellan, 1992). In the present study, the overall model uncertainty is considered through a model uncertainty factor for the system strength(R). The mean value for model uncertainty of system strength (R) is taken as 1.0 and the corresponding COV of 0.15. The latter has been selected conservatively as an order of magnitude of the uncertainties in the calculation of system strength. However, in the previous studies by (Hovde and Hellan, 1992), (Sigurdsson et al, 1993) and (Hansen et al, 1995) the COV of strength model uncertainty has been varied in the range of 0.05-0.15.

The pile and soil parameters and pile-soil interaction modelling are defined as random to account for the uncertainties involved in each of these parameters. The wave load model uncertainty is taken into account by assuming wave height as random in calculation of (S). The ultimate limit state of collapse function is defined as follows:

$$g(x) = R(x) - S(x) \tag{6.1}$$

where $g(x)$ is the failure function, $S(x)$ is the load function, $R(x)$ as the system strength function and (x) representing the corresponding random parameters.

The annual probability of failure would be defined in the following form:

$$P_{f(a)} = P(g_a(x) \leq 0) \tag{6.2}$$

where $P_{f(a)}$ is the annual probability of failure of the pile-soil-jacket system. It may be note worthy that $S(x)$ and $R(x)$ have to be calculated at the design point. For annual probability of failure $P_{f(a)}$, the annual maximum load at the first iteration $S_i(x)$ and the annual ultimate system strength at the first iteration $R_i(x)$ may be considered. Also note that $S_i(x)$ is calculated from base shear vs. wave height relationships and $R_i(x)$ is obtained at the first iteration as a function of the mean values of the random variables x. At the next iterations of the analysis, the design values of the random parameters $x*$ are considered(see also the following subsections). It is also noteworthy that the load pattern related to calculation of $S(x)$ may vary from the initial values of the wave height to the final converged values close to the design point. However, this variation effect is not considered to have a very significant impact on the reliability analysis results, if the waves do not reach the deck of the platform.

6.2.2 System uncertainty modelling

In the present study, a simple approach is adopted by incrementing the gravitational loads to unity and incrementing the environmental loads until collapse without factoring with their partial safety factors. Hence, the ultimate capacity factors are obtained for the global system strength for each variation of the random variable which is described in the following.

The system strength may be expressed as follows:

$$R(x) = R(x_s, x_p, x_{psim}, x_{st}) \tag{6.3}$$

where x_s, x_p, x_{psim} represent respectively soil, pile and pile-soil interaction modelling random parameters and x_{st} denotes the model uncertainty in the calculation of structural strength. In USFOS analysis, the ultimate strength $R(x)$ is obtained as a function of the components strength. Hence, parametric function Eq.6.3 is numerically evaluated in our reliability analysis (RELJPS) procedure(no explicit form of these functions are given here). It may also be argued that system strength function evaluated numerically from a non-linear pushover analysis might be (in general) dependent on the wave pattern as well. While the global load function $S(x)$ may be expressed as follows:

$$S(x) = S(x_{wlm}, x_{ss}) \tag{6.4}$$

where x_{wlm} represents the model uncertainty in the wave load modelling due to uncertainties in evaluation of drag and inertia coefficients, current velocity profile and the wave theory itself. In Eq.6.4 x_{ss} denotes the random sea state parameters and is only taken as the annual maximum wave height or H_1.

6.2.3 Uncertainty measures of structural resistance parameters

The uncertainties related to the structural resistance parameters might be due to fabrication, installation and measurements according to the standards of the materials. Actual structure's material properties for each structural component(leg, brace, node etc.) has to be traced from shop drawings, where the material standard certificate of each manufactured (steel) component is issued etc. The actual distribution of the material properties can then be compiled from the

referenced steel manufacturing certificates.

The work required to obtain the actual material properties is out of the scope of this work. The required data is acquired from study carried out by Hovde and Hellan, (1992) based on survey of Swedish yield stress data(Melchers, 1987) and also API database(API RP2A, 1993).
Based on study of Hovde and Hellan, (1992), the model uncertainty and cov values related to the yield stress of the steel material of the jacket structure are taken as 1.04 and 0.07, respectively. These values are somewhat conservatively chosen.

The initial imperfection is another source of uncertainty. Specially, the assumption of a linear relationship between buckling strength and out-of-straightness may be questioned. At initial deformations δ_0/l (deflection to length of element ratio) between 0 and 0.001(0.002) which might be realistic values, the relationship is non-linear or at least have a steeper gradient than the (usually) applied linearization.

6.2.4 Uncertainty measures of pile-soil resistance parameters

The soil input parameters may be considered as random by nature. Due to this fact, the associated uncertainty with the pile-soil resistance characteristics is partly inherent. However, other sources of uncertainty may also contribute to the pile-soil resistance calculations such as measurement uncertainties(sampling and testing and reading methods etc.), statistical uncertainties(due to limited database) and model uncertainty(related to the prediction of (t-z), (p-y) and (q-z) curves).

The pile-soil parameters can be defined based on their mean values, standard deviations and relevant probability of distribution functions. To obtain the mean and variance of the soil resistance parameters, basic theories of statistics might be used (for e.g. see Nadim, 1988, Keaveny et al., 1989 and Lacasse and Nadim, 1996).

Fig.6.1 summarizes the mean and cov values and distribution types adopted for various pile-soil parameters in the current work based on survey of NGI and API databases (API RP2A 1993). The adopted cov values for clay and sand are somewhat conservatively taken with respect to the values recommended in NGI report(Lacasse and Goulois, 1989). It is seen that the cov values are generally taken somewhat higher than those for clay. This conservatism may be partly related to the dependency of the resistance of the pile on fewer parameters of sand which are quite crucial such as internal friction angle of soil and lateral earth coefficient and partly to the testing methods. However, in the case of clay, depending on the quality of the triaxial tests such as consolidated triaxial compression/extension, direct simple shear the cov may be taken slightly less. The relative importance of each parameter in pile's axial or lateral resistance calculation is another issue which has been considered in the choice of model uncertainty and cov values listed in Table.6.1.
*model uncertainty values are based on the API RP2A 1993 pile-soil models.

**The upper bound value of COV for the random parameter would be used for which fewer data

Table 6.1: The probability distribution and COV of random pile-soil parameters

Description	Random Param.	Physical Param.	n	μ	COV%	Distribution
Undrained shear strength (clay)	x_1	$S_{u,i}$	2	-	$5-20$	Lognormal
Total unit weight (clay-sand)	x_2	$\gamma_{tot,i}$	6	-	$0-10$	Normal
Friction angle (sand)	x_3	ϕ_i	4	-	$2-5$	Normal
Half of failure strain (clay)	x_4	$\epsilon_{50,i}$	2	-	40	Normal
Initial stiffness (sand)	x_5	k_i	4		40	Normal
Model uncertainty p-y (clay)	x_6	x_{cp}	1	$1.0-1.2$	>= 15	Normal
Model uncertainty t-z, q-z (clay)	-	-	-	-	-	
in compression	x_7	x_{cqc}	1	$1.0-1.2$	15	Normal
Model uncertainty t-z, q-z (clay)	-	-	-	-	-	
in tension	x_8	x_{cqt}	1	$1.0-1.2$	15	Normal
Model uncertainty p-y (sand)	x_9	x_{sp}	1	$1.0-1.3$	30	Normal
Model uncertainty t-z, q-z (sand)	-	-	-	-	-	
in compression	x_{10}	x_{sqc}	1	1.3	40	Normal
Model uncertainty t-z, q-z (sand)	-	-	-	-	-	
in tension	x_{sqt}	x_{11}	1	$1.0-1.3$	30	Normal
Yield stress	σ_{y_i}	x_{12}	4	-	-	Normal
Diameter	D_i	x_{13}	1	-	-	Normal
Thickness	t_i	x_{14}	1	-	-	Normal
E-modulus	E_i	x_{15}	-	-	-	Normal

are available .

*** Each physical parameter in Table.6.1 refers to a random variable defined as x in Eq.6.9.

*****full list of random parameters are given in Appendix.F.
The choice of normal distribution function for most pile-soil material properties is because the variation of soil parameters usually average out over a large volume of soil particularly for deeply embedded foundations such as piles. The selection of a lognormal type distribution as for instance for undrained shear strength of soil (S_u) is because such parameters can not have negative values.

As seen from Table.6.1, the COV values are higher for sand than for clay. Also the COV values are chosen higher for the axial loading than those for the lateral loading. The COV value for the end bearing is the highest in the pile-soil modelling due to large uncertainties involved in anticipating the plugging condition at the pile tip(the effective plug area), the coefficient of tip resistance etc. (see Chapter.2).

6.2.5 Uncertainty Modelling of pile-soil interaction

The axial pile-soil modelling is defined as t-z load transfer- displacement curve for sand and clayey soils according to API RP2A 1993 (see Sec.2.1 and 3.1). A modified API model (Emami,

1994) for clay is used. The t-z curve for clay includes a post peak strain softening with an ultimate residual axial soil resistance t_{res}. The ratio t_{res} to t_{peak} varies from 0.99 to about 0.70 for clay from top to the bottom of pile. Due to degradation of the soil layers near the surface, t-z curves in that zone have a t_{peak} nearly equal to the theoretical t_{res} value while this varies with depth and for the bottom layers the value of t_{peak} is modified (Emami, 1994) by a factor which is greater than 1.0. The end bearing of the pile-soil system is modelled as q-z model defined in API RP2A 1993 recommendations given in Chapter.2.

The lateral load-displacement behaviour of the pile-soil system is modelled according to the (p-y) model of API as described in Sec.3.1 of Chapter.2.
The associated uncertainty with pile-soil interaction (t-z), (p-y) and (q-z) models are obtained based on the following :

. Engineering judgment (expert opinion) for e.g. API, NGI etc.

. Comparisons of the LDPT data with the prediction results (for e.g. ref. to Ch.2)

. Statistical approaches such as Monte-Carlo simulations (see for e.g. Lacasse and Nadim, 1996 etc)

With respect to the above items the mean and cov values of various pile-soil parameters are listed in Table.6.1 which are used throughout this study.

6.2.6 Wave load uncertainty

The uncertainties in the wave load estimation as outlined briefly in the introduction above may be partly due to the inherent randomness of the sea state parameters such as wave height and period and partly because of the wave theory, the coefficients of mass and drag and the wave load distribution pattern over the jacket structure (ref. to Chapters.3 and 5).

In the present study, the total uncertainty due to the sea-state and wave load calculation are attributed to the model uncertainty of annual wave height (H_1) and that of the wave load (S). The mean value of the model uncertainty of sea load is considered as 0.9 which means that the calculated procedure based on a single regular wave is assumed to be conservative compared to a long term stochastic sea wave approach(see Yu-Lin, 1989 and Hovde and Hellan, 1992). It may be argued that the mean value of 0.9 for the model uncertainty of sea load is based on quasi-static response assumption for the jacket system. However, in the absence of a detailed analysis and more data, it is assumed that this 0.9 adopted here could be a rather reasonable value.

Previous studies by Sigurdsson et al, (1994) and Hansen et al, (1995) showed that the effects of uncertainties in the prediction of the maximum annual wave height are dominant. The associated wave period with the H_1 is not considered as an independent random variable.

The wave load is computed according to the Morison's equation as follows:

$$F_{sea} = F_D + F_I \tag{6.5}$$

where F_{sea} represents the wave and current induced forces ,F_D and F_I denote respectively drag and inertia forces which are computed as follows:

$$F_D = C_D.\rho.\frac{D}{2}u.|u| \tag{6.6}$$

$$F_I = C_M.\rho.\frac{\pi}{4}.D^2.\frac{du}{dt} \tag{6.7}$$

where C_D and C_M are drag and inertia(mass) coefficients respectively, ρ is the density of sea water, D is the element diameter, u and du/dt denote respectively the wave velocity and acceleration which are calculated as functions of wave height from an appropriate wave theory. Thus computation of sea load on the platform is subjected to some major uncertainties in evaluation of drag and inertia coefficients, wave height and the wave theory used for calculating the wave kinematics.

The distribution of model uncertainty of load (S) is assumed to be lognormal with a mean value of 0.9 and COV of 0.25 (Yu-Lin, 1989). A lognormal distribution with mean value of 1.0 and COV of 0.15 is used for the annual wave height parameter H_1 (Hovde and Hellan, 1992). The values might be compared with those computed by Hansen et al, (1995) and Olufsen and Moan, (1989).

The distribution function of the maximum annual wave height is computed according to the long term exponential distribution of individual wave heights as follows(see e.g. Almar N æs):

$$H_1 = H_{100}(1 - \frac{logN_1}{logN_{100}}) \approx 0.77H_{100} \tag{6.8}$$

where $H_1 and H_{100}$ are respectively the most probable maximum wave heights for 1 and 100 years. Alternatively the statistics of the observed annual maximum wave height can be used. H_1 then could be computed from the annual maximum significant wave height H_s obtained by long term statistical procedure.

6.2.7 Evaluation of system strength

An approximate first order variational form is established for the system strength parameter (R) as follows:

$$R(x) = R(x_0) + \sum \frac{\partial R(x)}{\partial x}(x - x_0) \tag{6.9}$$

where x_0 represents the base or reference parameters. It is assumed that the first order variational form will provide sufficient approximation to the exact nonlinear relationship for small variations of x parameters. The above partial derivatives are calculated numerically by 10 to 20 percent variation of each x parameter. The finite element model of the pile-soil system is shown in Fig.6.1. The model consists of two node beam elements which discretize the pile

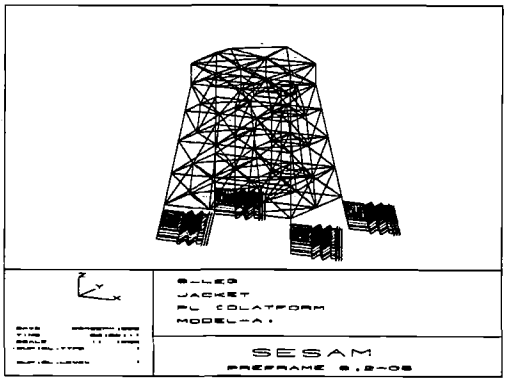

Figure 6.1: 8-leg jacket platform with modified height of cellar deck

and a set of uncoupled nonlinear springs which idealize the pile-soil interaction. The stiffness characteristics of the latter elements are defined by the t-z, p-y and q-z curves as described above.

The basic assumption here is that all pile-soil parameters involved in p-y, q-z and t-z calculations are the actual parameters and thus the only uncertainties are in the pile-soil stiffness calculations as described by the preceding curves.

The model uncertainty and COV values given in Table.6.1 of each of these interaction curves for both sand and clayey layers are determined based on recommended values by NGI (Nadim, 1994) and Hansen et al, (1995) and the author's studies of several LDPT results (Clarke et al, 1992) and API test data base (API, 1993). For the lateral loading, we update the characteristic lateral soil resistance (P(y)) after each iteration of reliability analysis as follows:

$$P_i = k_{p,i} P_0(y) \tag{6.10}$$

where $k_{p,i}$ is the design point factor for lateral loading computed at each iteration of RELAP analysis, In Eq.6.10 P_0 is the reference lateral capacity as follows:

$$P_0 = \int D(\zeta).p(\zeta).d\zeta \tag{6.11}$$

where $p(\zeta)$ is the lateral load transfer as given in API RP2A 1993 or modified API 93 pile-soil model (Emami, 1994). $D(\zeta)$ is the diameter of pile which would vary with depth ζ. (Note that ζ is taken differently from z which represents the axial displacement)

For the axial loading, the shaft and tip resisting forces are combined as follows:

$$N_i = k_{t,i} T_0 + k_{q,i} Q_0 \tag{6.12}$$

where $k_{t,i}$ and $k_{q,i}$ are the design point factors associated with the shaft skin friction and the tip resistance of the pile. T_0 and Q_0 represent the reference shaft skin friction capacity and end-bearing resistance of the pile, respectively, which are defined as follows:

$$T_0 = \int \pi D(\zeta).t_0(\zeta).d\zeta \tag{6.13}$$

where $t_0(\zeta)$ is the reference(base) axial load transfer as described in Chapter.2
Q_0 is the reference end bearing capacity of pile which is expressed as:

$$Q_0 = A_{tip} \cdot q_0(\zeta) \tag{6.14}$$

where $q_0(\zeta)$ is the reference end bearing load transfer and A_{tip} is the end bearing area which for the unplugged pile is the pile wall area and for the plugged condition is the whole pile tip area. It may be noted that the reference(base) case is referred to the mean values of the pile-soil parameters.

6.3 Case studies

6.3.1 Structural description

The original structure (Model-A1) is an 8-leg Jacket platform located at a water depth of 110m. The jacket consists of two longitudinal and four transversal frames with diagonal, K and X bracings at different levels (see Fig.6.1) The total height of structure is 142m and its horizontal dimension at mudline 56mx70m. The module support system(MSF) is modelled by an extra horizontal frame at deck level.
The structure has four pile connections to the ground. Each connection consists of 6 skirt piles which are modelled as a centered equivalent pile throughout this study. Figure.6.1 shows the structural model of the studied 8-leg platform.

6.3.2 Foundation model

The foundation of the jacket system in this study is modelled as equivalent single piles penetrating to a depth of 28m below the mud-line. Due to the relatively short lengths of the designed skirt piles in this case, they have been grouted at the bottom where the piles have penetrated into a sand layer. Hence, the pile-tip is considered to be plugged to ensure end-bearing. Since the lateral resistance may be mobilized at the upper part of the soil, the designed pile condition is not modified and will be used in the first part of this study. The pile-soil interaction is modelled as non-linear disks as described above. The soil profile consists mainly of sand layers with only two stiff clayey layers encountered at depths 18.5m and 25.5m below mudline level as described in Table.6.2.

6.3.3 Loading

Gravity loading

The gravity loads are assumed as deterministic and include the topside loads,the weight of jacket, pile, pile guides, bottle legs, mud-mats and buoyancy as given in Table.6.3.

Table 6.2: The soil layer data for the foundation of the 8-Leg jacket platform

Layer	Z(m)	γ(t/m3)	ϕ(deg)	Su(KPa)	G0(Mn/m3)	ϵ_{50}	T_{max}(KPa)
1	3.5	20.5	37.0	0	31.5	0	10.3
2	4.5	20.5	37.0	0	47.5	0	23.5
3	5.5	20.5	37.5	0	53.1	0	30.0
4	6.5	20.5	38.0	0	58.2	0	36.6
5	8.5	20.5	38.0	0	65.1	0	45.8
6	10.5	20.5	38.0	0	73.3	0	58.0
7	12.5	20.5	38.0	0	80.6	0	70.3
8	14.5	20.5	38.0	0	87.3	0	82.5
9	15.9	20.5	38.0	0	92.6	0	94.0
10	18.5	21.6	0.0	174	58.0	0.013	99.7
11	23.5	20.5	34.0	0	109.6	0	104.2
12	25.5	21.6	0.0	180	60.0	0.011	121.4
13	29.5	20.5	37.0	0	125.7	0	115.8

Table 6.3: The gravity loads related to the 8-Leg jacket platform

Gravity load	weight (tons)
Topside	22 339
Jacket*	9 401
equipment	2 042
bottle legs	2 976
mudmat	4 296
piles	3 750
buoyancy	9 400

Wave and current loading

The wave and current loading is considered as random thus uncertainties are modelled as described in the following section. A reference(base) load is defined as a combination of 100 year wave with the 10 year current. Wave and current descriptions are given in Table.6.4. Model uncertainty related to the wave calculation is described above.

Table 6.4: The 100-year wave height and period data

The wave direction	**wave height** (m)	**wave period** (s)	**current velocity** (m/s)
West-East wave	30.2	16.7	1.1
North-South wave	27.3	15.8	1.05

6.3.4 Total base shear-wave height relationship

The total wave load on the platform might be related to the wave height via a power relationship by a series of single(regular) wave analyses. The following power relationships is obtained for the total base shear at mudline:

$$BS_w = a_1 H^{b_1} + a_2 (H - H_d)^{b_2} \tag{6.15}$$

in which H = the scaled wave height, H_d = the wave height that hits the bottom of the deck, T = the period associated with a scaled wave height H, T_{100} = the period corresponding to the 100 year wave height, $a_i and b_i$ = are the coefficients of the curve fitting (regression coefficients). The coefficients of Eq.6.15 are given in Table.6.5. The values of exponents are between 1.5 and 2.0 which indicate a mixed drag-inertia regime for both directions and air gap conditions. The fitted relationships above for the studied 8-leg Jacket platform are comparable with those found by Heideman and Weaver, (1992) for the 8-leg Tern platform for three different storms from N-NE and W-SW directions.

Table 6.5: The coefficients of base shear vs. wave height correlation

Case	a_1	a_2	b_1	b_2	H_d
Northbound waves					(m)
Model A0	0.77	0	1.54	0	∞
Westbound waves					
Model A0	0.77	0	1.52	0	∞

6.3.5 Reliability analysis at the design point

In Sec.6.2 an annual probability of failure function has been described. An ideal reliability analysis requires evaluation of failure function $f(x)$ at the design point x* as follows:

$$g(x^*) = X_R R(x^*) - X_S . S(x^*) = 0 \tag{6.16}$$

where X_R and X_S denote the uncertainties(bias) associated with system strength at the design point and the loading, respectively. The resistance function $R(x)$ in the above equation is computed from the following:

$$R(x) = R_0(x) + \Delta R(x) \tag{6.17}$$

where $\Delta R(x)$ is the sum of variations given in Eq.6.9 and becomes zero when x approaches x^* i.e. the design point. An explicit form of the base shear vs. wave height relationship is used to calculate $S(x)$ function.

The distribution type of x^* is assumed to be normal or lognormal at least for its central part. For a normal distribution x^* might be computed from the following relationship for the load (Hovde and Moan, 1994):

$$x_i^* = \mu_{x_i}(1 + \alpha_i . \beta_m . V_i) \tag{6.18}$$

and for the system strength as follows:

$$x_i^* = \mu_{x_i}(1 - \alpha_i.\beta_m.V_i) \quad . \tag{6.19}$$

where μ_{x_i} is the mean value of x_i random parameter , V_i is the coefficient of variation for the x_i. α_i is the square root of the importance factor for x_i and β_m is the reliability index which varies for different failure modes.
A lognormal distribution form is used for S_u the undrained strength of clayey layers as follows:

$$S_{u_i}{}^* = \mu_{S_{ui}} \exp(\alpha_i.\beta_m.V_i - \frac{1}{2}V_i^2) \tag{6.20}$$

where in this case the square root of importance factor α_i is taken as 0.07 for clay. Eq.6.20 implies that $S_{u_i}{}^* <= \mu_{S_{u_i}}$. i.e. the design parameter (e.g. undrained shear strength) is smaller or equal to the mean value of parameter. It should be noted that the computed design values from the above equations are not the 'true' design values and only are used here in the first iteration of reliability analyses.

The next step in the current simulation procedure is to generate the pile-soil stiffnesses or load transfer-displacement data for the computed first iteration design values for the base case by computer program GENSODM (Emami,1994).

The partial derivatives of S with respect to each of 62 selected random strength parameters (as listed in Appendix.F) are computed in the third step of the analysis. This is achieved numerically by varying each design pile-soil parameter by about 10 to 20 percent at a single run of GENSODM program, thus generating 62 pile-soil interaction characteristic files. It is noteworthy that the design parameter here is referred to the mean value of the parameter multiplied by a design factor obtained from previous iteration of the reliability analysis. Thus it may not be the true design parameter of pile-soil.

In the fourth step a series of pushover analyses are performed by using nonlinear structural analysis program USFOS (Søreide et al, 1994) for each of the pile-soil characteristic files to calculate the ultimate capacity of the system R.

The final step is the reliability analysis of the system by using the ultimate capacity values obtained in the previous step and the model uncertainty and cov values given in Table.6.1. The total base shear-wave height relationship as described in Sec.6.4 and the annual maximum wave height formulation as given in Sec.1.3 are written as a subroutine called calno.f into the reliability analysis program RELAP (Hovde, 1995). Subroutine calno.f calculates the ultimate limit state function for each iteration of analysis.

Both FORM and SORM reliability methods are used in the RELAP analysis. In each method, first the limit state surface is transformed into a standard normal U-space and then is approximated by a first order tangent hyperplane or a quadratic surface at the design point u^* as follows:

$$g(x) = g(T^{-1}(u)) \rightarrow g_u(u) = g(u, \beta, \alpha^*) \tag{6.21}$$

The Taylor expansion of the latter might be expressed as follows (Tvedt, 1990):

$$g_u(u) = \frac{(-1)^n}{n!}(u-u^*)^n \frac{\partial^n g_u(u^*)}{\partial u_i u_j ... u_k} \cdot \frac{1}{|\nabla g_u(u^*)|}(i,j,...,k = 1,2,...,n) \tag{6.22}$$

where $g_u(u)$ is the failure function in the U-space, n is the order of the approximation, u^* is the u at the design point, the second term in the right hand side of Eq.6.22 is performed vectorially.

The first order form of Eq.6.22 may be simplified as:

$$g_u(u) = -\alpha^{*T}(u-u^*) = \beta - \alpha^{*T}u \tag{6.23}$$

which can also be written in the following form:

$$\beta = \alpha^{*T}u^* \tag{6.24}$$

And also :

$$\alpha^* = -\frac{\partial g_u(u^*)}{\partial u_i} \cdot \frac{1}{|\nabla g_u(u^*)|}(i = 1,2,...,n) \tag{6.25}$$

The latter means that α^* is a unit vector normal to the failure surface with an inward direction and this implies that $\alpha^{*T}.\alpha^* = 1$ and thus from Eq.6.24 the following can be obtained:

$$u^* = \beta.\alpha^* \tag{6.26}$$

The latter indicates that the design point is the nearest point on the $g_u(u)$ surface to the origin of the U-space and likewise β is the minimum distance from the failure surface to the origin(see for e.g. Madsen et al, 1986).
From Eq.6.25, it is seen that α^* is a function of variations in each of x random parameters at the design point therefore it is an indicate of importance of each of these variations. The α^{*2} is usually referred to as the importance factor and the pre-described derivatives are called sensitivity factors.

A second order formulation follows by truncating the Taylor expansion in Eq.6.22 after two first terms as:

$$g_u(u) = g_{u,1}(u) + \frac{1}{2}(u-u^*)^T \frac{\partial^2 g_u(u^*)}{\partial u_i u_j} \cdot \frac{1}{\nabla g_u(u^*)}(u-u^*)(i,j = 1,2,...,n) \tag{6.27}$$

For each iteration of the analysis, the design values used in the previous analysis are updated by multiplying the initial values of the random parameters with the computed design factors in the X-space from the last iteration.

Due to the number of non-linear pushover static analyses required in the iterative approach which amounts to 62 in each wave direction, more iterations require much longer running time of computer(in average about $62 * 2 * 4 * 1500/3600 \approx 207$ CPU-hrs). It is therefore assumed that a few number of iterations will be sufficient to reach the vicinity of design point. However, the accuracy and the convergence of iterations depend on the reliability method used for the

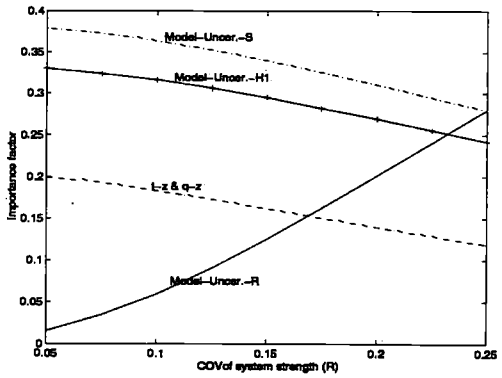

Figure 6.2: Variation of importance factors with COV of R

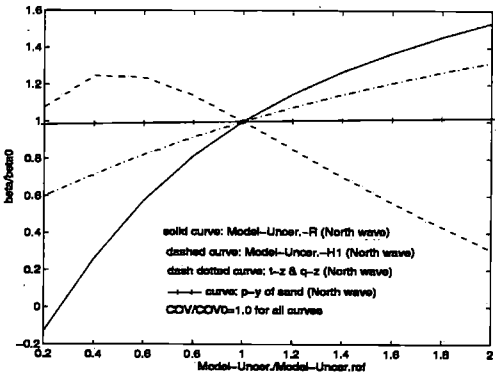

Figure 6.3: Variation of reliability index with model uncertainty of various random parameters

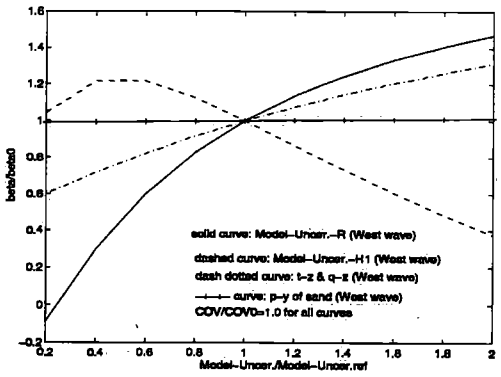

Figure 6.4: Variation of reliability index with model uncertainty of various random parameters

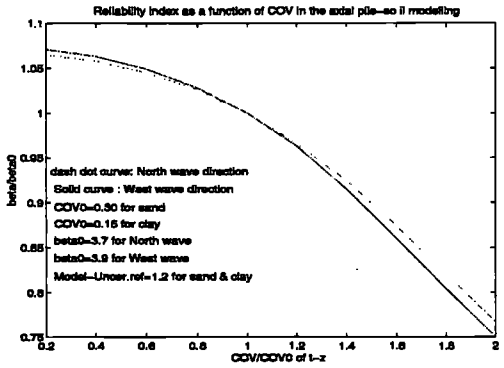

Figure 6.5: Variation of reliability index with the COV of t-z

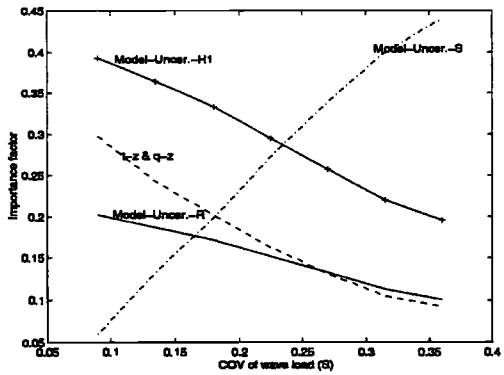

Figure 6.6: Variation of importance factors as a function of COV of system wave load

Table 6.6: Failure mechanisms of the jacket-pile-soil system under end-on and broad-side loadings

Wave direction	pile-soil failure	member failure
Broad-side(North)	uplift (axial pile failure)	K-bracing(elev.4-5)
End-on (West)	axial failure & plastic hinge	Diagonal-bracing(elev.5-6)

Table 6.7: The annual probability of the failure and the reliability index results of jacket-pile-soil system analysis

wave load direction	β FORM	p_f FORM	β SORM	p_f SORM
North(Model A0)	3.637	1.377E-04	3.592	1.640E-04
West (Model A0)	3.850	5.908E-05	3.807	7.027E-05

analyses. Therefore both FORM and SORM methods are used and the obtained results are compared for each iteration.
Note that the above α values are chosen based on our judgment and then compared and corrected against the analysis results. Since $\alpha_i \geq 0.0$, $\beta_m \geq 0.0$ and $V_i >= 0.0$ then we might have the following for the system strength: $x_i^* <= \mu_{x_i}$. α_i values are taken for e.g. as 0.25 for sand and 0.07 for clay. α_i is taken as 0.45 for pile-soil modelling of sand layers and 0.30 for pile-soil modelling of clayey layers. V_i values are given in Table.6.1.

6.3.6 Discussion of results

The annual probability of failure of the studied platform is found to be approximately an order of magnitude higher for the North wave direction than that for the west wave direction as given in Table.6.7. The agreement between the FORM and SORM results is good for both studied wave directions.

It may be noted that the variations of the wave height indicated here are related to a reference wave height used in RELAP program not related to the real sea surface variation). Also it may be worth mentioning that we have applied wave load incrementation approach in this reliability study. The corresponding real sea surface elevation generated by WAJAC program are far below main deck level for all the iterations of the analyses.
The overall uncertainty contribution of the pile-soil interaction modelling for $t-z$ and $q-z$ axial loading and end bearing is found to be significantly higher than those for p_s-y_s and p_c-y_c lateral loading of both sand and clayey layers for both wave directions.

The importance factor of $t-z$ and $q-z$ for the broadside loading of platform is computed to be 16.19% while that for the end on loading of platform is obtained to be 12.84%. Therefore the uncertainty in the axial modelling of soil is more pronounced for the northern wave than that for the westerly wave (see Tables.6.9 and 6.10).

The overall uncertainty contribution due to the model uncertainty in the calculation of the structural strength (R) is about 12.5 percent for the North and 12.8 percent for the west direction. The sum of importance factors related to the uncertainties in soil parameters are calculated to

Table 6.8: The reference wave height(H_{ref}) values after each iteration

Iteration no.	**wave height** (North)	**wave height** (West)
1	30.2	27.3
2	31.5	28.7
3	30.7	28.5
4	31.3	28.3

Table 6.9: The importance factors related to the sea load and pile-soil modelling parameterR(North-wave)

random parameter (North wave)	**importance factor Model A0 %**
Model uncert. of wave load	34.0
Annual wave height	29.5
Model uncert. of struc. strength	12.5
Axial pile-soil model	16.2
Lateral pile-soil model	0.0
Soil&pile parameters	8.0

be around 8 percent for the North wave direction (broadside loading) and about 10 percent for the West wave direction (end on loading) (see Tables.6.9 and 6.10).

The randomness in the annual wave height H_1 accounts for almost 29.5% of the total system uncertainty for each wave direction. However, the importance factor of model uncertainty in the wave load calculation varies from 34.0% for the North wave up to 34.8% for the westerly wave(see Tables.6.9 and 6.10). These results show that the total uncertainty in predicting the platform's collapse behavior largely is due to sea state and wave load modelling.

Any further improvement in the pile-soil-structure model uncertainty may also reduce the global uncertainty and thus would increase β the reliability index values. Sensitivity studies indicate that the index of reliability is largely dependent on the variation of COV of the annual wave height and the wave load model(see Fig.6.7).

The effects of proportional reduction in the cov of (t-z) and (q-z) of pile-soil system is somewhat greater than the effect of reducing the uncertainty related to the calculation of the ultimate structural strength (R). By comparison, a proportional increase of cov in (t-z) and (q-z) has smaller effect on the overall reliability index of the jacket-pile-soil system than the increase of cov of the annual wave height and the wave load model(see Fig.6.5).

The results plotted in Figs.6.3 and 6.4 suggest that the reliability index does not vary much with COV of (p-y) modelling. For instance, Fig.6.5 shows that the the reliability index varies with the wave directions. The discrepancy increases as the cov/cov0 ratio varies from the unity.

Table 6.10: The importance factors related to the sea load and pile-soil modelling parameters (West-wave)

random parameter (West wave)	**importance factor Model A %**
Model uncert. of wave load	34.9
Annual wave height	29.4
Model uncert. of struc. strength	12.8
Axial pile-soil model	12.8
Lateral pile-soil model	0.0
Soil&pile parameters	10.1

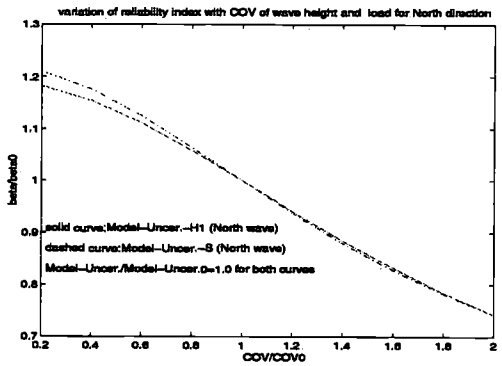

Figure 6.7: Variation of reliability index with COV of wave height

The results also indicate that the decrease of the reliability index is relatively larger by an increase of cov of (t-z) and (q-z) random parameters than the decrease for the same amount of reduction of cov(see Fig.6.5). For instance, a reduction of about half in the cov of (t-z) and (q-z) increases the reliability index by about 5 percent while an increase of the same magnitude reduces the β value approximately 10 percent.

The study of the results on variation of the mean value(model uncertainty/model uncertainty-ref) suggests a power relationship between the model uncertainty of R and the reliability index. As expected, the value of β increases rapidly with increasing the model uncertainty of R while variation of cov of (t-z) & (q-z) less affects the β index.

It is seen that the reliability index increases with the increase of the model uncertainty in the wave height calculation from (model uncertainty/model uncertainty-ref) equal to 0.2 up to 0.4 and is almost constant up to (model uncertainty/model uncertainty-ref) equal to 0.6 and then it decreases almost linearly up to the $beta/beta0$ equal to 2.0. The change in the sign of variation of β for (model uncertainty/model uncertainty-ref) less than 0.4 might be to prevailing effects of other uncertain parameters such as current and also due to inaccuracy in the wave theory for

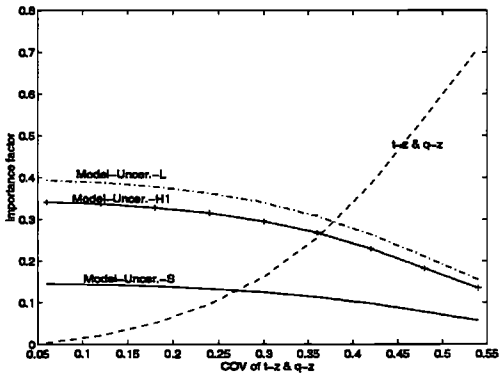

Figure 6.8: Variation of importance factors with COV of (t-z) & (q-z)

that range of wave height.

As shown in Figs.6.3 the model uncertainty in calculation of (p-y) curves has negligible effect on the β index. This is largely due to the fact that the overturning moment induced by wave and current loads on the platform is resisted by the axial pile-soil reaction.

The variation of β with (model uncertainty/model uncertainty-ref) suggests a full correlation between the β versus model uncertainty of $(t-z)$ & $(q-z)$ of pile-soil system with respect to the wave direction. The maximum discrepancy of β of wave height for two different wave directions in the range of model uncertainty=0 to (model uncertainty/model uncertainty-ref) equal to 2.0 is around 10 percent.

The study of the global importance factors shows that using a 5% cov for model uncertainty-R instead of 15% which is conservatively taken in this study, would reduce the overall importance factor for model uncertainty-R to about 2% while increases the contribution of (t-z)&(q-z) model of pile-soil system from about 16% to nearly 20% (see Fig.6.2). A similar parametric study on the variation of cov of model uncertainty of S indicated that by increasing the cov of model uncertainty of S, the importance factor of model uncertainty of S increases almost linearly while those of other parameters decrease rather slowly(see Fig.6.6). For instance an increase of 10 percent in cov of model uncertainty of S, would increase the importance factor of model uncertainty of S by about 20 percent while it would reduce the importance of (t-z) & (q-z) modelling from around 16 percent to 10 percent (See Fig.6.8).

The results of parametric studies on variation of various importance factors with changes of cov in the axial modelling (t-z) & (q-z) of pile-soil system are plotted in Fig.6.6.

It is found that a reduction of 10 percent in cov of the axial modelling of pile-soil would reduce the corresponding importance factor from 16 to about 5 percent whilst a 10 percent increase of cov in the (t-z) & (q-z) modelling, would increase the corresponding overall uncertainty contri-

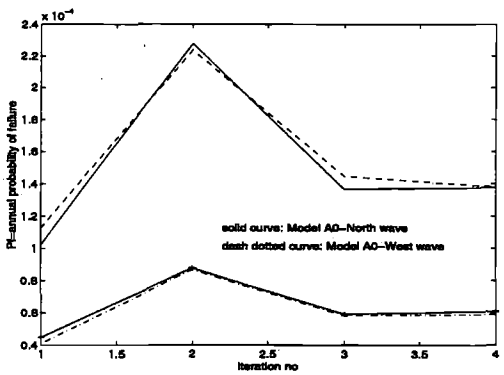

Figure 6.9: Convergence of the anuual probability of failure(P_f) with no. of iterations

bution to about 38 percent.

The annual probability of failure of platform is an order of magnitude higher for broad-side loading of platform (see Table.6.7). In general the second order reliability method has resulted in higher probability of failure values.

The study also shows that the tension axial pile-soil failure particularly for the broad-side loading is more sensitive to uncertainties in the axial modelling of pile-soil. Since there is no end-bearing for tension piles ,the overall pile-soil uncertainty contribution is largely attributed to (t-z) modelling. However for the compression failure of pile-soil system, the effects of uncertainties in (q-z) modelling can not be neglected.

Since most layers in the site of the studied platform consist of sand, thus any improvement in the axial pile-soil modelling would significantly reduce the existing uncertainty in the API RP2A 1993 model which are used in this study to model axial loading of sand layers. To extend the modifications by (Emami, 1994) which are specifically introduced for clayey soils to sand, further verifications are required. Fig.6.9 shows the convergence of the annual probability of failure with no of iterations. A convergence rate of about 1.0E-06 has been achieved for p_f.

6.4 Concluding remarks

The reliability analyses of the pile-soil-jacket system indicate that the contributions to the overall uncertainties are mainly due to the wave load and pile-soil modelling. This is because the lateral pile-soil behaviour is not governing in the failure mechanism of the platform.

The importance factors for random soil parameters are very small compared with those for the model uncertainty of annual maximum wave height H_1, the model uncertainty in load calculation and the model uncertainty of system strength calculation.

The reliability index from the last iteration of analyses is found to be about 3.64 for the North wave direction and 3.85 for the west wave direction. These results show that the annual probability of failure depends on the loading direction of platform and thus varies with the imposed wave direction.

The overall uncertainty contribution of the annual maximum wave height and the model uncertainty in the wave load modelling is found to be in the range of 60-65 percent. While the importance factor of pile-soil modelling is obtained to be in the range of 12-16 percent. The results also show that the uncertainty contribution of the structural strength calculation is less important than those for the wave load and pile-soil modelling.

The importance of uncertainties in the lateral modelling of pile-soil system are quite insignificant compared to those of axial pile-soil modelling.

Parametric studies on the variation of importance factors and the reliability index with COV of $(t-z)$ and $(q-z)$ suggested that any further improvement of axial modelling of pile-soil system might reduce the probability of collapse.

Further work is needed:
1)To study more structural models to investigate the effects of wave on deck.

2)To verify modification of (t-z) model of pile-soil for more LDP tests on sand.

3)To refine the wave theory and wave height estimation.

4) To investigate an overturning based failure function for jacket-pile-soil systems whose global failure is governed mainly by pile pull out or plunge

CHAPTER 7

SUMMARY AND CONCLUDING REMARKS

Static pile-soil interaction

A review of the most widely used state of practice pile-soil interaction models is done in Chapter.2. In addition, two new (t-z) and (p-y) load transfer-displacement models for pile-soil systems are introduced. The presented models are based on disk idealization of the pile-soil system.

The disk models are established based on a Mohr-Coloumbian form effective/total stress relationship and a shear tangent stiffness criterion of the soil. The derivation of the model is based on simple continuum and soil mechanics theories. However, the model's tangent stiffness parameters α and β are dependent on the available triaxial test data.

The advantage of the disk models are their simplicity, efficiency and fairly good accuracy and non-site specificness. The disk model(s) in general can be applied for any kind of soil but they are specifically validated in Chapter.2 against the recent large diameter pile tests in clay.

The comparison of the disk model results with LDPT data in Chapter.2 showed that they are fairly capable in different soil conditions such as normally and overconsolidated clayey soils. The studied cases showed that the current practice code of API RP2A 1993 model might be unconservative in the case of the normally consolidated clay while the other cases indicate that the API RP2A 1993 model for overconsolidated clay might be rather conservative. A recent literature review is conducted which indicated that the current practice models of API RP2A 1993 are generally conservative.

Static jacket-pile-soil interaction

The static behaviour of the jacket-pile-soil systems under extreme environmental loading such as hurricane intensity waves and severe earthquakes is studied in Chapter.3.

The ultimate collapse response of the jacket-pile-soil systems were determined by static pushover analysis approach. In addition of the traditional wave load incrementation(WLI) method, a new approach based on wave height incrementation(WHI) is also applied.

The influence of foundation modelling on the static behaviour of the jacket platform near the ultimate collapse is investigated in Chapter.3. It is shown that a linear lumped spring to ground model might offer a fairly good estimate of the initial response (stiffness) of the jacket-pile-soil system.

It is found that the linear spring model may not be capable to predict accurately the ultimate collapse behaviour of the jacket-pile-soil system. It is observed that near collapse behaviour of the jacket platform might be influenced by the pile-soil failure.

It is shown that soil-structure interaction may change the failure mode of the structural element and hence the overall system. It is observed that for e.g a soil yield simulated by a non-linear pile-soil model may cause a spring back behaviour of the studied 4-leg jacket-pile-soil system while a linear spring or fixed support system was unable to capture such significant change of behaviour after collapse.

It is also shown that a non-linear pile-soil model is capable to simulate the collapse of a 2D-jacket system mainly due to pile-soil failure.

It is observed that the effect of pile tip plug can be quite significant on the near collapse behaviour of the jacket platforms supported on relatively short piles.

The influence of different soil types such as sand, normally consolidated clay and overconsolidated clay on the overall response of the jacket-pile-soil system is also studied in Chapter.3. It is shown that the global static collapse behaviour of the jacket-pile-soil system might significantly vary depending on the soil condition.

The influence of the wave load modelling based on WHI approach is studied for an 8-leg jacket platform of North-sea. It is observed that a more realistic wave load modelling based on wave height incrementation may result in slightly (about 8%-9%) less ultimate collapse capacity than WLI approach. The observed discrepancy may be attributed to the change in the wave load distribution on the structural members as well as the shift of the centroid of the wave load on the entire jacket. The accumulated plasticity is also manifested on the onset of the collapse(failure cycle).

Stiffness degradation is also observed in the quasi-static cyclic response histories. The observed stiffness degradation might be attributed to the change in sea surface elevation as well as structural and pile-soil element stiffness/strength degradation.

Dynamic pile-soil interaction

The static disk model of pile-soil established in Chapter.2 might only be applicable for the environmental load conditions with low frequency of vibration such as extreme sea waves with typical duration periods of about 10-20 secs.

For the high frequency loading such as seismic loading due to strong earthquakes a static pile-soil model may not be applicable due to its lack of account for the dynamic(non-linear and resonance) effects.

To this aim, a dynamic pile-soil model is introduced in Chapter.4 based on a cone-disk idealization of the pile-soil system. The model is a non-linear and non-homogeneous version of Wolf's model. An indirect formulation of the model is initially introduced by Emami et al, (1996) by coupling the non-linear multi-stack of disks with dynamic soil cone properties.

The main feature of the dynamic disk-cone model is its use of finite and boundary elements simultaneously. The advantages of the cone-disk model are illustrated as its simplicity, efficiency and fairly good accuracy.

By using the disk-cone model, more insight is gained into the dynamic behaviour of the pile-soil systems. It is shown that disk-cone model is capable to account for radiation as well as material damping. It is also shown that both radiation and material damping can be formulated with the disk-cone model of pile-soil.

It is shown that the disk-cone model can be applied both in layered and non-layered soils with different boundary conditions. Both reflections and refractions at the boundaries of layers are formulated.

The solution procedures of the disk-cone model are established in frequency and time domains. Although the frequency domain analysis procedure is established in Chapter.4 based on superposition approach for the linear elastic pile-soil system. Nonetheless, the procedure can be easily extended to the non-linear pile-soil system. The time domain solution procedure is derived for the non-linear pile-soil system.

The disk-cone model is applied for several single pile-soil cases under dynamic loading. The predictive ability of the disk-cone model is examined in comparison with the static disk and also the current practice API RP2A 1993 pile-soil models.

The effects of soil non-linearity on the pile-soil response is illustrated within the studied examples.

The hysteretic soil damping effects are quantified by means of elasto-plastic and hyper-elastic soil models.

Simple lumped models of pile-soil system such as SDOF, 2DOF and 3DOF are also presented in Chapter.4. Such models are shown to be quite efficient to study the effects of various soil and

pile parameters in an extensive manner.

A number of parametric studies based on simplified lumped parameter models of pile-soil are presented at the end of Chapter.4. Such studies demonstrated the sensitivity of the pile-soil stiffness to the variations of the soil and pile parameters.

Ductility demand analysis of jacket-pile-soil systems

Dynamic performance of a jacket-pile-soil system is found to depend on both structural-pile-soil characterestics and dynamic loading effects. The key structural characteresics of a dynamic system are considered to be mass, stiffness related via natural period relationship. The key soil parameter is chosen as soil shear modulus. The loading effects are considered to be intensity, frequency content, duration, shape and randomness.

A ductility demand concept is introduced in Chapter.5 based on non-linear dynamic analyses of jacket-pile-soil systems. The ductility ratio and overload ratios are defined as key elements to the establishment of ductility spectra. The presented ductility approach can be applied either to determine:

. the maximum damage potential to a jacket-pile-soil system under a given extreme environmental loading history

.or the maximum overload ratio for a jacket-pile-soil system with a given maximum ductility ratio

.or the natural period(stiffness or mass) of a jacket-pile-soil system for a given overload ratio and ductility ratio

Simplified non-linear SDOF based analysis approach is established for ductility demand analysis of equivalent jacket-pile-soil system. A simple ductility-overload ratio relationship is obtained based on the analyses of simplified systems such as SDOF.

For the purpose of illustration of the approach, a number of ductility demand spectra are established in Chpater.5 based upon the analysis of simplified dynamic models such as non-linear SDOF and 3DOF.

The predictive capability of the obtained formulation is assessed against the results of more complex 3D-Jacket analyses, 2D-plane frame analyses and also other existing relationships.

Several interesting results are obtained from ductility spectra analyses such as:
. ductility demand of the jacket-pile-soil system increases in general with decreasing the natural period of the system

. Considerable peaks and valleys are observed in the ductility spectra in the region of $T_n < 2 - 3secs$ which might be attributed to the resonance effects superimposed on the non-linear

dynamic response of the system

. It is observed that the peaks in the ductility spectra decrease significantly by increase of the damping ratio from $1 to 10\%$.

. It is generally observed that ductility demand for the wave loading are much larger than that of seismic loading.

. It is shown that the increase of bandwidth of hysteresis loops shifts the spectra towards smaller values.

. The results of ductility spectra suggest that an effective period concept may better describe the dynamic response near failure.

The following results are also obtained from MDOF analyses of jacket-pile-soil systems:

. The inertial resistance of the structure is shown to be important in providing an additional reserve strength for structures with sufficient ductility.

. It may be concluded that the effect of ductility can be significant in providing an overload factor of large than unity. Overload factors in the range of 1.1-1.2 were obtained for the systems with ductile behaviour. On the contrary overload ratios slightly lower or closer to unity were found for systems with semi-brittle type behaviour.

. The foundation modelling is found to have significant influence on the near collapse behaviour of the system. Hence, it is concluded that realistic (nonlinear) pile-soil models should be used in the ULS based analysis.

. The effects of superimposed harmonics are shown to be important in reducing the overload ratio for brittle behaving systems. The reduction for jacket system under wave loading studied here found to be less than about 5%.

. It is observed that for the relatively stiff(rigid) jacket systems studied in the Chapter.5, the ultimate dynamic collapse capacity is increased in the range of $3-7\%$ through accounting for relative velocity in the wave load calculation.

. The smaller influence was obtained for the linear spring type foundation model and the plugged type pile foundation with relatively smaller displacement response at the deck level compared to the jacket with un-plugged pile for which we found a greater influence.

. In the cases studied in Chapter.5, it is observed that the maximum displacement response of the jacket at the deck level often exceeds the largest diameter of the leg member and also found that no high frequency motion is involved at the deck level. The implication of these observation and those reported by previous studies is to consider seriously the relative velocity effect on the

ultimate near collapse behaviour of the jacket-pile-soil system.

Reliability analysis of jacket-pile-soil system

It is concluded that the sea state and wave load modelling are the major contributors to the overall uncertainty of the jacket-pile-soil system. The reliability analysis of the jacket-pile-soil system indicates that the importance factors related to the sea state and wave theory are about $60 - 70\%$.

It is also observed that the soil and pile-soil interaction modelling together contribute about $20 - 25\%$ to the overall uncertainty of the jacket-pile-soil system. The influence of the axial pile-soil model is more than that of the lateral pile-soil model. This might be due to the fact the overall wave and current forces on the jacket platform are mainly resisted through the axial pile-soil resistance.

The bias in the calculation of the ultimate structural strength is found to be least contributor to the overall uncertainty of the jacket-pile-soil system. The importance factor associated with the structure's ultimate strength calculation is obtained to be about $9 - 10\%$ for the studied jacket-pile-soil system. Hence, assuming the structural model parameters (strength) as deterministic may be quite reasonable.

An extensive sensitivity study of various jacket-pile-soil parameters are carried out showed that increase of the uncertainty of the sea, wave load and pile-soil model random variables might result in considerable reduction of the overall reliability index of the system.

Any improvement of the sea state or wave load modelling may enhance the reliability of the system. Further improvement of the shaft friction and pile tip resistance modelling might also result in reducing the probability of failure of the jacket-pile-soil system.

Main contribution of this work

The main contributions of this work may be listed as follows:

. Evaluation of the current practice pile-soil interaction models which are widely used today in the design of offshore pile foundations

. Establishment of simplified (t-z) and (p-y) interaction models based on disk idealization of pile-soil system

. Validation of the static disk models based on recent large diameter pile test data carried out by BP and NGI (complementary to API database)

. Modification of the Wolf's disk-cone model for non-linear and non-homogeneous soil conditions

. Verification of disk-cone model results against other more rigorious methods such as BEM

. Static and dynamic analysis of the integrated jacket-pile-soil system

. Assessment of the traditional static pushover analysis approach based on wave load incrementation and a more realistic pushover analysis approach based on wave height incrementation

. Investigating the influence of foundation (pile-soil) failure on the ultimate response of the jacket-pile-soil system near collapse

. Examining the influence of the wave load modelling on the ultimate response of the jacket-pile-soil system near collapse

. Performing other parametric studies to assess for e.g. the effect of member fracture on the ultimate response of the jacket-pile-soil system

. Establishing an efficient ductility demand analysis approach based on simplified SDOF and 3DOF models to evaluate the dynamic performance and loading effects on jacket-pile-soil systems

. Introducing a simple procedure for reliability analysis of jacket-pile-soil system at the limit state of collapse

Recommendations for further investigations

Throughout this work attempts made to get more insight into the non-linear behaviour of the jacket-pile-soil systems near collapse. This work could introduce some ideas about the effects such as influence of the pile-soil failure on the response of the jacket platform near failure, structural/pile-soil as well as wave load modelling and dynamic effects.

The cyclic soil behaviour is considered in this study to be nondilatant type and hence the associated flow rules of plasticity are applied in modelling the pile-soil interaction. However, it is mentioned that cyclic soil behaviour might be significantly different for dilatant type soils such as OC clay and sand. It is recommended to consider the non-associative type hardening/softening models in dealing with these kind of soils.

With respect to the static pile-soil modelling, the coupling effects under combined axial and lateral loadings between (t-z) and (p-y) response are not treated. However, it is recognized that the coupling might have some considerable effects particularly for the jacket pile foundations under simultaneous axial and lateral loading. The effect might be more significant for the cyclic loading of the piles due to extreme storms or earthquakes. The pile-soil interaction issue has to be studied further by including the coupling effects under extreme cyclic loading.

Within this study the jacket foundations are modelled as single piles and the pile-soil-pile interaction(pile group effect) is not modelled. However, some preliminary studies have been conducted by the author(SINTEF memo) and the topic has to be investigated further.

The ductility analysis approach established within this work proved to be a simple but efficient tool for studying the ultimate dynamic response of the jacket-pile-soil systems. Studies on several key parameters such as natural period, the overload ratio, ductility ratio, soil shear modulus and hysteretic model parameters are performed. More ductility spectra studies of these and other structural and pile-soil as well as load model parameters have to be considered.

In the dynamic analysis of the jacket-pile-soil systems under extreme waves, the main focus is placed on the wave on jacket forces while the horizontal and vertical wave forces on the cellar and the main deck are also considered. Due to the importance of the impulsive forces on the deck, it is required to study more cases with inclusion of wave on deck forces.

The dynamic pile group effect is not treated in this study and is recommended to be considered in future study of jacket platforms. This issue is quite crucial for the jacket pile foundations subjected to strong ground motions or significant subsidence and encountering wave on deck forces.

Further verification of the (t-z) and (q-z) models against the large scale pile test results are needed to provide additional data about uncertainty model parameters. However, the assumed values for bias and COV of pile-soil random parameters in Chapter.6 based on available API and NGI database are thought to be quite reasonable.

CHAPTER 8

References

Abbassian F., Lau T.B. and Zintilis (1991): "3-D inelastic behaviour of tubular members supported on non-linear rotational springs", J. Offshore Mechanics and Arctic Engineering, 113, pp 320-326.

Amdahl J., Johansen A. and Svanø G. (1994): "Ultimate Capacity of Jack-Ups Considering Foundation Behavior", Proceedings of OMAE Conference 1994, USA.

Anagnostopoulos C. and Georgiadis M. (1993): "Interaction of Axial and Lateral Pile Responses", Journal of Geotechnical Engineering, ASCE, Vol.119, No.4.

Apsel R.J. and Luco J.E. (1987): "Impedance functions for Foundations Embedded in a Layered Medium": An Integral Approach, Earthquake Engineering and Structural Dynamics, Vol.15-pp.213-231, USA.

API RP2A (1993): "Recommended Practice for Planning, Designing and Constructing Fixed Offshore Platforms-Load and Resistance factor Design", American Petroleum Institute, Washington, DC, USA.

API RP2A (1994): "Recommended Practice for Planning, Designing and Constructing Fixed Offshore Platforms-Load and Resistance factor Design", American Petroleum Institute, 20th Edition, Draft Section 17.0, USA.

Audibert J.M.E. and Dover A.R.(1982):"Pile Load Tests", Cyclic Loads and Varying Load Rates, Discussion, Journal of the Geotechnical Engineering, Proc, of ASCE, Vol.108, GT3.

Baguelin F., Frank R. and Said Y.H. (1977):"Theoretical study of lateral reaction mechanism of piles", Geotechnique, Vol. 27, Issue 3, pp.405-434.

Baker M.J. and Vrouwendvelder A.C.M. (1992):"Reliability Methods for the Design and Operation of Offshore Structures", Proc. of Offshore Mechanical and Arctic Eng.(OMAE), Vol.2, pp.123-132, New York, ASME, USA.

Barton Y.O., Finn W.D.L., Parry R.H.G. and Towhata I.(1983):"Lateral Pile Response and p-y Curves from Centrifuge Tests", Proc. of Offshore Tech. Conf., OTC 4502, Houston, USA.

Bea R.G. and Audibert J.M.F. (1979):"Performance of Dynamically Loaded Pile Foundation", Proc. of the 2nd Int. Conf. on the Behaviour of Offshore Structures(BOSS), London, UK.

Bea R.G., Audibert J.M.E. and Dover A.R. (1980):"Dynamic Response of Laterally and Axially Loaded Piles", Proc. of Offshore Technology Conf., OTC 3749, Houston, USA.

Bea R.G., Litton R.W., Nour-Omid S. and Chang J.Y.(1984):"A Specialized Design and Research Tool for the Modelling of Near-Field Pile-Soil Interactions", Proc. of Offshore Tech. Conf., OTC 4806, Houston, USA.

Bea R.G., Vahdani S., Guttman S.I., Meith R.M. and Paulson S.F.(1986):"Analysis of the Performance of Piles in Silica Sands and Carbonate Formations", Proc. of Offshore Tech. Conf., OTC 5145, Houston, USA.

Bea R.G. (1991):" Offshore Platform Reliability Acceptance Criteria", J. of Drilling Engineering, Soc. of Petroleum Engineers, June, pp.131-137.

Bea R.G. and Young C.N. (1993): "Loading and Capacity Effects on Platform Performance In Extreme Storm Waves and Earthquakes", Proceeding of OTC 1993, Houston, Texas, USA.

Bea R.G. (1995):" Probability Based LRFD Criteria For Offshore Platforms", Proc. of Int. Workshop on Wind and Earthquake Eng. Univ. of Calif., Berkeley, USA.

Bea R.G. (1995b):" Simplified Earthquake Spectra For Equipment on Offshore Platforms", Proc. of Int. Workshop on Wind and Earthquake Eng., Univ. of Calif., Berkeley, USA.

Bea R.G. and Mortazavi M.M., Loch K.J. and Young P.L. (1995):"Verification of a Simplified Method to Evaluate the Capacities of Template-Type Platforms", Proc. of Offshore Tech. Conf., OTC 7780, Houston, USA.

Bea R.G. (1996):"Probability Based Earthquake LRFD Criteria for Offshore Platforms", Proc. of Offshore Technology Conf., OTC 8106, Houston, Texas, USA.

Bessason B. (1993): "Seismically isolated bridges", Dr.ing Thesis, NTH, Trondheim, Norway.

Beyer W.H. (1981): "CRC Standard Mathematical Tables", 26th Edition, CRC Press Inc., Boca Raton, Fla, USA.

Bond A.J. (1989):"Behaviour of Displacement Piles in Overconsolidated Clays", Ph.D. Thesis, Univ. of London(Imperial College), UK.

Bouc R. (1968): "Forced vibration of mechanical systems with hysteresis", Abstract, Proceedings of the Fourth Conference on Non-linear Oscillation, Prague, Czechoslovakia, 1967.

Bradshaw H., Barton R.R. and McKenzie R.H.(1984):"The Hutton TLP Foundation Design", Proc. of the 16th Annual Offshore Technology Conf., OTC 4807, Houston, USA.

Broms B.B. (1964):"Lateral Resistance of Piles in Cohesive Soils", J. of Soil Mechanics and Foundation Design, American Society of Civil Engineers(ASCE), Vol. 90, Vol.2, pp.27-63

Caltech Seismic Lab. (1994): "Seismic data and correction procedures", Univ. of California, Berkeley, USA.

Chan S.L. (1989): "Inelastic post-buckling analysis of tubular beam-columns and frames",J. Eng. Strucs., 11, pp23-30, UK.

Chow F.C. (1996):"Investigation into Displacement Pile Behaviour for Offshore Foundations", Ph.D. Thesis, Univ. of London(Imperial College), UK.

Clarke J. (1992): "The Axial Tension Test of An Instrumented Pile in Over-Consolidated Clay at Tilbrook Grange", Proceedings of the Conference on Recent Large Scale Fully Instrumented Pile Tests, In Clay, Institution of Civil Engineers, London, UK.

Clarke J., Rigden W.J. and Senner D.W.F. (1985): "Reinterpretation of the West Sole Platform WC Pile Load Tests", Geotechnique, UK.

Clausen C.F. (1992): "SPLICE soil-pile-structure interaction analysis program", NGI, Norway.

Clough R.W. and Penzien J. (1975):" Dynamics of Structures", Mc-Graw Hill Company, New York, USA.

Constantinou M.C. and Tadjbaksh I.G.(1985):"Hysteretic Dampers in Base Isolation: Random Approach, Journal of Structural Engineering, Vol.111, No.4, USA.

Cox W.R., Reese L.C. and Grubbs B.R. (1974):"Field Testing of Laterally Loaded Piles in Sand", Proc. of Offshore Tech. Conf., OTC 2079, Houston, USA.

Cox W.R., Solomon I.J. and Cameron K. (1992): "Instrumentation and Calibration of Two 762-mm-Diameter Pipe Piles for Axial Load Tests in Clays", UK.

Cox W.R., Cameron K. and Clarke J.(1992): "Static and Cyclic Axial Tests on Two 762mm

Diameter Pipe Piles in Clays", Proceedings of the Conference on Recent Large Scale Fully Instrumented Pile Tests In Clay, Institution of Civil Engineers, London, UK.

Coyle H.M. and Reese L.C. (1996): "Load Transfer For Axially Loaded Piles In Clay", ASCE Journal of Geotechnical Engineering Division, USA.

Crisfield M.A. (1991): "Non-linear Finite Element Analysis of Solids and Structures", Vol.1, John Wiley and Sons, UK.

Daghigh Y. (1993): "Numerical Simulation of dynamic behaviour of an earthdam during seismic loading", Ph.D. Thesis, Delft Univ. of Technology, The Netherlands.

Das B.J. (1985): "Advanced Soil Mechanics", McGraw-Hill, New York, USA.

Det norske Veritas (1992):" Wajac Computer Program for Generating Wave Forces on the Jacket", Høvik, Norway.

Digre K.A., Puskar F.J., Aggarwal R.K., Irick J.T., Krieger W. and Petrauskas, C. (1995): "Modification to and Applications of the Guidelines for Assessment of Existing Platforms", Contained in Sec.17 of API RP2A, Proc. of Offshore Tech. Conf., OTC 7779, Houston, USA.

Dunnavant T.D. and O'Neill W. (1989): "Experimental p-y Model For Submerged Stiff Clay", The Journal of Geotechnical Engineering, American Society of Civil Engineers, USA.

Eberg E., Hellan Ø. and Amdahl J. (1993): "Non-linear Re-Assessment of Jacket Structures Under Extreme Storm Cyclic Loading", Part II, The Development of Structural Models for Cyclic Response," Proc., 12th Int. Conf. On Offshore Mech. Arctic Eng. Symp., ASME, Vol.1, p 517-523, USA.

Eberg E. and Amdahl J. (1992): "Phase 2 Time Domain Integration in USFOS", Div. of Structural Engineering, SINTEF, Trondheim, Norway.

El Naggar M.H. and Novak M. (1995): "Nonlinear lateral interaction in pile dynamics", J. Soil Dynamics and Earthquake Eng., Vol.14, Issue.2, pp-141-157.

Emami Azadi M.R. (1994):"GENSODM - A Computer Program for Generating Soil Data", Dept. of Marine Struc., NTNU, Trondheim, Norway.

Emami Azadi M.R., Moan T. and Amdahl J. (1995): "Dynamic Effects on The Performance of Steel Offshore Jacket Platforms Under Extreme Waves", Proceedings of EuroSteel'95, Athens, Greece.

Emami Azadi M.R and Moan T. (1996): "Ductility Demand of Simplified Pile-Soil-Jacket System Under Extreme Sea waves and Earthquakes", Proc. of Eurodyn'96, vol.2, pp.1029-1038

Florence, Italy.

Emami Azadi M.R. (1998): "GENSODM- A modified Version of Gensod program Based on Modified API 93 and Disk Pile-Soil Models due to be published.

Emami Azadi, M.R. and Nordal, S. and Moan, T. (1998): "The predictive abilities of various t-z and p-y models", due to be submitted to J. of Geotechnical Engineering, American Society of Civil Engineers, USA.

Emami Azadi M.R. and Nordal S. (1998): "Non-linear disk-cone model of soil for dynamic loading of offshore pile foundations, due to be published.

Emami Azadi M.R., Hovde G. and Moan T. (1998): "Reliability analysis of jacket-pile-soil system", due to be published.

Fajfar P., Vidic T. and Fischinger M. (1993):"Influence of Damping Model on the Seismic Response of Non-linear SDOF Systems", Proc. of European Conf. on Structural Dynamics(EURODYN'93), Vol.1, pp.77-84.

Finn W.D.L. and Lee M.K.W. (1982): "DESRA-2: Dynamic effective stress response analysis of soil deposits with energy transmitting boundary including assessment of liquefaction potential, The Univ. of British Columbia, Faculty of Applied Science, Canada.

Fugro-McClelland Ltd., (1989):"Field and Laboratory Report", Supplemental site invesitigation-Tilbrook Grange, Cambridgeshire, Prop. Report to BP Int. on Behalf of Participants, LDPT, Report 89/0503-1.

Gabr M. (1994): "P-Y Analysis of Laterally Loaded Piles in Clay Using DMT approach", The Journal of Geotechnical Engineering, American Society of Civil Engineers, USA.

Gazetas G. and Dobry R. (1984): "Horizontal response of the pile in layered soil", J. of Geotechnical Eng., ASCE, Vol.110, pp.20-40, USA.

Gazetas G. (1987):"Simple Physical Methods for Foundation Impedance", in Dynamic Behaviour of Foundation and Buried Structures(Developments in Soil Mechanics and Foundation Engineering, Vol.3), Applied Science, Elsevier, Edited by P.K.Banerjee and Butterfield, Chapter.2, pp.45-93.

Gazioglu S.M. and O'Neill M.W. (1984):"Evaluation of p-y Relationships in Cohesive Soils", Analysis and Design of Pile Foundations, ASCE, OCT. 1984, pp. 192-213.

Gibbs C.E., Mcauley J., Mirza U.A. and Cox W.R. (1992): "Reduction of Field data and Interpretation of Lateral Load Tests Instrumented Pile Tests of Two 762mm Diameter Pipes in Clays", Proceedings of the Conference on Recent Large Scale Fully Instrumented Pile Tests In

Clay, Institution of Civil Engineers, London, UK.

Grande L. and Nordal S. (1979): "Pile-Soil Interaction Analysis on Effective Stress Basis", Proceedings of ICE, Recent Developments In the Design and Construction of Piles, London, UK.

Granli, T.(—): "Behaviour of tubular beam columns under cyclic loading", personal communication.

Hahn G.D. (1991): "A Modified Euler Method For Dynamic Analyses", Int. J. of Numerical Methods in Engineering, Vol.32, pp.943-955, USA.

Hamilton J.M. and Dunnavant T.W. (1992):" Analysis of Behaviour of the Tilbrook Grange Lateral Test Pile", Proc. of Conf. on Recent Large Scale Fully Instrumented Piles in Clay, Institution of Civil Engineer, London, UK.

Hamilton J.M. and Murff J.D.(1988):"Probabilistic Assessment of the Foundation Collapse Strength of Piled Offshore Platforms", Proc. of Behaviour of Offshore Struc. (BOSS'88), Trondheim, Norway.

Hansen P.F., Madsen H.O. and Tjelta T.I. (1995): "Reliability Analysis of a Pile Design", Technical University of Denmark, Lyngby, Denmark.

Hara A. (1980):" Dynamic Deformation Characteristics of Soils and Seismic Response Analysis of the Ground", Dissertation submitted to the Univ. of Tokyo, Japan.

Hardin B.O and Drnevich V.P. (1972):"Closure to Vibration Modulus of Normally Consolidated Clay", JSMFD, ASCE, Vol.95, No.SM6, Nov., pp.1531-1537.

Heideman J.C. and Weaver T.O.(1992): "Static Wave Force Procedure for Platform Design", Proceedings of Civil Engineering in the Oceans V, ASCE ,Texas ,USA.

Hellan Ø., Skallerud B., Amdahl J. and Moan T. (1991): "Re-assessment of Offshore Steel Structures": Shakedown and Cyclic Non-linear FEM Analysis," Proc. of 1st Int. Offshore Polar Conf., Publ. by Int. Soc. of Offshore and Polar Engineers(ISOPE), p 34-42, UK.

Hellan Ø, Tandberg T. and Hellevig N.C. (1993):"Non-linear Re-assessment of Jacket Structures under Extreme Storm Cyclic Loading", Part IV- Case studies on existing North sea platforms. Proc. of Offshore Mechanics and Arctic Engineering Conference(OMAE), Glasgow, UK.

Hellan Ø. (1994): "Re-assessment of Marine Structures", Parameter Studies, SINTEF Report STF70 F94031, SINTEF, Structures and Concrete, Trondheim, Norway.

Hellan Ø. (1995): "Non-linear Pushover and Cyclic Analyses In Ultimate Limit State Design and Re-Assessments Of Tubular Steel Offshore Structures", Dr.ing thesis, NTH, Trondheim, Norway.

Hilber H.M, Hughes T.J.R. and Taylor R.L (1976): "Improved numerical dissipation algorithms in structural dynamics". Rep.no. 76-29, Earthquake Eng. Res. Center, Univ. of California, LA, USA.

Hobbs R. (1992):"The Impact of Axial Pile Load Tests at Pentre and Tilbrook on the Design and Certification of Offshore Piles in Clay", Proc. of Conf. on Recent Large Scale Fully Instrumented Piles in Clay, Institution of Civil Engineer, London, UK.

Holmås T. and Amdahl J. (1994): "USFOS- A Computer Program for Progressive Collapse Analysis of of Steel Offshore Structures", Version 6.7, SINTEF, Norway

Horsnell M.R. and Toolan F.E. (1996): "Risk of Foundation Failure of Offshore Jacket Piles", The 28th Offshore Technology Conf.(OTC), p381-392, USA.

Hovde.G.O , Hellan Ø. (1992): "Probabilistic Analysis of An 8-leg Jacket Platform", Dept. of Marine Structures, NTH, Norway.

Hovde G.O. and Moan T. (1994):"Fatigue Reliability of TLP Tether Systems", Proc. of Offshore Mechanical and Arctic Eng.(OMAE), Vol.2, pp.141-150, ASME, New York, USA.

Hovde G.O. (1995): RELAP- A Reliability Analysis Program, Dept. of Marine Structures, NTH, Norway.

ISO (1995): "Analysis Modelling ISO Adhoc Group, Draft Section X, Den Haag, The Netherlands.

Janbu N. (1976):" Soils under Cyclic Loading", Chairman report, Spec. Sess. No.1 on Soils, Proc. Behaviour of Offshore Structures (BOSS'76), NTH, Trondheim, Norway.

Janbu N. (1985): "Soils In Offshore Engineering", The 25th Rankine Lecture, Geotechnique, Vol 35, No.3, UK.

Jardine R.J.(1985):"Investigations of Pile-Soil Behaviour with Special Reference to the Foundations of Offshore Structures", Ph.D. Thesis, Univ. of London(Imperial College), UK.

Jardine R.J. and Lehane B.M.(1994):"Research Into The Behaviour of Offshore Piles", Field experiments in sand and clay, UK Health and Safety Executives, OTH 93 401, HSE Books, London, UK.

Karamchandani A. (1990):"New Methods in Systems Reliability", Ph.D. Thesis, Stanford, CA., Dept. of Civil Eng., Stanford Univ., USA.

Karlsrud K., Hansen S.B., Dyvik R. and Kalsnes B. (1992): "NGI's Pile Tests at Tilbrook and

Pentre", Review of Testing Procedures and Results, Proceedings of the Conference on Recent Large Scale Fully Instrumented Pile Tests, In Clay, Institution of Civil Engineers, London, UK.

Kaynia A.M. and Kausel E. (1982): "Dynamic behaviour of pile groups", Proceedings of 2nd International Conference on Numerical Methods of Offshore Piling, pp.509-532 , Texas, USA.

Kraft L.M., Focht J.A., Amerasinghe S.F. (1981): "Friction Capacity of Piles Driven into Clay", ASCE Journal of Geotechnical Engineering Division, USA.

Lacasse S. and Goulois A.M. (1989):"Uncertainty in API Parameters for Prediction of Axial Capacity of Driven Piles in Sand", Proc. of Offshore Tech. Conf., OTC 6001, Houston, USA.

Lacasse S. and Nadim F.(1996): "Model Uncertainty in Pile Axial Capacity Calculations", Proceedings of the Offshore Technology Conference, OTC 7996, Houston, Texas, USA.

Lambson M.D., Clarke D.G., Senner D.W.F. (1992): "Investigation and Interpretation of Pentre and Tilbrook Grange Soil Conditions", Proceedings of the Conference on Recent Large Scale Fully Instrumented Pile Tests, In Clay, Institution of Civil Engineers, London, UK.

Langen H.V. (1991):"Numerical Analysis of Soil-Structure Interaction", Ph.D. Thesis, Delft Univ., The Netherlands.

Langø H.V. (1991): "Cyclic shear modulus of natural intact clays", Dr.ing Thesis, NTH, Trondheim, Norway.

Lloyd J.R. and Clawson W.C. (1983):"Reserve and Residual Strength of Piled Founded Offshore Platforms", Int. Symp. on the Role of Design, Inspection and Redundancy in Marine Structural Reliability, Williamsburg, USA.

Madsen H.O., Krenk S. and Lind N.C. (1986): "Methods of Structural Safety", Prentice-Hall Inc., USA.

Madshus C. (1997):"Soil Non-linearity and its Effects on the Dynamic Behaviour of Offshore Platform Foundations", D.Sc. Thesis, Dept. of Geology, Univ. of Oslo, Oslo, Norway.

Marshall P.W., Gates W.E. and Anagnostopoulos S. (1977): "Inelastic Dynamic Analysis of Tubular Offshore Structures", Proc. Offshore Structures, Proc. of Offshore Technology Conf. (OTC), Paper No. 2908, Houston, USA.

Matlock H. (1970): "Correlations for Design of Laterally Loaded Piles in Soft Clays", Proc. 2nd Annual Offshore Technology Conference, paper no. 1204, Vol.1, pp 577-588, Houston, USA.

Meek J.W. and Wolf J.P. (1992): "Cone models for homogeneous soil", Journal of Geotechnical Engineering, ASCE, Vol.118- PP.667-685, USA.

Meek J.W. and Wolf J.P. (1993): "Cone models for nearly incompressible soil", Earthquake Engineering and Structural Dynamics, Vol.22- pp.649-663.

Melchers R.E. (1987):"Structural Reliability Analysis and Prediction, Chichester, UK. Ellis Horwood Ltd., UK.

Meyerhof G.G. (1976):" Bearing Capacity and Settlement of Pile Foundations", J. of Geotech. Eng., Div., ASCE, Vol. 102, No. GT3, pp. 1-29.

Miller G.F. and Pursey H. (1955): "The field and radiation impedance of mechanical radiators on the free surface of the semi-infinite Isotropic Solid", Proceedings Royal Society, Vol.A 223-pp.521-541, UK.

Moan T., Amdahl J., Engseth A.G. and Granli T. (1985): "Collapse behaviour of Trusswork Steel Platforms", BOSS'85, Delft, Holland.

Moan T., Hellan Ø. and Emami Azadi M.R.(1997): "Non-linear Dynamic versus Static Analysis of Jacket Systems for Ultimate Limit State Check", J. of Marine Science and Technology, (in print)

Moan T., Amdahl J., Engseth A.G. and Granli T. (1985): " Collapse behavior of Trusswork steel platforms", Int. Conf. On Behavior of Offshore Structures, BOSS' 85, Delft, Holland.

Moan T. (1997):"Current Trends in the Safety of Offshore Structures", Proc. of the 7th Int. Offshore and Polar Engineering Conference(ISOPE), Honolulu, USA.

Moe O. and Moan T. (1984): "Environmental Load Effect Analysis of Guyed Towers", Proc. of the Third International Offshore Mechanics and Arctic Engineering Symposium, Vol.1, 68-79, ASME, USA.

Molenkamp F. and Smith M. (1980):"Hysteretic and Viscous Material Damping", Int. J. for Numerical and Analytical Methods in Geomechanics, Vol.4, pp.293-311.

Moses F. and Liu Y.W. (1992):"Methods of Redundancy Analysis for Offshore Platforms, Proc. of Offshore Mechanical and Arctic Eng.(OMAE), Vol.2, pp.411-416, ASME, New York, USA.

Nadim F. (1988):"Geotechnical Site Description Using Stochastic Interpolation", Norwegian Geotech. Inst., Oslo, Norway.

Nadim F.(1994):" NGI report, Uncertainty modelling of pile-soil system, Oslo, Norway.

Nadim F. and Dahlberg R. (1996): "Numerical Modelling of Cyclic Pile Capacity in Clay", Proc. of Offshore Technology Conf. (OTC), Vol.1, 347-356, USA.

Newmark N.M. (1959): "A method of computation for structural dynamics", J. of Eng. Mechanics Division, ASME, Vol.85, No.EM3, pp.67-94, USA.

NGI (1994):"Database of Norwegian Geotech. Inst., personal communication

Nogami T. and Konagai K. (1986): "Time domain axial response of dynamically loaded single piles", J. of Eng. Mechanics, ASCE, Vol.112, No.11, pp.1241-1252, USA.

Nogami T. and Konagai K. (1988): "Time domain flexural response of dynamically loaded single piles", J. of Eng. Mechanics, ASCE, Vol.114, No.9, pp.1512-1525, USA.

Nogami T. and Konagai K. (1989): "Time Domain Flexural Response of Dynamically Loaded Single Piles", ASCE, USA.

Nonaka J. (1973): "An elastic-plastic analysis of a bar under repeated axial loading ", Int. J. Solids and Structures, Vol.9, pp569-580, Pergamon Press, New York, USA.

Nordal S., Grande L. and Janbu N. (1985): "Prediction of pile behavior", Geotechnical Division, Bul.15, NTH, Norway.

Nordal S.(1986):"Soil Modelling", Lecture Notes, Division of Geotech. Eng., NTH, Trondheim, Norway.

Nordal S., Eiksund G. and Bernardes G. (1992):"Large Scale Model Piles: Measured and Calculated Response During Driving", Proc. of Int. Conf. on the Application of Stress-Wave Theory to Piles", pp.589-594. Balkema, Rotterdam, Holland.

Nordal S. (1998):"Personal communications based on guidance for Dr.ing Thesis".

Nordic Committee on Building Regulations (1978): "Recommendations for Loading and Safety Regulations for Structural Design", NKB-Report No.36, Denmark.

Norwegian Petroleum Directorate (1992): "Guidelines for fixed offshore structures", Oslo, Norway.

Ogawa K., Yamanari M., Makino Y., Kurobane Y., Kumanato U. and Yamashita M. (1987): "Buckling and post-buckling behaviour of complete tubular trusses under cyclic loading", Proc. of Offshore Technology Conference, paper no. 5439, Houston, USA.

Olufsen A. and Moan T.(1989): "Reliability Analysis of A Fixed Jacket Platform, NTNF Research Program: Report No.STF71 A89034, Marine Structures, SINTEF, Norway.

Poulos H. and Davis E.H. (1980):"Pile Foundation Analysis and Design", John Wiley and Sons,

New York, USA.

Poulos H.G. (1982):"Influence of Cyclic Loading on The Axial Pile Response", Proc. of the 2nd Int. Conf. on Numerical Methods in Offshore Piling, Austin, Texas, USA.

Przemieniecki R. (1968): "The matrix structural analysis", Prentice Hall, New York, USA.

Ramberg W. and Osgood W.T. (1943):"Description of Stress-Strain Curves by Three Parameters", Technical Note 902, National Advisory Committee for Aeronautics, Washington D.C., USA.

Randolph M.F. (1990):"Impact: Dynamic Analysis of Pile Driving", User manual(2 Volumes), The Univ. of Western Australia, Australia.

Randolph M.F. (1992):"Analysis of Stress-Wave Data from Pile Tests at Pentre and Tilbrook", Proc. of Conf. on Recent Large Scale Fully Instrumented Piles in Clay, Institution of Civil Engineer, London, UK.

Rashed S.M.H. (1980): "Behaviour to Ultimate Strength of Tubular Offshore Structures by the Idealized Structural Unit Method", Report SK/R51, Division of Marine Structures, NTH, Norway.

Reddy J.N. (1985): "An Introduction to the Finite Element Method", McGraw-Hill Company, New York, USA.

Reese L. C., Cox W.R. and Koop F. D. (1974): "Analysis of Laterally Loaded Piles in Sand", Proc. of Offshore Technology Conference, OTC2080, Houston, USA.

Reese L.C. and Cox. W.R. and Koop F.D. (1975):"Field Testing and Analysis of Laterally Loaded Piles in Stiff Clay", Proc. of Offshore Tech. Conf., OTC 2312, Houston, USA.

Richart F.E. (1975):"Some Effects of Dynamic Soil Properties on Soil Structure Interaction", Proc. of ASCE, Vol.101, GT12, pp.1193-1240.

Rigden W.J. and Semple R.M. (1983):"Design and Installation of the Magnus Foundations", Predictions of Pile Behaviour. In: Design in Offshore Structures, Thomas Telford Ltd., London, UK.

Samier P., Paygnard J.C. and Birades M. and Colliat J.L. (1994):"Nonlinear Deterministic Analysis Versus Reliability Study for the Assessment of A Jacket", Proc. of Offshore Mechanical and Arctic Eng.(OMAE), Vol.2, pp.203-210, ASME, New York, USA.

Schmucker D.G and Cornell C.A.(1994): "Dynamic behaviour of Semi-Ductile Jackets Under Extreme Wave and Wave-In-Deck Forces", Civil Eng. Dept., Stanford Univ., USA.

Schmucker D.G. (1996): "Near Failure behaviour of Jacket-Type Offshore Platforms in The Extreme Wave Environment", Ph.D. thesis, report no. RMS-21, June, 1996, Stanford Univ., USA.

Shahrour I. and Meimon Y. (1990): "Analysis of the Behavior of the Offshore Piles under Inclined Loads", Canadian Geotechnical Journal, No.27, Canada.

Shetty N.K. (1992):"System Reliability of Fixed Offshore Structures under Fatigue Deterioration", Ph.D. Thesis, Imperial College, London, UK.

Sigurdsson G., Skallerud B., Skjong R. and Amdahl J. (1993): "Probabilistic Collapse Analysis of Jackets", DNV and SINTEF, Norway.

Skotheim A.Å., Stordal A. and Svanø G.(1980): "Geotechnical stability of Statfjord platform A", OTTER Project No.881121.02-07508,A, Trondheim, Norway.

Søreide T.H. and Amdahl J. (1986): "USFOS A computer program for ultimate strength analysis of framed offshore structures", Theory manual, Report STF71 A86049, SINTEF Structural Engineering, Trondheim, Norway.

Søreide T.H., Amdahl J. (1994): "USFOS- A Computer Program for Ultimate Strength Analysis of Framed Offshore Structures", Theory manual, Report STF71 A86049, SINTEF Structural Engineering, Trondheim, Norway.

Spiegel M. (1968): "Mathematical Handbook", Schaum's series, McGraw-Hill Company, New York, USA.

Stewart G., Efthymiou M. and Vugts J.H.(1988):" Ultimate Strength and Integrity Assessment of Fixed Offshore Platforms", Int. Conf. on the Behaviour of Offshore Structures(BOSS), Trondheim, Norway.

Stewart G., Moan T. and Eide O. (1993): "Non-linear Re-Assessment of Jacket Structures Under Extreme Storm Cyclic Loading", Part I : Philosophy and Acceptance Criteria , Proc. of Int. Offshore and Polar Engineering (ISOPE), USA.

Stewart G. (1995): "The Response of Non-linear Structures by the Pseudo-Force Influence Method", Ph.D. Thesis, Dept. of Naval Architecture and Ocean Eng., Univ. of Glasgow, UK.

Sugmimoto H. and Chen W.F. (1985): "Inelastic post-buckling behaviour of tubular members", J. of Struc. Eng., Vol.111, no.9, American Society of Civil Engineers, USA.

Sullivan W.R. and Reese L.C. and Fenske C.W.(1980):"Unified Method for Analysis of Laterally Loaded Piles in Clay", Numerical Methods in Offshore Piling, ICE, London, pp.135-146.

Svanø G. (1992): "Long Term Processes In Geomaterials" , SINTEF Geotech. Division , Norway.

Svanø G., Tjelta and Eide (1992): "Model Verification by Using LDPT data, Proceedings of the Conference on Recent Large Scale Fully Instrumented Pile Tests, In Clay, Institution of Civil Engineers, London, UK.

Svanø G., Madshus C. and LangøH. (1993): "On the validity of non-linear spring idealization of soil-structure interaction", The third European Conference on Structural Dynamics, Vol.1, pp.403-410, EURODYN'93, Trondheim, Norway.

Timoshenko S.P. and Goodier J.N. (1982):"Theory of Elasticity", McGraw-Hill Company, New York, USA.

Trochanis A.M., Bielak J. and Christiano P. (1991): "Three-dimensional Non-linear Study of Piles", Journal of Geotechnical Engineering, ASCE, Vol.113, No.3, USA.

Tromans P.S., Anaturk A.R. and Hagemeijer P. (1991): "A New Model for the Kinematics of Large Ocean Waves", Application as a Design Wave, The Proc. of the First Int. Offshore and Polar Engineering Conf. (ISOPE), UK.

Tvedt L. (1990): "Distribution of Quadratic Forms in Normal Space", Application to Structural Reliability, Journal Engineering Mechanics ,Vol.116, No.6, USA.

Ueda Y. and Rashed S.M.H. (1974): "An Ultimate Transverse Strength Analysis of Ship Structures", J. of Society of Naval Architecture of Japan, Vol.136, Japan.

Vijayvergia V.N. (1977): "Loaded Movement Characteristics of Piles", Proceedings of the Ports'77 Conference, ASCE, USA.

Vugts J.H. and Edwards G. (1992):"Offshore Structural Reliability Assessment- From research to reality? Proc. of Behaviour of Offshore Structures(BOSS), Imperial College, London, UK.

Warburton G.B. (1976):"The Dynamic Behaviour of Structures", Pergamon Press Ltd., UK.

Wolf J.P. and Meek J.W. and Song Ch. (1992): "Cone models for a pile foundation", Piles under dynamic loads, Edited by S.Prakash. Geotechnical Special Publication, Vol.34- pp.94-113, ASCE, USA.

Wolf J.P. and Meek J.W. (1994): "Cone models for an embedded foundation in a layered soil medium", J. of Geotechnical Eng., ASCE, Vol.120, pp.210-228, USA.

Wolf J.P. (1994): "Foundation vibration analysis using simple physical models", PTR, Prentice-Hall, Engelwood Cliffs, USA.

Wolf and Song (1995):"Consistent Infinitesimal Finite-Element Cell Method: In-Plane Motion", J. of Comput. Methods, App. Mech. Eng., Elsevier, No. 123, pp. 355-370.

Wu Y.L. and Moan T. (1989):"A Structural System Reliability of Jacket Using An Improved Truss Model", Proc. of Int. Conf. on Structural Statistics and Reliability (ICOSSAR),Vol.2, pp.887-894, ASME, New York, USA.

Yu-Lin Wu (1989):"System Reliability Analysis of Offshore Structures Using Improved Truss and Beam Models", Dr.ing. Report No.1989:70, Div. of Marine Struc., NTH, Trondheim, Norway.

Zayas V.A., Mahin S.A. and Popov E.P, (1980): "Cyclic inelastic buckling of tubular steel braces", Report No. UBC/EERC-80/16, Earthquake Eng. Research Centre, Univ. of California, Berkeley, USA.

Zienkiewicz O.C. and Taylor R.L. (1989): "The Finite Element Method", Vol.1, Basic Formulation, McGraw-Hill Company, UK.

APPENDIX A

Static pile-soil disk model

A.1 (t-z) disk model for perfectly overconsolidated layered soil

For a special case of clay with $\beta = 1$ from Eq.4.28, a linear relationship between G^T and τ is obtained as:

$$G^T = G_i(1 - \alpha\frac{\tau}{\tau_{ps}}) \tag{A.1}$$

where τ_{ps} is defined in the main text of Chapter.2 as the failure stress at the pile-soil interface and obtained in Eq.2.45 based on Mohr-Coulomb criteria.
The shear strain γ may be obtained as follows:

$$\gamma = \int_{\tau_0}^{\tau} \frac{d\tau}{G^T} = \int_{\tau_0}^{\tau} \frac{d\tau}{G_i(1 - \alpha\frac{\tau}{\tau_{ps}})} \tag{A.2}$$

integrating the Eq.A.2 results in:

$$\gamma = -\frac{\tau_{ps}}{\alpha G_i} Ln(\frac{1 - \alpha\frac{\tau}{\tau_{ps}}}{1 - \alpha\frac{\tau_0}{\tau_{ps}}}) \tag{A.3}$$

Now integrating γ over the radius of the soil disk will result in the axial displacement z as a function of τ in the following form:

$$z = \int_{r_i}^{r_{id}} \gamma(r)dr = \int_{r_i}^{r_{id}} -\frac{\tau_{ps}}{\alpha G_i} Ln(\frac{1 - \alpha\frac{\tau}{\tau_{ps}}}{1 - \alpha\frac{\tau_0}{\tau_{ps}}}) \tag{A.4}$$

Substituting for τ in Eq.A.4 from Eq.2.13 will yield:

$$z = \int_{r_i}^{r_{id}} -\frac{\tau_{ps}}{\alpha G_i} Ln(\frac{1 - \alpha\tau_i\frac{exp(\frac{r_i - r}{2r_i})}{\tau_{ps}}}{1 - \alpha\frac{\tau_0}{\tau_{ps}}}) \tag{A.5}$$

Integration of Eq.A.5 may be performed numerically. The results of numerical integration and the fitted functions are prsenented in the following sections.

A.2 A general case of (p-y) model for partially drained soil

For the case of a partially drained soil, the radial strain after time (t) may be related approximately to the circumferencial strain at time (t) and the amount of drained soil since loading process begins at time ($t = 0$)as follows:

$$|\epsilon_r(t)| = |\epsilon_\theta(t)| + \alpha_d|\epsilon_r(0)| \tag{A.6}$$

in which $\epsilon_r(t)$ may be related to $\epsilon_r(0)$ in a simple way as follows:

$$\epsilon_r(t) = f_\epsilon(t).\epsilon_r(0) \tag{A.7}$$

Combining Eqs.A.6 and A.7, one might obtain:

$$\frac{|\epsilon_r(0)|}{|\epsilon_\theta(0)|} = \frac{f_\epsilon(t)}{\alpha_d - f_\epsilon(t)} \tag{A.8}$$

The distortion caused by shearing in the soil infinitesimal element at time (t) $\gamma(t)$ may be expressed approximately as follows:

$$|\gamma(t)| = |\epsilon_r(0)|[\alpha_d + 2(f_\epsilon(t) - \alpha_d)] \tag{A.9}$$

From Eq.A.9, $\epsilon_r(0)$ may be obtained as follows:

$$|\epsilon_r(0)| = \frac{|\gamma(t)|}{\alpha_d + 2(f_\epsilon(t) - \alpha_d)} \tag{A.10}$$

Hence, $\epsilon_r(t)$ may be obtained from Eqs.A.10 and A.7 as follows:

$$\epsilon_r(t) = \int_{\tau_0}^{\tau} \frac{f_\epsilon(t)}{\alpha_d + 2(f_\epsilon(t) - \alpha_d)} . \frac{d\tau}{G^T(t,\tau)} \tag{A.11}$$

The lateral soil displacement function y(t) may be obtained through integration of $\epsilon_r(t)$ over the disk radius as follows:

$$y(t) = \int_{r_i}^{\eta r_i} \int_{\tau_0}^{\tau} \frac{f_\epsilon(t)}{\alpha_d + 2(f_\epsilon(t) - \alpha_d(t))} . \frac{d\tau}{G_i(1 - \alpha \frac{r_i}{r_{ps}(t)} exp(\frac{\tau - r_i}{2r_i}))^\beta} . dr \tag{A.12}$$

$f_\epsilon(t)$ may be considered as consolidation function of soil and several empirical as well as theoretical forms exist in the soil mechanics literature for it(see for e.g. Das, (1985)).

A.3 Comparison of fitted functions and integration of (t-z) and (p-y) disk models

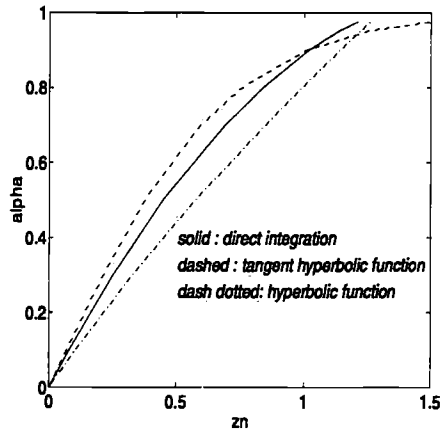

Figure A.1: Comparison of fitted tangent hyperbolic and hyperbolic (t-z) functions with the direct integration results for $\beta = 1.05$

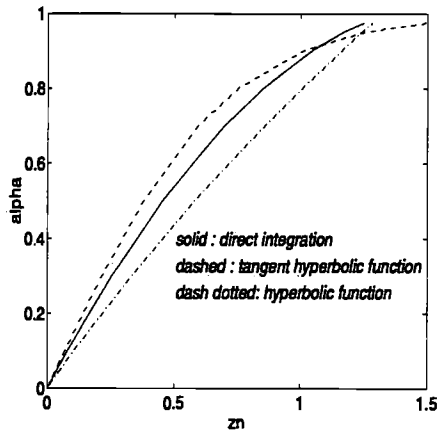

Figure A.2: Comparison of fitted tangent hyperbolic and hyperbolic (t-z) functions with the direct integration results for $\beta = 1.1$

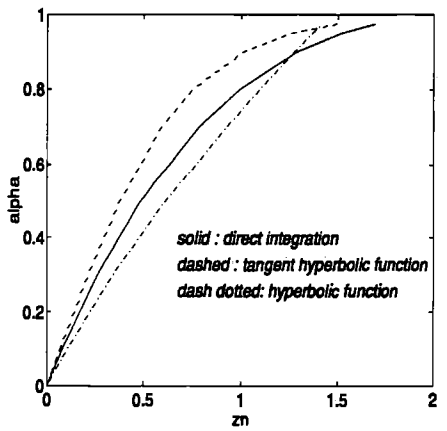

Figure A.3: Comparison of fitted tangent hyperbolic and hyperbolic (t-z) functions with the direct integration results for $\beta = 1.5$

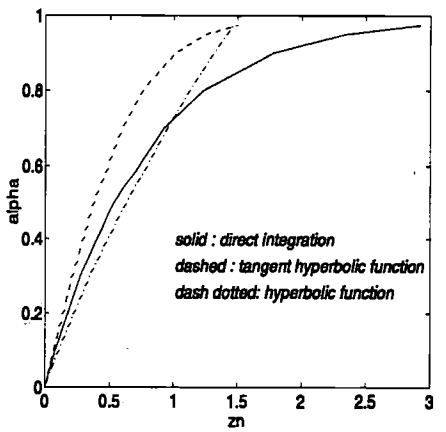

Figure A.4: Comparison of fitted tangent hyperbolic and hyperbolic (t-z) functions with the direct integration results for $\beta = 2.0$

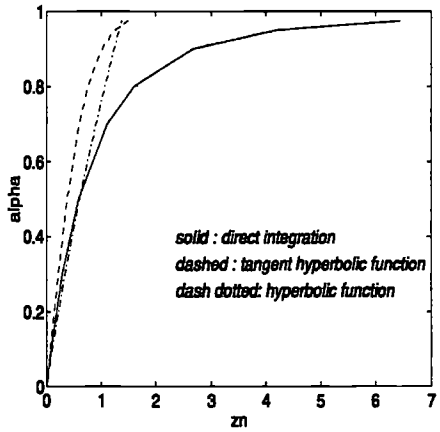

Figure A.5: Comparison of fitted tangent hyperbolic and hyperbolic (t-z)functions with the direct integration results for $\beta = 2.5$

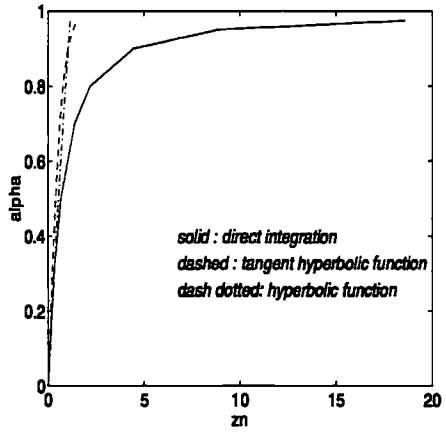

Figure A.6: Comparison of fitted tangent hyperbolic and hyperbolic (t-z)functions with the direct integration results for $\beta = 3.0$

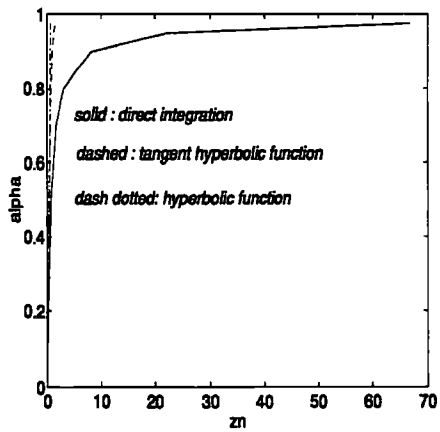

Figure A.7: Comparison of fitted tangent hyperbolic and hyperbolic (t-z)functions with the direct integration results for $\beta = 3.5$

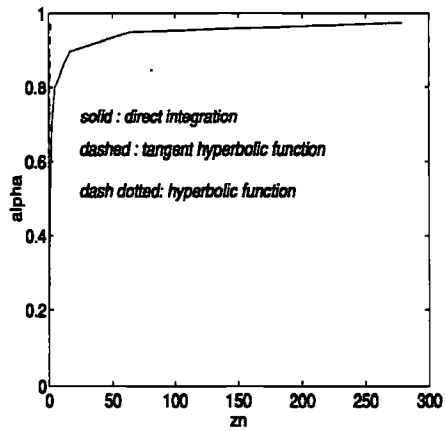

Figure A.8: Comparison of fitted tangent hyperbolic and hyperbolic (t-z)functions with the direct integration results for $\beta = 4.0$

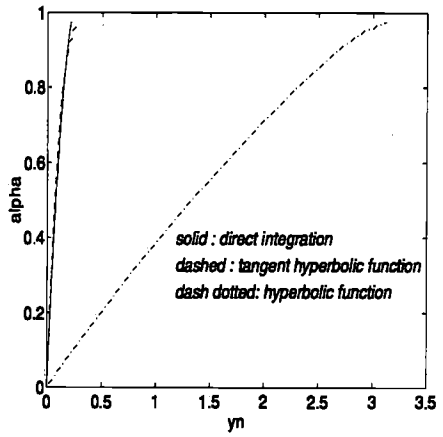

Figure A.9: Comparison of fitted tangent hyperbolic and hyperbolic (p-y)functions with the direct integration results for $\beta = 1.05$

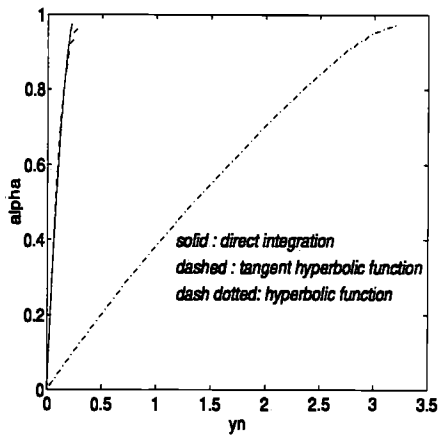

Figure A.10: Comparison of fitted tangent hyperbolic and hyperbolic (p-y)functions with the direct integration results for $\beta = 1.1$

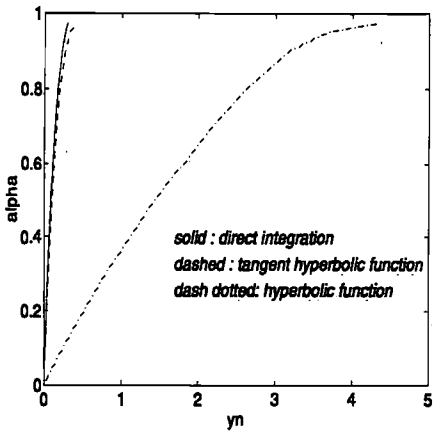

Figure A.11: Comparison of fitted tangent hyperbolic and hyperbolic (p-y)functions with the direct integration results for $\beta = 1.5$

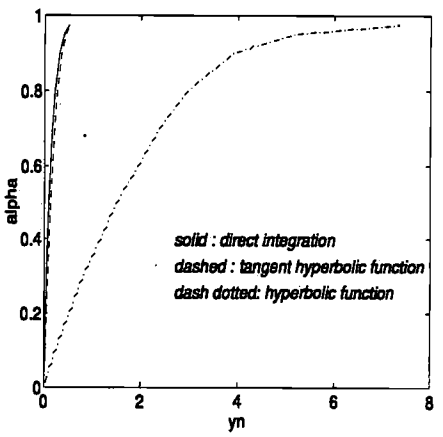

Figure A.12: Comparison of fitted tangent hyperbolic and hyperbolic (p-y)functions with the direct integration results for $\beta = 2.0$

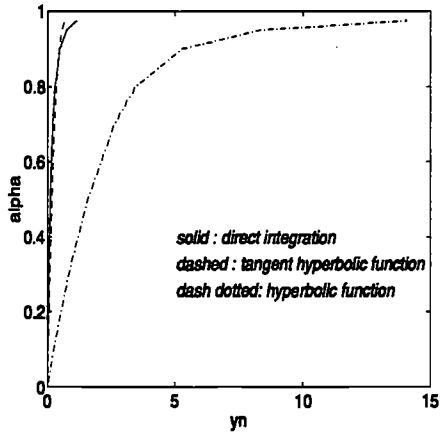

Figure A.13: Comparison of fitted tangent hyperbolic and hyperbolic (p-y)functions with the direct integration results for $\beta = 2.5$

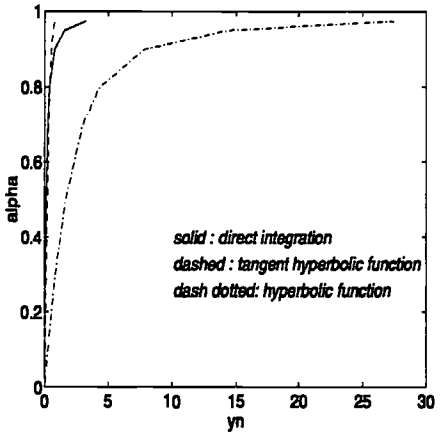

Figure A.14: Comparison of fitted tangent hyperbolic and hyperbolic (p-y)functions with the direct integration results for $\beta = 3.0$

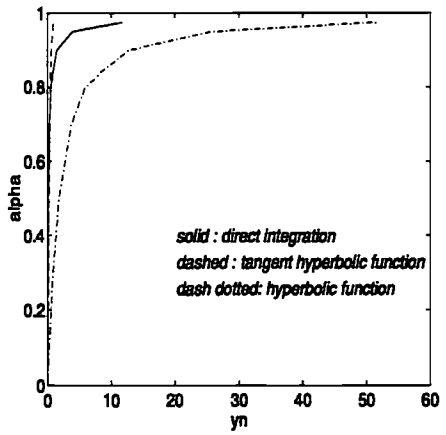

Figure A.15: Comparison of fitted tangent hyperbolic and hyperbolic (p-y)functions with the direct integration results for $\beta = 3.5$

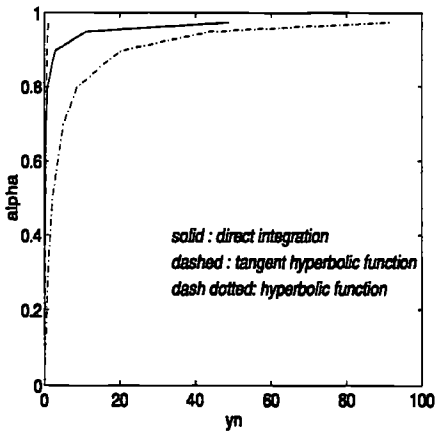

Figure A.16: Comparison of fitted tangent hyperbolic and hyperbolic (p-y)functions with the direct integration results for $\beta = 4.0$

APPENDIX B

LDPT verification cases(Pentre, Tilbrook and Houston)

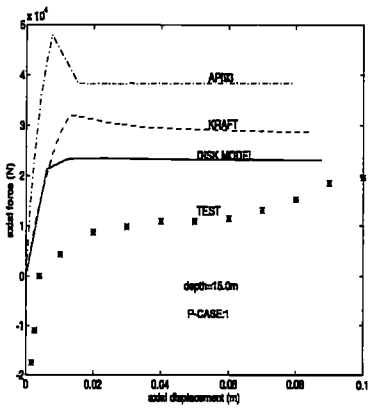

Figure B.1: Comparison of (t-z) response curves for Pentre pile(NC case)at depth 15m

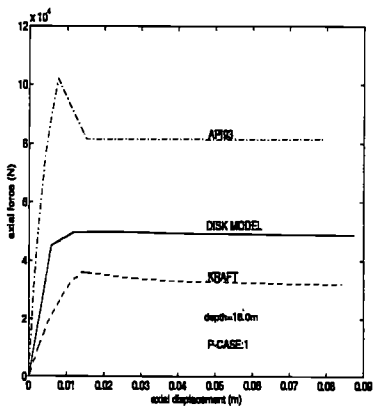

Figure B.2: Comparison of (t-z) response curves for Pentre pile(NC case)at depth 16m

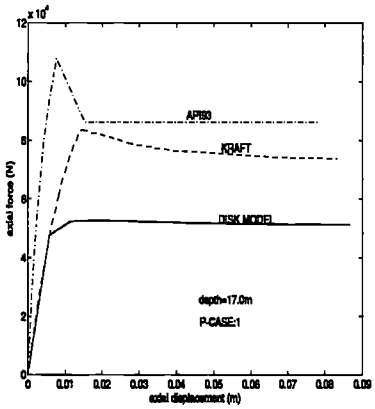

Figure B.3: Comparison of (t-z) response curves for Pentre pile(NC case)at depth 17m

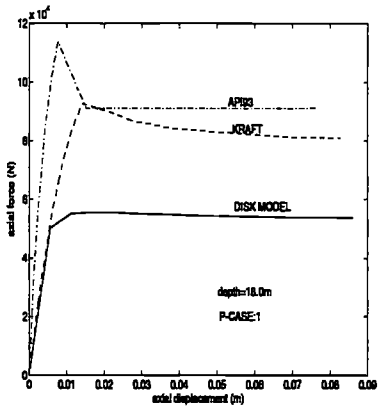

Figure B.4: Comparison of (t-z) response curves for Pentre pile(NC case)at depth 18m

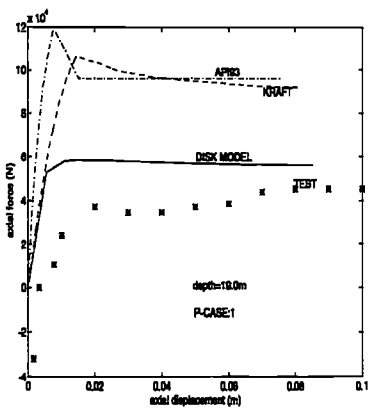

Figure B.5: Comparison of (t-z) response curves for Pentre pile(NC case)at depth 19m

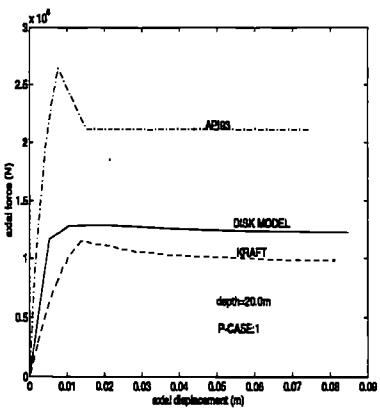

Figure B.6: Comparison of (t-z) response curves for Pentre pile(NC case)at depth 20m

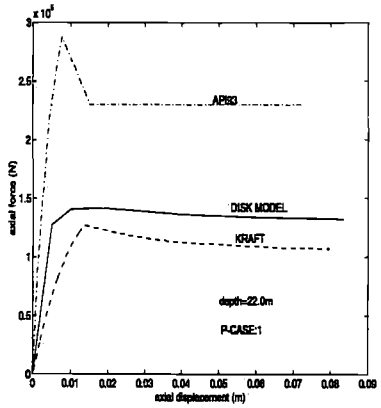

Figure B.7: Comparison of (t-z) response curves for Pentre pile(NC case)at depth 22m

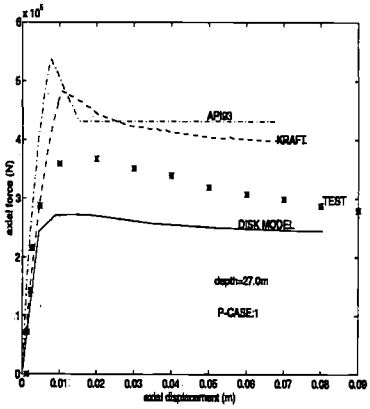

Figure B.8: Comparison of (t-z) response curves for Pentre pile(NC case)at depth 27m

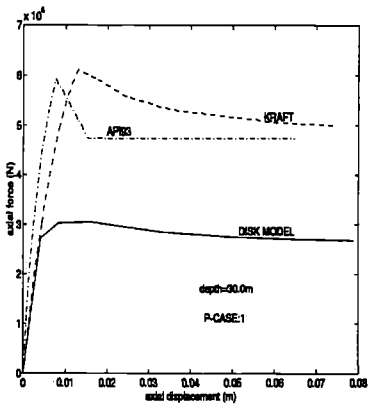

Figure B.9: Comparison of (t-z) response curves for Pentre pile(NC case)at depth 30m

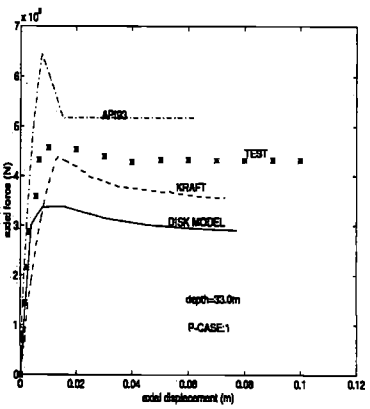

Figure B.10: Comparison of (t-z) response curves for Pentre pile(NC case)at depth 33m

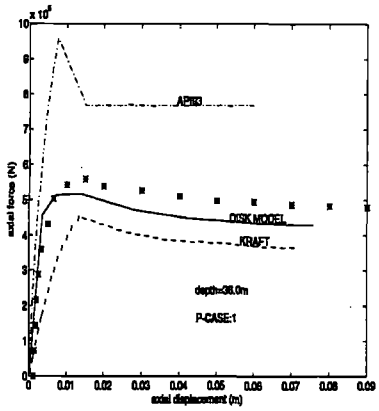

Figure B.11: Comparison of (t-z) response curves for Pentre pile(NC case)at depth 36m

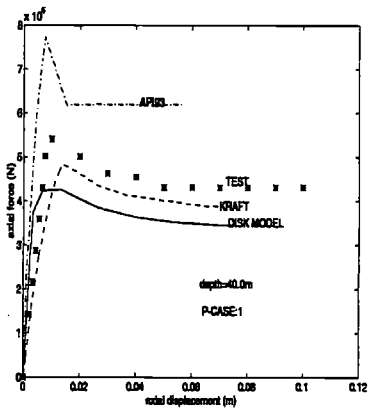

Figure B.12: Comparison of (t-z) response curves for Pentre pile(NC case)at depth 40m

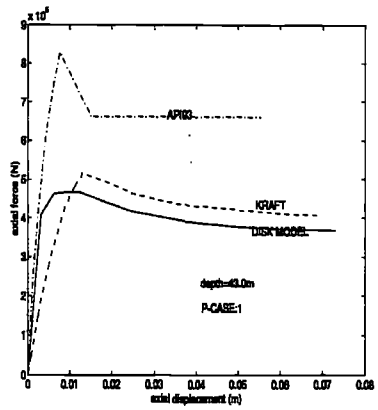

Figure B.13: Comparison of (t-z) response curves for Pentre pile(NC case)at depth 43m

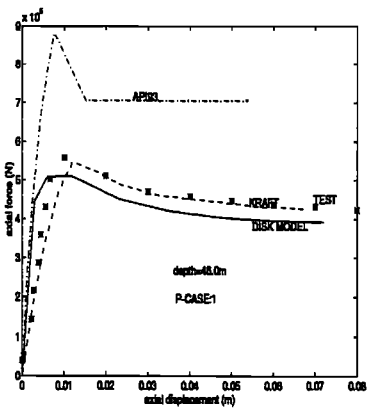

Figure B.14: Comparison of (t-z) response curves for Pentre pile(NC case)at depth 46m

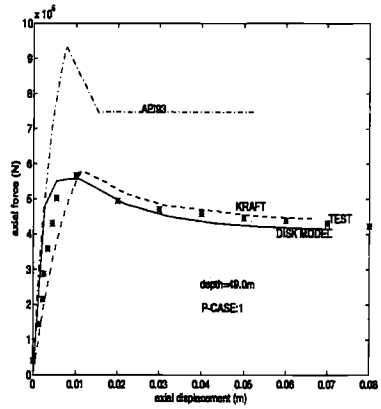

Figure B.15: Comparison of (t-z) response curves for Pentre pile(NC case)at depth 49m

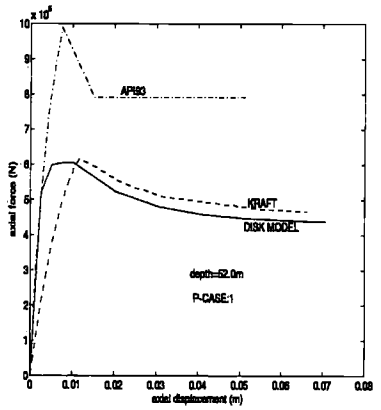

Figure B.16: Comparison of (t-z) response curves for Pentre pile(NC case)at depth 52m

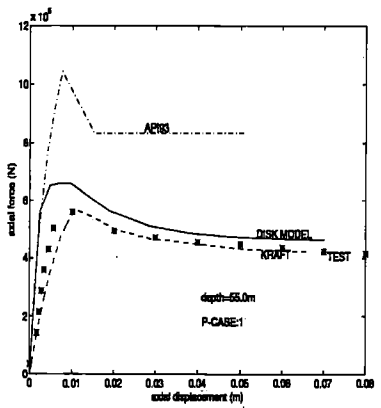

Figure B.17: Comparison of (t-z) response curves for Pentre pile(NC case)at depth 55m

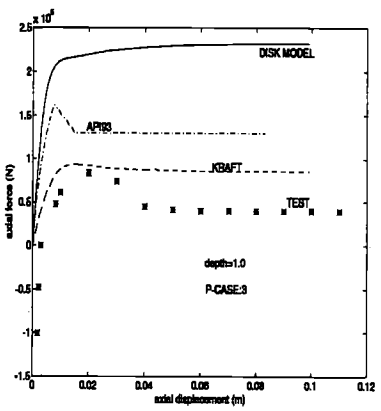

Figure B.18: Comparison of (t-z) response curves for Tilbrook pile(OC case)at depth 1m

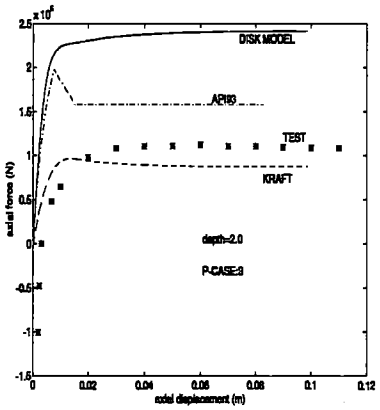

Figure B.19: Comparison of (t-z) response curves for Tilbrook pile(OC case)at depth 2m

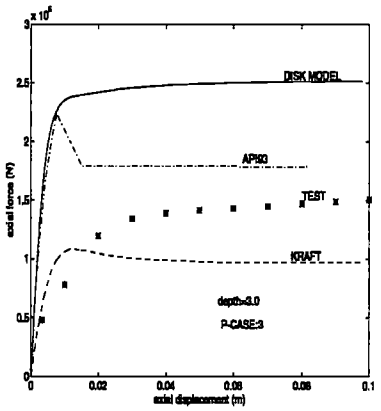

Figure B.20: Comparison of (t-z) response curves for Tilbrook pile(OC case)at depth 3m

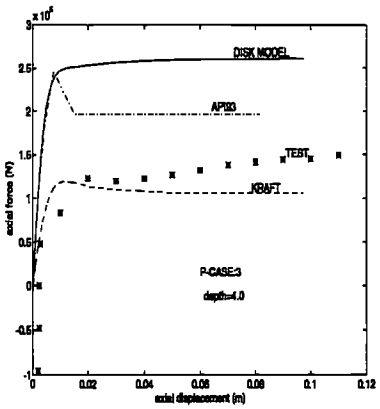

Figure B.21: Comparison of (t-z) response curves for Tilbrook pile(OC case)at depth 4m

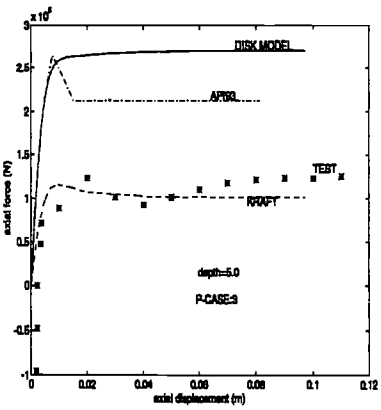

Figure B.22: Comparison of (t-z) response curves for Tilbrook pile(OC case)at depth 5m

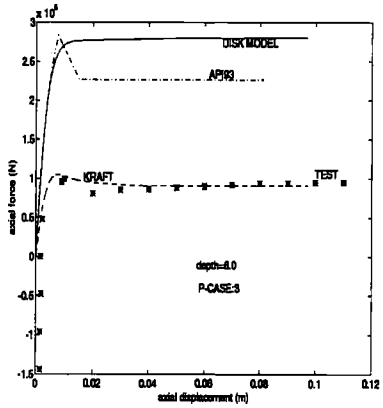

Figure B.23: Comparison of (t-z) response curves for Tilbrook pile(OC case)at depth 6m

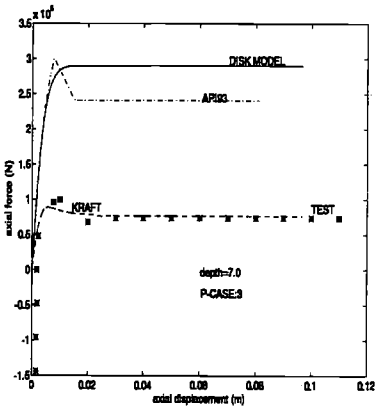

Figure B.24: Comparison of (t-z) response curves for Tilbrook pile(OC case)at depth 7m

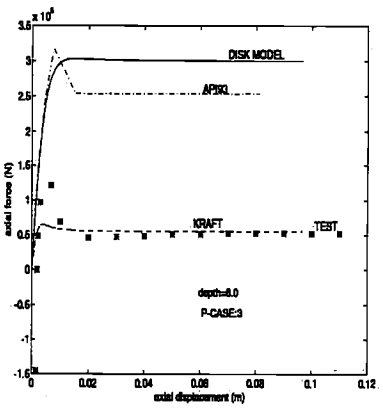

Figure B.25: Comparison of (t-z) response curves for Tilbrook pile(OC case)at depth 8m

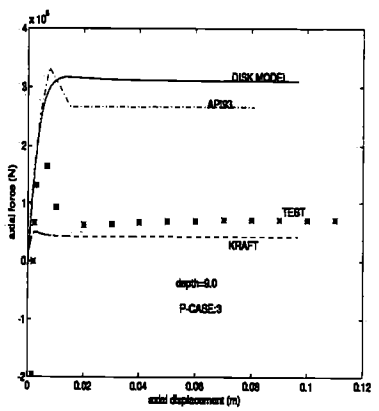

Figure B.26: Comparison of (t-z) response curves for Tilbrook pile(OC case)at depth 9m

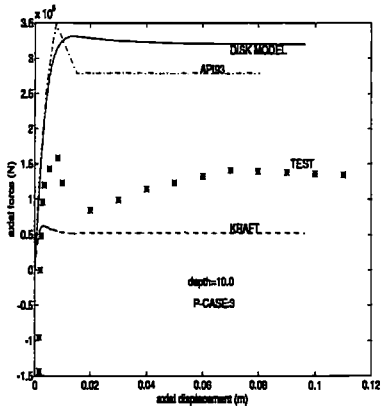

Figure B.27: Comparison of (t-z) response curves for Tilbrook pile(OC case)at depth 10m

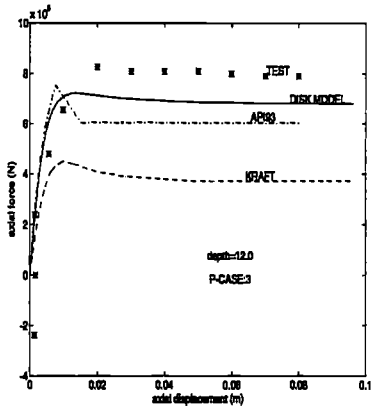

Figure B.28: Comparison of (t-z) response curves for Tilbrook pile(OC case)at depth 10m

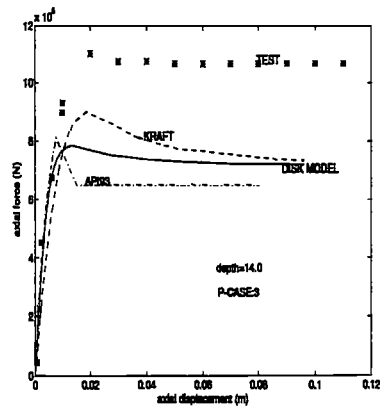

Figure B.29: Comparison of (t-z) response curves for Tilbrook pile(OC case)at depth 14m

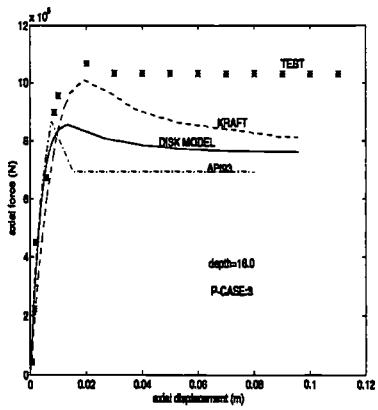

Figure B.30: Comparison of (t-z) response curves for Tilbrook pile(OC case)at depth 16m

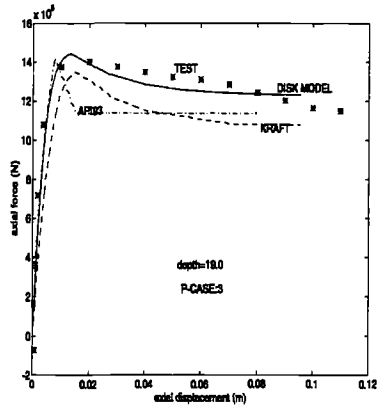

Figure B.31: Comparison of (t-z) response curves for Tilbrook pile(OC case)at depth 19m

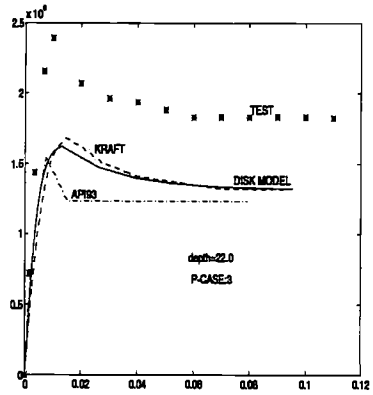

Figure B.32: Comparison of (t-z) response curves for Tilbrook pile(OC case)at depth 22m

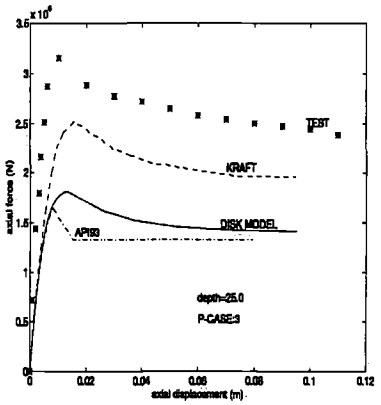

Figure B.33: Comparison of (t-z) response curves for Tilbrook pile(OC case)at depth 25m

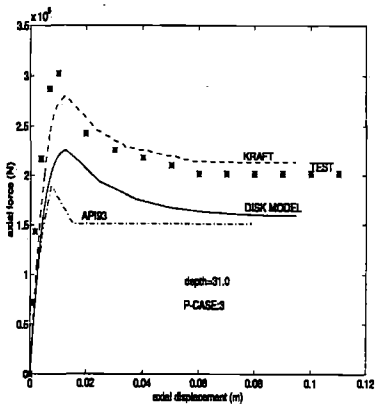

Figure B.34: Comparison of (t-z) response curves for Tilbrook pile(OC case)at depth 31m

APPENDIX C

LDPT verification cases (Tilbrook and Houston)

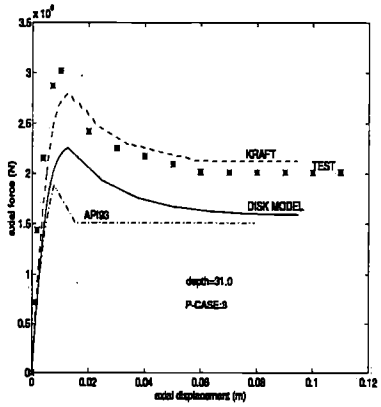

Figure C.1: Comparison of (t-z) response curves for Tilbrook pile(OC case)at depth 31.0m

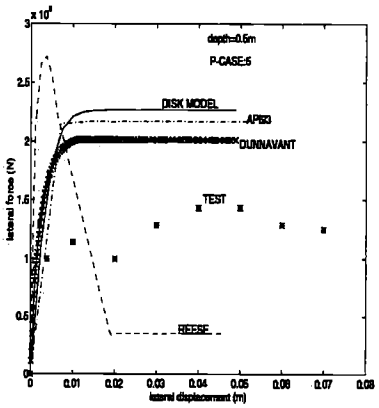

Figure C.2: Comparison of (p-y) response curves for Tilbrook pile(OC case)at depth 0.5m

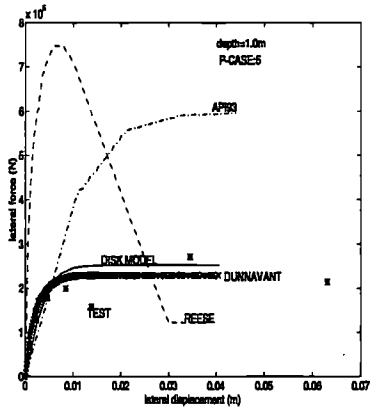

Figure C.3: Comparison of (p-y) response curves for Tilbrook pile(OC case)at depth 1.0m

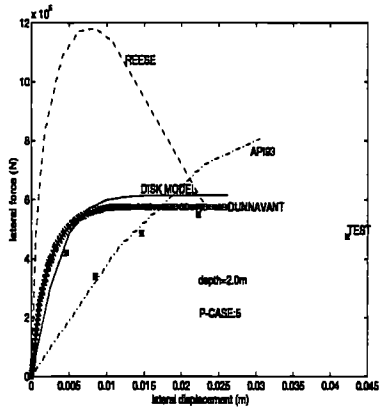

Figure C.4: Comparison of (p-y) response curves for Tilbrook pile(OC case)at depth 2.0m

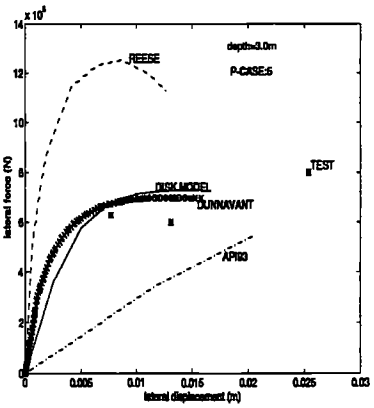

Figure C.5: Comparison of (p-y) response curves for Tilbrook pile(OC case)at depth 3.0m

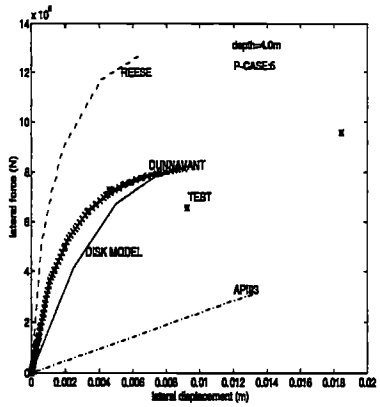

Figure C.6: Comparison of (p-y) response curves for Tilbrook pile(OC case)at depth 4.0m

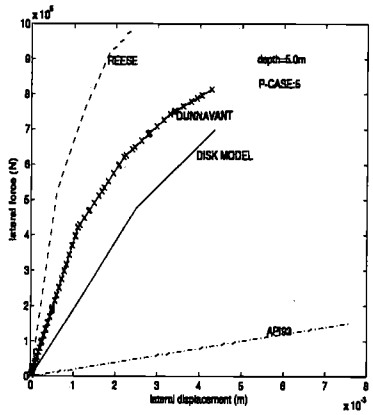

Figure C.7: Comparison of (p-y) response curves for Tilbrook pile(OC case)at depth 5.0m

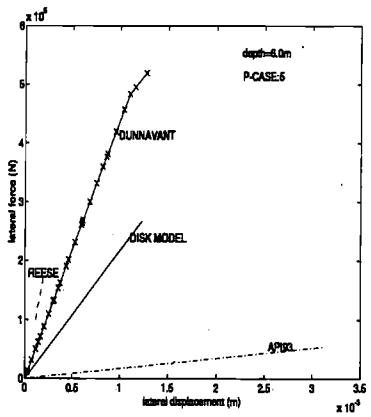

Figure C.8: Comparison of (p-y) response curves for Tilbrook pile(OC case)at depth 6.0m

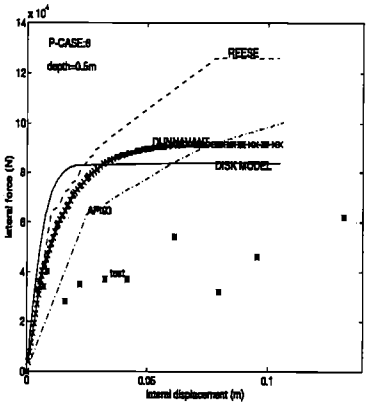

Figure C.9: Comparison of (p-y) response curves for Houston pile(OC case)at depth 0.5m

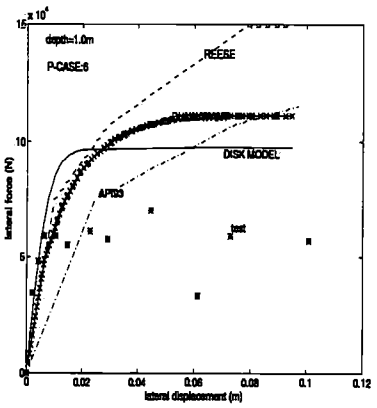

Figure C.10: Comparison of (p-y) response curves for Houston pile(OC case)at depth 1.0m

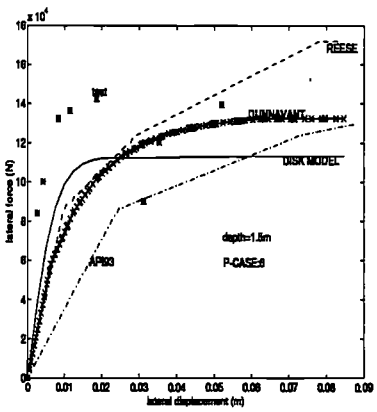

Figure C.11: Comparison of (p-y) response curves for Houston pile(OC case)at depth 1.5m

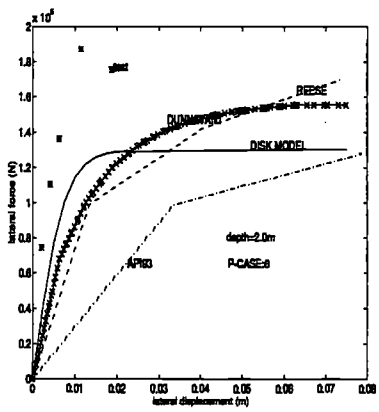

Figure C.12: Comparison of (p-y) response curves for Houston pile(OC case)at depth 2.0m

APPENDIX D

Descriptions of disk-cone model

D.1 Geometrical properties of cone model

The following contains a list of geometrical properties of cone which are given for vertical, horizontal and rocking motions, respectively.
(I) Vertical motion of disk:

For this case, the vertical velocity for $0 < \nu \leq 1/3$ will be c_p and for $1/3 < \nu \leq 1/2$ as $2c_s$ (Gazetas et al, 1984). The horizontal wave velocity for this case may be considered as Rayleigh wave velocity denoted by c_R (Wolf and Meek et al, 1994). Fig.4.47 illustrates schematically the wave propagation from a vertically loaded disk. Now substituting the corresponding values of c_h and c_v into Eq. 4.5, we will have:

$$\theta_{c,i} = tg^{-1}(\frac{r_i}{z_i}) = tg^{-1}(\frac{c_R}{c_v}) \tag{D.1}$$

c_R may be obtained by equating the initial static stiffness of a disk under translational motion to that of exact value obtained by Gazetas et al, (1984) as follows:

$$c_R = \frac{4c_s^2}{\pi(1-\nu)c_p} \tag{D.2}$$

As seen, the Rayleigh wave velocity is a function of c_s, c_p and ν. The shear and compression wave velocities are given as functions of the soil's shear modulus and poisson ratio (see for e.g. Gazetas et al, 1984, Wolf et al, 1994) as:

$$c_s = \sqrt{\frac{E_s}{2\rho}(\frac{1-2\nu}{1-\nu})} = \sqrt{\frac{G}{\rho}} \tag{D.3}$$

$$c_p = \sqrt{\frac{E_s}{\rho}} = \sqrt{\frac{2G}{\rho}(\frac{1-\nu}{1-2\nu})} \tag{D.4}$$

By substituting for c_s and c_p in Eq. D.2, we will have:

$$c_R = \frac{2\sqrt{\frac{2G}{\rho}(\frac{1-2\nu}{1-\nu})}}{\pi(1-\nu)} \tag{D.5}$$

which implies that c_R can be expressed as non-linear function of time and space by means of Eq. 4.28 in the following form:

$$c_R = \frac{2\sqrt{\frac{2G_i(1-\alpha.s)^\beta}{\rho}(\frac{1-2\nu}{1-\nu})}}{\pi(1-\nu)} \tag{D.6}$$

After re-arranging the terms in 4.140 , we will have:

$$\theta_{c,i} = tg^{-1}\frac{4}{\pi(1-\nu)}(\frac{c_s}{c_p})^2 \qquad \nu \leq 1/3 \tag{D.7}$$

$$\theta_{c,i} = tg^{-1}\frac{1}{\pi(1-\nu)} \qquad 1/3 < \nu \leq 1/2 \tag{D.8}$$

(II) For a horizontal motion of disk:
c_h may be assumed as a function of c_p and c_s (or simply as an average of them):

$$c_h = \frac{c_s + c_p}{2} \tag{D.9}$$

From a horizontally loaded disk as shown in Fig. 4.48 two different types of waves may emanate dilatational waves in the direction of the disk's motion with a velocity of c_p and shear waves perpendicular to that moving with a velocity of c_s. In the vertical direction, the wave will travel with a shear wave velocity $c_v = c_s$. Hence, the corresponding aspect ratio of the cone may be obtained as follows:

$$\theta_{c,ii} = tg^{-1}(\frac{r_i}{z_i} = \frac{c_h}{c_v} = \frac{c_p + c_s}{2c_s}) \tag{D.10}$$

Inserting Eqs.D.4 and D.3 into Eq.D.10 will result in:

$$\theta_{c,ii} = tg^{-1}(\frac{1+\sqrt{2(\frac{1-\nu}{1-2\nu})}}{2}) \tag{D.11}$$

From D.11 and D.10 the aspect ratio may be obtained as follows:

$$\frac{z_i}{r_i} = \frac{2}{1+\sqrt{2(\frac{1-\nu}{1-2\nu})}} \tag{D.12}$$

For e.g. for a perfectly compressible soil with $\nu = 0$ the aspect ratio corresponding to the horizontal motion of the disk will become:

$$\frac{z_i}{r_i} = \frac{2}{1+\sqrt{2}} \approx 0.83 \tag{D.13}$$

and for a perfectly saturated soil(incompressible) with $\nu = 0.5$ the cone's apex height corresponding to horizontal motion of disk will approach zero. (i.e. the cone is transformed to a plane disk). For a partially saturated soil with $\nu = 1/3$ from Eq.D.12, we get:

$$\frac{z_i}{r_i} = \frac{2}{3} \tag{D.14}$$

Comparing the above obtained values based on cone model and the exact values from Gazetas's solution as:

$$lim \frac{z_i}{r_{i\,\nu \to 0}} = \frac{\pi}{4} = 0.76 \tag{D.15}$$

$$lim \frac{z_i}{r_{i\,\nu \to 1/3}} = \frac{\pi}{8}(2 - \frac{1}{3}) = 0.65 \tag{D.16}$$

$$lim \frac{z_i}{r_{i\,\nu \to 0.5}} = \frac{\pi}{8}(2 - \frac{1}{2}) = 0.59 \tag{D.17}$$

As seen the only theoretical shortcoming is associated with the case of $\nu = 0.5$ which is already addressed. Since c_p approaches infinity at this limit of ν hence an asymptotic or limit is defined for $limc_{p_{\nu \to 0.5}} \to 2c_s$. Inserting this asymptotic value in Eq.D.10 will result in:

$$lim \frac{z_i}{r_{i\,\nu \to 1/2}} = \frac{2}{3} \approx 0.67 \tag{D.18}$$

compared to exact value of $\pi/4$. The max. discrepancy for this limit of ν is about 14.6%. For the compressible soil the max. discrepancy is less than 6% which is very good.

(III) Rocking motion of disk:
For the rocking motion of the disk as shown in Fig. 4.49, the vertical wave velocity may be considered as $c_v = c_p$ while that of the horizontally propagating waves from the disk may be considered as the Rayleigh wave velocity $c_h = c_R$. Hence, the aspect ratio of the cone or the associated apex angle for this case may be obtained as follows:

$$\frac{z_i}{r_i} = \frac{c_v}{c_h} = \frac{c_p}{c_R} \qquad ;\nu \leq 1/3 \tag{D.19}$$

$$= \frac{2c_s}{c_R} \qquad ;1/3 < \nu \leq 1/2 \tag{D.20}$$

Comparing the obtained values from latter with the exact solution of Gazetas et al, (1984) as :

$$\frac{z_i}{r_i} = \frac{9\pi}{32}(\frac{c}{c_s})^2 \tag{D.21}$$

$$\frac{z_i}{r_i} = \frac{\pi(1-\nu)}{4}(\frac{c}{c_s})^2 \tag{D.22}$$

The discrepancy is about 10.7% which is quite satisfactory.

D.2 Dynamic stiffness coefficients of a frictional system

The derivation of impedance functions $k_{dy}(a_0)$ and $c_{dy}(a_0)$ according to frictional damping model are given in the following. For a harmonic type of response for which $u = u_{max}sin(\omega t)$, $\dot{u} = \omega u_{max}cos(\omega t)$, $\ddot{u} = -u_{max}\omega^2 sin(\omega t)$ and $\dddot{u} = -\omega^3 u_{max}cos(\omega)$ and with initial values $u_0 = \dot{u}_0 = \ddot{u}_0 = \dddot{u}_0 = 0$, Then $N(\omega)$ may be expanded as follows:

$$N(\omega) = Ku_{max}sin(\omega t) + K\omega u_{max}tan(\delta)sgn(cos(\omega t)) + C\omega u_{max}cos(\omega t)$$
$$-C\omega^2 u_{max}0.5tan(\delta)sgn(sin(\omega t)) - \Delta M.\omega^2 u_{max}sin(\omega t) - \Delta M.\omega^3 u_{max}.tan(\delta).sgn(cos(\omega t)) \quad \text{(D.23)}$$

Now dividing Eq. D.23 by Ku_{max} will result in modified dynamic stiffness function based on frictional damping as follows:

$$\frac{S(\omega)}{K} = sin(\omega t) + tan(\delta)\omega sgn(cos(\omega t)) + \frac{C\omega}{K}cos(\omega t) - 0.5tan(\delta)\frac{C\omega^2}{K}sgn(sin(\omega t)) -$$
$$\frac{\Delta M}{K}.\omega^2.sin(\omega t) - \frac{\Delta M}{K}.\omega^3.tan(\delta).sgn(cos(\omega t)) \quad \text{(D.24)}$$

If the sgn function in Eq. D.24 is expanded by means of Fourier expansion, we will have:

$$\frac{S(\omega)}{K} = sin(\omega t) - \frac{\omega C}{K}\eta_m\frac{4}{\pi}(sin\omega t + \frac{1}{3}sin3\omega t + \frac{1}{5}sin5\omega t + ...) + \frac{\omega C}{K}cos\omega t$$
$$+2\eta_m\frac{4}{\pi}(cos\omega t - \frac{1}{3}cos3\omega t + \frac{1}{5}cos5\omega t + ...) - \omega^2.\frac{\Delta M}{K}.sin(\omega t) - \omega^2\frac{\Delta M}{K}.2\eta_m.\frac{4}{\pi}(cos\omega t$$
$$-\frac{1}{3}cos3\omega t + \frac{1}{5}cos\omega t + ...) \quad \text{(D.25)}$$

Now truncating the above expansion by omitting the superharmonics would result in the following approximate form:

$$\frac{S(\omega)}{K} = (1 - \frac{4}{\pi}\frac{z_0}{r_0}\frac{c_s}{c}\eta_m a_0 - \omega^2\frac{\Delta M}{K})sin\omega t + a_0(\frac{z_0}{r_0}\frac{c_s}{c} + 2\frac{\eta_m}{a_0}\frac{4}{\pi} - \omega^2\frac{\Delta M}{K}.2\eta - m\frac{4}{\pi})cos\omega t \quad \text{(D.26)}$$

D.3 Recursive computation of Green functions

The recursive method for evaluation of Green function g_{n-k} as described earlier in the main text of chapter.4 will be discussed in detail in this section. The basis for evaluation of g_{n-k} may be described as the correspondence between the coefficients of the following convolution integral and a mathematical recursive function of a general response function in terms of its previous values and its variables:

$$u(t) = \int_0^t h(t-\tau)P(\tau)d\tau \quad \text{(D.27)}$$

In which the unit impulse function $h(t-\tau)$ which can be obtained from the solution of a the following differential equation of a single linear cone (modified after Meek and Wolf et al, 1994):

$$\frac{z_i}{c}(\dot{h}_1(t-\tau)) + h_1(t-\tau) = \delta(t-\tau) \quad \text{(D.28)}$$

in which $h_1(t-\tau)$ refers to the response in one degree of freedom, say vertical or horizontal etc. at time t due to the corresponding unit impulse at time τ. The term $\delta(t)$ on the right hand-side of Eq. D.28 denotes a unit impulse load (force) applied only at time $t = \tau$ so the value of the latter function will be zero elsewhere (i.e. $\delta = 0$ for $t \neq \tau$). The solution of Eq. D.28 may be obtained by inspection as follows:

$$h_1(t-\tau) = \delta^{''}(t-\tau)\frac{c}{z_i}e^{-\frac{c}{z_i}(t-\tau)\delta^{'}(t-\tau)} \tag{D.29}$$

in which the first function on the right hand-side of Eq. D.29 may be defined as:

$$\begin{aligned} \delta^{''}(t-\tau) &= \frac{z_i}{2c}; & t = \tau \\ &= 1; & t \neq \tau \end{aligned} \tag{D.30}$$

The $\delta^{'}(t-\tau)$ function may be defined as follows:

$$\begin{aligned} \delta^{'}(t-\tau) &= -1; & t = \tau \\ &= 1; & t \neq \tau \end{aligned} \tag{D.31}$$

By combining Eqs. D.29 to D.31 and inserting into Eq. D.28, the equilibrium can be satisfied for all values of t. (Including $t = \tau$ in which the right hand-side exists). By comparison the original solution given by Meek and Wolf et al,(1994) does seem to only satisfy the general differential equation without the non-zero term at the time $t = \tau$ as follows:

$$h(t-\tau) = \frac{c}{z_i}e^{-\frac{c}{z_i}(t-\tau)} \tag{D.32}$$

As seen the latter is a particular case of the solution given above for $t \neq \tau$. To obtain the solution of Eq. D.27 for a linearly varying stepwise load as described above. The following recursive relationship is obtained by Wolf et al, (1994) for a general stepwise load variation between two successive stations n-1 and n as follows:

$$y_n = ay_{n-1} + b_0x_n + b_1x_{n-1} \tag{D.33}$$

in which y_n, y_{n-1}, x_n and x_{n-1} represent the values of response and its variable (load) at time stations n and n-1, respectively. By analogy between the convolution integration Eq. D.27 and a the general recursive relationship of Eq. D.33, Wolf et al, (1994) obtained the coefficients of the latter equation as follows:

$$a = e^{-\frac{c}{z_i}\delta t} \tag{D.34}$$

which is a particular form of Eq. D.32 by inserting $\tau = 0$ and $t = \delta t$. And the two other coefficients are computed as:

$$b_0 = -\frac{1}{K}\left(\frac{e^{-\frac{c}{z_i}\delta t} - 1}{-\frac{c}{z_i}\delta t} - 1\right) \tag{D.35}$$

$$b_1 = -\frac{1}{K}\left(\frac{e^{-\frac{c}{z_i}\delta t} + 1}{-\frac{c}{z_i}\delta t} + e^{-\frac{c}{z_i}\delta t}\right) \tag{D.36}$$

Now continuing the recursive relationship Eq. D.33 for the time stations (k+1), k and (k-1),we may have:

$$y_{k+1} = ay_k + b_0 x_{k+1} + b_1 x_k \tag{D.37}$$

$$y_k = ay_{k-1} + b_0 x_k + b_1 x_{k-1} \tag{D.38}$$

$$y_{k-1} = ay_{k-2} + b_0 x_{k-1} + b_1 x_{k-2} \tag{D.39}$$

Noting that $x_{k-1} = 0$, $x_k = 1$ and $x_{k+1} = 0$ and inserting these in Eqs. D.37 to D.39, we may obtain:

$$y_k = a^{k-1}(ab_0 + b_1) \tag{D.40}$$

in which all the parameters are as defined above. The latter equation is the only relationship which is needed to calculate the flexibility (Green) matrix $[G_{n-k}]$. The explicit form of this function is then written as:

$$g_{n-k} = e^{\frac{-c(n-k)}{z_i}} \frac{z_i}{c\delta t}(e^{\frac{c\delta t}{z_i}} + e^{\frac{-c\delta t}{z_i}} - 2) \tag{D.41}$$

Comparison of the Green unit impulse functions for the triangular pulse and a concentrated load at infinitesimal time interval shows that the Green function of a concentrated load for the same time station as the time of load application is several order of magnitude higher than that of a triangular pulse within a finite time interval ($2\delta t = t_{k+1} - t_{k-1}$) it is assumed that the intervals have the same lengths). The latter can be easily understood in both mathematical and physical senses. From mathematics point of view, the impulse response function at the time of a unit impulse within $dt = d\tau$ time can be obtained from either Eqs. D.29 or D.32 as follows:

$$h(t = \tau) = \frac{c}{Kz_i} \tag{D.42}$$

Using Eq. D.41 for n=k , we may obtain:

$$g_{n=k} = \frac{1}{K}(e^{\frac{c\delta t}{z_i}} + e^{\frac{-c\delta t}{z_i}} - 2) \tag{D.43}$$

It is quite obvious that the for an infinitesimal time interval $\delta = dt$, the $g_{n=k} = 0$ which means only an infinitesimal loading portion of the whole time history is considered, hence its contribution as expected will proportionally be negligible. On the other hand, from physical point of view, this means that the Eq. D.43 does not consider a unit load's very significant contribution at the time of application or close to that time (after the incident). On the contrary, Eq. D.42 considers only the effects of an impulse (shock) at an extremely short duration (dt). It is clear from Eq. D.42 that the response of a unit impulse dissipates very rapidly in the medium as the source load disappears and the waves earlier generated propagate towards infinity and carry the energy to the far field of soil medium which is referred to as the radiation damping of the cone model.

The implication of the latter discussion is that it is very important to recognize the loading type for this cone model .(i.e. if the load is impulsive or consists of very short impulses such as shock waves then the Green matrix must be assembled based on the concentrated load impulses as given by Eqs. D.42 or D.32. However, for a steady-type of loading over a finite period of

duration which is often the case for e.g sea and seismic wave loading, then Eq. D.41 or D.43 would be relevant.
However, from mathematical point of view this discontinuity of two formulations at their limits may be resolved by adding the corresponding concentrated impulse term on the right hand-side of Eq. D.41 as follows:

$$g_{n-k} = g_{n-k,d} + \delta(\delta t - dt) g_{n-k,c} \tag{D.44}$$

in which Dirac-δ function will be equal to unity for $\delta t = dt$ and elsewhere will be zero.
A particular form of the Green function is the instantaneous Green function $g_{ij}(a,\omega)$ which can be derived according to the above general procedure as follows:

$$g_{ij}(a,\omega) = \int_{-\infty}^{+\infty} \int_0^t \left[h(t-\tau) = \delta^*(t-\tau) \frac{c}{z_i} e^{-\frac{c}{z_i}(t-\tau)\delta'(t-\tau)} \right] exp(-i\omega t) d\tau dt \tag{D.45}$$

where all the terms involved in the latter equations are as defined above.

D.4 A procedure for generating hysteretic loops

The soil hysteretic behaviour may be simulated by using the backbone relationship and a standard procedure such as Massing's rule or other magnification methods such as constant with linear elastic or hyper-elastic unloading, elasto-plastic re-loading or hyperelasto-plastic re-loading etc. The latter models can be generated by applying the initial stiffness G_i, the tangent stiffness G^T or secant stiffness G^{sec} of the soil (see for e.g. Langø et al, 1991 and Svanø et al,1993).
It can be seen from Eq. 4.21 through Eq. 4.28 that the nonlinear dynamic stiffness of the pile-soil system is a function of the soil's shear modulus G. In the previous section, G assumed to be constant for a linear type of pile-soil interaction. However in general, this modulus may vary with the shear strain increase of soil and also the number of the hysteresis cycles as shown schematically in Figs.4.29 and 4.28.
The following steps may be applied to generate the cyclic hysteresis from the above established skeleton curve:
a) A loading branch can be generated by using $g^T = f_g(s)$ and the given displacement or computed one at the time step i of analysis
b) The unloading may be detected through the variation of the internal loading which can also be explicitly related to the changes in the displacement at element level based on the type of the cyclic loading whether is load controlled or displacement controlled, respectively can be applied. The latter check may be written as:

$$\dot{u}_{n+1}.\dot{u}_n <= 0 \tag{D.46}$$

or similarly:

$$\dot{p}_{n+1}.\dot{p}_n <= 0 \tag{D.47}$$

The unloading branch may be constructed by using the initial part of the hysteresis curve (or the first branch of loading) and using the proper magnification or mirror rule as:

$$\frac{\tau - \tau_{ps}}{\alpha_{mf}} = f\left(\frac{\gamma - \gamma_{ps}}{\alpha_{mf}}\right) \tag{D.48}$$

where α_{mf} may be defined as the magnification factor. For e.g Massing's rule assumes that $\alpha_{mf} = 2$ for a constant mirror hysteresis $\alpha_{mf} = 1$ etc.
c) The above procedure may be applied similarly for the re-loading part of the this time with the same curvature sign and according to the magnification rule Eq. D.48.
d) for a degrading hysteretic system, procedure described in steps a) to c) may be coupled with an excess pore water pressure model such as the one proposed by Janbu, 1975. The following cyclic degradation formula may be derived based on Janbu's cyclic resistance concept:

$$s_N = log\frac{N + N_m - N_s - 1}{N_m} s_1 \tag{D.49}$$

in which s_N and s_1 correspond to the normalized shear stress as defined by Eq. D.75, at the Nth and the 1st cycles, respectively. The other parameters involved such as N_m, N_s are determined according to the cyclic resistance concept of Janbu, 1975 through a series of one -way and two-way cyclic triaxial tests on various soil samples, including NC, OC clay and sand.
The unloading for soil type material may be assumed elastic or hyper-elastic depending on the type of model used. The hyper-elastic model is particularly suited for the soil type materials (see for e.g. Crisfield, 1991).

D.5 Refraction coefficients of cone at the layer boundaries

The refraction coefficient at the boundary of two flexible layers may be obtained as follows. The displacement induced by the incident and reflected wave at the lower boundary may be obtained as:

$$u_l(z) = \frac{z_l}{z_l + z} f(t - \frac{z}{c_l}) + \frac{z_l}{z_l + 2d - z} g(t - \frac{2d}{c_l} + \frac{z}{c_l}) \tag{D.50}$$

The displacement associated with the refracted wave at the lower boundary $u_r(z)$ can be obtained as:

$$u_r(z) = \frac{\frac{z_l z_r}{z_l + z}}{z_r - d + z} h(t - \frac{d}{c_l} + \frac{d}{c_r} - \frac{z}{c_r}) \tag{D.51}$$

The normal cone forces associated with $u_l(z)$ and $u_r(z)$ may be obtained according to continuum mechanics theory as follows:

$$N_l(d,t) = \sigma_l . A_l = E_l . \epsilon_l . A_l = \rho_l . c^2{}_l A_l . \frac{\partial u_l}{\partial z} \tag{D.52}$$

$$N_r(d,t) = \sigma_r . A_r = E_r . \epsilon_r . A_r = \rho_r . c^2{}_r A_r . \frac{\partial u_r}{\partial z} \tag{D.53}$$

The strain components can be calculated according to Eqs.D.50 and D.51 as follows:

$$\epsilon_l = \frac{-z_l}{(z_l + z)^2} f - \frac{1}{c_l} . \frac{\partial f}{\partial (t - \frac{z}{c_l})} . \frac{z_l}{z_l + z} + \frac{z_l}{(z_l + 2d - z)^2} . g + \frac{z_l}{z_l + 2d - z} . \frac{\partial g}{\partial (t - \frac{2d}{c_l} + \frac{z}{c_l})} . (\frac{1}{c_l}) \tag{D.54}$$

and so the strain component related to the refraction may be derived as follows:

$$\epsilon_r = \frac{-z_l z_r}{(z_l + d)(z_l - d + z)^2} . h + \frac{z_l z_r}{(z_l + d)(z_r - d + z)} . \frac{\partial h}{\partial (t - \frac{d}{c_l} + \frac{d}{c_r} - \frac{z}{c_r})} . (-\frac{1}{c_r}) \tag{D.55}$$

Satisfying the equilibrium condition of the forces at the lower boundary between two adjacent layers (i) and (i+1) where $z = d$ and $A_l = A_r$, we shall have:

$$N_l(d,t) = N_r(d,t) \tag{D.56}$$

Hence, we will have:

$$(\rho_l c_l + \rho_r c_r)g' + (\frac{\rho_l c^2{}_l}{z_l + d} + \frac{\rho_r c^2{}_r}{z_r})g = (\rho_l c_l - \rho_r c_r)f' + (\frac{\rho_l c^2{}_l}{z_l + d} - \frac{\rho_r c^2{}_r}{z_r})f \tag{D.57}$$

From latter first order differential equation the refraction coefficient η may be obtained for lower and higher limits of the frequency range of excitation as follows:

$$lim\eta_{j,d_{\omega\to 0}} = 1 + \frac{\frac{\rho_l c^2{}_l}{z_l+d} - \frac{\rho_r c^2{}_r}{z_r}}{\frac{\rho_l c^2{}_l}{z_l+d} + \frac{\rho_r c^2{}_r}{z_r}} \tag{D.58}$$

$$lim\eta_{j,d_{\omega\to\infty}} = 1 + \frac{\rho_l c_l - \rho_r c_r}{\rho_l c_l + \rho_r c_r} \tag{D.59}$$

For a more general form of cone($n \neq 1$), the following coupled first order differential equation is obtained as follows:

$$g(\rho_l.c^2{}_l.A_l.(\frac{n}{z_l+2d-z})(\frac{z_l}{z_l+2d-z})^n - \rho_r.c^2{}_r.A_r.n.(\frac{z_l z_r(z_r-d+z)}{z_l+d})^n.(\frac{-1}{z_r-d+z}))$$
$$+\dot{g}(-\rho_l.c_l.A_l.(\frac{z_l}{z_l+2d+z})^n + \rho_r.c_r.A_r.\frac{z_l z_r(z_r-d+z)}{z_l+d}) = f(\rho_l.c^2{}_l.A_l.(\frac{-n}{z_l+z}).(\frac{z_l}{z_l+z})^n$$
$$+\rho_r.c^2{}_r.A_r.n.\frac{z_l z_r(z_r-d+z)}{z_l+d})^n(\frac{-1}{z_r-d+z}) + \dot{f}(\rho_l.c_l.A_l.(\frac{z_l}{z_l+z})^n - \rho_r.c_r.A_r.\frac{z_l z_r(z_r-d+z}{z_l+d} \tag{D.60}$$

For the low frequency limit of the excitation(static case), the refraction coefficient η_j may be obtained as follows:

$$lim\eta_{j_{\omega\to 0}} = 1 + \frac{\rho_l.c^2{}_l.A_l(\frac{n}{z_l+d})(\frac{z_l}{z_l+d})^n - \rho_r.c^2{}_r.A_r.n.(\frac{z_l z_r(z_r-d+z)}{z_l+d})^n(\frac{1}{z_r-d+z})}{\rho_l.c^2{}_l.A_l.(\frac{n}{z_l+2d-z})(\frac{z_l}{z_l+2d-z})^n + \rho_r.c^2{}_r.A_r.n(\frac{z_l z_r(z_r-d+z)}{z_l+d})^n(\frac{1}{z_r-d+z})} \tag{D.61}$$

For the higher frequency limit of the excitation ($\omega \to \infty$), η_j may be obtained as follows:

$$lim\eta_{j\to\infty} = 1 + \frac{\rho_l.c_l.A_l.(\frac{z_l}{z_l+z})^n - \rho_r.c_r.A_r.(\frac{z_l z_r(z_r-d+z)}{z_l+d})}{-\rho_l.c_l.(\frac{z_l}{z_l+2d-z})^n + \rho_r.c_r.A_r.(\frac{z_l z_r(z_r-d+z)}{z_l+d})} \tag{D.62}$$

By inserting $z = d$ the refraction coefficients may be obtained at the lower boundary as follows:

$$lim\eta_{j,d_{\omega\to 0}} = 1 + \frac{\frac{\rho_l c^2{}_l}{z_l+d} - \frac{\rho_r c^2{}_r}{z_r}}{\frac{\rho_l c^2{}_l}{z_l+d} + \frac{\rho_r c^2{}_r}{z_r}} \tag{D.63}$$

$$lim\eta_{j,d_{\omega\to\infty}} = 1 + \frac{\rho_l.c_l(\frac{z_l}{z_l+d})^{n-1} - \rho_r.c_r}{\rho_l.c_l.(\frac{z_l}{z_l+d})^{n-1} + \rho_r.c_r} \tag{D.64}$$

As seen, for the low frequency limit (static) the refraction relationship for a general cone($n >= 1$) is exactly the same as obtained in Eq.D.63 for a particular case of cone ($n = 1$). Hence, the static energy transmission through one flexible layer of soil to the adjacent one does not depend on the shape of the cone in general. Thus, even for $n = 0$ a prismatic bar the refraction coefficient at boundary of two considered layers $\eta_{j,d}$ will be the same. However, as Eq.D.62indicates ,the limit of the refraction coefficient for the higher frequency of excitation is dependent on the shape of the cone and the two adjacent layer properties but independent of the frequency of excitation. For a particular case of cone $n = 1$ (or wedge) the latter equation results in Eq.D.59 which is independent of the layer thickness and the shape of cone.

D.6 Particular cases of cone's refraction coefficients

If $G_l >> G_r \rightarrow c_l >> c_r$ which means a layer on the air, we will have from Eq.D.63:

$$lim\eta_{j\,c_l>>c_r} = 2 \tag{D.65}$$

The latter coefficient was used in the main text and was also obtained from a general relationship for the mud-line. If $G_l << G_r$ which is the case for a layer lying on a rigid bed-rock, we will have: $c_l << c_r$ the following refraction coefficient can be obtained from Eq.eq:eta-refraction-layer-static:

$$lim\eta_{j\,c_l<<c_r} = 0 \tag{D.66}$$

which means that no refraction occurs in this case and all the wave energy is reflected. Let us consider another particular case, $G_l = G_r$ when two layers have the same properties which is the case of a homogeneous soil half space with finite element layering. From Eq.eq:eta-refraction-layer-static, we shall have:

$$lim\eta_{j\,c_l=c_r} = 1 \tag{D.67}$$

which means that the whole propagated energy is refracted through the boundary of the layers and no portion of it will be reflected through the half-space layer. All the latter conclusions can be easily verified by means of Eq.D.64. For an intermediate frequency of excitation, however, the general solution of differential equation has to be obtained either in time or frequency domains. For a harmonic loading with a frequency of ω the solution of Eq.D.60 can be easily obtained as follows:

$$lim\eta_j = 1 +$$

$$\frac{\rho_l.c^2{}_l.A_l(\frac{n}{z_l+d})(\frac{z_l}{z_l+d})^n - \rho_r.c^2{}_r.A_r.n(\frac{z_l z_r(z_r-d+z)}{z_l+d})^n(\frac{1}{z_r-d+z}) + i\omega(\rho_l.c_l.A_l.(\frac{z_l}{z_l+z})^n - \rho_r.c_r.A_r.(\frac{z_l z_r(z_r-d+z)}{z_l+d}$$

$$\rho_l.c^2{}_l.A_l.(\frac{n}{z_l+2d-z})(\frac{z_l}{z_l+2d-z})^n + \rho_r.c^2{}_r.A_r.n(\frac{z_l z_r(z_r-d+z)}{z_l+d})^n(\frac{1}{z_r-d+z}) - i\omega(\rho_l.c_l.(\frac{z_l}{z_l+2d-z})^n + \rho_r.c_r.A_r.(\frac{z_l z_r(z_r-d}{z_l+d}$$

D.7 Cyclic degradation criterion for clayey soil

The derivation of the cyclic degradation formula of soil based on Janbu's resistance concept (Janbu, 1976) and formula of Skotheim et al, (1982) which is presented in the main text:

$$u_{cu} = \frac{\Delta\sigma_d}{r_u} \int_1^N \frac{dN}{N_0 + N + N_{eq}} \tag{D.69}$$

where u_{cu} is the generated cyclic access pore pressure of water, $\Delta\sigma_d$ = the deviatoric shear stress as $\Delta\sigma_1 - \Delta\sigma_3$, r_u = a resistance ratio obtained from cyclic triaxial test, N =number of the cycles in a current shear stress block, N_0 =a resistance reference no, N_{eq} = an equivalent no of cycles accounting for the past cyclic stress history of the soil Skotheim et al, (1982) presented a formula based on Janbu's cyclic resistance concept as follows:

$$N_{eq} = (N_0 + 1)exp(\frac{u_{cu}.r_u}{\Delta\sigma_d}) - 1) \tag{D.70}$$

Inserting Eq.D.70 into Eq.D.69 and integrating will result in:

$$u_{cu} = \frac{\Delta\sigma_d}{r_u}.Ln\frac{N + exp(\frac{u_{cu}.r_u}{\Delta\sigma_d})(N_0 + 1) - 1 - N_s}{exp(\frac{u_{cu}.r_u}{\Delta\sigma_d})(N_0 + 1)} \tag{D.71}$$

Now considering that the principle of superposition may not apply for some particular cases of cyclic soil mobilization a shear stress number may be considered to account for such interaction effect and may be simply subtracted from the numerator of Eq.D.71 which will be re-written as :

$$u_{cu} = \frac{\Delta\sigma_d}{r_u}.Ln\frac{N + N_m - N_s - 1}{N_m} \tag{D.72}$$

where : $N_m = exp(\frac{u_{cu}.r_u}{\Delta\sigma_d})(N_0 + 1)$ and N_s may be determined from cyclic triaxial tests for each particular soil type such as NC and OC clays and sand.

D.8 Tangent shear modulus G^T relationship

The relationship between the tangent shear modulus of soil G^T and its shear strain γ may be derived from Svanø's cyclic shear mobilization(CSM) model(Svanø et al, 1993) as follows:

$$g = g_{max}(\frac{1}{a + h.s} - \lambda.s) \tag{D.73}$$

where g is the normalized shear modulus as:

$$g = \frac{G_s}{\sigma'_m + a_d} \tag{D.74}$$

where G_s is the shear modulus of soil, σ'_m the mean effective stress and a_d the dynamic attraction of soil. In Eq.D.78, g_{max} is the maximum normalized shear modulus of soil which then is easily followed from Eq.D.74 by only replacing G_s with G_{max}. h, λ are curve fitting parameters obtained

empirically and s is the normalized shear stress at the pile-soil interface which can be written as:

$$s = \frac{\tau}{\sigma'_m + a_d} \tag{D.75}$$

where τ is the cyclic shear stress at the pile-soil interface and the other parameters are defined above. The relationship between τ and γ near the pile shaft may be written as:

$$\tau = G_s.\gamma \tag{D.76}$$

The tangent shear modulus of soil can be found as:

$$G^T = \frac{\partial s}{\partial \gamma} \tag{D.77}$$

By combining Eqs.D.78 to D.77, yields:

$$G^T = \frac{g_{max}(\sigma'_m + a_d)(1 - \lambda s - \lambda h s^2)}{(1 + 2hs)} \tag{D.78}$$

By combining Eqs.D.78 to D.77, the following relationship between s and γ is obtained:

$$s = \frac{-1 + \sqrt{1 + \frac{4bh}{c}}}{2h} \tag{D.79}$$

where $b = g_{max}.\gamma$ and $c = (b.\lambda + 1)$. By combining Eqs.D.78 and D.79, G^T is obtained as:

$$G^T = \frac{G_i(1 - \lambda\frac{b}{c})}{\sqrt{1 + 4\frac{bh}{c}}} \tag{D.80}$$

where $G_i = g_{max}.(\sigma'_m + a_d)$. b and c are given above. By inserting b, c and G_i into Eq.D.80, the following expression for the tangent of the pile-soil's skeleton curve emerges:

$$G^T = \frac{g_{max}(\sigma'_m + a_d)(1 - \frac{\lambda.\gamma.g_{max}}{\lambda.\gamma.g_{max}+1})}{\sqrt{1 + 4\frac{h\gamma g_{max}}{\lambda\gamma g_{max}+1}}} \tag{D.81}$$

From Eq.D.81, for $\gamma = 0$, the initial shear modulus will be equal to G_s given in Eq.D.74, while for $\gamma \to \infty$ the ultimate tangent shear modulus of soil will approach zero.

D.9 A simple procedure to determine the coefficients of the tangent shear modulus of soil

Based on available triaxial test data for a specific type of soil such as NC or OC clay and sand, a polynomial relationship may be fit as follows:

$$g = \sum_{i}^{n} a_i s^i \tag{D.82}$$

where g and s refer as before to a normalized shear modulus of soil and a normalized shear stress parameter. The coefficients of the polynomial a_i may be determined through a linear regression analysis or a simply a least square of error method(see for e.g. Matlab manual, 1992).
Particular cases of g function may be fit as described by for e.g. Langø, (1991) and Svanø et al, (1993):

$$g = g_i(1 - \alpha.s)^{\beta} \tag{D.83}$$

The coefficients of the latter two parameter relationship can be obtained from triaxial test data for any particular type of soil. For e.g. Langø et al, (1991) has described some typical values of α and β parameters obtained for NC and OC clays of Eberg, Gløva and Drammen in Norway.
A hyperbolic type relationship for g is described by Svanø, (1992) for clay soils with two material parameters as h and λ as follows:

$$g = g_i(\frac{1}{a + h.s} - \lambda.s) \tag{D.84}$$

Based on data provided by Daghigh, (1993), the parameters of Eq.D.83 are calibrated for sand as given in the following Table:

Table D.1: Soil tangent stiffness related material parameters

soil parameter/type	NC Clay	OC clay	sand
α	0.5-1.0	0.5-1.0	0.5-1.0
β	1.5-4.0	1.0-1.5	$\geq$ 4.0

D.10 An iterative procedure for calculating the coefficients of Bouc's model

The coefficients c1 and c2 are determined with respect to the sign of $\dot{u}$ and z_b functions at any time step. Since the value of function z_b is dependent on c coefficient in Eq.4.206, hence, its value from previous step is used to determine the coefficient c_2 and so c. After initial prediction of parameter c, z_b can be updated from Eq.4.206 and its value is used to correct c2 and hence c. This iterative procedure can be continued until the convergence criterion is satisfied.

D.11 Correspondence principle

The dynamic stiffness function $S(\omega)$ according to Eq.4.77 can be expressed as:

$$S(\omega) = K + i\omega C - \omega^2 M_t \tag{D.85}$$

where all the parameters are as defined in Chapter.4. According to the correspondence principle the linear hysteretic type material may be introduced by pre-multiplying the elastic stiffness properties of the soil such as G by a complex value as: $(1+2i\eta_m)$ where η_m denotes the material damping ratio of the soil material.

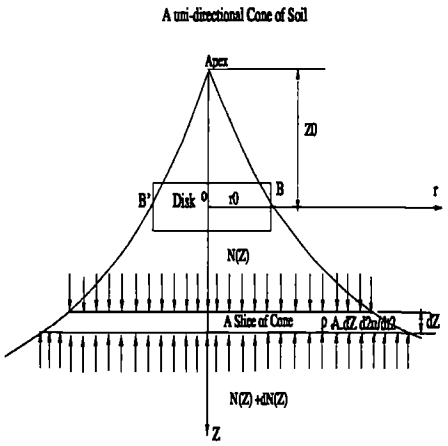

Figure D.1: Equilibrium of dynamic forces for a thin slice of soil cone

For e.g the shear wave velocity can be modified due to the influence of the material damping as follows:

$$c^* = \sqrt{\frac{G(1+2i\eta_m}{\rho})} = c\sqrt{(1+2i\eta_m)} \tag{D.86}$$

Considering that in $(1+i\eta_m)^2 = 1+2i\eta_m - \eta_m^2$ the last term might be neglected if $\eta_m << 1.0$. Then, Eq.D.86 may be simplified as follows:

$$c^* = c(1+i\eta_m) \tag{D.87}$$

Knowing that $K = \rho c^2 A(z)$ and $C = \frac{\rho c}{z_0}$ then it is evident that:

$$K^* = K(1+2i\eta_m - \eta_m^2) \approx K(1+2i\eta_m) \tag{D.88}$$

$$C^* = C(1+i\eta) \tag{D.89}$$

D.12 A rotational cone model(modified After Wolf et al, 1994)

For a slice of cone shown on Fig.D.1 the equilibrium of dynamic forces may be written as follows:

$$-M_z + (M_z + dM_z) = \rho I \ddot{v} dz \tag{D.90}$$

where M_z =the bending moment at the depth z of cone, dM_z = the difference of bending moment at depth z, ρ = the mass density, I = the moment of inertia of the cone's cross section, $\ddot{v}$ =

the rotational acceleration of the cone and dz = the infinitesimal thickness of a slice of cone as shown in Fig.D.1. Note that the damping forces are inherent in Eq.D.90.
The bending moment-rotation relationship for a small strain condition may be written as follows:

$$M_z = E.I.v_{,z} \tag{D.91}$$

Combining Eqs.D.90 and D.91 will lead to:

$$d(EIv_{,z}) = \rho I\ddot{v}dz \tag{D.92}$$

Expanding the L-H-S of Eq.D.92 will yield:

$$EI.v_{,zz} + \frac{\partial E}{\partial z}.dz.I.v_{,z} + E.\frac{\partial I}{\partial z}.dz.v_{,z} - \rho.I.\ddot{v}dz = 0 \tag{D.93}$$

Assuming that $E = f_E(z)$ and $I = f_I(z)$ for a non-homogeneous arbitrary uni-directional single(one-sided) cone, we will have :

$$E = (\frac{z}{z_0})^m \tag{D.94}$$

and so for I:

$$I = (\frac{z}{z_0})^n \tag{D.95}$$

Taking the first derivatives of E and I functions w.r.t z will lead to:

$$\frac{\partial E}{\partial z} = \frac{m}{z}.E(z) \tag{D.96}$$

and so:

$$\frac{\partial I}{\partial z} = \frac{n}{z}.I(z) \tag{D.97}$$

Now inserting Eqs.D.94, D.95, D.96 and D.97 into Eq.D.93 and noting that:

$$E(z) = \rho.c^2 \tag{D.98}$$

will yield:

$$v_{,zz} + (\frac{m+n}{z}).v_{,z} - \frac{\ddot{v}}{c^2} = 0 \tag{D.99}$$

For a special case of homogeneous cone Wolf et al, (1994) obtained the following DEQ:

$$v_{,zz} + \frac{4}{z}.v_{,z} - \frac{\ddot{v}}{c^2} = 0 \tag{D.100}$$

c the wave's shear velocity in general is a temporal as well as spatial varying parameter for a non-linear and non-homogeneous type soil as:

$$c = f_c(z,t) \tag{D.101}$$

The approximate analytical solution of DEQ. of Eq.D.100 may be obtained through a step-wise linearization. Let us write Eq.D.100 for an increment of rotation $v + \delta v$ instead of v:

$$(v_{,zz} + \delta v_{,zz}) + \frac{m+n}{z}(v_{,z} + \delta v_{,z}) - \frac{\ddot{v} + \delta\ddot{v}}{c^2} = 0 \tag{D.102}$$

By a linearization of the Taylor expansions will be truncated in two first terms as follows:

$$\frac{d}{dt}(v+\delta v) = \frac{d}{dt}v + \delta\frac{dv}{dt} \tag{D.103}$$

$$\frac{d^2}{dt^2}(v+\delta v) = \frac{d^2}{dt^2}v + \delta\frac{dt^2}{dt^2} \tag{D.104}$$

Subtracting approximate Eq.D.102 from Eq.D.99 will yield:

$$\delta v_{,zz} + \frac{m+n}{z}\delta v_{,z} - \frac{\rho\delta\ddot{v}}{E(z,t_i)} = 0 \tag{D.105}$$

which is an approximate incremental form of Eq.D.99 w.r.t time. $E(z,t_i)$ function on the denominator of last term on the R-H-S of Eq.D.105 is approximated as follows:

$$E(z,t_i) = E_i(z).f_\tau(t) \tag{D.106}$$

where $E_i(z)$ denotes the initial soil's elastic modulus w.r.t time(response history). $E_i(z)$ varies with z and indicates the soil's non-homogeneity w.r.t depth only.
Substituting for $E(z,t_i)$ from Eq.D.106 into Eq.D.105 leads to:

$$\delta v_{,zz} + \frac{m+n}{z}\delta v_{,z} - \frac{\rho\delta\ddot{v}}{E_i(z=z_0,t=0)f_\tau(t_i)} = 0 \tag{D.107}$$

in which $f_\tau(t_i)$ is evaluated as the disk's non-linear (t-z) or (p-y) functions at the current time station t_i.
Re-arranging Eq.D.107 as:

$$\delta v_{,zz} + (m+n)z^{m-1}\delta v_{,z} - \frac{z^m{}_0\rho\delta\ddot{v}}{E_i(z=z_0,t=0)f_\tau(t_i)} = 0 \tag{D.108}$$

The solution of Eq.D.108 may be obtained analytically by using Bessel and Hankel's functions as follows. Note that $f_\tau(t)$ in the denominator of last term of Eq.D.108 is assumed as constant at the time interval $(t,t+\delta t)$ due to step-wise linearization.
Eq.D.108 can be written in frequency domain by assuming that $\delta v = \delta v_0 sin(\omega t)$ as follows:

$$\delta v_{,zz} + (m+n)z^{m-1}\delta v_{,z} - \frac{z^m{}_0\rho\omega^2\delta\ddot{v}}{E_i(z=z_0,t=0)f_\tau(t_i)} = 0 \tag{D.109}$$

The solution of differential equation in the form of Eq.D.109 is discussed in the main text of Chapter.4.

D.13 Linear hysteretic and visco-elastic type damping

The correspondence principle states that for a dynamic (e.g. pile-soil) system which is damped the dynamic stiffness may be modified by simply multiplying the elastic stiffness properties of the system by $(1+2i\eta_m)$ where $i=\sqrt{-1}$ and η_m represents the material damping ratio of the soil. In this section, we shall try to establish the basis for the this principle which is referred to

in the main text of Chapter.4.

Let us consider a simple linear SDOF system, with the mass, spring and a dashpot whose parameters are denoted by M, K and C, respectively. The dynamic equilibrium of the forces (equation of motion) can be written as follows:

$$M\ddot{u} + C\dot{u} + Ku = F_e(t) \tag{D.110}$$

where u and $F_e(t)$ denote the displacement response and the excitation force applied on the dynamic system.

For a simple harmonic type excitation force such as $F_e(t) = F_0 e^{i\omega t}$ where F_0 is a constant which is equal to initial excitation force at time ($t = 0$) and ω represents the circular frequecny of vibration of the system. The solution of Eq.D.110 may be written as: $u = u_0 e^{i\omega t}$. where u_0 denotes the initial displacement response of the SDOF system. Inserting the latter function into Eq.D.110 and simplifying it , we will have:

$$-M\omega^2 + i\omega C + K = \frac{F_0}{u_0} \tag{D.111}$$

where k_0 represents the initial(linear) dynamic stiffness of the SDOF system. Now considering the ratio of the equivalent viscous damping to the critical damping as η, we have:

$$\eta = \frac{C}{C_{cr}} = \frac{C}{2\sqrt{KM}} \tag{D.112}$$

Noting that the fundamental natural frequency of the undamped SDOF system may be written as ω_n:

$$\omega_n^2 = \frac{K}{M} \tag{D.113}$$

Substituting Eq.D.113 into R-H-S of Eq.D.112 , we get:

$$\eta = \frac{C}{2M\omega_n} = \frac{C}{2K}.\omega_n \tag{D.114}$$

C can be obtained easily by inversing Eq.D.114 as:

$$C = \eta.\frac{2K}{\omega_n} \tag{D.115}$$

Combining Eq.D.111 and D.115, we may write:

$$-M\omega^2 + i\omega\eta.\frac{2K}{\omega_n} + K = K_0 \tag{D.116}$$

Re-arranging the L-H-S of the Eq.D.116, we can re-write it as:

$$\begin{aligned} -M\omega^2 + K(1 + 2i\frac{\eta}{\omega_n}\omega) &= K_0 \\ -M\omega^2 + K(1 + 2ia_m\omega) &= K_0 \end{aligned} \tag{D.117}$$

where $a_m = \frac{\eta}{\omega_n}$ represents a material damping coefficient for a visco-elastic type damping, which is directly proportional with the critical damping ratio η and inversely with the circular natural frequency of the SDOF system ω_n. Hence, $\eta_m = a_m.\omega$ which is a classical representation of the visco-elastic material damping of a SDOF system, can be written as:

$$\eta_m = a_m.\omega = \eta\frac{\omega}{\omega_n} \tag{D.118}$$

Considering that K and M are constant for a linear SDOF type dynamic system, and also η is by the same virtue may be considered as a constant from R-H-S of Eq.D.115, then a_m turns out to be a constant which is equal to:

$$a_m = \frac{C}{2K} \tag{D.119}$$

For a SDOF system, C representing the material (soil) damping C is often taken as 0.1 to 0.25 times the critical damping C_{cr}. If the coefficient a_m on the L-H-S of Eq.D.120 is replaced with $a'_m = a_m.\frac{\omega_n}{\omega}$ then we will have:

$$-M\omega^2 + K(1 + 2ia'_m) = K_0 \tag{D.120}$$

The latter is a much simpler form representing a linear hysteretic type damping. In this case, $a'_m = \eta$. Therefore, for a linear hysteretic type damping, the elastic stiffness might be multiplied by $(1 + 2i\eta)$ while for a visco-elastic system by $(1 + i\frac{\eta}{\omega_n}\omega)$.

D.14 The modified dynamic stiffness properties of the disk-cone model

The modified dynamic stiffness of a single disk-cone with material damping and attached (trapped) mass may be exprssed as follows:

$$S^*(a_0) = M_t\omega^2 + K(1 + 2ia_m\omega) + i\omega C(1 + ia_m\omega) \tag{D.121}$$

By assuming that $M_t = 0$ then Eq.D.121 may be re-written as follows:

$$S^*(a_0) = K_{st}(1 + 2i\eta_m.\frac{c_s}{r}a_0) + iC\frac{c_s}{r}a_0(1 + i\eta_m\frac{c_s}{r}a_0) \tag{D.122}$$

By taking the following ratio:

$$\frac{C}{K_{st}} = \frac{z_0}{c} \tag{D.123}$$

Hence, $S^*(a_0)$ may be re-written as follows:

$$\begin{aligned} S^*(a_0) &= K_{st}[(1 + 2i\eta_m a_0) + i\omega.\frac{z_0}{c}(1 + i\eta_m a_0)] \\ S^*(a_0) &= K_{st}[(1 + 2i\eta_m a_0) + ia_0\frac{c_s}{r_0}.\frac{z_0}{c}(1 + i\eta_m a_0)] \\ S^*(a_0) &= K_{st}[1 - \eta_m.\frac{c_s}{c}.\frac{z_0}{r_0}.a_0^2] + ia_0K_{st}[2\eta_m + \frac{c_s}{c}.\frac{z_0}{r_0}] \end{aligned} \tag{D.124}$$

The spring and dashpot coefficients can be obtained from decomposition of Eq.D.124 into real and imaginary parts as follows:

$$k_{dy} = 1 - \eta_m . \frac{c_s}{c} . \frac{z_0}{r_0} . a_0^2$$
$$c_{dy} = 2\eta_m + \frac{c_s}{c} . \frac{z_0}{r_0} \tag{D.125}$$

The dynamic stiffness coefficients expressed in Eq.D.125 are relevant for the visco-elastic type damping as assumed above (i.e. a material damping linearly dependent on the frequency of vibration of the disk-cone system).

For a disk-cone model with inclusion of the trapped mass of the soil (M_t), the dynamic stiffness may be modified as follows. The inertia (first) term on the L-H-S of Eq.D.121 may be re-written as:

$$S^*_{M_t}(a_0) = \frac{\mu \rho r_0^3 \omega^2}{K_{st}} = K_{st} . \frac{\mu}{\pi} . \frac{z_0}{c} . \frac{r_0}{c} . \omega^2$$
$$S^*_{M_t}(a_0) = \frac{\mu}{\pi} . \frac{z_0}{r_0} . \frac{c_s^2}{c^2} . a_0^2 \tag{D.126}$$

Hence, for a visco-elastic type damping, the spring and dashpot coefficients may be written as follows:

$$k_{dy} = 1 - a_{m,ve} . \frac{c_s}{r_0} . \frac{c_s}{c} . \frac{z_0}{r_0} . a_0^2 - \frac{\mu}{\pi} . \frac{z_0}{r_0} . \frac{c_s^2}{c^2} . a_0^2$$
$$c_{dy} = 2a_{m,ve} . \frac{c_s}{r_0} + \frac{c_s}{c} . \frac{z_0}{r_0} - 2a_{m,ve} . \frac{\mu}{\pi} . \frac{c_s}{r_0} . \frac{z_0}{r_0} . \frac{c_s^2}{c^2} . a_0^2 \tag{D.127}$$

In a similar manner, the expressions may be derived for the k_{dy} and c_{dy} corresponding to a disk-cone model with linear hysteretic type damping which are given in the main text of Chapter.4.

D.15 General discussion about earthquake loading

The earthquake usually occurs due to the movement of the earth's crust at the fault(rupture) lines. The intensity, direction of the propagation and the dissipation of the waves depend on the tectonic plates movement with respect to each other at the fault lines.

In general, three main types of the seismic waves are generated after an earthquake happens, namely, dilatational or contractant(P) waves, shear (S) waves, Rayleigh(R) waves (sometimes referred to as love waves). The R-waves propagate at the earth's surface from the point above the epicenter of the quake outwards along a main circle connecting it to the receiver point (station). The motion of the earth under R-waves is perpendicular to the direction of its propagation. Since R-waves and Love waves travel on the surface in tangential or radial directions from the source towards the station they trail the body waves(P and S) waves(see for e.g. Fig.D.4).

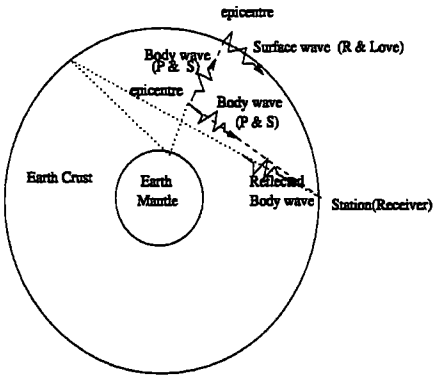

Figure D.2: A schematic illustration of body and surface (seismic) waves

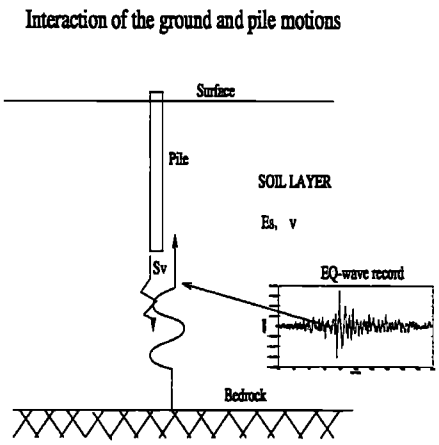

Figure D.3: A schematic illustration of interaction between the seismic(far-field) wave and the waves generated by the responding pile-soil system(near-field)

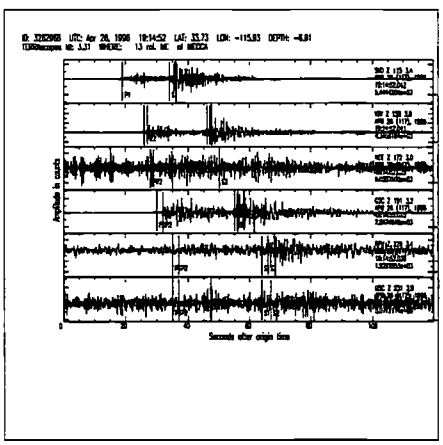

Figure D.4: A sample seismogram (recorded) earthquake from Caltech seismic lab(1996)

On the contrary, the P-waves and S-waves propagate from the epicenter of the quake often far below the earth's surface towards the receiver(station). On their way, they encounter the boundaries of the various layers and so they reflect and refract. Among the body waves, P-waves travel faster towards the station, because of their greater velocity than shear waves (For e.g. for a soil with a poission ratio of $\nu = 1/3$, it is found that $c_p = 2c_s$). The direction of propagation of the P-wave is the same as the soil's particle motion along that. The S-waves often take longer time to arrive at the station due to their associated motion which is perpendicular to the their direction of propagation(see e.g. Fig.D.2).

The earth's motion or the corresponding seismic waves are modified while they travel in various soil layers. The modification of the seismic waves in general, depend on the material and geometrical properties of the encountered soil layers. For instance, when a rigid bed rock underlying a softer layer of the soil is subjected to the earth motion, the waves which travel through the soil towards the foundation located in the softer soil might be significantly modified.

When a foundation embedded in the soil such as pile is subjected to the seismic waves, it starts responding (oscillating) depending on its mass, stiffness and damping characteristics. Hence, a pile-soil system will act as a dynamic mass, spring and dashpot system under the prescribed motion of earth. The motion of the pile might interact with that of the virgin soil(if there was not any foundation built in it). This interaction may result in modifying the ground's motion. The effective motion of the ground might therefore be applied on the dynamic pile-soil system. The motion of the earth which reaches the foundation is often called far-field motion. The motion of the ground(soil) at the vicinity of the pile foundation is often referred to as near-field motion. To obtain the near field motion of soil from its far-field counterpart and also the kinematic as well as inertial interaction of the foundation(pile) and the surrounding soil, various methods exist. Various analytical as well as numerical treatments exist for solution of the modified seismic waves such as those suggested by Clough and Penzien, (1968), Gazetas et al, (1976), Novak, (1968), Poulos, (1976), Wolf, (1985,1994).

Fig.D.3 schematically illustrates the interaction between the waves approaching from the far-field of the soil and the waves generated by the responding pile. Fig.D.5 illustrates a simple method to obtain the modified(near field) motion of the ground from the motion an underlying bedrock(far-field motion). This method is basically introduced by Clough and Penzien, (1968) which discretizes the soil layer above the bedrock as a system of springs and dashpots and masses lumped at the disk points. The far-field or bedrock motion is applied at the tip of this multi-stack of disks and the response is calculated at the nodal(disk) points which correspond to the modified or near field motion of the soil along the pile. It may be noted that this multi-stack of disks only corresponds to the cylinder of (virgin) soil itself not to the pile cylinder.

After determining the response or near-field motion of the soil, it is applied at the nodes of the multi-stack of disks-cones system representing the pile-soil foundation. The response is then calculated in the same manner as for the near-field motion of the soil. It is noteworthy that this may require more computing time, however, in most practical case, the following simplifying assumptions often used:

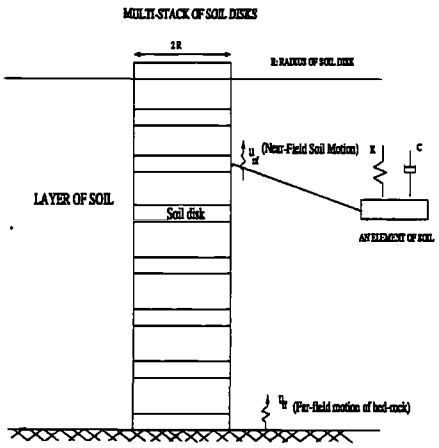

Figure D.5: Illustration of soil seismic near-field response of the multi-stack of soil disks subjected to an underlying bedrock(far-field)motion

. an equivalent static load say about 10% of the gravity load is applied on the pile head as a lateral load etc.

. an equivalent earthquake loading is applied as the mass of the pile-soil multiplied by the maximum ground acceleration etc. The frequency of such force might be taken as the dominant frequency of the vibration of the ground etc.

. an effective ground motion is applied at the pile tip where is closer to the bedrock as prescribed displacement, velocity or acceleration .

. an effective ground motion is applied at all the disks or nodes of the pile-soil system with full correlation.

The first assumption is very simplistic, since no account of the real amplitude of the seismic motion and the frequency of the vibration are taken. The second approach is often used only with a lumped model (SDOF) model of the pile-soil system and may give just an estimate of the response(with less accuracy). The third and fourth methods seem to be more relevant for the seismic analysis of a single pile-soil system. In the case studies presented in the main text of Chapter.4, we have applied the latter three methods.

D.16 Dynamic pile-soil input data

Table D.2: Soil layer input data for dynamic stiffness and damping functions of Figs.4.35 to 4.38

d/r_0	G (MPa)	ν	soil type	α	β
1-1000	35	1/3	NC	0.75	2.5

Table D.3: Soil layer input data for dynamic stiffness and damping functions of Figs.4.35 to 4.38

d/r_0	G (MPa)	ν	soil type	α	β
1.0	35	1/3	OC	0.75	1.1
1.0	35	1/3	NC	0.75	1.5
1.0	35	1/3	NC	0.75	2.0
1.0	35	1/3	NC	0.75	2.5
1.0	35	1/3	NC	0.99	2.5

Table D.4: Soil layer input data for dynamic stiffness and damping functions of Figs.4.35 to 4.38

d/r_0	G (MPa)	ν	soil type	α	β
1.0	35	1/3	NC	0.99	2.5
1.0	35	1/3	OC	0.75	1.0

Table D.5: The pile-soil input data for frequency domain analysis of pile-soil system Figs.4.63 and 4.64

pile type	O.D. (m)	t_w (m)	soil type	η	S.C.	α	β
Rigid	0.762	0.03	linear-elastic	0.25	OC	0.99	1.0
linear-elastic	0.762	0.03	linear-elastic	0.25	OC	0.99	1.0
elasto-plastic	0.762	0.03	elasto-plastic	-	OC	0.99	1.0

Table D.6: The pile-soil input data for displacement response of a single pile-soil system in Fig.4.65

pile type	O.D (m)	t_w (m)	soil type	S.C.	α	β
elasto-plastic	1.0	0.03	elasto-plastic	OC	0.75	1.00

Table D.7: The pile-soil input data for impedance function plotted in Fig.4.82 to 4.93

e/r_0	G	ν	S.C.	α	β
		0.4	OC	0.75	1.00
15	150	0.4	OC	0.75	1.00
30	150	0.4	OC	0.75	1.00
2.75	35.8	0.4	OC	0.75	1.00
2.0	35.8	0.4	OC	0.75	1.00
75.0	806.5	0.4	OC	0.75	1.00

APPENDIX E

Ductility demand analysis of jacket-pile-soil systems

Table E.1: Ductility demand spectra results for extreme wave(Hs=12.75m, Tz=12.5secs)

T_n (sec)	$\mu(F_\nu = 1)$	$\mu(F_\nu = 1.15)$	$\mu(F_\nu = 1.3)$
0.5	1.24	4.04	6.07
1.0	1.12	3.82	4.72
1.5	1.29	2.13	3.71
2.0	1.01	2.02	2.92
2.5	0.62	1.12	1.50
3.0	0.28	0.62	1.14
3.5	0.34	0.67	1.09
4.0	0.39	0.79	1.31
4.5	0.39	0.84	1.25
5.0	0.34	0.60	1.10

Table E.2: Ductility demand spectra results for an extreme wave (Hs=15m, Tz=15.8 esc)

T_n (sec)	$\mu(F_\nu = 1)$	$\mu(F_\nu = 1.15)$	$\mu(F_\nu = 1.3)$
0.5	0.84	1.49	7.67
1.0	2.80	2.48	9.16
1.5	2.80	6.94	12.13
2.0	5.61	9.42	14.36
2.5	3.36	5.70	9.41
3.0	1.68	2.73	4.46
3.5	1.12	2.73	3.71
4.0	2.24	3.47	5.45
4.5	1.12	1.49	2.18
5.0	0.95	0.99	1.31

Table E.3: Ductility demand spectra results for a simulated extreme wave with with $H_s = 12.75$ m and $T_z = 12.5$ sec with different viscous damping ratios

T_n (sec)	$\mu(F_\nu = 1.0, c = 0.01)$	$\mu(F_\nu = 1.0, c = 0.05)$	$\mu(F_\nu = 1.0, c = 0.1)$
0.5	1.01	1.01	1.01
1.0	2.02	2.42	5.52
1.5	2.02	2.32	5.49
2.0	2.02	2.83	7.68
2.5	1.62	2.53	4.75
3.0	1.92	1.41	2.09
3.5	1.21	1.21	1.21
4.0	1.01	1.31	4.34
4.5	0.81	0.91	1.72
5.0	0.61	0.81	0.86

Table E.4: Ductility demand spectra results for a severe earthquake(El Centro, 1940)

T_n (sec)	$\mu(F_\nu = 1.0)$	$\mu(F_\nu = 2.0)$	$\mu(F_\nu = 3.0)$
0.5	1.54	3.33	8.33
1.0	1.03	2.05	4.23
1.5	0.77	1.54	3.85
1.75	1.03	1.67	3.92
2.0	0.77	1.79	3.59
2.25	0.77	1.54	3.01
2.5	0.71	1.41	2.76
2.75	0.64	1.28	2.31
3.0	0.51	1.24	1.90
3.5	0.51	1.05	1.58
4.0	0.38	0.77	1.28
4.5	0.32	0.64	1.06
5.0	0.26	0.51	0.90

Table E.5: Ductility demand spectra results for a severe earthquake(El Centro, 1940) with variation of soil's shear modulus with reference shear modulus of $G_0 = 42MPa$

T_n (sec)	$\mu(F_\nu = 1.0, G/G_0 = 1)$	$\mu(F_\nu = 1.0, G/G_0 = 2.0)$	$\mu(F_\nu = 1.0, G/G_0 = 3.0)$
0.5	1.54	1.31	1.36
1.0	1.39	1.26	1.30
1.5	1.34	1.20	1.20
2.0	1.20	1.16	1.13
2.5	1.11	1.06	1.05
3.0	1.07	1.10	1.08
3.5	1.07	1.05	1.06
4.0	1.05	1.05	1.06
4.5	1.07	1.06	1.06
5.0	1.05	1.05	1.06

Table E.6: Ductility demand spectra results for a severe earthquake(El Centro, 1940) with variation of bandwidth parameter α_1

T_n (sec)	$\mu(F_\nu = 1.0, \alpha = 1.0)$	$\mu(F_\nu = 1.0, \alpha = 0.1)$	$\mu(F_\nu = 1.0, \alpha = 0.01)$
0.50	1.57	1.80	1.80
1.00	1.39	1.40	1.63
1.50	1.01	1.01	1.24
2.00	0.78	0.79	0.90
2.50	0.56	0.58	0.56
3.00	0.53	0.55	0.51
3.50	0.54	0.58	0.52
4.00	0.54	0.55	0.46
4.50	0.52	0.53	0.50
5.00	0.53	0.55	0.44

Table E.7: Ductility demand spectra results for a severe earthquake(Big bear, 1940) with variation of post-peak hardening/softening parameter β

T_n (sec)	$\mu(F_\nu = 1.0, \beta = 0.1)$	$\mu(F_\nu = 1.0, \beta = 0.5)$	$\mu(F_\nu = 1.0, \beta = 1.0)$
0.26	0.39	0.43	0.50
0.52	0.79	0.83	1.08
0.78	0.52	0.57	0.62
1.04	0.59	0.61	0.67
1.30	0.50	0.50	0.52
1.57	0.49	0.49	0.49
1.83	0.48	0.48	0.49
2.09	0.47	0.48	0.48
2.35	0.47	0.47	0.47
2.61	0.47	0.47	0.47

Table E.8: Ductility demand spectra results for a severe earthquake(El Centro, 1940) with variation of yield stress with reference $f_y = 300$ MPa

T_n (sec)	$\mu(F_\nu = 1.0, f_y/f_{y0} = 0.2)$	$\mu(F_\nu = 1.0, f_y/f_{y0} = 1.0)$	$\mu(F_\nu = 1.0, f_y/f_{y0} = 5.0)$
0.5	1.61	1.50	1.45
1.0	1.46	1.43	1.32
1.5	1.35	1.29	1.22
2.0	1.20	1.16	1.13
2.5	1.12	1.11	1.09
3.0	1.09	1.09	1.08
3.5	1.07	1.10	1.09
4.0	1.07	1.09	1.08
4.5	1.05	1.08	1.08
5.0	1.04	1.08	1.08

Table E.9: Ductility demand spectra results for a severe earthquake(Santa cruz, 1989)

T_n (sec)	$\mu(F_\nu = 1.0)$	$\mu(F_\nu = 1.5)$
0.32	2.84	7.11
0.64	1.78	1.24
0.96	1.07	1.42
1.28	0.53	0.71
1.60	0.36	0.98
1.92	0.27	0.36
2.24	0.27	0.31
2.56	0.22	0.27
2.88	0.18	0.18
3.20	0.18	0.09

Table E.10: Ductility demand spectra results for a severe earthquake(Woodfords, 1995)

T_n (sec)	$\mu(F_\nu = 1.0)$	$\mu(F_\nu = 2.0)$	$\mu(F_\nu = 3.0)$
0.32	3.87	6.27	12.00
0.64	2.67	5.60	9.07
0.96	1.23	1.73	2.80
1.28	1.20	1.33	1.87
1.60	0.73	1.07	1.87
1.92	0.56	1.20	1.93
2.24	0.53	0.80	1.33
2.56	0.40	0.67	1.60
2.88	0.32	0.47	1.00
3.20	0.27	0.53	0.13

Table E.11: Ductility demand spectra results for a severe earthquake(Parkfield, 1994)

T_n (sec)	$\mu(F_\nu = 1.0)$	$\mu(F_\nu = 1.5)$	$\mu(F_\nu = 3.0)$
0.61	2.56	2.81	6.00
0.94	1.19	1.65	2.66
1.25	1.14	1.31	1.81
1.55	0.70	1.06	1.79
1.88	0.53	1.11	1.94
2.18	0.41	0.63	1.23
2.49	0.60	0.39	1.45
2.79	0.29	0.44	0.63
3.12	0.24	0.44	0.48

Table E.12: Ductility demand spectra results for a severe earthquake(Taft, 1952)

T_n (sec)	$\mu(F_\nu = 1.0)$	$\mu(F_\nu = 2.0)$	$\mu(F_\nu = 3.0)$
1.0	1.60	7.00	15.60
1.5	1.28	3.30	5.60
2.0	0.80	3.20	3.60
2.5	1.00	2.00	4.00
3.0	0.40	1.50	2.40
3.5	0.40	1.20	1.40
4.0	0.20	1.80	1.20
4.5	0.20	0.80	1.30
5.0	0.20	0.80	1.20

Table E.13: Comparison of the computed overload ratio of one storey plane frame with single and double bracings

single braced		double braced	
F_ν	μ	F_ν	μ
0.26	0.19	0.40	0.30
0.26	0.34	0.72	0.23
0.50	0.49	0.36	0.53
1.00	0.53	0.52	0.60
1.00	0.64	0.74	0.68
1.00	1.06	1.44	1.06
1.24	1.74	1.38	1.74
1.00	2.00	1.24	2.04
1.96	1.96	1.76	2.64
1.48	2.72	1.46	3.17
1.46	3.21	1.70	7.25

Table E.14: The predicted versus computed overload ratios of double-braced two-storey plane frame with varying natural periods from 0.28 to 0.82 secs

Predictive method	F_ν $T_n = 0.28$ sec	$T_n = 0.56$ sec	$T_n = 0.82$ sec
Plane frame analysis	1.10	1.98	2.77
Schmucker, 1996	1.57	2.13	2.67
Eq.5.14	1.10-1.12	1.08-1.12	1.47-2.03

Table E.15: The predicted versus computed overload ratios of jacket platform with with hydrodynamic Model-1 and plugged pile foundation under regular wave loading

Predictive Method	F_ν (end-on)	F_ν (broad-side)
MDOF(abs.velocity)	1.05-1.25	0.9-1.18
Stewart et al, 1993	1.1-1.2	1.0-1.2
Schmucker, 1996	1.16	1.15
Eq.5.14	1.10	1.09

Table E.16: The predicted versus computed overload ratios of jacket platform with with hydrodynamic Model-1 and plugged pile foundation under multiple wave loading

Predictive Method	F_ν (end-on)	F_ν (broad-side)
MDOF(abs.velocity)	1.14	1.04
Stewart et al, 1993	1.1-1.2	1.0-1.05
Schmucker, 1996	1.13	1.35
Eq.5.14	1.12	1.05

Table E.17: The predicted versus computed overload ratios of jacket platform with lumped linear spring to ground foundation under end-on and broad-side loading(Model-1)

Predictive Method	F_ν (end-on)	F_ν (broad-side)
MDOF(abs.velocity)	1.10	0.90
Stewart et al, 1993	1.1-1.2	≤ 1.0
Schmucker, 1996	1.06	0.99
Eq.5.14	1.08	0.95

Table E.18: The predicted versus computed overload ratios of jacket platform with plugged pile foundation under end-on and broad-side loading(Model-1)

Predictive Method	F_v (end-on)	F_v (broad-side)
MDOF(abs.velocity)	1.12	0.96
MDOF(rel.velocity)	1.16	0.99
Stewart et al, 1993	1.10-1.20	$\leq$1.00
Schmucker, 1996	1.04	0.91
Eq.5.14	1.13	0.96

APPENDIX F

Jacket-pile-soil random variables

The following is the list of input random variables used in the routine RELAP with their corresponding mean ,std values and distribution types:
I N P U T
Name : PilSoi-N4
Description : Pushover of Jacket - Pile/Soil foundation Analysis method : FORM and SORM
Joint study by : Geir Olaf Hovde and M.Reza Emami Azadi
Description of variables : Variable No. 1 - GamS : Gamma of sand - layer nos. 1,2,3 and 5
Variable No. 2 - GamC : Gamma of clay - layer nos. 4 and 6
Variable No. 3 - Phi1 : Phi of sand - layer no. 1

Variable No. 4 - Phi2 : Phi of sand - layer no. 2

Variable No. 5 - Phi3 : Phi of sand - layer no. 3

Variable No. 6 - Phi5 : Phi of sand - layer no. 5

Variable No. 7 - Su4 : Su of clay - layer no. 4

Variable No. 8 - Su6 : Su of clay - layer no. 6

Variable No. 9 - Epsc4 : Epsc of clay - layer no. 4

Variable No. 10 - Epsc6 : Epsc of clay - layer no. 6

Variable No. 11 - Tresmax : Tres/Tmax - all layers

Variable No. 12 - Tzzres : Tzzres - all layers

Variable No. 13 - Tcmax1 : Tcmax - no. 1

Variable No. 14 - Tcmax2 : Tcmax - no. 2

Variable No. 15 - Tcmax3 : Tcmax - no. 3

Variable No. 16 - Tcmax4 : Tcmax - no. 4

Variable No. 17 - Tcmax5 : Tcmax - no. 5

Variable No. 18 - Tcmax6 : Tcmax - no. 6

Variable No. 19 - Tcmax7 : Tcmax - no. 7

Variable No. 20 - Tcmax8 : Tcmax - no. 8

Variable No. 21 - Tcmax9 : Tcmax - no. 9

Variable No. 22 - Tcmax10 : Tcmax - no. 10

Variable No. 23 - Tcmax11 : Tcmax - no. 11

Variable No. 24 - Tcmax12 : Tcmax - no. 12

Variable No. 25 - Tcmax13 : Tcmax - no. 13

Variable No. 26 - Ttmax1 : Ttmax - no. 1

Variable No. 27 - Ttmax2 : Ttmax - no. 2

Variable No. 28 - Ttmax3 : Ttmax - no. 3

Variable No. 29 - Ttmax4 : Ttmax - no. 4

Variable No. 30 - Ttmax5 : Ttmax - no. 5

Variable No. 31 - Ttmax6 : Ttmax - no. 6

Variable No. 32 - Ttmax7 : Ttmax - no. 7

Variable No. 33 - Ttmax8 : Ttmax - no. 8

Variable No. 34 - Ttmax9 : Ttmax - no. 9

Variable No. 35 - Ttmax10 : Ttmax - no. 10

Variable No. 36 - Ttmax11 : Ttmax - no. 11

Variable No. 37 - Ttmax12 : Ttmax - no. 12

Variable No. 38 - Ttmax13 : Ttmax - no. 13

Variable No. 39 - Gs1 : Gs - no. 1

Variable No. 40 - Gs2 : Gs - no. 2

Variable No. 41 - Gs3 : Gs - no. 3

Variable No. 42 - Gs4 : Gs - no. 4

Variable No. 43 - Gs5 : Gs - no. 5

Variable No. 44 - Gs6 : Gs - no. 6

Variable No. 45 - Gs7 : Gs - no. 7

Variable No. 46 - Gs8 : Gs - no. 8

Variable No. 47 - Gs9 : Gs - no. 9

Variable No. 48 - Gs10 : Gs - no. 10

Variable No. 49 - Gs11 : Gs - no. 11

Variable No. 50 - Gs12 : Gs - no. 12

Variable No. 51 - Gs13 : Gs - no. 13

Variable No. 52 - Dsptzdiam : Dsptz/diam - nos. 1-13

Variable No. 53 - Bias-Es : Bias of Es0+f(z)*Es1

Variable No. 54 - Nus : Nus

Variable No. 55 - Dspqzdiam : Dspqz/diam - nos. 1-13

Variable No. 56 - Diameter : Diameter

Variable No. 57 - Pc-yc : Pc-yc

Variable No. 58 - Ps-ys : Ps-ys

Variable No. 59 - T-z,Q-z : T-z,Q-z

Variable No. 60 - Fy21 : Yield stress - Mat.no. 21

Variable No. 61 - Fy20 : Yield stress - Mat.no. 20

Variable No. 62 - H1 : Annual maximum wave height

Variable No. 63 - Bias-L : Bias of load calculation

Variable No. 64 - Bias-S : Bias of strength calculation

Variable No. 65 - Bias-H1 : Bias of wave height

Variable No. 66 - Lcode : Type of load calculation

Variable No. 67 - Href : Wave height in strength calculation
Type of statistical parameters :
Distrib. No. 1 - Fixed : Value
Distrib. No. 2 - Normal : Mean, StD
Distrib. No. 3 - Lognormal : Mean, StD, Low
Declaration of variables :
Variable No. 1 - GamS : Normal 1.0000D+00 1.0000D-01
Variable No. 2 - GamC : Normal 1.0000D+00 1.0000D-01
Variable No. 3 - Phi1 : Normal 1.0000D+00 5.0000D-02
Variable No. 4 - Phi2 : Normal 1.0000D+00 5.0000D-02
Variable No. 5 - Phi3 : Normal 1.0000D+00 5.0000D-02
Variable No. 6 - Phi5 : Normal 1.0000D+00 5.0000D-02
Variable No. 7 - Su4 : Lognormal 1.0000D+00 2.0000D-01 .0000D+00
Variable No. 8 - Su6 : Lognormal 1.0000D+00 2.0000D-01 .0000D+00
Variable No. 9 - Epsc4 : Normal 1.0000D+00 4.0000D-01
Variable No. 10 - Epsc6 : Normal 1.0000D+00 4.0000D-01
Variable No. 11 - Tresmax : Normal 1.0000D+00 2.0000D-01
Variable No. 12 - Tzzres : Fixed 1.0000D+00
Variable No. 13 - Tcmax1 : Normal 1.2000D+00 3.0000D-01
Variable No. 14 - Tcmax2 : Normal 1.2000D+00 3.0000D-01
Variable No. 15 - Tcmax3 : Normal 1.2000D+00 3.0000D-01
Variable No. 16 - Tcmax4 : Normal 1.2000D+00 3.0000D-01
Variable No. 17 - Tcmax5 : Normal 1.2000D+00 3.0000D-01
Variable No. 18 - Tcmax6 : Normal 1.2000D+00 3.0000D-01

Variable No. 19 - Tcmax7 : Normal 1.2000D+00 3.0000D-01
Variable No. 20 - Tcmax8 : Normal 1.2000D+00 3.0000D-01
Variable No. 21 - Tcmax9 : Normal 1.2000D+00 3.0000D-01
Variable No. 22 - Tcmax10 : Normal 1.2000D+00 3.0000D-01
Variable No. 23 - Tcmax11 : Normal 1.2000D+00 3.0000D-01
Variable No. 24 - Tcmax12 : Normal 1.2000D+00 3.0000D-01
Variable No. 25 - Tcmax13 : Normal 1.2000D+00 3.0000D-01
Variable No. 26 - Ttmax1 : Normal 1.2000D+00 3.0000D-01
Variable No. 27 - Ttmax2 : Normal 1.2000D+00 3.0000D-01
Variable No. 28 - Ttmax3 : Normal 1.2000D+00 3.0000D-01
Variable No. 29 - Ttmax4 : Normal 1.2000D+00 3.0000D-01
Variable No. 30 - Ttmax5 : Normal 1.2000D+00 3.0000D-01
Variable No. 31 - Ttmax6 : Normal 1.2000D+00 3.0000D-01
Variable No. 32 - Ttmax7 : Normal 1.2000D+00 3.0000D-01
Variable No. 33 - Ttmax8 : Normal 1.2000D+00 3.0000D-01
Variable No. 34 - Ttmax9 : Normal 1.2000D+00 3.0000D-01
Variable No. 35 - Ttmax10 : Normal 1.2000D+00 3.0000D-01
Variable No. 36 - Ttmax11 : Normal 1.2000D+00 3.0000D-01
Variable No. 37 - Ttmax12 : Normal 1.2000D+00 3.0000D-01
Variable No. 38 - Ttmax13 : Normal 1.2000D+00 3.0000D-01
Variable No. 39 - Gs1 : Normal 1.0000D+00 1.5000D-01
Variable No. 40 - Gs2 : Normal 1.0000D+00 1.5000D-01
Variable No. 41 - Gs3 : Normal 1.0000D+00 1.5000D-01
Variable No. 42 - Gs4 : Normal 1.0000D+00 1.5000D-01
Variable No. 43 - Gs5 : Normal 1.0000D+00 2.5000D-01
Variable No. 44 - Gs6 : Normal 1.0000D+00 2.5000D-01
Variable No. 45 - Gs7 : Normal 1.0000D+00 2.5000D-01
Variable No. 46 - Gs8 : Normal 1.0000D+00 2.5000D-01
Variable No. 47 - Gs9 : Normal 1.0000D+00 3.0000D-01
Variable No. 48 - Gs10 : Normal 1.0000D+00 3.0000D-01
Variable No. 49 - Gs11 : Normal 1.0000D+00 3.0000D-01
Variable No. 50 - Gs12 : Normal 1.0000D+00 3.0000D-01
Variable No. 51 - Gs13 : Normal 1.0000D+00 3.0000D-01
Variable No. 52 - Dsptzdiam : Normal 1.0000D+00 4.0000D-01
Variable No. 53 - Bias-Es : Lognormal 1.0000D+00 1.5000D-01 .0000D+00
Variable No. 54 - Nus : Lognormal 1.0000D+00 1.5000D-01 .0000D+00
Variable No. 55 - Dspqzdiam : Normal 1.0000D+00 4.0000D-01
Variable No. 56 - Diameter : Fixed 1.0000D+00
Variable No. 57 - Pc-yc : Normal 1.1000D+00 1.6500D-01
Variable No. 58 - Ps-ys : Normal 1.2000D+00 3.0000D-01
Variable No. 59 - T-z,Q-z : Normal 1.2000D+00 3.0000D-01
Variable No. 60 - Fy21 : Lognormal 1.0400D+00 7.2800D-02 .0000D+00
Variable No. 61 - Fy20 : Lognormal 1.0400D+00 7.2800D-02 .0000D+00
Variable No. 62 - H1 : Fixed 2.3273D+01

Variable No. 63 - Bias-L : Lognormal 9.0000D-01 2.2500D-01 .0000D+00
Variable No. 64 - Bias-S : Lognormal 1.0000D+00 1.5000D-01 .0000D+00
Variable No. 65 - Bias-H1 : Lognormal 1.0000D+00 1.5000D-01 .0000D+00
Variable No. 66 - Lcode : Fixed 1.0000D+00
Variable No. 67 - Href : Fixed 3.1300D+01

APPENDIX G

An algorithm for reliability analysis of jacket-pile-soil system

G.1 Reliability analysis algorithm

The following describes an algorithm for reliability analysis of jacket-pile-soil system under extreme wave loading. This algorithm is used in study of Chapter.6.

1) Generate the pile-soil load transfer-displacement (p-y), (t-z) and (q-z) curves by using the mean values of the soil-pile input parameters as listed in Appendix.C
For this aim FORTRAN program GENSODM and MATLAB program GENSDISKD are used in Chapter 6.

2) Use the generated pile-soil stiffness data and the mean values of structural input parameters as listed in Appendix.c to perform a static pushover analysis at the reference point for all the assumed random parameters
Program USFOS is used for pushover analysis of jacket-pile-soil system in Chapter.6.

3) Post-process the output from pushover analysis of step (2) to generate the global load-deflection curves at the deck level
Program Postfos is used for post-processing of the analysis results of step (2) in Chpater.6.

4) Vary each random pile-soil and structural input parameter by about $10 - 20\%$ and generate the corresponding (p-y), (t-z) and (q-z) data from step (1) for each given variation

5) Perform static pushover analyses for each variation of the pile-soil and structural parameters and post-process the results as described in steps (2) and (3)

6) Establish a limit state function as described in Chapter.6 and compute the reliability index, annual probability of failure and importance factors by using the values of the random parameters from step (4) and the strength parameters from steps (3) and (5)
Program RELJPS is used in Chapter.6 to perform FORM and SORM reliability analyses of the integrated jacket-pile-soil system at the limit state of collapse.

7) Post-process the results of the reliability analyses of step (6) and obtain the new values of the random pile-soil and structural parameters
Program RELJPS is used to post-process the results of reliability analysis in Chapter.6.

8) Use the computed values of the random parameters in X-space to generate the corresponding (p-y), (t-z) and (q-z) curves and repeat the steps(4) to (7) if the condition of step (9) is not satisfied

9) Check if the maximum absolute difference between the current and the previous values of the random parameters is less than a pre-defined tolerance value or a Euclidean norm as specified in RELJPS algorithm then stop the analysis

10) Process and print the results of the reliability analyses

G.2 RELJPS algorithm

The following describes the algorithm for RELJPS program:

1) Input the mean values of the random parameters

2) Compute the limit state function $g(x)$

3) Compute the distance normal to the yield surface of the system

4) Calculate the load and strength from calno subroutine by using the base shear vs. the wave height relationship as described in Chapter.6 and compute the limit state function as step (2)

5) Compute the reliability index and importance factors from FORM and SORM analyses

6) update the strength random table STRETAB from static pushover analyses and also the values of the updated random variables, their derivatives and variations from previous RELJPS analysis

7) Follow the steps (1) to (6) if the convergence requirement set in step (9) of algorithm for reliability analysis is not met

G.3 GENSODM algorithm

The following is an algorithm which describes the generation of the pile-soil load transfer-displacement curves according to disk and API RP2A 1993 (t-z), (p-y) and (q-z) models.

1) Define the pile geometry (length, diameter and thickness)

2) Define the soil profile(layers type, thickness, strength characteristic data such as shear strength S_u, the effective overburden pressure $p^{'}$, the overconsolidation ratio OCR, the strain at half deviatoric stress level ϵ_{50} etc).

3) Define cyclic soil parameter such as α_s and β_s parameters no of cycles, one way or two way cyclic indicator parameter such as τ_{av} and τ_{cyc}, stabilization switch etc.

4) Assign the pile and soil layer data

5) Specify additional data such as hydraulic scour or gapping for API RP2A 1993 models

6) Compute other necessary soil data if not supplied as input such as OCR and G_i according to relationships described in Chapter.2.

7) Compute the effective soil parameters such as internal soil angle or interface angle if not supplied

8) Compute the peak or ultimate values of the shaft skin friction, the lateral soil resistance and the tip end-bearing and the associated displacement values according to the relationships given in Chapter.2

9) Generate the (t-z), (p-y) and (q-z) curves according to the relationships described in secs.2.2.1, 2.3.1, 2.2.3 and 2.3.3 for API RP2A 1993 and disk models, respectively

10) Repeat the steps (8) and (9) for all the specified pile segments or the given soil layers in steps (1) to (4)

11) If the force-displacement (MISOPL) record of USFOS is required then compute the corresponding forces by integrating simply (t) and (p) stress or load transfer values over the segments of the shaft at each layer

12) Calculate the tension (t-z), (p-y) curves with using the mirror image of the compression (t-z) and (p-y) curves according to API RP2A 1993 recommendation or apply a reduction factor (due to suction or reduction of the effective vertical stress in soil as described in Chapter.2

Appendix H

Colour displays of deformed models

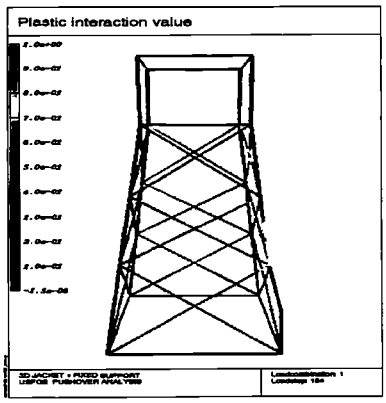

Figure H.1: Failure mode of 4-leg (Malaysian) Jacket with fixed support

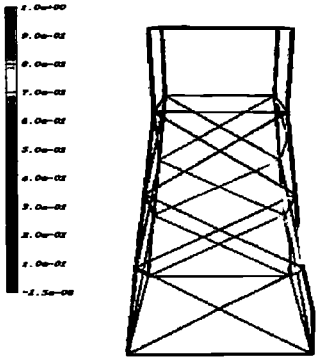

Figure H.2: The Failure mode of the 4-leg (Malaysian) Jacket with linear spring to ground

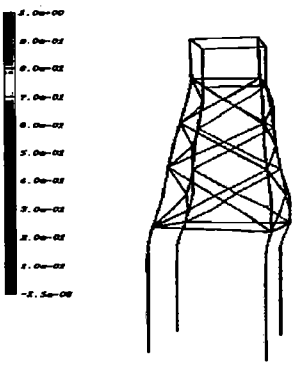

Figure H.3: The Failure mode of the 4-leg (Malaysian) Jacket with non-linear pile-soil model(NC clay)

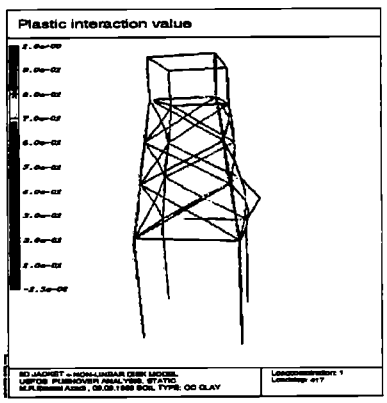

Figure H.4: The Failure mode of the 4-leg (Malaysian) Jacket with non-linear pile-soil model(OC clay)

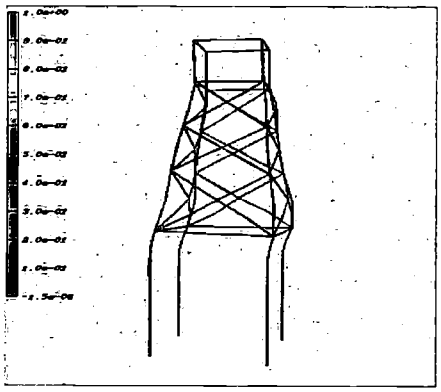

Figure H.5: The Failure mode of the 4-leg (Malaysian) Jacket with non-linear pile-soil model(NC clay)

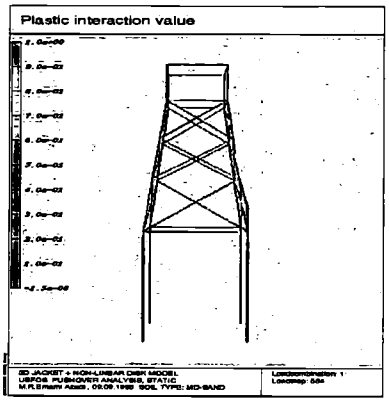

Figure H.6: The failure mode of the 4-leg (Malaysian) Jacket with non-linear pile-soil model(sand)

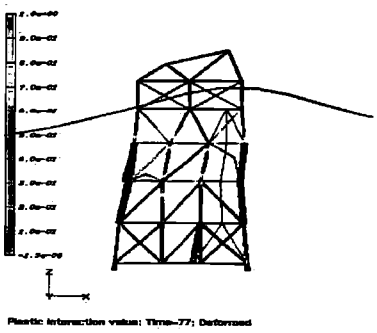

Figure H.7: The deformed model of the Jacket(Model-1) with linear spring to ground under end-on loading

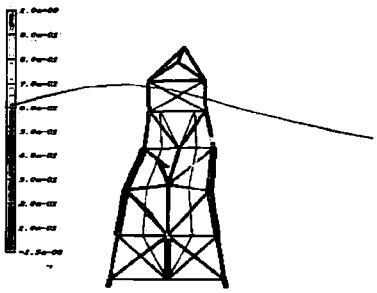

Figure H.8: The deformed model of the jacket (Model-1) with linear spring to ground under broad-side loading

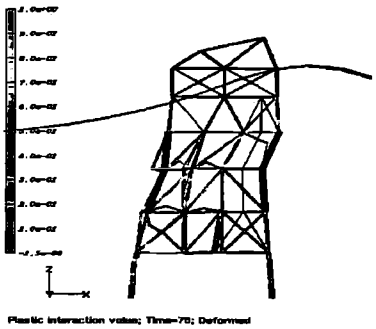

Figure H.9: The deformed model and plastic interaction model of the jacket(Model-1) with un-plugged pile foundation under end-on loading

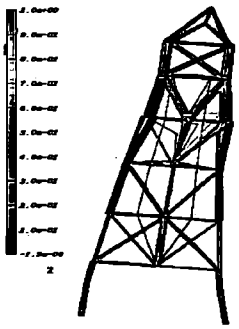

Figure H.10: The deformed model and plastic interaction model of the jacket(Model-1) with un-plugged pile foundation under broad-side loading

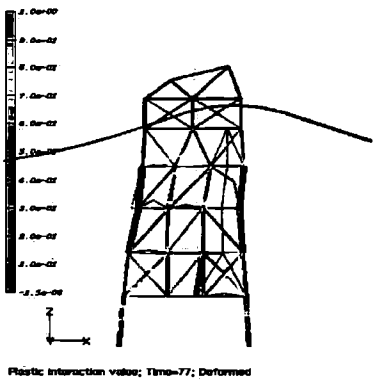

Figure H.11: The deformed plastic interaction model of platform with plugged non-linear pile-soil system under end-on loading

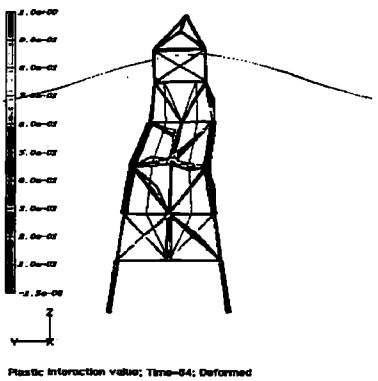

Figure H.12: The deformed plastic interaction model of platform with plugged pile-soil system under broad-side loading

PREVIOUS DR.ING. THESES

Department of Marine Structures

Kavlie, Dag	:	Optimization of Plane Elastic Grillages. 1967.
Hansen, Hans R.	:	Man-Machine Communication and Data-Storage Methods in Ship Structural Design. 1971.
Gisvold, Kaare M.	:	A Method for non-linear mixed -integer programming and its Application to Design Problems.
Lund, Sverre	:	Tanker Frame Optimalization by means of SUMT-Transformation and Behaviour Models. 1971.
Vinje, Tor	:	On Vibration of Spherical Shells Interacting with Fluid. 1972.
Lorentz, Jan D.	:	Tank Arrangement for Crude Oil Carriers in Accordance with the new Anti-Pollution Regulations. 1975.
Carlsen, Carl A.	:	Computer-Aided Design of Tanker Structures. 1975.
Larsen, Carl M.	:	Static and Dynamic Analysis of Offshore Pipelines during Installation. 1976.
Hatlestad, Brigt	:	The Finite Element Method used in a Fatigue Evaluation of Fixed Offshore Platforms. 1979.
Valsgård, Sverre	:	Finite Difference and Finite Element Method Applied to Non-Linear Analysis of Plated Structures. 1979.
Pettersen, Erik	:	Analysis and Design of Cellular Structures. 1979.
Nordsve, Nils T.	:	Finite Element Collapse Analysis of structural Members considering Imperfections and Stresses due to Fabrication. 1980.
Fylling, Ivar J.	:	Analysis of towline Forces in Ocean towing Systems. 1980.
Haver, Sverre	:	Analysis of Uncertainties related to the stochastic Modelling of Ocean Waves. 1980.
Odland, Jonas	:	On the Strength of welded Ring stiffened cylindrical Shells primarily subjected to axial Compression. 1981.
Engesvik, Knut	:	Analysis of Uncertainties in the fatigne Capacity of Welded Joints. 1982.
Eide, Oddvar Inge	:	On Cumulative Fatigue Damage in Steel Welded Joints. 1983.
Mo, Olav	:	Stochastic Time Domain Analysis of Slender Offshore Structures. 1983.
Amdahl, Jørgen	:	Energy absorption in Ship-platform impacts 1983.
Czujko, Jerzy	:	Collapse Analysis of Plates subjected to Biaxial Compression and Lateral Load. 1983.
Soares, C. Guedes	:	Probabilistic models for load effects in ship structures. 1984.
Mørch, Morten	:	Motions and mooring forces of semi submersibles as determined by full-scale measurements and theoretical analysis. 1984.

Engseth, Alf G.	:	Finite Element Collapse Analysis of Tubular Steel Offshore Structures. 1985.
Baadshaug, Ola	:	Systems Reliability Analysis of Jacket Platforms. 1985. (Confidential)
Hessen, Gunnar	:	Fracture Mechanics Analysis of Stiffened Tubular Members. 1986.
Taby, Jon	:	Ultimate and post-ultimate strength of dented tubular members. 1986.
Wessel, Heinz-J.	:	Fracture mechanics analysis of crack growth in plate girders. 1986.
Leira, Bernt Johan	:	Gaussian Vector-processes for Reliability Analysis involving Wave-induced Load Effects. 1987.
Xu JUN	:	Non-linear Dynamic Analysis of Space-framed Offshore Structures. 1988.
Guoyang Jiao	:	Reliability Analysis of Crack Growth under Random Loading considering Model Updating. 1989.
Olufsen, Arnt	:	Uncertainty and Reliability Analysis of Fixed Offshore Structures. 1989.
Wu Yu-Lin	:	System Reliability Analyses of Offshore Structures using improved Truss and Beam Models. 1989.
Farnes, Knut-Aril	:	Long-term Statistics of Response in Non-linear Marine Structures. 1990.
Sotberg, Torbjørn	:	Application of Reliability Methods for Safety Assessment of Submarine Pipelines. 1990.
Hoen, Christopher	:	System Identification of Structures Excited by Stochastic Load Processes. 1991.
Sødahl, Nils	:	Methods for Design and Analysis of Flexible Risers. 1991.
Haugen, Stein	:	Probabilistic Evaluation of Frequency of Collision between Ships and Offshore Platforms. 1991.
Ormberg, Harald	:	Non-linear Response Analysis of Floating Fish Farm Systems. 1991.
Marley, Mark J.	:	Time Variant Reliability Under Fatigue Degradation. 1991.
Bessason, Bjarni	:	Assessment of Earthquake Loading and Response of Seismically Isolated Bridges. 1992.
Sævik, Svein	:	On Stresses and Fatigue in Flexible Pipes. 1992.
Dalane, Jan Inge	:	System Reliability in Design and Maintenance of Fixed Offshore Structures. 1993.
Karunakaran, Daniel	:	Nonlinear Dynamic Response and Reliability Analysis of Drag-dominated Offshore Platforms. 1993.
Passano, Elizabeth	:	Efficient Analysis of Nonlinear Slender Marine Structures. 1994.
Bech, Sidsel M.	:	Experimental and Numerical Determination of Stiffness and Strength of GRP/PVC Sandwich Structures. 1994.

Hovde, Geir Olav	:	Fatigue and Overload Reliability of Offshore Structural Systems, Considering the Effect of Inspection and Repair. 1995.
Wang, Xiaozhi	:	Reliability Analysis of Production Ships with Emphasis on Load Combination and Ultimate Strength. 1995.
Hellan, Øyvind	:	Nonlinear Pushover and Cyclic Analyses in Ultimate Limit State Design and Reassessment of Tubular Steel Offshore Structures. 1995.
Hermundstad, Ole A.	:	Theoretical and Experimental Hydroelastic Analysis of High Speed Vessels. 1995.
Eknes, Monika Løland	:	Escalation Scenarios Initiated by Gas Explosions on Offshore Installations. 1996.
Halse, Karl Henning	:	On Vortex Shedding and Prediction of Vortex-Induced Vibrations of Circular Cylinders. 1997.
Igland, Ragnar Torvanger	:	Reliability Analysis of Pipelines during Laying, Considering Ultimate Strength under Combined Loads. 1997.
Vikestad, Kyrre	:	Multi-Frequency Response of a Cylinder Subjected to Vortex Shedding and Support Motions. 1998
Azadi, Mohammad R. Emami	:	Analysis of Static and Dynamic Pile-Soil-Jacket Behaviour. 1998.